

الجمهورية الجزائرية الديمقراطية الشعبية
REPUBLIQUE ALGERIENNE DEMOCRATIQUE ET POPULAIRE
وزارة التعليم العالي والبحث و العلمي
MINISTERE DE L'ENSEIGNEMENT SUPERIEUR ET DE LA RECHERCHE
SCIENTIFIQUE
جامعة فرحات عباس سطيف - 1 -
UNIVERSITE FERHAT ABBAS SETIF-1-

THESE

Présenté à la Faculté de Technologie
Pour l'Obtention du Diplôme de

DOCTORAT

Domaine : Sciences et Technologie

Filière : Electrotechnique

Option : Commande Electrique

Par

Mr : Fayssal AMRANE.

Contribution à la Commande d'un Système de Conversion Eolien à base de la Génératrice Double Alimentée

Soutenu le: 13/05/2018 devant un Jury composé de:

Pr. RADJELI Hammoud.	Professeur.	Université de Sétif-1.	Président.
Dr. CHAIBA Azeddine.	MCA.	Université de Khenchela.	Directeur de Thèse.
Pr. AOZELLAG Djamel.	Professeur.	Université de Bejaia.	Examineur.
Dr. BENAICHA Samira.	MCA.	Université de Sétif-1.	Examineur.
Dr. BOUAFIA Abdelouahab.	MCA.	Université de Sétif-1.	Examineur.

الجمهورية الجزائرية الديمقراطية الشعبية
PEOPLE'S DEMOCRATIC REPUBLIC OF ALGERIA
وزارة التعليم العالي والبحث و العلمي
MINISTRY OF HIGHER EDUCATION AND SCIENTIFIC RESEARCH
جامعة فرحات عباس سطيف - 1 -
UNIVERSITY FERHAT ABBAS SETIF -1-

THESIS

Submitted at Faculty of Technology
This thesis is submitted in fulfillment of the requirement for the degree

PhD

Field: Sciences and Technology
Specialty: Electrical Engineering
Option: Electrical Control

By

Mr. Fayssal AMRANE

Contribution to the Control of Wind Energy Conversion System based on Doubly Fed Induction Generator

University Ferhat ABBAS of Setif-1 (UFAS-1), ALGERIA
Fayssal AMRANE© 2018.

Dedication

I dedicate this thesis to my

Mother and my Father

To my wife for her patience and encouragement

To my Brother and my Sister

I dedicate this thesis to the memory of my

cousin: KERAGHUEL Yacine (Allah yarahmou)

I dedicate this thesis to the memory of my

best friend MEDJBER Walid (Allah yarahmou)...

To my colleagues and friends in my social and academic life.

30 December 2017.

Mr. AMRANE Fayssal.

Acknowledgement

Above all, I would like to thank The Almighty **God** (*ALLAH le tous puissant*) for the wisdom and perseverance that he has been bestowed upon me during this research work, and indeed, throughout my life.

It has been a pleasure for me to work on this thesis. I hope the reader will find it not only interesting and useful, but also comfortable to read.

First and foremost, I would like to express my sense of gratitude and indebtedness to my supervisor **Mr. CHAIBA Azeddine**, Associate Professor at Department of Industrial Engineering University of Khenchela, Algeria, for his inspiring guidance, encouragement, and untiring effort throughout the course of this work. His timely help and painstaking efforts made it possible to present the work contained in this thesis. I consider myself fortunate to have worked under his guidance during **03 years** (*December 2014- December 2017*).

Also, I express my heartfelt thanks to **Mr. FRANCOIS Bruno**, Full professor at Ecole Centrale de Lille for giving me a great opportunity to do a training long period (*under the Franco-Algerian scholarship program PROFAS b+*: Oct 2016- June. 2017) at Ecole Centrale de Lille, France in L2EP Laboratory (*Laboratoire de d'Electrotechnique et d'Electronique de Puissance*), for his time and for his valuable advices and comments.

I also wish to thank President of jury **Mr. RADJEAI Hammoud** Full Professor at the university of Setif-1 and member of the Automatic Laboratory of Setif LAS, and the members of the jury: **Mr. AOUZELLAG Djamel**, Full Professor at the University of Bejaia, **Mrs. BENAICHA Samira** Associate Professor at University of Setif-1, and member of the Automatic Laboratory of Setif LAS and **Mr. BOUAFIA Abdelouahab** Associate Professor at University of Setif-1 and member of the Power Quality in Electric Networks Laboratory, for serving as my committee members and taking the time to revise my thesis. I am thankful that in the midst of all their activities, they accepted to be members of the reading committee.

Last but not the least, I am grateful to my parents for their prayers, guidance and support throughout my education. Their inspiration and encouragement has been invaluable.

ملخص:

تشكل هذه الأطروحة مساهمة في دراسة السيطرة على نظام إنتاج طاقة الرياح. وهو موضوع مقارنة تقني اقتصادي بين الهياكل المختلفة لمولد الرياح الغير المتزامن ذو التغذية المزدوجة (DFIG) المكرس لنظم تحويل طاقة الرياح. ونظرا للطبيعة المتقلبة للرياح، الأمر الذي يسبب التغير المتكرر للتردد عند مخرج المولد، فمن الضروري ربط الأخير مع الحمل أو الشبكة من خلال محولات ثابتة من أجل تحسين نوعية الطاقة في الجهد والتردد باستخدام تقنيات التحكم المناسبة. في هذا السياق تم اقتراح العديد من وحدات التحكم الغير الخطية المحسنة (IDPC, I/OLDC, FOC) باستخدام محولات AC-DC-AC (عن طريق PWM أو SVM) للسيطرة على الدوار ولتحسين أداء نظام الرياح. استنادا إلى DFIG فيما يتعلق بالتغير المفاجئ لسرعة الرياح واقتراح متغيرات الحالة على طول المحاورين (d و q) لاستخراج القدرة القصوى. تم وضع استراتيجية MPPT في العمل من أجل الحفاظ على طاقة رديه شبه معدومة (معامل القدرة يساوي الوحدة 1). تم تنفيذ اثنين من مناصب الاختبار التجريبية (عن طريق dSPACE1103 و dSPACE1104 على التوالي باستخدام اثنين من المحاكاة التوربينية المختلفة) لضمان الأداء العالي لوحدات التحكم المقترحة تحت اختبارات متانة لتتبع مرجع تيارات الدوار (I_{rd}^* و I_{rq}^*) والسرعة (في كل من سائظ: هايبو وفرط متزامن). تم اقتراح وحدات تحكم قوية وذكية (مثل: PID, IP, MRAC, T1-FLC, T2-FLC, NFC و HCC) للسيطرة على الطاقة النشطة والردية (P_s^* و Q_s^*) صور الخوارزميات غير الخطية (المذكورة سابقا) من DFIG في الوقت الحقيقي مع / بدون استراتيجية MPPT. تم دراسة وضعين للاتصال في المحاكاة والتجريب (واسطة مع شحن معزول ووضع مترابطة مع الشبكة) في الوقت الحقيقي من أجل التحقق من صحة هذه الخوارزميات. وقد تم ربط الدراسة المقارنة التجريبية بين ثلاثة أنواع من المرشحات L, LC, LCL لكل تحت الدوار الحالي الاختلاف (I_{rd}^* و I_{rq}^*), بين الدوار والعاكس (SEMIKUBE) لتصفية التوافقيات من الفولتية الساكنة والدوار، وجعلها في شكل جيبي لضمان مراجع جيدة للسيطرة على السلطة. الاختبارات التجريبية تؤكد متانة وأداء الضوابط المقترحة التي تم علاج العديد من المشاكل من نظام الرياح من حيث؛ وفصل متغيرات الدولة من كلا المحاورين (d و q) والحساسية للتغير البارامتري، وتتبع المراجع، وخطأ القدرة، ووقت الاستجابة والتجاوز.

كلمات مفتاحية:

أنظمة تحويل طاقة الرياح، مولد الغير المتزامن ذو التغذية المزدوجة، تتبع نقطة القدرة القصوى، معالج الإشارات الرقمية.

Abstract:

This thesis constitutes contribution to the study of the control of a wind energy production system. It is the subject of a technical-economic comparison of the different structures of the wind-turbine based doubly fed induction generator (DFIG), dedicated to wind energy conversion systems (WECS's). Due to the fluctuating nature of the wind speed, which causes frequent frequency variation at the output of the generator, it is necessary to link this latter with the load or the grid by static converters in order to improve the voltage energy quality and in frequency using appropriate control techniques. In this context several improved nonlinear controls (IDPC, I/OLDC and FOC) have been proposed using AC-DC-AC converters (via PWM or SVM) to control the DFIG's rotor in order to improve the performance of the DFIG wind system compared to the sudden variation of the wind speed and the coupling of the state variables along the two axes (d and q). To extract the maximum power; the MPPT strategy is achieved to keep the reactive power maintains to zero level (Power factor near to 1). Two experimental test benches were implemented (via dSPACE1103 and dSPACE1104 respectively using two different wind turbine emulators) in order to ensure the high performance of the proposed controls under robustness tests of rotor current reference tracking (I_{rd}^* and I_{rq}^*) and speed (under the two modes: Sub- and Super-synchronous). Robust and intelligent controllers (such as: PID, IP, MRAC, T1-FLC, T2-FLC, NFC and HCC) have been proposed to control the images of active and reactive power (P_s^* and Q_s^*) for nonlinear algorithms (already mentioned above) of the DFIG in real time with/without MPPT strategy. Two modes of connection have been studied in simulation and experimentation (Stand-alone mode and Grid-connection mode) in real time in order to validate these algorithms. An experimental comparison between three types of filters: L, LC and LCL under rotor current variation (I_{rd}^* and I_{rq}^*), have been connected between the DFIG's rotor and the inverter (SEMIKUBE) to filter the harmonics of the stator and rotor voltages waveforms, and render them in sinusoidal form to ensure good references for power control. Experimental tests prove the robustness and high efficiency of the proposed controls in which several wind system problems have been remedied in terms of; decoupling the variables state of the two axes (d and q), sensitivity to the parametric variation, references tracking, power error, response time and overshoot.

Keywords:

Wind Energy Conversion Systems, Doubly Fed Induction Generator, Maximum Power Point Tracking, Digital Signal Processor.

Résumé:

Cette thèse constitue une contribution à l'étude de la commande d'un système de production d'énergie éolienne. Il fait l'objet d'une comparaison technico-économique des différentes structures de l'aérogénérateur asynchrone à double alimentée (GADA), dédiées aux systèmes de conversion d'énergie éolienne. A cause de la nature fluctuante du vent qui provoque une variation fréquente de fréquence à la sortie du générateur, il est nécessaire de lier ce dernier avec la charge ou le réseau par des convertisseurs statiques afin d'améliorer la qualité d'énergie en tension et en fréquence en utilisant des techniques de commande adéquates. Dans ce contexte plusieurs commandes non-linéaires améliorées (IDPC, I/OLDC et FOC) ont été proposées en utilisant des convertisseurs AC-DC-AC (via MLI ou MLI vectorielle) pour contrôler le rotor afin d'améliorer les performances du système éolien à base de la GADA vis-à-vis la variation brusque de la vitesse du vent et du couplage des variables d'état selon les deux axes (d et q). Pour extraire le maximum de puissance du vent; la stratégie MPPT est mise en action afin de garder la puissance réactive maintient la valeur nulle (Facteur de puissance proche de 1). Deux bancs d'essais expérimentaux ont été mis en œuvre (via dSPACE1103 et dSPACE1104 respectivement en utilisant deux émulateurs de turbine différents) afin d'assurer une haute performance des commandes proposés sous des tests de robustesses de suivi de référence de courants rotoriques (I_{rd}^* et I_{rq}^*) et de vitesse (sous les deux modes : Hypo- et Hyper-synchrones). Des régulateurs robustes et intelligents (tels que: PID, IP, MRAC, T1-FLC, T2-FLC, NFC et HCC) ont été proposés afin de contrôler les images de puissances active et réactive (P_s^* et Q_s^*) des algorithmes non linéaires (déjà précités) de la GADA en temps réel avec/sans la stratégie MPPT. Deux modes de connexion ont été étudiés en simulation et expérimentation (mode à Charge isolée et mode Interconnecté au réseau) en temps réel afin de valider ces algorithmes. Une étude comparative expérimentale entre trois type de filtres : L, LC et LCL sous variation de courant rotoriques (I_{rd}^* et I_{rq}^*), ont été connectés entre le rotor et l'onduleur (SEMIKUBE) ont pour objectif de filtrer les harmoniques des tensions statoriques et rotoriques, et les rendre sous forme sinusoïdale afin d'assurer de bon références pour le contrôle de puissances. Les tests expérimentaux affirment la robustesse et la performance des commandes proposées dont plusieurs problèmes du système éolien ont été remédiés en termes de; découplage des variables d'état des deux axes (d et q), sensibilité par rapport à la variation paramétrique, le suivie des références, l'erreur de puissance, le temps de réponse et le dépassement.

Mots clés:

Systèmes de conversion d'énergie éolienne, Générateur asynchrone à double alimentation, Suivi de point de puissance maximale, Processeur de signal numérique.

Table of contents:

Dedication	I
Acknowledgments	II
ملخص -Abstract -Résumé-	III
Table of Contents.....	IV
List of Figures	IX
List of Tables	XIV
List of Abreviation	XV
List of Acronymes	XVI
Chapter 0: General Introduction.....	01
0.1 General Introduction.....	02
0.2 The Main Contributions	03
0.3 Thesis Organization	06
0.4 Thesis Limitations	07
0.5 Scientific Production during the PhD (<i>Conference Papers, Chapter in Book and Journal Papres</i>).....	08
0.5.1 <i>International Conference Papers presented in Algeria, France and Bulgaria (2015, 2016 and 2017)</i>	08
0.5.2 <i>Chapter in Book (2017)</i>	09
0.5.3 <i>Journal Papers (2016)</i>	09
0.6 References.....	09
Chapter 1: State of the Art: An Overview of Wind Energy Conversion Systems (WECS) based on DFIG.....	12
1.1 Development of Wind Power Generation.....	13
1.2 Wind Turbine Concepts.....	14
1.2.1 <i>Fixed Speed Wind Turbines (WT Type A)</i>	14
1.2.2 <i>Partial Variable Speed Wind Turbine with Variable Rotor Resistance (WT Type B)</i>	14
1.2.3 <i>Variable Speed Wind Turbine with Partial Scale Power Converter (WT Type C)</i>	14
A- <i>Advantages of the DFIG-based WT generator scheme</i>	14
B- <i>Disadvantages of the DFIG-based wind turbine-generator system</i>	15
1.2.4 <i>Variable Speed Wind Turbine with Full Scale Power Converter (WT Type D)</i>	15
1.3 Control Structure of WTs.....	15
1.4 Literature Survey	16
1.4.1 <i>Modelling of a WTGS</i>	16
A- <i>DFIG modelling</i>	16
1.4.2 <i>Control Strategies for a WTGS</i>	17
A- <i>Maximum power point tracking control</i>	17
A.1 <i>Intelligent control</i>	17
A.2 <i>Other control strategies</i>	17
B- <i>DFIG control</i>	17
B.1 <i>Field oriented control</i>	18
B.2 <i>Direct torque/power control (DTC/DPC)</i>	18
B.3 <i>Adaptive control (MRAS observer/MRAC controller)</i>	18
B.4 <i>Adaptive Disturbance Rejection Control (ADRC)</i>	19
B.5 <i>Sliding mode control (SMC)</i>	19
B.6 <i>Backstepping control (BSC)</i>	19
B.7 <i>Predictive Direct power control (PDPC)</i>	20
B.8 <i>Input/output Linearizing control</i>	20
1.5 References.....	21
Chapter 2: Indirect Power Control (IDPC) of DFIG using Classical Controllers under MPPT Strategy.....	25
2.1 Introduction	26

2.2 Mathematical model of DFIG	26
2.3 Conventional Indirect Power Control (IDPC) of DFIG	27
2.3.1 Relationship between rotor voltages and rotor currents (generally form)	28
2.3.2 Relationship between stator power and rotor currents	29
2.3.3 Relationship between rotor voltages and rotor currents (detailed form)	29
2.3.4 Synthesis of the Proportional-Integral (PI) regulator	30
2.4 Wind turbine mathematical model	30
2.4.1 Maximum Power Point Tracking (MPPT) strategy	31
2.5 Grid Side Converter (GSC) and DC-link voltage control	33
2.6 Rotor Side Converter (RSC).....	34
2.6.1 Space Vector Modulation (SVM)	35
2.6.2 LC Filter	38
2.7 Operating principle of DFIG	40
2.8 Proposed IDPC based on PID Controllers	42
2.9 Simulation results	43
2.9.1 Conventional IDPC based on PI controllers	44
2.9.2 Proposed IDPC based on PID controllers	49
2.9.3 Power Factor (PF) tests for three (03) modes	54
2.10 Conclusion.....	55
2.11 References.....	55

**Chapter 3: A Novel IDPC using Adaptive, Robust and Intelligent
Controllers..... 58**

3.1 Introduction	59
3.2 Drawbacks and performances limitation of conventional IDPC.....	60
3.3 Proposed Power control based on Model Reference Adaptive Control (MRAC)	61
3.4 Proposed Power control based on Type-1 Fuzzy Logic Control (T1-FLC).....	62
3.4.1 Reasons for Choosing Fuzzy Logic.....	62
3.4.2 Fuzzy Set Theory and Fuzzy Set Operations.....	62
3.4.3 Membership Functions	62
3.4.4 Mamdani Fuzzy Inference Method	63
A. Fuzzifier	63
B. Knowledge Base	63
C. Inference Engine	63
D. Defuzzifier	63
3.4.5 Membership Functions and Rule Base	64
3.5 Proposed Power control based on Type-2 Fuzzy Logic Control (T2-FLC).....	65
3.5.1 Overview of Type-2 Fuzzy Logic Controller Toolbox	66
3.5.2 Design of Type-2 Fuzzy Logic Controller	66
3.6 Proposed Power control based on Neuro-Fuzzy Control (NFC).....	68
3.6.1 Layer I: Input layer	68
3.6.2 Layer II: membership layer.....	68
3.6.3 Layer III: rule layer	69
3.6.4 Layer IV: output layer.....	69
3.7 Simulation Results.....	70
3.7.1 Topology 1: Improved IDPC (based on MRAC controllers)	71
3.7.2 Topology 2: Improved IDPC (based on T1-FLC controllers)	76
3.7.3 Topology 3: Improved IDPC (based on T2-FLC controllers)	81
3.7.4 Topology 4: Improved IDPC (based on NFC controllers)	86
3.8 Wind-system performances recapitulation under six (06) proposed IDPC algorithms	91
3.9 Conclusion.....	91
3.10 References.....	92

**Chapter 4: A New Input/output Linearizing and Decoupling Control
(I/OLDC) of DFIG in WECS using an Adaptive Control**

through Multi-Level Converters.....	94
4.1 Introduction	95
4.2 Classical Input/output Linearizing and Decoupling Control (<i>I/OLDC</i>) based on PI controller.....	95
4.2.1 <i>General Concept of The Input-Output Linearizing Control</i>	95
4.2.2 <i>Control of rotor side converter</i>	96
4.3 Proposed I/OLDC based on MRAC under three modes using MPPT Strategy	98
4.3.1 <i>Model Reference Adaptive control (MRAC) strategy</i>	98
4.3.2 <i>Back-to-back two Level converter using three (03) modes</i>	99
4.3.3 <i>Back-to-back Three Level NPC converter using three (03) modes</i>	99
A. <i>NPC (Neutral-Point Clamped) Topology</i>	99
B. <i>Modeling structure of one inverter arm</i>	100
C. <i>Comparative simulation study of two level and three level inverter under RL-load</i>	101
4.4 Simulation Results.....	101
4.4.1 <i>Back-to-back two Level converter using PI controller</i>	103
4.4.2 <i>Back-to-back two Level converter using MRAC controller</i>	108
4.4.3 <i>Back-to-back three Level Inverter (NPC) based on MRAC controller</i>	113
4.5 The high power evaluation tests (<i>using improved I/OLDC with 2LC and 3LC</i>).....	118
4.6 Decoupling parameter tests (<i>using all the proposed control: chapter 2, chapter 3 and chapter 4</i>).....	118
4.7 Conclusion.....	120
4.8 References.....	120

Chapter 5: Experimental Design of IDPC of DFIG for Variable Speed Wind-Turbine in Isolated Mode with LCL-Filter. 121

5.1 Introduction	122
5.2 Proposed control (<i>Stand-alone topology</i>)	123
5.3 Indirect Power Control (<i>IDPC</i>) based on Integral-Proportional (<i>IP</i>) regulators	123
5.3.1 <i>DFIG control (Rotor Side Converter-RSC)</i>	123
5.3.2 <i>Integral Proportional (IP) regulators</i>	124
5.3.3 <i>Emulator turbine control (Induction motor torque and flux control)</i>	126
5.3.4 <i>Hardware implementation</i>	127
5.4 Experimental studies using a new inverter named SEMIKUBE (<i>100kW, version 2016</i>).....	128
5.4.1 <i>SEMIKUBE components description</i>	128
A. <i>PWM input signals</i>	128
B. <i>Dead time generation</i>	128
C. <i>LED Diagnostic</i>	129
5.4.2 <i>Isolation card</i>	129
5.4.3 <i>SEMIKUBE with isolation card</i>	130
5.4.4 <i>dSPACE1103 and Control Desk software</i>	130
A. <i>PWM Outputs</i>	130
B. <i>ADC Inputs</i>	130
C. <i>DAC Outputs</i>	130
D. <i>Master PPC Digital I/Os</i>	130
5.4.5 <i>SEMIKUBE with R-L load under open loop using dSPACE1103 card</i>	131
5.5 Impact of Filters in RSC using the Fast Fourier Transform (<i>FFT</i>).....	133
5.5.1 <i>Mode I: L Filter</i>	134
5.5.2 <i>Mode II: LC Filter</i>	135
5.5.3 <i>Mode III: LCL Filter</i>	136
5.6 Robustness tests of proposed control (<i>under Trapezoid, Step form of rotor d-q axes rotor currents</i>)	139
5.6.1 <i>Topology 1 : Stator not connected to R-L load</i>	139
A. <i>Trapezoid form</i>	140
B. <i>Step form</i>	141
5.6.2 <i>Topology 2 : Stator under load (connected to R-L load)</i>	141
A. <i>Trapezoid form</i>	142
B. <i>Step form</i>	142
5.7 Experimental results of proposed control under Sub & Super-synchronous operations	143

5.7.1 Case 1 : Nr = 0 (rpm).....	144
5.7.2 Case 2 : Nr = 500 (rpm).....	146
5.7.3 Case 3 : Nr = 1000 (rpm).....	147
5.7.4 Case 4 : Nr = 1500 (rpm).....	148
5.7.5 Case 5 : Nr = 1700 (rpm).....	149
5.8 Conclusion.....	149
5.9 References.....	150

Chapter 6: Design and Real Time Implementation of FOC based on HCC in WECS Variable Speed-DFIG using dSPACE1104 for: Grid-connection and Stand-alone Modes..... 152

6.1 Introduction	153
6.2 Field Oriented Control (FOC)	155
6.3 Hysteresis Current Controllers (HCC) Topology	155
6.4 Experimental Studies using a SEMIKRON Inverter (60 kW, 2008 version)	156
6.4.1 SEMIKRON Components Description.....	157
A. Diode Bridge	157
B. DC-link Capacitors	157
C. IGBT Modules.....	157
D. IGBT Drivers.....	157
E. Snubber Capacitors	157
6.4.2 Isolation card (realized in LAS Laboratory).....	159
6.4.3 dSPACE1104	159
6.4.4 SEMIKRON with Isolation Card	159
A. PWM Outputs.....	159
B. ADC Inputs	159
C. DAC Outputs	159
D. Master PPC Digital I/Os.....	159
6.5 Proposed control strategies.....	160
6.5.1 Mode I: Stand-alone topology	160
6.5.2 Mode II: Grid-connection topology	161
A. Synchronous Reference Frame Phase Locked Loop (SRF-PLL).....	162
B. Selection of witching frequency.....	163
6.6 Hardware implementation (Stand-alone and Grid-connection Topologies)	163
6.7 Experimental results	164
6.7.1 Stand-alone mode	164
A. Rotor side converter (Stand-alone topology).....	164
B. Stator side converter (Stand-alone topology)	164
6.7.2 Grid-connection mode	166
A. Grid side converter (Grid-connection topology)	166
B. Rotor side converter (Grid-connection topology)	167
6.8 Conclusion.....	170
6.9 References.....	170

Chapter 7: General Conclusion and Future Works 173

7.1 General Conclusion.....	173
7.2 Future Works	174

Appendix : A, B and C..... 175

Appendix.A. WECS Parameters (Chapters n°: 2, 3, 4, 5 and 6) + Real time implementation (PWM and SVM Strategies) + Parameters' identification topology + List of Wind Turbine Manufacturers.....	176
A.1 Simulation part.....	176
A.2 Experimental part.....	176
A.3 Real time implementation.....	176

A.4 Parameters' identification topology of the Experimental part (chapter n°5 and Chapter n°6)	178
Appendix.B. Isolation cards of dSPACE1103 and dSPACE1104.....	180
B.1 dSPACE1103 Isolation Card (L2EP Laboratory/ France)	180
B.2 dSPACE1104 Isolation Card (LAS Laboratory, UFASétif-1/Algeria)	181
Appendix.C. DFIG and Emulator turbine using in chapter n°5 and Chapter n°6.....	182
C.1 Wind Energy conversion system used in Chapter n°5 (L2EP Laboratory).....	182
C.2 Wind Energy conversion system used in Chapter n°6 (LAS Laboratory).	182
C.3 The gains's values of the proposed controllers (chapters n°; 2, 3, 4, 5 and 6).	182
C.4 Neutral Point Clamped (NPC) realized in L2EP Laboratory.	183

List of Figures:

Figures of Chapter-1 :

Figure.1.1	Global cumulative wind power capacity from 2001 to 2020.....	13
Figure.1.2	Evolution of WT size and the power electronics seen from 1980 to 2020 (estimated). Orange circle: means the power coverage by power electronics, D: means diameter of the rotor.	13
Figure.1.3	Power conversion stages in a typical WTS.	14
Figure.1.4	A: Variable-speed wind turbine with partial-scale power converter and a DFIG and B: Variable-speed wind turbine with full-scale power converter.	15
Figure.1.5	Control structure for power electronics converter in WTS. (v_{dc} : dc-link voltage, I_{rotor} : rotor current, ω_{rotor} : rotational speed of rotor, θ : pitch angle of rotor blade, X_{filter} : filter impedance, I_{grid} : grid current, V_{grid} : grid voltage, P_{meas} : measured active power, Q_{meas} : measured reactive power, PCC: point of common coupling).....	16

Figures of Chapter-2 :

Figure.2.1	Schematic diagram of wind-turbine DFIG based on conventional indirect power control (IDPC).	26
Figure.2.2	Stator and rotor flux vectors in the synchronous d-q frame.	28
Figure.2.3	The DFIG simplified power model.	30
Figure.2.4	DFIG's conventional indirect power control.	30
Figure.2.5	Closed loop transfer function topology based on PI controller.....	30
Figure.2.6	Schematic block of wind turbine.	31
Figure.2.7	Theoretical maximum power coefficient ($C_p = (16/27) \approx 0.59$).	31
Figure.2.8	MPPT control strategy without wind speed measurement.....	31
Figure.2.9	C_p under different pitch angles (B°).	32
Figure.2.10	3D Power coefficient versus Tip speed ratio (TSR) and Pitch angle degree (B°).	32
Figure.2.11	Simulation results of MPPT strategy: (C_p versus λ "or TSR", Wind speed versus time, C_p versus time) Taero, Tgearbox and T_{em} using two wind speed profiles	32
Figure.2.12	Main circuit topology of a back-to-back PWM converter for DFIG.....	32
Figure.2.13	GSC configuration.....	33
Figure.2.14	Grid side converter topology (DC-link voltage control).	34
Figure.2.15	RSC configuration (three-phase voltage source PWM Inverter+ DFIG).	34
Figure.2.16	Rotor side converter topology (of Indirect Power Control DFIG).....	35
Figure.2.17	The eight inverter voltage vectors (V_0 to V_7).....	36
Figure.2.18	Voltage space vector and its components in (d, q).	37
Figure.2.19	The eight (08) basic switching vectors and sectors.	37
Figure.2.20	Reference vector as a combination of adjacent vectors at sector 1	37
Figure.2.21	Space vector PWM switching patterns at each sector	37
Figure.2.22	Rotor side converter topology with LC-Filter (of Indirect Power Control DFIG).....	39
Figure.2.23	Operating modes of a DFIM: Mode 1 (Sub-synchronous motoring mode), Mode 2 (Super-synchronous motoring mode), Mode 3 (Sub-synchronous generating mode), and Mode 4 (Super-synchronous generating mode).	41
Figure.2.24	DFIM's torque/speed characteristic in 04 quadrants.....	41
Figure.2.25	Power-flow diagram of a DFIM for (1): Sub-synchronous motoring mode, (2): Super-synchronous motoring mode, (3): Sub-synchronous generating mode, and (4): Super-synchronous generating mode	41
Figure.2.26	Proportional-Integral-Derivative controller topology.....	42
Figure.2.27	Proposed IDPC (based on PID) of DFIG.....	42
Figure.2.28	The proposed wind turbine-DFIG algorithm (based on PID) using 3 MPPT modes	43
Figure.2.29	Simulation results of conventional control based on PI using three (03) modes; (a): stator active and reactive powers, (b): stator active power, (c): stator reactive power, (d): stator direct and transversal currents, (e): rotor direct and transversal currents, (f): stator active and reactive power error, (g): rotor direct and transversal fluxes, (h): stator currents, (i): rotor currents, (j): power factor	46
Figure.2.30	Simulations results of tow modes MPPT strategy for conventional control based on PI; (a): stator active and reactive powers, (b): stator active power using different B° pitch angles, (c): stator reactive power using different pitch angles B° , (d): wind speed, (e): generator speed, (f): power coefficient, (g): slip, (h): rotor currents.....	47
Figure.2.31	Robustness tests of conventional control based on PI using three (03) modes; (a): stator active powers, (b): stator reactive powers	48

Figure.2.32	Simulation results of conventional control based on PID using three (03) modes; (a): stator active and reactive powers, (b): stator active power, (c): stator reactive power, (d): stator direct and transversal currents, (e): rotor direct and transversal currents, (f): stator active and reactive power error, (g): rotor direct and transversal fluxes, (h): stator currents, (i): rotor currents, (j): power factor.....	51
Figure.2.33	Simulations results of tow modes MPPT strategy for proposed control based on PID; (a): stator active and reactive powers, (b): stator active power using different B° pitch angles, (c): stator reactive power using different pitch angles B° , (d): wind speed, (e): generator speed, (f): power coefficient, (g): slip, (h): rotor currents... Robustness tests of proposed control based on PID using three (03) modes; (a): stator active powers, (b): stator reactive powers	52
Figure.2.34	53
Figure.2.35	Simulations results of grid voltage' and stator currents behavior under power profiles' and wind speed variation	54

Figures of Chapter-3 :

Figure.3.1	Schematic diagram of wind-turbine DFIG based on novel indirect power control (IDPC).	59
Figure.3.2	Global wind-turbine system scheme based on fourths proposed controllers.....	60
Figure.3.3	Proposed MRAC to control I_{rd} and I_{rq} respectively	61
Figure.3.4	Block diagram of Mamdani Type-1 fuzzy logic inference system..	63
Figure.3.5	Global Memberships structure (2 inputs and 1 output).	64
Figure.3.6	Schematic structure of Type-1 fuzzy logic controller under Matlab/Simulink.....	64
Figure.3.7	Simulation results of the membership functions (a and b: 2 inputs, c: 1 output and d: the fuzzy logic surface). ..	64
Figure.3.8	FIS editor A: type-1 fuzzy logic toolbox, B: type-2 fuzzy logic toolbox.	66
Figure.3.9	Type-2 fuzzy logic interface; A: Membership function editor of Type-2 fuzzy logic toolbox, B: Rule editor of type-2 fuzzy logic toolbox, C: 2 Inputs-1output Membership function editor of type-2 fuzzy logic Toolbox, D: Surface viewer of type-2 fuzzy logic toolbox.....	66
Figure.3.10	Block diagram of Mamdani Type-2 fuzzy logic inference system.	67
Figure.3.11	(a) The FOU for a type-2 fuzzy set, (b) The secondary membership functions.....	67
Figure.3.12	Membership functions (A: inputs and B: output).	68
Figure.3.13	Schematic structure of Type-2 fuzzy logic controller under Matlab®/Simulink.....	68
Figure.3.14	Block diagram of the neuro-fuzzy controller under Matlab®/Simulink..	69
Figure.3.15	Simulation results of training error (0.05) using 1000 epochs.....	69
Figure.3.16	Schematic diagram of the neuro-fuzzy network.....	69
Figure.3.17	Simulations results of proposed control based on MRAC using three (03) modes; a: stator active and reactive powers, b: stator active power, c: stator reactive power, d: stator direct and transversal currents, e: rotor direct and transversal currents, f: stator active and reactive power error, g: rotor direct and transversal fluxes, h: stator currents, i: rotor currents, j: power factor.....	73
Figure.3.18	Simulations results of two MPPT strategy modes of proposed control based on MRAC; (a): stator active and reactive powers, (b): stator active power using different B° pitch angles, (c): stator reactive power using different pitch angles B° , (d): wind speed, (e): generator speed, (f): power coefficient, (g): slip, (h): rotor currents.	74
Figure.3.19	Robustness tests of proposed control based on MRAC using three (03) modes; a: stator active powers, b: stator reactive powers.....	75
Figure.3.20	Simulations results of proposed control based on T1-FLC using three (03) modes; a: stator active and reactive powers, b: stator active power, c: stator reactive power, d: stator direct and transversal currents, e: rotor direct and transversal currents, f: stator active and reactive power error, g: rotor direct and transversal fluxes, h: stator currents, i: rotor currents, j: power factor.	78
Figure.3.21	Simulations results of tow MPPT strategy modes of proposed control based on T1-FLC; (a): stator active and reactive powers, (b): stator active power using different B° pitch angles, (c): stator reactive power using different pitch angles B° , (d): wind speed, (e): generator speed, (f): power coefficient, (g): slip, (h): rotor currents.	79
Figure.3.22	Robustness tests of proposed control based on T1-FLC using three (03) modes; a: stator active powers, b: stator reactive power.....	80
Figure.3.23	Simulations results of proposed control based on T2-FLC using three (03) modes; a: stator active and reactive powers, b: stator active power, c: stator reactive power, d: stator direct and transversal currents, e: rotor direct and transversal currents, f: stator active and reactive power error, g: rotor direct and transversal fluxes, h: stator currents, i: rotor currents, j: power factor.	83
Figure.3.24	Simulations results of tow MPPT strategy modes of proposed control based on T2-FLC; (a): stator active and reactive powers, (b): stator active power using different B° pitch angles, (c): stator reactive power using different pitch angles B° , (d): wind speed, (e): generator speed, (f): power coefficient, (g): slip, (h): rotor	

	currents.	84
Figure.3.25	Robustness tests of proposed control based on T2-FLC using three (03) modes; a: stator active powers, b: stator reactive powers.	85
Figure.3.26	Simulations results of proposed control based on NFC using three (03) modes; a: stator active and reactive powers, b: stator active power, c: stator reactive power, d: stator direct and transversal currents, e: rotor direct and transversal currents, f: stator active and reactive power error, g: rotor direct and transversal fluxes, h: stator currents, i: rotor currents, j: power factor.	88
Figure.3.27	Simulations results of tow MPPT strategy modes of proposed control based on NFC; (a): stator active and reactive powers, (b): stator active power using different B° pitch angles, (c): stator reactive power using different pitch angles B° , (d): wind speed, (e): generator speed, (f): power coefficient, (g): slip, (h): rotor currents.	89
Figure.3.28	Robustness tests of proposed control based on NFC using three (03) modes; a: stator active power, b: stator active power.	90

Figures of Chapter-4 :

Figure.4.1	The DFIG power model.	95
Figure.4.2	The doubly fed induction generator simplified model.	96
Figure.4.3	Schematic diagram of input-output linearizing control	96
Figure.4.4	Schematic diagram of classical input/output linearizing control based on PI controllers.....	98
Figure.4.5	Model reference adaptive control scheme	98
Figure.4.6	Schematic diagram of new input/output linearizing control.	98
Figure.4.7	Schematic diagram of the proposed I/OLDC based on two level back-to-back converter.....	100
Figure.4.8	NPC inverter arm and AC waveform.....	100
Figure.4.9	Simulation results for load current and load voltage fed by two levels inverter (left) and three Level Inverter (right) using PWM strategy.....	102
Figure.4.10	Schematic diagram of the proposed I/OLDC based on NPC back-to-back converter.....	102
Figure.4.11	Simulations results for proposed control (I/OLDC based on PI with PWM two levels) under three modes; a: Stator active and reactive powers, b: stator active power, c: stator reactive power, d: stator direct and transversal currents, e: rotor direct and transversal currents, f: stator active and reactive power error, g: rotor direct and transversal fluxes, h: stator currents, i: rotor currents, j: power factor	105
Figure.4.12	Simulations results of tow modes MPPT strategy for proposed control (I/OLDC based on PI with PWM two levels) under three modes; (a): stator active and reactive powers, (b): Stator active power using different B° pitch angles, (c): stator reactive power using different pitch angles B° , (d): wind speed, (e): the generator speed, (f): power coefficient, (g): the slip, (h): the rotor currents.	106
Figure.4.13	Robustness tests of proposed control (I/OLDC based on PI with PWM two levels) under three Modes; a: stator active powers, b: stator active powers.....	108
Figure.4.14	Simulations results for proposed control (I/OLDC based on MRAC with PWM two levels) under three (03) modes; a: Stator active and reactive powers, b: stator active power, c: stator reactive power, d: stator direct and transversal currents, e: rotor direct and transversal currents, f: stator active and reactive power error, g: rotor direct and transversal fluxes, h: stator currents, i: rotor currents, j: power factor.	110
Figure.4.15	Simulations results of tow modes MPPT strategy for proposed control (I/OLDC based on MRAC with PWM two levels) under three (03) modes; (a): stator active and reactive powers, (b): Stator active power using different B° pitch angles, (c): stator reactive power using different pitch angles B° , (d): wind speed, (e): the generator speed, (f): power coefficient, (g): the slip, (h): the rotor currents	111
Figure.4.16	Robustness tests of proposed control (I/OLDC based on MRAC with PWM two levels) under three Modes; a: stator active powers, b: stator active powers.....	113
Figure.4.17	Simulations results for proposed control (I/OLDC based on MRAC with PWM three levels inverter/NPC) under three modes; a: stator active and reactive powers, b: stator active power, c: stator reactive power, d: stator direct and transversal currents, e: rotor direct and transversal currents, f: stator active and reactive power error, g: rotor direct and transversal fluxes, h: stator currents, i: rotor currents, j: power factor.....	115
Figure.4.18	Simulations results of tow modes MPPT strategy for proposed control (I/OLDC based on MRAC with PWM three levels inverter/NPC); (a): stator active and reactive powers, (b): stator active power using different B° pitch angles, (c): stator reactive power using different pitch angles B° , (d): wind speed, (e): the generator speed, (f): power coefficient, (g): the slip, (h): the rotor currents	116
Figure.4.19	Robustness tests of proposed control (I/OLDC based on MRAC with PWM three levels inverter/NPC) under three modes; a: stator active powers, b: stator active powers.....	118
Figure.4.20	Simulations results of the high power' evaluation tests (using improved I/OLDC with 2LC and 3LC).....	119
Figure.4.21	Simulations results of decoupling terms (between active and reactive power) in each topology.....	119

Figures of Chapter-5 :

Figure.5.1	<i>Schematic diagram of DFIG using indirect power control in stand-alone mode</i>	122
Figure.5.2	<i>Proposed control scheme based on DFIG power control in stand-alone mode</i>	123
Figure.5.3	<i>Schematic diagram of IP and PI regulators</i>	124
Figure.5.4	<i>System controlled by IP regulator (according to d and q axes)</i>	125
Figure.5.5	<i>(a and b): Stator active and reactive powers controlled by PI and IP controllers respectively</i>	125
Figure.5.6	<i>Induction motor torque and rotor flux control system</i>	126
Figure.5.7	<i>Hardware connexion of emulator wind turbine and dSPACE1103 panel via incremental sensor connector</i>	127
Figure.5.8	<i>WECS hardware implementation :(emulator turbine + DFIG + inductances (L-Filter))</i>	127
Figure.5.9	<i>Experimental test bench developed in L2EP Laboratory (Ecole Centrale de Lille/France)</i>	128
Figure.5.10	<i>Isolation card for the dSPACE1104 realizing in L2EP Laboratory (Ecole Centrale de Lille)</i>	129
Figure.5.11	<i>Inverter type SEMIKUBE® with isolation card developed in L2EP laboratory (Ecole Centrale de Lille), A: Inverter + Isolation card, B: Isolation card is connected, C: The isolation card components and D: Printed circuit board (copper side)</i>	129
Figure.5.12	<i>dSPACE1103 panel (to the left) and dSPACE1103 Card (to the right)</i>	130
Figure.5.13	<i>ControlDesk interface (for the proposed control)</i>	131
Figure.5.14	<i>a: Open loop hardware scheme using SEMIKUBE with R-L Load (Stand-alone) and b: PWM signals for three SEMIKUBE Legs</i>	131
Figure.5.15	<i>The R-L load used in Semikube performance tests</i>	132
Figure.5.16	<i>Switching signals: high (Sa, Sb, Sc) and low (Sa', Sb', Sc')</i>	132
Figure.5.17	<i>Dead time between the switching signals for each leg</i>	132
Figure.5.18	<i>Current and voltage waveforms of RL-load under Vdc= 80 (V)</i>	133
Figure.5.19	<i>Single Phase LCL Filter Schematic</i>	133
Figure.5.20	<i>Proposed Filters (L, LC and LCL) topologies</i>	133
Figure.5.21	<i>Experimental results of the rotor' and stator' voltages in transient and steady states under d-q axes rotor currents variation using L-Filter</i>	134
Figure.5.22	<i>Experimental results of the rotor' and stator' voltages FFT in transient and steady states under d-q axes rotor currents variation using L-Filter</i>	135
Figure.5.23	<i>Experimental results of the rotor and stator voltages FFT in transient and steady states under d-q axes rotor currents variation using LC-Filter</i>	136
Figure.5.24	<i>LCL's elements filter with their values</i>	137
Figure.5.25	<i>Experimental results of the rotor and stator voltages FFT in transient and steady states under d-q axes rotor currents variation using LCL-Filter</i>	139
Figure.5.26	<i>SEMIKUBE-LCL-DFIG topology without load</i>	140
Figure.5.27	<i>Robustness tests (rotor currents variation: Ir_meas(A) and Irq*(A)) in steady and transient states without RL-load</i>	140
Figure.5.28	<i>Robustness tests under Trapezoid form (rotor currents variation: Ird*(A), Ird_meas (A) and Irq*(A), Irq_meas (A)) without RL-load</i>	140
Figure.5.29	<i>Robustness tests under Step form (rotor currents variation: Ird*(A), Ird_meas (A) and Irq*(A), Irq_meas (A)) without RL-load</i>	141
Figure.5.30	<i>SEMIKUBE-LCL-DFIG topology with R-L load</i>	141
Figure.5.31	<i>Robustness tests under trapezoid form (rotor currents variation: Ird*(A), Ird_meas (A) and Irq*(A), Irq_meas (A)) with RL-load</i>	142
Figure.5.32	<i>Robustness tests under Step form (rotor currents variation: Ird*(A) and Ird_meas (A) and Irq*(A), Irq_meas (A)) with RL-load</i>	142
Figure.5.33	<i>a and b: Measured rotor current variation and slip angle, c and d: Rotor speed variation and rotor current measured</i>	143
Figure.5.34	<i>DFIG's operating modes (Motor/Generator) using Doubly Fed Induction Machine (DFIM) and Torque/speed characteristic</i>	143
Figure.5.35	<i>Rotor speed tests: 0 rpm, 1500 rpm, 1700 rpm and 200 rpm (Sub and Super synchronous modes) with slip' and grid angle</i>	144
Figure.5.36	<i>Rotor and stator voltages behavior under currents variation (Ird*(A) and Irq*(A)) at 0 (rpm) with/without load</i>	145
Figure.5.37	<i>Rotor currents variation (Ird*(A) and Irq*(A)) under 500 (rpm) with RL-load</i>	147
Figure.5.38	<i>Rotor currents variation (Ird*(A) and Irq*(A)) under 1000 (rpm) with RL-load</i>	147
Figure.5.39	<i>Rotor currents variation (Ird*(A) and Irq*(A)) under 1500 (rpm) with RL-load</i>	148
Figure.5.40	<i>Rotor currents variation (Ird*(A) and Irq*(A)) under 1700 (rpm) with RL-load</i>	149

Figures of Chapter-6 :

Figure.6.1	<i>Schematic diagram of wind energy conversion system based on DFIG using field oriented control</i>	153
Figure.6.2	<i>Proposed FOC-HCC for wind turbine-DFIG for both modes: stand-alone and grid-connection.....</i>	154
Figure.6.3	<i>Rotor flux vector in the synchronous d-q frame.....</i>	156
Figure.6.4	<i>Hysteresis current control structure for two-level inverter</i>	156
Figure.6.5	<i>Hysteresis band validation using four (04) cases.....</i>	156
Figure.6.6	<i>Isolation card for the dSPACE1104 realizing in LAS laboratory (UFASétif-1).....</i>	159
Figure.6.7	<i>Inverter type SEMIKRON® with isolation card developed in LAS laboratory (UFASétif-1), A: Inverter + Isolation card, B: Isolation card not connected, C: The isolation card components and D: Printed circuit board (copper side).....</i>	159
Figure.6.8	<i>Deference between dSPACE1103 panel and dSPACE1104 panel</i>	159
Figure.6.9	<i>WECS Hardware implementation (Emulator turbine + DFIG).....</i>	160
Figure.6.10	<i>Detailed scheme of proposed stand-alone of FOC-HCC based on DFIG.....</i>	161
Figure.6.11	<i>Stator side converter of stand-alone topology</i>	161
Figure.6.12	<i>Detailed scheme of proposed grid-connection of FOC-HCC based on DFIG.</i>	162
Figure.6.13	<i>PLL structure scheme; a: Scheme of slip angle calculation and b: Hardware PLL implementation.....</i>	162
Figure.6.14	<i>PLL block implementation in Matlab/Simulink®.....</i>	163
Figure.6.15	<i>Hardware connection of proposed FOC-HCC for stand-alone topology</i>	163
Figure.6.16	<i>Hardware connection of proposed FOC-HCC for grid-connection topology.</i>	164
Figure.6.17	<i>Experiental test bench developed in LAS Laboratory (UFASétif/Algeria) 1: PC, 2: Speed sensor, 3: Power analyzer, 4: Oscilloscopes, 5: inverter (SEMIKRON), 6: Current sensors, 7: Voltage sensors, 8: dSPACE1104, 9: DCM, 10: DFIG, 11: Grid, 12: Resistive load (Resistance), 13: Capacitor, 14: DC variable supply power) ..</i>	164
Figure.6.18	<i>Steady and transient states of the RSC parameters under the variation of the speed and rotor direct and quadrature respectively (stand-alone mode).</i>	165
Figure.6.19	<i>The performances of SSC under rotor direct and quadrature currents variation in both steady and transient states (stand-alone mode).....</i>	166
Figure.6.20	<i>The performances of GSC under rotor direct and quadrature currents variation in both steady and transient states (grid-connection mode).....</i>	167
Figure.6.21	<i>Sub-synchronous mode under rotor speed variation (grid-connection mode).....</i>	168
Figure.6.22	<i>Robustness tests by variation of reference quadrature current to ensure the unity power factor (grid-connection mode).....</i>	169

List of Tables:

Tables of Chapter-2 :

Table.2.1	<i>Switching vectors, phase voltages and output line to line voltages</i>	36
Table.2.2	<i>Switching time calculation at each sector</i>	37
Table.2.3	<i>The proposed profiles of the active and reactive power references.</i>	45
Table.2.4	<i>Recapitulation results for classical control (based on PI).</i>	48
Table.2.5	<i>Recapitulation results for the proposed control (based on PID).....</i>	53

Tables of Chapter-3 :

Table.3.1	<i>Type-1 fuzzy logic inferences.....</i>	65
Table.3.2	<i>Type-2 fuzzy logic inferences.....</i>	67
Table.3.3	<i>The parameters of the proposed Neuro-fuzzy controller.</i>	68
Table.3.4	<i>The proposed profiles of the active and reactive power references.</i>	71
Table.3.5	<i>Performances results for proposed control based on MRAC using back-to-back SVM converter.....</i>	75
Table.3.6	<i>Performances results for proposed control based on T1-FLC using back-to-back SVM converter.....</i>	80
Table.3.7	<i>Performances results for proposed control based on T2-FLC using back-to-back SVM converter.....</i>	85
Table.3.8	<i>Performances results for proposed control based on NFC using back-to-back SVM converter.....</i>	90
Table.3.9	<i>Wind-system performances (under six proposed IDPC algorithms).....</i>	91

Tables of Chapter-4 :

Table.4.1	<i>Excitation switches of NPC's IGBTs.....</i>	101
Table.4.2	<i>The proposed active and reactive power references</i>	104
Table.4.3	<i>Results recapitulation for conventional I/OLDC based on PI using two level converter.....</i>	107
Table.4.4	<i>Results recapitulation for proposed I/OLDC based on MRAC using two level converter.....</i>	112
Table.4.5	<i>Results recapitulation for proposed I/OLDC based on MRAC using NPC three level converter.....</i>	117
Table.4.6	<i>The proposed references profiles of high power</i>	118

Tables of Chapter-5 :

Table.5.1	<i>The advantages and disadvantages (difficulties) of the proposed controls (in chapters 3, 4 and 5).....</i>	125
Table.5.2	<i>Incremental sensor connector</i>	127
Table.5.3	<i>SEMIKUBE connector pin assignment.....</i>	128
Table.5.4	<i>Slave I/O PWM connector (dSPACE1103).....</i>	130
Table.5.5	<i>References rotor current variation using L-filter.....</i>	134
Table.5.6	<i>LCL Filter's elements with their values.....</i>	137

Tables of Chapter-6 :

Table.6.1	<i>Recapitulation results for proposed hysteresis band (HB) performances using 04 cases... ..</i>	157
Table.6.2	<i>The interfaces / connectors of the SEMIKRON®.</i>	157
Table.6.3	<i>Slave I/O PWM connector (dSPACE1104).....</i>	160

List of Abreviation :

DFIG :	<i>Doubly Fed Induction Generator.</i>
WECS :	<i>Wind Energy Conversion System.</i>
VS-WECS :	<i>Variable Speed-Wind Energy Conversion System.</i>
DFIM :	<i>Doubly Fed Induction Machine.</i>
HCC :	<i>Hysteresis Current Controller.</i>
T1-FLC :	<i>Type1-Fuzzy Logic Control.</i>
T2-FLC :	<i>Type2-Fuzzy Logic Control.</i>
FIS :	<i>Fuzzy Inference System.</i>
ANFIS :	<i>Adaptive Neuro-Fuzzy Inference System.</i>
NFC :	<i>Neuro Fuzzy Control.</i>
PI :	<i>Proportional Integral.</i>
IP :	<i>Integral Proportional.</i>
PID :	<i>Proportional Integral Derivate.</i>
PWM :	<i>Pulse Width Modulation.</i>
SVM :	<i>Space Vector Modulation.</i>
AC :	<i>Alternating Current.</i>
DC :	<i>Direct Current.</i>
ADC :	<i>Analog to Digital Converter.</i>
DAC :	<i>Digital to Analog Converter.</i>
DSP :	<i>Digital Signal Processor.</i>
MPPT :	<i>Maximum Power Point Tracking.</i>
P-DPC :	<i>Predictive-Direct Power Control.</i>
DPC :	<i>Direct Power Control.</i>
FOC :	<i>Field Oriented Control.</i>
VOC :	<i>Vector Oriented Control.</i>
SMC :	<i>Sliding Mode Control.</i>
I/OLDC :	<i>Input/Output Linearizing and Decoupling Control</i>
FFT	<i>Fast Fourier Transform.</i>
IGBT :	<i>Insulated Gate Bipolar Transistor.</i>
DCM :	<i>Direct Current Motor.</i>
IM :	<i>Induction Motor.</i>
NPC :	<i>Neutral Point Clamped.</i>
MRAC	<i>Model Reference Adaptive Control (Controller).</i>
LAS :	<i>Automatic Laboratory of Setif.</i>
L2EP :	<i>Laboratoire de l'Electrotechnique et de l'Electronique de Puissance.</i>
MRAS :	<i>Model Reference Adaptive System (Observer).</i>
PF :	<i>Power Factor.</i>
MATLAB® :	<i>Matrix Laboratory.</i>
THD :	<i>Total Harmonic Distorsion.</i>
I/O PWM :	<i>Input/output Pulse Width Modulation (dSPACE1103' or dSPACE1104 card)</i>
Rpm:	<i>Revolution per minutes.</i>
PLL:	<i>Phase locked loop.</i>
ANN:	<i>Artificial neural network</i>
GSC:	<i>Grid side converter.</i>
RSC:	<i>Rotor side converter.</i>
SA-IDPC	<i>Stand-alone-Indirect power control</i>
VS-WT	<i>Variable speed-wind turbine</i>
2-LC:	<i>Two level converter.</i>
3-LC:	<i>Three level converter.</i>
VSI:	<i>Voltage source inverter.</i>
FPGA:	<i>Field Programmable Gate Array</i>
PSO:	<i>Particle Swarm Optimization.</i>
MPC:	<i>Model Predictive Control.</i>
GA:	<i>Genetic Algorithm.</i>
RTI:	<i>Real Time Interface.</i>
IDPC:	<i>Indirect Power Control.</i>
FLS:	<i>Fuzzy Logic System (FLS)</i>
FOU:	<i>The footprint of uncertainty of T2-FLC.</i>
MFs	<i>The membership functions</i>
IEEE:	<i>Institute of Electrical and Electronics Engineering.</i>

List of Acronymes :

B	Degree (°).	Blade pitch angle.
TSR	-	Tip Speed Ratio or λ (Lambda).
C_p	-	Power coefficient.
ρ	(Kg/m ³).	Air density.
v	(m/sec).	Wind speed.
R_s	(Ω).	Stator Resistance.
R_r	(Ω).	Rotor Resistance.
I_{sq}	(A).	Stator quadrature (or transversal) current component.
I_{sd}	(A).	Direct axis current of stator.
I_{rq}^* & I_{rd}^*	(A).	Rotor reference quadrature (or transversal) and direct current components.
I_{rq_meas} & I_{rd_meas}	(A).	Rotor measured quadrature (or transversal) and direct current components.
L_s	(H).	Stator inductance.
L_r	(H).	Rotor inductance.
L_m	(H).	Magnetizing (mutual) inductance.
Φ_{rq} & Φ_{rd}	(Wb).	Rotor quadrature (or transversal) and direct flux components.
Φ_{sq} & Φ_{sd}	(Wb).	Stator quadrature (or transversal) and direct flux components.
V_{rq} & V_{rd}	(V).	Rotor quadrature (or transversal) and direct voltage components.
V_{sq} & V_{sd}	(V).	Stator quadrature (or transversal) and direct voltage components.
P_s , P_r & P_m	(W).	Stator power, Rotor power and Mechanical power.
P_s^* & Q_s^*	(W & Var).	Stator reference active power and Stator reference reactive power.
P_{s_meas} & Q_{s_meas}	(W & Var).	Stator measured active power and Stator measured reactive power.
T_{em} , T_{aero} & $T_{gearbox}$	(N.m).	Electromagnetic torque, Aerodynamic torque and Gearbox torque.
T_r & T_{vis}	(N.m).	Load torque and Viscous torque.
J_G , $J_{Turbine}$ & J	(Kg.m ²).	Generator moment inertia, Turbine inertia and Total inertia.
P	-	Number of Pole pairs.
Ω_{mec}	(Rad/sec).	Mechanical speed.
N_r	(rpm).	Rotor speed.
$N_{synchronous}$	(rpm).	Synchronous speed (=1500 (rpm)).
G	-	The gain of the gearbox.
f_{DFIG}	(N.m/sec).	DFIG's Friction coefficient.
$f_{Turbine}$	(N.m/sec).	Turbine's Friction coefficient.
S	-	Slip.
ω_s & ω_r	(rad/sec).	Stator and rotor pulsations.
θ_s , θ_r & θ_{slip}	(rad).	Stator', rotor' and slip angles.
Z_s	-	Stator impedance.
V_{dc}	(V).	DC-Link voltage.
C_{dc}	(F)	DC-capacitance
R_{Load} , C_{Load} & P_{Load}	(Ω , F & W).	Load resistance, Load capacitance and Load power.
f_{grid} , f_{stator} & f_{rotor}	(Hz).	Grid, stator and rotor frequencies.
$ V_{grid} $ & $ V_{stator} $	(V).	Grid and stator voltage magnitudes.
I_{s_abc} & I_{r_abc}	(A).	Stator and rotor currents (line to neutral).
V_{s_abc} & V_{r_abc}	(V).	Stator and rotor voltages (line to neutral).
K_p , K_i & K_D	-	Proportional gain, Integral gain and Derivative gain.
I_{sa_meas} & I_{ra_meas}	(A).	Stator and rotor measured current (line to neutral).
S_w	(m ²).	Wind turbine blades swept area (= $\pi \cdot R^2$).
R	(m).	Blades diameter of the turbine.
I_{g_abc} & $I_{g_abc}^*$	(A).	Grid measured and reference currents (line to neutral).
I_{rec}	(A).	Rectifier current.
C_{p_max} & $\lambda_{optimal}$	-	Maximum power coefficient and optimal Tip speed ratio (TSR or λ).
T_{ij} & K_{ij}	-	IGBTs of the rectifier and inverter respectively ($i=1, 2$ 'lines' & $j=1, 2, 3$ 'columns').
S_{ij}	-	IGBT variable states (1 or 0).
C_f & L_f	(F and H)	Filter capacitance and filter inductance.
I_{fa} , I_{fb} & I_{fc}	(A).	Filter currents (in each phase).
V_{fab} , V_{fbc} and V_{fca}	(V).	Filter voltages (line to line).
I_{inv} , I_c & I_{rotor}	(A).	Inverter (SEMIKUBE) current, capacitance current and rotor current.
V_{inv} & V_{Rotor}	(V).	Inverter (SEMIKUBE) voltage and rotor voltage.
L_1 & L_2	(H).	Inverter side inductance and Rotor side inductance.
R_1 , R_2 & R_D	(Ω).	Inverter (SEMIKUBE) side resistance, Inverter side resistance & Damping resistance
$L_f^*h(x)$	-	Lie derivative.
T_1 , T_2 & T_0	(sec).	The SVM switching time duration.
μ_4 , μ_3 , μ_2 & μ_1	-	The NFC's learning-rate parameters.

Chapter 0 :

General Introduction

- 0.1 General Introduction 02
- 0.2 The Main Contributions 03
- 0.3 Thesis Organization 06
- 0.4 Thesis Limitations 07
- 0.5 Scientific Production during the PhD (12 Conference papers, 01 Chapter in Book and 05 Journal Papers) 08
 - 0.5.1 International Conferences papers presented in Algeria, France and Bulgaria (2015, 2016 and 2017) 08
 - 0.5.2 Chapter in Book (2017) 09
 - 0.5.3 Journal Papers (2016) 09
- 0.6 References 09

Abstract:

In this chapter a brief general introduction focuses on the well-known topologies of wind energy conversion systems, on proposed controls and generators by the scientific researchers. One part will be devoted to the latest research that has addressed the performance problems of wind systems and their results (in simulation and experimentation). There will also be some arguments that reflect the main proposed ideas in this manuscript, the proposed selections and their applications in simulation and experiments. We present the selecting criteria in particular the type of: generator, controls and theirs application in experimental and simulation studies. Also, we discuss a detailed section on the different contributions of thesis that define the improvement of the proposed algorithms in each chapter. The organization and structure of thesis takes a place in this chapter: chapter one is based on the state of the art of wind systems and their controls, in particular using the doubly fed induction machine. The simulation part is based on three chapters (2, 3 and 4) and the experimental part focuses on chapters (5 and 6). The limitations and problems encountered during the realization of this thesis are well described in the following section (technical problems of simulation and experimentation). After solving problems, very satisfactory (simulation and experimentation) results have been found which reflect the quality of the scientific contribution including more papers of conferences; Journal papers were published during this thesis.

0.1 General Introduction

The cumulative installation of wind turbines has increased at a fast pace over the last decades. Installed wind power generation, which is currently larger than 440 GW¹, is expected to exceed 760 GW by 2020, making this form of renewable energy a significant component of the modern and future energy supply systems [1-2-3]. The wind power grows more significant than any other renewable energy sources and is becoming really an important player in the modern energy supply system [4].

In the 1980s, the power electronics (PEs) for wind turbines (WTs) was just a soft starter used to initially interconnect the squirrel-cage induction generator with the power grid, and only simple thyristors were applied and they did not need to carry the power continuously [5]. In the 1990s the PE technology was basically used for the rotor resistance control of wound-rotor induction generator (WRIG), where more advanced diode bridges with a chopper were used to control the rotor resistance for generator [6], especially at rated power operation to reduce mechanical stress and loading. Since 2000, even more advanced voltage source converters with bidirectional power flow have been introduced; the PEs started to handle the generated power from the WTs continuously, first, by partial scale of power capacity for doubly fed induction generators (DFIGs), and then by the full scale of power capacity for asynchronous or synchronous generators (A/SGs) [1], [6].

Although the wind turbine system can be categorized into several concepts in terms of the generator type, with and without the gearbox, or the rating of the power electronic converter, it is common to divide the WTs system into a partial-scale power converter equipped with a DFIG and a full-scale power converter together with either a synchronous generator or an induction generator (IG) [4-7-8]. Currently, the configuration of the DFIG system occupies close to 50% of the wind energy market, due to its light weight, small size, and cost-effectiveness of the generator, as well as the relatively small and economic power converter [9-10].

The variable-speed WECSs can be operated in the maximum power point tracking (MPPT) mode to extract the maximum energy from wind. For this purpose, well-calibrated mechanical sensors, such as anemometers and encoders/resolvers, are indispensable in order to acquire the information of wind speed and generator rotor position/speed. However, the use of mechanical sensors increases the cost, hardware complexity and failure rate of WECSs [11-12]. These problems can be solved by adopting position/speed sensorless control schemes [13].

The DFIG' classical control strategies are normally based on voltage oriented control (VOC) algorithms [14-15]. In the past few decades it suffers from the problem of the machine parameters variations, which comes to compromise the robustness of the control device. Therefore, the controller should accommodate the effects of uncertainties and keep the system stable against a large variation of system parameters. The conventional PI-based controllers cannot fully satisfy stability and performance requirements [15]. Their optimal PI's parameters can be determined by other methods such as particle swarm optimization (PSO) or genetic algorithm (GA) [16-17-18]. Power converter and drive system possess inherent characteristics, such as non-linearities, unavailability of a precise model or excessive complexity, that call for intelligent control techniques such as fuzzy logic (FL), neural networks (NN) [19-20]. The dynamic performance of a wind turbine system can be substantially improved by the introduction of intelligent techniques for the control of the PES that are used in WPG systems. Hence, the objectives of reliable and efficient wind power integration in the power system can be effectively realized.

Fuzzy logic has been proposed for wind power generation control [21-22]. The FL based controller of a given system is capable of implanting, in the control strategy, the qualitative knowledge and experience of an operator or field engineer about the process, but has been criticized for its limitations, such as the lack of a formal design methodology, the difficulty in predicting stability and robustness of FL controlled systems [23]. The artificial neural networks (ANNs) based controllers have been used as these controllers can be formed directly by using the input-output data of the unknown system, without need any prior model structure. However, to select an optimal structure, parameter values and the number of training sets are still key concerns. To take advantage of their strengths and to eliminate their drawbacks, several hybrid methods have been proposed [24]. A hybrid system can be obtained by, for example, combining a fuzzy inference system and adaptive neural networks (i.e., the adaptive neuro-fuzzy inference system (ANFIS)) [25]. ANFIS based controllers have been successfully imp-

¹ Please refer to Appendix.A (Table.A.7 illustrated a detailed list of wind turbine manufacturers).

-mented for several power systems and power electronics applications [26-27].

On the other hand, the system is highly nonlinear and has a large range of operating points. Thus, linearization around one operating point cannot be employed to design the controller. Nonlinear control methods can be used to effectively solve this problem [28] and [29]. In attempt to achieve high performances in the steady state as well as during the transients, a different nonlinear control structure must be applied. In the recent two decades, many modified nonlinear state feedback such as Input-output feedback linearization control, Sliding mode and Backstepping have been applied to more improve the control performances [30].

0.2 The Main Contributions

In the review of the DFIG-based wind system in last decade, it can be seen that the majority relies on the regulation of: *speed, flux, torque, current and powers*. More than 75% of the published articles (mainly based on "IEEE and Science Direct" databases between 2005 and 2017) in the study and development of the DFIG-based wind system are basically focused on three (03) main controls: vector control (*rotor flux and torque*), predictive control and direct power control (*stator active and reactive power*). In this thesis, we are interested in power control (*in terms of modeling and experimentation*) whose main objective is to improve the quality of energy transmitted into the network by integrating and developing new algorithms in order to overcome drawbacks of conventional controls in transient and steady states during the wind speed variation and under robustness tests.

A detailed simulation study in power control using PI (*Proportional-Integral*) regulators (*in order to control the stator powers " P_s and Q_s " and the rotor currents " I_{rd} and I_{rq} " according to 04 loops respectively*) is developed according to three modes, as follows:

- **Mode 1:** *Without the MPPT strategy (imposed power profiles).*
- **Mode 2:** *With the MPPT strategy (wind in step form).*
- **Mode 3:** *With the MPPT strategy (wind in random form).*

(Knowing that all control algorithms in this thesis are developed using these three modes).

The MPPT (*maximum power point tracking*) is used in order to extract the maximum power despite the wind speed variation (*step or random wind forms*) by maintaining the reactive power at zero level means power factor near to the unity.

Some drawbacks appears in simulation studies especially in with/without robustness tests (Knowing that we used the same robustness tests in chapters: 2, 3 and 4) such as:

- *An important overshoot is noted (more than + 50%).*
- *The coupling terms between the parameters of the both axes (d and q) has negative influence on the wind-system performances, especially in high wind-power generation (HWPG)*
- *The long response time (a visible delay of the measured value relative to that of the reference) order of $10e^{-2}$ (sec).*
- *A bad power tracking of the measured value relative to that of the reference especially if the profile is in the step form.*
- *Poor power/voltage quality which will be transmitted to the grid; a bad THD that exceeds IEEE standards ($>> + 5\%$).*
- *A remarkable power error for conventional power control sometimes exceeding 25% of the rated power (± 1000 (W) for a rated power of 4 kW).*
- *The conventional regulators (PI regulators) depend on the DFIG's parameters.*

In this context, several approaches have been proposed in order to overcome or minimize these drawbacks (*already mentioned above*). As a first step, a conventional regulator called PID (*Proportional-Integral-Derivate*) more developed in term of minimization error and overshoot is proposed instead the PI controllers to control P_s , Q_s , I_{rq} and I_{rd} respectively. Remarkable improved performances are noted

for the three modes -Mode: 1, Mode: 2 and Mode: 3; already mentioned above- especially without robustness tests. After applying the 3rd test (green color of the curves/robustness tests section in each chapter) a bad tracking of the active power is particularly apparent when the wind speed varies severely, which means that the PID regulator -for rotor current control: I_{rd} and I_{rq} - is unable to track the power reference during the sudden wind speed variation and DFIG's parameters variation.

For this reason, adaptive and intelligent controllers are used to correct the failure of conventional controllers in transient and steady states, such as: "Model Reference Adaptive Control (MRAC)", "Type-1 Fuzzy Logic Control (T1-FLC)", "T2-FLC (Type-2 fuzzy logic control)" and "NFC (Neuro-fuzzy control)"; knowing that all these proposed controllers (already mentioned above) are used in order to control the d - q axes rotor currents components (I_{rd} and I_{rq}) by keeping PID controllers for stator active and reactive powers tuning (P_s and Q_s). MRAC regulators have been proposed for the control of " I_{rq} and I_{rd} ", in same time; there will be more improved results than used only for " P_s , Q_s , I_{rq} and I_{rd} ", the aim of this select is minimizing time computing and in same time maintaining a good performance², then it is to look for a robust controllers which does not depend on DFIG's mathematical model.

In this context, the high-performance regulators known by the name of "intelligent regulators"; are set up to remedy these problems -performances limitation-, three (03) intelligent regulators: T1-FLC, T2-FLC and NFC are used to correct power error especially under robustness tests. T2-FLC and T1-FLC are fuzzy controllers based on the inferences (inputs and outputs in triangular or trapezoid forms) and linguistic rules -depends on the inferences number choosing for studied system to the power of number of inputs, exp: 7 inferences in triangular form "for inputs and output respectively" and 2 inputs; means: $7^2 = 49$ rules³- to initiate the optimal calculation of the desired value, noting that the computational algorithm interface is integrated in Matlab®/Simulink software. Knowing that; T2-FLC controller based on three (03) dimensions more than T1-FLC (only two dimensions) this difference in dimensional form generates a complexity of mathematical model of the controller itself and aims to minimize error of the desired value known by optimal value despite the parameters variation of the wind-system. T2-FLC represents the most developed fuzzy family generation in terms of precision and robustness. NFC regulator is a combination between the fuzzy logic strategy and the artificial neural network (ANN) to have theirs qualities at the same time: to remedy the dependence problem of the wind-system mathematical model and to minimize the calculation of the optimal value while maintaining the robustness despite the parametric variation. Excellent results have been found compared to those found for the last proposed controllers which reflect the robustness of the proposed controller.

A wind-system linearity and coupling problem has not been fully treated in the previously proposed controls, in this context a robust control called "Input / Output linearizing and decoupling control: I / OLDC", which will deal with the problem of decoupling between the terms of the two axes " d and q ". A well-detailed simulation study -based on the three modes mentioned above- is developed using classical regulators 'PI' for controlling active and reactive powers only P_s and Q_s , has some problems; whose majority of them are based on the power error and a small overshoot in transient and steady states. In order to improve the wind-system performances, a novel topology using the MRAC controllers (already used in Chapter 3) has been proposed to definitively remedy the problem of power error, overshoot and the decoupling " d and q " axes components. A multilevel converter (in this case, a Neutral Point Clamped (NPC) three level converter) has been proposed to provide high output power to the rotor-side converter (RSC) in the case of high wind speed. A detailed study of the simulation results was presented for both topologies -two and three-level converter- using robustness tests, which presented a good performances in transient and steady states, compared to those found in previous proposed controls.

² This choice is used in chapter: 4, because in this case the proposed control based only on two (02) loops (to control P_s and Q_s respectively without necessity of control d - q axis rotor currents components), proposes a good linearity and perfect decoupling control using MRAC.

³ The same rules number applied in chapter: 3 (for T1-FLC and T2-FLC respectively).

The stand-alone indirect power control (*SA-IDPC*) is proposed to control the *DFIG's* rotor via the six (06) *IGBTs* of the *SEMIKUBE* (*inverter*) and the *DFIG's* stator is connected to *RL-load*; knowing that the *LCL-Filter* is connected between the *DFIG's* rotor and the *SEMIKUBE* in order to improve the power quality in *RSC* and *GSC*. In order to test the feasibility and robustness of the proposed control, an experimental test bench was developed in *L2EP Laboratory* (*Ecole Centrale de Lille / France*) using *dSPACE1103* card. The wind turbine emulator is chosen as an induction motor (*IM*) is controlled by a variable speed drive in order to vary easily the rotor speed in real time according to rotor flux vector control; *i.e.*: achieve Sub-synchronous operation and Super-synchronous operation respectively. An indirect power control is proposed in order to be able to control the images⁴ of the stator active and reactive powers using *IP* (*Integral-Proportional*) regulators. Its purpose is to minimize the excesses created by using *PI* regulators. Sensors for measuring voltages and currents have been used to capture good measurements and without noise of signals. The test bench is implemented via *dSPACE1103* card and *ControlDesk* software that allows controlling the wind-system references and measured values by the mean of the sensors in real time, in case of danger a single click on "OFF" will be sufficient to protect the *SEMIKUBE's* isolation card and the measurement devices of and *dSPACE1103*. Comparative studies have been carried out using three types of filters (*L*, *LC* and *LCL*) to filter the stator and rotor voltages, in order to get a higher power quality (good *THD* under *IEEE-519 standards*), the optimal choice in this case is selected by *LCL filter* (*3rd order transfer function*) which has made the "stator and rotor" voltages well filtered and the "stator and rotor" currents well smooth. It is very necessary to keep this filter for the next experimental tests which is well argued with several results; especially *FFT* (*Fast Fourier Transform*) of experimental results. Several experimental tests were carried out on the basis of the rotor currents variation with/ without connection to the stator in order to ensure the robustness of the proposed algorithms; using different conditions in each experimental test. Profiles in the form of "steps and trapezoid" have been proposed for reference rotor currents; in order to confirm the good tracking of the measured currents compared to those references, a negligible current error has been noted with a very short response time. The 'Sub-synchronous and Super-synchronous' modes were performed by varying the rotor speed via the variable speed drive where the variation of the slip angle is visible. Many experimental tests on the behavior of "stator and rotor" currents under a speed fixation (0 (*rpm*), 500 (*rpm*), 1000 (*rpm*), 1500 (*rpm*) and 1700 (*rpm*) respectively) have been established at each test. Very satisfactory results have been observed, hence the waveforms of currents and voltages (*rotor and stator*) are purely sinusoidal in transient and steady states.

A vector control is established via the rotor flux orientation which based on the hysteresis controller using *low band*= ± 0.01 (A), to control the *DFIG's* rotor currents, has been proposed for an experimental study via *dSPACE1104* card in two modes: *Grid-connection mode* via a robust *PLL* and a *Stand-alone mode* using *nonlinear load*. The experimental study is carried out using a test bench developed in *LAS Laboratory* (*University of Setif-1*), the turbine emulator of wind-system is a *DC* motor with shunt excitation (3 *kW*) and *DFIG* has a rated power of 3.5 (*kW*). Measurement sensitive sensors are essential to keep good inputs waveforms of rotor currents, stator and speed. The proposed control is essentially based on hysteresis bands, in this thesis $\Delta I_r = \pm 0.01$ (A) is chosen as band optimal one for the next experimental tests and in the same context a detailed simulation study described more the performances of each band, means that the measured rotor current is near to its reference (*error minimization*) to generate the *PWM* switching signals to control the six (06) *IGBT's* of the *SEMIKRON* (*inverter used in this section*). The first topology is to synchronize the stator voltages and the grid voltages in terms of *frequency*, *sequence* and *amplitude* in order to activate the switch, there is a specific device that makes the synchronization by using the *PLL algorithm*; manually or atomically via a specific algorithm that will be developed in *Matlab* software and will be compiled in real time using the *dSPACE1104* card. Very satisfactory experimental results show a soft synchronization between the

⁴ The images of stator active and reactive powers are I_{rq} and I_{rd} respectively.

stator and the grid, stator 'voltages and currents' waveforms meet the requirements of the IEEE-519 standard ($THDi < 5\%$) which will be injected into the network (*grid*). The *Sub-synchronous operation mode* (< 1500 rpm) and the *Super-synchronous operation mode* (> 1500 rpm) have been established by varying the rotor speed (*between 0 rpm and 1700 rpm and the inverse*) to be able to verify the waveforms of the rotor currents and its frequencies. Several experimental robustness tests are developed using the same algorithm to ensure the performance of rotor tracking currents, overshoot, response time and current error. The second proposed approach deals principally with the behavior of the rotor currents variation in the stand-alone mode; in this case the DFIG's stator is connected to the *R-load* via rectifier - *nonlinear load*- and the bank capacitances for the stator voltage filtering. Experimental results in GSC and RSC respectively for both modes: *grid-connection and stand-alone mode*, show high performances of the proposed control under different conditions in transient and steady states.

0.3 Thesis Organization

The content of this thesis is divided into seven chapters. This first chapter is restricted to a brief introduction to the subjects related to this thesis in order to contextualize the presented work and to elucidate its relevance. Furthermore, the main contributions and the structure of the thesis are succinctly described. The detailed study based on art of the state (*in last ten years*) of different WECS' topologies (*especially using DFIG*), the controls and its applications will be presented in **Chapter 1**.

Chapter 2 will deal on a simulation study of power vector control (*stator active and reactive power*) based on classical *PI regulators* by the means of the stator flux orientation. A mathematical model of the turbine is established in order to use the *MPPT* strategy; means the maximum power will be extracted by keeping the reactive power at zero. A mathematical model of DFIG is defined using the stator flux orientation to simplify the model and create the decoupling terms (*needed later for the power control algorithm*). A well-detailed schematic explanation of the *Hypo* and *Hyper synchronous* cases according to: motor mode and generator mode (*in order to use these principles in the simulation and experimental part*). In order to control the rotor side converter (RSC), the SVM (*space vector modulation*) has been proposed (*based on six (06) sectors using the 'dq' frame*) to minimize the harmonics of the rotor currents in order to get good reference voltages (V_{rd} and V_{rq}) to fed again the DFIG's rotor. A detailed simulation study based on robustness tests shows the inability means performances' limitation with/without robustness tests of this classical algorithm, for this reason an improved topology -*based on PID controllers*- is proposed in order to overcome the present problems. Robustness tests were applied to confirm its performances, the problem of overshoot was solved and on other hand the great power error and a bad power tracking were observed especially in the third test (*robustness tests*).

Chapter 3 will focus on the improvement of the previous control strategy in order to eliminate the observed disadvantages especially during the sudden variation of the wind and the parametric variation of the DFIG. For this, four topologies have been proposed based on robust, adaptive and intelligent regulators. *MRAC*, *T1-FLC*, *T2-FLC* and *NFC* represent the proposed regulators for controlling the rotor currents (I_{rd} and I_{rq}) while keeping the *PID* controllers for power control (P_s and Q_s). A remarkable improvement was noted in the simulation results, particularly in the robustness tests, which proves the right choice and the proposed thorough study in order to improve the power quality transmitted in the networks.

Chapter 4 will be essentially based on a robust control called "*Input / Output linearizing and decoupling control (I/OLDC)*" whose main interest is to eliminate the coupling between the two axes (d and q) and also to improve the wind system performances. A mathematical model of I/OLDC is established to control the DFIG's rotor. First of all, the '*I/OLDC*' was established using classical *PI regulators* in order to test the performance of the system according to the three (03) modes. Some defects appear in simulation results developed via *Matlab/Simulink*®, are essentially based on: a poor reference power tracking and a remarkable overshoot. In order to overcome this problem; *MRAC* is proposed instead the *PI* to control the (P_s and Q_s) powers and to eliminate the observed drawbacks in

the previous topologies. A comparative study using new power profiles has been established between the six (06) topologies (*chapter 2, 3 and 4*) without the MPPT strategy to confirm that the decoupling problem is solved. The simulation results show the performances superior quality of the improved nonlinear control (*via MRAC*) in transient and steady states.

Chapter 5 will deal on the novel topology of indirect power control in stand-alone mode means *the stator is connected to RL-load*. The proposed control is mainly based on IP controllers in order to control the rotor currents (I_{rd} and I_{rq}), then a detailed study to justify the IP controller's choice. Including an LCL-filter which will be mounted between the rotor and the SEMIKUBE (*inverter*), which aims to filter the rotor voltages and also the stator voltages. In this chapter, a comparative experimental study will be carried out between three (03) filter's types: L, LC and LCL, where the FFT performance will be displayed to show the rotor' and stator frequencies (f_r and f_s) of the impair harmonics (3th, 5th, 7th, 9th, ...). Several tests have been developed (*using an experimental test bench via a dSPACE1103 board, DFIG (4.5 kW) a wind turbine emulator (4 kW)*) by varying the rotor currents along the two axes (I_{rd} and I_{rq}) by connecting the stator with/without the RL-load to display the measured rotor currents tracking compared to those references ones. Other experimental tests on several speed values will be established to illustrate *Sub- and Super-synchronous* operations and on the other hand to see the robustness of the proposed control in terms of reference current tracking, response time and overshoot in transient and steady states.

Chapter 6 will presents the study and implementation of a vector control (*based on rotor flux orientation*) to control the DFIG's rotor according to two (02) proposed modes: (*Grid-connection and stand-alone modes*). Hysteresis current regulators have been proposed to control the rotor currents (I_{rd} & I_{rq}) respectively in order to generate the switching signals to control the six (06) IGBT's of SEMIKRON (*inverter*) in accordance with fixed hysteresis bands. In this context a detailed study was established in order to choose the optimal hysteresis band which can be controlled the RSC with high performances. In order to validate the robustness of the proposed algorithm, a PLL is implemented for the grid-connection mode in order to synchronize the stator voltages with those of the network in terms of *amplitude, frequency and sequence*. A nonlinear load (*rectifier + resistance R*) has been connected to the stator in order to create the stand-alone mode, then in order to filter the stator voltage the capacitance bank has been implemented between the stator and the nonlinear. A *Sub- and Super-synchronous* operations have been established ($< \text{and } >1500$ (rpm)) for the both modes in order to vary the rotor speed, and on the other hand to test the robustness of the proposed algorithms in particular in terms of power quality, reference tracking and low current error of the wind-system. The experimental results have proved the high robustness of the proposed modes in transient and steady states.

In **Chapter 7** provides conclusion of this thesis and some topics for future research in this field.

0.4 Thesis Limitations

During the thesis, we found several problems of which the majority of them were reminded i.e.; *the Simpower Systems model in Matlab/Simulink takes a long time in simulation; sometimes for several minutes especially if the sampling time is between $1e^{-6}$ (sec) and $1e^{-5}$ (sec)*, and this can cause problems in the computer (*the PC*). If the studied system includes a simple algorithm with a few *Simulink-blocks* (*maximum 2 control loops*) this does not pose a problem in general, and if the studied system is complicated with several loops -*as in the majority of the algorithms of this thesis*- the solution is translated in this case by the realization of the blocks based on the mathematical model of the studied system because the *Simpower Systems library* contains dozens of algorithms in the same block *means that; the studied system is near to the real one; exp: DTC control*. By using these simulation blocks, the simulation time is minimized to just a few seconds. It is necessary to note that the calculation time of the proposed power algorithm using T2-FLC will be took more time (nearly twice) than T1-FLC; the

reason was the complexity of T2-FLC structure (using three (03) dimensions) compared to T1-FLC (based only on two (02) dimensions).

In the practical part (*experimental studies*), several technical problems were noted during the experimental tests, particularly in the measurements of the currents and voltages (*In this thesis: the inputs of studied algorithm*), to solve this problem, very sensitive sensors (*exp: "Fluke"*) were used to capture exact measured values, namely *currents, voltages and speed*. The parameters identification of the wind system possesses a real' experimental problem, the exactness of the parameters of the DFIG presents the greatest technical obstacle, to remedy this problem two solutions have been proposed; the first is based on a mathematical method from which the values of stator, rotor or magnetizing inductances can be determined. The second method is only experimental and is based on an apparatus which measures the inductances of the rotor and stator windings (*even resistances and capacitances*). The synchronization between the stator and the network has a major problem in term; *sequence, frequency & amplitude*. The risk of DFIG's rotor runaway is possible as long as the three factors (*already mentioned above*) are not equal between the stator and the grid. Two solutions have also been proposed, the first one is theoretical whose objective is to calculate the slip angle and after that we use the block of the PLL (*Phase Locked Loop*) of Matlab/Simulink® software to synchronize the voltages. Another proposed solution is the installation of a device, which acts as a switch that connects the stator phases to those of the network (*which has two techniques: manual or automatic via the dSPACE1103*). In most experimental tests, the sampling time value was near into $1e^{-4}$ (sec), several trials were based on a smaller time in the order of $1e^{-6}$ (sec) and were unsuccessful from the start (*the compilation was not even done*) using the dSPACE1104 card.

0.5 Scientific Production during the PhD (12 Conference papers, 01 Chapter in Book and 05 Journal Papers)

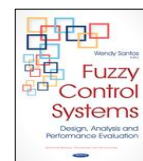
0.5.1 International Conferences papers presented in Algeria, France and Bulgaria (2015, 2016 and 2017):

1. **Fayssal AMRANE** and Azeddine CHAIBA: "Model Reference Adaptive Control for DFIG based on DPC with a Fixed Switching Frequency" International Electrical Computer Engineering Conference, IECEC 23-25th May 2015 Setif-Algeria.
2. **Fayssal AMRANE** and Azeddine CHAIBA: "Direct Power Control for grid-connected DFIG using Fuzzy Logic with a Fixed Switching Frequency" Conférence Internationale d'Automatique et de la Mécatronique, CIAM 10-11th Nov 2015 Oran-Algeria.
3. **Fayssal AMRANE** and Azeddine CHAIBA: "Comparative Study on the performance of Fuzzy-PID and MRAC-PID Controllers based on DPC with SVM for DFIG using MPPT Strategy" International Conference on Automatic Control, Telecommunication and Signals, ICATS 16-18th Nov 2015 Annaba-Algeria.
4. **Fayssal AMRANE** and Azeddine CHAIBA: "A Hybrid Intelligent Control based on DPC for grid-connected DFIG with a Fixed Switching Frequency using MPPT Strategy" 4th International Conference on Electrical Engineering, IEEE Conference, ICEE 13-15th Dec 2015 Boumerdes-Algeria.
5. **Fayssal AMRANE**, Azeddine CHAIBA and Khaled Eben el-Oualid. MEDANI: "Neuro-Fuzzy Control based on DPC for grid-connected DFIG with a Fixed Switching Frequency" International conference on electrical engineering and first workshop on robotics and controls, 9th CEE 2-4th October 2016 Batna-Algeria.
6. **Fayssal AMRANE**, Azeddine CHAIBA and Khaled Eben el-Oualid. MEDANI: "Improved Input-Output Linearizing Control using MRAC in Variable Speed DFIG-based on WECS Fed by Three-Level Voltage Source Inverter" International conference on electrical engineering and first workshop on robotics and controls, 9th CEE 2-4th October 2016 Batna-Algeria.
7. **Fayssal AMRANE**, Azeddine CHAIBA and Ali CHEBABHI: "Improved Active and Reactive Power Control WECS for grid-connected DFIG using Type-1 and Type-2 Fuzzy Logic Control" International Conference on Technological Advances in Electrical Engineering, ICTAEE 24-26th October 2016 Skikda-Algeria.
8. **Fayssal AMRANE**, Azeddine CHAIBA and Ali CHEBABHI: "Robust and Simplified Input-Output Linearizing Control in Variable Speed DFIG using MRAC with Fixed Switching Frequency" International Conference on Technological Advances in Electrical Engineering, ICTAEE 24-26th October 2016 Skikda-Algeria.

9. **Fayssal AMRANE**, Azeddine CHAIBA and Bruno FRANCOIS: "Application of Adaptive T2FLC in Stator Active and Reactive power Control WECS based on DFIG via Hypo/Hyper-Synchronous Modes", 4^{ème} Conférence des Jeunes Chercheurs en Génie Electrique, JCGE, 30 Mai et 1^{er} Juin 2017, Arras, France.
10. **Fayssal AMRANE**, Azeddine CHAIBA, Bruno FRANCOIS and Badr Eddine BABES: "Experimental Design of Stand-alone Field Oriented Control for WECS in Variable Speed DFIG-based on Hysteresis Current Controller", 15th International Conference on Electrical Machines, Drives and Power Systems, *IEEE Conference, ELMA*, 1-3th June 2017 Sofia-Bulgaria.
11. **Fayssal AMRANE**, Azeddine CHAIBA, Bruno FRANCOIS and Badreddine BABES: "Real Time Implementation of Grid-connection control using Robust PLL for WECS in Variable Speed DFIG-based on HCC", 5th International Conference on Electrical Engineering, *IEEE Conference, ICEE* 29-31th Oct 2017 Boumerdes-Algeria.
12. **Fayssal AMRANE**, Azeddine CHAIBA and Bruno FRANCOIS: "Suitable Power Control based on Type-2 Fuzzy Logic Control for Wind-Turbine DFIG Under Hypo-Synchronous Mode Fed by NPC Converter" 5th International Conference on Electrical Engineering, *IEEE Conference, ICEE* 29-31th Oct 2017 Boumerdes-Algeria.

0.5.2 Chapter in Book (2017):

- **Fayssal AMRANE** and Azeddine CHAIBA, "Type2 Fuzzy Logic Control: Design and Application in Wind Energy Conversion System based on DFIG via Active and Reactive Power Control", Chapter-1, pp.1-35, Title Book: "Fuzzy Control Systems, Analysis and Performances Evaluation", Nova Science Publishers, Inc., New York, USA, January 2017. ISBN: 978-1-63485-889-2.



0.5.3 Journal Papers (2016):

1. **Fayssal AMRANE**, Azeddine CHAIBA and Saad MEKHILEF: "High performances of grid-connected DFIG based on direct power control with fixed switching frequency via MPPT strategy using MRAC and Neuro-Fuzzy control" *Journal of power technologies*, Vol, 96, n°: 1, pp. 27-39, 2016.
2. **Fayssal AMRANE** and Azeddine CHAIBA, "Performances of Type-2 Fuzzy Logic Control and Neuro-Fuzzy Control Based on DPC for Grid Connected DFIG with Fixed Switching Frequency", *International Journal of Electrical, Computer, Energetic, Electronic and Communication Engineering*, Vol: 10, n°: 7, 2016.
3. **Fayssal AMRANE** and Azeddine CHAIBA, "A Novel Direct Power Control for Grid-Connected Doubly Fed Induction Generator based on Hybrid Artificial Intelligent Control with Space Vector Modulation", *Rev. Roum. Sci. Techn.- Électrotechn. et Énerg* Vol: 61, n°: 3, pp. 263-268 , 2016.
4. **Fayssal AMRANE**, Azeddine CHAIBA and Ali CHEBABHI: "Improvement Performances of Doubly Fed Induction Generator via MPPT Strategy using Model Reference Adaptive Control based on Direct Power Control with Space Vector Modulation", *Journal of Electrical Engineering*, Vol: 16, n°: 3, pp. 218-225, 2016.
5. **Fayssal AMRANE**, Azeddine CHAIBA, Badr Eddine BABES and Saad MEKHILEF, "Design and Implementation of High Performance Field Oriented Control for Grid-Connected Doubly Fed Induction Generator via Hysteresis Rotor Current Controller", *Rev. Roum. Sci. Techn.- Électrotechn. et Énerg* Vol: 61, n°: 4, pp. 319-324, 2016.

0.6 References

- [1] Frede BLAABJERG; Ke MA, "Wind Energy Systems", *Proceedings of the IEEE*, vol: 105, no: 11, pp.: 2116 – 2131, 2017.
- [2] REN21, "Renewables 2016: Global Status Report (GSR)". [Online]. Available: <http://www.ren21.net>, 2017.
- [3] GWEC, "Global Wind Statistics 2016". [Online]. Available: www.gwec.net, 2017.
- [4] Frede BLAABJERG, and Ke MA, "Future on Power Electronics for Wind Turbine Systems", *IEEE Journal of Emerging and Selected Topics in Power Electronics*, vol: 1, no: 3, 2013.
- [5] Zhe. CHEN, Josep M. GUERRERO, and Frede. BLAABJERG, "A review of the state of the art of power electronics for wind turbines," *IEEE Trans. Power Electron.*, vol. 24, no. 8, pp. 1859–1875, Aug. 2009.

- [6] Anca D. HANSEN, Florin IOV, Frede BLAABJERG, and Lars H. HANSEN, "Review of contemporary wind turbine concepts and their market penetration," J. Wind Eng., vol. 28, no. 3, pp. 247-263, 2004.
- [7] Venkata YARAMASU, Bin WU, Paresh C. SEN, Samir KOURO and Mehdi NARIMANI, "High-power wind energy conversion systems: state-of-the-art and emerging technologies", in Proceeding of the IEEE, vol: 103, no: 5, pp. 740-788, 2015.
- [8] Dao ZHOU, Frede BLAABJERG, "Bandwidth oriented proportional-integral controller design for back-to-back power converters in DFIG wind turbine system", IET Renewable Power Generation, Vol. 11, no: 7, pp. 941-951, DOI: 10.1049/iet-rpg.2016.0760, 2017.
- [9] Marco LISERRE, Roberto CARDENAS, Marta MOLINAS, and José RODRIGUEZ, "Overview of multi-MW wind turbines and wind parks", IEEE on Transactions in Industrial Electronics, vol: 58, no: 4, pp. 1081-1095, 2011.
- [10] Roberto CARDENAS, Rubén PENA, Salvador ALEPUZ and Greg ASHER, "Overview of control systems for the operation of DFIGs in wind energy applications", IEEE Transactions on Industrial Electronics, vol: 60, no: 7, pp. 2776-2798, 2013.
- [11] Yue ZHAO, Chun WEI, Zhe ZHANG and Wei QIAO, "A Review on Position/Speed Sensorless Control for Permanent-Magnet Synchronous Machine-Based Wind Energy Conversion Systems", IEEE Journal of Emerging and Selected Topics in Power Electronics, vol: 1, no: 4, pp.:203-216, 2013.
- [12] Wei QIAO, Xu YANG and Xiang GONG, "Wind speed and rotor position sensorless control for direct-drive PMG wind turbines," IEEE Transaction on Industry Applications, vol. 48, no. 1, pp. 3-11, 2012.
- [13] Wei QIAO, "Intelligent mechanical sensorless MPPT control for wind energy systems," in Proc. IEEE Power and Energy Society General Meeting, pp. 1-8, 2012.
- [14] Nihel KHEMIRI, Adel KHEDHER and Mohamed Faouzi MIMOUN, "Wind Energy Conversion System using DFIG Controlled by Backstepping and Sliding Mode Strategies," International Journal of Renewable Energy Research, vol. 2, no. 3, pp. 3-11, 2012.
- [15] Álvaro LUNA, Kleber LIMA, Pedro RODRÍGUEZ, Edson H. WATANABE and Remus TEODORESCU, "Comparison of Power Control Strategies for DFIG Wind Turbines", Industrial Electronics, IECON 2008. 34th Annual Conference of IEEE, 2008
- [16] Bo YANG, Lin JIANG, Lei WANG, Wei YAO and Q.H. WU, "Nonlinear maximum power point tracking control and modal analysis of DFIG based wind turbine", Industrial Electronics, Electrical Power and Energy Systems, vol:74, no: xx, pp: 429-436, 2016.
- [17] Mohsen RAHIMI and Mostafa PARNIANI "Dynamic behavior analysis of doubly-fed induction generator wind turbines-the influence of rotor and speed controller parameters", International Journal of Electric Power Energy Systems, vol: 32, pp: 464-77, 2010.
- [18] Feng WU, Xiao-ping ZHANG, Keith GODFREY and Ping JU, "Small signal stability analysis and optimal control of a wind turbine with doubly fed induction generator", IET Generation, Transmission & Distribution; vol: 1, no: 5, pp: 751 - 760, 2007.
- [19] Gilberto C. D. SOUSA and Bimal K. BOSE, "Fuzzy logic applications to power electronics and drives - an overview," Proceedings of IECON 1995, pp.57-62, 1995.
- [20] Y. DOTE and R. G. HOFT, "Intelligent Control: Power Electronic Systems", Oxford University Press, New-York, 1998.

- [21] Marcelo Godoy SIMOES, Bimal K. BOSE, and Ronald J. SPIEGEL, "Design and performance evaluation of a fuzzy-logic-based variable-speed wind generation system", IEEE Transactions on Industry Applications, vol. 33, no. 4, pp. 956-965, 1997.
- [22] Hany M. SOLOUMAH, Narayan C. KAR, "Fuzzy logic based vector control of a doubly-fed induction generator for wind power application," Wind Engineering, vol. 30, no. 3, pp. 201-224, 2006.
- [23] Bharat SINGH, Elias KYRIAKIDES, and Sri Niwas SINGH, "Intelligent Control of Grid Connected Unified Doubly-Fed Induction Generator," IEEE Conference, DOI: 978-1-4244-6551-4/10, 2010.
- [24] Peter VAS, "Artificial-intelligence-based electrical machines and drives", Oxford University Press, New-York, 1999.
- [25] Jyh-S hing Roger JANG, "ANFIS: Adaptive-network based fuzzy inference system," IEEE Transactions on System Man, Cybernetics, vol. 23, no. 2, pp.665-685, 1993.
- [26] Praveen TRIPATHY, "Development of Adaptive Supplementary Feedback Controller for GUPFC", Master Thesis (in English Language), IIT Kanpur, India, 2006.
- [27] Cameron POTTER, Michael NEGNEVITSKY, "Very short-term wind forecasting for Tasmanian power generation," IEEE Transactions on Power Systems, vol. 21, no. 2, pp. 965-972, 2006.
- [28] Ja KARTHIKEYAN, Sujan Kumar KUMMARA, C. NAGAMANI and G Saravana ILANGO, " Power control of grid connected Doubly Fed Induction Generator using Adaptive Back Stepping approach", in Proc 10th IEEE International Conference on Environment and Electrical Engineering EEEIC'2011, Rome, 2011.
- [29] Karim ABBASZADEH and Sam ROOZBEHANI "A New Approach for Maximum Power Extraction from Wind Turbine Driven by Doubly Fed Induction Generator Based on Sliding Mode Control", Energy Management, vol: 1, no: 2, 2012.
- [30] Ahmed Lokmane NEMMOUR, Fateh MEHAZZEM, Abdelmalek KHEZZAR, Rachid ABDESSEMED, "Advanced Backstepping controller for induction generator using multi-scalar machine model for wind power purposes", Journal of Renewable Energy, vol: 35, no: 10, pp. 2375-2380, 2010.

Arab proverb:

Science does not consist in what is preserved in books, but in what is engraved in hearts.

Chapter 1 :

State of the Art: An Overview of Wind Energy Conversion Systems (WECS) based on DFIG

1.1 Development of Wind Power Generation.....	13
1.2 Wind Turbine Concepts	14
1.2.1 Fixed Speed Wind Turbines (WT Type A).....	14
1.2.2 Partial Variable Speed Wind Turbine with Variable Rotor Resistance (WT Type B).....	14
1.2.3 Variable Speed Wind Turbine with Partial Scale Power Converter (WT Type C)	14
A- Advantages of the DFIG-based WT generator scheme	14
B- Disadvantages of the DFIG-based wind turbine-generator system	15
1.2.4 Variable Speed Wind Turbine with Full Scale Power Converter (WT Type D)	15
1.3 Control Structure of WTs	15
1.4 Literature Survey	16
1.4.1 Modelling of a WTGS	16
A- DFIG modelling	16
1.4.2 Control Strategies for a WTGS	17
A- Maximum power point tracking control	17
A.1 Intelligent control.....	17
A.2 Other control strategies.....	17
B-DFIG control	17
B.1 Field oriented control.....	18
B.2 Direct torque/power control (DTC/DPC).....	18
B.3 Adaptive control (MRAS observer/MRAC controller)	18
B.4 Adaptive Disturbance Rejection Control (ADRC).....	19
B.5 Sliding mode control (SMC).....	19
B.6 Backstepping control (BSC).....	19
B.7 Predictive Direct power control (PDPC).....	20
B.8 Input/output Linearizing control	20
1.5 References.....	21

Abstract:

The scope of this chapter is to provide a status overview of the technologies and to discuss some technology trends in the power electronics used for wind power applications. First, the technology and market developments of wind power generation are generally reviewed. Next, the wind turbine concept is illustrated and more explained using different types of generator. The control structure of wind-turbines (WTs) is explained using Doubly Fed Induction Generator (DFIG), Asynchronous and Synchronous Generator (ASG and SG). Finally, the last section focuses on a detailed literature review describing DFIG based wind turbine-generator systems in terms of modeling and control strategies.

1.1 Development of Wind Power Generation

The cumulative wind power capacity from 1999 to 2020 is shown in *figure.1.1*, and it can be seen that the wind power has grown fast to a capacity of 283 GW with ~45 GW installed only in 2012, and this number is expected to achieve 760 GW in 2020 on moderate scenario [1-2-3]. Wind power grows more significant than any other renewable energy sources and is becoming really an important player in the modern energy supply system. For example, Denmark has a high penetration by wind power and today >30% of the electric power consumption is covered by wind. This country has even the ambition to achieve 100% non-fossil based power generation system by 2050 [4].

Regarding the markets and manufacturers, the U.S. became the largest markets with over 13.1 GW capacity installed in 2012, together with China (13 GW) and the EU (11.9 GW) sharing around 87% of the global market. The Danish company Vestas first gives out the top position among the largest manufacturers since 2000, while GE catches up to the first because of the strong U.S. market in 2012 [4]

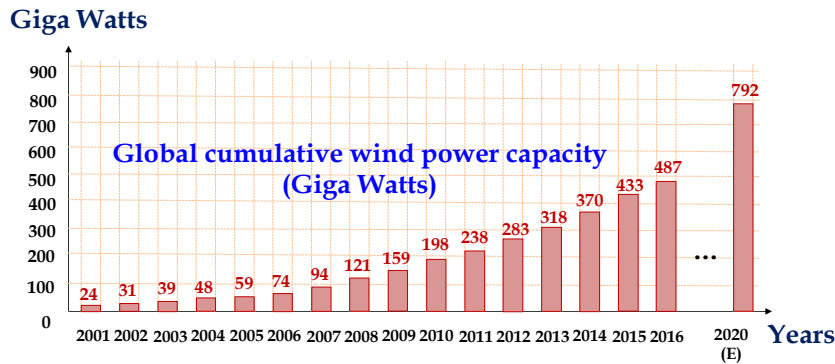


Figure.1.1 Global cumulative wind power capacity from 2001 to 2020 [1].

In addition to the quick growth in the total installed capacity, the size of individual WT is also increasing dramatically to obtain a reduced price per generated kilowatt hour. In 2012, the average turbine size delivered to the market was 1.8-MW, among which the average offshore turbine has achieved a size of 4-MW. The growing trends of emerging turbine size between 1980 and 2018 are shown in *figure.1.2*, where the development of power electronics in the WTS (*rating coverage and function role*) is also shown. It is noted that the cutting-edge 8-MW WTs with a diameter of 164 m have already shown up in 2012 [5]. Right now most of the turbine manufacturers are developing products in the power range 4.5–8 MW, and it is expected that more and more large WTs even up to 10-MW will appear in 2018, will be present in the next decade [1].

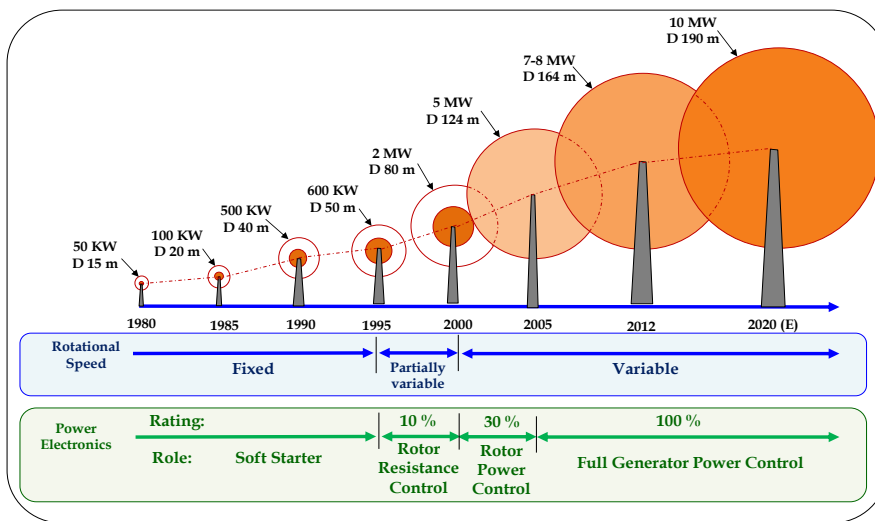


Figure.1.2 Evolution of WT size and the power electronics seen from 1980 to 2020 (estimated). Orange circle: means the power coverage by power electronics, D: means diameter of the rotor [1].

1.2 Wind Turbine Concepts

The overall system of Wind Energy Conversion System (WECS) consisting of *electro-mechanical* and aerodynamic components which converts wind energy to electrical energy as shown in figure 1.3.

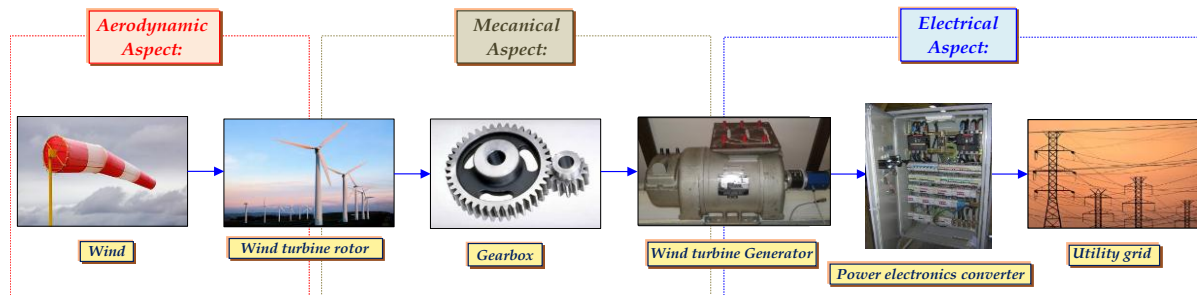


Figure.1.3 Power conversion stages in a typical WTS.

Wind power generation uses either fixed speed or variable speed turbines which can be characterized into four major types. The main changes between these wind turbine types are the ways how the aerodynamic efficiency of the rotor would be imperfect for different wind speed conditions. These four types are briefly described below [6]:

1.2.1 Fixed Speed Wind Turbines (WT Type A)

An asynchronous squirrel-cage induction generator (SCIG) directly connected to the grid via a transformer dealing with type 'A' wind turbine. The so-called "fix speed WT" comes from the point that the rotational speed of the wind turbine cannot be automatically controlled and will only differ by the wind speed. This type of wind turbine needs a switch to prevent motoring operation during low wind speeds, and also suffers a major drawback of reactive power consumption subsequently there is no reactive power regulator. Besides, this type of wind turbine transfers the wind variations to mechanical instabilities and further converts these into electrical power oscillations due to the fact that there are no speed or torque control loops. These electrical power oscillations can lead to an effect in the case of a weak grid.

1.2.2 Partial Variable Speed Wind Turbine with Variable Rotor Resistance (WT Type B)

A wound rotor induction generator (WRIG) directly connected to the grid deals with this type of wind turbine. The controlled resistances are connected in series with the rotor phase windings of the generator. In this way, the total rotor resistances can be regulated, and thus the slip and the output power can be controlled. Due to the limitation of the serial resistance sizes, the variable speed range is usually small, typically 0-10% above synchronous speed.

1.2.3 Variable Speed Wind Turbine with Partial Scale Power Converter (WT Type C)

This arrangement, known as the doubly-fed induction generator (DFIG) concept, uses a variable speed controlled wind turbine. The stator phase windings of the doubly fed induction generator are directly connected to the grid, while the rotor phase windings are connected to a back-to-back converter via slip rings. The power converters could control the rotor frequency and thus the rotor speed. The power rating of the power converters is typically rated $\pm 30\%$ around the rated power since the rotor of the DFIG would only deal with slip power. The smaller rating of the power converters makes this concept eye-catching from a cost-effective sight. Besides, this type of wind turbine can also achieve the desired reactive power compensation.

A- Advantages of the DFIG-based WT generator scheme [7]

- It has the ability of decoupling the active and reactive power by adjusting the rotor terminal voltages. Hence, the power factor control can be implemented in this scheme.
- The DFIG is usually a wound rotor induction generator, which is simple in construction and cheaper than a PMSG.

- In a DFIG based wind turbine generator system, the power rating of the power converters is typically rated $\pm 30\%$ around the rated power, and this characteristic leads to many merits, such as, reduced converter cost, reduced filter volume and cost, less switching losses, less harmonic injections into the connected grid, and improved overall efficiency (approx. 2-3% more than full scale frequency converter) if only the generator and power converters are considered [6].

B- Disadvantages of the DFIG-based wind turbine-generator system [8-9-10] and [11]

- Needs slip-rings and gearbox, which will require frequent maintenance.
- Has limited fault ride through capability and needs protection schemes.
- Has complex control schemes and limited reactive power capability.

1.2.4 Variable Speed Wind Turbine with Full Scale Power Converter (WT Type D)

This structure usually uses a permanent magnet synchronous generator (PMSG) and a full-scale power converter. The stator phase windings are connected to the grid through a full-scale power converter. Some of this type of wind turbines adopts a gearless concept, which means that instead of connecting a gearbox to the generator, a direct driven multi-pole generator is used without a gearbox.

The first two types of wind turbines have many disadvantages. Examples of these disadvantages are: **1)** they do not support any speed control, **2)** they do not have reactive compensation, **3)** they require a stiff grid, **4)** their mechanical structure must be able to support high mechanical stress caused by wind gusts, and so on. Therefore, this thesis does not show any detailed work about these considerations. The advantages and disadvantages of type C wind turbine systems are summarized in paragraphs: §.1.4.3-(A and B).

Nowadays, DFIGs are most frequently used in the wind turbine industry for large wind turbines. Considering these merits of the DFIG-based wind turbine-generator systems, this thesis will only focus on DFIGs and obviously in the next chapters; we will provide some detailed work about the modeling and control schemes.

1.3 Control Structure of WTs

Controlling a wind turbine involves both fast and slow control dynamics [1-12] and [13], as shown in figure.1.5, where a general control structure for a WTS, including turbine, generator, filter, and converter, is shown. The wind turbine concept can either be the type shown in figure.1.4-(A), or the type shown in figure.1.4-(B). Generally, the power flowing in and out of the generation system has to be managed carefully. The generated power by the turbines should be controlled by means of mechanical parts (e.g., pitch angle of blades). Meanwhile, the whole control system has to follow the power production commands given by distribution system operator (DSO)/transmission system operator (TSO). More advanced features of the wind turbine control may be considered such as the maximization of the generated power, ride through operation of the grid faults, and providing grid supporting functions in both normal and abnormal operations, and so on.

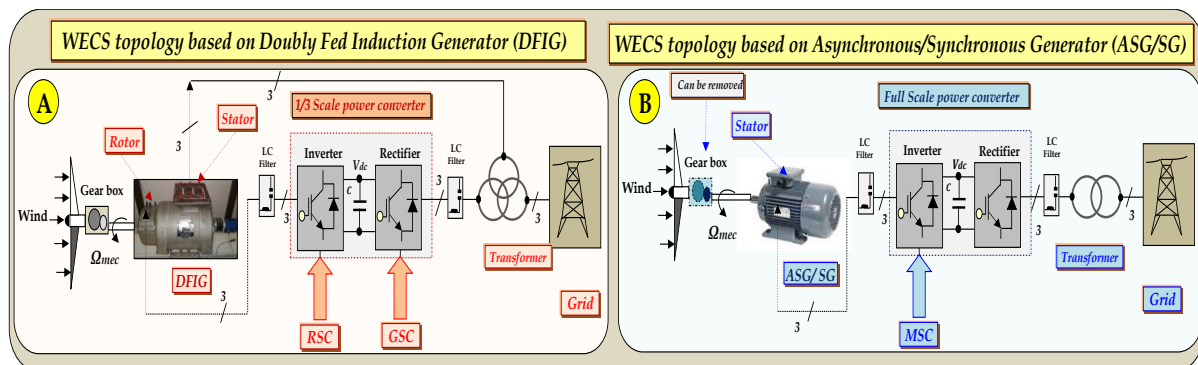


Figure.1.4 A: Variable-speed wind turbine with partial-scale power converter and a DFIG and B: Variable-speed wind turbine with full-scale power converter.

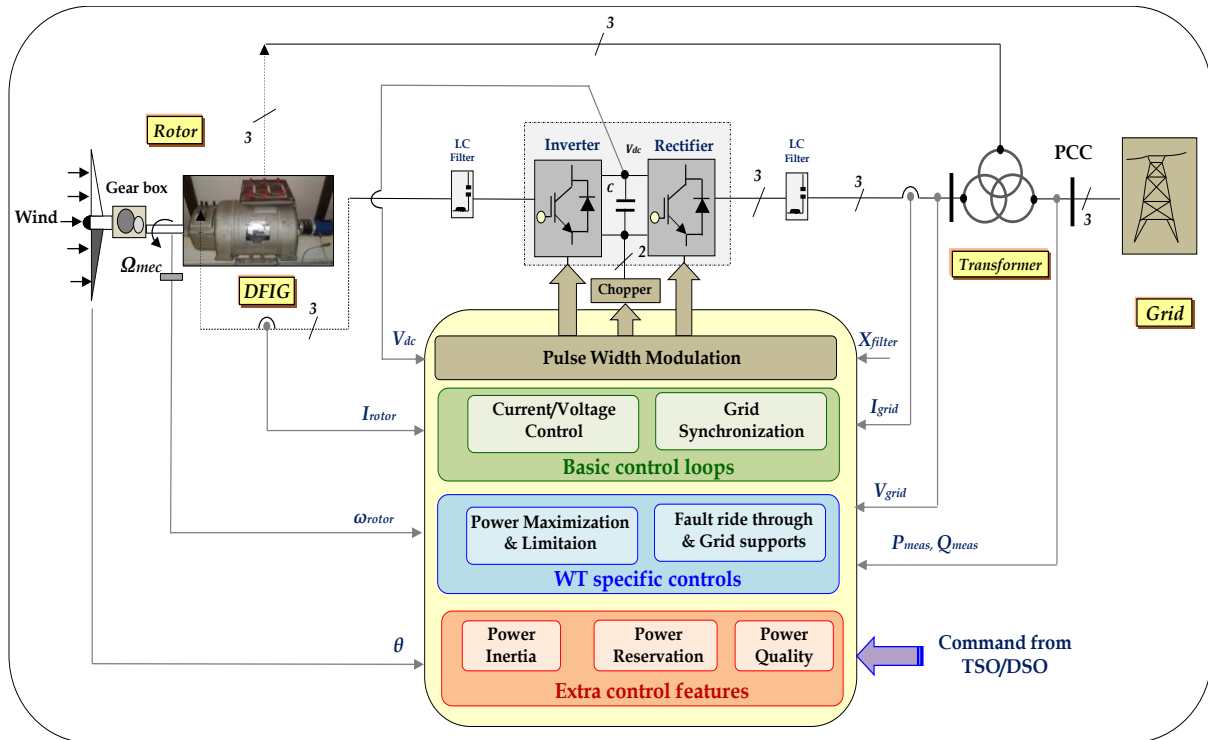


Figure.1.5 Control structure for power electronics converter in WTS. (v_{dc} : dc-link voltage, I_{rotor} : rotor current, ω_{rotor} : rotational speed of rotor, θ : pitch angle of rotor blade, X_{filter} : filter impedance, I_{grid} : grid current, V_{grid} : grid voltage, P_{meas} : measured active power, Q_{meas} : measured reactive power, PCC: point of common coupling).

In the variable-speed wind turbine concept, the current in the generator will typically be changed by controlling the generator side converter, and thereby the rotational speed of turbine can be adjusted to achieve maximum power production based on the available wind power. In respect to operation under grid fault, coordinated control of several subsystems in the wind turbine such as *the generator/grid side converters, braking chopper/crowbar*, and pitch angle controller are necessary. Finally, the basic controls such as current regulation, dc bus stabilization, and the grid synchronization have to be quickly performed by the wind power converter, where the proportional-integral controller and proportional-resonant controllers are typically used [14-15] and [16].

1.4 Literature Survey

In this section, a detailed literature review describing doubly-fed induction generator (DFIG) based wind turbine-generator systems will be presented. More specifically, the related previous studies and researches on the modelling, the control strategies, and the state of the art converter topologies applied in DFIG-based wind turbine-generator systems will be presented [17].

1.4.1 Modelling of a WTGS

The modelling of a wind turbine generator system involves the aerodynamic modelling, the drive train system modelling, the DFIG modelling, and the power converter modelling, see *figure.1.3*. Hence, this part of the study will only focus on the DFIG modelling.

A- DFIG modelling

The doubly-fed induction machines (DFIMs) can be categorized into four types. These types are: the standard DFIM, the cascaded DFIM, the single-frame cascaded doubly-fed induction machine and the brushless DFIM [18]. However, only the standard type and brushless type of doubly-fed induction machines have been applied in wind turbine-generator systems. In reference [19], the authors developed the brushless-DFIG by employing two cascaded induction machines to eliminate the brushes and copper rings, and used a closed-loop SFO control scheme to achieve active and reactive power control. In [20] and [21], the authors adopted the synchronously rotating reference frame in order to simplify the controller design

because of the fact that all the currents and voltages expressed under this reference frame will be of a dc nature. The DFIG model can usually be expressed by reduced order models, which can yield a third order model by neglecting the derivative terms of the stator flux and first order model by neglecting both the derivative terms of the stator flux and rotor flux [22]. But in [21], the authors proposed an enhanced third order model which considered the dc-components of the stator currents, and gave a comparison between a full order model and the proposed model for wind ramp conditions. Alvaro Luna, in [23], deduced a new reduced third order model by ignoring the stator resistances and inductances through applying the Laplace transformation, and compared the proposed model with a full order model for transient analysis.

1.4.2 Control Strategies for a WTGS

The control schemes for a wind turbine-generator system include the pitch angle control, MPPT control, and the DFIG control. The traditional control techniques and advanced control techniques for wind turbine-generator systems are reviewed in this section.

A- Maximum power point tracking control

To achieve the MPPT control, some regulator schemes have been presented. The maximum power point tracking control can be mainly divided into two types. They are the conventional control schemes and intelligent control schemes. The conventional control schemes can also be divided into current mode control and speed mode control, which depends on the setting of reference values. The reference values are the active power and electromagnetic torque for current mode control [24-25], and the rotational speed for the speed mode control [26-27]. In [28], the author compared these two control strategies for dynamic transient analysis, and concluded that the current mode control has slow response with simple construction, while the speed mode control has fast response with complex construction. The discussions and limitations of these two control schemes were presented in [29]. In fact, the wind speeds in above conventional control schemes need to be exactly measured. However, the anemometer cannot precisely measure the wind speed because of the flow misrepresentation, complex landscape and tower shadow influence [30]. Hence, some studies on maximum wind energy tracking without wind velocity measurement had been developed in [31], [32] and [33].

A.1 Intelligent control

The intelligent control strategies usually apply the hill-climbing control and the fuzzy logic control to the MPPT control. However, this control method is usually slow in speed because the step disturbance is fixed. Therefore, some improved hill-climbing control methods were proposed. For example, a method of using variable-step wind energy perturbation method to control the captured wind power was analysed in [34]. Fuzzy logic control based MPPT strategies have the advantages of having robust speed control against wind gusts and turbine oscillatory torque, having superior dynamic and steady performances, and being independent of the turbine parameters and air density, see [35] and [36].

A.2 Other control strategies

In [37], the authors presented a novel adaptive MPPT control scheme in which the wind speed was projected by the output power and the productivity of the generator, and the maximum efficiency was estimated by the maximum tip-speed ratio tracker. A novel MPPT strategy that was proposed in [38], in which there was no requirement for the knowledge of wind turbine characteristic and measurements of the wind speed.

B- DFIG control

Control of the DFIGs is more complex than the control of a squirrel-cage induction generator, because the DFIGs can operate at sub-synchronous speed and super-synchronous speed by regulating the rotor terminal voltages. Through the years, many researchers have presented various types of DFIG control strategies, such as FOC, direct torque/power control, predictive control, sensorless control and nonlinear control.

B.1 Field oriented control

Field oriented control (FOC) or vector control is commonly used in DFIG controls due to its ability of controlling the motor speed more efficiently, and the low economic cost to build an FOC system. Field oriented control also provides the ability of separately controlling the active and reactive power of the generator. Currently, there are mainly two types of field oriented control for DFIGs, which are stator voltage oriented control and stator flux oriented control, respectively [17].

B.2 Direct torque/power control (DTC/DPC)

In [39], the authors proposed a new direct power control (DPC) strategy for a DFIG-based wind energy generation system. The strategy is based on the direct control of stator active and reactive power by selecting appropriate voltage vectors on the rotor side. The proposed method only utilizes the estimated stator flux so as to remove the difficulties associated with rotor flux estimation. Simulation results on a 2 MW DFIG system are provided to demonstrate the effectiveness and robustness of the proposed control strategy during variations of active and reactive power, rotor speed, machine parameters, and converter dc link voltage. In [40], the authors presented an implementation of a direct active and reactive power control for a DFIG, which is applied to a wind generation system as an alternative to the classical field-oriented control (FOC). The proposed direct power control (DPC) method produces a fast and robust power response without the need of complex structure and algorithms. One drawback, however, is its high power ripple during a steady state. The active and reactive power controllers and space-vector modulation (SVM) are combined to replace hysteresis controllers used in the original DPC drive, resulting in a fixed switching frequency of the power converter. Simulation results with the FOC and DPC for a 3kW DFIG are given and discussed, and the experimental results of a test involving identical machines are presented to illustrate the feasibility of the proposed control strategy. In [41], the authors focused on the analysis on the control of DFIG based high-power wind turbines when they operate under presence of voltage dips. The main objective of the control strategy proposed for DFIG based wind turbines is to eliminate the necessity of the crowbar protection when low-depth voltage dips occurs. The proposed control does not totally eliminate the necessity of the typical crowbar protection for turbines it eliminates the activation of this protection during low depth voltage dips. Due to voltage dip in the wind turbine causes three main problems they are control difficulties, disturbance in the stator flux, increase of voltage and currents in the rotor of the machine. Simulation results show the proposed control strategy that mitigates the necessity of the crowbar protection during low depth voltage dips.

B.3 Adaptive nonlinear control (MRAS observer/MRAC controller)

An adaptive nonlinear controller for wind energy doubly fed induction machines is proposed by [42]. The proposed controller is based on the feedback linearization technique and includes a disturbance observer for estimation of parameter uncertainties. Estimated uncertainties values are injected in order to construct the control law, improving in this way the system's performance. The controller behavior, when tracking power references, is tested with realistic Electromagnetic Transients for dc/Power Systems Computer-Aided Design simulations. In addition, the controller performance is checked in the presence of parameter uncertainties and nearby faults. In [43] proposed a sensorless control strategy for DFIGs in variable speed wind turbine systems (WTS). The proposed scheme uses an extended Kalman filter (EKF) for estimation of rotor speed and rotor position. The EKF is used to estimate the mechanical torque of the generator to allow for maximum power point tracking control for wind speeds below the nominal wind speed. The estimation and control performance of the proposed sensorless control method are illustrated by simulation results at low, high, and close to the synchronous speed. The performances of the EKF and a model reference adaptive system (MRAS) observer are compared for time-varying wind speeds. In [44] the authors proposed design and the implementation of a model reference adaptive control (MRAC) of the active and reactive power regulation of a grid connected wind turbine based on a doubly fed induction generator. This regulation is achieved below the synchronous speed, by means of a maximum powerpoint tracking algorithm. The experiment was conducted on a 1kW didactic wound

rotor induction machine in association with a wind turbine emulator. This implementation is realized using a dSPACE1104 single-board control and acquisition interface. The obtained results show a permanent track of the available maximum wind power, under a chosen wind speed profile. Furthermore the proposed controller exhibits a smooth regulation of the stator active and reactive power amounts exchanged between the machine and the grid.

B.4 Adaptive Disturbance Rejection Control (ADRC)

In [45], the authors proposed a new control structure is presented to extract maximum power from a wind regime. In this novel approach a discrete-time higher order sliding mode controller is designed as an observer to construct the reference value for the extractable power based on the condition that it operates. The presented structure improves performance under abrupt changes in the wind speed, and can be used for any type of optimum active power tracking algorithms. The simulations show the significant improvement in performance of the nonlinear discrete-time backstepping controller utilizing this technique.

B.5 Sliding mode control (SMC)

In [46] a second-order sliding-mode control (2-SMC) scheme for a wind turbine-driven DFIG was proposed. The tasks of grid synchronisation and power control are undertaken by two different algorithms, designed to command the rotor-side converter at a fixed switching frequency. Effective tuning equations for the parameters of both controllers are derived. A procedure is also provided that guarantees bumpless transfer between the two controllers at the instant of connecting the DFIG to the grid. In [47], the main control problem is the estimation of maximum power operating points of wind turbine under stochastic wind velocity profiles and tracking them using conventional offline and innovative adaptive online method. In this control strategy the wind speed and consequent aerodynamics torque is considered as the disturbance. Results under different operating conditions show the superior performance of the proposed online input-output linearization sliding mode technique.

B.6 Backstepping control (BSC)

In [48], the authors proposed a sort of nonlinear backstepping-based algorithm combining with direct power control (DPC) to wind turbine DFIG under normal and especially harmonic grid voltage. The comparative simulation results between vector control (VC) with resonant controller, look-up table DPC (LUT-DPC) and BS-DPC under normal grid voltage verify that the proposed BS-DPC realizes the decoupling control of active and reactive power of DFIG, with better dynamic performance than VC, as well as with better steady performance than LUT-DPC. The proposed backstepping-based direct power control (BS-DPC) in order to control DFIG under normal and harmonic grid voltage situation, which adopts space vector pulse width modulation (SVPWM) in the last step to achieve fixed switching frequency. In [49], the authors proposed a resonant based backstepping direct power control (BS-DPC) strategy for doubly fed induction generator (DFIG) under both balanced and unbalanced grid conditions. Furthermore, a resonant based improved strategy is proposed to achieve different control targets under unbalanced grid condition without the need of decomposition of positive and negative sequence components. In [50], the decoupling control strategy has been applied to control the active and reactive powers generated by a DFIG. A robust nonlinear control based on Backstepping has been proposed with integral actions in order to control the power of the wind turbine transmitted to the grid and to make the wind turbine adaptable to different constraints. The proposed control laws are derived from the Lyapunov approach which is well suited for this nonlinear system. Furthermore, the proposed integral backstepping control is compared with the classical backstepping controller. The results obtained by simulation prove the effectiveness of the control strategies in terms of decoupling, robustness and dynamic performance for different operating conditions. In [51], the main objective of the study is to derive a control strategy which will be applied to a bidirectional converter supplying a DFIG based on the combination of vector and backstepping control. Vector control approach has been initially carried out in order to get a decoupled active and reactive power with proportional-integral compensator (PI). In order to enhance some of the drawbacks of the PI compensator in terms of robustness, transient response

and steady state error a backstepping approach has been used. Simulation study carried out on the DFIG generating both real powers extracted from the turbine and the required reactive power have shown good performances compared to those obtained by using PI compensator for the overall expected performance parameters.

B.7 Predictive Direct power control (PDPC) and Deadbeat control

In [52]; the authors proposed a control scheme for a wind turbine using a DFIG electromechanical converter, implemented through an NPC three-level back to back converter, that keeps a unitary power factor injection to the grid and maximizes the energy harvested from wind, using a maximum power point tracking algorithm (MPPT). A predictive direct power control (PDPC) strategy drives the grid-side converter, to maintain the DC bus reference voltage. Whereas, a predictive direct torque control (DTC) strategy drives the machine-rotor-side converter, to control the power extraction, the power factor and balancing of the DC bus capacitors. Simulation results endorse the effectiveness of the advanced control techniques for the whole wind spectrum, including the pitch angle control. A sensitivity analysis shows that the predictive DTC control strategy is robust with an uncertainty up to 20% of the induction machine parameters. In [53], authors proposed a new control strategy of DFIGs under unbalanced grid voltage conditions. The proposed controller includes a model predictive direct power control (MPDPC) method and a power compensation scheme. In MPDPC, the appropriate voltage vector is selected according to an optimization cost function, hence the instantaneous active and reactive powers are regulated directly in the stator stationary reference frame without the requirement of coordinate transformation, PI regulators, switching table, or PWM modulators. In [54], the application of the model predictive control (MPC) approach was proposed to control the voltage and frequency of a stand alone wind generation system. The MPC is used to calculate the optimal control actions including system constraints. To alleviate computational effort and to reduce numerical problems, particularly in large prediction horizon, an exponentially weighted functional model predictive control (FMPC) is employed. The proposed controller has been tested through step changes in the wind speed and the load impedance. Simulation results show that adequate performance of the proposed wind energy scheme has been achieved. In [55], the authors proposed a power control scheme for doubly fed induction generator for variable speed wind power generation. This scheme uses a deadbeat control loop. The algorithm of the deadbeat calculates at each sample period the voltage vector to be supplied to the rotor in order to guarantee that the active and reactive power reach their desired reference values. The robustness of the controller against rotor resistance variation was evaluated. Simulations results are carried out for validation of the digital controller operation. In [56], the aim is to provide the designing and the modeling of a deadbeat power control scheme for DFIG in accordance with the present state of the art. In this way, the deadbeat power control aims the stator active and reactive power control using the discretized DFIG equations in synchronous coordinate system and stator flux orientation. The deadbeat controller calculates the rotor voltages required to guarantee that the stator active and reactive power reach their desired references values at each sample period using a rotor current space vector loop. Experimental results using a TMS320F2812 platform are presented to validate the proposed controller.

B.8 Input/output Linearizing and decoupling control

In [57], the authors proposed a non-linear control algorithm based on the simplified input-output linearizing and decoupling control (I/OLDC) strategy. Both rotor side controller and grid side controller are presented. The control strategy is implemented and tested in a 160 kW wind power test rig, and the experiment results validate that the simplified input-output linearizing and decoupling control provides improved dynamic responses and decoupled control of the wind turbine driven DFIG. In [58], a new type control strategy for maximum power point tracking (MPPT) of doubly-fed induction generator based wind turbine (DFIG-WT) has been proposed. The strategy adopts proportional-integral (PI) based regulators and feedback linearization control (FLC) based regulators in the power and current control loops of DFIG, respectively. The FLC based regulator can fully decouple and linearize the nonlinear system and provide optimal control performance in a wide range operating conditions. However, since

the FLC strategy might require some unaccessible state variables of the mechanical system, the PI based regulators are able to simplify the control implementation in the power loop. Simulation studies are undertaken in a single-machine system operating under ramp-change and random wind profiles, respectively. Simulation results reveal that the proposed strategy performs better than the conventional vector control (VC) scheme under varying operation conditions.

1.5 References

- [1] Frede. BLAABJERG, Ke MA. "Future on power electronics for wind turbine systems", IEEE Journal of Emerging and Selected Topics in Power Electronics, vol. 1, no. 3, pp: 139-152, 2013
- [2] REN21 – Renewables 2012 Global Status Report [Online]". Available: <http://www.ren21.net>, 2012.
- [3] Frede BLAABJERG; Ke MA, "Wind Energy Systems", Proceedings of the IEEE, vol: 105, no: 11, pp: 2116 – 2131, 2017.
- [4] Green Energy – "The Road to a Danish Energy System without Fossil Fuels [Online]". Available: <http://www.klimakommissionen.dk/en-US/>, 2010.
- [5] Vestas Wind Power, Aarhus, Denmark, "Wind Turbines Overview [Online]". Available: www.vestas.com/, 2011.
- [6] Hyong Sik KIM and Dylan Dah-Chuan LU, "Wind Energy Conversion System from Electrical Perspective -A Survey," Smart Grid and Renewable Energy, vol:1, no: 3, pp: 119-131, 2010
- [7] S. MULLER, M. DEICKE and RikW. De DONCKER, "Doubly fed induction generator systems for wind turbines," IEEE, Industry Applications Magazine, vol: 8, no: 3, pp: 26-33, 2002.
- [8] "Wind Energy Background [Online]". Available: <http://www.dolcera.com>.
- [9] Stephan ENGELHARDT, Istvan ERLICH, Christian FELTES, Jörg KRETSCHMANN, and Fekadu SHEWAREGA, "Reactive Power Capability of Wind Turbines Based on Doubly Fed Induction Generator," IEEE Transaction on Energy Conversion, vol: 26, no: 1, pp: 364-372, 2011.
- [10] "Asynchronous Generators [Online]". Available: <http://www.windturbines.net>.
- [11] Frede RAYMOND, W. FLUMERFELT and Su Su WANG, "Wind turbines," in Access Science, ©Mc Graw-Hill Companies, 2009, <http://www.accessscience.com>.
- [12] Mohamed S. EL-MOURSI, Birgitte Bak-JENSEN, and Mansour H. ABDEL-RAHMAN, "Novel STATCOM controller for mitigating SSR and damping power system oscillations in a series compensated wind park," IEEE Transaction Power Electronics, vol: 25, no: 2, pp: 429-441, 2010.
- [13] Pedro RODRIGUEZ, Adrian V. TIMBUS, Remus TEODORESCU, Marco LISERRE and Frede BLAABJERG, "Flexible active power control of distributed power generation systems during grid faults," IEEE Transactions on Industrial Electronics, vol: 54, no: 5, pp: 2583-2592, 2007.
- [14] Adrian TIMBUS, Marco LISERRE, Remus TEODORESCU, Pedro RODRIGUEZ and Frede BLAABJERG, "Evaluation of current controllers for distributed power generation systems," IEEE Transaction on Power Electronics, vol: 24, no: 3, pp: 654-664, 2009.
- [15] Remus TEODORESCU, Marco LISERRE, and Pedro RODRIGUEZ, "Grid Converters for Photovoltaic and Wind Power Systems", New York, NY, USA: Wiley, 2011.
- [16] Frede BLAABJERG, Remus TEODORESCU, Marco LISERRE, and Adrian V. TIMBUS, "Overview of control and grid synchronization for distributed power generation systems," IEEE Transaction on Industrial Electronics, vol: 53, no: 5, pp: 1398-1409, 2006.

- [17] Sushanta Kumar SENAPATI, "Modelling and Simulation of a Grid Connected Doubly Fed Induction Generator for Wind Energy Conversion System", Master Thesis (English language), National Institute of Technology, Rourkela, INDIA, 2014.
- [18] Andreas PETERSSON, "Analysis, Modeling and Control of Doubly-Fed Induction Generators for Wind Turbines", Chalmers University of Technology, Ph.D. Thesis (English language), Sweden, 2005.
- [19] Kostyantyn PROTSENKO and Dewei XU, "Modeling and Control of Brushless Doubly-Fed Induction Generators in Wind Energy Applications", IEEE Transactions on Power Electronics, vol: 23, no: 3, pp.1191- 1197, 2008.
- [20] Janaka B. EKANAYAKE, Lee HOLDSWORTH, Xueguang WU and Nicholas JENKINS "Dynamic Modeling of Doubly Fed Induction Generator Wind Turbines", IEEE Transactions on Power Systems, vol: 18, no: 2, pp. 803-809, 2003.
- [21] Istvan ERLICH, Jörg KRETSCHMANN, Jens FORTMANN, Stephan MUELLER-ENGELHARDT and Holger WREDE, "Modeling of Wind Turbine Based on Doubly-Fed Induction Generators for Power System Stability Studies", IEEE Transactions on Power Systems, vol: 22, no: 3, pp. 909-919, 2007.
- [22] Istvan ERLICH and F. SHEWAREGA, "Modeling of Wind Turbines Equipped with Doubly-Fed Induction Machines for Power System Stability Studies", IEEE Power Systems Conference and Exposition, pp: 978-985, 2006.
- [23] Alvaro LUNA, Francisco Kleber de ARAUJO LIMA, David SANTOS, Pedro RODRÍGUEZ, Edson H. WATANABE, and Santiago ARNALTES, "Simplified Modeling of a DFIG for Transient Studies in Wind Power Applications", IEEE Transactions on Industrial Electronics, vol: 58, no: 1, pp: 9-20, 2011.
- [24] Ruben PENA, J. C. CLARE and Greg ASHER, "Doubly fed induction generator using back-to-back PWM converters and its application to variable-speed wind energy generation," IEE Proceedings Electric Power Applications, vol. 143, no. 3, pp. 231-241, May 1996.
- [25] Xie ZHEN, Zhang XING, Yang SHUYING, Li QIN and Zhai WENFENG, "Study on Control Strategy of Maximum Power Capture For DFIG in Wind Turbine System", 2nd IEEE International Symposium on Power Electronics Distributed Generation Systems, pp: 110-115, 2010.
- [26] Yunqi XIAO and Pengxiao JIA, "VSCF Wind Turbine Control Strategy for Maximum Power Generation", Proceedings of the 8th World Congress on Intelligent Control and Automation, Jinan, China, pp: 4781-4786, 2010.
- [27] Rajib DATTA and V. T. RANGANATHAN, "A Method of Tracking the Peak Power Points for a Variable Speed Wind Energy Conversion System", IEEE Transactions on Energy Conversion, vol: 18, no: 1, pp: 163-168, 2003.
- [28] Baike SHEN, Bakari MWINYIWIWA, Yongzheng ZHANG and Boon-Teck OOI, "Sensorless Maximum Power Point Tracking of Wind by DFIG Using Rotor Position Phase Lock Loop (PLL)", IEEE Transactions on Power Electronics, vol: 24, no: 4, pp: 942-951, April 2009.
- [29] Changhong SHAO, Xiangjun CHEN and Zhonghua LIANG. "Application Research of Maximum Wind energy Tracing Controller Based Adaptive Control Strategy in WECS", IEEE 5th International Power Electronics and Motion Control Conference, pp: 1-5, 2006.
- [30] Eftichios KOUTROULIS and Kostas KALAITZAKIS, "Design of a Maximum Power Tracking System for Wind-Energy-Conversion Applications", IEEE Transactions on Industrial Electronics, vol: 53, no: 2, pp. 486-494, 2006.
- [31] Wei QIAO, Wei ZHOU, José M. ALLER, and Ronald G. HARLEY, "Wind Speed Estimation Based Sensorless Output Maximization Control for a Wind Turbine Driving a DFIG", IEEE Transactions on Power Electronics, vol: 23, no: 3, pp: 1156-1169, 2008.

- [32] S. CHONDROGIANNIS and Mike BARNES, "Stability of Doubly-Fed Induction Generator under Stator Voltage Orientated Vector Control", IET Renewable Power Generation, vol: 2, no: 3, pp. 170-180, 2008.
- [33] Carles BATLLE, Arnau Doria-CEREZO and Romeo ORTEGA, "A Stator Voltage Oriented PI Controller For The Doubly-Fed Induction Machine", Proceedings of the American Control Conference, New York City, USA, pp. 5438-5443, 2007.
- [34] Chen WANG and George WEISS, "Integral Input-to-State Stability of the Drive- Train of a Wind Turbine", Proceedings of the 46th IEEE Conference on Decision and Control, New Orleans, LA, USA, pp: 6100-6105, 2007.
- [35] Yazhou LEI, Alan MULLANE, Gordon LIGHTBODY, and Robert YACAMINI, "Modeling of the Wind Turbine With a Doubly Fed Induction Generator for Grid Integration Studies", IEEE Transactions on Energy Conversion, vol. 21, no. 1, pp. 257-264, 2006.
- [36] M. TAZIL, V. KUMAR, R. C. BANSAL, S. KONG, Z. Y. DONG, W. FREITAS and H. D. MATHUR, "Three-phase doubly fed induction generators: an overview", IET Electric Power Applications, vol: 4, no: 2, pp: 75-89, 2010.
- [37] Domenico CASADEI, Francesco PROFUMO, Giovanni SERRA and Angelo TANI, "FOC and DTC: Two Viable Schemes for Induction Motors Torque Control", IEEE Transactions on Power Electronics, vol: 17, no: 5, pp: 779-787, 2002.
- [38] K. C. WONG, S. L. HO and K. W. E. CHENG, "Direct Torque Control of a Doubly fed Induction Generator with Space Vector Modulation", Electric Power Components and Systems, vol: 36, no: 12, pp: 1337-1350, 2008.
- [39] Lie XU, and Phillip CARTWRIGHT, "Direct Active and Reactive Power Control of DFIG for Wind Energy Generation", IEEE Transactions on Energy Conversion, vol: 21, no: 3, 2006
- [40] Sung-Tak JOU, Sol-Bin LEE, Yong-Bae PARK, and Kyo-Beum LEE, "Direct Power Control of a DFIG in Wind Turbines to Improve Dynamic Responses", JPE Journal of Power Electronics, vol: 9, no: 5, pp.: 781 - 790, 2012.
- [41] Yerra Sreenivasa RAO, A. Jaya LAXMI, "Direct Torque Control of Doubly Fed Induction Generator based Wind Turbine under Voltage Dips", International Journal of Advances in Engineering & Technology, vol: 3, no: 2, pp.: 711-720, 2012.
- [42] Juan Manuel MAURICIO, Andres E. LEON, Antonio Gomez-EXPOSITO, and Jorge A. SOLSONA, "An Adaptive Nonlinear Controller for DFIM-Based Wind Energy Conversion Systems", IEEE Transactions on Energy Conversion, vol: 23,no: 4, 2008
- [43] Mohamed ABDELRAHEM, Christoph HACKL, Ralph KENNEL, "Sensorless Control of Doubly-Fed Induction Generators in Variable-Speed Wind Turbine Systems", International Conference on Clean Electrical Power (ICCEP), IEEE conference, pp: 406 - 413, 2015.
- [44] Sabrina ABDEDDAIM, Achour BETKA, Said DRID, Mohamed BECHERIF, "Implementation of MRAC controller of a DFIG based variable speed grid connected wind turbine", Energy Conversion and Management, vol: 79, , pp: 281-288, 2014.
- [45] Akbar TOHIDI, Hadi HAJIEGHRARY and M. Ani HSIEH, "Adaptive Disturbance Rejection Control Scheme for DFIG-Based Wind Turbine: Theory and Experiments", IEEE Transactions on Industry Applications, vol: 52, no: 03, pp: 2006-2015, 2016.
- [46] Ana SUSPERREGUI, Miren Itsaso MARTINEZ, Gerardo TAPIA and Ionel VECHIU, "Second-Order Sliding-Mode Controller Design and Tuning for Grid Synchronization and Power Control of a Wind Turbine-Driven Doubly Fed Induction Generator", IET Renewable Power Generation, vol: 7, no: 5, pp: 540-551, 2013.

- [47] Akbar TOHIDI, Ali SHAMSADDINLOU and Ali Khaki SEDIGH, "Multivariable input-output linearization sliding mode control of DFIG based wind energy conversion system", 9th Asian Control Conference (ASCC), , IEEE Conference, pp: 1-6, 2013.
- [48] Pinghua XIONG and Dan SUN, "Backstepping-Based DPC Strategy of a Wind Turbine-Driven DFIG under Normal and Harmonic Grid Voltage", IEEE Transactions on Power Electronics, vol: 31, no: 6, pp: 4216- 4225, 2016.
- [49] Xiaohe WANG, Dan SUN and Z. Q. ZHU, "Resonant-Based Backstepping Direct Power Control Strategy for DFIG under Both Balanced and Unbalanced Grid Conditions", IEEE Transactions on Industry Applications, vol: 53, no: 5, pp: 4821- 4830, 2017.
- [50] M'hamed DOUMI, Abdel Ghani AISSAOUI, Ahmed TAHOUR, Mohamed ABID, and Khalfallah TAHIR, "Nonlinear Integral Backstepping Control of Wind Energy Conversion System Based on a Double-Fed Induction Generator", PRZEGLĄD ELEKTROTECHNICZNY, vol: xx, no: xx, pp: 130 - 135, 2016.
- [51] Riyadh ROUABHI, Rachid ABDESSEMED, Aissa CHOUDER and Ali DJERIOUI, "Hybrid Backstepping Control of a Doubly Fed Wind Energy Induction Generator", The Mediterranean Journal of Measurement and Control, vol: 11, no: 1, 2015
- [52] José SAYRITUPAC; Eduardo ALBÁNEZ; Johnny RENGIFO; José M. ALLER and José RESTREPO, "Predictive control strategy for DFIG wind turbines with maximum power point tracking using multilevel converters", IEEE Workshop on Power Electronics and Power Quality Applications (PEPQA), pp: 1-6, 2015.
- [53] Jiefeng HU, Jianguo ZHU and David G. DORRELL, "Predictive Direct Power Control of Doubly Fed Induction Generators Under Unbalanced Grid Voltage Conditions for Power Quality Improvement", IEEE Transactions on Sustainable Energy, vol: 6, no: 3, pp: 943-950, 2015.
- [54] Ahmed. M. KASSEM, "Predictive Voltage Control of Stand Alone Wind Energy Conversion System", WSEAS TRANSACTIONS on SYSTEMS and CONTROL, vol: 7, no: 3, pp: 97-107, 2012.
- [55] Alfeu . J. SGUAREZI FILHO and Ernesto RUPPERT, "A Deadbeat Active and Reactive Power Control for Doubly Fed Induction Generator", Taylor & Francis Group, LLC, Electric Power Components and Systems, vol: 38, pp: 592-602, 2010.
- [56] Alfeu J. SGUAREZI FILHO and Ernesto RUPPERT, "Modeling and Designing a Deadbeat Power Control for Doubly-Fed Induction Generator", Chapter n°:06 from eBook: "Wind Energy Management"; Edited by Dr Paritosh Bhattacharya, pp: 113-128, 2017.
- [57] Luhua ZHANG, Xu CAI and Jiahu GUO, "Simplified input-output linearizing and decoupling control of wind turbine driven doubly-fed induction generators", IEEE 6th International Power Electronics and Motion Control Conference, pp: 632-637, 2009.
- [58] X. LIN, K. S. XIAHOU, Y. LIU, Y. B. ZHANG and Q. H. WU, "Maximum Power Point Tracking of DFIG-WT Using Feedback Linearization Control Based Current Regulators", IEEE Innovative Smart Grid Technologies - Asia (ISGT-Asia), pp: 718-723, 2016.

Chapter 2 :

Indirect Power Control (IDPC) of DFIG using Classical Controllers under MPPT Strategy.

2.1 Introduction	26
2.2 Mathematical model of DFIG	26
2.3 Conventional Indirect Power Control (IDPC) of DFIG	27
2.3.1 Relationship between rotor voltages and rotor currents(generally form)	28
2.3.2 Relationship between stator power and rotor currents	29
2.3.3 Relationship between rotor voltages and rotor currents(detailed form)	29
2.3.4 Synthesis of the Proportional-Integral (PI) regulator	30
2.4 Wind turbine mathematical model	30
2.4.1 Maximum Power Point Tracking (MPPT) strategy	31
2.5 Grid Side Converter (GSC) and DC-link voltage control	33
2.6 Rotor Side Converter (RSC)	34
2.6.1 Space Vector Modulation (SVM)	35
2.6.2 LC Filter	38
2.7 Operating principle of DFIG	40
2.8 Proposed IDPC based on PID Controllers	42
2.9 Simulation results	43
2.9.1 Conventional IDPC based on PI controllers	44
2.9.2 Proposed IDPC based on PID controllers	49
2.9.3 Power Factor (PF) tests for three (03) modes	54
2.10 Conclusion	55
2.11 References	55

Abstract:

In this chapter, we present a comparative study of conventional Indirect Power Control (IDPC) algorithm of DFIG-Wind turbine in grid-connection mode, using PI and PID controllers via Maximum power point tracking (MPPT) strategy. Firstly, the conventional IDPC based on PI controllers will be described using simplified model of DFIG through stator flux orientation and wind-turbine model. The MPPT strategy is developed using Matlab/Simulink® with two wind speed profiles in order to ensure the robustness of wind-system by maintaining the Power coefficient (C_p) at maximum value and reactive power at zero level; regardless unexpected wind speed variation. Secondly, the rotor side converter (RSC) and Grid side converter (GSC) are illustrated and developed using Space vector modulation (SVM) in order to minimize the stress and the harmonics and to have a fixed switching frequency. In this context, the switching frequency generated by IDPC to control the six IGBTs of the inverter (RSC), and this control algorithm works under both Sub- and Super-synchronous operation modes and depending to the wind speed profiles. The quadrants operation modes of the DFIG are described in details using real DFIG to show the power flow under both modes (motor and generator in the four (04) quadrants). Finally, the conventional IDPC have several drawbacks as: response time, power error and overshoot. In this context, the PID controllers are proposed instead the PI; to improve the wind-system performances via MPPT strategy with/without robustness tests. The obtained simulation results under Matlab/Simulink® show high performances (in terms of power error, power tracking and response time) in steady and transient states despite sudden wind speed variation, whereas big power error and remarkable overshoot are noted using robustness tests, so the proposed IDPC can't offer big improvement under parameter variation.

2.1 Introduction

Wind energy conversion system (WECSs) based on the doubly-fed induction generator (DFIG) dominated the wind power generations due to the outstanding advantages, including small converters rating around 30 % of the generator rating, lower converter cost. Several novel control strategies have been investigated in order to improve the DFIG operation performance [1-2-3] and [4]. Nowadays, since DFIG-based WECSs (figure.2.1) are mainly installed in remote and rural areas [2]. In literature [5] vector control is the most popular method used in the DFIG-based wind turbines (WTs). In most applications, the proportional-integral (PI) controller based Power Vector Control (PVC) scheme is used to control DFIG in wind energy conversion systems [6-7]. Although this control scheme is easy to implement, it has some drawbacks. One of the most important drawbacks of this control scheme is that the performance of the PVC (known also by Indirect Power Control 'IDPC'¹) scheme largely depends on the tuning of the PI controller's parameters (K_p and K_i). Another drawback of this controller is that its performance also depends on the accuracy of the machine parameters and on grid voltage conditions such as harmonic level, distortion, etc. [7]. However, the switching frequency of the converter is still affected significantly by active and reactive power variations and operating speed. In this context, Space Vector modulation (SVM) will present the best solution [8-9] compared to Pulse Width Modulation (PWM) in order to minimize the harmonic and keeping the fixed switching frequency of AC-DC-AC converters (especially in Rotor Side Converter 'RSC'). To extract the maximum power despite sudden variations in wind speed, the maximum power point tracking (MPPT) strategy [10-11-12-13] and [14] is proposed, the stator active power is extracted from wind power and stator reactive power is maintained at zero level to ensure unity power.

In order to improve the performance of the IDPC scheme, Proportional-Integral-Derivate (PID) [15] is proposed instead the PI controllers [16-17-18] to hence wind-system performance in terms of power tracking, power error and overshoot.

In this chapter, a WECS's study was presented which described in details the mathematical model of; the DFIG, the IDPC, the turbine, the MPPT strategy, the GSC, the RSC based on SVM and finally the comparative simulation study of the conventional and proposed IDPC with/without robustness tests to show the improve-ment offered by the proposed control in transient and steady states.

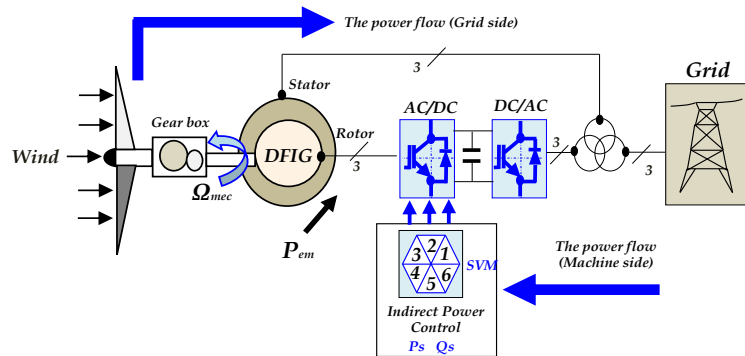


Figure.2.1 Schematic diagram of wind-turbine DFIG based on conventional indirect power control (IDPC).

2.2 Mathematical model of DFIG

The generator chosen for the conversion of wind energy is a double-fed induction generator, DFIG modeling described in the two-phase reference (Park). The general electrical state model of the induction machine obtained using Park transformation is given by the following equations [19-20]: Stator and rotor voltages:

$$V_{sd} = R_s * I_{sd} + \frac{d}{dt} \Phi_{sd} - \omega_s * \Phi_{sq} \quad (2.1)$$

$$V_{sq} = R_s * I_{sq} + \frac{d}{dt} \Phi_{sq} + \omega_s * \Phi_{sd} \quad (2.2)$$

$$V_{rd} = R_r * I_{rd} + \frac{d}{dt} \Phi_{rd} - (\omega_s - \omega_r) * \Phi_{rq} \quad (2.3)$$

¹ In global world literature the Vector Power Control (VPC) is the same as Stator Active and Reactive Power Control under stator flux' orientation, whereas in French literature the VPC is well-known by Indirect Power Control (Commande Indirecte de Puissances).

$$V_{rq} = R_r * I_{rq} + \frac{d}{dt} \Phi_{rq} + (\omega_s - \omega_r) * \Phi_{rd}. \quad (2.4)$$

Stator and rotor fluxes:

$$\Phi_{sd} = L_s * I_{sd} + L_m * I_{rd}. \quad (2.5)$$

$$\Phi_{sq} = L_s * I_{sq} + L_m * I_{rd}. \quad (2.6)$$

$$\Phi_{rd} = L_r * I_{rd} + L_m * I_{sd}. \quad (2.7)$$

$$\Phi_{rq} = L_r * I_{rq} + L_m * I_{sd}. \quad (2.8)$$

The electromagnetic torque is given by:

$$T_{em} = P * L_m * (I_{rd} * I_{sq} - I_{rq} * I_{sd}). \quad (2.9)$$

And its associated motion equations are:

$$T_{vis} = f * \Omega_{mec}. \quad (2.10)$$

$$T_{em} - T_r = J * \frac{d}{dt} \Omega_{mec} + T_{vis}. \quad (2.11)$$

$$J = \frac{J_{turbine}}{G^2} + J_g. \quad (2.12)$$

Where; R_s , R_r , L_r and L_s are respectively the resistances and the inductances of the stator and the rotor of the DFIG. V_{sd} , V_{sq} , V_{rd} , V_{rq} , I_{sd} , I_{sq} , I_{rd} , I_{rq} , Φ_{sd} , Φ_{sq} , Φ_{rd} and Φ_{rq} respectively represent the components along the d and q axes of the stator and rotor voltages, currents and flux. T_{em} , T_r , T_{vis} , T_{aero} and $T_{gearbox}$ present the electromagnetic', load', viscous, aerodynamic' and gearbox torques. J_g , $J_{turbine}$ and J are the generator', turbine' and total inertia in DFIG's rotor respectively, Ω_{mec} is the mechanical speed, and G is the gain of gear box.

The active and reactive powers of DFIG's stator and rotor are respectively:

$$P_s = V_{sd} * I_{sd} + V_{sq} * I_{sq} \quad (2.13)$$

$$Q_s = V_{sq} * I_{sd} - V_{sd} * I_{sq} \quad (2.14)$$

$$P_r = V_{rd} * I_{rd} + V_{rq} * I_{rq} \quad (2.15)$$

$$Q_r = V_{rq} * I_{rd} - V_{rd} * I_{rq} \quad (2.16)$$

The frequency of the stator voltage being imposed by the electrical network (*grid*), the pulsation of the rotational currents (*slip*) is given by:

$$\omega_{slip} = \omega_s - \omega_r \text{ and } (\omega_r = P * \Omega_{mec}) \quad (2.17)$$

Where: ω_r and ω_s represent respectively the pulsations of rotor and stator voltages in *rad/sec*. The angles θ_s and θ_r are obtained respectively by integration of ω_s and ω_r .

$$\theta_s = \int_0^t \omega_s \cdot dt + \theta_{s0}. \quad (2.18)$$

$$\theta_r = \int_0^t \omega_r \cdot dt + \theta_{r0}. \quad (2.19)$$

2.3 Conventional Indirect Power Control (IDPC) of DFIG

The DFIG model can be described by the following state equations in the synchronous reference frame whose axis " d " is aligned with the stator flux vector as shown in *figure.2.2*. [19-20]:

$$\dot{\Phi}_{sd} = L_s * \dot{i}_{sd} + L_m * \dot{i}_{rd} \quad (2.20)$$

$$0 = L_s * \dot{i}_{sq} + L_m * \dot{i}_{rq} \quad (2.21)$$

From the equations of the direct and quadrature components of the stator flux, we obtain the following expressions of the stator currents:

$$i_{sd} = \frac{\Phi_{sd}}{L_s} - \frac{L_m}{L_s} * i_{rd}. \quad (2.22)$$

$$I_{sq} = -\frac{L_m}{L_s} * I_{rq}. \quad (2.23)$$

By replacing in the equations of the rotor flux, it finds:

$$\Phi_{rd} = L_r \left(1 - \frac{L_m^2}{L_s * L_r} \right) * I_{rd} + \frac{L_m}{L_s} * \Phi_{sd} = L_r * \sigma * I_{rd} + \frac{L_m}{L_s} * \Phi_{sd}. \quad (2.24)$$

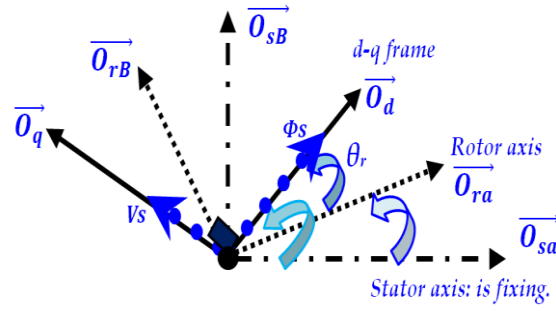


Figure.2.2 Stator and rotor flux vectors in the synchronous d-q frame.

$$\Phi_{rq} = L_r \left(1 - \frac{L_m^2}{L_s L_r}\right) I_{rq} = L_r * \sigma * I_{rq}. \quad (2.25)$$

σ : is the dispersion coefficient between windings d and q :

$$\sigma = 1 - \frac{L_m^2}{L_s L_r}. \quad (2.26)$$

By integrating the equations of the stator currents and the rotor flux into the equations of the stator and rotor voltages, we will have:

$$V_{sd} = \frac{R_r}{L_s} * \Phi_{sd} - \frac{R_r}{L_s} * L_m * I_{rd} + \frac{d\Phi_{sd}}{dt}. \quad (2.27)$$

$$V_{sq} = \frac{R_r}{L_s} * L_m * I_{rq} + \omega_s * \Phi_{sd}. \quad (2.28)$$

$$V_{rd} = R_r * I_{rd} + L_r * \sigma * \frac{dI_{rd}}{dt} + \frac{L_m}{L_s} * \frac{d\Phi_{sd}}{dt} - L_r * (\omega_s - \omega_r) * \sigma * I_{rq}. \quad (2.29)$$

$$V_{rq} = R_r * I_{rq} + L_r * \sigma * \frac{dI_{rq}}{dt} + \frac{L_m}{L_s} * (\omega_s - \omega_r) * \Phi_{sd} + L_r * (\omega_s - \omega_r) * \sigma * I_{rd}. \quad (2.30)$$

For control of the generator, expressions are established showing the relationship between the currents and the rotor voltages applied to it:

$$\frac{dI_{rd}}{dt} = \frac{1}{\sigma * L_r} * (V_{rd} - R_r * I_{rd} - e_d). \quad (2.31)$$

$$\frac{dI_{rq}}{dt} = \frac{1}{\sigma * L_r} * (V_{rq} - R_r * I_{rq} - e_q - e_\phi). \quad (2.32)$$

With the electromotive forces:

$$e_d = \frac{L_m}{L_s} * \frac{d\Phi_{sd}}{dt} - L_m * (\omega_s - \omega_r) * \sigma * I_{rq}. \quad (2.33)$$

$$e_\phi = \frac{L_m}{L_s} * (\omega_s - \omega_r) * \Phi_{sd}. \quad (2.34)$$

$$e_q = L_r * (\omega_s - \omega_r) * \sigma * I_{rd}. \quad (2.35)$$

On the other hand the expression of the electromagnetic torque becomes:

$$T_{em} = P * \left(\frac{L_m}{L_s}\right) * \Phi_{sd} * I_{rq}. \quad (2.36)$$

2.3.1 Relationship between rotor voltages and rotor currents (generally form)

If we neglect the stator resistance, which is a valid assumption for the medium and large power machines used in wind energy. So we simplify the expressions of the stator voltages as follows:

$$V_{sd} = \frac{d\Phi_{sd}}{dt}. \quad (2.37)$$

$$V_{sq} = \omega_s * \Phi_{sd}. \quad (2.38)$$

If we assume that the electrical network is stable, having for simple voltage V_s and for stator pulsation ω_s (supposed constant), this leads to a constant stator flux Φ_{sd} , with a zero variation in steady state, which makes it possible to write:

$$V_{sd} = 0, V_{sq} = \omega_s * \Phi_{sd}. \quad (2.39)$$

So the decoupling relationships are:

$$e_d^* = +L_r * \sigma * (\omega_s - \omega_r) * I_{rq}^* \quad (2.40)$$

$$e_q^* = -L_r * \sigma * (\omega_s - \omega_r) * I_{rd}^* \quad (2.41)$$

From the equation of the slip² (S), we replace $\omega_s - \omega_r$ as follows:

$$S = \frac{\omega_s - \omega_r}{\omega_s} \text{ and } \omega_s - \omega_r = S * \omega_s \quad (2.42)$$

$$e_d^* = +L_r * \sigma * S * \omega_s * I_{rq}^* \quad (2.43)$$

$$e_q^* = -L_r * \sigma * S * \omega_s * I_{rd}^* \quad (2.44)$$

Regulators of rotor currents:

$$V_{rd}^* = PI (I_{rd}^* - I_{rd_meas}). \quad (2.45)$$

$$V_{rq}^* = PI (I_{rq}^* - I_{rq_meas}). \quad (2.46)$$

2.3.2 Relationship between stator power and rotor currents

In a two-phase reference, the stator active and reactive powers of a DFIG are written as follows:

$$P_s = V_{sd} * I_{sd} + V_{sq} * I_{sq} \quad (2.47)$$

$$Q_s = V_{sq} * I_{sd} - V_{sd} * I_{sq} \quad (2.48)$$

With $V_{sd} = 0$ and replacing " I_{sd} " and " I_{sq} " with their expressions, with $\Phi_s = V_s / \omega_s$, we gets:

$$P_s^* = -V_s * \frac{L_m}{L_s} * I_{rq}^* \quad (2.49)$$

$$Q_s^* = \frac{V_s^2}{\omega_s * L_s} - V_s * \frac{L_m}{L_s} * I_{rd}^* \quad (2.50)$$

Regulators of stator powers:

$$I_{rd}^* = PI (Q_s^* - Q_{s_meas}). \quad (2.51)$$

$$I_{rq}^* = PI (P_s^* - P_{s_meas}). \quad (2.52)$$

2.3.3 Relationship between rotor voltages and rotor currents (detailed form)

By replacing the stator currents by their expressions in the rotor flux expressions, we will have:

$$\Phi_{rd} = \left(L_r - \frac{L_m^2}{L_s} \right) * I_{rd} + \frac{L_m * V_s}{\omega_s * L_s} \quad (2.53)$$

$$\Phi_{rq} = \left(L_r - \frac{L_m^2}{L_s} \right) * I_{rq} \quad (2.54)$$

The expressions of the rotor fluxes of d and q axes are introduced into the expressions of the two-phase rotor voltages. We are getting:

$$V_{rd} = R_r * I_{rd} + \left(L_r - \frac{L_m^2}{L_s} \right) * \frac{dI_{rd}}{dt} - S * \omega_s * \left(L_r - \frac{L_m^2}{L_s} \right) * I_{rq} \quad (2.55)$$

$$V_{rq} = R_r * I_{rq} + \left(L_r - \frac{L_m^2}{L_s} \right) * \frac{dI_{rq}}{dt} + S * \omega_s * \left(L_r - \frac{L_m^2}{L_s} \right) * I_{rd} + S * \frac{L_m * V_s}{L_s} \quad (2.56)$$

In steady state, the terms involving derivatives of out of phase rotor currents disappear, so we can write:

$$V_{rd} = R_r * I_{rd} - S * \omega_s * \left(L_r - \frac{L_m^2}{L_s} \right) * I_{rq} \quad (2.57)$$

$$V_{rq} = R_r * I_{rq} + S * \omega_s * \left(L_r - \frac{L_m^2}{L_s} \right) * I_{rd} + S * \frac{L_m * V_s}{L_s} \quad (2.58)$$

With: V_{rd} , V_{rq} : are the out of phase components of the rotor voltages to be imposed on the generator (DFIG) to obtain the desired rotor currents.

$\left(L_r - \frac{L_m^2}{L_s} \right)$: Is the coupling term between the both axes (d and q);

$\left(S * \frac{L_m * V_s}{L_s} \right)$: Represents an electromotive force dependent on the speed of rotation.

Figure.2.3 illustrates the simplified model of the DFIG and figure.2.4 presents the conventional Indirect Power Control (IDPC based on PI controllers) of DFIG.

² In this case the slip varies between $\pm 0.05 \rightarrow \pm 0.07$ (means the stable zone), refer to paragraph §.5.7 (Chapter.5); will be explained by experimental results.

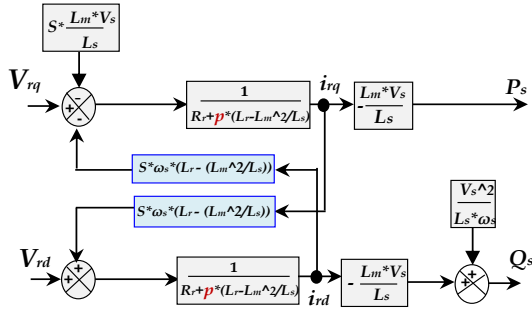


Figure.2.3 The DFIG simplified power model.

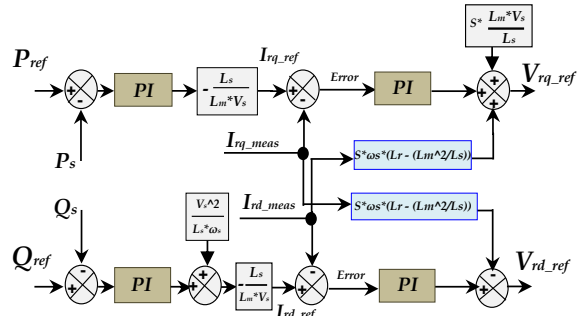


Figure.2.4 DFIG's conventional indirect power control.

2.3.4 Synthesis of the Proportional-Integral (PI) regulator

To carry out the looped control; conventional regulators 'PI' are used. This type of regulator ensures a zero static error thanks to the integral action while the speed of the response is established by the proportional action. The reference quantities for these regulators will be active and reactive power [16-17-18]. Figures.2.5 (a and b) show the PI controller structure with the closed loop transfer function of the wind-system based on PI.

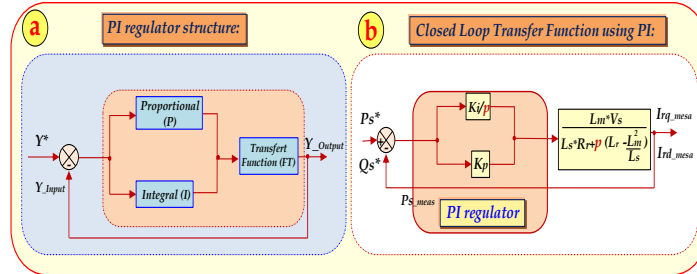


Figure.2.5 Closed loop transfer function topology based on PI controller.

The open loop transfer function (OLTF) with the controllers is written in the following way:

$$OLTF = \frac{p + \frac{K_i}{K_p}}{\frac{p}{K_p}} * \frac{L_m * V_s}{L_s * (L_r - \frac{L_m^2}{L_s})} * \frac{1}{p + (L_r - \frac{L_m^2}{L_s})} \quad (2.59)$$

By the compensation method: $\frac{K_i}{K_p} = L_s * (L_r - \frac{L_m^2}{L_s})$, we get the next OLTF:

$$OLTF = \frac{K_p * \frac{L_m * V_s}{L_s * (L_r - \frac{L_m^2}{L_s})}}{p} \quad (2.60)$$

And the closed loop transfer function (CLTF):

$$CLTF = \frac{1}{1 + \tau_{cl} * p} \quad \text{with} \quad \tau_{cl} = \frac{1}{K_p} * \frac{L_s * (L_r - \frac{L_m^2}{L_s})}{L_m * V_s} \quad (2.61)$$

With τ_{cl} is the response time of the system that is fixed at 10 (ms). Corresponding to a sufficiently fast value for the use made on the wind turbine and where the variations of the wind are not very fast and the mechanical constants time are important. From (2.61), we can determine the gains K_p and K_i according to the parameters of the machine and the response time:

$$K_p = \frac{1}{\tau_{cl}} * \frac{L_s * (L_r - \frac{L_m^2}{L_s})}{L_m * V_s} \quad \text{and} \quad K_i = \frac{1}{\tau_{cl}} * \frac{L_s * R_r}{L_m * V_s} \quad (2.62)$$

2.4 Wind turbine mathematical model

The wind turbine⁴ input power usually is [12-14]:

³ Please refer to Appendix.C (The gains of PI and PID controllers are illustrated in details in Table.C-2).

⁴ Schematic block of wind turbine is described in details in figure.2.6.

$$P_v = \frac{1}{2} * \rho * S_w * v^3 \tag{2.63}$$

Where ρ is air density; S_w is wind turbine blades swept area in the wind; v is wind speed.

The output mechanical power of wind turbine is:

$$P_m = C_p * P_v = \frac{1}{2} * C_p * \rho * S_w * v^3 \tag{2.64}$$

Where power coefficient ⁵ (C_p) represents the wind turbine power conversion efficiency (as shown in figure.2.6). C_p is a non-linear function of Tip Speed Ratio (TSR or λ) and the blade angle β [°]. λ is defined as the ratio of the tip speed of the turbine blades to wind speed. λ is given by:

$$\lambda = \frac{R * \Omega_t}{v} \tag{2.65}$$

Where R is blade radius, Ω_t is angular speed of the turbine. The expression for $C_p(\lambda, \beta)$ can be described as [12-14]:

$$C_p(\lambda, \beta) = (0.5 - 0.0167 * (\beta - 2)) * \sin \left[\frac{\pi * (\lambda + 0.1)}{18.5 - 0.3 * (\beta - 2)} \right] - 0.00184 * (\lambda - 3) * (\beta - 2) \tag{2.66}$$

2.4.1 Maximum Power Point Tracking (MPPT) strategy

The MPPT strategy without wind speed measurement is illustrates in figure.2.8; “So the P_{s_ref} (reference stator power) is calculated by the product of the MPPT’s output (the mechanical speed Ω_{mec}) by the electromagnetic torque T_{em_ref} ”; so $P_{s_ref} = \Omega_{mec} * T_{em_ref}$. Using Matlab/Simulink® to show the behavior of the Power coefficient (C_p) under different pitch angles (B°) as shown in figure.2.9, it is clear the zero pitch angle ($B^\circ = 0^\circ$) offered the maximum C_p which correspond to Optimal Tip Speed Ratio (TSR). Figure.2.10 illustrates the three dimensions (3D) of C_p versus TSR and pitch angles (B°) respectively. The main aim of the MPPT strategy; is to adapt the speed of the turbine to the wind speed, in order to maximize the converted power, this will improve its energy efficiency and its integration with the electrical grid.

In this thesis, two wind speed profiles are proposed (step wind speed and random wind speed), as shown in figure.2.11-(top side of figure.2.11 present the simulation results of the step wind speed and the bottom side of figure.2.11 illustrates the simulation results of random wind speed). From the simulation results of figure.2.11, it can be seen that the maximum value of C_p ($C_{p_max} = 0.4785$) is achieved for $B^\circ = 0^\circ$ and for

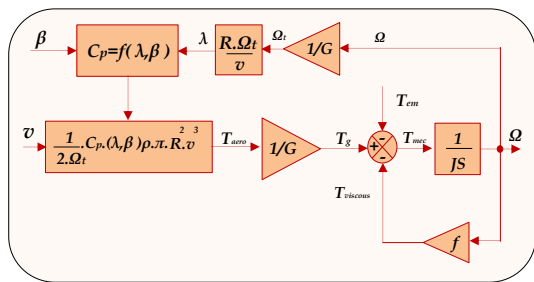


Figure.2.6 Schematic block of wind turbine.

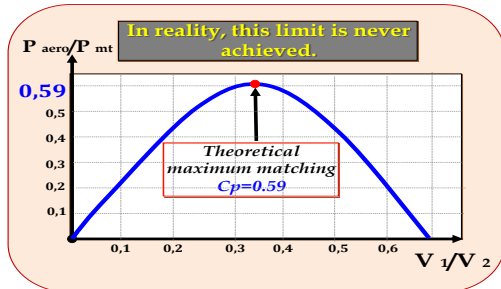


Figure.2.7 Theoretical maximum power coefficient ($C_p = (16/27) \approx 0.59$).

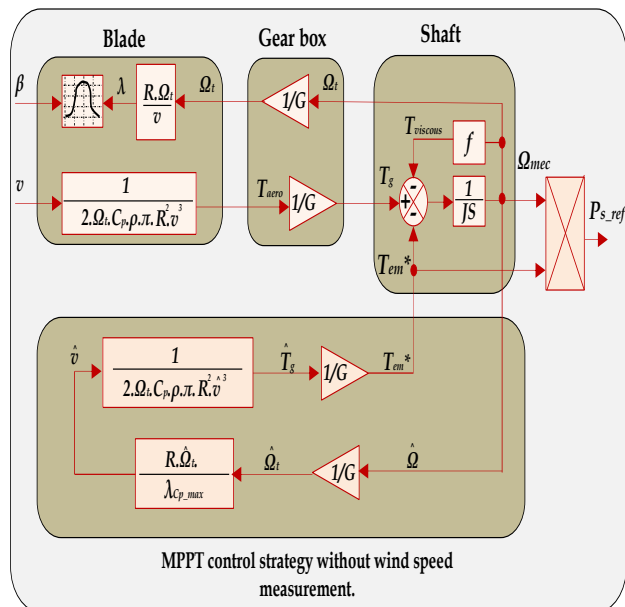


Figure.2.8 MPPT control strategy without wind speed measurement.

⁵ Knowing that in reality $C_p = 16/27 \approx 0.59$; (Betz limit) and this value is never achieved “Ref [18]” as shown in figure.2.7.

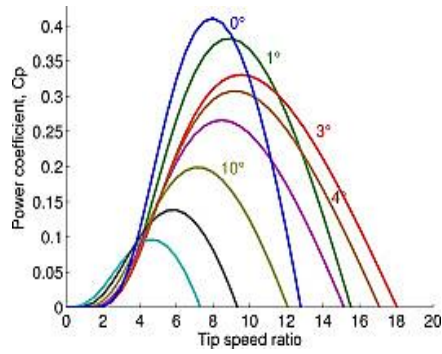


Figure.2.9 C_p under different pitch angles (B°).

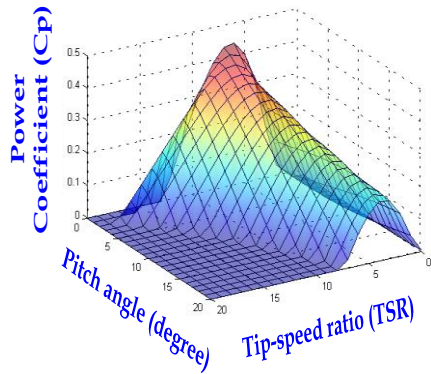


Figure.2.10 3D Power coefficient versus Tip speed ratio (TSR) and Pitch angle degree (B°).

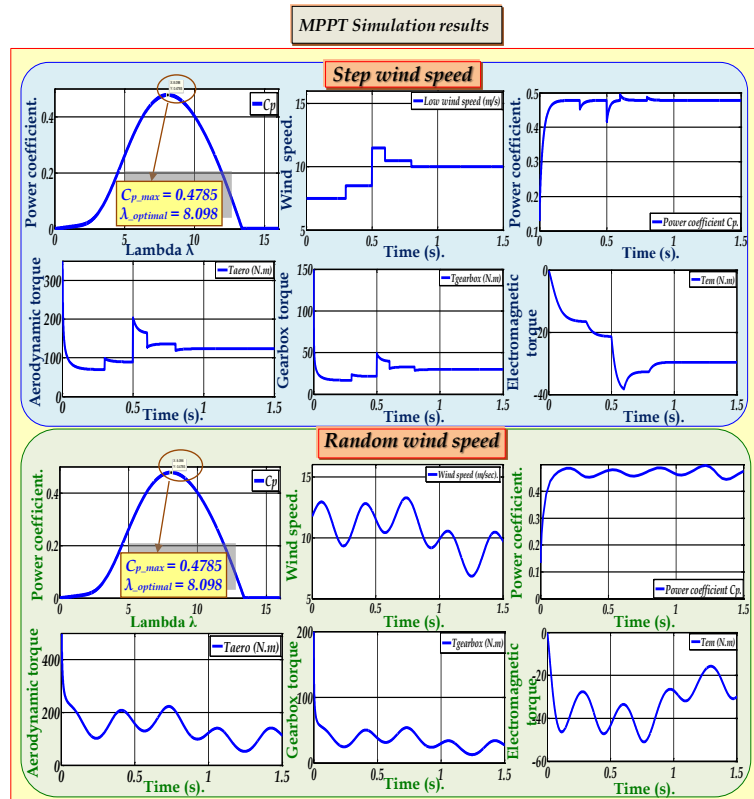


Figure.2.11 Simulation results of MPPT strategy: (C_p versus λ "or" TSR", Wind speed versus time, C_p versus time) T_{aero} , $T_{gearbox}$ and T_{em} using two wind speed profiles.

$\lambda_{opt}=8.098$. This point corresponds at the maximum power point tracking (MPPT) [14] as shown in figure.2.11-(The top-left side of both proposed cases). After the simulation of the wind turbine model using proposed wind pro-files, we test the robustness of the MPPT algorithm; we have as results the C_p versus time for both pro-posed wind speed profiles; this latter achieved the maximum value mentioned in figure.2.11 ($C_{p_max}= 0.4785$) despite the sudden variation of the wind speed. T_{aero} , $T_{gearbox}$ and T_{em} are depicts respectively in figure. 2.11 (at the bottom) for both proposed wind speed. Knowing that: T_{em} takes negative value (Generator mode).

Figure.2.12 illustrates the full circuit topology of a DFIG system with a back-to-back PWM converter, which is composed of a GSC (Grid Side Converter), a RSC (Rotor Side Converter) and a DC-link capacitor.

Though a few schemes of control, the DC-link voltage of the back-to-back PWM converter have been studied [21-22]. In the back-to-back PWM converter of DFIG, the bidirectional power is transferred between the GSC and the RSC.

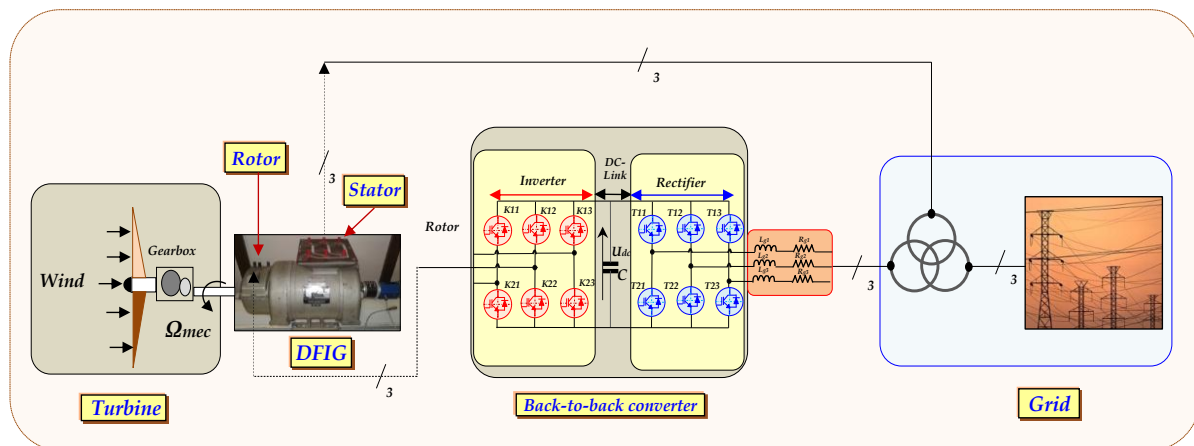


Figure.2.12 Main circuit topology of a back-to-back PWM converter for DFIG.

2.5 Grid Side Converter (GSC) and DC-link voltage control [22, 24]:

Figure.2.13 presents the GSC configuration. In this case, we use balanced network voltages, so we will have the following relationships:

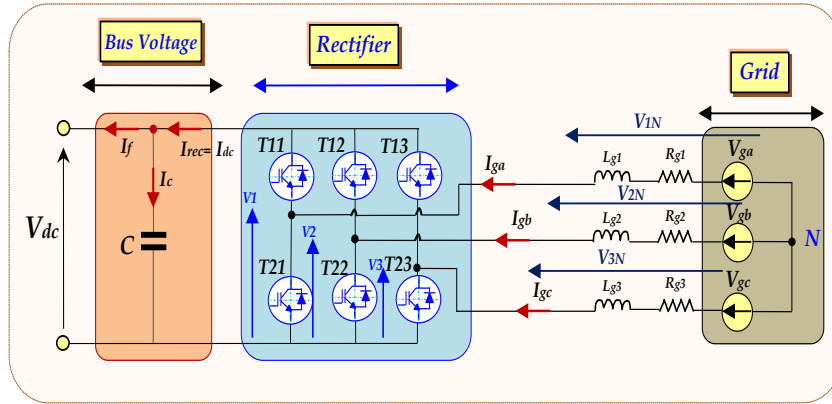


Figure.2.13 GSC configuration.

$$\begin{cases} V_{1N} = \frac{1}{3} * (+2 * V_1 - V_2 - V_3) \\ V_{2N} = \frac{1}{3} * (-V_1 + 2 * V_2 - V_3) \\ V_{3N} = \frac{1}{3} * (-V_1 - V_2 + 2 * V_3) \end{cases} \quad (2.67)$$

According to the closing or the opening of the switches⁶ T_{ij} , the voltages of branch (leg) V_i can be equal to V_{dc} or 0 . Other variables such as S_{11} , S_{12} and S_{13} are introduced which take 1 if the switch T_{ij} is closed or 0 if it is blocked. Equation (2.67) can be rewritten as:

$$\begin{pmatrix} V_{1N} \\ V_{2N} \\ V_{3N} \end{pmatrix} = \frac{V_{dc}}{3} * \begin{pmatrix} +2 & -1 & -1 \\ -1 & +2 & -1 \\ -1 & -1 & +2 \end{pmatrix} * \begin{pmatrix} S_{11} \\ S_{12} \\ S_{13} \end{pmatrix} \quad (2.68)$$

The rectified current can be written as:

$$I_{rec} = S_{11} * I_{ga} + S_{12} * I_{gb} + S_{13} * I_{gc} \quad (2.69)$$

Where S_{ii} presents a logical signal deduced from the application of the control technique of PWM. In this section, the switching signals are determined by the comparison (using hysteresis controllers) between the measured grid currents I_{g_abc} and the reference grid currents $I_{g_abc}^*$.

The terminal voltage of the capacitor is calculated by:

$$C * \frac{dV_{dc}}{dt} = I_c = I_{rec} - I_f = (S_{11} * I_{ga} + S_{12} * I_{gb} + S_{13} * I_{gc}) - I_f \quad (2.70)$$

Figure.2.14 displays the control block diagram of a vector control strategy for the GSC. This grid PWM converter is operated to keep the DC-link voltage at a constant value. The GSC is usually controlled with a vector control strategy with the grid voltage orientation. This voltage frame corresponds to the $d-q$ axes, which makes it possible to decouple the expressions from the active and the reactive power exchanged between the grid and the rotor side. A DC capacitor is used in order to remove ripple and keep the DC-link voltage relatively smooth. Therefore, a hysteresis controller is used in which the error between the desired and actual currents is passed through a controller [23].

The control of active power and consequent control of the DC-link voltage are realized by the intermediary of reference direct grid current I_d^* and the reactive power by the intermediary of reference transversal grid current I_{gq}^* . In order to guarantee the unity power factor ($PF \approx 1$) at the grid-side; the reference transversal grid current I_{gq}^* is maintained to zero value ($I_{gq}^* = 0$ (A)).

⁶ Knowing that: T_{ij} ($i=1, 2$ 'lines' and $j=1, 2, 3$ 'columns').

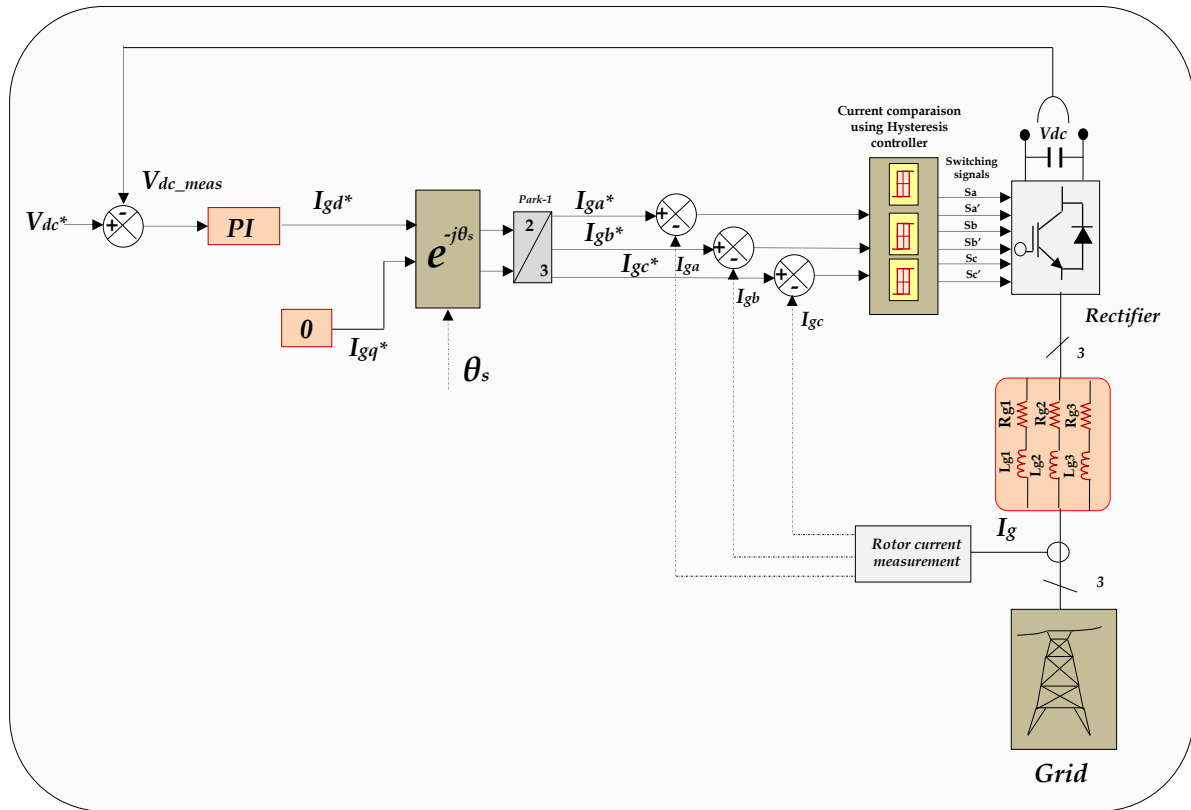


Figure.2.14 Grid side converter topology (DC-link voltage control).

2.6 Rotor side converter (RSC)

The control of the rotor side converter (RSC) enables us to control the stator active and reactive powers independently. From equations (2.49) and (2.50), it's clear that the active and reactive powers are based on the q and d axes rotor currents respectively. Therefore, the powers are checked by controlling the rotor currents. These currents are controlled by PI controllers. Then, we must add terms of compensation and decoupling (figure.2.15 illustrates the global RSC configuration).

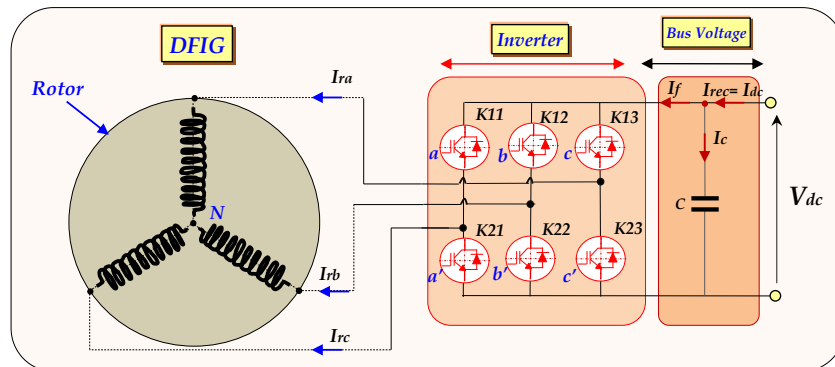


Figure.2.15 RSC configuration (three-phase voltage source PWM Inverter+ DFIG).

The voltages obtained are transformed to 'abc' frame using 'dq' to 'abc' transformation which the angle is the difference between the stator angle obtained using PLL (Phase locked Loop)⁷ and the rotor angle (as shown in figure.2.16). Finally, the 'abc' results voltages are transformed to 'Alpha-Beta' and by the means of the DC bus voltage and sectors; it can be converted to SVM (Space vector modulation) signals in order to control the gates of IGBTs used in the rotor side converter (RSC) as set forth in figure.2.15 [21-24-25].

⁷ Please refer to chapter.6 for more information (paragraph § 6.6.2; a robust PLL is described with descriptive schemes).

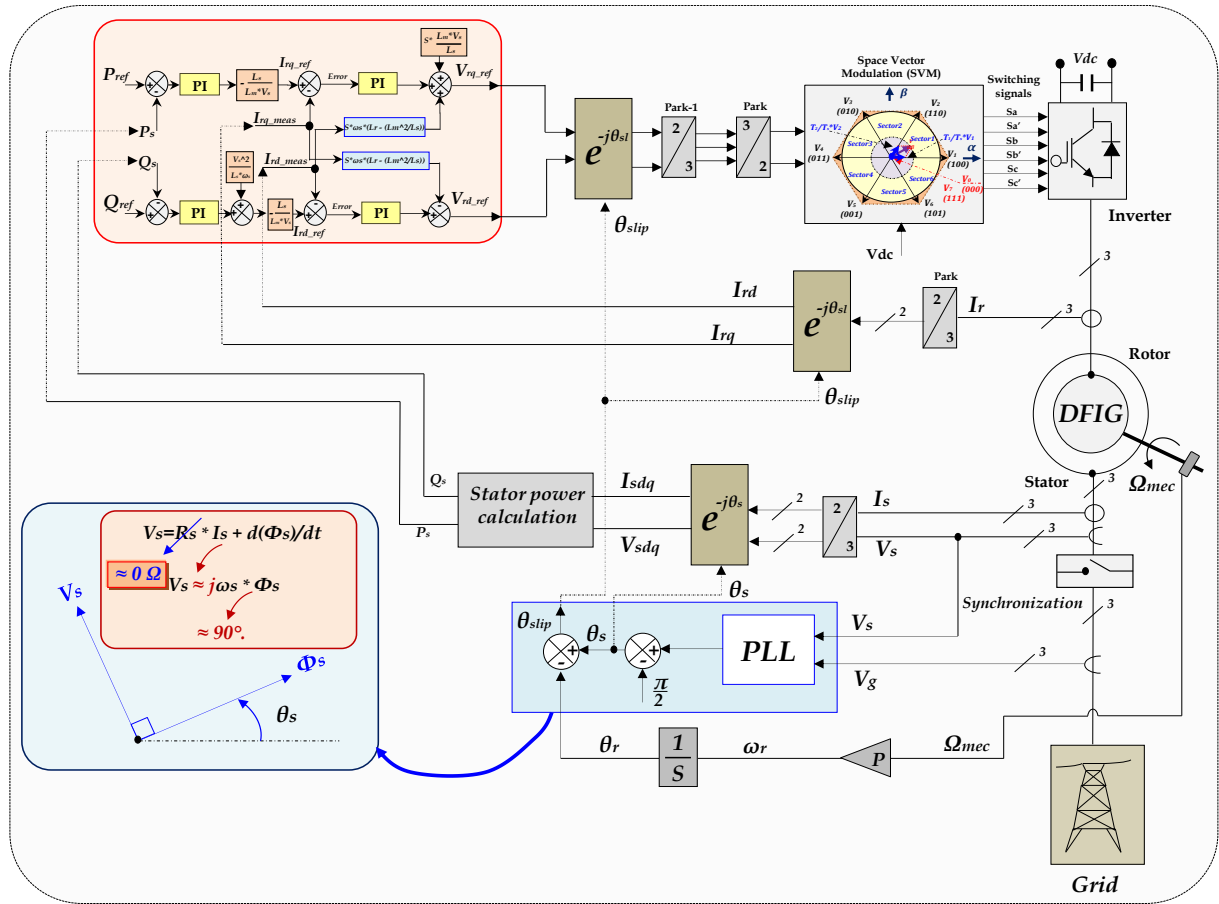


Figure.2.16 Rotor side converter topology (of Indirect Power Control DFIG).

2.6.1 Space Vector Modulation (SVM) [26-27]

The circuit model of a typical three-phase voltage source PWM (Pulse width modulation)⁸ inverter is shown in figure.2.15. K_{11} to K_{23} are the six power switches⁹ that shape the output, which are controlled by the switching variables a, a', b, b', c and c' . When an upper transistor is switched on, i.e., when a, b or c is 1, the corresponding lower transistor is switched off, i.e., the corresponding a', b' or c' is 0. Therefore, the on and off states of the upper transistors K_{11}, K_{12} and K_{13} can be used to determine the output voltage.

The relationship between the switching variable vector $[a, b, c]^t$ and the line-to-line voltage vector $[V_{rab} \ V_{rbc} \ V_{rca}]^t$ is given by equation (2.71) in the following:

$$\begin{pmatrix} V_{rab} \\ V_{rbc} \\ V_{rca} \end{pmatrix} = V_{dc} * \begin{pmatrix} +1 & -1 & 0 \\ 0 & +1 & -1 \\ -1 & 0 & +1 \end{pmatrix} * \begin{pmatrix} a \\ b \\ c \end{pmatrix} \tag{2.71}$$

Also, the relationship between the switching variable vector $[a, b, c]^t$ and the phase voltage vector $[V_a \ V_b \ V_c]^t$ can be expressed below (equation (2.72)).

$$\begin{pmatrix} V_{ran} \\ V_{rbn} \\ V_{rcn} \end{pmatrix} = \frac{V_{dc}}{3} * \begin{pmatrix} +2 & -1 & -1 \\ -1 & +2 & -1 \\ -1 & -1 & +2 \end{pmatrix} * \begin{pmatrix} a \\ b \\ c \end{pmatrix} \tag{2.72}$$

As illustrated in figure.2.15, there are eight possible combinations of on and off patterns for the three upper power switches. The on and off states of the lower power devices are opposite to the upper one and so are easily determined once the states of the upper power transistors are determined.

⁸ Please refer to Appendix.A (illustrates the real time implementation of PWM and SVM strategies using dSPACE1103 with experimental results).

⁹ Knowing that: K_{ij} ($i=1, 2, 3$ 'are the lines' and $j=1, 2, 3$ 'are the columns').

According to equations (2.71) and (2.72), the eight switching vectors, output line to neutral voltage (phase voltage), and output line-to-line voltages in terms of DC-link V_{dc} are given in table.2.1 and figure.2.17 shows the eight inverter voltage vectors (V_0 to V_7).

Table.2.1 Switching vectors, phase voltages and output line to line voltages.

Voltage vectors	Switching vectors:			Line to neutral voltage:			Line to line voltage:		
	a	b	c	V_{an}	V_{bn}	V_{cn}	V_{ab}	V_{bc}	V_{ca}
V_0	0	0	0	0	0	0	0	0	0
V_1	1	0	0	$2/3$	$-1/3$	$-1/3$	+1	0	-1
V_2	1	1	0	$1/3$	$1/3$	$-2/3$	0	+1	-1
V_3	0	1	0	$-1/3$	$2/3$	$-1/3$	-1	+1	0
V_4	0	1	1	$-2/3$	$1/3$	$1/3$	-1	0	+1
V_5	0	0	1	$-1/3$	$-1/3$	$2/3$	0	-1	+1
V_6	1	0	1	$1/3$	$-2/3$	$1/3$	+1	-1	0
V_7	1	1	1	0	0	0	0	0	0

NB: The respective voltage should be multiplied by V_{dc} .

Space Vector PWM (SVPWM) refers to a special switching sequence of the upper three power transistors of a three-phase power inverter. It has been shown to generate less harmonic distortion in the output voltages and or currents applied to the phases of an AC motor and to provide more efficient use of supply voltage compared with sinusoidal modulation technique.

As described in figure.2.18, this transformation is equivalent to an orthogonal projection of $[a, b, c]^t$ onto the two-dimensional perpendicular to the vector $[1, 1, 1]^t$ (the equivalent $d-q$ plane) in a three-dimensional coordinate system. As a result, six non-zero vectors and two zero vectors are possible. Six non-zero vectors ($V_1 - V_6$) shape the axes of a hexagonal as depicted in figure.2.19, and feed electric power to the load. The angle between any adjacent two non-zero vectors is sixty degrees (60°). Meanwhile, two zero vectors (V_0 and V_7) are at the origin and apply zero voltage to the load. The eight vectors are called the basic space vectors and are denoted by $V_0, V_1, V_2, V_3, V_4, V_5, V_6,$ and V_7 . The same transformation can be applied to the desired output voltage to get the desired reference voltage vector V_{ref} in the $d-q$ plane. The objective of space vector PWM technique is to approximate the reference voltage vector V_{ref} using the eight switching patterns. One simple method of approximation is to generate the average output of the inverter in a small period, T to be the same as that of V_{ref} in the same period. Knowing that the main aim of the SVM strategy is to fix the IGBT's switching frequency.

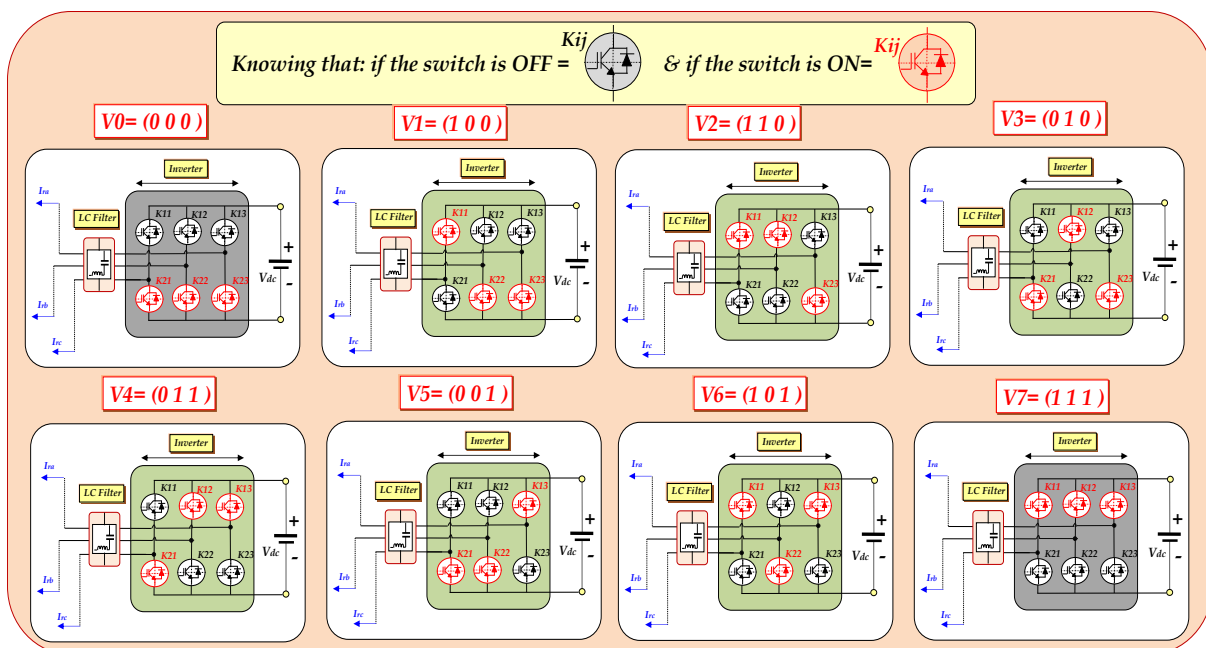


Figure.2.17 The eight inverter voltage vectors (V_0 to V_7).

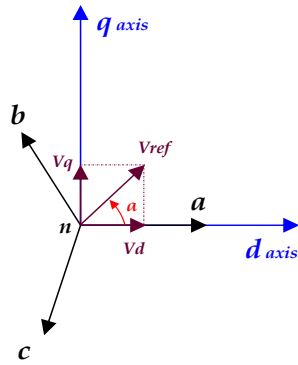


Figure.2.18 Voltage space vector and its components in (d, q) axes.

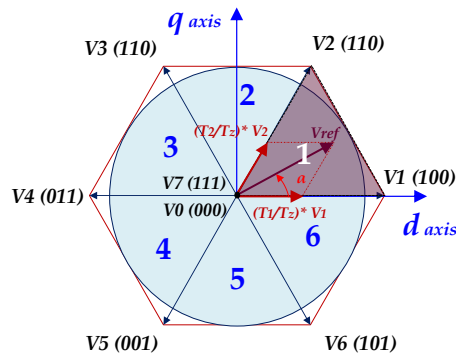


Figure.2.19 The eight (08) basic switching vectors and sectors.

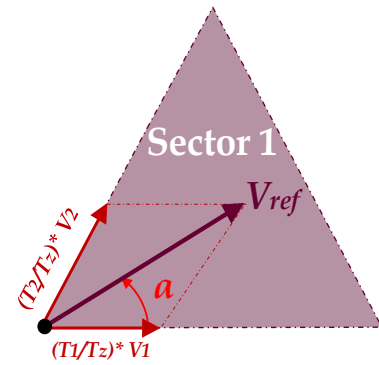


Figure.2.20 Reference vector as a combination of adjacent vectors at sector 1.

Table.2.2 Switching time calculation at each sector.

Sector:	Upper switches (K_{11}, K_{12}, K_{13}):	Lower switches (K_{21}, K_{22}, K_{23}):
1	$K_{11} = T_1 + T_2 + T_0/2$ $K_{12} = T_2 + T_0/2$ $K_{13} = T_0/2$	$K_{21} = T_0/2$ $K_{22} = T_1 + T_0/2$ $K_{23} = T_1 + T_2 + T_0/2$
2	$K_{11} = T_1 + T_0/2$ $K_{12} = T_1 + T_2 + T_0/2$ $K_{13} = T_0/2$	$K_{21} = T_2 + T_0/2$ $K_{22} = T_0/2$ $K_{23} = T_1 + T_2 + T_0/2$
3	$K_{11} = T_0/2$ $K_{12} = T_1 + T_2 + T_0/2$ $K_{13} = T_2 + T_0/2$	$K_{21} = T_1 + T_2 + T_0/2$ $K_{22} = T_0/2$ $K_{23} = T_1 + T_0/2$
4	$K_{11} = T_0/2$ $K_{12} = T_1 + T_0/2$ $K_{13} = T_1 + T_2 + T_0/2$	$K_{21} = T_1 + T_2 + T_0/2$ $K_{22} = T_2 + T_0/2$ $K_{23} = T_0/2$
5	$K_{11} = T_2 + T_0/2$ $K_{12} = T_0/2$ $K_{13} = T_1 + T_2 + T_0/2$	$K_{21} = T_1 + T_0/2$ $K_{22} = T_1 + T_2 + T_0/2$ $K_{23} = T_0/2$
6	$K_{11} = T_1 + T_2 + T_0/2$ $K_{12} = T_0/2$ $K_{13} = T_1 + T_0/2$	$K_{21} = T_0/2$ $K_{22} = T_1 + T_2 + T_0/2$ $K_{23} = T_2 + T_0/2$

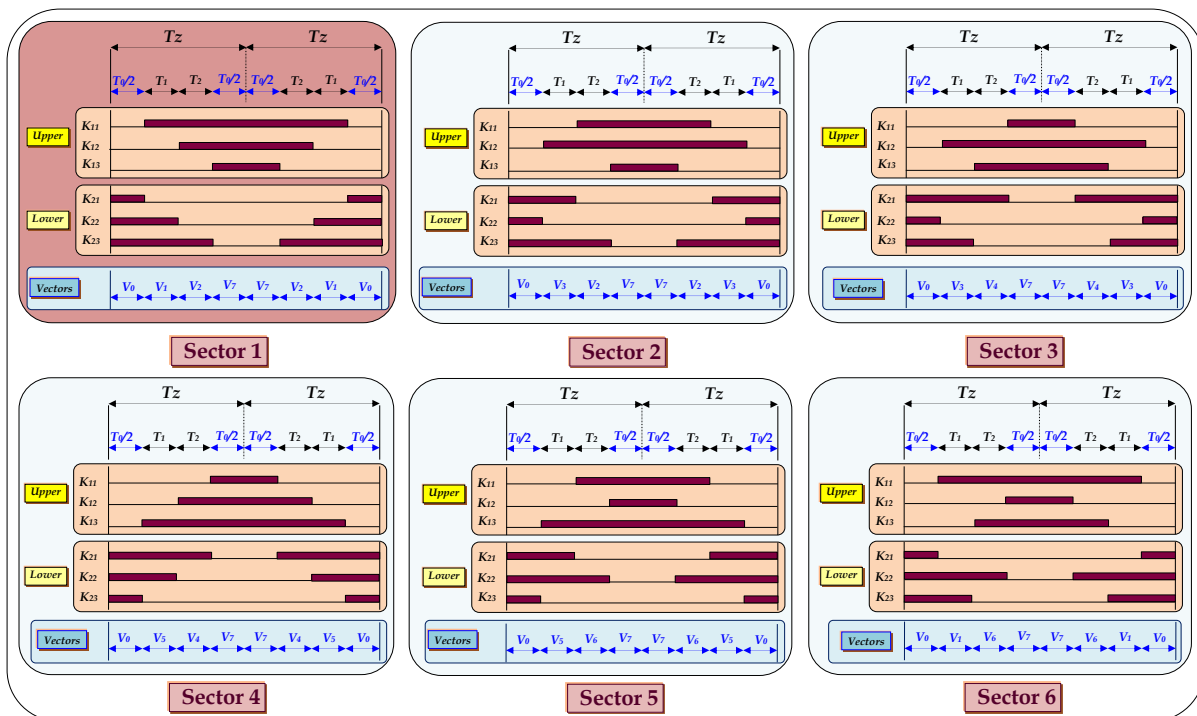


Figure.2.21 Space vector PWM switching patterns at each sector.

Therefore, space vector PWM can be implemented by the following steps:

Step 1: Determine V_d , V_q , V_{ref} , and angle (a):

From figure.2.18, the V_d , V_q , V_{ref} , and angle (a) can be determined as follows:

$$V_d = V_{an} - V_{bn} * \cos(60^\circ) - V_{cn} * \cos(60^\circ) = V_{an} - \frac{1}{2} * V_{bn} - \frac{1}{2} * V_{cn}. \quad (2.73)$$

$$V_q = 0 - V_{bn} * \cos(30^\circ) - V_{cn} * \cos(30^\circ) = V_{an} + \frac{\sqrt{3}}{2} * V_{bn} - \frac{\sqrt{3}}{2} * V_{cn}. \quad (2.74)$$

$$\begin{pmatrix} V_d \\ V_q \end{pmatrix} = \frac{2}{3} * \begin{pmatrix} 1 & -\frac{1}{2} & -\frac{1}{2} \\ 0 & +\frac{\sqrt{3}}{2} & -\frac{\sqrt{3}}{2} \end{pmatrix} * \begin{pmatrix} V_{an} \\ V_{bn} \\ V_{cn} \end{pmatrix}. \quad (2.75)$$

$$|\vec{V}_{ref}| = \sqrt{V_d^2 + V_q^2}. \quad (2.76)$$

$$a = \tan^{-1}\left(\frac{V_q}{V_d}\right) = \omega \cdot t = 2 * \pi * f. \quad (2.77)$$

Where ' f ' is fundamental frequency.

Step 2: Determine time duration T_1 , T_2 , T_0 :

From figure.2.20, the switching time duration can be calculated as follows:

Switching time duration at Sector 1:

$$\int_0^{T_z} \vec{V}_{ref} dt = \int_0^{T_1} \vec{V}_1 dt + \int_{T_1}^{T_1+T_2} \vec{V}_2 dt + \int_{T_1+T_2}^{T_z} \vec{V}_0 dt. \quad (2.78)$$

$$T_z \cdot \vec{V}_{ref} = (T_1 * \vec{V}_1 + T_2 * \vec{V}_2). \quad (2.79)$$

$$T_z \cdot |\vec{V}_{ref}| \cdot \begin{pmatrix} \cos(a) \\ \sin(a) \end{pmatrix} = T_1 * \frac{2}{3} * V_{dc} * \begin{pmatrix} 1 \\ 0 \end{pmatrix} + T_2 * \frac{2}{3} * V_{dc} * \begin{pmatrix} \cos \pi/3 \\ \sin \pi/3 \end{pmatrix} \quad (2.80)$$

Where: $0^\circ \leq a \leq 60^\circ$.

$$T_1 = T_z * a * \frac{\sin(\pi/3 - a)}{\sin(\pi/3)}. \quad (2.81)$$

$$T_2 = T_z * a * \frac{\sin(a)}{\sin(\pi/3)}. \quad (2.82)$$

$$T_0 = T_z - (T_1 + T_2) \quad (2.83)$$

Where: $T_z = (1/f_z)$ and $a = |\vec{V}_{ref}| / (\frac{2}{3} * V_{dc})$.

Switching time duration at any Sector:

$$T_1 = \frac{\sqrt{3} * T_z * |\vec{V}_{ref}|}{V_{dc}} * \left(\sin\left(\frac{\pi}{3} - \alpha + \frac{n-1}{3} \pi\right) \right) = \frac{\sqrt{3} * T_z * |\vec{V}_{ref}|}{V_{dc}} * \left(\sin\left(\frac{n}{3} \pi - \alpha\right) \right) = \frac{\sqrt{3} * T_z * |\vec{V}_{ref}|}{V_{dc}} * \left(\sin\left(\frac{n}{3}\right) \pi \cdot \cos(\alpha) - \cos\left(\frac{n}{3}\right) \pi \cdot \sin(\alpha) \right). \quad (2.84)$$

$$T_2 = \frac{\sqrt{3} * T_z * |\vec{V}_{ref}|}{V_{dc}} * \left(\sin\left(\alpha - \frac{n-1}{3} \pi\right) \right) = \frac{\sqrt{3} * T_z * |\vec{V}_{ref}|}{V_{dc}} * \left(-\cos(\alpha) \cdot \sin\left(\frac{n-1}{3}\right) \pi + \sin(\alpha) \cos\left(\frac{n-1}{3}\right) \pi \right). \quad (2.85)$$

$$T_0 = T_z - (T_1 + T_2) \quad (2.86)$$

Where, $n=1$ through 6 (that is: Sector 1 to 6) and $0^\circ \leq a \leq 60^\circ$.

Step 3: Determine the switching time of each transistor (K_{11} to K_{23})

Figure.2.21 shows space vector PWM switching patterns at each sector. The switching time at each sector is summarized in table.2.2, and it will be built in Simulink model to implement SVM.

2.6.2 LC Filter

Figure.2.22 shows L-C output filter to obtain current and voltage equations. By applying Kirchhoff's current law to nodes a, b, and c, respectively, the following current equations are derived:

Node "1":

$$I_{fa} + I_{ca} = I_{ab} + I_{ra} \Rightarrow I_{fa} + C_f \cdot \frac{dV_{rca}}{dt} = C_f \cdot \frac{dV_{rab}}{dt} + I_{ra}. \quad (2.87)$$

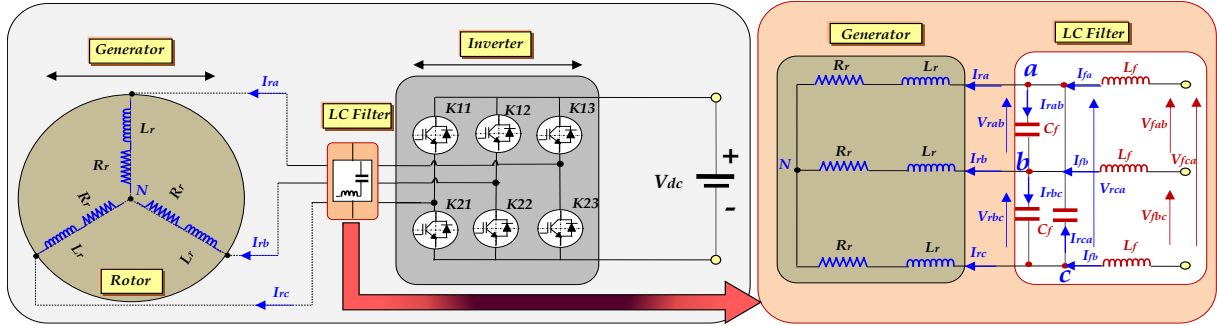


Figure.2.22 Rotor side converter topology with LC-Filter (of Indirect Power Control DFIG).

Node "2":

$$I_{fb} + I_{ab} = I_{bc} + I_{rb} \Rightarrow I_{fb} + C_f \cdot \frac{dV_{rab}}{dt} = C_f \cdot \frac{dV_{rbc}}{dt} + I_{rb}. \quad (2.88)$$

Node "3":

$$I_{fc} + I_{bc} = I_{ca} + I_{rc} \Rightarrow I_{fa} + C_f \cdot \frac{dV_{rbc}}{dt} = C_f \cdot \frac{dV_{rca}}{dt} + I_{rc}. \quad (2.89)$$

Where:

$$I_{ab} = C_f \cdot \frac{dV_{rab}}{dt}, I_{bc} = C_f \cdot \frac{dV_{rbc}}{dt} \text{ and } I_{ca} = C_f \cdot \frac{dV_{rca}}{dt} \quad (2.90)$$

Also, equations: (2.87) to (2.89) can be rewritten as the following equations, respectively:

1/subtracting equations: (2.88) from (2.87):

$$\begin{aligned} I_{fa} - I_{fb} + C_f \cdot \left(\frac{dV_{rca}}{dt} - \frac{dV_{rab}}{dt} \right) &= C_f \cdot \left(\frac{dV_{rab}}{dt} - \frac{dV_{rbc}}{dt} \right) + I_{ra} - I_{rb} \\ \Rightarrow C_f \cdot \left(\frac{dV_{rca}}{dt} + \frac{dV_{rbc}}{dt} - 2 \cdot \frac{dV_{rab}}{dt} \right) &= -I_{fa} + I_{fb} + I_{ra} - I_{rb}. \end{aligned} \quad (2.91)$$

2/subtracting equations: (2.89) from (2.88):

$$\begin{aligned} I_{fb} - I_{fc} + C_f \cdot \left(\frac{dV_{rab}}{dt} - \frac{dV_{rbc}}{dt} \right) &= C_f \cdot \left(\frac{dV_{rbc}}{dt} - \frac{dV_{rca}}{dt} \right) + I_{rb} - I_{rc} \\ \Rightarrow C_f \cdot \left(\frac{dV_{rab}}{dt} + \frac{dV_{rca}}{dt} - 2 \cdot \frac{dV_{rbc}}{dt} \right) &= -I_{fb} + I_{fc} + I_{rb} - I_{rc}. \end{aligned} \quad (2.92)$$

3/subtracting equations: (2.87) from (2.89):

$$\begin{aligned} I_{fc} - I_{fa} + C_f \cdot \left(\frac{dV_{rbc}}{dt} - \frac{dV_{rca}}{dt} \right) &= C_f \cdot \left(\frac{dV_{rca}}{dt} - \frac{dV_{rab}}{dt} \right) + I_{rc} - I_{ra} \\ \Rightarrow C_f \cdot \left(\frac{dV_{rab}}{dt} + \frac{dV_{rbc}}{dt} - 2 \cdot \frac{dV_{rca}}{dt} \right) &= -I_{fc} + I_{fa} + I_{rc} - I_{ra}. \end{aligned} \quad (2.93)$$

To simplify equations: (2.91) to (2.93), we use the following relationship that an algebraic sum of line to line rotor voltages is equal to zero:

$$V_{rab} + V_{rbc} + V_{rca} = 0. \quad (2.94)$$

Based on (2.94), the (2.91) to (2.93) can be modified to a first-order differential equation, respectively:

$$\begin{cases} \frac{dV_{rab}}{dt} = \frac{1}{3 \cdot C_f} * I_{fab} - \frac{1}{3 \cdot C_f} * I_{rab} \\ \frac{dV_{rbc}}{dt} = \frac{1}{3 \cdot C_f} * I_{fbc} - \frac{1}{3 \cdot C_f} * I_{rbc} \\ \frac{dV_{rca}}{dt} = \frac{1}{3 \cdot C_f} * I_{fca} - \frac{1}{3 \cdot C_f} * I_{rca} \end{cases} \quad (2.95)$$

Where : $I_{fab} = I_{fa} - I_{fb}$, $I_{fbc} = I_{fb} - I_{fc}$, $I_{fca} = I_{fc} - I_{fa}$ and $I_{rab} = I_{ra} - I_{rb}$, $I_{rbc} = I_{rb} - I_{rc}$, $I_{rca} = I_{rc} - I_{ra}$.

By applying Kirchoff's voltage law on the side of inverter output, the following voltage equations can be derived:

$$\begin{cases} \frac{dI_{fab}}{dt} = \frac{1}{L_f} * V_{rab} + \frac{1}{L_f} * V_{fab} \\ \frac{dI_{fbc}}{dt} = \frac{1}{L_f} * V_{rbc} + \frac{1}{L_f} * V_{fbc} \\ \frac{dI_{fca}}{dt} = \frac{1}{L_f} * V_{rca} + \frac{1}{L_f} * V_{fca} \end{cases} \quad (2.96)$$

By applying *Kirchhoff's* voltage law on the rotor side, the following voltage equations can be derived:

$$\begin{cases} V_{rab} = L_r \frac{dI_{ra}}{dt} + R_r * I_{ra} - L_r \frac{dI_{rb}}{dt} - R_r * I_{rb} \\ V_{rbc} = L_r \frac{dI_{rb}}{dt} + R_r * I_{rb} - L_r \frac{dI_{rc}}{dt} - R_r * I_{rc} \\ V_{rca} = L_r \frac{dI_{rc}}{dt} + R_r * I_{rc} - L_r \frac{dI_{ra}}{dt} - R_r * I_{ra} \end{cases} \quad (2.97)$$

Equation (2.97) can be rewritten as:

$$\begin{cases} \frac{dI_{rab}}{dt} = -\frac{R_r}{L_r} * I_{rab} + \frac{1}{L_r} * V_{rab} \\ \frac{dI_{rbc}}{dt} = -\frac{R_r}{L_r} * I_{rbc} + \frac{1}{L_r} * V_{rbc} \\ \frac{dI_{rca}}{dt} = -\frac{R_r}{L_r} * I_{rca} + \frac{1}{L_r} * V_{rca} \end{cases} \quad (2.98)$$

Therefore, we can rewrite (2.95), (2.96) and (2.98) into a matrix form, respectively:

$$\begin{cases} \frac{dV_r}{dt} = \frac{1}{3 * C_f} * I_f - \frac{1}{3 * C_f} * I_r \\ \frac{dI_f}{dt} = -\frac{1}{L_f} * V_r + \frac{1}{L_f} * V_f \\ \frac{dI_r}{dt} = \frac{1}{L_r} * V_r - \frac{R_r}{L_r} * I_r \end{cases} \quad (2.98)$$

Where: $V_r = [V_{rab} \ V_{rbc} \ V_{rca}]^T$, $I_f = [I_{fab} \ I_{fbc} \ I_{fca}]^T = [I_{fa}-I_{fb} \ I_{fb}-I_{fc} \ I_{fc}-I_{fa}]^T$, $V_f = [V_{fab} \ V_{fbc} \ V_{fca}]^T$, $I_r = [I_{rab} \ I_{rbc} \ I_{rca}]^T = [I_{ra}-I_{rb} \ I_{rb}-I_{rc} \ I_{rc}-I_{ra}]^T$.

Finally, the given plant model (2.98) can be expressed as the following continuous-time state space equation:

$$\dot{x}(t) = A \cdot x(t) + B \cdot u(t) \quad (2.99)$$

Where:

$$x = \begin{bmatrix} V_r \\ I_f \\ I_r \end{bmatrix}_{9 \times 1} \quad A = \begin{bmatrix} 0_{3 \times 3} & \frac{1}{3 \cdot C_f} \cdot I_{3 \times 3} & -\frac{1}{3 \cdot C_f} \cdot I_{3 \times 3} \\ -\frac{1}{L_f} \cdot I_{3 \times 3} & 0_{3 \times 3} & 0_{3 \times 3} \\ \frac{1}{L_{rotor}} \cdot I_{3 \times 3} & 0_{3 \times 3} & -\frac{R_{rotor}}{L_{rotor}} \cdot I_{3 \times 3} \end{bmatrix}_{9 \times 9} \quad B = \begin{bmatrix} 0_{3 \times 3} \\ \frac{1}{L_f} \cdot I_{3 \times 3} \\ 0_{3 \times 3} \end{bmatrix}_{9 \times 3}, \quad u = [V_f]_{3 \times 1}$$

2.7 Operating principle of DFIG

In spite of the disadvantages associated with the slip-rings, the wound-rotor induction machine has long been a wind electric generator choice. By using a suitable integrated approach in the design of a WECS, use of a slip-ring induction generator has been found to be economically competitive. Control of grid-connected and isolated variable-speed wind turbines with a doubly fed induction generator has been implemented and reported [28-29].

A wound-rotor induction machine can be operated as a doubly-fed induction machine (DFIM) when a power converter is present in its rotor circuit. This converter directs the power flow into and out of the rotor windings. Because the DFIM can operate as either a motor or a generator at sub-synchronous and super-synchronous speeds¹⁰, there exist four operational modes in which the DFIM operates. All the four modes are explained in *figure .2.23*. When the machine runs above synchronous speed, this operation is termed super-synchronous operation. Similarly, operation below synchronous speed is called sub-synchronous operation. In both sub- and super-synchronous operation, the machine can be operated either as a motor or a generator. In the motoring mode of operation, the torque produced by the machine is positive. On the other hand, during generating operation, the machine needs mechanical torque as input; thus, the torque is negative during generating operation. The principle of a DFIM control in these modes can be understood more clearly by the power-flow diagram given in *figure.2.25*. In this figure, P_s is the stator power, P_r is the rotor power, and P_m is the mechanical

¹⁰ In French literature, Sub-synchronous and Super-synchronous speeds are replaced by "Hypo-synchrone and Hyper-synchrone".

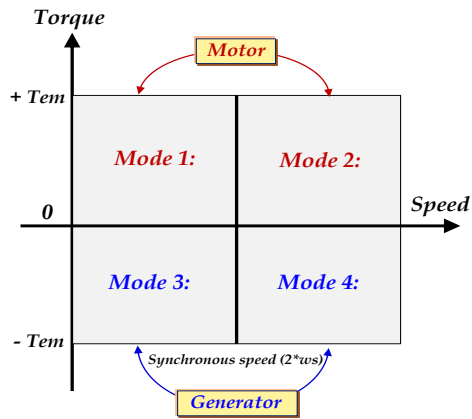


Figure.2.23 Operating modes of a DFIM: Mode 1 (Sub-synchronous motoring mode), Mode 2 (Super-synchronous motoring mode), Mode 3 (Sub-synchronous generating mode), and Mode 4 (Super-synchronous generating mode).

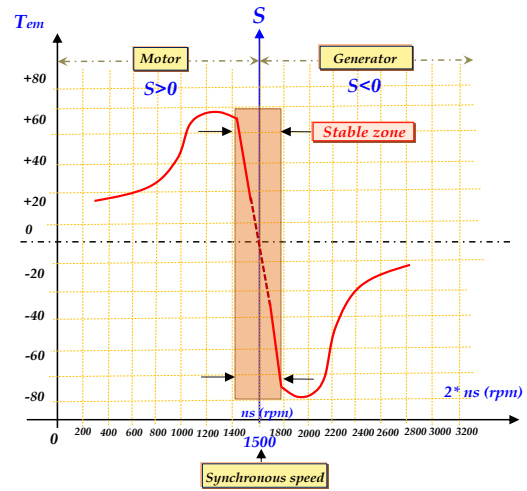


Figure.2.24 DFIM's torque/speed characteristic in 04 quadrants.

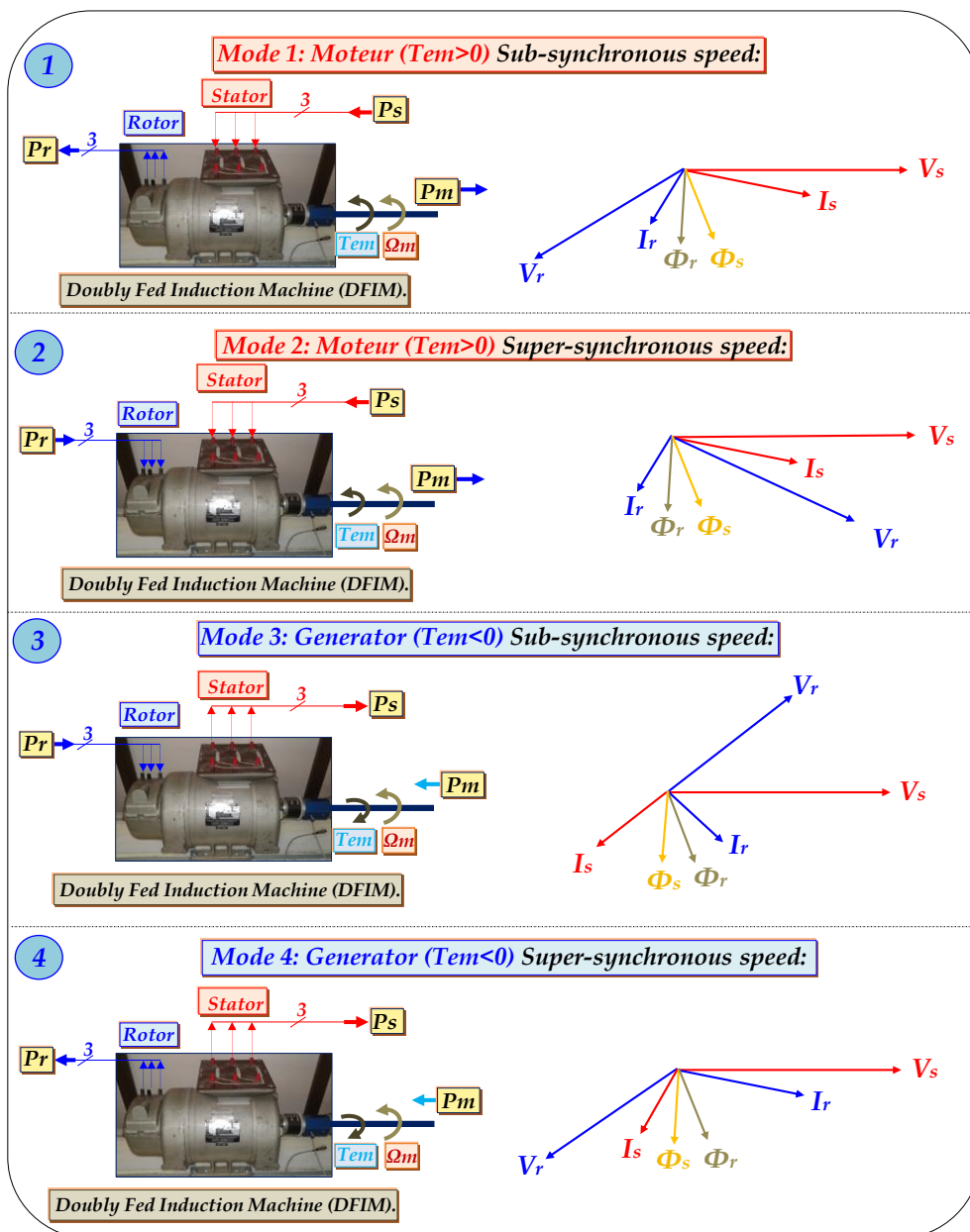


Figure.2.25 Power-flow diagram of a DFIM for (1): Sub-synchronous motoring mode, (2): Super-synchronous motoring mode, (3): Sub-synchronous generating mode, and (4): Super-synchronous generating mode.

power. When the *DFIM* is operating as a motor in the sub-synchronous speed range (figure 2.25-[1]), power is taken out of the rotor. This operational mode is commonly known as slip-power recovery. If the speed increases so that the machine is operating at super-synchronous speeds (figure 2.25-[2]), the rotor power then changes direction [28-29].

When the *DFIM* is operating as a generator in the sub-synchronous speed range (figure .2.25-[3]), power is delivered to the rotor. If the speed increases so that the machine is operating at super-synchronous speeds (figure.2.25-[4]) the rotor power again changes direction.

Because the machine will be predominantly working as a generator for a wind-energy application, operation in *Mode 3* and *Mode 4* is more important than *Mode 1* and *Mode 2*. However, for an ideal WECS system, all four operating modes are desirable. Motoring modes are useful when the generator needs to speed up quickly in order to achieve the best operating speed and efficiency [28]. However, because of the high inertia of the wind generator power train, the acceleration of the machine may be achieved by the wind torque itself. Hence, motoring operations may be sacrificed if the cost of the system can be reduced substantially. Figure.2.24 displays the *Torque/Speed* characteristic of *DFIM* in four (04) quadrants under both modes: *Motoring and Generating*.

It should be noted that for Sub- and Super-synchronous generating modes, the power flows through the rotor are of opposite directions. Hence, the power converter connected with such system should have bi-directional power flow capability.

2.8 Proposed IDPC based on PID Controllers

Proportional-Integral-Derivative (*PID controller*¹¹) is widely used in industrial control system. *PID* controller has all the necessary dynamics: fast reaction on change of the controller input (*D controller*), increase in control signal to lead error towards zero (*I controller*) and suitable action inside control error area to eliminate oscillations (*P controller*). Derivative mode improves stability of the system and enables increase in gain K_p , which increases speed of the controller response. The output of *PID* controller consists of three terms the error signal, the error integral and the error derivative. The error signal is computed by equation (2.100). Figure.2.26 shows the block diagram of *PID* controller. The transfer function of *PID* controller is expressed as [30]:

$$\frac{Y}{Y_{ref}} = K_p + \frac{K_i}{p} + K_d \cdot p \tag{2.100}$$

Where K_p is the proportional gain, K_d is the derivative gain, K_i is the integral gain, and $Y(s)$ is the output control signal which represent stator active and reactive power (P_s and Q_s) respectively. Figure.2.27 illustrates the proposed *IDPC* scheme (The inputs are = P_s, Q_s , and the output are= V_{rd}, V_{rq}).

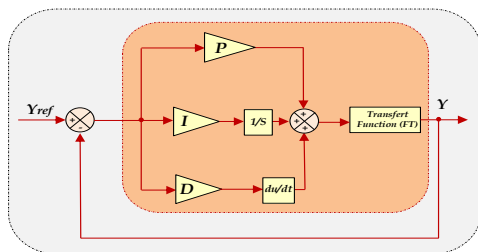


Figure.2.26 Proportional-Integral-Derivative controller topology.

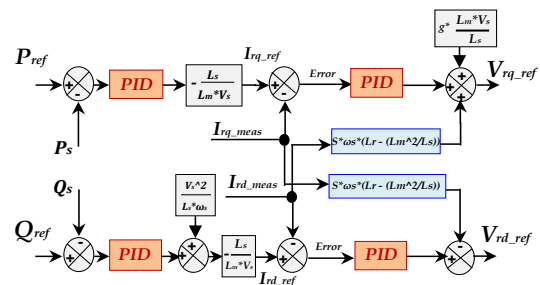


Figure.2.27 Proposed IDPC (based on PID) of DFIG.

Figure.2.28 presents the whole proposed *IDPC* control which is composed on six (06) important parts as follows; 1: Back-to-back two level converter (based on SVM strategy), 2: The proposed power profiles, 3: The MPPT strategy under three (03) proposed mode, 4: SVM modulation strategy, 5: proposed *IDPC* (based on *PID* controllers) and 6: *PID* block diagram.

¹¹ Please refer to Appendix.C (PID's gain values are mentioned in table.C.2).

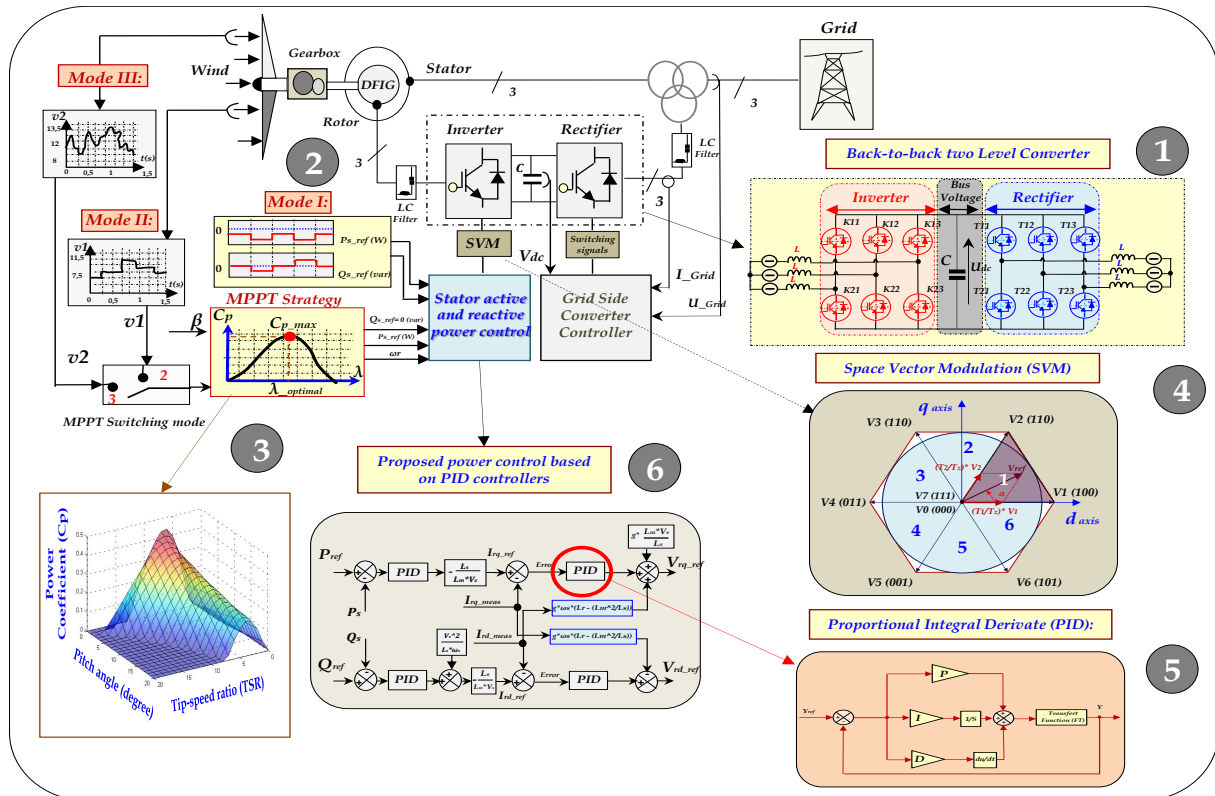


Figure.2.28 The proposed wind turbine-DFIG algorithm (based on PID) using 3 MPPT modes.

2.9 Simulation results

The proposed system (DFIG control + wind turbine)¹² is validated using Matlab/Simulink® software under MPPT strategy by keeping stator reactive power equals to zero and to ensure unity power factor (PF=1). The figures.2-(29 and 32) respectively presents the simulation results for conventional IDPC and proposed IDPC using PI and PID respectively under two level converters. These figures are divided into three parts; the left part (red color) presents the simulation results of the wind system without using the MPPT strategy by imposing stator active and reactive power profiles, in the middle (blue color) depicts the simulation results of the wind-system under MPPT strategy using step form of wind speed; Which it can only illustrate Sub-synchronous mode because the generator speed is still less than the synchronous speed, and finally at right part (green color) illustrates the simulation results of the wind-system under MPPT strategy using random form of wind speed; which can illustrate both modes; Sub- and Super-synchronous mode because the generator speed vary above and below the synchronous speed. The three (03) modes applied in simulation section in transient and steady states are described as flows:

- 1- **Mode I (Red color/** to the left side of figures.2-(29 and 32)): Without MPPT Strategy, in this case we impose the P_s and Q_s reference profiles.
- 2- **Mode II (Blue color/** to the middle of figures.2-(29 and 32)): With MPPT strategy, in this case we propose a low wind speed based on step form (Max wind speed = 11.5 m/sec) by keeping stator reactive power equal to Zero level " $Q_s = 0$ (Var)"; to ensure only the exchange of the stator active power to the grid; means following the maximum active power point.
- 3- **Mode III (Green color/** to the right side of figures.2-(29 and 32)): With MPPT strategy, in this case we propose a medium wind speed based on random form (Max wind speed = 13.5 m/sec) by keeping stator reactive power equal to Zero level " $Q_s = 0$ Var"; to ensure only the exchange of the stator active power to the grid; means following the maximum active power point.

¹² Please refer to Appendix A :(The DFIG' and wind turbine parameters are indicated in Table.A.1 and Table.A.2 respectively).

The second part focuses on the comparative simulation study between the MPPT strategy (using step' and random wind speed) for conventional and proposed IDPC algorithms (using PI and PID respectively) is described in details in figures.2-(30 and 33) respectively. This section is developed in order to illustrate the Sub- and Super-synchronous modes and the behavior of slip under generator speed variation.

The third part deals on robustness tests using a comparative simulation study, for three modes (with/without MPPT strategy) for conventional and proposed IDPC algorithms (using PI and PID respectively) is described in details in figures.2-(31 and 34) respectively. This section is developed in order to verify the robustness of wind-system under parameter variation (using three tests)¹³ in transient and steady states.

2.9.1 Conventional IDPC (based on PI controllers)

The simulation results of this topology (conventional IDPC based on PI controllers) are described in details in figures.2-(29 and 30). Figure.2.29 shows the behavior of the wind-system (using DFIG (4 kW) and wind turbine (4.5 kW)) under three modes (that already presented above) in transient and steady states. Following are detailed description of the simulation results under three (03) modes:

Mode 1 (red color/figure.2.29 to the left side): The measured stator active and reactive powers (P_{s_meas} and Q_{s_meas}) and their references (P_{s_ref} and Q_{s_ref}) profiles are presented together in figure.2.29-(a) and are presented separately in figures.2.29.(b and c) respectively. The reference powers are indicated in table.2.3. It is clear that the measured powers (active and reactive) have bad tracking power (big error) compared to their reference powers in transient and steady states (refer to figure.2.29-(b and c)), a remarkable (70%) overshoot is noted at 0.2, 0.4, 0.6, 0.8, 1.0, 1.2, 1.4 and 1.5 (sec) respectively in measured stator active' and reactive power (P_{s_meas} and Q_{s_meas}) (because the PI controller is not robust in terms of overshoot especially if the step power' changement is big). The direct and quadrature components of currents and flux (I_{rd} , I_{rq} and Φ_{rd} , Φ_{rq}) are presented respectively in figure.2.29-(e and g), which present the inverse diagrams compared to reactive and active powers. The inverse case for stator direct and quadrature currents (I_{sd} , I_{sq}) which have the same diagrams of reactive and active powers, and they are presented in figure.2.29-(d). The power error is presented in figure.2.29-(f); we observe a big power error of active and reactive powers $-200 \text{ (W_Var)} \leq \Delta P_s \Delta Q_s \leq +200 \text{ (W_Var)}$. The stator' and rotor currents; I_{s_abc} and I_{r_abc} are shown in figure.2.29-(h and i) respectively, we remark the sinusoidal form of the three rotor and stator phases currents. The power factor (PF) of the conventional control is presented in figure.2.29-(j), knowing that PF is the ratio of P to S (apparent power), had the top value (with remarkable ripples) when the reactive power equals to zero value; refer to these time interval in figures.2.29-(a, b, c and j): 0-0.3 (sec), 0.9-1.0 (sec) and 1.2-1.5(sec); and this is the main aim of MPPT strategy/keeping at any time the unity power factor regardless wind speed variation. In 1.0-1.2 (sec) remarkable ripples are noted. Table.2.4 depicts in details the obtained results of the conventional IDPC based on PI for Mode: I.

Mode 2 (blue color/figure.2.29 to the middle): The reference stator active power (P_{s_ref}) (figure.2.29-(a)) is extracted from MPPT strategy (in this case, the wind speed will take step form); it takes the inverse diagram of wind speed. The stator reactive power (Q_{s_ref}) equals to 0 (Var), represents power factor unity. It is clear that the poor power tracking of the measured powers compared to their reference powers in transient and steady states, a remarkable overshoot (40%) is noted at 0.6 (sec) in measured stator reactive' and active power (P_{s_meas} and Q_{s_meas}) (because the PI controller is not so robust in terms of overshoot especially if the wind power' changement is big). The direct and quadrature components of currents and flux (I_{rd} , I_{rq} and Φ_{rd} , Φ_{rq}) are presented respectively in figures.2.29-(e and g), which present the inverse diagrams compared to reactive and active powers. The inverse case for stator direct and quadrature currents (I_{sd} , I_{sq}) which have the same diagrams of reactive and active powers, and they are presented respectively in figure.2.29-(d). The power error is presented in figure.2.29-(f), we observe a big power error of active and reactive powers $-180 \text{ (W_Var)} \leq \Delta P_s \Delta Q_s \leq +180 \text{ (W_Var)}$. The stator' and rotor currents; I_{s_abc} and I_{r_abc} are shown in figures.2.29-(h and i) respectively, we rem-

¹³ Knowing that in this chapter the robustness tests are based on three tests as follows: [Test-1: without parameter changement → Blue color, Test-2: +100% of R_r and -25% of (L_s , L_r and L_m) → Brown color and Test-3: +100% of (J and R_r), -25 % of (L_r , L_s and L_m) → Green color] respectively.

Table.2.3 The proposed profiles of the active and reactive power references.

Time (sec):	Stator active power (W):	Stator reactive power (Var):
[0 - 0.2]	-700.	0.
[0.2-0.4]	-1400.	-1400.
[0.4-0.6]	-700.	0.
[0.6-0.8]	-1400.	+1400.
[0.8-1.0]	-700.	0.
[1.0-1.2]	-1400.	-1400.
[1.2-1.4]	-700.	0.
[1.4-1.5]	-1400.	+1400.

mark the sinusoidal form of the waveforms with ripples. The power factor (PF) of the conventional control is presented in figure.2.29-(j), knowing that PF is the ratio of P to S (apparent power), it reaches the top value when the reactive power equals to zero value, in this case the stator reactive power equals to zero value means the PF had taken always the unity; and this is the main aim of MPPT strategy/keeping at any time the unity power factor regardless wind speed variation. Table.2.4 described in details the obtained results of the conventional IDPC based on PI for Mode: II.

Mode 3 (green color/figure.2.29 to the right): The reference stator active power (P_{s_ref}) (figure.2.29-(a)) is extracted from MPPT strategy (in this case, the wind speed will take random form); it takes the inverse diagram of wind speed. The stator reactive power (Q_{s_ref}) equal to 0 (Var), represents power factor unity. It is clear that the measured powers (active and reactive) have acceptable tracking with remarkable undulations (big error) compared to their reference powers in transient and steady states, a big overshoot (40%) is noted at 0.5 (sec) and 0.8 (sec) in measured stator reactive' and active power (P_{s_meas} and Q_{s_meas}) (because the PI controller is not so robust in terms of overshoot especially if the wind power' chngement is big). The direct and quadrature components of currents and flux (I_{rd} , I_{rq} and Φ_{rd} , Φ_{rq}) are presented respectively in figures.2.29-(e and g), which present the inverse diagrams compared to reactive and active powers. The inverse case for stator direct and quadrature currents (I_{sd} , I_{sq}) which have the same diagrams of reactive and active powers, and they are presented in figure.2.29-(d). The power error is depicted in figure.2.29-(f), we observe a big power error of active and reactive powers $-250 (W_Var) \leq \Delta P_s _ \Delta Q_s \leq +250 (W_Var)$. The stator' and rotor currents; I_{s_abc} and I_{r_abc} are shown in figures.2.29-(h and i) respectively, we remark the sinusoidal form of the waveforms with presence of undulations. The power factor (PF) of the conventional control is presented in figure.2.29-(j), knowing that PF is the ratio of P to S (apparent power), it reaches top the value when the reactive power equals to zero value (refer to these time interval in figures.2.29-(a, b and j): and this is the main aim of MPPT strategy/ keeping at any time the unity power factor regardless wind speed variation. Table.2.4 described in details the obtained results of the conventional IDPC based on PI for Mode: III.

MPPT Strategy: Knowing that in the left side of figure.2.30 (Mode: II); the wind speed had taken the step form and in the right side of figure.2.30 (Mode: III); the wind speed had taken the random form. Figure.2.30-(a) presents the stator active and reactive powers and its references profiles using conventional IDPC based on PI for pitch angle equals to 0° ($B^\circ=0^\circ$) means the maximum power. It can be seen that the measured powers (active and reactive) follow theirs references despite the sudden variation of wind speed) in transient and steady states with a poor tracking power (remarkable ripples and undulation are noted). Figures.2.30-(b) illustrate the stator active power under different pitch angle ($B^\circ=0^\circ, 1^\circ, 1.5^\circ, 2^\circ$ and 2.05°), it can be seen the inverse proportionality between the active powers and pitch angle and big undulations were noted. Figures.2.30-(c) illustrate the stator reactive power under different pitch angle ($B^\circ=0^\circ, 1^\circ, 1.5^\circ, 2^\circ$ and 2.05°), it is clear that the reactive power doesn't maintain the zero level despite the pitch angle variation (the maximum wind power is reached at $B^\circ=0^\circ$ "black color" as mentioned from MPPT strategy/refer to §2.4.1) and big power error was noted due to wind speed variation especially at 0.6 (sec) which present the DFIG' rated power (4 kW). Figure.2.30-(d) depicts the wind speed forms; figure.2.30-(d/to the left) presents the step wind speed (maximum value equals to 11.5 m/sec) and figure.2.30-(d/to the right) displays the random wind speed (maximum value equals to 13.5 m/sec). Figure.2.30-(e) presents the generator speed (rpm); figure.2.30-(e/to the left) presents the generator speed (<1500 rpm) means the Sub-synchronous operation, noted by '1') and figure.2.30-(e/to the right) displays the generator speed (below and above the synchronous speed (1500 rpm) means the Sub-synchronous and Super-synchronous operations noted by '1' and '2' respectively). Figure.2.30-(f) displays the power coefficient (C_p); figure.2.30-(f/to

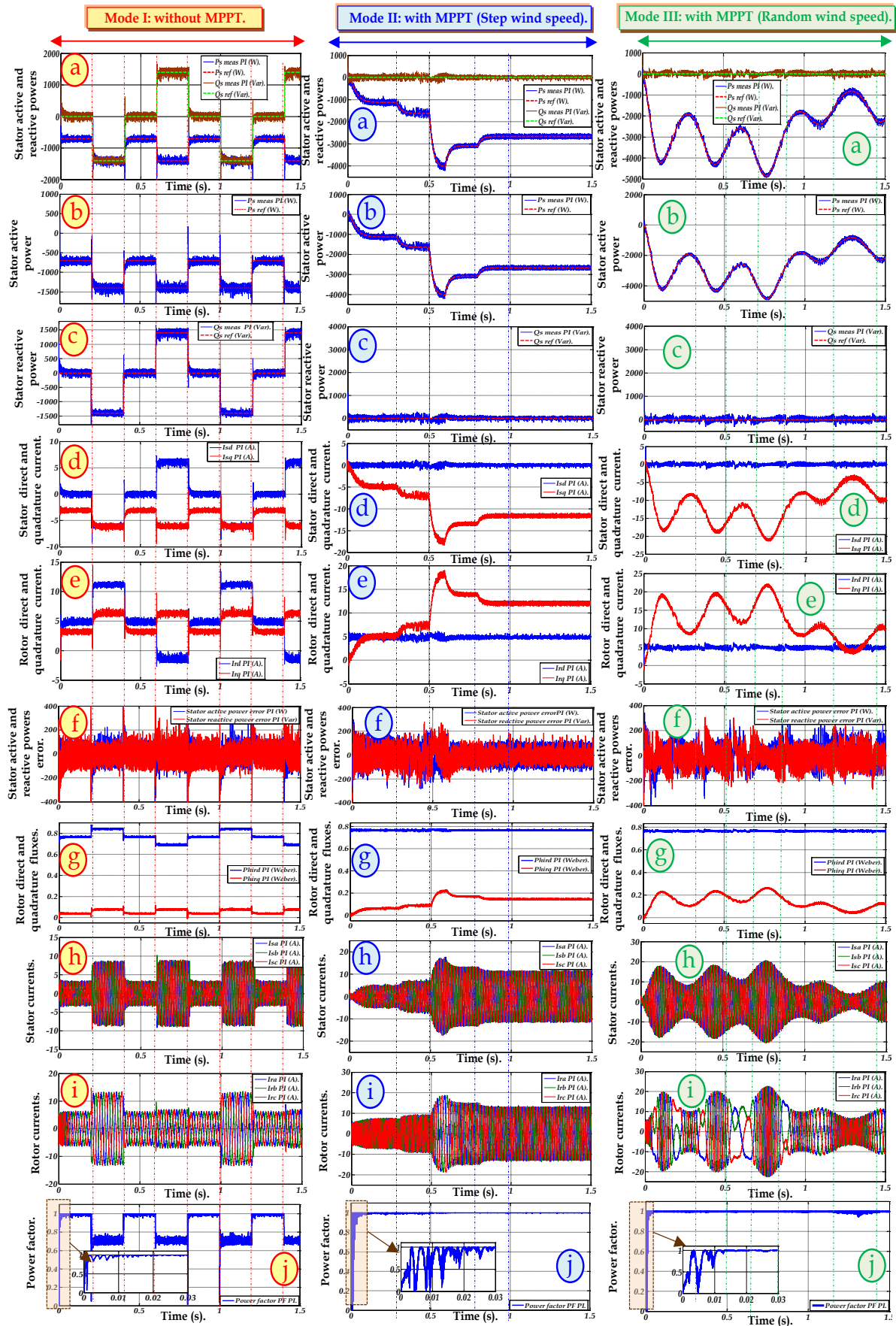


Figure.2.29 Simulation results of conventional control based on PI using three (03) modes; (a): stator active and reactive powers, (b): stator active power, (c): stator reactive power, (d): stator direct and quadrature currents, (e): rotor direct and quadrature currents, (f): stator active and reactive power error, (g): rotor direct and quadrature fluxes, (h): stator currents, (i): rotor currents, (j): power factor.

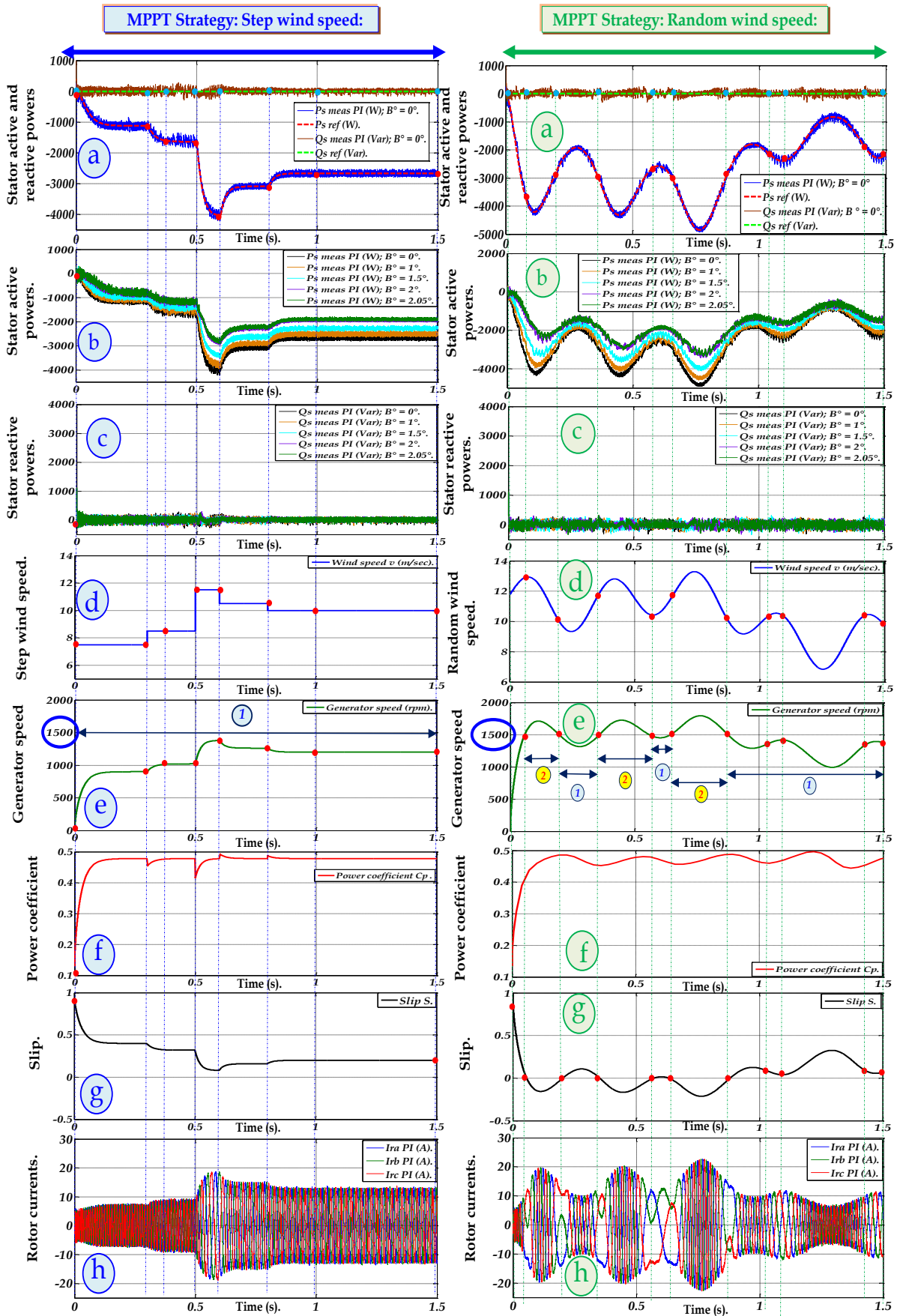


Figure.2.30 Simulations results of two modes MPPT strategy for conventional control based on PI; (a): stator active and reactive powers, (b): stator active power using different B° pitch angles, (c): stator reactive power using different pitch angles B° , (d): wind speed, (e): generator speed, (f): power coefficient, (g): slip, (h): rotor currents.

this case C_p had maintained the maximum value despite of wind speed variation. Figure.2.30-(g) displays the slip (S) behavior during the generator speed variation; figure.2.30-(g/to the left) illustrates the behavior of S under generator speed variation, in this case S varies between '+1' and '0' $\rightarrow 0 < S \leq +1$ means the generator speed didn't reach the synchronous speed (always < 1500 (rpm)), figure.2.30-(g/to the right) represents the S behavior under generator speed variation, in this case S varies between '+1' and '-1' $\rightarrow -1 < S \leq +1$ means the generator speed varies below and above the synchronous speed (superior and inferior 1500 (rpm)), in the case when S reaches zero value means the mechanical speed $N_r=1500$ (rpm) this case called the synchronous mode (because S equals $(N_s-N_r)/N_s$), for exp: in the case of mechanical speed $N_r=1500$ (rpm) and $N_s =1500$ (rpm) $= (60*f)/P = (60*50) /2 =1500$ (rpm) means $S = (1500-1500)/1500 = 0$ is the stable zone, please refer to Appendix.A, DFIG's parameters (Table.A.1). Figure.2.30-(h) displays the behavior of rotor currents under generator speed variation; figure.2.30-(h/to the left) illustrates the sinusoidal waveforms of rotor currents with remarkable ripples (in this case the rotor currents did not change the sense because the Slip (S) did not reach the zero value) and figure.2.30-(h/to the right) demonstrates the rotor currents behavior under generator speed variation, it can be seen the rotor currents had changed the sense in the case when S equals to zero value means when the generator speed varied near the synchronous speed.

Robustness tests¹⁴: Knowing that in the left side of figure.2.31-(Mode: I/without MPPT strategy); the middle side of figure.2.31-(Mode: II/ using step wind speed) and right side of figure.2.31-(Mode: III/ using random wind speed). In Mode: I (red color), figures.2.31-(a and b/to the left) illustrate the behavior of stator active and reactive powers under parameters variations. It can be noted big power in active and reactive power especially using the 2nd test (brown color/please refer to the bottom of the page) and 3rd test (green color) with remarkable undulations especially in transient and steady states (please refer to zoom) and the value of power error reaches nearly ± 200 (W_Var) in Test-1, and nearly ± 1000 (W_Var) in Test-2 and Test-3. A remarkable overshoot is noted under all robustness tests at: 0.2, 0.4, 0.6, 0.8, 1.0 1.2, 1.4 and 1.5 (sec). Figures.2.31-(a and b/to the mid-

Table.2.4 Recapitulation results for classical control (based on PI)¹⁵.

	THD I_{s_abc} (%) :	THD I_{r_abc} (%) :	Overshoot (%) :	Response time (Sec):	Power Error (W_Var) :
Mode I:	01.23 %	50.74 %	Remarquable ($\approx 70\%$).	$1 * 10^{-3}$.	+/- 200.
Mode II:	0.78 %	36.46 %	Remarquable ($\approx 40\%$).	$1,3 * 10^{-3}$.	+/- 180.
Mode III:	0.42 %	36.46 %	Remarquable ($\approx 40\%$).	$1,3 * 10^{-3}$.	+/- 250.

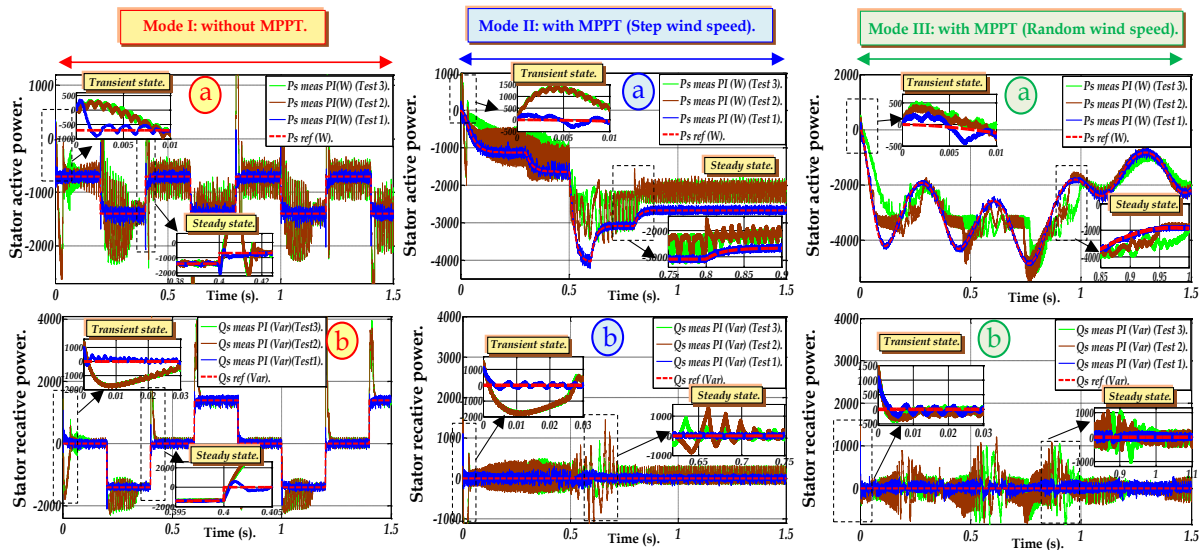


Figure.2.31 Robustness tests of conventional control based on PI using three (03) modes; (a): stator active powers, (b): stator reactive powers.

¹⁴ Knowing that in this chapter the robustness tests are based on three tests as follows: [Test-1: without parameter changment \rightarrow Blue color, Test-2: +100% of R_r and -25% of (L_s, L_r and L_m) \rightarrow Brown color and Test-3: +100% of (J and R_r), -25 % of (L_r, L_s and L_m) \rightarrow Green color] respectively.

¹⁵ Knowing that the recapitulations results of tables.2-(4 and 5) are taken without robustness test.

-dle) display the behavior of stator active and reactive powers under MPPT strategy by maintaining the reactive power equals to zero value. In this case the active power had taken the inverse step profile of wind speed. Using robustness tests a remarkable undulations are noted (using tests: 2 and 3) especially at 0.6 (sec) which presents the rated power of DFIG ($P=4$ (kW)), on other hand and in the same time a remarkable power error is noted in stator reactive power (which means that the PI controllers can't maintain the unity power factor under maximum wind power and parameters variation), also a very big overshoot is noted in transient and steady states of active and reactive power. Figures.2.31-(a and b/to the right) display the behavior of stator active and reactive powers under MPPT strategy by maintaining the reactive power equals to zero value. In this case the active power had taken the inverse random profile of wind speed. Using robustness tests a remarkable undulations are noted (using tests: 2 and 3) especially at 0.75 (sec) and 0.8 (sec) which presents the over rated power of DFIG ($P=4$ (kW) and the measured active power maintain 4.6 (kW)), on other hand and in the same time a remarkable power error is noted in stator reactive power (which means that the PI controllers can't maintain the unity power factor under maximum wind power), also a very high overshoot is noted in transient and steady states of active and reactive power.

2.9.2 Proposed IDPC (based on PID controllers)

The simulation results of this topology (proposed IDPC based on PID controllers) are described in details in figures.2-(32 and 34). Figure.2.32 presents the behavior of the wind-system (using DFIG (4 kW) and wind turbine (4.5 kW)) under three modes in transient and steady states. Following are detailed description of the simulation results under three (03) modes:

Mode 1 (red color/figure.2.32 to the left side): The measured stator active and reactive powers (P_{s_meas} and Q_{s_meas}) and their references (P_{s_ref} and Q_{s_ref}) profiles are presented together in figure.2.32-(a) and are presented separately in figures.2.32.(b and c) respectively. The reference powers are indicated in table.4.2. It is clear that the measured powers (active and reactive) have good tracking power of the measured powers compared to their reference powers in transient and steady states (refer to figure.2.32-(b and c)), a neglected overshoot (<5%) is noted in time interval: 0 (sec) to 1.0 (sec) respectively in measured stator reactive' and active power (P_{s_meas} and Q_{s_meas}) (because the PID controller is robust in terms of overshoot especially if the step power' changement is big). The direct and quadrature components of currents and flux (I_{rd} , I_{rq} and Φ_{rd} , Φ_{rq}) are presented respectively in figure.2.32-(e and g), which present the inverse diagrams compared to reactive and active powers. The inverse case for stator direct and quadrature currents (I_{sd} , I_{sq}) which have the same diagrams of reactive and active powers, and they are presented in figure.2.32-(d). The power error is presented in figure.2.32-(f); we observe a few power error of active and react-ve powers -80 (W_Var) $\leq \Delta P_s \Delta Q_s \leq +80$ (W_Var). The stator' and rotor currents; I_{s_abc} and I_{r_abc} are shown in figure.2.32-(h and i) respectively, we remark the sinusoidal form of the three rotor and stator phases currents with neglected ripples. The power factor (PF) of the proposed control is presented in figure.2.32-(j), knowing that PF is the ratio of P to S (apparent power), took the top value when the reactive power equals to zero value; refer to these time interval in figures.2.32-(a, b, c and j): 0-0.3 (sec), 0.9-1.0 (sec) and 1.2-1.5(sec); and this is the main aim of MPPT strategy/keeping at any time the unity power factor regardless wind speed variation. In 1.0-1.2 (sec) neglected ripples are noted. Table.2.5 described in details the obtained results of the proposed IDPC based on PID for Mode: 1.

Mode 2 (blue color/figure.2.32 to the middle): The reference stator active power (P_{s_ref}) (figure.2.32-(a)) is extracted from MPPT strategy (in this case, the wind speed will take step form); it takes the inverse diagram of wind speed. The stator reactive power (Q_{s_ref}) equals to 0 (Var), represents power factor unity. It is clear that the measured powers (active and reactive) have good tracking power of the measured powers compared to their reference powers in transient and steady states, a neglected overshoot (< 3%) is noted at 0.6 (sec) in measured stator reactive' and active power (P_{s_meas} and Q_{s_meas}) (because the PID controller is robust in terms of overshoot especially if the wind power' changement is big). The direct and quadrature components of currents and flux (I_{rd} , I_{rq} and Φ_{rd} , Φ_{rq}) are presented respectively in figures.2.32-(e and g), which present the inverse diagrams compared to reactive and active powers. The inverse case for stator direct and quadrature currents (I_{sd} , I_{sq}) which have the same diagrams of reactive and active powers, and they are presented in figure.2.32-(d). The power error is presented in figure.2.32-(f), we observe a big power error of active and reactive powers -80 (W_Var) \leq

$\Delta P_s \Delta Q_s \leq +80$ (W_Var). The stator' and rotor currents; I_{s_abc} and I_{r_abc} are shown in figures.2.32-(h and i) respectively, we remark the sinusoidal form of the waveforms. The power factor (PF) of the proposed control is presented in figure.2.32-(j), knowing that PF is the ratio of P to S (apparent power), it reaches the top value when the reactive power equals to zero value, in this case the stator reactive power equals to zero value means the PF had taken always the unity; and this is the main aim of MPPT strategy/keeping at any time the unity power factor regardless wind speed variation. Table.2.5 described in details the obtained results of the proposed IDPC based on PID for Mode: II.

Mode 3 (green color/figure.2.32 to the right): The reference stator active power (P_{s_ref}) (figure.2.32-(a)) is extracted from MPPT strategy (in this case, the wind speed will take random form); it takes the inverse diagram of wind speed. The stator reactive power (Q_{s_ref}) equal to 0 (Var), represents power factor unity. It is clear that the measured powers (active and reactive) have good tracking power of measured powers compared to their reference powers in transient and steady states, a neglected overshoot (<3%) is noted at 0.5 (sec) and 0.8 (sec) in measured stator reactive' and active power (P_{s_meas} and Q_{s_meas}) (because the PID controller is so robust in terms of overshoot especially if the wind power' changement is big). The direct and quadrature components of currents and flux (I_{rd} , I_{rq} and Φ_{rd} , Φ_{rq}) are presented respectively in figures.2.32-(e and g), which present the inverse diagrams compared to reactive and active powers. The inverse case for stator direct and quadrature currents (I_{sd} , I_{sq}) which have the same diagrams of reactive and active powers, and they are presented in figure.2.32-(d). The power error is presented in figure.2.32-(f), we observe a lower power error: -90 (W_Var) $\leq \Delta P_s \Delta Q_s \leq +90$ (W_Var). The stator' and rotor currents; I_{s_abc} and I_{r_abc} are shown in figures.2.32-(h and i) respectively, we remark the sinusoidal form of the waveforms with neglected ripples. The power factor (PF) of the proposed control is presented in figure.2.32-(j), knowing that PF is the ratio of P to S (apparent power), it reaches top the value when the reactive power equals to zero value, and this is the main aim of MPPT strategy/ keeping at any time the unity power factor regardless wind speed variation. Table.2.5 described in details the obtained results of the proposed IDPC based on PID for Mode: III.

MPPT Strategy: Knowing that in the left side of figure.2.33 (Mode: II); the wind speed had taken the step form and the right side of figure.2.33 (Mode: III); the wind speed had taken the random form. Figure.2.33-(a) presents the stator active and reactive powers and its references profiles using of the proposed IDPC based on PID for pitch angle equals to 0° ($B^\circ=0^\circ$) means the maximum power. It can be seen that the measured powers (active and reactive) follow exactly theirs references despite the sudden variation of wind speed in transient and steady states with a good tracking power (neglected undulation are noted). Figures.2.32-(b) illustrate the stator active power under different pitch angle ($B^\circ=0^\circ, 1^\circ, 1.5^\circ, 2^\circ$ and 2.05°), it can be seen the inverse proportionality between the active powers and pitch angle. Figures.2.33-(c) illustrate the stator reactive power under different pitch angle ($B^\circ=0^\circ, 1^\circ, 1.5^\circ, 2^\circ$ and 2.05°), it is clear that the reactive power maintain the zero level despite the pitch angle variation (the maximum wind power is reached at $B^\circ=0^\circ$ (black color) as mentioned from MPPT strategy/refer to §.2.4.1) and neglected power error was noted. Figure.2.33-(d) depicts the wind speed forms; figure.2.33-(d/to the left) presents the step wind speed (maximum value equals to 11.5 m/sec) and figure.2.33-(d/to the right) displays the random wind speed (maximum value equals to 13.5 m/sec). Figure.2.33-(e) presents the generator speed (rpm); figure.2.33-(e/to the left) presents the generator speed (<1500 (rpm) means the Sub-synchronous operation, noted by '1') and figure.2.33-(e/to the right) displays the generator speed (below and above the synchronous speed (1500 rpm) means the Sub-synchronous and Super-synchronous operations noted by '1' and '2' respectively). Figure.2.33-(f) displays the power coefficient (C_p); figure.2.33-(f/to the left) illustrates the power coefficient under Mode: II, it is clear that C_p had maintained the maximum value (≈ 0.48) regardless the wind speed variation and figure.2.33-(f/to the right) presents the C_p under Mode: III, in this case C_p had maintained the maximum value despite of wind speed variation. Figure.2.33-(g) displays the slip (S) behavior during the generator speed variation; figure.2.33-(g/to the left) illustrates the behavior of S under generator speed variation, in this case S varies between '+1' and '0' $\rightarrow 0 < S \leq +1$ means the generator speed did not reach the synchronous speed (always < 1500 (rpm)), figure.2.33-(g/to the right) represents the S behavior under generator speed variation, in this case S varies between '+1' and '-1' $\rightarrow -1 < S \leq +1$ means the generator speed varies below and above the synchronous speed (superior and inferior 1500 (rpm)), in the case when S reaches zero value means the mechanical speed $N_r=1500$ (rpm) this case called the synchronous mode (because S

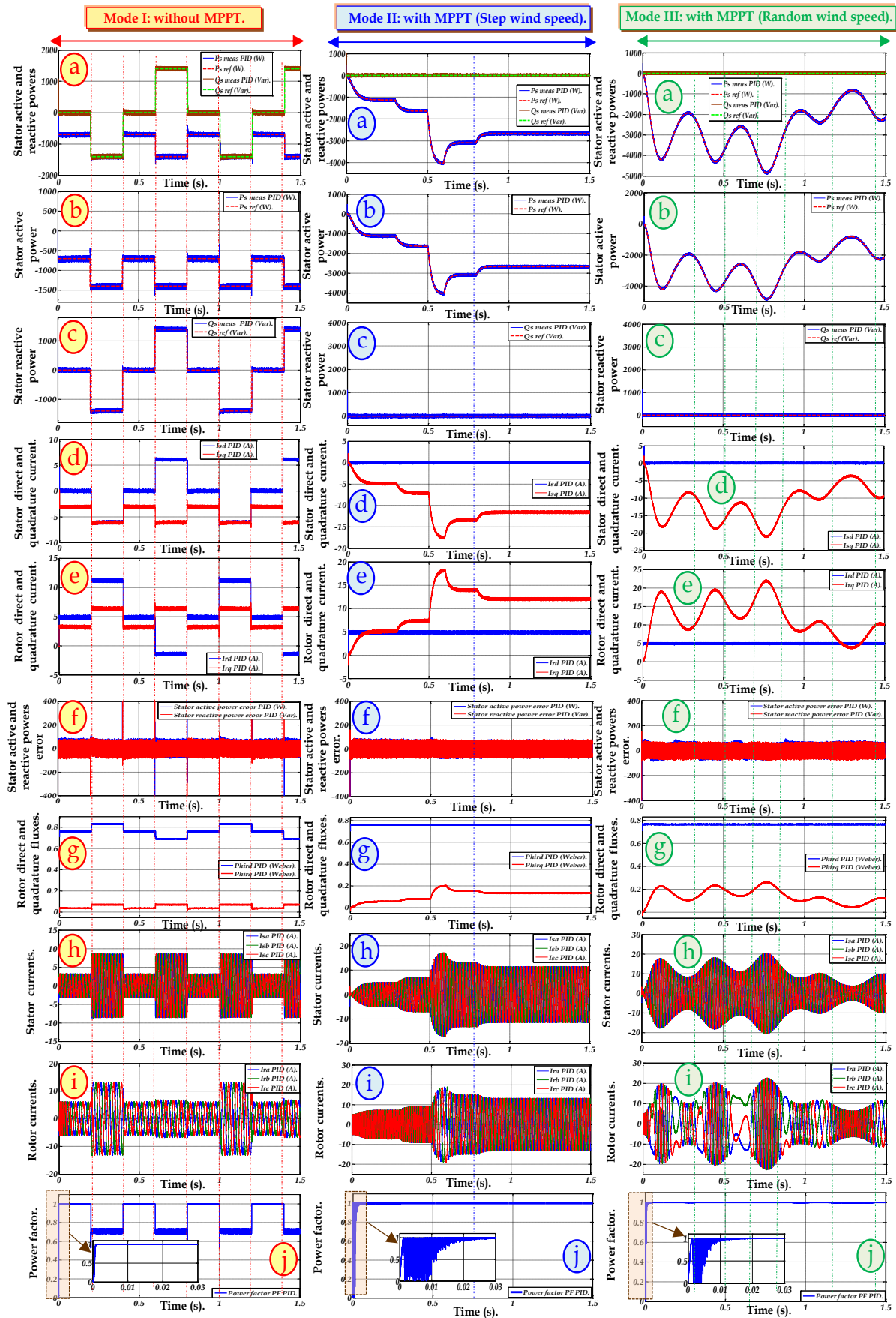


Figure.2.32 Simulation results of conventional control based on PID using three (03) modes; (a): stator active and reactive powers, (b): stator active power, (c): stator reactive power, (d): stator direct and quadrature currents, (e): rotor direct and quadrature currents, (f): stator active and reactive power error, (g): rotor direct and quadrature fluxes, (h): stator currents, (i): rotor currents, (j): power factor.

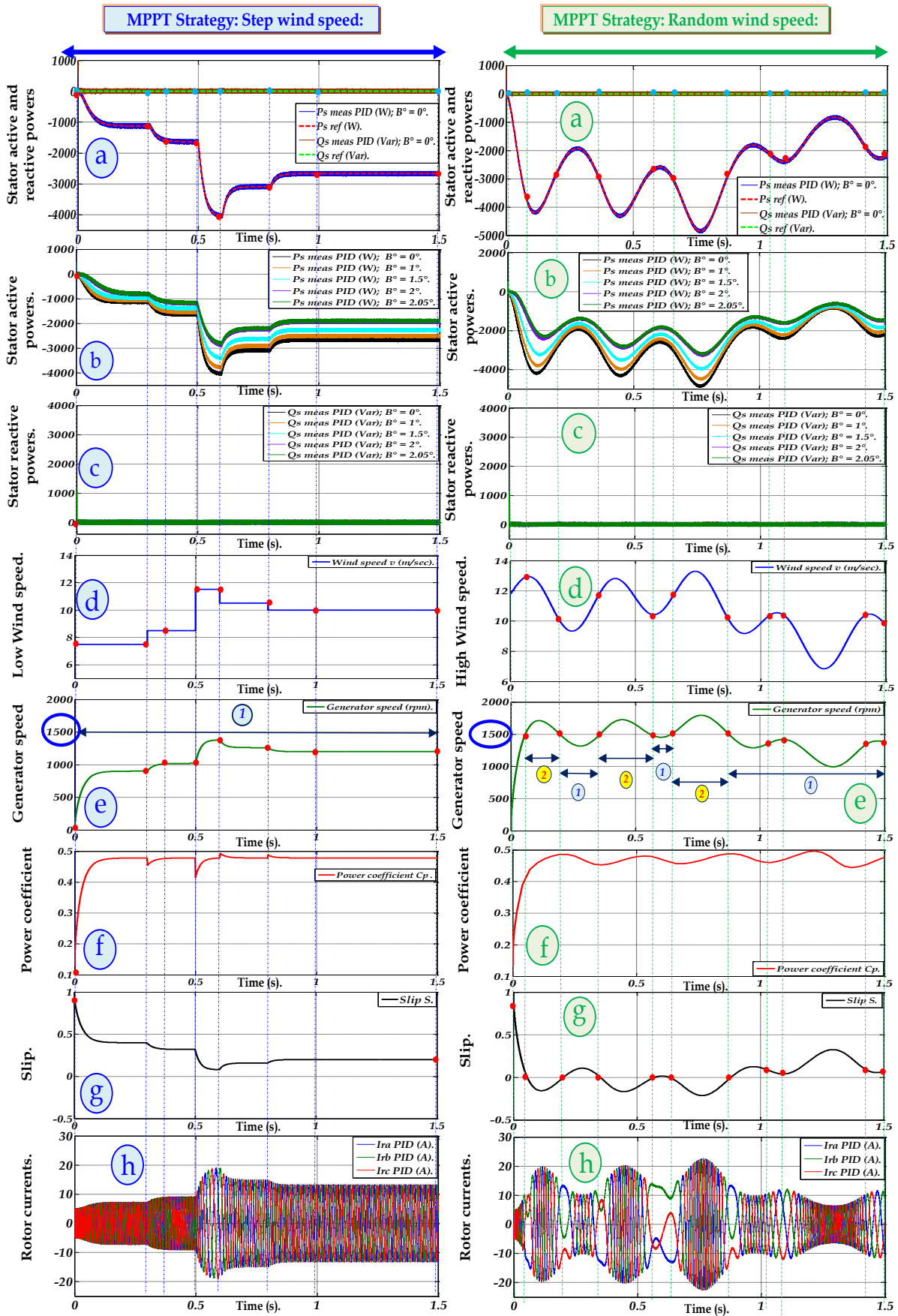


Figure.2.33 Simulations results of two modes MPPT strategy for proposed control based on PID; (a): stator active and reactive powers, (b): stator active power using different B° pitch angles, (c): stator reactive power using different pitch angles B° , (d): wind speed, (e): generator speed, (f): power coefficient, (g): slip, (h): rotor currents.

equals $(N_s - N_r) / N_s$, for exp: in the case of mechanical speed $N_r = 1500$ (rpm) and $N_s = 1500$ (rpm) $= (60 * f) / P = (60 * 50) / 2 = 1500$ (rpm) means $S = (1500 - 1500) / 1500 = 0$ is the stable zone, please refer to Appendix.A, DFIG's parameters (Table.A.1). Figure.2.33-(h) displays the behavior of rotor currents under generator speed variation; figure.2.33-(h/to the left) illustrates the sinusoidal waveforms of rotor currents with neglected ripples (in this case the rotor currents did not change the sense because the S did not reach the zero value) and figure.2.33-(h/to the right) demonstrates the rotor currents behavior under generator speed variation, it can be seen the rotor currents had changed the sense in the case when S equals to zero value means when the generator speed varied near the synchronous speed.

Robustness tests¹⁶: Knowing that in the left side of figure.2.34-(Mode: I/without MPPT strategy); the middle side of figure.2.34-(Mode: II/ using step wind speed) and right side of figure.2.34-(Mode: III/ using random wind speed). In Mode: I red color), figures.2.34-(a and b/to the left) illustrate the behavior of stator active and reactive powers under parameters variations. It can be noted big power in active and reactive power especially using the 2nd test (brown color/please refer to the bottom of the page) and 3rd test (green color) with remarkable undulations especially in transient and steady states (please refer to zoom) and the value of power error reaches nearly ± 80 (W_Var) in Test-1, and nearly ± 500 (W_Var) in Test-2 and Test-3. A remarkable overshoot is noted under all robustness tests especially at 0.2, 0.6 and at 1.0 (sec). Figures.2.34-(a and b/to the middle) display the behavior of stator active and reactive powers under MPPT strategy by maintaining the reactive power equals to zero value. In this case the active power had taken the inverse step profile of wind speed. Using robustness tests a remarkable undulations are noted (using tests: 2 and 3) especially at 0.6 (sec) which presents the rated power of DFIG ($P = 4$ (kW)), on other hand and in the same time a remarkable power error is noted in stator reactive power (which means that the PID controllers can't maintain the unity power factor under parameters variation), also a remarkable overshoot is noted in transient and steady states of active and reactive power. Figures.2.34-(a and b/to the right) display the behavior of stator active and reactive powers under MPPT strategy by maintaining the reactive power equals to zero value. In this case the active power had taken the inverse random

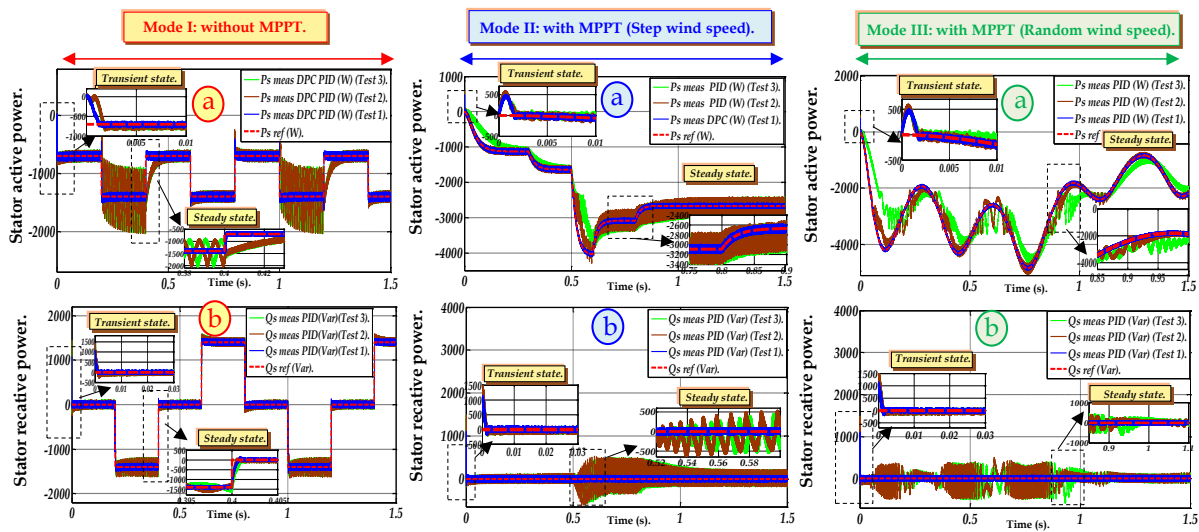


Figure.2.34 Robustness tests of proposed control based on PID using three (03) modes; (a): stator active powers, (b): stator reactive powers

Table.2.5 Recapitulation results for the proposed control (based on PID).

	THD _{Is_abc} (%) :	THD _{Ir_abc} (%) :	Overshoot :	Response time (Sec):	Power Error (W_Var) :
Mode I:	0.73 %	39.27 %	Neglected (< 5%).	$1,2 * 10^{-4}$.	+/- 80.
Mode II:	0.32 %	5.89 %	Neglected (< 3%).	$1,5 * 10^{-4}$.	+/- 80.
Mode III:	0.25 %	1.81 %	Neglected (< 3%).	$1,6 * 10^{-4}$.	+/- 90.

¹⁶ Knowing that in this chapter the robustness tests are based on three tests as follows: [Test-1: without parameter change → Blue color, Test-2: +100% of R_r and -25% of $(L_s, L_r$ and $L_m)$ → Brown color and Test-3: +100% of $(J$ and $R_r)$, -25% of $(L_r, L_s$ and $L_m)$ → Green color] respectively.

profile of wind speed. Using robustness tests, a remarkable undulations are noted (using tests: 2 and 3) especially at 0.75 (sec) and 0.8 (sec) which presents the over rated power of DFIG ($P=4$ (kW) and the measured active power maintain 4.6 (kW)), on other hand and in the same time a remarkable power error is noted in stator reactive power (which means that the PID controllers can't maintain the unity power factor under parameters changing), also a big overshoot is noted in transient and steady states of active and reactive power (please refer to zoom).

2.9.3 Power Factor (PF) tests for three (03) modes

Mode 1 (red color/figure.2.35 to the left): in this case the generator speed was proposed basically constant (≈ 1450 rpm) is illustrated in figure.2.35-(a) and "1" means the simulation study is developed in Sub-synchronous operation. Figure.2.35-(b) displays the power factor (PF), It is clear that the PF depends on the reactive power variation ($PF= P_s/(P_s^2+Q_s^2)^{1/2}$; if Q_s is near than zero (Var)). If the reactive power (Q_s (Var)) takes the zero level means the PF maintain the unity ($0 \rightarrow 0.2$ (sec), $0.4 \rightarrow 0.6$ (sec), $0.8 \rightarrow 1$ (sec) and $1.2 \rightarrow 1.4$ (sec)) is clear in zoom ($PF=0.995$), otherwise the PF doesn't maintain the unity factor ($0.2 \rightarrow 0.4$ (sec), $0.6 \rightarrow 0.8$ (sec), $1 \rightarrow 1.2$ (sec) and $1.4 \rightarrow 1.5$ (sec)); is clear in the zoom ($PF < 0.7$). Figure.2.35-(c) presents the behavior of the grid voltage (V_{ga}) and stator currents (I_{sa})¹⁷ under stator powers variation. It is remarkable that the angle between stator current and grid voltage $\theta_{I_{sa}-V_{ga}}$ equals to 180° in the time interval: $0 \rightarrow 0.2$ (sec), $0.4 \rightarrow 0.6$ (sec), $0.8 \rightarrow 1$ (sec) and $1.2 \rightarrow 1.4$ (sec); which correspond at the unity power factor. And the this angle is $<< 180^\circ$ in the time interval: $0.2 \rightarrow 0.4$ (sec), $0.6 \rightarrow 0.8$ (sec), $1 \rightarrow 1.2$ (sec) and $1.4 \rightarrow 1.5$ (sec); which correspond a decrease power factor value.

Mode 2 (red color/figure.2.35 to the middle): in this case the generator speed took the same wind-speed profile (< 1500 rpm) is illustrated in figure.2.35-(a) and "1" means the simulation study is developed in Sub-synchronous operation. Figure.2.35-(b) displays the power factor (PF), it is clear that the PF depends on the reactive power variation ($PF= P_s/(P_s^2+Q_s^2)^{1/2} = 1$; if Q_s is near than zero (Var)). In this case, MPPT strategy is applied in order to maintain the reactive power (Q_s (Var)) at the zero level in all simulation time means that the PF maintain always the unity factor; is clear in the zoom ($PF=0.999$ at 0.5 sec and $PF \approx 0.997$ at 0.3 sec).

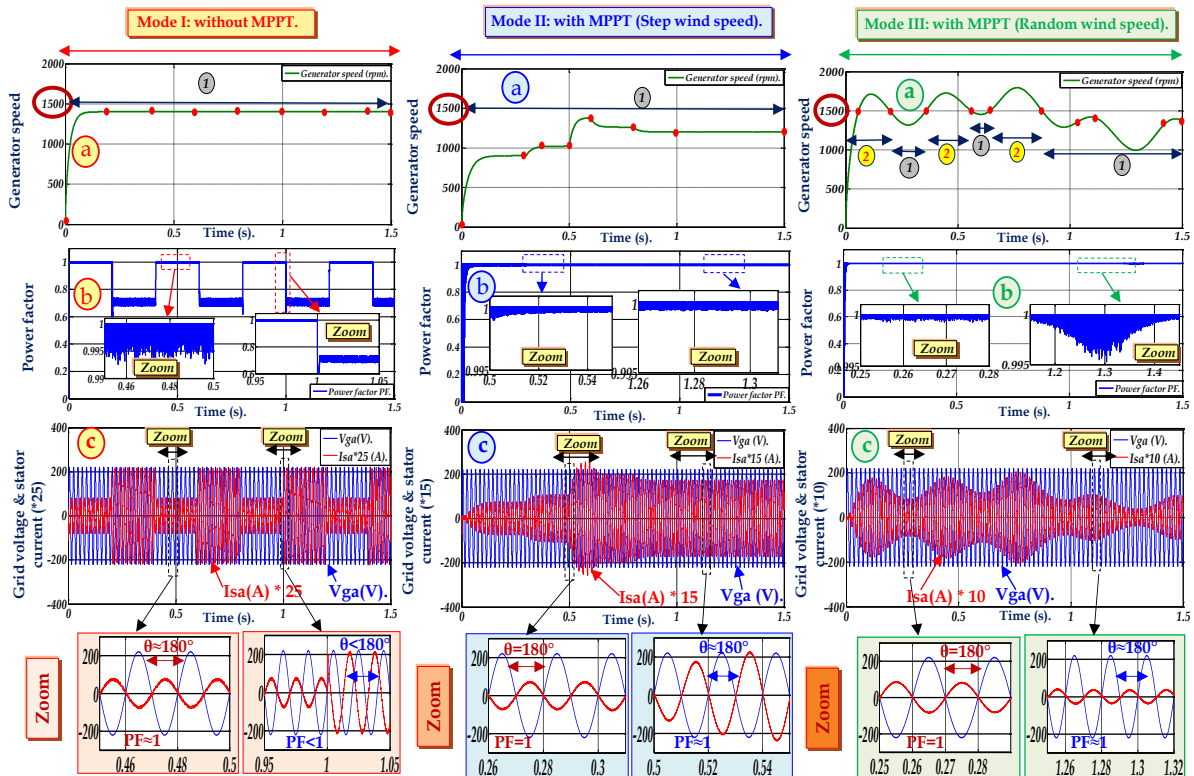


Figure.2.35 Simulations results of grid voltage' and stator currents behavior under power profiles' and wind speed variation.

¹⁷ Knowing that (in Mode: I) the stator current (I_{sa}) is multiplied by 25.

Figure.2.35-(c) presents the behavior of the grid voltage (V_{ga}) and stator currents (I_{sa})¹⁸ under MPPT strategy. It is obvious that the angle between stator current and grid voltage $\theta_{I_{sa}_V_{ga}}$ equals exactly to 180° (between 0.26 sec and 0.28 sec); which correspond at the unity power factor.

Mode 3 (red color/figure.2.35 to the right): in this case the generator speed took the same wind-speed profile (< and > 1500 rpm) is illustrated in figure.2.35-(a), "1" and "2" means the simulation study is developed in Sub- and Super-synchronous operations respectively. Figure.2.35-(b) displays the power factor (PF) behavior, it is clear that the PF depends on the reactive power variation ($PF = P_s / (P_s^2 + Q_s^2)^{1/2} = 1$; if Q_s is near than zero (Var)). In this case, MPPT strategy is applied in order to maintain the reactive power (Q_s (Var)) at the zero level in all simulation time means that the PF maintain always the unity factor is clear in zoom ($PF = 0.999$ at 0.26 sec and $PF \approx 0.995$ at 1.3 sec). Figure.2.35-(c) presents the behavior of the grid voltage (V_{ga}) and stator current (I_{sa})¹⁹ under MPPT strategy. It is remarkable that the angle between stator current and grid voltage $\theta_{I_{sa}_V_{ga}}$ equals exactly to 180° (between 0.25 sec and 0.29 sec); which correspond at the unity power factor.

So, after the simulation' comparative study between the both topologies (using PI and PID respectively), we observe the high performance of wind-turbine using PID compared to PI without robustness tests. In this context, it is necessary to keep PID controllers for the power regulation (P_s^* and Q_s^*) in the next chapter. In the same time we will propose (for the chapter n° 03) adaptive and intelligent regulators (such as: MRAC, T1-FLC, T2-FLC and NFC respectively) to control I_{rd}^* and I_{rq}^* in order to improve the dynamic response (in steady and transient) and to overcome the parameter sensibility (under robustness tests).

2.10 Conclusion

This chapter presents a detailed power control (based on classical PI controllers) study for DFIG-grid connection. In order to control independently DFIG's stator power; conventional indirect power control with SVM (in order to maintain the fixed switching frequency) have been combined to adjust active and reactive powers and rotor currents. MPPT strategy was proposed in order to extract the maximum wind-power despite unexpected wind speed variation (in this chapter we proposed two wind speed profiles: the step wind speed and the random wind speed) and to maintain power factor at unity ($PF \approx 1$). Several drawbacks appears in transient and steady states, in terms of tracking power and dynamic performances. In this context, improved IDPC algorithm was proposed, PID controllers are proposed instead of PI to control stator powers and rotor currents respectively in order to overcome the disadvantages of the conventional controllers. The simulation results have been developed via Matlab/ Simulink® environment, show high dynamics response and improved wind-system performances using proposed algorithm compared to the conventional one. Using the robustness tests, the wind-performances are remarkably decreasing (in conventional and proposed algorithm respectively) which demonstrate the inability of tracking reference power during the parameter change and sudden wind speed variation. In the next chapter, robust and intelligent algorithms will be proposed in order to overcome these drawbacks.

2.11 References

- [1] Gonzalo ABAD, Jesus LOPEZ, Miguel A. RODRIGUEZ, Luis MARROYO and Grzegorz IWANSKI, "Doubly Fed Induction Machine Modeling And Control For Wind Energy Generation", IEEE Book; John Wiley & Sons, 2011.
- [2] Akbar TOHIDI, Hadi HAJIEGHRARY and M. Ani HSIEH, "Adaptive Disturbance Rejection Control Scheme for DFIG-Based Wind Turbine: Theory and Experiments", IEEE Transactions on Industry Applications, vol: 52, no: 3, pp: 2006 - 2015, 2016.
- [3] Longqi LI; Heng NIAN; Lijie DING and Bo ZHOU, "Direct Power Control of DFIG System without Phase-Locked Loop under Unbalanced and Harmonically Distorted Voltage", IEEE Transactions on Energy Conversion, 2017.

¹⁸ Knowing that (in Mode: II) the stator current (I_{sa}) is multiplied by 15.

¹⁹ Knowing that (in Mode: III) the stator current (I_{sa}) is multiplied by 10.

- [4] Heng NIAN and Longqi LI, "Direct Power Control of Doubly Fed Induction Generator without Phase-Locked Loop under Harmonically Distorted Voltage Conditions", IEEE Transactions on Power Electronics, 2017.
- [5] Jafar MOHAMMADI, Sadegh VAEZ-ZADEH, Saeed AFSHARNIA, Ehsan DARYABEIGI, "A Combined Vector and Direct Power Control for DFIG-Based Wind Turbines", IEEE Transactions on Sustainable Energy, vol: 5, no: 3, pp: 767 - 775, 2014.
- [6] Roberto CARDENAS; Rubén PENA; Salvador ALEPUZ and Greg ASHER, "Overview of Control Systems for the Operation of DFIGs in Wind Energy Applications", IEEE Transactions on Industrial Electronics, vol: 60, no: 7, pp: 2776-2798, 2013.
- [7] Etienne TREMBLAY, Sergio ATAYDE and Ambrish CHANDRA, "Comparative Study of Control Strategies for the Doubly Fed Induction Generator in Wind Energy Conversion Systems: A DSP-Based Implementation Approach", IEEE Transactions on Sustainable Energy, vol: 2, no: 3, pp: 288-299, 2011.
- [8] Fayssal AMRANE and Azeddine CHAIBA, "A Novel Direct Power Control for grid-connected Doubly Fed Induction Generator based on Hybrid Artificial Intelligent Control with Space Vector Modulation", Rev. Roum. Sci. Techn.- Électrotechn. et Énerg., vol. 61, no.3, pp: 263-268, 2016.
- [9] Fayssal AMRANE, Azeddine CHAIBA and Ali CHEBABHI: "Improvement Performances of Doubly Fed Induction Generator via MPPT Strategy using Model Reference Adaptive Control based on Direct Power Control with Space Vector Modulation", Journal of Electrical Engineering, vol: 16, no: 3, pp. 218-225, 2016.
- [10] Yu ZOU; Malik E. ELBULUK and Yilmaz SOZER, "Stability Analysis of Maximum Power Point Tracking (MPPT) Method in Wind Power Systems", IEEE Transactions on Industry Applications, vol: 49, no: 3, pp: 1129-1136, 2013.
- [11] Shenghu LI, "Power Flow Modeling to Doubly-Fed Induction Generators (DFIGs) Under Power Regulation", IEEE Transactions on Power Systems, vol: 28, no: 3, pp: 3292 - 3301, 2013.
- [12] Baike SHEN; Bakari MWINYIWIWA; Yongzheng ZHANG and Boon-Teck OOI, "Sensorless Maximum Power Point Tracking of Wind by DFIG Using Rotor Position Phase Lock Loop (PLL)", IEEE Transactions on Power Electronics, vol: 24, no: 4, pp: 942 - 951, 2009.
- [13] Z. -S. ZHANG; Y. -Z. SUN; J. LIN and G. -J. LI, "Coordinated frequency regulation by doubly fed induction generator-based wind power plants", IET Renewable Power Generation, vol: 6, no: 1, pp: 38 - 47, 2012.
- [14] N. K. Swami NAIDU and Bhim SINGH, "Experimental Implementation of a Doubly Fed Induction Generator Used for Voltage Regulation at a Remote Location", IEEE Transactions on Industry Applications, vol: 52, no: 6, pp: 5065 - 5072, 2016.
- [15] Li WANG and Dinh-Nhon TRUONG, "Stability Enhancement of DFIG-Based Offshore Wind Farm Fed to a Multi-Machine System Using a STATCOM", IEEE Transactions on Power Systems, vol: 28, no: 3, pp: 2882 - 2889, 2013.
- [16] N. K. Swami NAIDU and Bhim SINGH, "Grid-Interfaced DFIG-Based Variable Speed Wind Energy Conversion System With Power Smoothing", IEEE Transactions on Sustainable Energy, vol: 8, no: 1, pp: 51 - 58, 2017.
- [17] Armand BOYETTE, "Contrôle-Commande d'un Générateur Asynchrone à Double Alimentation avec Système de Stockage pour la Production Eolienne", PhD Thesis (French language), Université Henri Poincaré Nancy-1, France, 2006.

- [18] Frédéric POITIERS, "*Etude Et Commande De Generatrices Asynchrones pour L'utilisation de L'Energie Eolienne : - Machine asynchrone à cage autonome ; -Machine asynchrone à double alimentation reliée au réseau*", PhD Thesis (French language), Université de Nantes, France, 2003.
- [19] Linyun XIONG; Jie WANG; Xiao MI and Muhammad Waseem KHAN, "*Fractional Order Sliding Mode Based Direct Power Control of Grid-Connected DFIG*", IEEE Transactions on Power Systems, 2017.
- [20] Dan SUN; Xiaohe WANG; Heng NIAN; Z. Q. ZHU, "*A Sliding-Mode Direct Power Control Strategy for DFIG under Both Balanced and Unbalanced Grid Conditions Using Extended Active Power*", IEEE Transactions on Power Electronics, vol: 33, no: 3, pp: 1313 - 1322, 2018.
- [21] M. Itsaso MARTINEZ; Gerardo TAPIA; Ana SUSPERREGUI and Haritza CAMBLONG, "*Sliding-Mode Control for DFIG Rotor- and Grid-Side Converters Under Unbalanced and Harmonically Distorted Grid Voltage*", IEEE Transactions on Energy Conversion, vol: 27, no: 2, pp: 328 - 339, 2012.
- [22] Youcef BEKAKRA and Djilani BEN ATTOUS, "*DFIG sliding mode control fed by back-to-back PWM converter with DC-link voltage control for variable speed wind turbine*", Front. Energy, vol: 8, no: 3, pp 345-354, 2014.
- [23] Aman Abdulla TANVIR, Adel MERABET and Rachid BEGUENANE, "*Real-Time Control of Active and Reactive Power for Doubly Fed Induction Generator (DFIG)-Based Wind Energy Conversion System*", Energies, vol: 8, 2015.
- [24] Julius MWANIKI, Hui LIN, and Zhiyong DAL, "*A Condensed Introduction to the Doubly Fed Induction Generator Wind Energy Conversion Systems*", Hindawi Journal of Engineering, vol: xx, no: xx, pp: xx-xx, 2017.
- [25] A. SUSPERREGUI; G. TAPIA; I. ZUBIA and J. X. OSTOLAZA, "*Sliding-Mode control of Doubly-Fed Generator for Optimum Power Curve Tracking*", Electronics Letters, vol: 46, no: 6, pp: 126 - 127, 2010.
- [26] Keliang ZHOU and Danwei WANG, "*Relationship between Space-Vector Modulation and Three-Phase Carrier-Based PWM: A Comprehensive Analysis*", IEEE Transactions on Industrial Electronics, vol. 49, no. 1, pp. 186-196, 2002.
- [27] Behzad VAFAKHAH, "*Multilevel Space Vector PWM for Multilevel Coupled Inductor Inverters*", University of Alberta, Ph.D. Thesis (English language), Canada, 2010.
- [28] Gonzalo Abad BIAIN, "*Predictive Direct Control Techniques of The Doubly Fed Induction Machine for Wind Energy Generation Applications*", PhD Thesis (English language), Mondragon Unibersitatea, Spain, 2008.
- [29] Gonzalo ABAD and Grzegorz IWANSKI, "*Chapter-10: Properties and Control of a Doubly Fed Induction Machine*" from the Book: "*Power Electronics for Renewable Energy Systems, Transportation and Industrial Applications*", EEE Press and John Wiley & Sons Ltd, 2014.
- [30] Fayssal AMRANE, Azeddine CHAIBA and Saad MEKHILEF: "*High performances of grid-connected DFIG based on direct power control with fixed switching frequency via MPPT strategy using MRAC and Neuro-Fuzzy control*" Journal of power technologies (JPT), vol, 96, no: 1, 2016.

Chapter 3 :

A Novel IDPC using Adaptive, Robust and Intelligent Controllers.

3.1 Introduction	59
3.2 Drawbacks and performances limitation of conventional IDPC	60
3.3 Proposed Power control based on Model Reference Adaptive Control (MRAC).....	61
3.4 Proposed Power control based on Type-1 Fuzzy Logic Control (T1-FLC)	62
3.4.1 Reasons for Choosing Fuzzy Logic.....	62
3.4.2 Fuzzy Set Theory and Fuzzy Set Operations.....	62
3.4.3 Membership Functions	62
3.4.4 Mamdani Fuzzy Inference Method	63
3.4.5 Membership Functions and Rule Base.....	64
3.5 Proposed Power control based on Type-2 Fuzzy Logic Control (T2-FLC)	65
3.5.1 Overview of Type-2 Fuzzy Logic Controller Toolbox	66
3.5.2 Design of Type-2 Fuzzy Logic Controller.....	66
3.6 Proposed Power control based on Neuro-Fuzzy Control (NFC)	68
3.6.1 Layer I: Input layer	68
3.6.2 Layer II: membership layer.....	68
3.6.3 Layer III: rule layer	69
3.6.4 Layer IV: output layer	69
3.7 Simulation results	70
3.7.1 Topology 1: Improved IDPC (based on MRAC controllers)	71
3.7.2 Topology 2: Improved IDPC (based on T1-FLC controllers)	76
3.7.3 Topology 3: Improved IDPC (based on T2-FLC controllers)	81
3.7.4 Topology 4: Improved IDPC (based on NFC controllers)	86
3.8 Wind-system performances recapitulation under six (06) proposed IDPC algorithms.....	91
3.9 Conclusion	91
3.10 References	92

Abstract:

This chapter presents an improved Indirect power control (compared to the conventional one illustrated in chapter: 2) based on robust and suitable controllers (Adaptive, Robust and Intelligent controllers) to control the d-q axes currents (I_{rd} and I_{rq}) respectively. In order to overcome the speed/efficiency trade-off and divergence from peak power under fast variation of wind speed; fourth robust topologies (based on MRAC, T1-FLC, T2-FLC and NFC) are proposed to control the rotor direct and quadrature currents (I_{rd} and I_{rq}) instead of PID controllers, for grid-connected doubly fed induction generator (DFIG). The same wind-turbine (DFIG (4kW) and turbine (4.5 kW)) used in last chapter will be developed again in order to make a comparative study between the wind-system performance algorithms. The SVM strategy (to ensure the fixed switching frequency and to minimize the harmonics) is used in RSC for switching signals generation to control the inverter. In this chapter, mathematical model of each proposed controller were described in details. The MPPT strategy also is developed in the fourth proposed algorithms in order to extract the maximum wind power by keeping the reactive power equals to zero value. The main aim of the proposed control is to improve the wind system performance despite the sudden wind speed variation and the DFIG's parameter variation in transient and steady states. The simulation results using the Matlab/Simulink environment (under three proposed modes and using robustness tests) show that the intelligent controller offered high power quality in spite of wind-speed variation have superior dynamic performance and are more robust during parameter variation.

3.1 Introduction

Model Reference Adaptive Control (MRAC) is a kind of control method that follows the response signal at the output of reference model. It has the advantages of simple structure and fast and stable reconfiguration. The general idea underpinning MRAC is to incorporate a reference model to acquire the preferred closed-loop reactions. MRAC has the ability to control a system that undergoes parameter and/or environmental variations. It designs the mechanism law and adjustments technique to drive the desired trajectories for the system to track the reference model output [1-2]. The analysis and performance of several model reference adaptive system (MRAS) observers for sensorless vector control of DFIG is proposed in [3]. A model reference adaptive control (MRAC) speed estimator speed sensorless direct torque and flux control of an induction motor is proposed in [4] to achieve high performance sensorless drive.

In recent years, novel classes of fuzzy logic systems-known by type-2 fuzzy logic control (T2FLC) are useful for incorporating uncertainties is introduced [5]. The advantages of fuzzy logic controllers over conventional controllers are that they do not need an accurate mathematical model, can work with imprecise inputs, can handle non-linearity and are more robust than conventional PID controllers [6-7]. Type-2 fuzzy logic is able to handle uncertainties because it can model them and minimize their effects than Type-1 fuzzy logic control. Unfortunately, type-2 fuzzy sets are more difficult to use and understand than traditional type-1 fuzzy sets. Therefore, their use is not widespread yet. Even in the face of these difficulties, type-2 fuzzy logic has found applications in the classification of coded video streams, co-channel interference elimination from nonlinear time-varying communication channels, connection admission control, extracting knowledge from questionnaire surveys, forecasting of time-series, function approximation, pre-processing radio-graphic images and transport scheduling [8-9]. T2 FLCs found successful application in many engineering areas, demonstrating their ability to outperform T1 FLCs in the presence of dynamic uncertainties. The fundamental difference between T1 and T2 FLCs is in the model of individual fuzzy sets. T2 fuzzy sets employ membership degrees that are themselves fuzzy sets. This additional uncertainty dimension provides new degrees of freedom for modeling dynamic uncertainties. Now the research is concentrating on Control applications using Type-2 fuzzy logic. It noted that in recent years, the application of fuzzy logic is extended especially in the wind energy conversion systems (WECS).

Furthermore fuzzy-neural techniques have been proposed as a robust control for electrical drives [10-11-12]. Neuro-fuzzy systems combine the advantages of neural networks and fuzzy logic systems. The main purpose of using the ANFIS (Adaptive Neuro-Fuzzy Inference Systems) approach is to automatically deliver the fuzzy system by using neural network methods [13-14]. The ANFIS architecture has well known advantages of modeling a highly Non-Linear system, as it combines the capability of fuzzy reasoning in handling the uncertainties and capability of an artificial neural network (ANN) in learning from processes. A combination of the strengths of Fuzzy Logic controllers and Neural Networks creates systems capable of controlling complex systems and adaptively learning to optimize control parameters [13-14]. These advantages justify the necessity of applying this kind of system for the DFIG used in wind energy conversion systems.

In this chapter the main contribution is the validation (via MATLAB/Simulink®) of the proposed IDPC based on robust and intelligent controllers: MRAC, T1-FLC, T2FLC and NFC instead the PID controller (as shown in

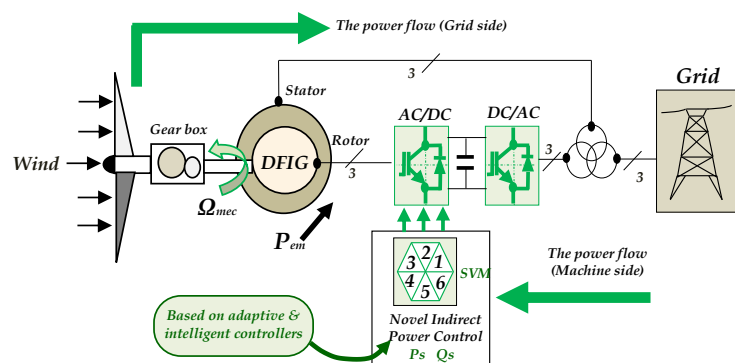


Figure.3.1 Schematic diagram of wind-turbine DFIG based on novel indirect power control (IDPC).

figure.3.2) in order to control rotor quadrature and direct currents (I_{rd} and I_{rq}) respectively under MPPT strategy. The robustness tests against parameters variation have been validated also using three MPPT modes in order to confirm that the drawbacks of the conventional IDPC are been treated. In order to more explain the advantages/disadvantages of all the proposed algorithms (six proposed algorithms: chapter 2 + chapter 3); a comparative study based on proposed controls will be proposed using several criteria.

3.2 Drawbacks and performances limitation of conventional IDPC:

The conventional algorithm developed in chapter 2 presents several drawbacks such as:

- An important overshoot is noted (more than + 50%).
- The coupling terms between the parameters of the both axis (d and q) has negative influence on the wind-system performances, especially in high wind power-wind generation (HWPG).
- The long response time -a visible delay of the measured value relative to that of the reference- order of $10e^{-2}$ (sec).
- A bad power tracking of the measured value relative to that of the reference especially if the profile is in the step form.
- Poor power/voltage quality which will be transmitted to the grid; a bad THD that exceeds IEEE standards ($>> + 5\%$).
- A remarkable power error for conventional power control; sometimes exceeding at 25% of the rated power (± 1000 (W) for a rated power of 4 kW).
- The conventional regulators (PI regulators) depend on the DFIG's parameters.

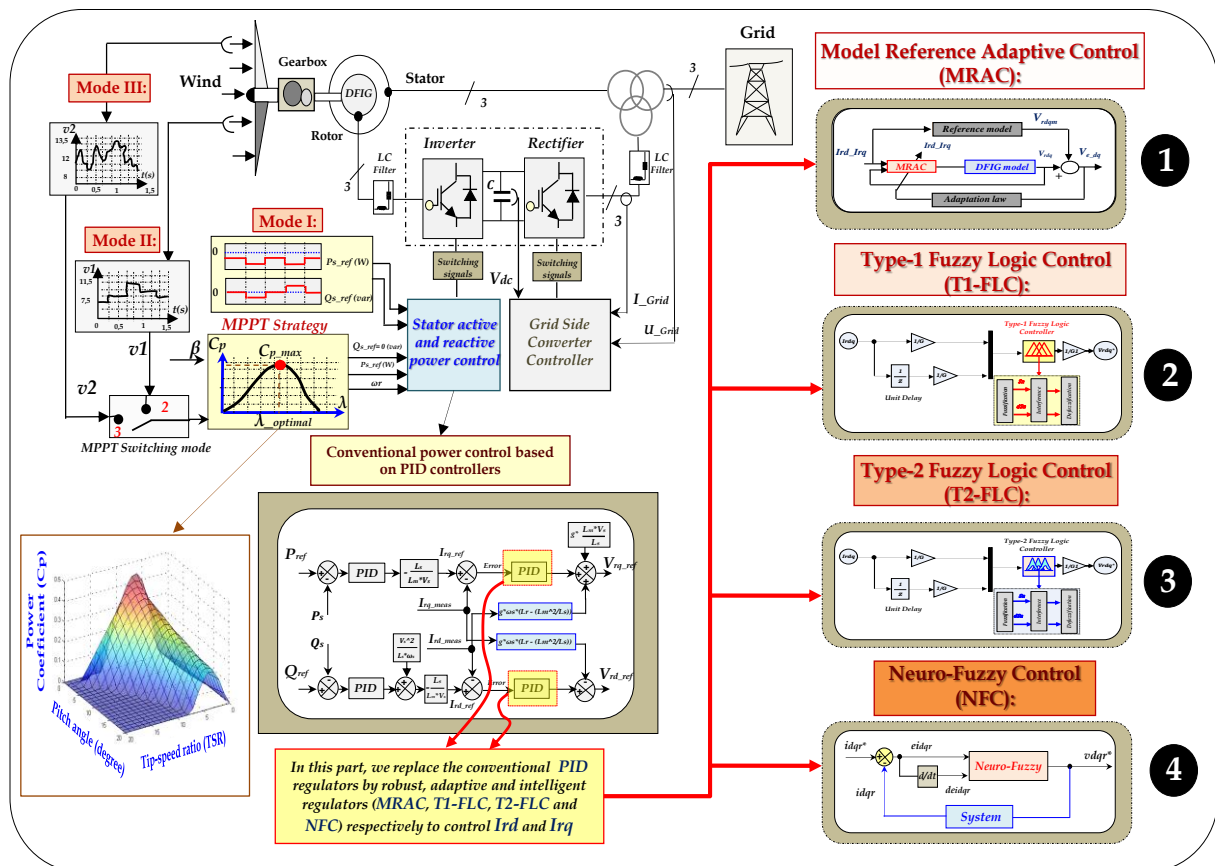


Figure.3.2 Global wind-turbine system scheme based on fourths proposed controllers.

In this context and to overcome these drawbacks; the adaptive and intelligent controllers are proposed instead the PID controllers, in order to improve power quality and wind-system performance, figure.3.2 present the adequate solution to ameliorate the power control under sudden wind speed variation and parameters changement.

The mathematical model of each proposed controller is described in details in the next sections, then the simulation results are described in details (*simulation results for each controller topology under three modes "as developed in chapter 2"*).

3.3 Proposed Power control based on Model Reference Adaptive Control (MRAC)

The system studied in this chapter is based on a first-order linear plant approximation given by [15]:

$$\dot{x}(t) = -a \cdot x(t) + b \cdot u(t) \quad (3.1)$$

Where $x(t)$ is the plant state, $u(t)$ is the control signal and a and b are the plant parameters. The control signal is generated from both the state variable and the reference signal $r(t)$, multiplied by the adaptive control gains K and K_r such that:

$$u(t) = K(t) \cdot x(t) + K_r(t) \cdot r(t) \quad (3.2)$$

Where $K(t)$ is the feedback adaptive gain and $K_r(t)$ the feed forward adaptive gain. The plant is controlled to follow the output from a reference model

$$\dot{x}_m(t) = a_m \cdot x_m(t) + b_m \cdot r(t) \quad (3.3)$$

Where x_m is the state of the reference model and a_m and b_m are the reference model parameters which are specified by the controller designer. The object of the MRAC algorithm is for $x_e \rightarrow 0$ as $t \rightarrow \infty$, where $x_e = x_m - x$ is the error signal. The dynamics of the system may be rewritten in terms of the error such that:

$$\dot{x}_e(t) = a_m \cdot x_e(t) + (a - a_m - b \cdot K(t)) \cdot x(t) + (b_m - b \cdot K_r(t)) \cdot r(t) \quad (3.4)$$

Using Equations (3.2), (3.3) and (3.4), it can be seen that for exact matching between the plant and the reference model, the following relations hold.

$$K = K^E = \frac{a - a_m}{b} \quad (3.5)$$

$$K_r = K_r^E = \frac{b_m}{b} \quad (3.6)$$

Where K^E denotes the (constant) Erzberger gains [15].

Equations (3.5) and (3.6) can be used to express Equation (3.4) as:

$$\dot{x}_e(t) = -a_m \cdot x_e + b \cdot (K^E - K) \cdot (x_m - x_e) + b \cdot (K_r^E - K_r) \cdot r \quad (3.7)$$

For general model reference adaptive control, the adaptive gains are commonly defined in a proportional plus integral formulation

$$K(eI_{rd_ref}, t) = \int_0^t a \cdot y_e \cdot I_{rd_ref}^T \cdot dt + b \cdot y_e \cdot I_{rd_ref}^T \quad (3.8)$$

$$K_r(eI_{rd}, t) = \int_0^t a \cdot y_e \cdot I_{rd}^T \cdot dt + b \cdot y_e \cdot I_{rd}^T \quad (3.9)$$

$$K(eI_{rq_ref}, t) = \int_0^t a \cdot y_e \cdot I_{rq_ref}^T \cdot dt + b \cdot y_e \cdot I_{rq_ref}^T \quad (3.10)$$

$$K_r(eI_{rq}, t) = \int_0^t a \cdot y_e \cdot I_{rq}^T \cdot dt + b \cdot y_e \cdot I_{rq}^T \quad (3.11)$$

Where α and β are adaptive control weightings representing the adaptive effort. y_e is a scalar weighted function of the error state and its derivatives, $y_e = C_e \cdot x_e$, where C_e can be chosen to ensure the stability of the feed forward block.

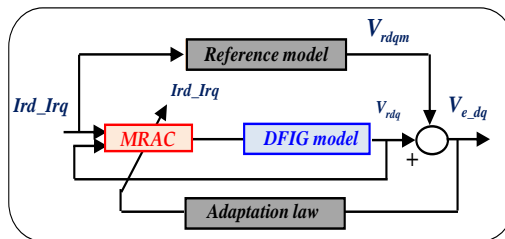


Figure.3.3 Proposed MRAC to control I_{rd} and I_{rq} respectively.

In this case, the MRAC controller is proposed to control rotor *direct and quadrature* currents respectively (I_{rd} and I_{rq}) instead the PID controllers, in order to improve the dynamic responses against parameter variation. The simulation results of the proposed algorithms will be presented in section §.3.7.1 in figures-(3.17, 3.18 and 3.19).

3.4 Proposed Power control based on Type-1 Fuzzy Logic Control (T1-FLC)

The Type-1 Fuzzy Logic Controller (T1-FLC) consists of four stages; Fuzzification of inputs, derivation of rules based on knowledge, inference mechanism and defuzzification. In general, the purpose of fuzzy logic system is to obtain a set of outputs for the given inputs in a nonlinear system, without using any mathematical model, but using linguistic rules [16].

3.4.1 Reasons for Choosing Fuzzy Logic

In general, the most powerful way of conveying information is by natural language. The conventional mathematical methods have not fully tapped this potential of language. The scientist [17] has said that the human thinking process is mainly based on conceptual patterns and mental images rather than on numerical quantities. So if the problem of assembling computers with the capability to work out complex issues has to be solved, the human thought process has to be modeled. The efficient way to do this is to use models that attempt to emulate the natural language; the creation of fuzzy logic has put this power to proper use. Many physical processes are not linear and especially to model them, a reasonable amount of approximation is necessary. For a simple system, the mathematical expressions give precise description of the system behavior.

Similarly, for more complicated systems with considerable amount of available data, model-free methods provide robust methods to reduce ambiguity and uncertainty in the system. But for complex systems with less numerical data, fuzzy reasoning furnishes a way to understand the system behavior by relying on approximate input-output approaches. The primary strength of fuzzy logic is that it makes use of linguistic variables rather than numerical variables to represent imprecise data [18].

3.4.2 Fuzzy Set Theory and Fuzzy Set Operations

In 1965, Zadeh introduced the concept of fuzzy set theory. He states that, "*Much of the decision making in the real world takes place in an environment in which the goals, the constraints and the consequences of possible actions are not known precisely*". In recent years, fuzzy set theory applications have received increasing attention in designing intelligent controllers for complex industrial processes. We live in a world of marvelous complexity and variety where events never repeat exactly. Real world solutions are very often not crisp; but are vague, uncertain, and imprecise. Fuzzy logic provides us not only with meaningful and powerful representation for measurement of uncertainties but also with a meaningful representation of vague concepts in natural language. A fuzzy set can be defined mathematically by assigning to each possible individual, in the universe of discourse, a value representing its grade of membership in the fuzzy set. The basic three fuzzy set operations are union (\cup), intersection (\cap) and complement ($\bar{}$). The fuzzy logic method uses fuzzy equivalents of logical AND, OR and NOT operations to build up fuzzy logic rules [18]. In conventional set theory, AND is said to be the intersection of the sets and OR the union. The fuzzy operators based on values between zero and one, are sometimes said to be true generalizations of the Boolean operators.

3.4.3 Membership Functions

The membership functions play an important role in designing fuzzy systems [19]. The membership functions distinguish the fuzziness in a fuzzy set, whether the elements in the set are discrete or continuous in a graphical form for eventual use in mathematical formalism of fuzzy set theory. The shape of membership function describes the fuzziness in graphical form. The shape of membership functions is also important in the development of fuzzy system. The membership functions can be symmetrical or asymmetrical. A uniform representation of membership functions is desirable. The

membership function defines how each point in the input space is mapped to a membership value in the interval $[0, 1]$ [19].

3.4.4 Mamdani Fuzzy Inference Method

Generally, the starting point of a fuzzy system is the formation of a knowledge base consisting of *IF-THEN* rules. These rules are obtained from human experts based on their respective domain of knowledge and from observations that they made. Combining these rules into a single system is a natural step forward which allows us to obtain an output that attains the assigned goals. The *Mamdani's* fuzzy inference method is the most commonly used fuzzy methodology. *Mamdani's* method is the first control system built using fuzzy set theory. The fuzzy logic controller consists of four main parts. Among these, two of which perform transformations as shown in the figure 3.4 [18-19].

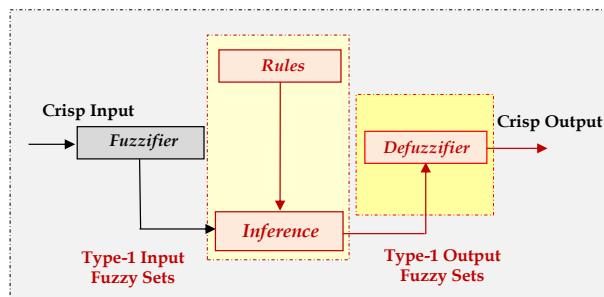


Figure.3.4 Block diagram of Mamdani Type-1 fuzzy logic inference system.

The four parts are: **1:** Fuzzifier (Transformation 1), **2:** Knowledge Base, **3:** Inference Engine (Fuzzy Reasoning) and **4:** Defuzzifier (Transformation 2):

A- Fuzzifier

The fuzzifier performs measurement of the input variables (input signals, real variables), scale mapping and Fuzzification (Transformation 1). Thus, all the monitoring input signals are scaled and the measured signals (crisp input quantities which have numerical values) are transformed into fuzzy quantities by the process of Fuzzification. This transformation is performed by using membership functions. In a conventional fuzzy logic controller, the number of membership functions and the shapes of these are initially determined by the user. There are many different types of membership functions, piecewise linear or continuous. The commonly used membership functions are bell-shaped, sigmoid, Gaussian, triangular and trapezoidal. A membership function has a value between 0 and 1, and it indicates the degree of belongingness of a quantity to a fuzzy set.

B- Knowledge Base

The knowledge base consists of the data base and the linguistic control rule base. The data base provides the information which is used to define the linguistic control rules and the fuzzy data manipulation in fuzzy controller. The rule base contains a set of *IF-THEN* rules and these rules specify the control goal actions by means of a set of linguistic control rules. In other words, the rule base contains rules which would be provided by an expert.

C- Inference Engine

It is the kernel of a fuzzy logic controller and has the capability of both simulating human decision-making based on fuzzy concepts and of inferring fuzzy control actions by using fuzzy implication and fuzzy logic rules of inference. In other words, once all the monitored input variables are transformed into their respective linguistic variables, the inference engine evaluates the set of *IF-THEN* rules and thus the result is obtained which is again a linguistic value for the linguistic variable. Then this linguistic result has to be transformed into a crisp output value of the fuzzy logic control.

D- Defuzzifier

The second transformation is performed by the Defuzzifier which performs scale mapping as well as defuzzification. The Defuzzifier yields a non-fuzzy, crisp control action from the inferred fuzzy control

action by using the consequent membership functions of the rules. There are many defuzzification techniques [18-19]. They are center of gravity method, height method, mean of maxima method, first of maxima method, sum of maxima method, center of average method, etc.

Fuzzy logic is an approach to computing based on degrees of truth rather than the usual true or false, 1 or 0. Boolean deals with reasoning that are approximate rather than fixed and exact. Fuzzy logic is the methodology for the handling of inexact, imprecise, qualitative, fuzzy, verbal information in a systematic and rigorous way.

Fuzzy logic is used for the following reasons:

- Parameter variations that can be compensated with designer judgments.
- Processes that can be modeled linguistically but not mathematically.
- Setting with the aim to improve efficiency as a matter of operator skill and attention.
- When the system depends on operator skill and attention.
- Whenever fuzzy logic based controller can be used as an advisor to the human operator.
- Data intensive modeling.

The block diagram given in figure 3.4, fuzzy logic controller was simulated using triangular membership function and the centroid method was used for defuzzification.

3.4.5 Membership Functions and Rule Base

Fuzziness in a fuzzy set is characterized by its membership functions. The membership functions convert the degree of fuzziness into the normalized interval (0, 1) where the boundary values 0 and 1 resemble membership degrees of crisp set members. The T1-FLC employed at RSC (rotor side converter) controller with seven (07) membership functions have been chosen for the inputs of: error rotor direct current ($eIrd$), with its derivate ($e dIrd$) and the output is the (Vrd); knowing that the same membership function will be applied for the rotor quadrature current (Irq). The purpose of T1-FLC in RSC controller is mainly used to stabilize the measured rotor direct and quadrature current (Ird and Irq) at their references. The chosen membership functions are triangular form which are the most accepted and balanced choice in many applications [20].

The seven (07) inputs and output membership functions (figure.3.5) are linguistically described as Negative Big-1 (NB1), Negative Medium-1 (NM1), Negative Small-1 (NS1), Zero-1 (ZE1), Positive Small-1 (PS1), Positive Medium-1 (PM1) and Positive Big-1 (PB1); knowing that “1” means the type-1 fuzzy logic. Figure.3.6 illustrates Schematic structure of Type-1 fuzzy logic controller under Matlab®/Si-

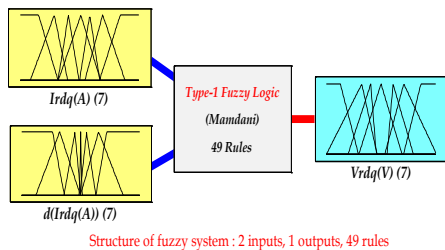


Figure.3.5 Global Memberships structure (2 inputs and 1 output).

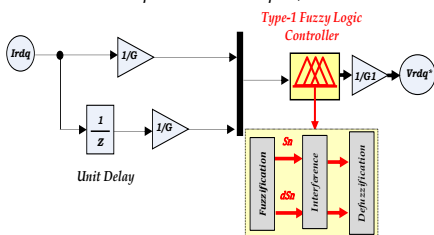


Figure.3.6 Schematic structure of Type-1 fuzzy logic controller under Matlab®/Simulink.

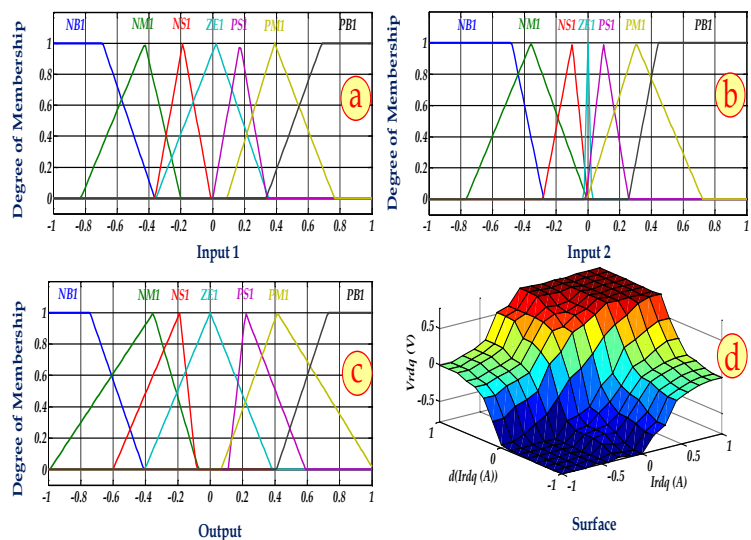


Figure.3.7 Simulation results of the membership functions (a and b: 2 inputs, c: 1 output and d: the fuzzy logic surface).

Table.3.1 Type-1 fuzzy logic inferences.

$U_{1,2}$		$dS_{1,2}$						
		NB1	NM1	NS1	EZ1	PS1	PM1	PB1
$S_{1,2}$	NB1	NB1	NB1	NB1	NM1	NS1	NS1	EZ1
	NM1	NB1	NM1	NM1	NM1	NS1	EZ1	PS1
	NS1	NB1	NM1	NS1	NS1	EZ1	PS1	PM1
	EZ1	NB1	NM1	NS1	EZ1	PS1	PM1	PM1
	PS1	NM1	NS1	EZ1	PS1	PS1	PM1	PB1
	PM1	NS1	EZ1	PS1	PM1	PM1	PM1	PB1
	PB1	EZ1	PS1	PS1	PM1	PB1	PB1	PB1

-mulink. Figure.3.7 depicts the simulation results of the membership functions using Matlab software; a and b: 2 inputs, c: 1 output and 4: the fuzzy logic surface).

The purpose of fuzzy logic controller is to make humanlike decisions by using the knowledge about controlling a target system. This is achieved by suitable fuzzy rules that constitute a fuzzy rule base. The fuzzy rules are formulated by means of IF-THEN rules. The rule table which is shown in Table 3.1 contains 49 rules (=7²). The structure of the fuzzy control rules for the two inputs and one output can be expressed as if (eI_{rd} is PB1 and deI_{rd} is PB1) THEN output Vrd is PB1.

The type-1 fuzzy rule base consists of a collection of linguistic rules¹ of the form [20-21]:

- Rule 1:** if $S_{1,2}$ is NB1, and $dS_{1,2}$ is NB1 then $U_{1,2}$ is NB1.
- Rule 2:** if $S_{1,2}$ is NM1, and $dS_{1,2}$ is NB1 then $U_{1,2}$ is NB1.
- Rule 3:** if $S_{1,2}$ is NS1, and $dS_{1,2}$ is NG1 then $U_{1,2}$ is NS1.
- ⋮
- ⋮
- ⋮
- Rule 49:** if $S_{1,2}$ is PB1, and $dS_{1,2}$ is PB1 then $U_{1,2}$ is PB1.

In this case, the T1-FLC controller is proposed to control rotor direct and quadrature currents respectively (I_{rd} and I_{rq}) instead the PID controllers, in order to improve the dynamic responses against parameter variation. The simulation results of the proposed algorithms will presented in section §.3.7.2 in figures-(3.20, 3.21 and 3.22).

3.5 Proposed Power control based on Type-2 Fuzzy Logic Control (T2-FLC)

Type-2 fuzzy logic systems (T2-FLS), introduced by Zadeh (1975) as an extension of ordinary Type-1 fuzzy logic systems (T1-FLS), are characterized by fuzzy membership functions represented by fuzzy sets in [0, 1] unlike a Type-1 fuzzy which have crisp membership functions [24].

Type-1 fuzzy logic controllers (FLCs) have proven effective in dealing with complex nonlinear systems containing uncertainties that are otherwise difficult to model or control. However, Type-1 FLCs have precise membership functions (MFs), i.e., there is nothing uncertain in such MFs. Consequently, using Type-1 FLCs may cause degradation in the performance of some systems with noise and uncertainties. On the other hand, the concept of Type-2 fuzzy sets is an extension of Type-1 fuzzy sets. The Type-2 fuzzy sets have grades of membership that are also fuzzy. The primary membership of Type-2 fuzzy sets can be any subset in [0, 1]. Moreover, corresponding to each primary membership, there is a secondary membership that is also in [0, 1], which defines the possibilities for the primary membership [24].

Both Type-1 fuzzy logic systems (FLSs) and Type-2 FLSs have the same four components: the fuzzifier, rule base, fuzzy inference engine, and output processor. Furthermore, unlike Type-1 FLSs, the output processor of Type-2 FLSs generates a Type-1 fuzzy set output using the type reducer or a crisp number using the Defuzzifier. A Type-2 FLS is also characterized by IF-THEN rules, but its antecedent or consequent sets are Type 2. Type-2 FLSs can be used when the circumstances are too

¹ Knowing that; the same linguistic rules (for T1-FLC) will be applied for the rotor quadrature current I_{rq}.

uncertain to determine membership grades exactly, such as for imprecise or vague data. Thus, the *Type-2 FLSs* have supplanted conventional technologies in many applications, especially in complex nonlinear systems. However, in general, *Type-2 FLSs* are computationally intensive due to the complexity of reducing *Type-2 FLSs* to *Type-1 FLSs* [24]. To simplify the computation, the secondary membership grade can be set to one, in which case the *Type-2 FLSs* become interval *Type-2 FLSs*. Currently, the most widely used *Type-2* fuzzy sets in *Type-2 FLCs* are interval *Type-2* fuzzy sets.

3.5.1 Overview of *Type-2* Fuzzy Logic Controller Toolbox

Figure.3.8 shows the FIS Editor by using *Type-1* fuzzy logic control (A) and *Type-2* fuzzy logic control (B) respectively via MATLAB/Simulink R2009a. Figure.3.9 depicts *Type-2* fuzzy logic toolbox interface.

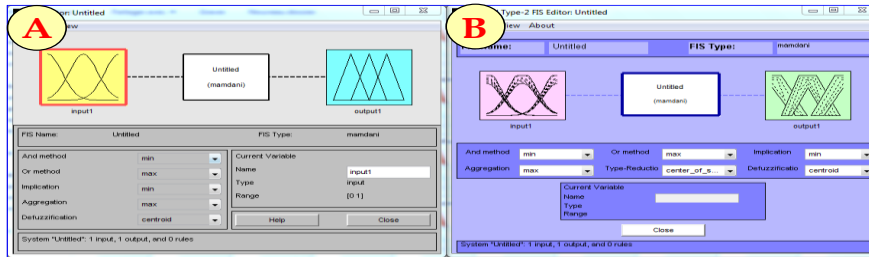


Figure.3.8 FIS editor A: type-1 fuzzy logic toolbox, B: type-2 fuzzy logic toolbox.

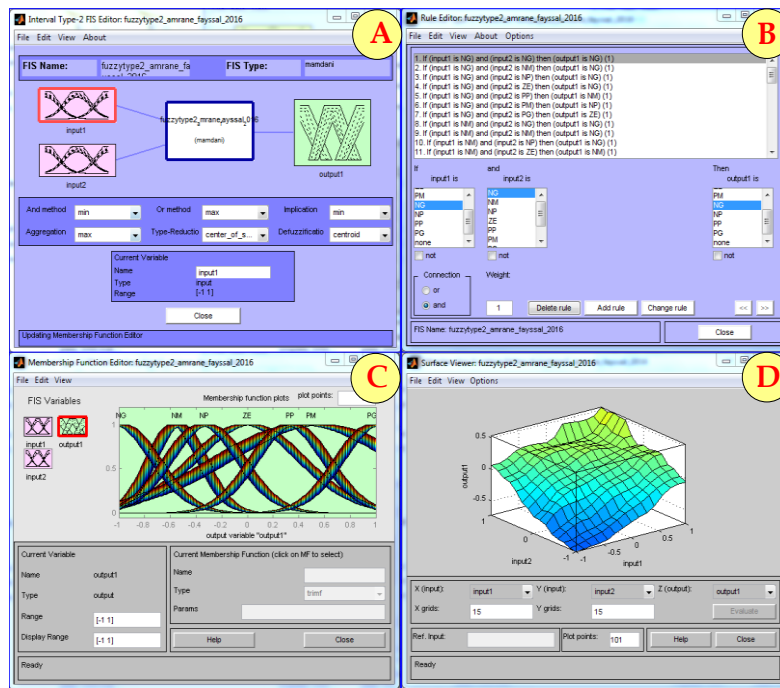


Figure.3.9 Type-2 fuzzy logic interface; A: Membership function editor of *Type-2* fuzzy logic toolbox, B: Rule editor of *type-2* fuzzy logic toolbox, C: 2 Inputs-1output Membership function editor of *type-2* fuzzy logic Toolbox, D: Surface viewer of *type-2* fuzzy logic toolbox.

3.5.2 Design of *Type-2* Fuzzy Logic Controller

As described in §.3.4.4, the *Type-2* fuzzy logic control (*T2-FLC*) have the same principle as *T1-FLC*, is also composed from four parts are: **1:** Fuzzifier (*Transformation 1*), **2:** Knowledge Base, **3:** Inference Engine (*Fuzzy Reasoning*) and **4:** Defuzzifier (*Transformation 2*). But the structure is different than *T1-FLC*.

The structure of a *type-2* Fuzzy Logic System (*FLS*) is shown in figure.3.10. It is actually very similar to the structure of an ordinary *type-1 FLS*. It is assumed in this chapter that the reader is familiar with *type-1 FLSs* and thus, in this section, only the similarities and differences between *type-2* and *type-1 FLSs* are underlined.

The fuzzifier shown in figure.3.10, as in a type-1 FLS, maps the crisp input into a fuzzy set. This fuzzy set can be a type-1, type-2 or a singleton fuzzy set. In singleton Fuzzification, the input set has only a single point of nonzero membership. The singleton fuzzifier is the most widely used fuzzifier due to its simplicity and lower computational requirements.

The shaded region in figure.3.11-(a) is the FOU for a type-2 fuzzy set. The primary memberships: J_{x1} and J_{x2} and their associated secondary membership functions $u_{\hat{A}}(x_1)$ and $u_{\hat{A}}(x_2)$ are shown at the points x_1 and x_2 . The upper and lower membership functions, $\bar{u}_{\hat{A}}(x)$ and $\underline{u}_{\hat{A}}(x)$, are also shown in figure.3.11-(a). The secondary membership functions, which are interval sets, are shown in figure.3.11-(b) [5].

The third dimension of type-2 fuzzy sets decides secondary membership function and the FOU decides the range of uncertainty, together provides additional degree of freedom in the design to compensate various uncertainties. Hence, wind energy systems, being highly uncertain, can utilize the special features of type-2 FLSs to improve its operational efficiency in the grid interaction [25]. The type2 fuzzy controller utilized in this work has two inputs and one output. The membership functions are defined in figure.3.12 (A and B). The inferences of T2-FLC can be made in a more explain as shown in table.3.2 [26-27].

The purpose of T2-FLC is to make humanlike decisions by using the knowledge about controlling a target system. This is achieved by suitable fuzzy rules that constitute a fuzzy rule base. The fuzzy rules are formulated by means of IF-THEN rules. The rule table which is shown in Table 3.2 contains 49 rules ($=7^2$). The structure of the fuzzy control rules for the two inputs and one output can be expressed as if (elrd is PB2 and delrd is PB2) THEN output Vrd is PB2.

The type-2 fuzzy rule base consists of a collection of linguistic rules² of the form [27-28]:

- Rule 1:** if $S_{1,2}$ is NB2, and $dS_{1,2}$ is NB2 then $U_{1,2}$ is NB2.
- Rule 2:** if $S_{1,2}$ is NM2, and $dS_{1,2}$ is NB2 then $U_{1,2}$ is NB2.
- Rule 3:** if $S_{1,2}$ is NS2, and $dS_{1,2}$ is NG2 then $U_{1,2}$ is NS2.
- ⋮
- Rule 49:** if $S_{1,2}$ is PB2, and $dS_{1,2}$ is PB2 then $U_{1,2}$ is PB2.

Table.3.2 Type-2 fuzzy logic inferences [29]:

$U_{1,2}$		$dS_{1,2}$						
		NB2	NM2	NS2	EZ2	PS2	PM2	PB2
$dS_{1,2}$	NB2	NB2	NB2	NB2	NM2	NS2	NS2	EZ2
	NM2	NB2	NM2	NM2	NM2	NS2	EZ2	PS2
	NS2	NB2	NM2	NS2	NS2	EZ2	PS2	PM2
	EZ2	NB2	NM2	NS2	EZ2	PS2	PM2	PM2
	PS2	NM2	NS2	EZ2	PS2	PS2	PM2	PB2
	PM2	NS2	EZ2	PS2	PM2	PM2	PM2	PB2
	PB2	EZ2	PS2	PS2	PM2	PB2	PB2	PB2

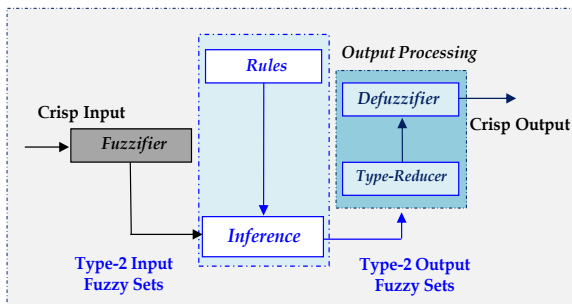


Figure.3.10 Block diagram of Mamdani Type-2 fuzzy logic inference system.

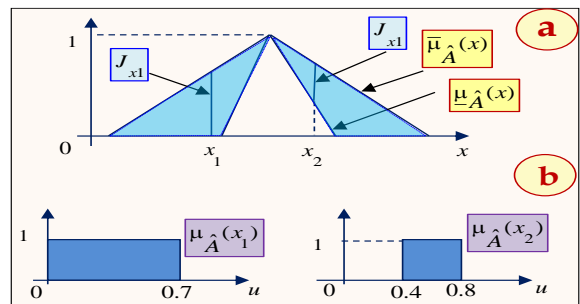


Figure.3.11-(a) The FOU for a type-2 fuzzy set, (b) The secondary membership functions.

² Knowing that; the same linguistic rules (for T2-FLC) will be applied for the rotor quadrature current I_{rq}.

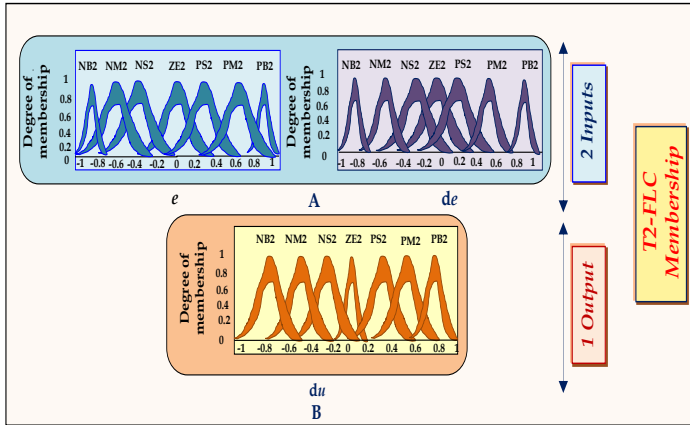


Figure.3.12 Membership functions (A: inputs and B: output).

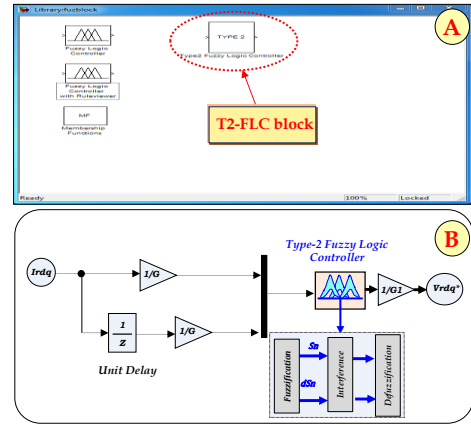


Figure.3.13 (A and B) Schematic structure of Type-2 fuzzy logic controller under Matlab®/Simulink.

Knowing that: the schematic structure of type-2 fuzzy logic controller under Matlab/Simulink® R2009a (in order to control I_{rd} and I_{rq}) is illustrated in details in figure.3.13-(A and B).

In this case, the T2-FLC controller is proposed to control rotor direct and quadrature currents respectively (I_{rd} and I_{rq}) instead the PID controllers, in order to improve the dynamic responses against parameter variation. The simulation results of the proposed algorithms will presented in section §.3.7.3 in figures-(3.23, 3.24 and 3.25).

3.6 Proposed Power control based on Neuro-Fuzzy Control (NFC)

The block diagram of the neuro-fuzzy controller (NFC) system is shown in figure.3.14. The NFC controller is composed of an on-line learning algorithm with a neuro-fuzzy network. The neuro-fuzzy network is trained using an on-line learning algorithm. The NFC has two inputs, the rotor current error e_{ird} and the derivative of rotor current error \dot{e}_{ird} . The output is rotor direct voltage V_{dr} . For the NFC of rotor current I_{rq} is similar with I_{rd} controller [30].

For the NFC, a four layer NN as shown in figure.3.16 is used. Layers I-IV represents the inputs of the network, the membership functions, the fuzzy rule base and the outputs of the network, respectively [30]. Knowing that: The parameters of the proposed NFC are illustrated in details in table.3.3. The training error is depicted in figure.3.15, which equals to 0.05; presents very good precision).

3.6.1 Layer I: Input layer

Inputs and outputs of nodes in this layer are represented as:

$$net_1^I = e_{idr}(t), y_1^I = f_1^I(net_1^I) = net_1^I = e_{idr}(t) \tag{3.12}$$

$$net_2^I = \dot{e}_{idr}(t), y_2^I = f_2^I(net_2^I) = net_2^I = \dot{e}_{idr}(t) \tag{3.13}$$

Where e_{idr} and \dot{e}_{idr} are inputs y_1^I and y_2^I are outputs of the input layer. In this layer, the weights are unity and fixed.

3.6.2 Layer II: membership layer

In this layer, each node performs a fuzzy set and the Gaussian function is adopted as a membership function.

Table.3.3 The parameters of the proposed Neuro-fuzzy controller.

Type:	Takagi Sugeno.
Number of iteration:	500.
Error tolerance:	5×10^{-3} .
Epochs:	1000.
Number of membership function:	7.
Number of hidden layer neuron:	14.

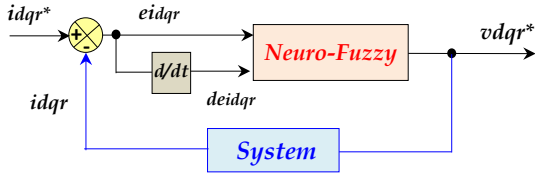


Figure.3.14 Block diagram of the neuro-fuzzy controller under Matlab/Simulink®.

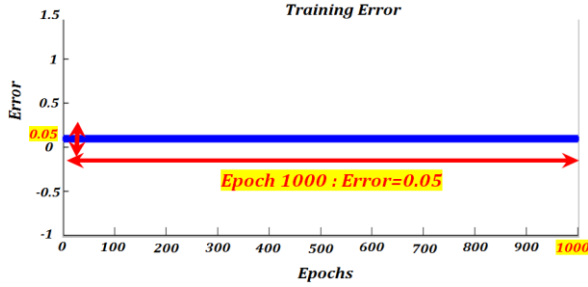


Figure.3.15 Simulation results of training error (0.05) using 1000 epochs.

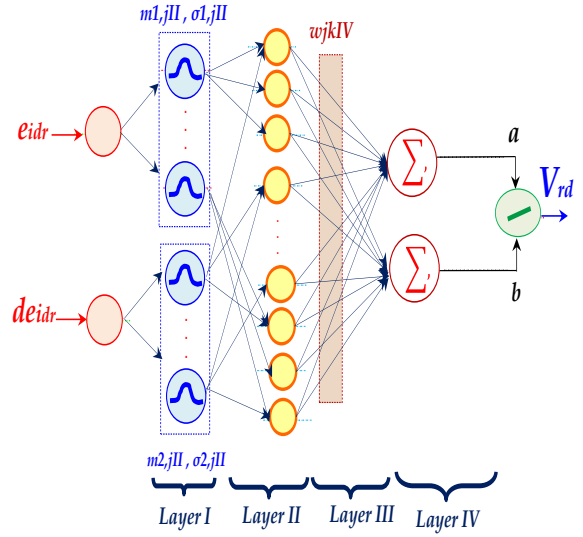


Figure.3.16 Schematic diagram of the neuro-fuzzy network.

$$net_{1,j}^{II} = -\frac{(x_{1,j}^{II} - m_{1,j}^{II})^2}{(\sigma_{1,j}^{II})^2}, y_{1,j}^{II} = f_{1,j}^{II}(net_{1,j}^{II}) = \exp(net_{1,j}^{II}) \quad (3.14)$$

$$net_{2,k}^{II} = -\frac{(x_{2,k}^{II} - m_{2,k}^{II})^2}{(\sigma_{2,k}^{II})^2}, y_{2,k}^{II} = f_{2,k}^{II}(net_{2,k}^{II}) = \exp(net_{2,k}^{II}) \quad (3.15)$$

Where: $m_{1,j}^{II}$, $m_{2,k}^{II}$ and $\sigma_{1,j}^{II}$, $\sigma_{2,k}^{II}$ are respectively, the mean and the standard deviation of the Gaussian function. There are $j + k$ nodes in this layer.

3.6.3 Layer III: rule layer

This layer includes the rule base used in the fuzzy logic control (FLC). Each node in this layer multiplies the input signals and outputs the result of product [10].

$$net_{j,k}^{III} = (x_{1,j}^{III} * x_{2,k}^{III}), y_{j,k}^{III} = f_{j,k}^{III}(net_{j,k}^{III}) = net_{j,k}^{III} \quad (3.16)$$

Where the values of link weights between the membership layer and rule base layer are unity.

3.6.4 Layer IV: output layer

This layer represents the inference and defuzzification used in the FLC. For defuzzification, the center of area method is used; therefore the following form can be obtained:

$$a = \sum_j \sum_k w_{jk}^{IV} y_{jk}^{III}, b = \sum_j \sum_k y_{jk}^{III} \quad (3.17)$$

$$net_0^{IV} = \frac{a}{b}, y_0^{IV} = f_0^{IV}(net_0^{IV}) = \frac{a}{b} \quad (3.18)$$

Where y_{jk}^{III} is the output of the rule layer; a and b are the numerator and the denominator of the function used in the center of area method, w_{jk}^{IV} is the center of the output membership functions used in the FLC, respectively.

The aim of the learning algorithm is to adjust the weights of w_{jk}^{IV} , $m_{1,j}^{II}$, $m_{2,k}^{II}$, $\sigma_{1,j}^{II}$, $\sigma_{2,k}^{II}$. The on-line learning algorithm is a gradient descent search algorithm in the space of network parameters.

The error expression for the input of Layer IV:

$$\delta_0^{IV} = -\frac{\partial e_{idr}(t) \dot{e}_{idr}(t)}{\partial y_0^{IV}} * \frac{\partial y_0^{IV}}{\partial net_0^{IV}} = \mu_5 e_{idr} \quad (3.19)$$

Where μ_5 is the learning-rate for w_{jk}^{IV} and it can be shown in following equation.

Therefore, the changing of w_{jk}^{IV} is written as:

$$\Delta w_{jk}^{IV} = -\frac{\partial e_{idr}(t) \dot{e}_{idr}(t)}{\partial net_0^{IV}} * \frac{\partial net_0^{IV}}{\partial a} * \frac{\partial a}{\partial w_{jk}^{IV}} = \frac{1}{b} \delta_0^{IV} y_{jk}^{III} \quad (3.20)$$

Since the weights in the rule layer are unified, only the approximated error term needs to be calculated and propagated by the following equation:

$$\delta_{jk}^{III} = -\frac{\partial e_{idr}(t)\dot{e}_{idr}(t)}{\partial net_0^{IV}} * \frac{\partial net_0^{IV}}{\partial y_{1,j}^{III}} * \frac{\partial y_{1,j}^{III}}{\partial net_{jk}^{III}} = \frac{1}{b} \delta_0^{IV} (w_{jk}^{IV} - y_0^{IV}) \quad (3.21)$$

The error received from *Layer III* is computed as:

$$\delta_{1k}^{II} = \sum_k \left[\left(-\frac{\partial e_{idr}(t)\dot{e}_{idr}(t)}{\partial net_{jk}^{III}} \right) * \frac{\partial net_{jk}^{III}}{\partial y_{1,j}^{II}} * \frac{\partial y_{1,j}^{II}}{\partial net_{1,j}^{II}} \right] = \sum_k \delta_{jk}^{III} y_{jk}^{III} \quad (3.22)$$

$$\delta_{2k}^{II} = \sum_j \left[\left(-\frac{\partial e_{idr}(t)\dot{e}_{idr}(t)}{\partial net_{jk}^{III}} \right) * \frac{\partial net_{jk}^{III}}{\partial y_{2,j}^{II}} * \frac{\partial y_{2,j}^{II}}{\partial net_{2,j}^{II}} \right] = \sum_k \delta_{jk}^{III} y_{jk}^{III} \quad (3.23)$$

The updated laws of: $m_{1,j}^{II}$, $m_{2,k}^{II}$, and $\sigma_{1,j}^{II}$, $\sigma_{2,k}^{II}$ also can be obtained by the gradient decent search algorithm:

$$\Delta m_{1,j}^{II} = -\frac{\partial e_{idr}(t)\dot{e}_{idr}(t)}{\partial net_{1,j}^{II}} * \frac{\partial net_{1,j}^{II}}{\partial m_{1,j}^{II}} = \mu_4 \delta_{1,j}^{II} * \frac{2 * (x_{1,j}^{II} - m_{1,j}^{II})}{(\sigma_{1,j}^{II})^2} \quad (3.24)$$

$$\Delta m_{2,k}^{II} = -\frac{\partial e_{idr}(t)\dot{e}_{idr}(t)}{\partial net_{2,k}^{II}} * \frac{\partial net_{2,k}^{II}}{\partial m_{2,k}^{II}} = \mu_3 \delta_{2,k}^{II} * \frac{2 * (x_{2,k}^{II} - m_{2,k}^{II})}{(\sigma_{2,k}^{II})^2} \quad (3.25)$$

$$\Delta \sigma_{1,j}^{II} = -\frac{\partial e_{idr}(t)\dot{e}_{idr}(t)}{\partial net_{1,j}^{II}} * \frac{\partial net_{1,j}^{II}}{\partial \sigma_{1,j}^{II}} = \mu_2 \delta_{1,j}^{II} * \frac{2 * (x_{1,j}^{II} - m_{1,j}^{II})^2}{(\sigma_{2,k}^{II})^3} \quad (3.26)$$

Where: μ_4 , μ_3 , μ_2 and μ_1 are the learning-rate parameters of the mean and the standard deviation of the Gaussian functions.

In this case, the NFC controller is proposed to control rotor *direct and quadrature* currents respectively (I_{rd} and I_{rq}) instead the *PID* controller, in order to improve the dynamic responses against parameter variation. The simulation results of the proposed algorithms will presented in section §.3.7.4 in figures-(3.26, 3.27 and 3.28).

3.7 Simulation results

The proposed system (*DFIG' control + wind turbine*)³ is validated using *Matlab/Simulink*[®] software under *MPPT* strategy by keeping stator reactive power equals to zero and to ensure unity power factor ($PF=1$). The figures.3-(17, 20, 23 and 26) respectively present the simulation results for *novel IDPC using MRAC, T1-FLC, T2-FLC and NFC* respectively under *two level converters*. These figures are divided into three parts; the left part (*red color*) presents the simulation results of the wind system without using the *MPPT* strategy by imposing stator active and reactive power profiles, in the middle (*blue color*) presents the simulation results of the wind-system under *MPPT* strategy using step form of wind speed; Which it can only illustrate *Sub-synchronous* mode because the generator speed is still less than the synchronous speed, and at right part (*green color*) presents the simulation results of the wind-system under *MPPT* strategy using random form of wind speed; which can illustrate both modes; *Sub* and *Super-synchronous* mode because the generator speed vary above and below the synchronous speed). The three (03) modes applied in simulation section in transient and steady states are described as flows:

- 1- **Mode I (Red color/** to the left side of figures.3-(17, 20, 23 and 26)): Without *MPPT* Strategy, in this case we impose the P_s and Q_s reference profiles.
- 2- **Mode II (Blue color/** to the middle of figures.3-(17, 20, 23 and 26)): With *MPPT* strategy, in this case we propose a low wind speed based on step form (Max wind speed = 11.5 m/sec) by keeping stator reactive power equal to Zero level " $Q_s = 0$ (Var)"; to ensure only the exchange of the stator active power to the grid; means following the maximum active power point.
- 3- **Mode III (Green color/** to the right side of figures.3-(17, 20, 23 and 26)): With *MPPT* strategy, in this case we propose a medium wind speed based on random form (Max wind speed = 13.5 m/sec) by keeping stator reactive power equal to Zero level " $Q_s = 0$ Var"; to ensure only the exchange of the stator active power to the

³ Please refer to Appendix A-"Section A-1"; (The *DFIG'* and wind turbine parameters are indicated in Table.A.1 and Table.A.2 respectively).

grid; means following the maximum active power point.

The second part focuses on the comparative simulation study between the MPPT strategy (using step' and random wind speed) for novel IDPC algorithms (using MRAC, T1-FLC, T2FLC and NFC respectively) is described in details in figures.3-(18, 21, 24 and 27) respectively. This section is developed in order to illustrate the Sub and Super-synchronous modes and the behavior of slip under generator speed variation.

The third part deals on robustness tests using a comparative simulation study, for three modes (with/without MPPT strategy) for novel IDPC algorithms (using MRAC, T1-FLC, T2FLC and NFC respectively) is described in details in figures.3-(19, 22, 25 and 28) respectively. This section is developed in order to verify the robustness of wind-system under parameter variation (using three tests)⁴ in transient and steady states.

3.7.1 Topology 1: Improved IDPC (based on MRAC controllers)

The simulation results of this topology (novel IDPC based on MRAC controller) are described in details in figures.3-(17, 18 and 19). Figure.3.17 presents the behavior of the wind-system (using DFIG (4 kW) and wind turbine (4.5 kW)) under three modes (that already presented above) in transient and steady states. Following are detailed description of the simulation results under three (03) modes:

Mode 1 (red color/figure.3.17 to the left side): The measured stator active and reactive powers (P_{s_meas} and Q_{s_meas}) and their references (P_{s_ref} and Q_{s_ref}) profiles are presented together in figure.3.17-(a) and are presented separately in figures.3.17.(b and c) respectively. The reference powers are indicated in table.3.4. It is clear that the measured powers (active and reactive) have good tracking power (neglected error) compared to their reference powers in transient and steady states (refer to figures.3.17-(b and c)), a neglected ($\approx 5\%$) overshoot is noted at 0.3 (sec) and 1.0 (sec) respectively in measured stator reactive' and active power (P_{s_meas} and Q_{s_meas}) (in this case the MRAC is robust in terms of overshoot especially if the step power' changement is big). The direct and quadratu-re components of currents and flux (I_{rd} , I_{rq} and Φ_{rd} , Φ_{rq}) are presented respectively in figure.3.17-(e and g), which present the inverse diagrams compared to reactive and active powers. The inverse case for stator direct and quadrature currents (I_{sd} , I_{sq}) which have the same diagrams of reactive and active powers, and they are presented in figure.3.17-(d). The power error is presented in figure.3.17-(f); we observe a small power error of active and reactive powers $-80 (W_Var) \leq \Delta P_s \Delta Q_s \leq +80 (W_Var)$. The stator' and rotor currents; I_{s_abc} and I_{r_abc} are shown in figure.3.17-(h and i) respectively, we remark the sinusoidal form of the three rotor and stator phases currents, and excellent THD of stator currents ($\ll 5\%$ respect the IEEE-519 Std). The power factor (PF) of the proposed control is presented in figure.3.17-(j), knowing that PF is the ratio of P to S (apparent power), took the top value when the reactive power equals to zero value; refer to these time interval in figures.3.17-(a, b, c and j): 0-0.3 (sec), 0.9-1.0 (sec) and 1.2-1.5(sec); and this is the main aim of MPPT strategy/keeping at any time the unity power factor regardless wind speed variation and parameters changement. In 1.0-1.2 (sec) neglected ripples are noted. Table.3.5 described in details the obtained results of the novel IDPC based on MRAC for Mode: 1.

Mode 2 (blue color/figure.3.17 to the middle): The reference stator active power (P_{s_ref}) (as shown in figure.3.17-(a)) is extracted from MPPT strategy (in this case, the wind speed will take step form); it takes the inverse

Table.3.4 The proposed profiles of the active and reactive power references.

Time (sec):	Stator active power (W):	Stator reactive power (Var):
[0 - 0.2]	-700.	0.
[0.2-0.4]	-1400.	-1400.
[0.4-0.6]	-700.	0.
[0.6-0.8]	-1400.	+1400.
[0.8-1.0]	-700.	0.
[1.0-1.2]	-1400.	-1400.
[1.2-1.4]	-700.	0.
[1.4-1.5]	-1400.	+1400.

⁴ Knowing that in this chapter the robustness tests are based on three tests as follows: [Test-1: without parameter changement → Blue color, Test-2: +100% of R_r and -25% of (L_s , L_r and L_m) → Brown color and Test-3: +100% of (J and R_r), -25 % of (L_r , L_s and L_m) → Green color] respectively.

diagram of wind speed. The stator reactive power (Q_{s_ref}) equals to 0 (Var), represents power factor unity. It is clear that the measured powers (active and reactive) have good tracking with neglected undulations compared to their reference powers in transient and steady states, a neglected ($\approx 5\%$) overshoot is noted at 0.6 (sec) in measured stator reactive' and active power (P_{s_meas} and Q_{s_meas}) (because the MRAC controller is very robust in terms of overshoot especially if the wind power' changement is big). The direct and quadrature components of currents and flux (I_{rd} , I_{rq} and Φ_{rd} , Φ_{rq}) are presented respectively in figures.3.17-(e and g), which present the inverse diagrams compared to reactive and active powers. The inverse case for stator direct and quadrature currents (I_{sd} , I_{sq}) which have the same diagrams of reactive and active powers, and they are presented in figure.3.17-(d). The power error is presented in figure.3.17-(f), we observe a small power error of active and reactive powers $-90 (W_Var) \leq \Delta P_s \Delta Q_s \leq +90 (W_Var)$. The stator' and rotor currents; I_{s_abc} and I_{r_abc} are shown in figures.3.17-(h and i) respectively, we remark the sinusoidal form of the waveforms and excellent THD of stator currents will be injected into the grid ($= 0.32\%$ respect the IEEE-519 Std). The power factor (PF) of the proposed control is presented in figure.3.17-(j), knowing that PF is the ratio of P to S (apparent power), it reaches the top value when the reactive power equals to zero value (refer to these time interval in figures.3.17-(a, b, c and j); in this case the stator reactive power equals to zero value means the PF had taken always the unity; and this is the main aim of MPPT strategy/keeping at any time the unity power factor regardless wind speed variation and parameter variation. Table.3.5 described in details the obtained results of the novel IDPC based on MRAC for Mode: II.

Mode 3 (green color/figure.3.17 to the right): The reference stator active power (P_{s_ref}) (figure.3.17-(a)) is extracted from MPPT strategy (in this case, the wind speed will take random form); it takes the inverse diagram of wind speed. The stator reactive power (Q_{s_ref}) equal to 0 (Var), represents power factor unity. It is clear that the measured powers (active and reactive) have good tracking with neglected undulations compared to their reference powers in transient and steady states, a neglected ($\approx 5\%$) overshoot is noted at 0.5 (sec) and 0.8 (sec) in measured stator reactive' and active power (P_{s_meas} and Q_{s_meas}) (because the MRAC controller is robust in terms of overshoot especially if the wind power' changement is big). The direct and quadrature components of currents and flux (I_{rd} , I_{rq} and Φ_{rd} , Φ_{rq}) are presented respectively in figures.3.17-(e and g), which present the inverse diagrams compared to reactive and active powers. The inverse case for stator direct and transversal currents (I_{sd} , I_{sq}) which have the same diagrams of reactive and active powers, and they are presented in figure.3.17-(d). The power error is presented in figure.3.17-(f), we observe a low power error of active and reactive powers $-90 (W_Var) \leq \Delta P_s \Delta Q_s \leq +90 (W_Var)$. The stator' and rotor currents; I_{s_abc} and I_{r_abc} are shown in figures.3.17-(h and i) respectively, we remark the sinusoidal form of the waveforms and excellent THD of stator currents will be injected into the grid ($= 0.26\%$ respect the IEEE-519 Std). The power factor (PF) of the proposed control is presented in figure.3.17-(j), knowing that PF is the ratio of P to S (apparent power), it reaches top the value when the reactive power equals to zero value (refer to these time interval in figures.3.17-(a, b and j); and this is the main aim of MPPT strategy/keeping at any time the unity power factor regardless wind speed variation and parameter variation. Table.3.5 described in details the obtained results of the novel IDPC based on MRAC for Mode: III.

MPPT Strategy: Knowing that in the left side of figure.3.18 (Mode: II); the wind speed had taken the step form and the right side of figure.3.18 (Mode: III); the wind speed had taken the random form. Figure.3.18-(a) presents the stator active and reactive powers and its references profiles using of the novel IDPC based on MRAC for pitch angle equals to 0° ($B^\circ=0^\circ$) means the maximum power. It can be seen that the measured powers (active and reactive) follow their references despite the sudden variation of wind speed in transient and steady states with a good tracking power. Figures.3.18-(b) illustrate the stator active power under different pitch angle ($B^\circ=0^\circ, 1^\circ, 1.5^\circ, 2^\circ$ and 2.05°), it can be seen the inverse proportionality between the active powers and pitch angle and neglected undulations were noted. Figures.3.18-(c) illustrate the stator reactive power under different pitch angle ($B^\circ=0^\circ, 1^\circ, 1.5^\circ, 2^\circ$ and 2.05°), it is clear that the reactive power maintain the zero level despite the pitch angle variation (the maximum wind power is reached at $B^\circ=0^\circ$ (black color) as mentioned from MPPT strategy/refer to §2.4.1). Figure.3.18-(d) illustrates the wind speed forms; figure.3.18-(d/to the left) presents the step wind speed (maximum value equals to 11.5 m/sec) and figure.3.18-(d/to the right) displays the random wind speed (maximum value equals to 13.5 m/sec). Figure.3.18-(e) presents the generator speed (rpm);

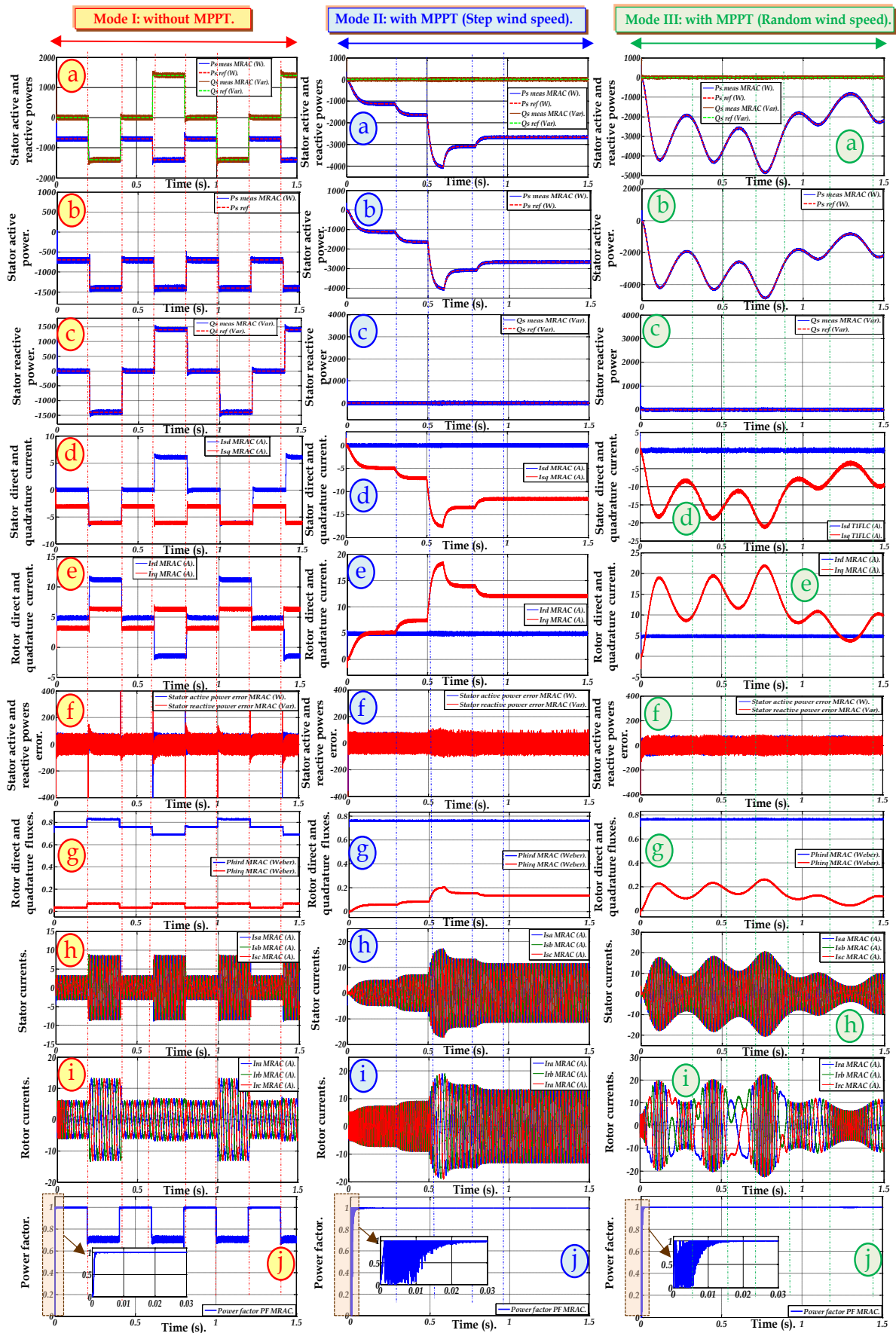


Figure.3.17 Simulations results of proposed control based on MRAC using three (03) modes; (a): stator active and reactive powers, (b): stator active power, (c): stator reactive power, (d): stator direct and quadrature currents, (e): rotor direct and quadrature currents, (f): stator active and reactive power error, (g): rotor direct and quadrature fluxes, (h): stator currents, (i): rotor currents, (j): power factor.

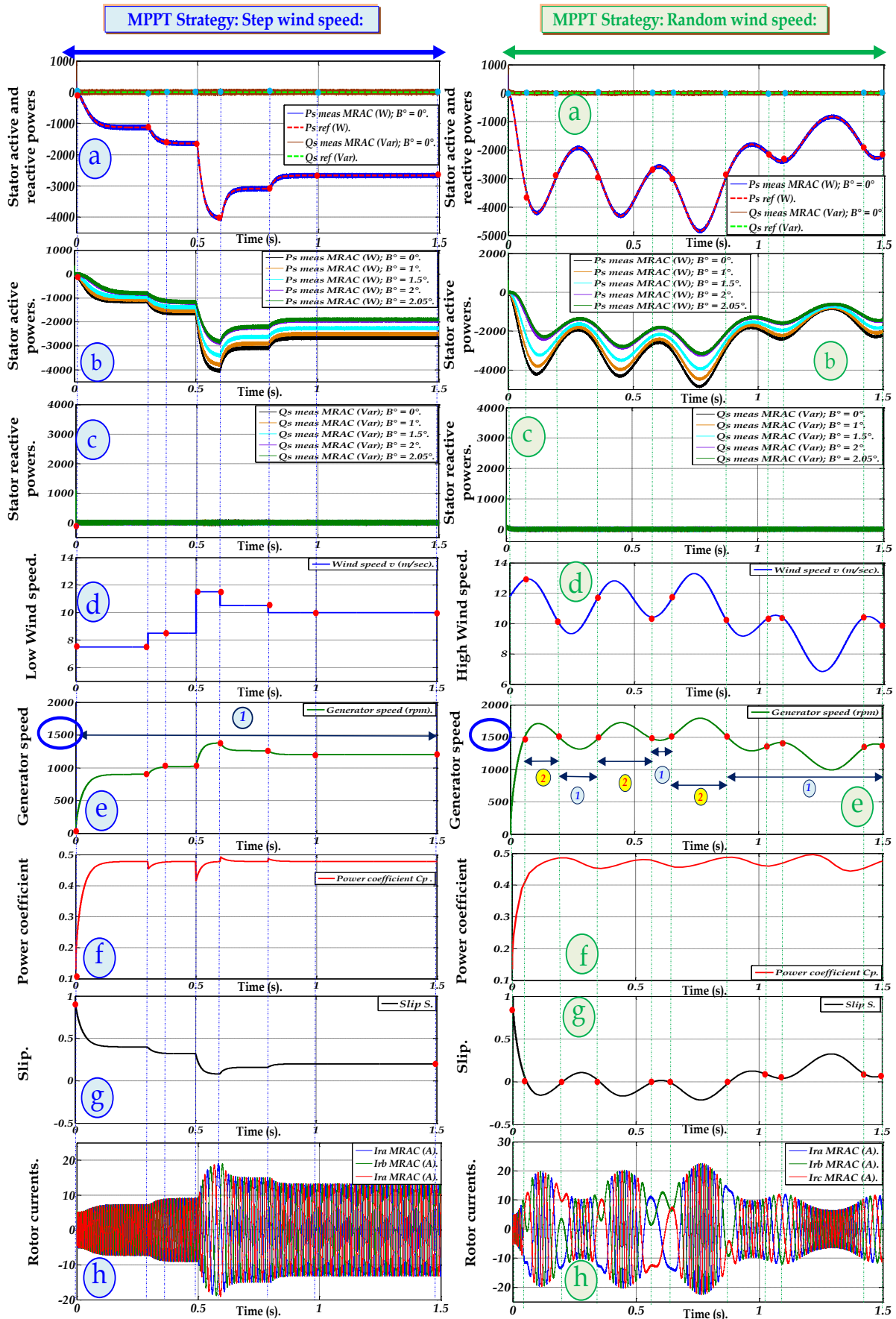


Figure 3.18 Simulations results of two MPPT strategy modes of proposed control based on MRAC; (a) stator active and reactive powers, (b) stator active power using different B° pitch angles, (c) stator reactive power using different pitch angles B° , (d) wind speed, (e) generator speed, (f) power coefficient, (g) slip, (h) rotor currents.

figure.3.18-(e/to the left) presents the generator speed (<1500 rpm) means the Sub-synchronous mode, noted by '1' and figure.3.18-(e/to the right) displays the generator speed (below and above the synchronous speed (1500 rpm) means the Sub-synchronous and Super-synchronous mode operations noted by '1' and '2' respectively). Figure.3.18-(f) displays the power coefficient (C_p); figure.3.18-(f/to the left) illustrates the power coefficient under Mode: II, it is clear that C_p had maintained the maximum value (≈ 0.48) regardless the wind speed variation and figure.3.18-(f/to the right) presents the C_p under Mode: III, in this case C_p had maintained the maximum value despite of wind speed variation. Figure.3.18-(g) displays the slip behavior (S) during the generator speed variation; figure.3.18-(g/to the left) illustrates the behavior of S under generator speed variation, in this case S varies between '+1' and '0' $\rightarrow 0 < S \leq +1$ means the generator speed did not reach the synchronous speed (always < 1500 rpm), figure.3.18-(g/to the right) represents the S behavior under generator speed variation, in this case S varies between '+1' and '-1' $\rightarrow -1 < S \leq +1$ means the generator speed varies below and above the synchronous speed (superior and inferior 1500 rpm), in the case when S reaches zero value means the mechanical speed $N_r=1500$ rpm this case called the synchronous mode (because S equals $(N_s-N_r)/N_s$), for exp: in the case of mechanical speed $N_r=1500$ rpm and $N_s=1500$ rpm $= (60 \cdot f)/P = (60 \cdot 50)/2 = 1500$ rpm means $S = (1500-1500)/1500 = 0$ is the stable zone, please refer to Appendix: A, DFIG's parameters (Table.A.1). Figure.3.18-(h) displays the behavior of rotor currents under generator speed variation; figure.3.18-(h/to the left) illustrates the sinusoidal waveforms of rotor currents (in this case the rotor currents did not change the sense because the S did not reach the zero value) and figure.3.18-(h/to the right) demonstrates the rotor currents behavior under generator speed variation, it can be seen the rotor currents had changed the sense in the case when S equals to zero value means when the generator speed varied near the synchronous speed.

Robustness tests⁵: Knowing that in the left side of figure.3.19-(Mode: I/without MPPT strategy); the middle side of figure.3.19-(Mode: II/using Step wind speed) and right side of figure.3.19-(Mode: III/using random

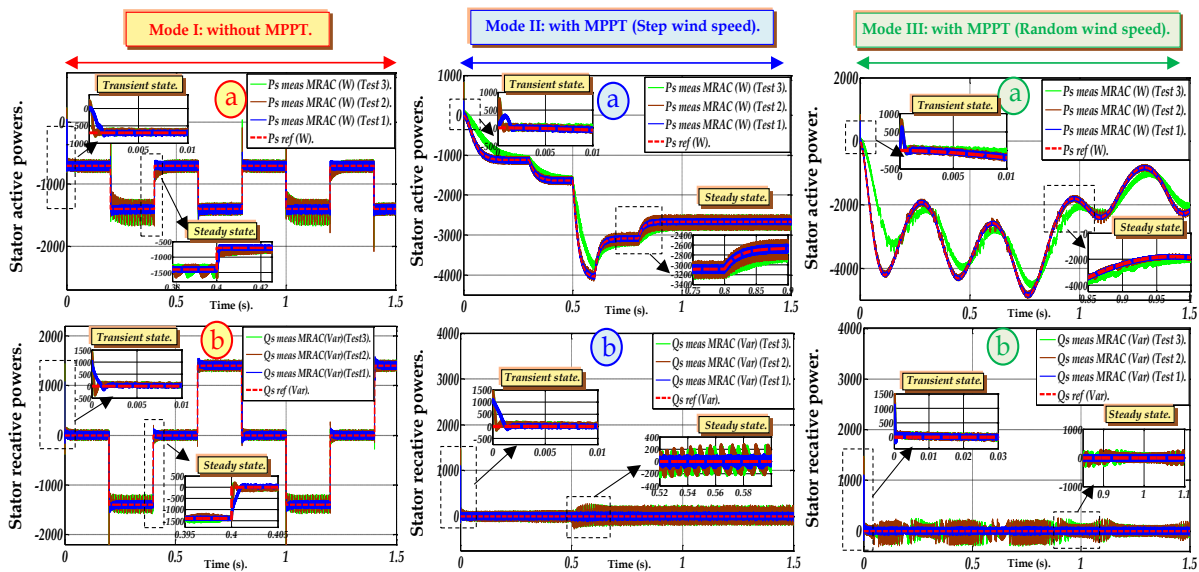


Figure.3.19 Robustness tests of proposed control based on MRAC using three (03) modes; a: stator active powers, b: stator reactive powers.

Table.3.5 Performances results for proposed control based on MRAC using back-to-back SVM converter⁶:

	THD_Is_abc (%) :	THD_Ir_abc (%) :	Overshoot :	Response time (sec) :	Power Error (W_Var) :
Mode I:	0.77 %	38.50 %	Neglected ($\approx 5\%$).	$1.45 \cdot 10^{-3}$.	+/- 80.
Mode II:	0.32 %	5.94 %	Neglected ($\approx 5\%$).	$1.4 \cdot 10^{-3}$.	+/- 90.
Mode III:	0.26 %	80.88 %	Neglected ($\approx 5\%$).	$1.3 \cdot 10^{-3}$.	+/- 90.

⁵ Knowing that in this chapter the robustness tests are based on three tests as follows: [Test-1: without parameter chngement \rightarrow Blue color, Test-2: +100% of R_r and -25% of $(L_s, L_r$ and $L_m)$ \rightarrow Brown color and Test-3: +100% of $(J$ and $R_r)$, -25% of $(L_r, L_s$ and $L_m)$ \rightarrow Green color] respectively.

⁶ Knowing that he performance' results of tables.3-(5, 6, 7 and 8) are taken without robustness test.

wind speed). In Mode: I (red color), figures.3.19-(a and b/to the left) illustrate the behavior of stator active and reactive powers under parameters variations. It can be noted big power in active and reactive power especially using the 2nd test (brown color/please refer to the bottom of the page) and 3rd test (green color) with remarkable undulations especially in transient and steady states (please refer to zoom) and the value of power error reaches nearly ± 80 (W_Var) in Test-1, and nearly ± 200 (W_Var) in Test-2 and Test-3. A few overshoot is noted under all robustness tests especially at 0.3 (sec) and at 1.0 (sec). Figures.3.19-(a and b/to the middle) display the behavior of stator active and reactive powers under MPPT strategy by maintaining the reactive power equals to zero value. In this case the active power had taken the inverse step profile of wind speed. Using robustness tests a remarkable ripples are noted (using tests: 2 and 3) especially at 0.6 (sec) which presents the rated power of DFIG ($P=4$ (kW)), on other hand and in the same time a remarkable power error is noted in stator reactive power, also a few overshoot is noted in transient and steady states of active and reactive power. Figures.3.19-(a and b/to the right) display the behavior of stator active and reactive powers under MPPT strategy by maintaining the reactive power equals to zero value. In this case the active power had taken the inverse random profile of wind speed. Using robustness tests a remarkable undulations are noted (using tests: 2 and 3) especially at 0.75 (sec) and 0.8 (sec) which presents the over rated power of DFIG ($P=4$ (kW) and the measured active power maintain 4.6 (kW)), on other hand and in the same time a remarkable power error is noted in stator reactive power, and a big overshoot is noted in transient and steady states of active and reactive power.

3.7.2 Topology 2: Improved IDPC (based on T1-FLC controllers)

The simulation results of this topology (novel IDPC based on T1-FLC controller) are described in details in figures.3-(20, 21 and 22). Figure.3.20 depicts the behavior of the wind-system (using DFIG (4 kW) and wind turbine (4.5 kW)) under three modes (that already presented above) in transient and steady states. Following are detailed description of the simulation results under three (03) modes:

Mode 1 (red color/figure.3.20 to the left side): The measured stator active and reactive powers (P_{s_meas} and Q_{s_meas}) and their references (P_{s_ref} and Q_{s_ref}) profiles are presented together in figure.3.20-(a) and are presented separately in figures.3.20.(b and c) respectively. The reference powers are indicated in table.3.6. It is clear that the measured powers (active and reactive) have good tracking power compared to their reference powers in transient and steady states (refer to figures.3.20-(b and c)), a few ($\approx 10\%$) overshoot is noted at 0.3 (sec) and 1.0 (sec) respectively in measured stator reactive' and active power (P_{s_meas} and Q_{s_meas}) (because the T1-FLC is robust in terms of overshoot especially if the step power' chngement is big). The direct and quadrature components of currents and flux (I_{rd} , I_{rq} and Φ_{rd} , Φ_{rq}) are presented respectively in figure.3.20-(e and g), which present the inverse diagrams compared to reactive and active powers. The inverse case for stator direct and quadrature currents (I_{sd} , I_{sq}) which have the same diagrams of reactive and active powers, and they are presented in figure.3.20-(d). The power error is presented in figure.3.20-(f); we observe a small power error of active and reactive powers -100 (W_Var) $\leq \Delta P_s - \Delta Q_s \leq +100$ (W_Var). The stator' and rotor currents; I_{s_abc} and I_{r_abc} are shown in figure.3.20-(h and i) respectively, we remark the sinusoidal form of the three rotor and stator phases currents and good THD of stator currents will be injected into the grid (= 01.20 % respect the IEEE-519 Std). The power factor (PF) of the proposed control is presented in figure.3.20-(j), knowing that PF is the ratio of P to S (apparent power), took the top value when the reactive power equals to zero value; refer to these time interval in figures.3.20-(a, b, c and j): 0-0.3 (sec), 0.9-1.0 (sec) and 1.2-1.5(sec); and this is the main aim of MPPT strategy/keeping at any time the unity power factor regardless wind speed variation and parameters chngement. In 1.0-1.2 (sec) neglected ripples are noted. Table.3.6 described in details the obtained results of the novel IDPC based on T1-FLC for Mode: I.

Mode 2 (blue color/figure.3.20 to the middle): The reference stator active power (P_{s_ref}) (figure.3.20-(a)) is extracted from MPPT strategy (in this case, the wind speed will take step form); it takes the inverse diagram of wind speed. The stator reactive power (Q_{s_ref}) equals to 0 (Var), represents power factor unity. It is clear that the measured powers (active and reactive) have good tracking power with neglected undulations compared to their reference powers in transient and steady states, a neglected ($\approx 7\%$) overshoot is noted at 0.6 (sec) in measured stator reactive' and active power (P_{s_meas} and Q_{s_meas}) (because the T1-FLC controller is robust in terms of overshoot especially if the wind power' chngement is big). The direct and quadrature components of currents

and flux (I_{rd} , I_{rq} and Φ_{rd} , Φ_{rq}) are presented respectively in figures.3.20-(e and g), which present the inverse diagrams compared to reactive and active powers. The inverse case for stator direct and quadrature currents (I_{sd} , I_{sq}) which have the same diagrams of reactive and active powers, and they are presented in figure.3.20-(d). The power error is presented in figure.3.20-(f), we observe a small power error of active and reactive powers $-130 (W_Var) \leq \Delta P_s \Delta Q_s \leq +130 (W_Var)$. The stator' and rotor currents; I_{s_abc} and I_{r_abc} are shown in figures.3.20-(h and i) respectively, we remark the sinusoidal form of the waveforms with an excellent THD of stator currents will be injected into the grid ($= 0.67\%$ respect the IEEE-519 Std). The power factor (PF) of the proposed control is presented in figure.3.20-(j), knowing that PF reaches the top value when the reactive power equals to zero value (refer to these time interval in figures.3.20-(a, b, c and j): in this case the stator reactive power equals to zero value means the PF had taken always the unity; and this is the main aim of MPPT strategy/keeping at any time the unity power factor regardless wind speed variation and parameter variation. Table.3.6 described in details the obtained results of the novel IDPC based on T1-FLC for Mode: II.

Mode 3 (green color/figure.3.20 to the right): The reference stator active power (P_{s_ref}) (figure.3.20-(a)) is extracted from MPPT strategy (in this case, the wind speed will take random form); it takes the inverse diagram of wind speed. The stator reactive power (Q_{s_ref}) equal to 0 (Var), represents power factor unity. It is clear that the measured powers (active and reactive) have good tracking, a few ($\approx 10\%$) overshoot is noted at 0.5 (sec) and 0.8 (sec) in measured stator reactive' and active power (P_{s_meas} and Q_{s_meas}) (because the T1-FLC is robust in terms of overshoot especially if the wind power' changement is big). The direct and quadrature components of currents and flux (I_{rd} , I_{rq} and Φ_{rd} , Φ_{rq}) are presented respectively in figures.3.20-(e and g), which present the inverse diagrams compared to reactive and active powers. The inverse case for stator direct and quadrature currents (I_{sd} , I_{sq}) which have the same diagrams of reactive and active powers, and they are presented in figure.3.20-(d). The power error is presented in figure.3.20-(f), we observe an acceptable power error of active and reactive powers: $-150 (W_Var) \leq \Delta P_s \Delta Q_s \leq +150 (W_Var)$. The stator' and rotor currents; I_{s_abc} and I_{r_abc} are shown in figures.3.20-(h and i) respectively, we remark the sinusoidal form of the waveforms with an excellent THD of stator currents will be injected into the grid ($= 0.44\%$ respect the IEEE-519 Std). The power factor (PF) of the proposed control is presented in figure.3.20-(j), knowing that PF is the ratio of P to S (apparent power), it reaches top the value when the reactive power equals to zero value (refer to these time interval in figures.2.20-(a, b and j): and this is the main aim of MPPT strategy/keeping at any time the unity power factor regardless wind speed variation and parameter variation. Table.3.6 described in details the obtained results of the novel IDPC based on T1-FLC for Mode: III.

MPPT Strategy: In the left side of figure.3.21 (Mode: II); the wind speed had taken the step form and in the right side of figure.2.21 (Mode: III); the wind speed had taken the random form. Figure.3.21-(a) presents the stator active and reactive powers and its references profiles using of the novel IDPC based on T1-FLC for pitch angle equals to 0° ($B^\circ=0^\circ$) means the maximum power. It can be seen that the measured powers (active and reactive) follow exactly theirs references regardless sudden variation of wind speed in transient and steady states with an acceptable tracking power. Figures.3.21-(b) illustrate the stator active power under different pitch angle ($B^\circ= 0^\circ, 1^\circ, 1.5^\circ, 2^\circ$ and 2.05°), it can be seen the inverse proportionality between the active powers and pitch angle and neglected undulations were noted. Figures.3.21-(c) illustrate the stator reactive power under different pitch angle ($B^\circ= 0^\circ, 1^\circ, 1.5^\circ, 2^\circ$ and 2.05°), it is clear that the reactive power maintain the zero level despite the pitch angle variation (the maximum wind power is reached at $B^\circ=0^\circ$ (black color) as mentioned from MPPT strategy/refer to §2.4.1). Figure.3.21-(d) illustrates the wind speed forms; figure.3.21-(d/to the left) presents the step wind speed (maximum value equals to 11.5 m/sec) and figure.3.21-(d/to the right) displays the random wind speed (maximum value equals to 13.5 m/sec). Figure.3.21-(e) presents the generator speed (rpm); figure.3.21-(e/to the left) presents the generator speed (<1500 rpm) means the Sub-synchronous mode, noted by '1' and figure.3.21-(e/to the right) displays the generator speed (below and above the synchronous speed (1500 rpm) means the Sub- synchronous and Super-synchronous modes noted by '1' and '2' respectively). Figure.3.21-(f) displays the power coefficient (C_p); figure.3.21-(f/to the left) illustrates the power coefficient under Mode: II, it is clear that C_p had maintained the maximum value (≈ 0.48) regardless the wind speed variation and figure.3.21-(f/to the right) presents the C_p under Mode: III, in this case C_p had maintained the maximum value despite of wind speed variation. Figure.3.21-(g) depicts the slip (S) behavior during the generator speed variation

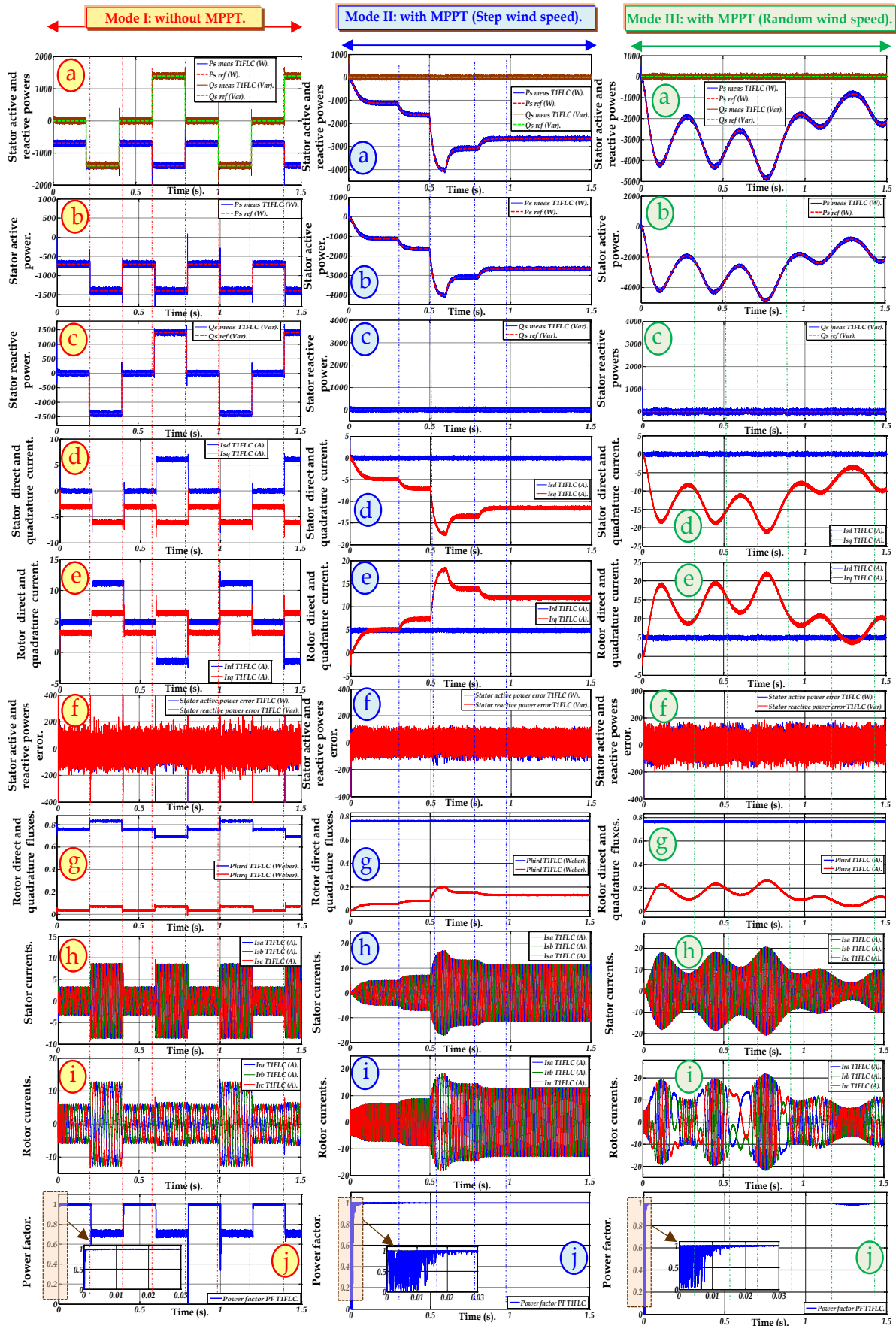


Figure.3.20 Simulations results of proposed control based on T1-FLC using three (03) modes; (a): stator active and reactive powers, (b): stator active power, (c): stator reactive power, (d): stator direct and quadrature currents, (e): rotor direct and quadrature currents, (f): stator active and reactive power error, (g): rotor direct and quadrature fluxes, (h): stator currents, (i): rotor currents, (j): power factor.

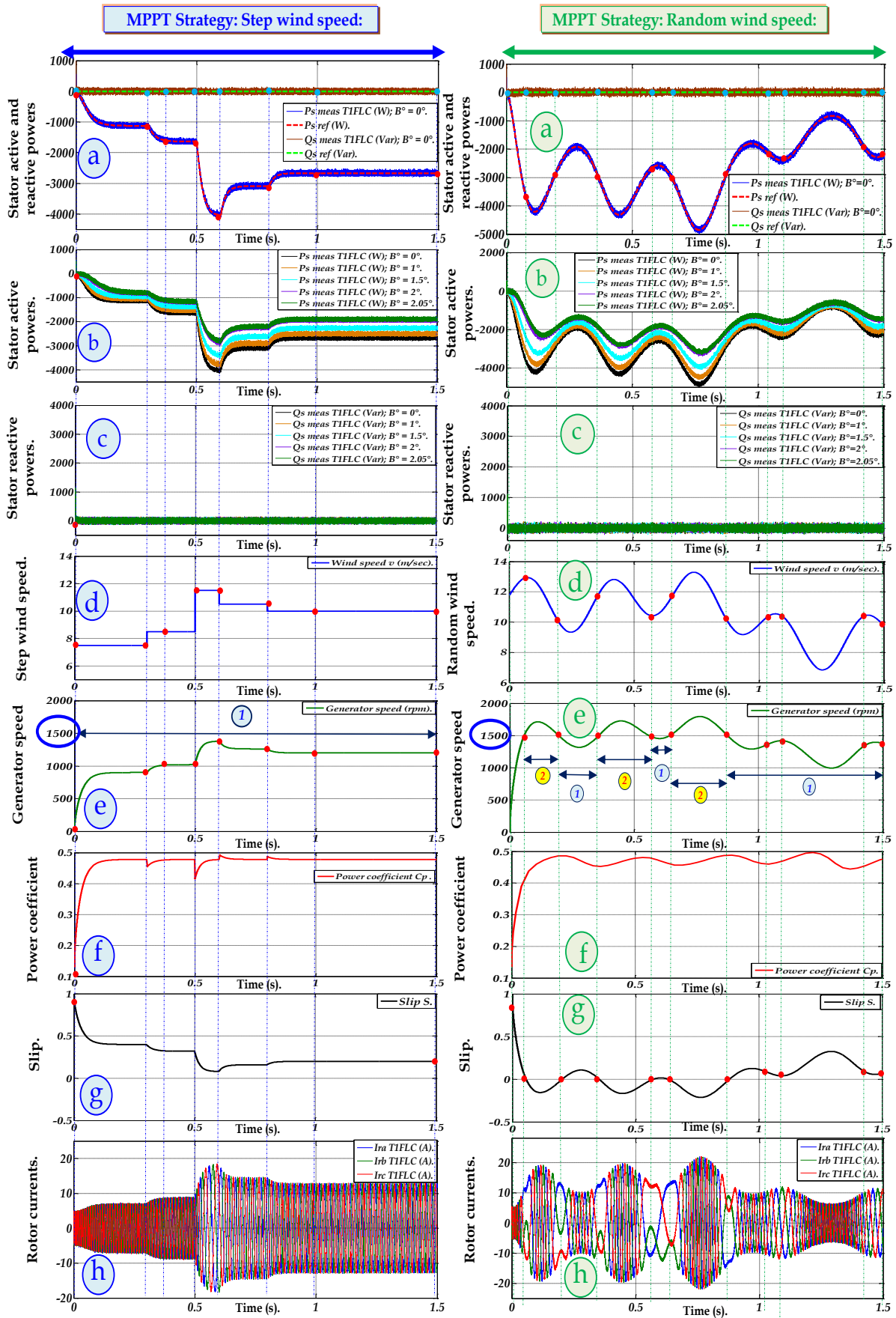


Figure.3.21 Simulations results of two MPPT strategy modes of proposed control based on T1-FLC; (a): stator active and reactive powers, (b): stator active power using different B° pitch angles, (c): stator reactive power using different pitch angles B° , (d): wind speed, (e): generator speed, (f): power coefficient, (g): slip, (h): rotor currents.

; figure.3.21-(g/to the left) illustrates the behavior of S under generator speed variation, in this case S varies between '+1' and '0' $\rightarrow 0 < S \leq +1$ means the generator speed did not reach the synchronous speed (always < 1500 (rpm)), figure.3.21-(g/to the right) represents the S behavior under generator speed variation, in this case S varies between '+1' and '-1' $\rightarrow -1 < S \leq +1$ means the generator speed varies below and above the synchronous speed (superior and inferior 1500 (rpm)), in the case when S reaches zero value means the mechanical speed $N_r=1500$ (rpm) this case called the synchronous mode (because S equals $(N_s-N_r)/N_s$), for exp: in the case of mechanical speed $N_r=1500$ (rpm) and $N_s =1500$ (rpm) $= (60 \cdot f)/P = (60 \cdot 50)/2 = 1500$ (rpm) means $S = (1500 - 1500)/1500 = 0$ is the stable zone, please refer to Appendix: A, DFIG's parameters (Table.A.1). Figure.3.21-(h) displays the behavior of rotor currents under generator speed variation; figure.3.21-(h/to the left) illustrates the sinusoidal waveforms of rotor currents with neglected ripples (in this case the rotor currents did not change the sense because the S did not reach the zero value) and figure.3.21-(h/to the right) demonstrates the rotor currents behavior under generator speed variation, it can be seen the rotor currents had changed the sense in the case when S equals to zero value means when the generator speed varied near the synchronous speed.

Robustness tests⁷: In the left side of figure.3.22-(Mode: I/without parameter changement); the middle side of figure.3.22-(Mode: II/ using Step wind speed) and in right side of figure.3.22-(Mode: III/ using random wind speed). In Mode: I red color), figures.3.22-(a and b/to the left) illustrate the behavior of stator active and reactive powers under parameters variations. It can be noted small power error in active and reactive power especially using the 2nd test (brown color/please refer to the bottom of the page) and 3rd test (green color) with few undulations especially in transient and steady states (please refer to zoom) and the value of power error reaches nearly ± 100 (W_Var) in Test-1, and nearly ± 190 (W_Var) in Test-2 and Test-3. A few overshoot is noted under all robustness tests especially at 0.3 (sec) and at 1.0 (sec). Figures.3.22-(a and b/to the middle) display the behavior of stator active and reactive powers under MPPT strategy by maintaining the reactive power equals to zero value. In this case the active power had taken the inverse step profile of wind speed. Using robustness tests a acceptable undulations are noted (using tests: 2 and 3) especially at 0.6 (sec) which presents the rated power of

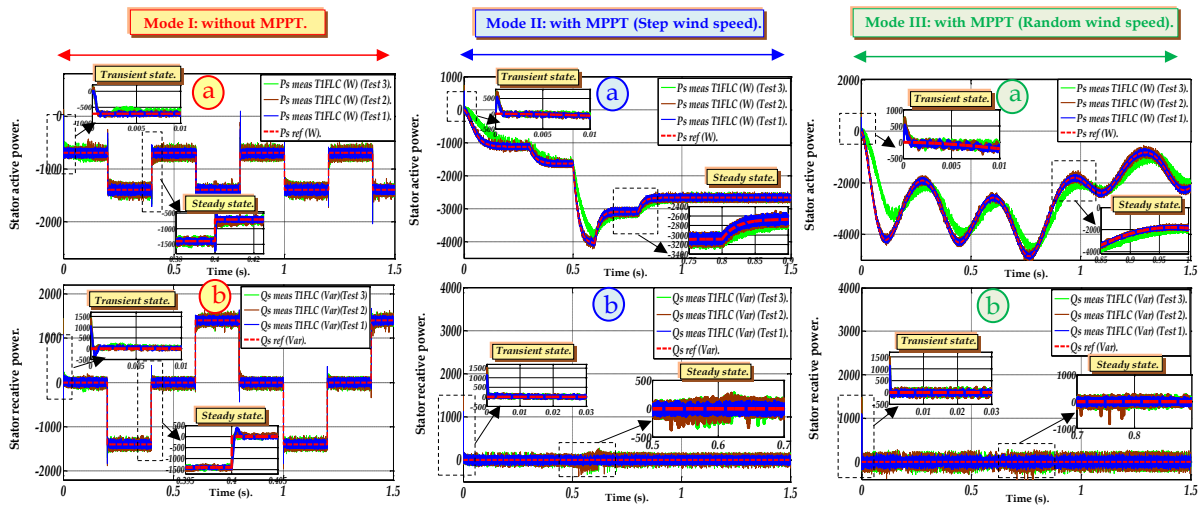


Figure.3.22 Robustness tests of proposed control based on T1-FLC using three (03) modes; a: sator active powers, b: sator reactive power.

Table.3.6 Performances results for proposed control based on T1-FLC using back-to-back SVM converter:

	THD_Is_abc (%) :	THD_Ir_abc (%) :	Overshoot :	Response time (sec) :	Power Error (W_Var) :
Mode I:	01.20 %	41.45 %	Few ($\approx 10\%$).	$0.8 \cdot 10^{-3}$.	+/- 100.
Mode II:	0.67 %	05.88 %	Neglected ($\approx 7\%$).	$0.7 \cdot 10^{-3}$.	+/- 130.
Mode III:	0.44%	06.54 %	Few ($\approx 10\%$).	$0.42 \cdot 10^{-3}$.	+/- 150.

⁷ Knowing that in this chapter the robustness tests are based on three tests as follows: [Test-1: without parameter changement \rightarrow Blue color, Test-2: +100% of R_r and -25% of $(L_s, L_r$ and $L_m)$ \rightarrow Brown color and Test-3: +100% of $(J$ and $R_r)$, -25 % of $(L_r, L_s$ and $L_m)$ \rightarrow Green color] respectively.

DFIG ($P=4$ (kW)), on other hand and in the same time a few power error is noted in stator reactive power (which means that the T1-FLC can maintain the unity power factor under maximum wind power and parameters variation), also a few overshoot is noted in transient and steady states of active and reactive power. Figures.3.22-(a and b/to the right) display the behavior of stator active and reactive powers under MPPT strategy by maintaining the reactive power equals to zero value. In this case the active power had taken the inverse random profile of wind speed. Using robustness tests a few undulations are noted (using tests: 2 and 3) especially at 0.75 (sec) and 0.8 (sec) which presents the over rated power of DFIG ($P=4$ (kW) and the measured active power maintain 4.6 (kW)), on other hand and in the same time a small power error is noted in stator reactive power (which means that the T1-FLC controllers can maintain the unity power factor under maximum wind power), also a few overshoot is noted in transient and steady states of active and reactive power.

3.7.3 Topology 3: Improved IDPC (based on T2-FLC controllers)

The simulation results of this topology (novel IDPC based on T2-FLC controller) are described in details in figures.3-(23, 24 and 25). Figure.2.23 presents the behavior of the wind-system (using DFIG (4 kW) and wind turbine (4.5 kW)) under three modes (that already presented above) in transient and steady states. Following are detailed description of the simulation results under three (03) modes:

Mode 1 (red color/figure.3.23 to the left side): The measured stator active and reactive powers (P_{s_meas} and Q_{s_meas}) and their references (P_{s_ref} and Q_{s_ref}) profiles are presented together in figure.3.23-(a) and are presented separately in figures.3.23.(b and c) respectively. The reference powers are indicated in table.4.2. It is clear that the measured powers (active and reactive) have good tracking power compared to their reference powers in transient and steady states (refer to figures.3.23-(b and c)), a few ($\approx 9\%$) overshoot is noted at 0.3 (sec) and 1.0 (sec) respectively in measured stator reactive' and active power (P_{s_meas} and Q_{s_meas}) (because the T2-FLC controller is robust in terms of overshoot especially if the step power' changement is big). The direct and quadrature components of currents and flux (I_{rd} , I_{rq} and Φ_{rd} , Φ_{rq}) are presented respectively in figure.3.23-(e and g), which present the inverse diagrams compared to reactive and active powers. The inverse case for stator direct and quadrature currents (I_{sd} , I_{sq}) which have the same diagrams of reactive and active powers, and they are presented in figure.3.23-(d). The power error is presented in figure.3.23-(f); we observe a small power error of active and reactive powers -100 (W_Var) $\leq \Delta P_s \Delta Q_s \leq +100$ (W_Var). The stator' and rotor currents; I_{s_abc} and I_{r_abc} are shown in figure.3.23-(h and i) respectively, we remark the sinusoidal form of the three rotor and stator phases currents with a good THD of stator currents will be injected into the grid (= 01.07 % respect the IEEE-519 Std). The power factor (PF) of the proposed control is presented in figure.3.23-(j), knowing that PF is the ratio of P to S (apparent power), took the top value when the reactive power equals to zero value; refer to these time interval in figures.3.23-(a, b, c and j): 0-0.3 (sec), 0.9-1.0 (sec) and 1.2-1.5(sec); and this is the main aim of MPPT strategy/keeping at any time the unity power factor regardless wind speed variation and parameters changement. In 1.0-1.2 (sec) neglected ripples are noted. Table.3.7 described in details the obtained results of the novel IDPC based on T2-FLC for Mode: I.

Mode 2 (blue color/figure.3.23 to the middle): The reference stator active power (P_{s_ref}) (figure.3.23-(a)) is extracted from MPPT strategy (in this case, the wind speed will take step form); it takes the inverse diagram of wind speed. The stator reactive power (Q_{s_ref}) equals to 0 (Var), represents power factor unity. It is clear that the measured powers (active and reactive) have acceptable tracking with neglected undulations compared to their reference powers in transient and steady states, a neglected ($< 6\%$) overshoot is noted at 0.6 (sec) in measured stator reactive' and active power (P_{s_meas} and Q_{s_meas}) (because the T2-FLC controller is robust in terms of overshoot especially if the wind power' changement is big). The direct and quadrature components of currents and flux (I_{rd} , I_{rq} and Φ_{rd} , Φ_{rq}) are presented respectively in figures.3.23-(e and g), which present the inverse diagrams compared to reactive and active powers. The inverse case for stator direct and quadrature currents (I_{sd} , I_{sq}) which have the same diagrams of reactive and active powers, and they are presented in figure.3.23-(d). The power error is presented in figure.3.23-(f), we observe a small power error of active and reactive powers -100 (W_Var) $\leq \Delta P_s \Delta Q_s \leq +100$ (W_Var). The stator' and rotor currents; I_{s_abc} and I_{r_abc} are shown in figures.3.23-(h and i) respectively, we remark the sinusoidal form of the waveforms with a good THD of stator currents will be injected into the grid (= 0.68 % respect the IEEE-519 Std). The power factor (PF) of the proposed control is

presented in figure.3.23-(j), knowing that PF is the ratio of P to S (apparent power), it reaches the top value when the reactive power equals to zero value (refer to these time interval in figures.3.23-(a, b, c and j)): in this case the stator reactive power equals to zero value means the PF had taken always the unity; and this is the main aim of MPPT strategy/keeping at any time the unity power factor regardless wind speed variation and parameter variation. Table.3.7 described in details the obtained results of the novel IDPC based on T2-FLC for Mode: II.

Mode 3 (green color/figure.3.23 to the right): The reference stator active power (P_{s_ref}) (figure.3.23-(a)) is extracted from MPPT strategy (in this case, the wind speed will take random form); it takes the inverse diagram of wind speed. The stator reactive power (Q_{s_ref}) equal to 0 (Var), represents power factor unity. It is clear that the measured powers (active and reactive) have good tracking power compared to their reference powers in transient and steady states, a neglected (< 6%) overshoot is noted at 0.5 (sec) and 0.8 (sec) in measured stator reactive' and active power (P_{s_meas} and Q_{s_meas}) (because the T2-FLC controller is robust in terms of overshoot especially if the wind power' changement is big). The direct and quadrature components of currents and flux (I_{rd} , I_{rq} and Φ_{rd} , Φ_{rq}) are presented respectively in figures.3.23-(e and g), which present the inverse diagrams compared to reactive and active powers. The inverse case for stator direct and quadrature currents (I_{sdr} , I_{sq}) which have the same diagrams of reactive and active powers, and they are presented in figure.3.23-(d). The power error is presented in figure.3.23-(f), we observe a low power error of active and reactive powers $-120 (W_Var) \leq \Delta P_s \Delta Q_s \leq +120 (W_Var)$. The stator' and rotor currents; I_{s_abc} and I_{r_abc} are shown in figures.3.23-(h and i) respectively, we remark the sinusoidal form of the waveforms with an excellent THD of stator currents will be injected into the grid (= 0.60 % respect the IEEE-519 Std). The power factor (PF) of the proposed control is presented in figure.3.23-(j), knowing that PF is the ratio of P to S (apparent power), it reaches top the value when the reactive power equals to zero value (refer to these time interval in figures.3.23-(a, b and j)): and this is the main aim of MPPT strategy/ keeping at any time the unity power factor regardless wind speed variation and parameter variation. Table.3.7 described in details the obtained results of the novel IDPC based on T2-FLC for Mode: III.

MPPT Strategy: Knowing that in the left side of figure.3.24 (Mode: II); the wind speed had taken the step form and the right side of figure.3.24 (Mode: III); the wind speed had taken the random form. Figure.3.24-(a) presents the stator active and reactive powers and its references profiles using of the novel IDPC based on T2-FLC for pitch angle equals to 0° ($B^\circ=0^\circ$) means the maximum power. It can be seen that the measured powers (active and reactive) follow exactly theirs references despite the sudden variation of wind speed in transient and steady states with an excellent tracking power. Figures.3.24-(b) illustrate the stator active power under different pitch angle ($B^\circ=0^\circ, 1^\circ, 1.5^\circ, 2^\circ$ and 2.05°), it can be seen the inverse proportionality between the active powers and pitch angle and neglected undulations were noted. Figures.3.24-(c) illustrate the stator reactive power under different pitch angle ($B^\circ=0^\circ, 1^\circ, 1.5^\circ, 2^\circ$ and 2.05°), it is clear that the reactive power maintain the zero level despite the pitch angle variation (the maximum wind power is reached at $B^\circ=0^\circ$ (black color) as mentioned from MPPT strategy/refer to §2.4.1). Figure.3.24-(d) illustrates the wind speed forms; figure.3.24-(d/to the left) presents the step wind speed (maximum value equals to 11.5 m/sec) and figure.3.24-(d/to the right) displays the random wind speed (maximum value equals to 13.5 m/sec). Figure.3.24-(e) presents the generator speed (rpm); figure.3.24-(e/to the left) presents the generator speed (<1500 (rpm) means the Sub-synchronous mode, noted by '1') and figure.3.24-(e/to the right) displays the generator speed (below and above the synchronous speed (1500 rpm) means the Sub-synchronous and Super-synchronous modes noted by '1' and '2' respectively). Figure.3.24-(f) displays the power coefficient (C_p); figure.3.24-(f/to the left) illustrates the power coefficient under Mode: II, it is clear that C_p had maintained the maximum value (≈ 0.48) regardless the wind speed variation and figure.3.24-(f/to the right) presents the C_p under Mode: III, in this case C_p had maintained the maximum value despite of wind speed variation. Figure.3.24-(g) displays the slip (S) behavior during the generator speed variation; figure.3.24-(g/to the left) illustrates the behavior of S under generator speed variation, in this case S varies between '+1' and '0' $\rightarrow 0 < S \leq +1$ means the generator speed did not reach the synchronous speed (always < 1500 (rpm)), figure.3.24-(g/to the right) represents the S behavior under generator speed variation, in this case S varies between '+1' and '-1' $\rightarrow -1 < S \leq +1$ means the generator speed varies below and above the synchronous speed (superior and inferior 1500 (rpm)), in the case when S reaches zero value means the mechanical speed $N_r =$

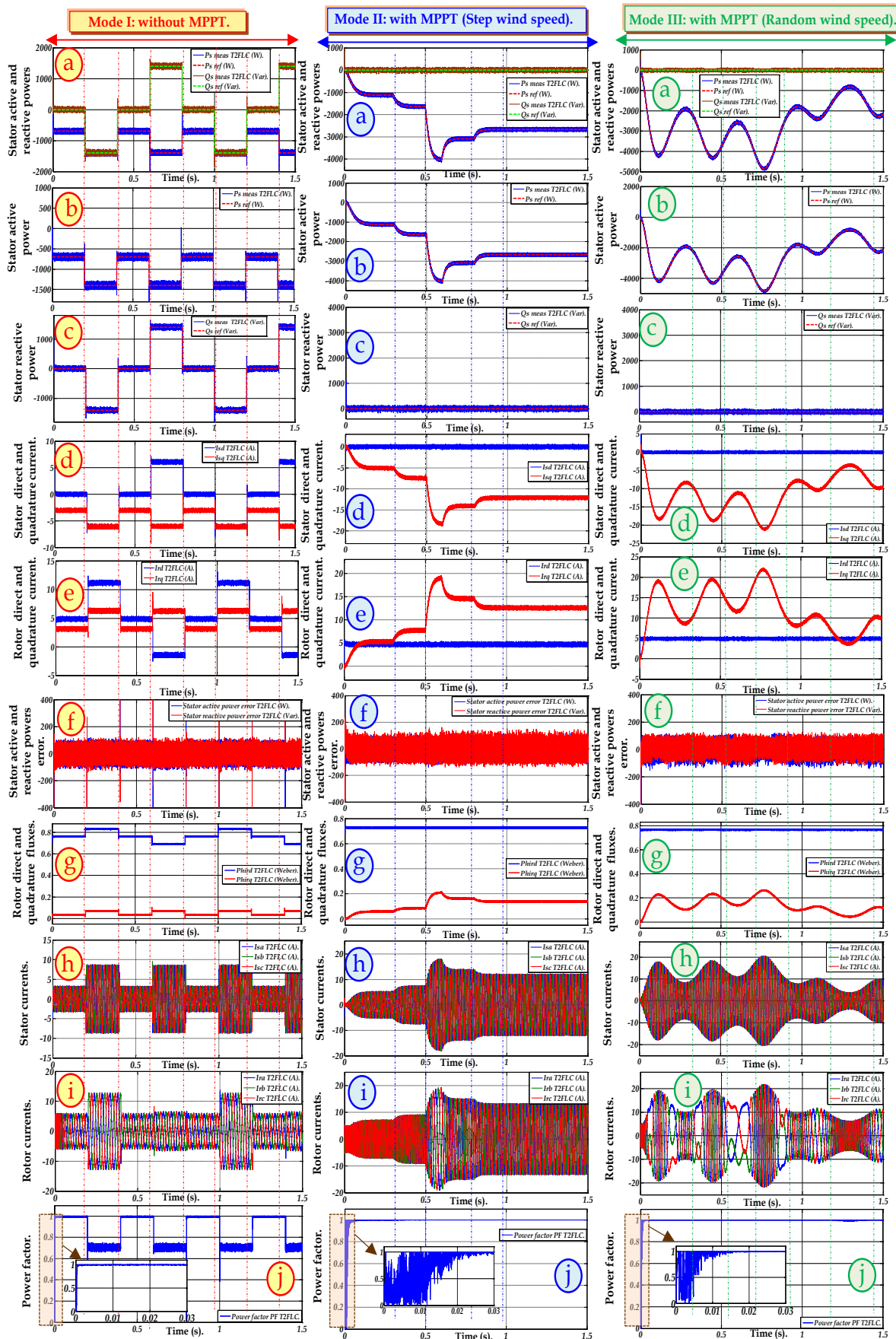


Figure.3.23 Simulations results of proposed control based on T2-FLC using three (03) modes; (a): stator active and reactive powers, (b): stator active power, (c): stator reactive power, (d): stator direct and quadrature currents, (e): rotor direct and quadrature currents, (f): stator active and reactive power error, (g): rotor direct and quadrature fluxes, (h): stator currents, (i): rotor currents, (j): power factor.

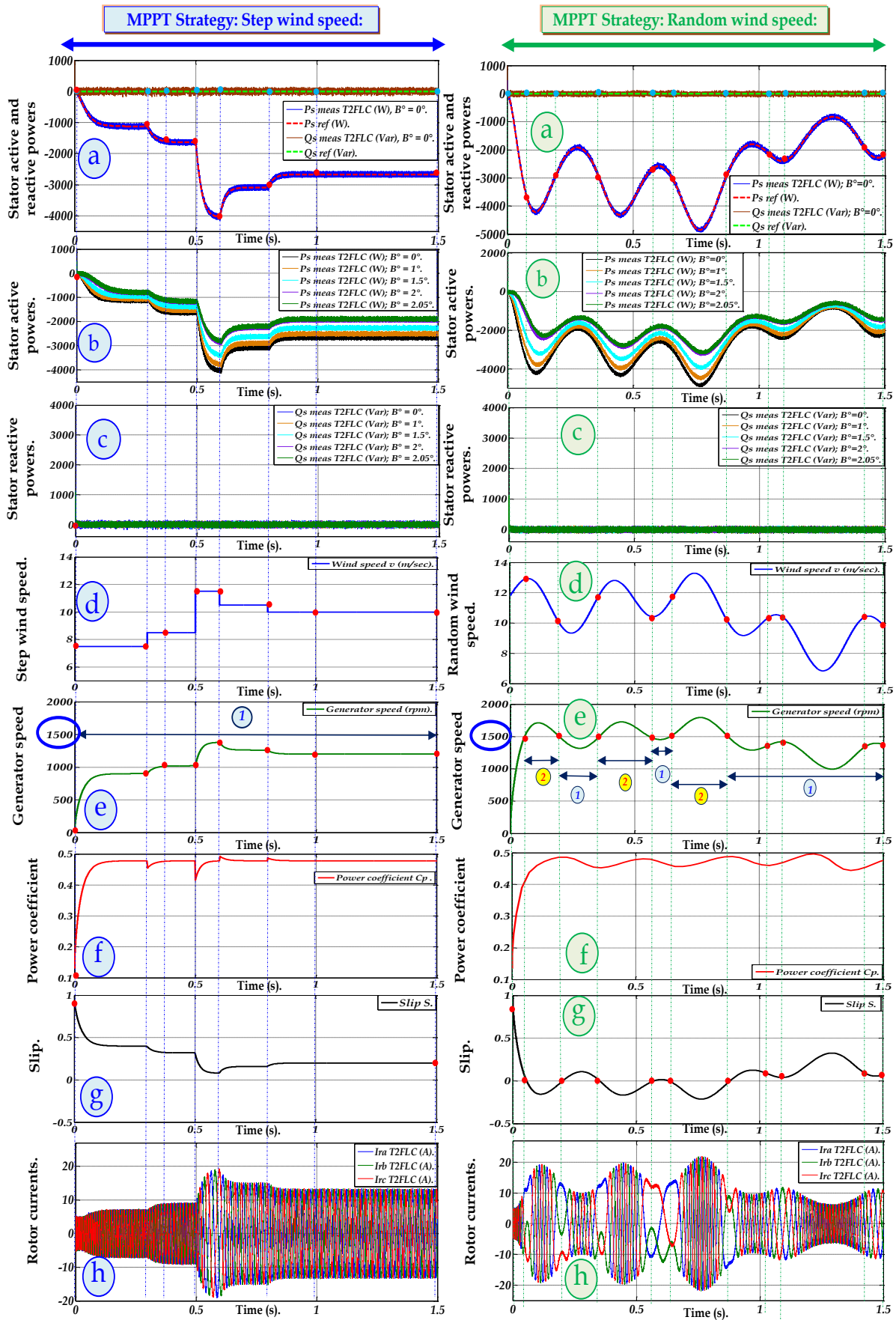


Figure.3.24 Simulations results of tow MPPT strategy modes of proposed control based on T2-FLC; (a): stator active and reactive powers, (b): stator active power using different B° pitch angles, (c): stator reactive power using different pitch angles B° , (d): wind speed, (e): generator speed, (f): power coefficient, (g): slip, (h): rotor currents.

=1500 (rpm) this case called the synchronous mode (because S equals $(N_s - N_r)/N_s$), for exp: in the case of mechanical speed $N_r=1500$ (rpm) and $N_s =1500$ (rpm) $= (60 \cdot f)/P = (60 \cdot 50)/2 = 1500$ (rpm) means $S = (1500 - 1500)/1500 = 0$ is the stable zone, please refer to Appendix: A, DFIG's parameters (Table.A.1). Figure.3.24-(h) displays the behavior of rotor currents under generator speed variation; figure.3.24-(h/to the left) illustrates the sinusoidal waveforms of rotor currents with few ripples (in this case the rotor currents did not change the sense because the S did not reach the zero value) and figure.3.24-(h/to the right) demonstrates the rotor currents behavior under generator speed variation, it can be seen the rotor currents had changed the sense in the case when S equals to zero value means when the generator speed varied near the synchronous speed.

Robustness tests⁸: Knowing that in the left side of figure.3.25-(Mode: I/without parameter chngement); the middle side of figure.3.25-(Mode: II/ using Step wind speed) and right side of figure.3.25-(Mode: III/ using random wind speed). In Mode: I red color), figures.3.25-(a and b/to the left) illustrate the behavior of stator active and reactive powers under parameters variations. It can be noted low power in active and reactive power especially using the 2nd test (brown color/please refer to the bottom of the page) and 3rd test (green color) with neglected undulations especially in transient and steady states (please refer to zoom) and the value of power error reaches nearly ± 100 (W_Var) in Test-1, and nearly ± 170 (W_Var) in Test-2 and Test-3. A few overshoot is noted under all robustness tests especially at 0.3 (sec) and at 1.0 (sec). Figures.3.25-(a and b/to the middle) display the behavior of stator active and reactive powers under MPPT strategy by maintaining the reactive power equals to zero value. In this case the active power had taken the inverse step profile of wind speed. Using robustness tests a neglected undulations are noted (using tests: 2 and 3) especially at 0.6 (sec) which presents the rated power of DFIG ($P=4$ (kW)), on other hand and in the same time a low power error is noted in stator reactive power (which means that the T2-FLC controllers can maintain the unity power factor under maximum wind power and parameters variation), also a neglected overshoot is noted in transient and steady states of active and reactive power. Figures.3.25-(a and b/to the right) display the behavior of stator active and reactive powers

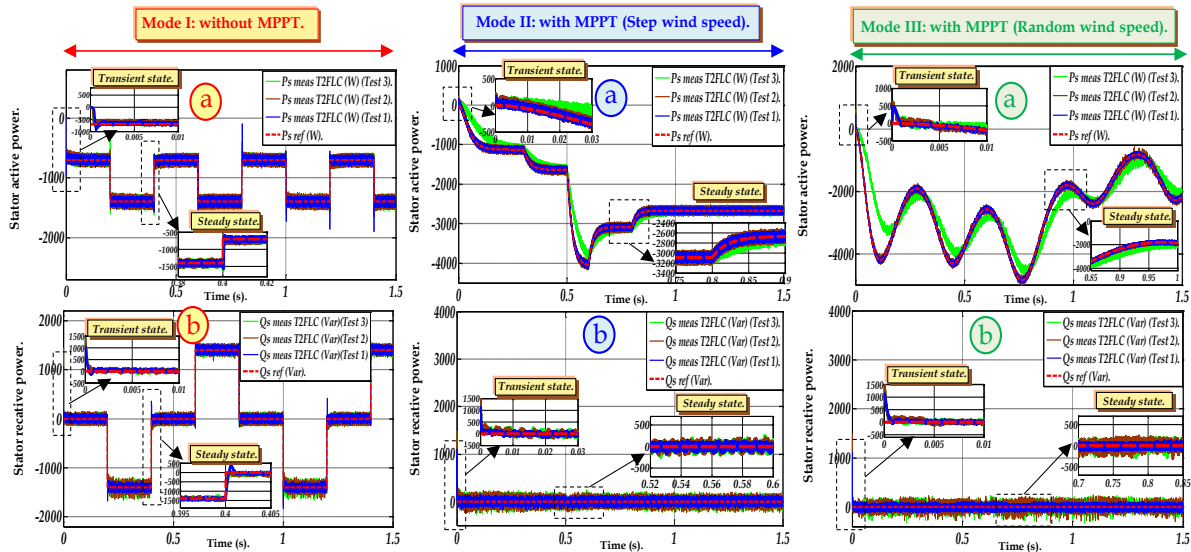


Figure.3.25 Robustness tests of proposed control based on T2-FLC using three (03) modes; a: stator active powers, b: stator reactive powers.

Table.3.7 Performances results for proposed control based on T2-FLC using back-to-back SVM converter:

	THD_Is_abc (%) :	THD_Ir_abc (%) :	Overshoot :	Response time (sec) :	Power Error (W_Var) :
Mode I:	01.07 %	40.48 %	Few ($\approx 9\%$).	$0.8 \cdot 10^{-3}$.	+/- 100.
Mode II:	0.68 %	05.99 %	Neglected ($< 6\%$).	$0.67 \cdot 10^{-3}$.	+/- 100.
Mode III:	0.60 %	04.90 %	Neglected ($< 6\%$).	$0.75 \cdot 10^{-3}$.	+/- 120.

⁸ Knowing that in this chapter the robustness tests are based on three tests as follows: [Test-1: without parameter chngement \rightarrow Blue color, Test-2: +100% of R_r and -25% of (L_s, L_r and L_m) \rightarrow Brown color and Test-3: +100% of (J and R_r), -25 % of (L_r, L_s and L_m) \rightarrow Green color] respectively.

under MPPT strategy by maintaining the reactive power equals to zero value. In this case the active power had taken the inverse random profile of wind speed. Using robustness tests a neglected undulations are noted (using tests: 2 and 3) especially at 0.75 (sec) and 0.8 (sec) which presents the over rated power of DFIG ($P=4$ (kW) and the measured active power maintain 4.6 (kW)), on other hand and in the same time a remarkable power error is noted in stator reactive power (which means that the T2-FLC controllers can maintain the unity power factor under maximum wind power), also a neglected overshoot is noted in transient and steady states of active and reactive power.

3.7.4 Topology 4: Improved IDPC (based on NFC controllers)

The simulation results of this topology (novel IDPC based on NFC controller) are described in details in figures.3-(26, 27 and 28). Figure.2.26 presents the behavior of the wind-system (using DFIG (4 kW) and wind turbine (4.5 kW)) under three modes (that already presented above) in transient and steady states. Following are detailed description of the simulation results under three (03) modes:

Mode 1 (red color/figure.3.26 to the left side): The measured stator active and reactive powers (P_{s_meas} and Q_{s_meas}) and their references (P_{s_ref} and Q_{s_ref}) profiles are presented together in figure.3.26-(a) and are presented separately in figures.3.26.(b and c) respectively. The reference powers are indicated in table.4.2. It is clear that the measured powers (active and reactive) have bad tracking power (big error) compared to their reference powers in transient and steady states (refer to figures.3.26-(b and c)), a few ($< 9\%$) overshoot is noted at 0.3 (sec) and 1.0 (sec) respectively in measured stator reactive' and active power (P_{s_meas} and Q_{s_meas}) (because the NFC controller is robust in terms of overshoot especially if the step power' changement is big). The direct and quadrature components of currents and flux (I_{rd} , I_{rq} and Φ_{rd} , Φ_{rq}) are presented respectively in figure.3.26-(e and g), which present the inverse diagrams compared to reactive and active powers. The inverse case for stator direct and quadrature currents (I_{sd} , I_{sq}) which have the same diagrams of reactive and active powers, and they are presented in figure.3.26-(d). The power error is presented in figure.3.26-(f); we observe a low power error of active and reactive powers -120 (W_Var) $\leq \Delta P_s \Delta Q_s \leq +120$ (W_Var). The stator' and rotor currents; I_{s_abc} and I_{r_abc} are shown in figure.3.26-(h and i) respectively, we remark the sinusoidal form of the three rotor and stator phases currents with a good THD of stator currents will be injected into the grid ($= 01.19\%$ respect the IEEE-519 Std). The power factor (PF) of the proposed control is presented in figure.3.26-(j), knowing that PF is the ratio of P to S (apparent power), took the top value when the reactive power equals to zero value; refer to these time interval in figures.3.26-(a, b, c and j): 0-0.3 (sec), 0.9-1.0 (sec) and 1.2-1.5(sec); and this is the main aim of MPPT strategy/ keeping at any time the unity power factor regardless wind speed variation and parameters changement. In 1.0-1.2 (sec) neglected ripples are noted. Table.3.8 described in details the obtained results of the novel IDPC based on NFC for Mode: I.

Mode 2 (blue color/figure.3.26 to the middle): The reference stator active power (P_{s_ref}) (figure.3.26-(a)) is extracted from MPPT strategy (in this case, the wind speed will take step form); it takes the inverse diagram of wind speed. The stator reactive power (Q_{s_ref}) equals to 0 (Var), represents power factor unity. It is clear that the measured powers (active and reactive) have excellent tracking power compared to their reference powers in transient and steady states, a neglected ($<5\%$) overshoot is noted at 0.6 (sec) in measured stator reactive' and active power (P_{s_meas} and Q_{s_meas}) (because the NFC controller is not so robust in terms of overshoot especially if the wind power' changement is big). The direct and quadrature components of currents and flux (I_{rd} , I_{rq} and Φ_{rd} , Φ_{rq}) are presented respectively in figures.3.26-(e and g), which present the inverse diagrams compared to reactive and active powers. The inverse case for stator direct and quadrature currents (I_{sd} , I_{sq}) which have the same diagrams of reactive and active powers, and they are presented in figure.3.26-(d). The power error is presented in figure.3.26-(f), we observe a small power error of active and reactive powers -150 (W_Var) $\leq \Delta P_s \Delta Q_s \leq +150$ (W_Var). The stator' and rotor currents; I_{s_abc} and I_{r_abc} are shown in figures.3.26-(h and i) respectively, we remark the sinusoidal form of the waveforms with an excellent THD of stator currents will be injected into the grid ($= 0.60\%$ respect the IEEE-519 Std). The power factor (PF) of the proposed control is presented in figure.3.26-(j), knowing that PF is the ratio of P to S (apparent power), it reaches the top value when the reactive power equals to zero value (refer to these time interval in figures.3.26-(a, b, c and j): in this case the stator reactive power equals to zero value means the PF had taken always the unity; and this is the aim

of MPPT strategy/keeping at any time the unity power factor regardless wind speed variation and parameter variation. Table.3.8 described in details the obtained results of the novel IDPC based on NFC for Mode: II.

Mode 3 (green color/figure.3.26 to the right): The reference stator active power (P_{s_ref}) (figure.3.26-(a)) is extracted from MPPT strategy (in this case, the wind speed will take random form); it takes the inverse diagram of wind speed. The stator reactive power (Q_{s_ref}) equal to 0 (Var), represents power factor unity. It is clear that the measured powers (active and reactive) have excellent tracking power compared to their reference powers in transient and steady states, a neglected (<5%) overshoot is noted at 0.5 (sec) and 0.8 (sec) in measured stator reactive' and active power (P_{s_meas} and Q_{s_meas}) (because the NFC controller is not so robust in terms of overshoot especially if the wind power' changement is big). The direct and quadrature components of currents and flux (I_{rd} , I_{rq} and Φ_{rd} , Φ_{rq}) are presented respectively in figures.3.26-(e and g), which present the inverse diagrams compared to reactive and active powers. The inverse case for stator direct and quadrature currents (I_{sd} , I_{sq}) which have the same diagrams of reactive and active powers, and they are presented in figure.3.26-(d). The power error is presented in figure.3.26-(f), we observe a low power error of active and reactive powers $-150 (W_Var) \leq \Delta P_s \Delta Q_s \leq +150 (W_Var)$. The stator' and rotor currents; I_{s_abc} and I_{r_abc} are shown in figures.3.26-(h and i) respectively, we remark the sinusoidal form of the waveforms with an excellent THD of stator currents will be injected into the grid (= 0.56 % respect the IEEE-519 Std). The power factor (PF) of the proposed control is presented in figure.3.26-(j), knowing that PF is the ratio of P to S (apparent power), it reaches top the value when the reactive power equals to zero value (refer to these time interval in figures.3.26-(a, b and j): and this is the main aim of MPPT strategy/keeping at any time the unity power factor regardless wind speed variation and parameter variation. Table.3.8 described in details the obtained results of the novel IDPC based on NFC for Mode: III.

MPPT Strategy: In the left side of figure.3.27 (Mode: II); the wind speed had taken the step form and in the right side of figure.3.27 (Mode: III); the wind speed had taken the random form. Figure.3.27-(a) presents the stator active and reactive powers and its references profiles using of the novel IDPC based on NFC for pitch angle equals to 0° ($B^\circ=0^\circ$) means the maximum power. It can be seen that the measured powers (active and reactive) follow exactly theirs references despite the sudden variation of wind speed in transient and steady states with an excellent tracking power. Figures.3.27-(b) illustrate the stator active power under different pitch angle ($B^\circ= 0^\circ, 1^\circ, 1.5^\circ, 2^\circ$ and 2.05°), it can be seen the inverse proportionality between the active powers and pitch angle and neglected undulations were noted. Figures.3.27-(c) illustrate the stator reactive power under different pitch angle ($B^\circ= 0^\circ, 1^\circ, 1.5^\circ, 2^\circ$ and 2.05°), it is clear that the reactive power maintain the zero level despite the pitch angle variation (the maximum wind power is reached at $B^\circ=0^\circ$ (black color) as mentioned from MPPT strategy/refer to §2.4.1). Figure.3.27-(d) illustrates the wind speed forms; figure.3.27-(d/to the left) presents the step wind speed (maximum value equals to 11.5 m/sec) and figure.3.27-(d/to the right) displays the random wind speed (maximum value equals to 13.5 m/sec). Figure.3.27-(e) presents the generator speed (rpm); figure.3.27-(e/to the left) presents the generator speed (<1500 (rpm) means the Sub-synchronous mode, noted by '1') and figure.3.27-(e/to the right) displays the generator speed (below and above the synchronous speed (1500 rpm) means the Sub-synchronous and Super-synchronous modes noted by '1' and '2' respectively). Figure.3.27-(f) displays the power coefficient (Cp); figure.3.27-(f/to the left) illustrates the power coefficient under Mode: II, it is clear that Cp had maintained the maximum value (≈ 0.48) regardless the wind speed variation and figure.3.27-(f/to the right) presents the Cp under Mode: III, in this case Cp had maintained the maximum value despite of wind speed variation. Figure.3.27-(g) displays the slip (S) behavior during the generator speed variation; figure.3.27-(g/to the left) illustrates the behavior of S under generator speed variation, in this case S varies between '+1' and '0' $\rightarrow 0 < S \leq +1$ means the generator speed did not reach the synchronous speed (always < 1500 (rpm)), figure.3.27-(g/to the right) represents the S behavior under generator speed variation, in this case S varies between '+1' and '-1' $\rightarrow -1 < S \leq +1$ means the generator speed varies below and above the synchronous speed (superior and inferior 1500 (rpm)), in the case when S reaches zero value means the mechanical speed $N_r=1500$ (rpm) this case called the synchronous mode (because S equals $(N_s-N_r)/N_s$), for exp: in the case of mechanical speed $N_r=1500$ (rpm) and $N_s =1500$ (rpm) $= (60*f)/P = (60*50)/2 = 1500$ (rpm) means $S = (1500 - 1500)/1500 = 0$) is the stable zone, please refer to Appendix: A, DFIG's parameters (Table.A.1). Figure.3.27-(h) displays the behavior of rotor currents under generator speed variation; figure.3.27-(h/to the left) illustrates the

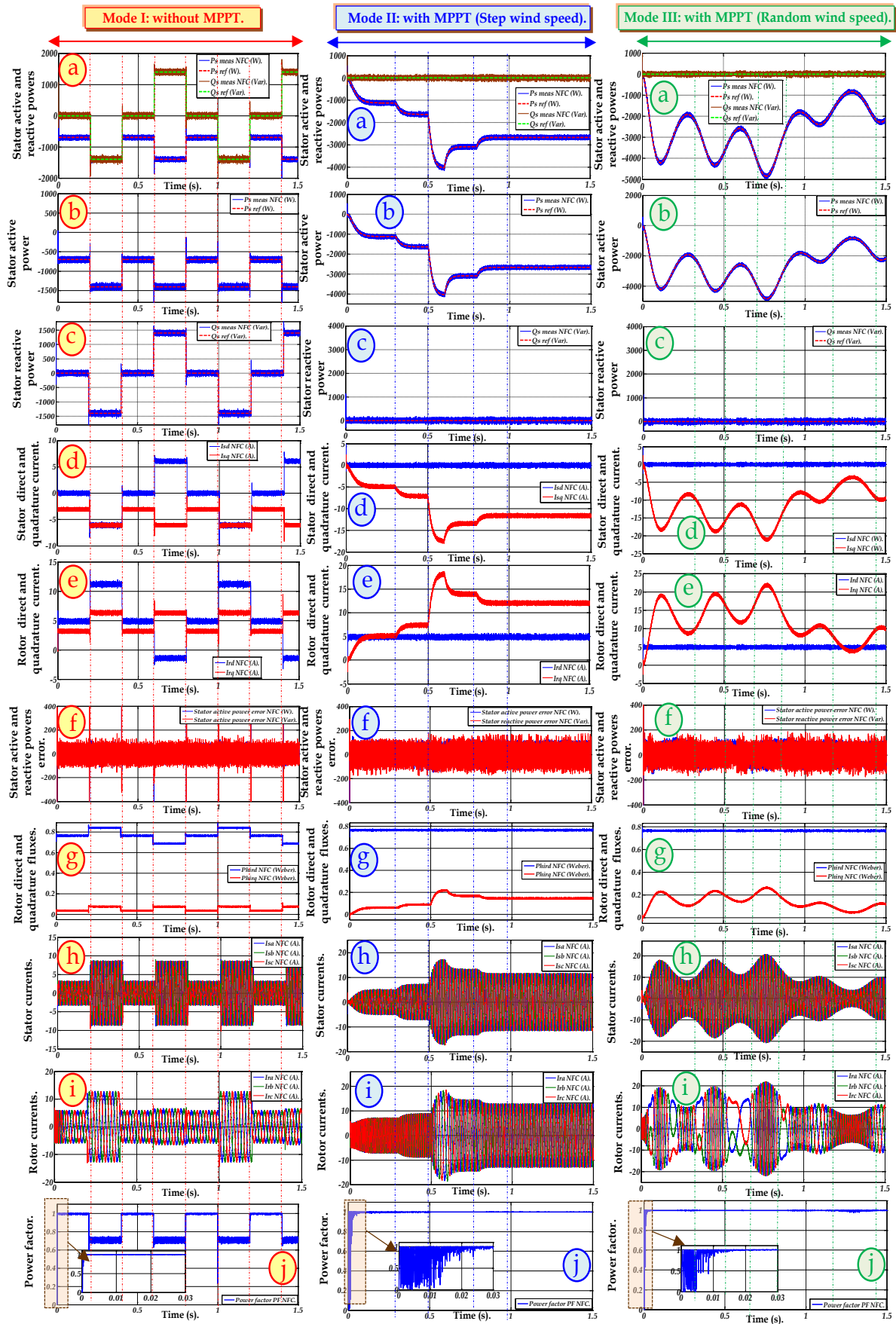


Figure.3.26 Simulations results of proposed control based on NFC using three (03) modes; (a): stator active and reactive powers, (b): stator active power, (c): stator reactive power, (d): stator direct and quadrature currents, (e): rotor direct and quadrature currents, (f): stator active and reactive power error, (g): rotor direct and quadrature fluxes, (h): stator currents, (i): rotor currents, (j): power factor.

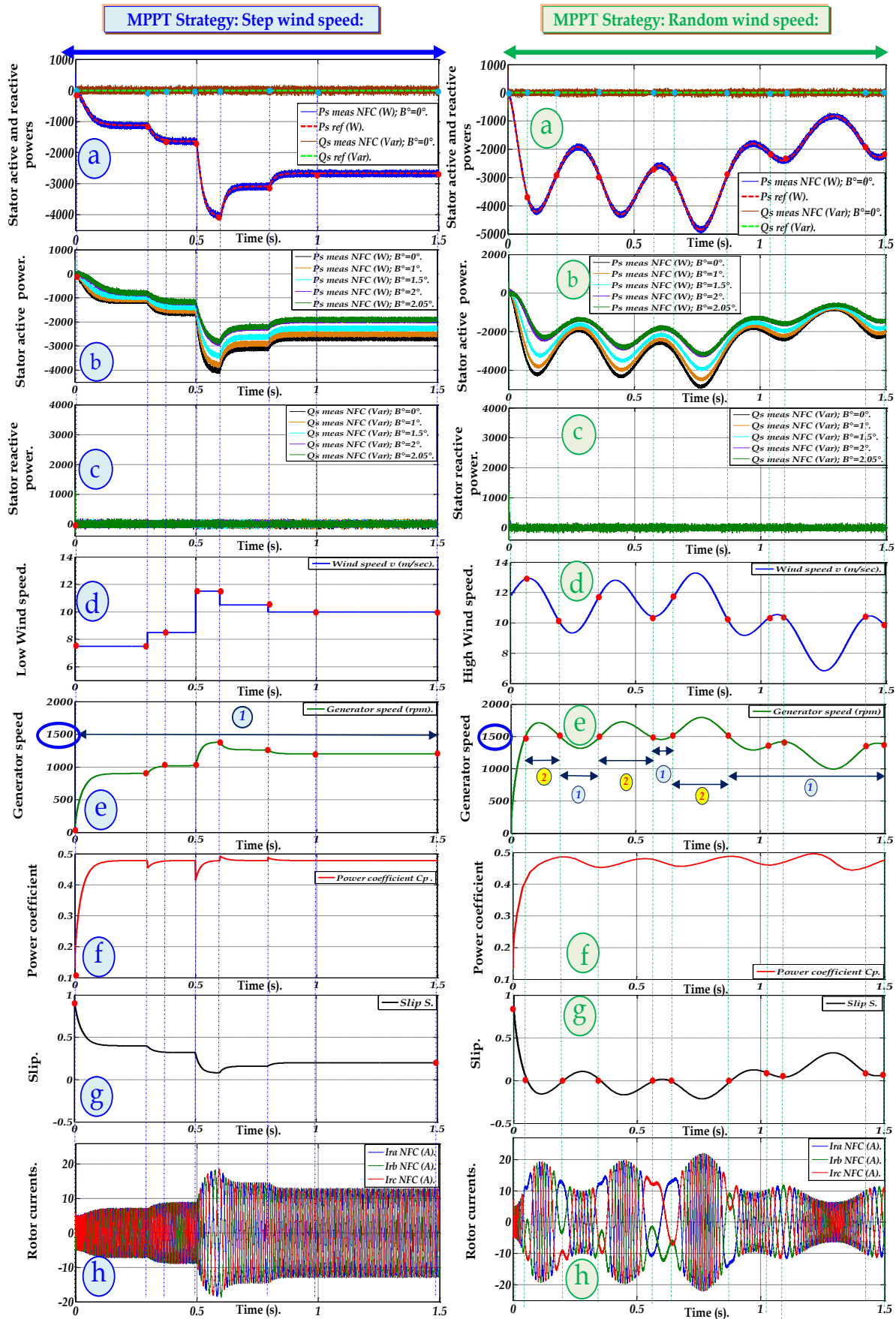


Figure.3.27 Simulations results of tow MPPT strategy modes of proposed control based on NFC; (a): stator active and reactive powers, (b): stator active power using different B° pitch angles, (c): stator reactive power using different pitch angles B° , (d): wind speed, (e): generator speed, (f): power coefficient, (g): slip, (h): rotor currents.

sinusoidal waveforms of rotor currents with neglected ripples (in this case the rotor currents did not change the sense because the S did not reach the zero value) and figure.3.27-(h/to the right) demonstrates the rotor currents behavior under generator speed variation, it can be seen the rotor currents had changed the sense in the case when S equals to zero value means when the generator speed varied near the synchronous speed.

Robustness tests⁹: Knowing that in the left side of figure.3.28-(Mode: I/without parameter changement); the middle side of figure.3.28-(Mode: II/ using Step wind speed) and right side of figure.3.28-(Mode: III/ using random wind speed). In Mode: I red color), figures.3.28-(a and b/to the left) illustrate the behavior of stator active and reactive powers under parameters variations. It can be noted neglected power error in active and reactive power especially using the 2nd test (brown color/please refer to the bottom of the page) and 3rd test (green color) with neglected undulations espacially in transient and steady states (please refer to zoom) and the value of power error reaches nearly ± 120 (W_Var) in Test-1, and nearly ± 160 (W_Var) in Test-2 and Test-3. A lower overshoot is noted under all robustnees tests espacially at 0.3 (sec) and at 1.0 (sec). Figures.3.28-(a and b/to the middle) display the behavior of stator active and reactive powers under MPPT strategy by maintaining the reactive power equals to zero value. In this case the active power had taken the inverse step profile of wind speed. Using robustnees tests a null undulations are noted (using tests: 2 and 3) espacially at 0.6 (sec) which presents the rated power of DFIG ($P=4$ (kW)), on other hand and in the same time a very small power error is noted in stator rea-ctive power (which means that the NFC controllers can maintain the unity power factor under maximum wind power and parameters variation), also a null overshoot is noted in transient and steady states of active and reactive power. Figures.3.28-(a and b/to the right) display the behavior of stator active and reactive powers under MPPT strategy by maintaining the reactive power equals to zero value. In this case the active power had taken the inverse random profile of wind speed. Using robustnees tests a null undulations are noted (using tests: 2 and 3) espacially at 0.75 (sec) and 0.8 (sec) which presents the over rated power of DFIG ($P=4$ (kW)

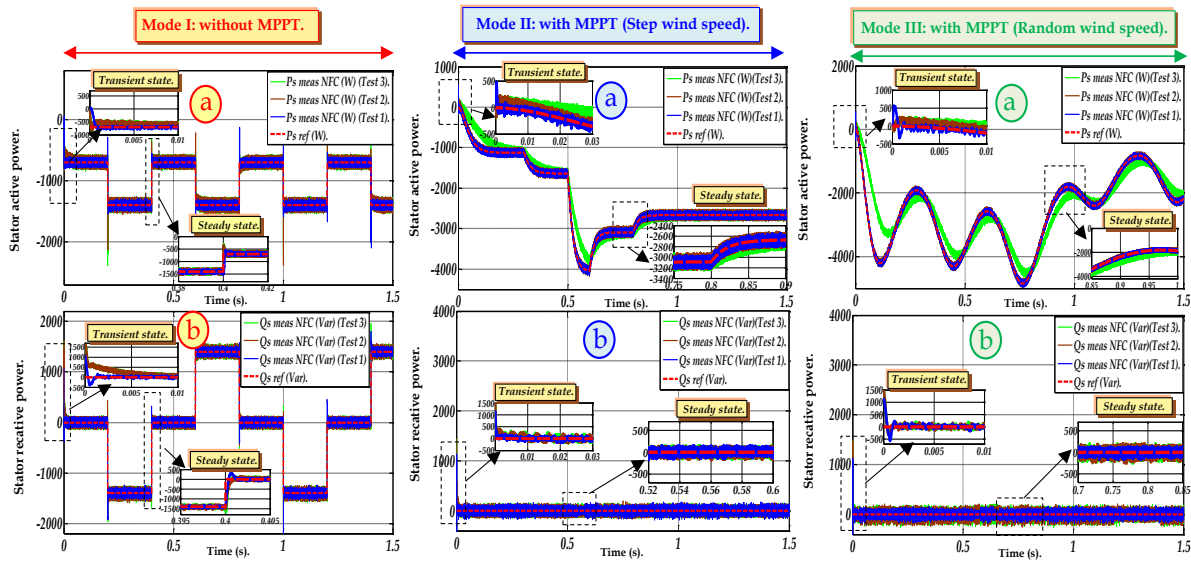


Figure.3.28 Robustness tests of proposed control based on NFC using three (03) modes; a: sator active power, b: sator active power.

Table.3.8 Performances results for proposed control based on NFC using back-to-back SVM converter:

	THD _{Is_abc} (%) :	THD _{Ir_abc} (%) :	Overshoot :	Response time (sec) :	Power Error (W_Var) :
Mode I:	01.19 %	88.20 %	Few ($\approx 9\%$).	$0.33 * 10^{-3}$.	+/- 120.
Mode II:	0.60 %	111.70 %	Neglected ($<5\%$).	$0.37 * 10^{-3}$.	+/- 150.
Mode III:	0.56 %	05.26 %	Neglected ($<5\%$).	$0.37 * 10^{-3}$.	+/- 150.

⁹ Knowing that in this chapter the robustness tests are based on three tests as follows: [Test-1: without parameter changement → Blue color, Test-2: +100% of R_r and -25% of (L_s, L_r and L_m) → Brown color and Test-3: +100% of (J and R_r), -25 % of (L_r, L_s and L_m) → Green color] respectively.

(kW) and the measured active power maintain 4.6 (kW)), on other hand and in the same time a low power error is noted in stator reactive power; which means that the NFC controllers can maintain the unity power factor under maximum wind power, also a null overshoot is noted in transient and steady states of active and reactive power.

3.8 Wind-system performances recapitulation under six (06) proposed IDPC algorithms

In this section, we present the advantages and disadvantages of each proposed algorithms (*Chapter: 2 and Chapter: 3*) using six (06) performance criteria, taken into account three (03) proposed modes and robustness tests; as shown in *table.3.9*:

Table.3.9 Wind-system performances (under six proposed IDPC algorithms):

Criteria:		Overshoot:	Response time:	THD:	Power error:	Power tracking:	Sensitivity of the parameters changement:
Topologies:							
Chapter 2:	Topology 1 (IDPC based on PI):	--	+	--	--	-	--
	Topology 2 (IDPC based on PID):	+	+	+	-	+	-
Chapter 3:	Topology 3 (IDPC based on MRAC):	++	+	+	+	++	+
	Topology 4 (IDPC based on T1-FLC):	+	++	++	++	++	++
	Topology 5 (IDPC based on T2-FLC):	++	++	+++	+++	+++	++
	Topology 6 (IDPC based on NFC):	++	+++	+++	+++	+++	+++

NB: "--" means Poor performance and "+" means High performance.

After analyzing the recapitulation results (as demonstrates in *table.3.9*), it is clear that the artificial intelligent controllers offer an improved' wind-system performances in transient and steady states, and we can confirm also that the best artificial intelligent controllers are T2-FLC and NFC.

After the simulation comparative study between the fourth topologies in this chapter (using MRAC, T1-FLC, T2-FLC and NFC respectively) high performance of wind-turbine (compared to those using PI and PID) are noted with/without robustness tests. It is clear that the intelligent controllers such as: T2-FLC and NFC present the best solution of the stator power control algorithm especially in MPPT modes (step and random wind speed). In this context, several drawbacks are solved such as: remarkable overshoot, long response time, the big power error and tracking power respectively in transient and steady states.

3.9 Conclusion

In this chapter, improved IDPC algorithms for DFIG-grid connection have been proposed. In order to control independely DFIG's stator powers; novel IDPC with SVM have been combined to adjust active and reactive powers and rotor currents. MPPT strategy was proposed in order to extract the maximum wind-power despite the sudden wind speed variation (*in this chapter we proposed two wind speed profiles: the step wind speed and the random wind speed*) and to maintain the unity power factor ($PF \approx 1$). In order to enhance the conventional IDPC; MRAC, T1-FLC, T2-FLC and NFC were proposed instead the PID controllers to control I_{rd} and I_{rq} respectively. In this context, several drawbacks in transient and steady states were treated using the adaptive and intelligent controllers, in terms of tracking power and dynamic response performances. The simulation results have been developed via *Matlab/ Simulink®* software, illustrate high dynamics response and improved wind-system performances regardless wind-speed variation. Using the robustness tests, the wind-peformances are

remarkably improved (*especially for Topology: 5 and Topology: 6 from table.3.9*) which demonstrate the high performance ability of artificial intelligent algorithms (*T2-FLC and NFC*) to keep the power tracking trajectory under parameter changing and sudden wind speed variation. In the next chapter, a new non-linear control will be proposed in order to overcome the coupling terms (*under d - q axes*).

3.10 References

- [1] Gil. D. MARQUES and Matteo F. IACCHETTI, "Stator frequency regulation in a field-oriented controlled DFIG connected to a DC link", IEEE Transactions on Industrial Electronics, vol: 61, no: 11, pp: 5930–5939, 2014.
- [2] Youssef Agrebi ZORGANI, Yassine KOUBAA and Mohamed BOUSSAK, "MRAS state estimator for speed sensorless ISFOC induction motor Drives with Luenberger load torque estimation", ISA Transactions, 2016.
- [3] Sabrina ABDEDDAIM, Achour BETKA, Said DRID and Mohamed BECHERIF, "Implementation of MRAC controller of a DFIG based variable speed grid-connected wind turbine", Energy Conversion and Management, vol: 79, no: xx, pp: 281–288, 2014.
- [4] R. CÁRDENAS, R. PEÑA, J. CLARE, G. ASHER and J. PROBOSTE, "MRAS observers for sensorless control of Doubly-Fed Induction Generators", IEEE Transactions on Power Electronics, vol: 23, no: 3, pp: 1075–1084., 2008.
- [5] Muzeyyen Bulut OZEK and Zuhtu Hakan AKPOLAT, "A Software tool: Type-2 fuzzy logic toolbox", JWPI, vol: 22, 2008.
- [6] Suresh MIKKILI and Anup Kumar PANDA, "Review and Analysis of Type-1 and Type-2 Fuzzy Logic Controllers", JASE, vol: 08, 2014.
- [7] Tejavathu RAMESH, Anup Kumar PANDA and Shiva Kumar "Type-2 fuzzy logic control based MRAS speed estimator for speed sensorless direct torque and flux control of an induction motor drive", ISA transactions, vol: 57, pp: 262–275, 2015.
- [8] N. Venkataramana NAIK and S. P. SINGH, "A Novel Type-2 Fuzzy Logic Control of Induction Motor Drive using Scalar Control", IEEE Conference, 5th India International Conference on Power Electronics (IICPE) 2012.
- [9] Q. LIANG and J. M. MENDEL, "Interval Type-2 Logic Systems: Theory and Design", IEEE Transactions on Fuzzy System, vol: 08, 2000.
- [10] Azeddine CHAIBA, Rachid ABDESSEMED M. L. BENDAAS, "Hybrid Intelligent Control based Torque Tracking approach for Doubly Fed Asynchronous Motor (DFAM) drive", Journal of Electrical Systems, vol: 08, no: 03, pp: 262-272., 2012
- [11] Cetin ELMAS, Oguz USTUN and Hasan H. SAYAN, "A neuro-fuzzy controller for speed control of a permanent magnet synchronous motor drive", Expert Systems with Applications, vol: 34, no: 1, pp: 657–664, 2008.
- [12] Muammer GÖKBULUT, Beşir DANDIL and Cafer BAL, "A hybrid neuro-fuzzy controller for brushless DC motors", Artificial Intelligence and Neural Networks, pp: 125–132, 2006.
- [13] K. KOUZI, M. NAIT-SAID, M. HILAIRET and É. BERTHELOT, "A fuzzy sliding-mode adaptive speed observer for vector control of an induction motor", IEEE International Conference on Industrial Electronics IECON, 2008.
- [14] Rodrigo MARCHI, Paulo DAINEZ, Fernando Von ZUBEN, Edson BIM, "A multilayer perceptron controller applied to the direct power control of a doubly fed induction generator", IEEE Transactions on Sustainable Energy, vol. 5, no.2, pp: 498-506, 2014.
- [15] Fayssal AMRANE and Azeddine CHAIBA: "Model Reference Adaptive Control for DFIG based on DPC with a Fixed Switching Frequency" International Electrical Computer Engineering Conference, IECEC 23-25th May 2015 Setif-Algeria.

- [16] Marcelo Godoy SIMOES, Bimal K. BOSE and Ronald J. SPIEGEL, "Design and Performance Evaluation of a Fuzzy-Logic-Based Variable-Speed Wind Generation System", Chapter-1, pp.1-35, Title Book: "Fuzzy Control Systems, Analysis and Performances Evaluation", IEEE Transactions on Industry Applications, vol: 33, no: 4, 1997.
- [17] Timothy J. ROSS, "Fuzzy Logic With Engineering Applications", Book: Second Edition, John Wiley & Sons Ltd, England, 2004.
- [18] Timothy J. ROSS, "Fuzzy Logic With Engineering Applications", Book: Third Edition, John Wiley & Sons Ltd, United Kingdom, 2010.
- [19] Kevin M. PASSINO and Stephen YURKOVICH, "Fuzzy Control", Book: First Edition, Addison-Wesley Longman, Inc, California-USA, 1998.
- [20] Fayssal AMRANE and Azeddine CHAIBA: "Direct Power Control for grid-connected DFIG using Fuzzy Logic with a Fixed Switching Frequency" Conférence Internationale d'Automatique et de la Mécatronique, CIAM 10-11th Nov 2015 Oran-Algeria.
- [21] Guanrong CHEN and Trung Tat PHAM, "Introduction to Fuzzy Sets, Fuzzy Logic, And Fuzzy Control Systems", Book: First Edition, CRC Press, New York-USA, 2001.
- [22] Abdeldjabbar KOUADRIA, Tayeb ALLAOUI, Mouloud DENAI and George PISSANIDIS, "Grid Power Quality Enhancement Using Fuzzy Control-Based Shunt Active Filtering", SAI Intelligent Systems Conference 2015 November 10-11th, 2015, London, UK
- [23] Dongrui WU and Jerry M. Mendel, "Designing Practical Interval Type-2 Fuzzy Logic Systems Made Simple", 2014 IEEE International Conference on Fuzzy Systems (FUZZ-IEEE) July 6-11, 2014, Beijing, China.
- [24] Faa-Jeng LIN, "Introduction to Type-2 Fuzzy Logic Control: Theory and Applications", Book, IEEE Systems, Man, & Cybernetics Magazine, 2015.
- [25] S. Krishnama RAJU and G. N. PILLAI, "Design and Implementation of Type-2 Fuzzy Logic Controller for DFIG-Based Wind Energy Systems in Distribution Networks", IEEE Transactions on Sustainable Energy, vol. 7, no. 1, 2016
- [26] L. Suganthia; S.INIYAN and Anand A.SAMUEL. *Applications of fuzzy logic in renewable energy systems – A review* JRSER. 2015, vol, 48.
- [27] Fayssal AMRANE and Azeddine CHAIBA, "Type2 Fuzzy Logic Control: Design and Application in Wind Energy Conversion System based on DFIG via Active and Reactive Power Control", Chapter-1, pp.1-35, Title Book: "Fuzzy Control Systems, Analysis and Performances Evaluation", Nova Science Publishers, USA, January 2017.
- [28] Fayssal AMRANE, Azeddine CHAIBA and Bruno FRANCOIS: "Application of Adaptive T2FLC in Stator Active and Reactive power Control WECS based on DFIG via Hypo/Hyper-Synchronous Modes", 4^{ième} Conférence des Jeunes Chercheurs en Génie Electrique, JCGE, 30 Mai et 1^{er} Juin 2017, Arras, France.
- [29] Fayssal AMRANE, Azeddine CHAIBA and Bruno FRANCOIS: "Suitable Power Control based on Type-2 Fuzzy Logic Control for Wind-Turbine DFIG Under Hypo-Synchronous Mode Fed by NPC Converter" 5th International Conference on Electrical Engineering, IEEE Conference, ICEE 29-31th Oct 2017 Boumerdes-Algeria
- [30] Fayssal AMRANE and Azeddine CHAIBA: "A Hybrid Intelligent Control based on DPC for grid-connected DFIG with a Fixed Switching Frequency using MPPT Strategy" 4th International Conference on Electrical Engineering, IEEE Conference, ICEE 13-15th Dec 2015 Boumerdes-Algeria.

Chapter 4 :

A New Input/output Linearizing and Decoupling Control (I/OLDC) of DFIG in WECS using an Adaptive Control through Multi-Level Converters.

4.1 Introduction.....	95
4.2 Classical Input/output Linearizing and Decoupling Control (I/OLDC) based on PI controller.....	95
4.2.1 General Concept of the Input-Output Linearizing Control.....	95
4.2.2 Control of rotor side converter.....	96
4.3 Proposed I/OLDC based on MRAC under three modes using MPPT strategy.....	98
4.3.1 Model Reference Adaptive control (MRAC) strategy.....	98
4.3.2 Back-to-back two Level converter using three (03) modes.....	99
4.3.3 Back-to-back Three Level NPC converter using three (03) modes.....	99
A. NPC (Neutral-Point Clamped) Topology.....	99
B. Modeling structure of one inverter arm.....	100
C. Comparative simulation study of two level and three level inverter under RL-load.....	101
4.4 Simulation Results.....	101
4.4.1 Back-to-back two Level converter using PI controller.....	103
4.4.2 Back-to-back two Level converter using MRAC controller.....	108
4.4.3 Back-to-back three Level Inverter (NPC) based on MRAC controller.....	113
4.5 The high power evaluation tests (using improved I/OLDC with 2LC and 3LC).....	118
4.6 Decoupling parameter tests (using all the proposed control: chapter 2, chapter 3 and chapter 4).....	118
4.7 Conclusion.....	120
4.8 References.....	120

Abstract:

This chapter presents an enhanced input/output-linearizing and decoupling control (I/OLDC), which is based on model reference adaptive control (MRAC). The improved I/OLDC is applied in variable speed for wind energy conversion system (WECS) using Doubly Fed Induction Generator (DFIG) fed by back-to-back three-phase voltage source inverter (VSI). The proposed control technique is used to control the active and reactive powers of wind turbine based on DFIG using different wind speed profiles (under three modes via MPPT strategy). By using the feedback linearization, the control algorithm is established. In order to improve the tracking of stator active and reactive power references, MRAC is used after the comparison between measured and reference of stator active and reactive powers respectively, instead of PI controllers. The proposed control is used to overcome the drawbacks of the classical control based on PI controllers in terms of; overshoot, response time, power error and the reference tracking. Two level back-to-back converter (2LC) and three level NPC back-to-back converter (3LC) are proposed for the improved I/OLDC control to evaluate the wind-system performances under high-wind power. Finally, simulation results demonstrate that the proposed control using MRAC provides improved dynamic responses and perfect decoupled control of the wind turbine has driven DFIG with high performances (good reference tracking, short response time and neglected power error) in steady and transient states for the both cases; 2LC and 3LC.

4.1 Introduction

During the past decade, the installed wind power capacity in the world has been increasing more than 30% [1-2]. DFIG-based wind turbines have many advantages over the fixed speed induction generators or variable speed synchronous generators with full-scale power converters, including variable speed operation for maximum power tracking, decoupled active and reactive power control, lower converter cost, and reduced power loss [3-4]. The electronic interface dealing with wind generator control is basically a back-to-back two-level converter; however, this kind of power converter is seldom used for high power applications [5]. As a result, multilevel converters using pulse-width modulation are being increasingly preferred for high power applications [6], [7], especially in wind energy. The advantages of multilevel structure are basically increasing in power rating, reducing stress across the switches, improving the voltage waveforms with low total harmonic distortion (THD) current. The neutral point clamped converter (NPC) is one of the most popular structures of the multilevel voltage source (VSI) proposed in 1981 by Nabae et al. [6]. With the development of nonlinear control theory, the corresponding methods can be applied for the control of doubly fed induction generator (DFIG). Among them, feedback linearization, integrator back-stepping and passivity based control are extensively applied for inductance electric machine [8]. The DFIG control using Input-Output Feedback Linearization and Decoupling (I/OLDC) method can operate below and above synchronous speed. A schematic diagram of variable speed wind turbine system with a DFIG based on classical I/OLDC using PI controllers (in order to control the rotor side converter) is shown in figure.4.1. The application of the classical input/output nonlinear control based on PI regulator generates some drawbacks or limitation of the performances (power error, tracking power, overshoot...etc.). Model reference adaptive control (MRAC) is an adaptive controller used instead the classical PI to avoid these drawbacks.

The main contribution of this chapter is the validation of the proposed control based on robust adaptive MRAC using input/output linearizing control to provide improved performance and parameter, also to control independently (decoupled control) the stator active and reactive powers of DFIG-wind turbine. MRAC used with multi-level converter to improve powers tracking and overcome the drawbacks of the classical nonlinear control based on PI regulators such as long response time, remarkable overshoot, and big power error.

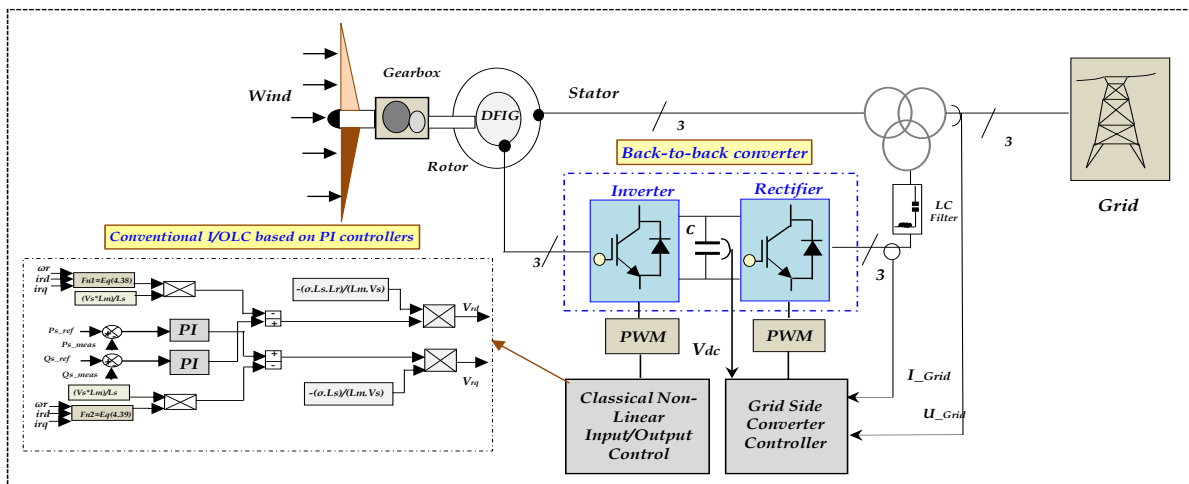


Figure.4.1 Conventional input/output linearizing and decoupling control of DFIG.

4.2 Classical Input/output Linearizing and Decoupling Control (I/OLDC) based on PI controller

4.2.1 General Concept of the Input-Output Linearizing Control

Given the system [9-10-11] as shown in figure.4.3; (knowing that the DFIG's¹ simplified model is described in figure.4.2). Where x is the state vector; u is the input; y is the output; f_n and g are the smooth vector fields; h is the smooth scalar function.

¹ The mathematical model (based on stator flux orientation) of the DFIG is described in details in chapter 2-(Paragraph §.2.2)

$$\begin{cases} \dot{x} = f_n(x) + g. u \\ y = h(x) \end{cases} \quad (4.1)$$

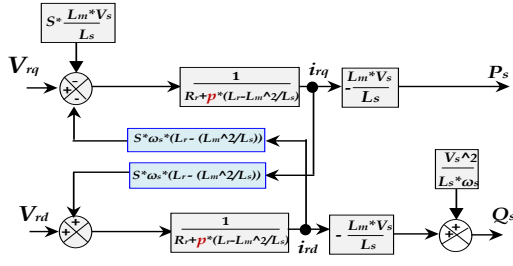


Figure.4.2 The DFIG power model.

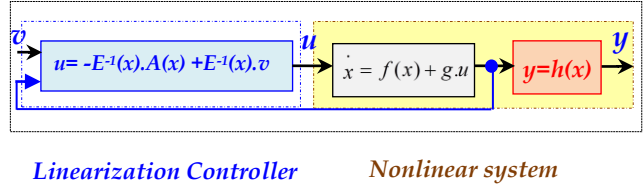


Figure.4.3 Schematic diagram of input-output linearizing control.

In order to obtain the input-output linearization of the multi-input multi-output (MIMO) system, the output y of the system is differentiated until the inputs appear.

$$\dot{y} = L_f h(x) + L_g h(x). u \quad (4.2)$$

Where: $L_f h(x) = \frac{\partial h}{\partial x} . f(x)$, $L_g h(x) = \frac{\partial h}{\partial x} . g(x)$; represent Lie derivatives of $h(x)$ with respect to $f(x)$ and $g(x)$ respectively. If $L_g h(x) = 0$ then the input u does not appear and the output is differentiated respectively.

$$y^{(r)} = L_f^r . h(x) + L_g^{r-1} . h(x). u \quad (4.3)$$

By neglecting resistances of the stator phases the stator voltage will be expressed by:

Where r is the relative rank of y . if we perform the above procedure for each input y_i , we get a total of m equations in the above form, which can be written completely as:

$$\begin{bmatrix} y_1^{(r)} \\ \vdots \\ y_m^{(r_m)} \end{bmatrix} = A(x) + E(x). \begin{bmatrix} u_1 \\ \vdots \\ u_m \end{bmatrix} \quad (4.4)$$

Where the $m \times m$ matrix $E(x)$ is defined as:

$$E(x) = \begin{bmatrix} L_{g1} L_f^{r-1} h_1 & \dots & \dots & L_{gm} L_f^{r-1} h_1 \\ \vdots & \vdots & \vdots & \vdots \\ L_{g1} L_f^{r_m-1} h_m & \dots & \dots & L_{gm} L_f^{r_m-1} h_m \end{bmatrix} \quad (4.5)$$

$$A(x) = [L_f^r h_1 \quad \dots \quad L_f^{r_m} h_m]^T \quad (4.6)$$

The matrix $E(x)$ is the decoupling matrix for the system. If $E(x)$ is nonsingular, then the original input u is controlled by the coordinate transformation:

$$u = -E^{-1}(x). A(x) + E^{-1}(x). v \quad (4.7)$$

Where: $v = [v_1 \quad \dots \quad v_m]^T$. Substituting (4.6) into (4.4) obtains a linear differential relation between the output y and the new input v .

$$\begin{bmatrix} y_1^{(r)} \\ \vdots \\ y_m^{(r_m)} \end{bmatrix} = \begin{bmatrix} v_1 \\ \vdots \\ v_m \end{bmatrix} \quad (4.8)$$

4.2.2 Control of rotor side converter ²

According (2.20) and (2.21), the direct and quadrature components of the stator and the rotor currents are linearly dependent respectively, thus we chooses state vectors of the DFIG as follows:

$$x = [x_1 \quad x_2]^T = [i_{rd} \quad i_{rq}]^T \quad (4.9)$$

² Knowing that; in this chapter we used the same Grid Side Converter (GSC) topology described in Chapter: 2-(paragraph §.2.5).

By substituting (2.9), (2.10), (2.11), (2.12), (2.18), (2.19), (2.20) and (2.21) to (2.7) and (2.8), the following equations hold:

$$V_{rd} = R_r \cdot i_{rd} + \sigma \cdot L_r \cdot \frac{di_{rd}}{dt} - (\omega_s - \omega_r) \cdot \sigma \cdot i_{rq} \quad (4.10)$$

$$V_{rq} = R_r \cdot i_{rq} + \sigma \cdot \frac{di_{rq}}{dt} - (\omega_s - \omega_r) \cdot \sigma \cdot L_r \cdot i_{rd} \quad (4.11)$$

Where: $\sigma = 1 - \frac{L_m^2}{L_s L_r}$

Arranging (4.10) and (4.11) in the form of (4.1):

$$\frac{di_{rd}}{dt} = -\frac{R_r}{\sigma \cdot L_r} \cdot i_{rd} + \frac{1}{L_r} \cdot (\omega_s - \omega_r) \cdot i_{rq} + \frac{u_{rd}}{\sigma \cdot L_r} \quad (4.12)$$

$$\frac{di_{rq}}{dt} = -\frac{R_r}{\sigma} \cdot i_{rq} - (\omega_s - \omega_r) \cdot L_r \cdot i_{rd} + \frac{u_{rq}}{\sigma} \quad (4.13)$$

Defining the input of the DFIG system:

$$u = [u_1 \quad u_2]^T = [u_{rd} \quad u_{rq}]^T \quad (4.14)$$

From (4.12) and (4.13), we have:

$$f_{n1} = -\frac{R_r}{\sigma \cdot L_r} \cdot i_{rd} + \frac{1}{L_r} \cdot (\omega_s - \omega_r) \cdot i_{rq} \quad (4.15)$$

$$f_{n2} = -\frac{R_r}{\sigma} \cdot i_{rq} - L_r \cdot (\omega_s - \omega_r) \cdot i_{rd} \quad (4.16)$$

$$g = \begin{bmatrix} \frac{1}{\sigma \cdot L_r} & 0 \\ 0 & \frac{1}{\sigma} \end{bmatrix} \quad (4.17)$$

Since the rotor side controller is set to decouple the active and reactive powers, the active and reactive powers of stator are selected as the output:

$$y = \begin{bmatrix} y_1 \\ y_2 \end{bmatrix} = \begin{bmatrix} P_s \\ Q_s \end{bmatrix} = \begin{bmatrix} v_{sd} \cdot i_{sd} + v_{sq} \cdot i_{sq} \\ v_{sq} \cdot i_{sd} - v_{sd} \cdot i_{sq} \end{bmatrix} \quad (4.18)$$

From (2.20), (2.21) and (4.18):

$$y_1 = \frac{\phi_s}{L_s} \cdot v_{sd} - \frac{L_m}{L_s} \cdot (v_{sd} \cdot i_{rd} - v_{sq} \cdot i_{rq}) \quad (4.19)$$

$$y_2 = \frac{\phi_s}{L_s} \cdot v_{sq} - \frac{L_m}{L_s} \cdot (v_{sq} \cdot i_{rd} - v_{sd} \cdot i_{rq}) \quad (4.20)$$

Differentiating (4.19) and (4.20) until an input appears:

$$\dot{y}_1 = \frac{u_{sd}}{L_s} \cdot (\phi_s - L_m \cdot i_{rd}) - \frac{L_m}{L_s} \cdot u_{sq} \cdot i_{rq} - \frac{L_m}{L_s} \cdot (v_{sd} \cdot f_{n1} - v_{sq} \cdot f_{n2}) - \frac{L_m \cdot V_{sd}}{\sigma \cdot L_r \cdot L_s} \cdot V_{rd} - \frac{L_m \cdot V_{sq}}{\sigma \cdot L_s} \cdot V_{rq} \quad (4.21)$$

$$\dot{y}_2 = \frac{u_{sq}}{L_s} \cdot (\phi_s - L_m \cdot i_{rd}) - \frac{L_m}{L_s} \cdot u_{sd} \cdot i_{rd} - \frac{L_m}{L_s} \cdot (v_{sq} \cdot f_{n1} - v_{sd} \cdot f_{n2}) - \frac{L_m \cdot V_{sq}}{\sigma \cdot L_r \cdot L_s} \cdot V_{rd} + \frac{L_m \cdot V_{sd}}{\sigma \cdot L_s} \cdot V_{rq} \quad (4.22)$$

Rewriting (4.21) and (4.22) in the form of (4.4):

$$\begin{bmatrix} \dot{y}_1 \\ \dot{y}_2 \end{bmatrix} = A(x) + E(x) \cdot \begin{bmatrix} u_1 \\ u_2 \end{bmatrix} \quad (4.23)$$

Where:
$$A(x) = \begin{bmatrix} \frac{V_{sd}}{L_s} \cdot (\phi_s - L_m \cdot x_1) - \frac{L_m}{L_s} \cdot V_{sq} \cdot x_2 - \frac{L_m}{L_s} \cdot (V_{sd} \cdot f_{n1} + V_{sq} \cdot f_{n2}) \\ \frac{V_{sq}}{L_s} \cdot (\phi_s - L_m \cdot x_1) + \frac{L_m}{L_s} \cdot V_{sd} \cdot x_2 - \frac{L_m}{L_s} \cdot (V_{sq} \cdot f_{n1} - V_{sd} \cdot f_{n2}) \end{bmatrix} \quad (4.24)$$

$$E(x) = \begin{bmatrix} -\frac{L_m \cdot V_{sd}}{\sigma \cdot L_r \cdot L_s} & -\frac{L_m \cdot V_{sq}}{\sigma \cdot L_s} \\ \frac{L_m \cdot V_{sq}}{\sigma \cdot L_r \cdot L_s} & \frac{L_m \cdot V_{sd}}{\sigma \cdot L_s} \end{bmatrix} \quad (4.25)$$

Since $E(x)$ is nonsingular, the control scheme is given from (4.34) as:

$$\begin{bmatrix} V_{rd} \\ V_{rq} \end{bmatrix} = E^{-1}(x) \cdot \left[-A(x) + \begin{pmatrix} V_1 \\ V_2 \end{pmatrix} \right] \quad (4.26)$$

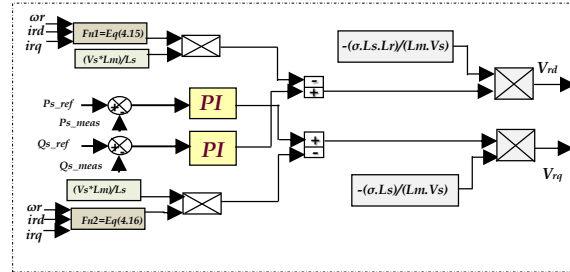


Figure.4.4 Schematic diagram of classical input/output linearizing control based on PI³ controllers.

In $A(x)$ and $E(x)$ most components relate to the factors L_m/L_s and σ that both are equal to one approximately, and the functions f_{n1} and f_{n2} have no relation with parameters of the stator windings. Hence, the control law is robust to machine parameter variations.

For a DFIG the demanded active power P_s^* is decided by the maximum power tracking scheme of the wind turbine according to the instant wind speed, and the demanded reactive power Q_s^* is set by the grid operator to support grid voltage. The model reference adaptive controller (MRAC) achieves the tracking of the powers. Hence, MRAC technique is described in details below.

4.3 Proposed I/OLDC based on MRAC under three modes using MPPT Strategy

4.3.1 Model Reference Adaptive control (MRAC) strategy

The system studied in this paper is based on a first-order linear plant approximation given by [12]:

$$\dot{x}(t) = -a \cdot x(t) + b \cdot u(t) \quad (4.27)$$

Where $x(t)$ is the plant state, $u(t)$ is the control signal and a and b are the plant parameters. The control signal is generated from both the state variable and the reference signal $r(t)$, multiplied by the adaptive control gains K and K_r such that

$$u(t) = K(t) \cdot x(t) + K_r(t) \cdot r(t) \quad (4.28)$$

Where $K(t)$ is the feedback adaptive gain and $K_r(t)$ the feed forward adaptive gain. The plant is controlled to follow the output from a reference model.

$$\dot{x}_m(t) = a_m \cdot x_m(t) + b_m \cdot r(t) \quad (4.29)$$

Where x_m is the state of the reference model and a_m and b_m are the reference model parameters

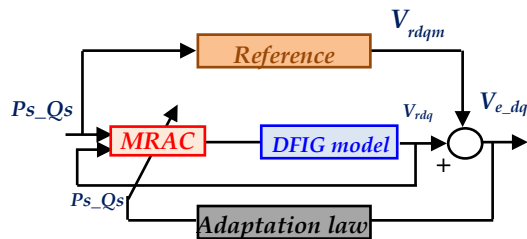


Figure.4.5 Model reference adaptive control scheme.

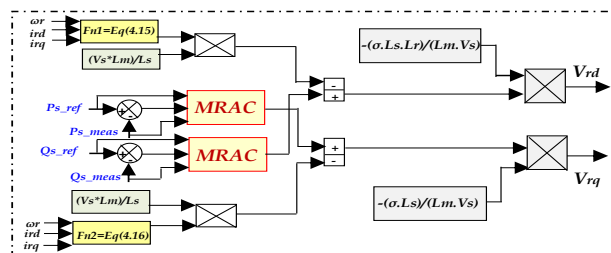


Figure.4.6 Schematic diagram of new input/output linearizing control.

³ Please refer to Appendix.C-“Section.C-3”: (The gain’s values used in chapter: 4 of PI controllers “Kp and Ki” are described in details in Table.C2).

which are specified by the controller designer. The object of the MRAC algorithm is for $x_e \rightarrow 0$ as $t \rightarrow \infty$, where $x_e = x_m - x$ is the error signal. The dynamics of the system may be rewritten in terms of the error such that:

$$\dot{x}_e(t) = a_m \cdot x_e(t) + (a - a_m - b \cdot K(t)) \cdot x(t) + (b_m - b \cdot K_r(t)) \cdot r(t) \quad (4.30)$$

Using Equations (4.28), (4.29) and (4.30), it can be seen that for exact matching between the plant and the reference model, the following relations hold.

$$K = K^E = \frac{a - a_m}{b} \quad (4.31)$$

$$K_r = K_r^E = \frac{b_m}{b} \quad (4.32)$$

Where $()^E$ denotes the (constant) Erzberger gains [12].

Equations (4.31) and (4.32) can be used to express Equation (4.30) as:

$$\dot{x}_e(t) = -a_m \cdot x_e + b \cdot (K^E - K) \cdot (x_m - x_e) + b \cdot (K^E - K) \cdot r \quad (4.33)$$

For general model reference adaptive control, the adaptive gains are commonly defined in a proportional plus integral formulation

$$K(eP, t) = \int_0^t a \cdot y_e \cdot P_s^T \cdot dt + b \cdot y_e \cdot P_s^T \quad (4.34)$$

$$K_r(eP, t) = \int_0^t a \cdot y_e \cdot P_{s_ref}^T \cdot dt + b \cdot y_e \cdot P_{s_ref}^T \quad (4.35)$$

$$K(eQ, t) = \int_0^t a \cdot y_e \cdot Q_s^T \cdot dt + b \cdot y_e \cdot Q_s^T \quad (4.36)$$

$$K_r(eQ, t) = \int_0^t a \cdot y_e \cdot Q_{s_ref}^T \cdot dt + b \cdot y_e \cdot Q_{s_ref}^T \quad (4.37)$$

Where α and β are adaptive control weightings representing the adaptive effort. y_e is a scalar weighted function of the error state and its derivatives, $y_e = C_e \cdot x_e$, where C_e can be chosen to ensure the stability of the feed forward block.

The equivalent scheme of MRAC for adjusting active and reactive powers in this work is shown in figure.4.5. The proposed control is described in details in figure.4.6.

4.3.2 Back-to-back two Level converter using three (03) modes

Figure.4.7 presents the proposed control which is composed on four (04) important parts as follows; 1: Back-to-back two level converter, 2: The imposed power profiles, 3: The MPPT strategy, 4: The proposed I/OLDC based on MRAC controller.

4.3.3 Back-to-back Three Level NPC⁴ converter using three (03) modes

Figure.4.10 presents the proposed control which is composed on four (04) important parts as follows; 1: The NPC back-to-back three level converter (which is explained below § 4.3.3-(A, B and C)), 2: The imposed power profiles, 3: The MPPT strategy, 4: The proposed I/OLDC (based on MRAC controller).

A. NPC (Neutral-Point Clamped) Topology

The trend towards multi MW wind turbine units has called up for new concepts in the design of wind energy conversion systems. Economic viability of wind turbines clearly scales with power and efficiency of generators and power conversion systems. Within this trend, power electronic multilevel converters have been seen as an appropriate technology for the wind energy conversion system because they can operate at high power and high voltage [13]. Among several proposed multilevel topologies the Three-level diode-clamped or simply called Neutral-Point Clamped (NPC) inverter was the first widely implemented by the industry and it continues to be extensively used in high voltage and high power applications. The NPC inverter leg is shown in figure.4.8. It is composed by four switches S11, S21, S31 and S41 and the anti-parallel diodes D1 to D2. Voltages across the switches are only half of the DC input voltage because diodes D1 and D2 are connected to the neutral point [13]. The three-phase NPC inverter presents a line-to-line voltage with five voltage levels which leads to a lower Total Harmonic Distortion (THD)

⁴ Please refer to Appendix C-“Section.C-4” (Figure.C.5 presents the real three level NPC converter developed in L2EP Laboratory, Ecole Centrale de Lille/France).

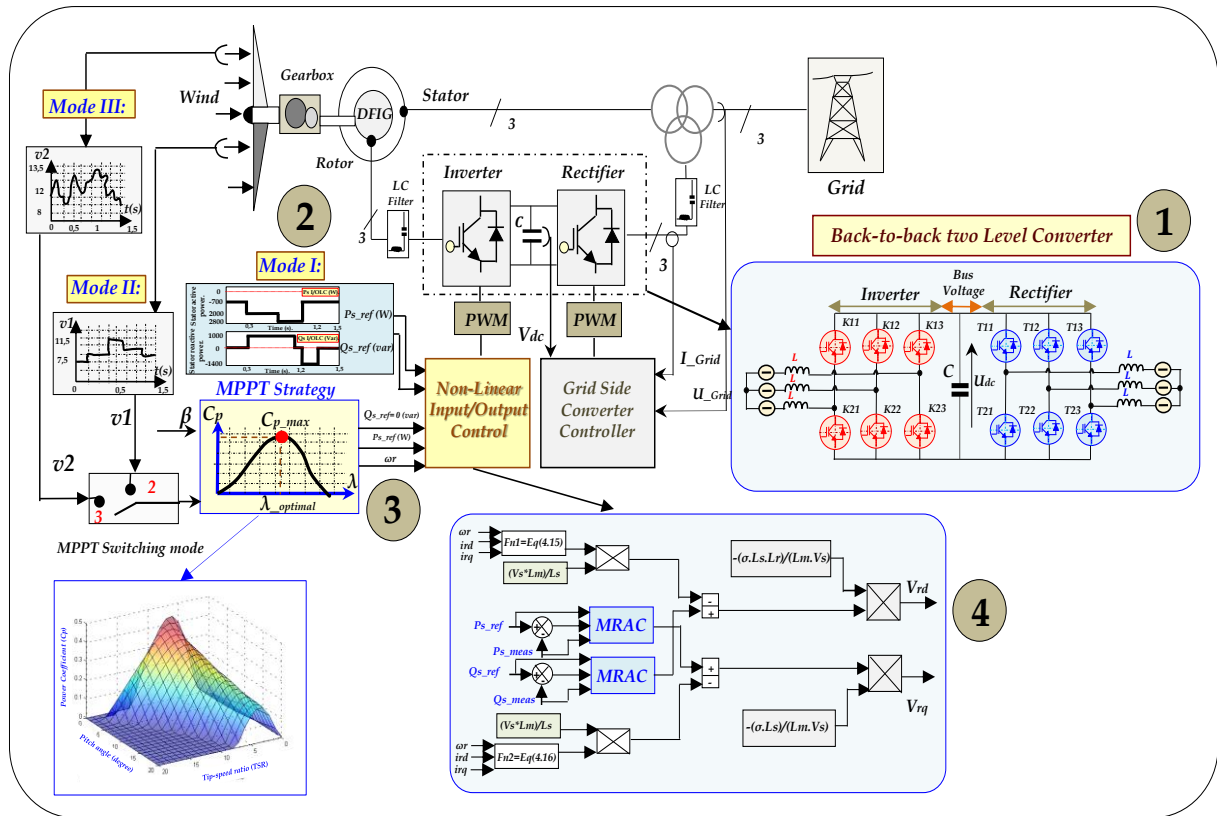


Figure.4.7 Schematic diagram of the proposed I/OLDC based on two level back-to-back converters.

and di/dt ; also resulting in lower Electromagnetic Interference EMI when compared to the conventional two-level inverter. On the other hand, as the number of levels of the inverter increases the THD of the output voltage waveform presents little improvement.

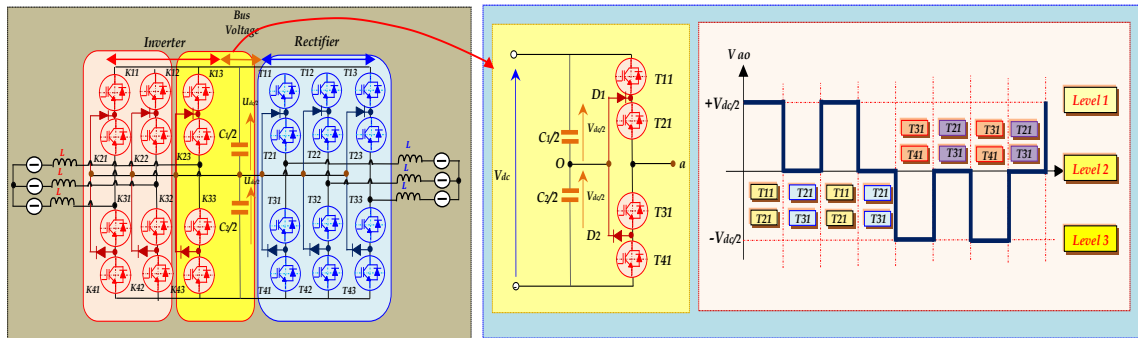


Figure.4.8 NPC inverter arm and AC waveform.

B. Modeling structure of one inverter arm:

The structure symmetry of the three level inverter inverter is described in figure.4.8. One initially defines the global model of an arm, and then deduces that of the complete inverter. Three complementary controls can be applied to the three level inverter arm.

$$\begin{aligned} G_{T31} &= \overline{G_{T11}}, G_{T21} = \overline{G_{T11}}, G_{T41} = \overline{G_{T11}} \\ G_{T41} &= \overline{G_{T21}}, G_{T41} = \overline{G_{T31}}, G_{T31} = \overline{G_{T21}} \end{aligned} \quad (4.38)$$

With G_{T5} the trigger controls of the T_5 switch of the arm's'.

In order to have the total commutable mode of the three-level inverter, one must eliminate the case which gives an unknown answer (as shown in table.4.1). By translating this complementary control using the connection functions of the switches of arm's', one finds:

$$\begin{cases} F_{T31} = 1 - F_{T41} \\ F_{T21} = 1 - F_{T31} \end{cases} \quad (4.39)$$

Table.4.1. Excitation switches of NPC's IGBTs.

G_{T11}	G_{T21}	G_{T31}	G_{T41}	V_{T0}
0	0	1	1	V_{c2}
0	1	0	1	0.
1	0	1	0	0
1	1	0	0	V_{c1}

One defines the connection function of the half-arms noted as F_{Tm}^b with:

$$\begin{aligned} m=1 & \text{ for the higher half arm composed of } TD_{T11} \text{ and } TD_{T21} \\ m=0 & \text{ for the lower half arm composed of } TD_{T31} \text{ and } TD_{T41} \end{aligned} \quad (4.40)$$

The connection functions of the half-arms are expressed by means of the connection functions of the switches as follows:

$$\begin{cases} F_{T11}^b = F_{T11} \cdot F_{T21} \\ F_{T11}^0 = F_{T31} \cdot F_{T41} \end{cases} \quad (4.41)$$

The nodal potentials a, b, c of the three -phase three -level inverter compared to the medium point, are given by the following system:

$$\begin{cases} V_{a0} = F_{11} \cdot F_{12} \cdot V_{c1} - F_{13} \cdot F_{14} \cdot V_{c2} \\ V_{b0} = F_{21} \cdot F_{22} \cdot V_{c1} - F_{23} \cdot F_{23} \cdot V_{c2} \\ V_{c0} = F_{31} \cdot F_{32} \cdot V_{c1} - F_{33} \cdot F_{34} \cdot V_{c2} \end{cases} \quad (4.42)$$

By introducing the connection functions of the half arms, one will obtain:

$$\begin{cases} V_{a0} = F_{11}^b \cdot V_{c1} - F_{10}^b \cdot V_{c2} \\ V_{b0} = F_{21}^b \cdot V_{c1} - F_{20}^b \cdot V_{c2} \\ V_{c0} = F_{31}^b \cdot V_{c1} - F_{30}^b \cdot V_{c2} \end{cases} \quad (4.43)$$

The inverter output phase voltages are deduced in terms of the nodal potentials compared to the medium point by the following relation:

$$\begin{cases} V_a = 1/3 \cdot (+2 \cdot V_{a0} - V_{b0} - V_{c0}) \\ V_b = 1/3 \cdot (-V_{a0} + 2 \cdot V_{b0} - V_{c0}) \\ V_c = 1/3 \cdot (-V_{a0} - V_{b0} + 2 \cdot V_{c0}) \end{cases} \quad (4.44)$$

From the relation (4.43) and (4.44), one obtains the matrix system linking the functions of the inverter half-arms to the phase voltages at the load terminals given as:

$$\begin{bmatrix} V_a \\ V_b \\ V_c \end{bmatrix} = \frac{1}{3} \cdot \begin{bmatrix} +2 & -1 & -1 \\ -1 & +2 & -1 \\ -1 & -1 & +2 \end{bmatrix} \cdot \begin{bmatrix} F_{11}^b \\ F_{21}^b \\ F_{31}^b \end{bmatrix} \cdot V_{c1} - \begin{bmatrix} F_{10}^b \\ F_{20}^b \\ F_{30}^b \end{bmatrix} \cdot V_{c2} \quad (4.45)$$

In the case where: $V_{c1} = V_{c2} = V_{dc}/2$, the relation (4.45) is reduced to:

$$\begin{bmatrix} V_a \\ V_b \\ V_c \end{bmatrix} = \frac{1}{3} \cdot \begin{bmatrix} +2 & -1 & -1 \\ -1 & +2 & -1 \\ -1 & -1 & +2 \end{bmatrix} \cdot \begin{bmatrix} F_{11}^b - F_{10}^b \\ F_{21}^b - F_{20}^b \\ F_{31}^b - F_{30}^b \end{bmatrix} V_{dc}/2 \quad (4.46)$$

C. Comparative simulation study of tow and three level inverter under RL-load:

Figure.4.9⁵ presents the currents and voltage waveforms of RL-load using twol levels and three levels inverter respectively. Figure.4.9-(a) presents the waveforms of RL-load current (via PWM two level inverter) of phase '1' $I_1(A)$ (peak to peak equals to 4 (A), simple voltage V_{an} (V), line to line voltage U_{ab} (V), switching signals for one IGBT and PWM carrier . Figure.4.9-(b) illustrates also the waveforms of RL-load (via PWM NPC three levels inverter): current of phase '1' $I_1(A)$ (peak to peak equals to 4 (A), simple voltage V_{an} (V), line to line voltage U_{ab} (V), switching signals for one IGBT and PWM carriers. The load current THD is improved using PWM-3LC (=1.29%) compared to 2LC (=1.61%).

4.4 Simulation results

The proposed system (DFIG' control + wind turbine)⁶ is validated using Matlab/Simulink[®] software under MPPT strategy by keeping stator reactive power equals to zero and to ensure unity power

⁵ In this case (figure.4.9) two inverter topologies (Bus voltage+Inverter+RL-Load) are studied and simulated in real time, knowing that the PWM two levels and three levels inverters are simulated using the same parameters, $V_{dc}=150$ (V), Load: (R=25 (Ω), L=50e⁻³ (H)), frequency: fs= 3 (KHz).

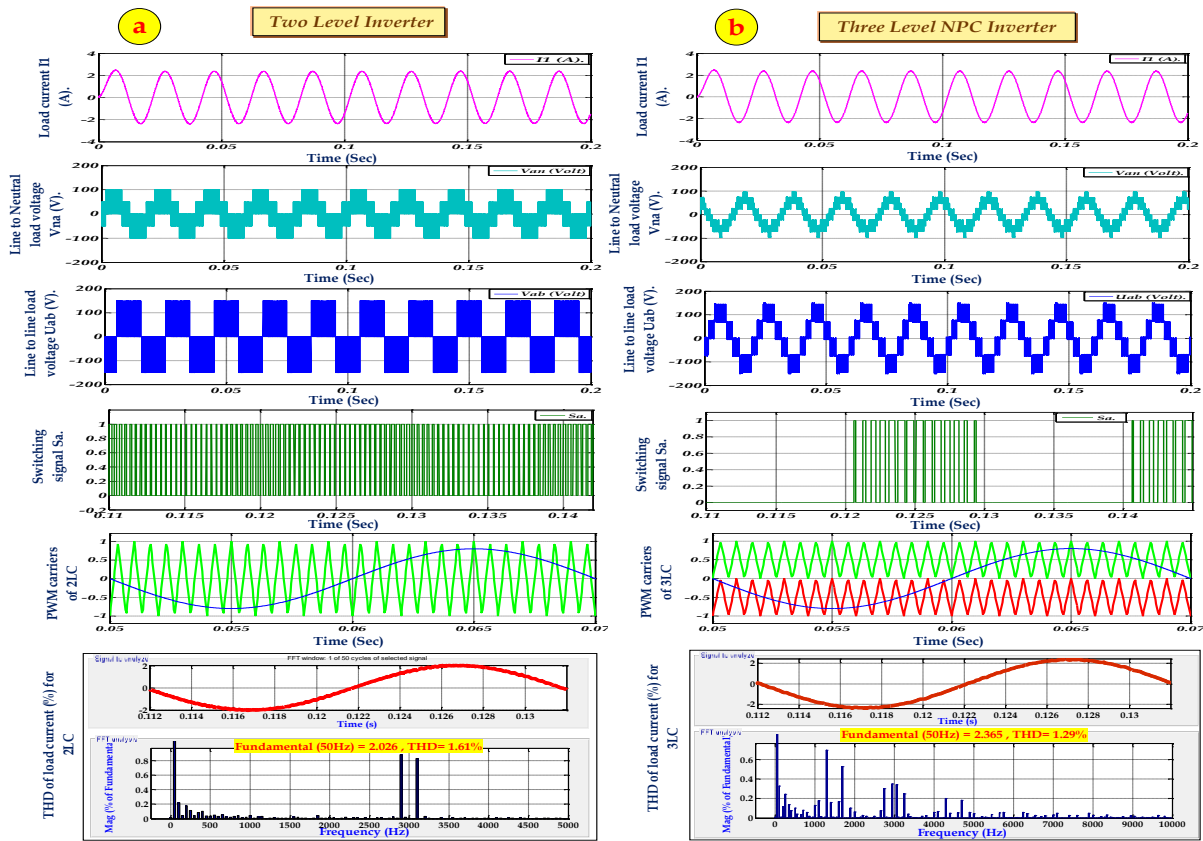


Figure.4.9 Simulation results for load current and load voltage fed by two levels (left) and three level inverter (right) using PWM strategy.

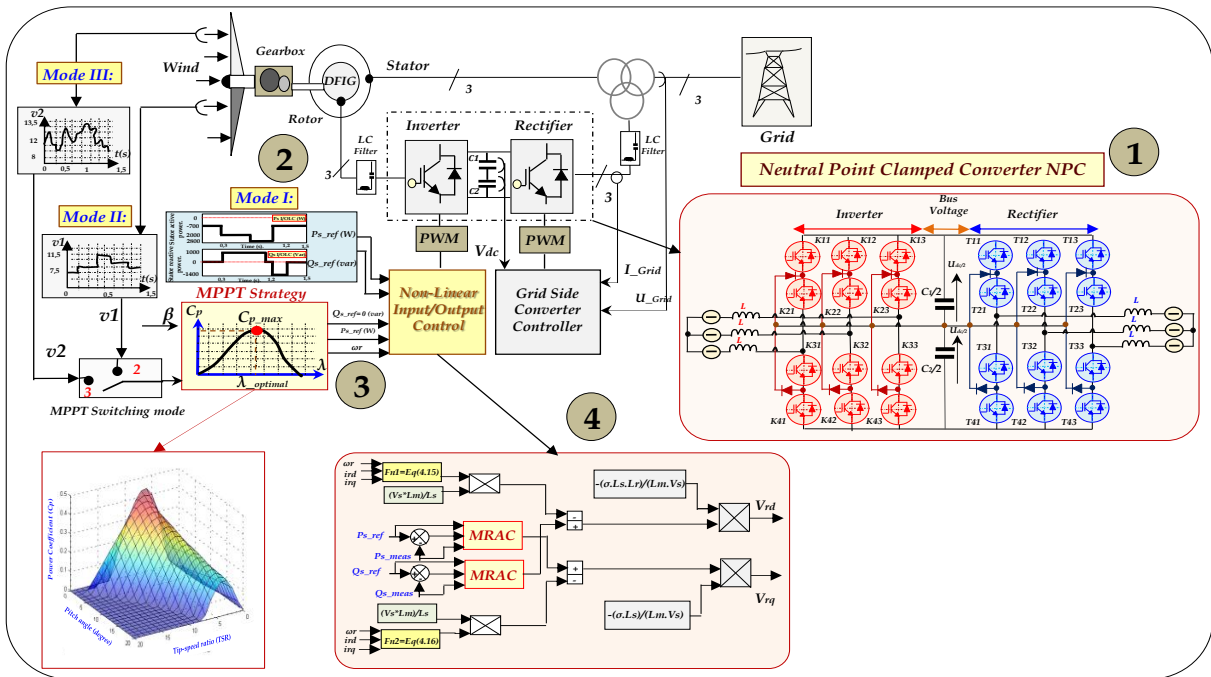


Figure.4.10 Schematic diagram of the proposed I/OLDC based on NPC back-to-back converter.

factor ($PF=1$). The figures.4-(11, 14 and 17) respectively present the simulation results for proposed I/OLDC using PI, MRAC under two and three level converters. These figures are divided into three parts; the left part (red color) presents the simulation results of the wind system without using the MPPT strategy by imposing stator active and reactive power profiles, in the middle (blue color) presents the

⁶ Please refer to Appendix.A-“Section.A-1”: (The DFIG’ and wind turbine parameters are indicated in Table.A.1 and Table.A.2 respectively).

simulation results of the wind-system under MPPT strategy using step form of wind speed which it can only illustrate *Sub-synchronous* operation because the generator speed is still less than the synchronous speed, and at right part (*green color*) presents the simulation results of the wind-system under MPPT strategy using random form of wind speed which can illustrate both modes; *Sub* and *Super-synchronous* operations because the generator speed vary above and below the synchronous speed). The three (03) modes applied in simulation section in transient and steady states are described as flows:

- 1- **Mode I (Red color/** to the left side of figures.4-(11, 14 and 17)): Without MPPT Strategy, in this case we impose the P_s and Q_s reference profiles.
- 2- **Mode II (Blue color/** to the middle of figures.4-(11, 14 and 17): With MPPT strategy, in this case we propose a low wind speed based on step form (Max wind speed = 11.5 m/sec) by keeping stator reactive power equal to Zero level " $Q_s = 0$ (Var)"; to ensure only the exchange of the stator active power to the grid; means following the maximum active power point.
- 3- **Mode III (Green color/** to the right side of figures.4-(11, 14 and 17)): With MPPT strategy, in this case we propose a medium wind speed based on random form (Max wind speed = 13.5 m/sec) by keeping stator reactive power equal to Zero level " $Q_s = 0$ Var"; to ensure only the exchange of the stator active power to the grid; means following the maximum active power point.

The second part focuses on the comparative simulation study between the MPPT strategy (using step' and random wind speed) for each proposed I/OLDC algorithm (using PI and MRAC for 2LC and 3LC⁷ respectively) is described in details in figures.4-(12, 15 and 18) respectively. This section is developed in order to illustrate the *Sub* and *Super-synchronous* modes and the behavior of slip under generator speed variation.

The third part deals on robustness tests using a comparative simulation study, for three modes (with/without MPPT strategy) for each proposed I/OLDC algorithm (using PI and MRAC for 2LC and 3LC respectively) is described in details in figures.4-(13, 14 and 19) respectively. This section is developed in order to verify the robustness of wind-system under parameter variation (using three tests)⁸ in transient and steady states.

4.4.1 Back-to-back two Level converter using PI controller

The simulation results of this topology (I/OLDC based on PI controller using 2LC) are described in details in figures.4-(11, 12 and 13). Figure.4.11 presents the behavior of the wind-system (using DFIG (4 kW) and wind turbine (4.5 kW)) under three modes (that already presented above) in transient and steady states. Following are detailed description of the simulation results under three (03) modes:

Mode 1 (red color/figure.4.11 to the left): The measured stator active and reactive powers (P_{s_meas} and Q_{s_meas}) and their references (P_{s_ref} and Q_{s_ref}) profiles are presented together in figure.4.11-(a) and are presented separately in figures.4.11.(b and c) respectively. The reference powers are indicated in table.4.2. It is clear that the measured powers (active and reactive) have bad tracking power (big error) compared to their reference powers in transient and steady states (refer to figure.4.11-(b and c)), a remarkable (70%) overshoot is noted at 0.3 (sec) and 1.0 (sec) respectively in measured stator reactive' and active power (P_{s_meas} and Q_{s_meas}) (because the PI controller is not robust in terms of overshoot especially if the step power' changement is big). The direct and quadrature components of currents and flux (I_{rd} , I_{rq} and Φ_{rd} , Φ_{rq}) are presented respectively in figure.4.11-(e and g), which present the inverse diagrams compared to reactive and active powers. The inverse case for stator direct and quadrature currents (I_{sd} , I_{sq}) which have the same diagrams of reactive and active powers, and they are presented in figure.4.11-(d). The power error is presented in figure.4.11-(f); we observe a big power error of active and reactive powers -120 (W_Var) $\leq \Delta P_s \Delta Q_s \leq +120$ (W_Var). The stator' and rotor currents; I_{s_abc} and I_{r_abc} are shown in figure.4.11-(h and i) respectively, we remark the sinusoidal form of the three rotor and stator

⁷ 2LC means two level converter and 3LC means three level converter.

⁸ Knowing that in this chapter the robustness tests are based on three tests as follows: [Test-1: without parameter changement → Blue color, Test-2: +100% of R_r and -25% of (L_s , L_r and L_m) → Brown color and Test-3: +100% of (J and R_r), -25 % of (L_r , L_s and L_m) → Green color] respectively.

Table.4.2 The proposed active and reactive power references.

Time (sec):	Stator active power (W):	Stator reactive power (Var):
[0 - 0.3]	-700.	0.
[0.3-0.7]	-2000.	+1000.
[0.7-1.0]	-2800.	0.
[1.0-1.2]	-700.	-1400.
[1.2-1.5]	-700.	0.

phases currents. The power factor (PF) of the proposed control is presented in figure.4.11-(j), knowing that PF is the ratio of P to S (apparent power), took the top value when the reactive power equals to zero value; refer to these time interval in figures.4.11-(a, b, c and j): 0-0.3 (sec), 0.9-1.0 (sec) and 1.2-1.5(sec); and this is the main aim of MPPT strategy/keeping at any time the unity power factor regardless wind speed variation and parameters changement. In 1.0-1.2 (sec) remarkable ripples are noted. Table.4.3 described in details the obtained results of the conventional I/OLDC based on PI using 2LC for Mode: I.

Mode 2 (blue color/figure.4.11 to the middle): The reference stator active power (P_{s_ref}) (figure.4.11-(a) to the middle) is extracted from MPPT strategy (in this case, the wind speed will take step form); it takes the inverse diagram of wind speed. The stator reactive power (Q_{s_ref}) equals to 0 (Var), represents power factor unity. It is clear that the measured powers (active and reactive) have acceptable tracking with remarkable undulations (big error) compared to their reference powers in transient and steady states, a few (15%) overshoot is noted at 0.6 (sec) in measured stator reactive' and active power (P_{s_meas} and Q_{s_meas}) (because the PI controller is not so robust in terms of overshoot especially if the wind power' changement is big). The direct and quadrature components of currents and flux (I_{rd} , I_{rq} and Φ_{rd} , Φ_{rq}) are presented respectively in figures.4.11-(e and g), which present the inverse diagrams compared to reactive and active powers. The inverse case for stator direct and quadrature currents (I_{sd} , I_{sq}) which have the same diagrams of reactive and active powers, and they are presented in figure.4.11-(d). The power error is presented in figure.4.11-(f), we observe a big power error of active and reactive powers $-160 (W_Var) \leq \Delta P_s \Delta Q_s \leq +160 (W_Var)$. The stator' and rotor currents; I_{s_abc} and I_{r_abc} are shown in figures.4.11-(h and i) respectively, we remark the sinusoidal form of the waveforms. The power factor (PF) of the proposed control is presented in figure.4.11-(j), knowing that PF is the ratio of P to S (apparent power), it reaches the top value when the reactive power equals to zero value (refer to these time interval in figures.4.11-(a, b, c and j): in this case the stator reactive power equals to zero value means the PF had taken always the unity; and this is the main aim of MPPT strategy/keeping at any time the unity power factor regardless wind speed variation and parameter variation. Table.4.3 described in details the obtained results of the conventional I/OLDC based on PI using 2LC for Mode: II.

Mode 3 (green color/figure.4.11 to the right): The reference stator active power (P_{s_ref}) (figure.4.11-(a) to the right) is extracted from MPPT strategy (in this case, the wind speed will take random form); it takes the inverse diagram of wind speed. The stator reactive power (Q_{s_ref}) equal to 0 (Var), represents power factor unity. It is clear that the measured powers (active and reactive) have acceptable tracking with remarkable undulations (big error) compared to their reference powers in transient and steady states, a relatively big (15%) overshoot is noted at 0.5 (sec) and 0.8 (sec) in measured stator reactive' and active power (P_{s_meas} and Q_{s_meas}) (because the PI controller is not so robust in terms of overshoot especially if the wind power' changement is big). The direct and quadrature components of currents and flux (I_{rd} , I_{rq} and Φ_{rd} , Φ_{rq}) are presented respectively in figures.4.11-(e and g), which present the inverse diagrams compared to reactive and active powers. The inverse case for stator direct and quadrature currents (I_{sd} , I_{sq}) which have the same diagrams of reactive and active powers, and they are presented in figure.4.11-(d). The power error is presented in figure.4.12-(f), we observe a low power error of active and reactive powers $-150 (W_Var) \leq \Delta P_s \Delta Q_s \leq +150 (W_Var)$. The stator' and rotor currents; I_{s_abc} and I_{r_abc} are shown in figure.4.11-(h and i) respectively, we remark the sinusoidal form of the waveforms. The power factor (PF) of the proposed control is presented in figure.4.11-(j), knowing that PF is the ratio of P to S (apparent power), it reaches top the value when the reactive power equals to zero value (refer to these time interval in figures.4.11-(a, b and j): and this is the main aim of MPPT strategy/ keeping at any time the unity power factor regardless wind speed variation and parameter variation. Table.4.3 described in details the obtained results of the conventional I/OLDC based on PI using 2LC for Mode: III.

MPPT Strategy: Knowing that in the left side of figure.4.12 (Mode: II); the wind speed had taken the step

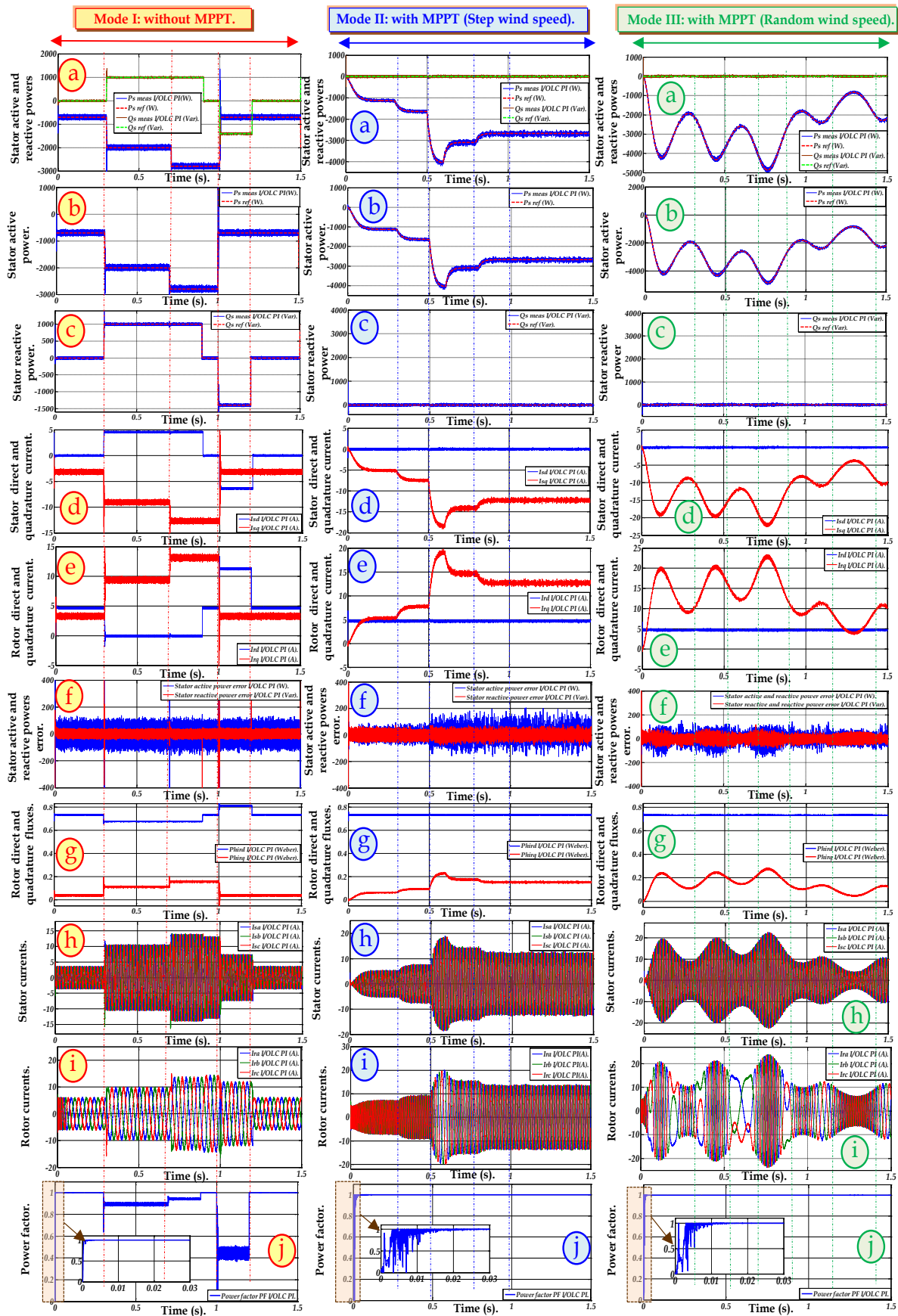


Figure.4.11 Simulations results for proposed control (I/O LDC based on PI with PWM two levels) under three modes; (a): stator active and reactive powers, (b): stator active power, c: stator reactive power, (d): stator direct and quadrature currents, (e): rotor direct and quadrature currents, (f): stator active and reactive power error, (g): rotor direct and quadrature fluxes, (h): stator currents, (i): rotor currents, (j): power factor.

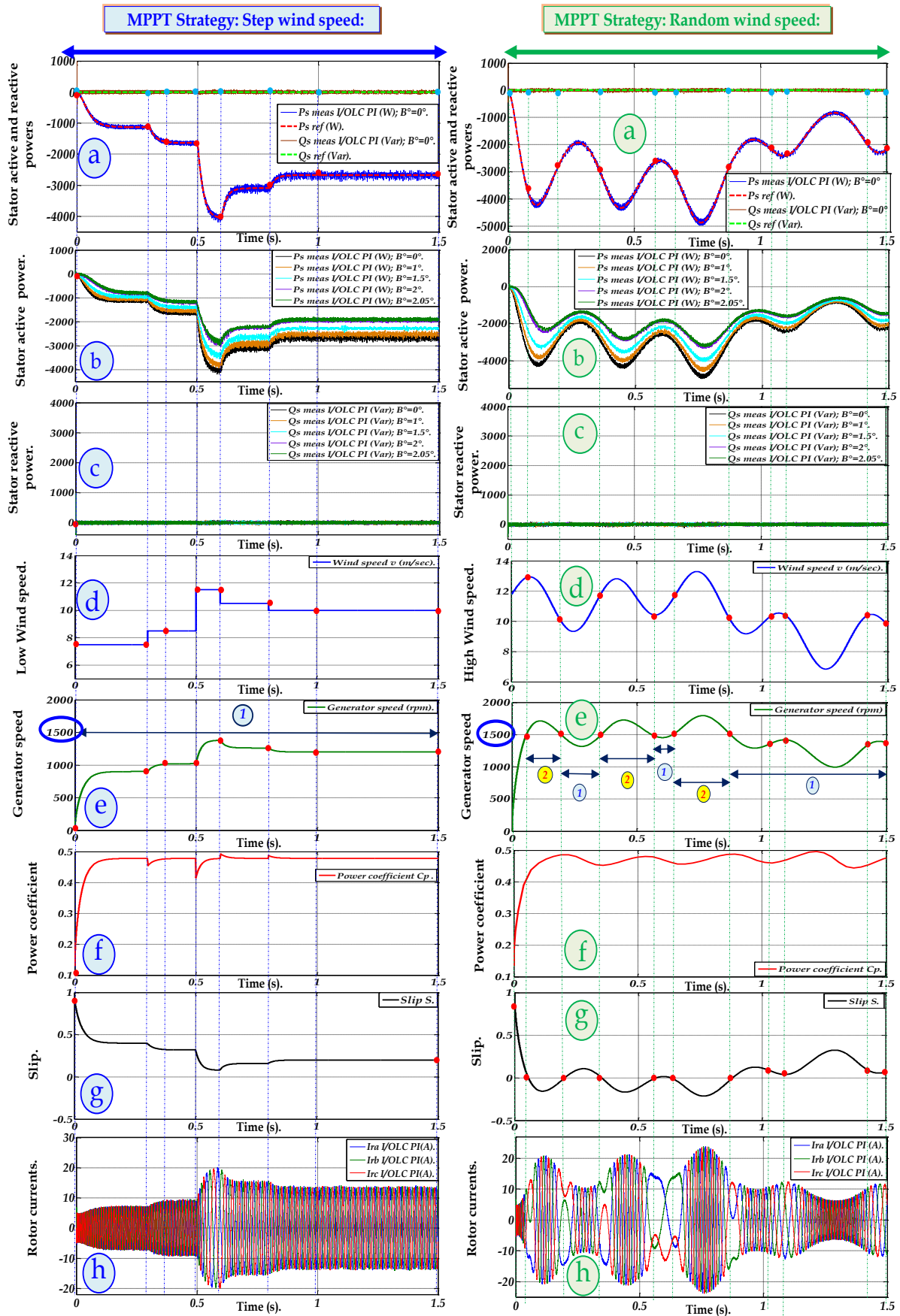


Figure.4.12 Simulations results of tow modes MPPT strategy for proposed control (I/OLDC based on PI with PWM two levels); (a): stator active and reactive powers, (b): stator active power using different B° pitch angles, (c): stator reactive power using different pitch angles B° , (d): wind speed, (e): generator speed, (f): power coefficient, (g): slip, (h): rotor currents.

form and the right side of figure.4.12 (Mode: III); the wind speed had taken the random form. Figure.4.13-(a) presents the stator active and reactive powers and its references profiles using of the conventional I/OLDC based on PI for pitch angle equals to 0° ($B^\circ=0^\circ$) means the maximum power. It can be seen that the measured powers (active and reactive) follow their references despite the sudden variation of wind speed in transient and steady states with an acceptable tracking power (ripples and undulation are noted). Figures.4.13-(b) illustrate the stator active power under different pitch angle ($B^\circ=0^\circ, 1^\circ, 1.5^\circ, 2^\circ$ and 2.05°), it can be seen the inverse proportionality between the active powers and pitch angle and big undulations were noted. Figures.4.13-(c) illustrate the stator reactive power under different pitch angle ($B^\circ=0^\circ, 1^\circ, 1.5^\circ, 2^\circ$ and 2.05°), it is clear that the reactive power maintain the zero level despite the pitch angle variation (the maximum wind power is reached at $B^\circ=0^\circ$ (black color) as mentioned from MPPT strategy/refer to Chapter:2) and big power error was noted due to wind speed variation. Figure.4.12-(d) illustrates the wind speed forms; figure.4.12-(d/to the left) presents the step wind speed (maximum value equals to 11.5 m/sec) and figure.4.12-(d/to the right) displays the random wind speed (maximum value equals to 13.5 m/sec). Figure.4.12-(e) presents the generator speed (rpm); figure.4.12-(e/to the left) presents the generator speed (<1500 rpm) means the Sub-synchronous mode, noted by '1') and figure.4.12-(e/to the right) displays the generator speed (below and above the synchronous speed (1500 rpm) means the Sub-synchronous and Super-synchronous modes noted by '1' and '2' respectively). Figure.4.12-(f) displays the power coefficient (C_p); figure.4.12-(f/to the left) illustrates the power coefficient under Mode: II, it is clear that C_p had maintained the maximum value (near than 0.48) regardless the wind speed variation and figure.4.12-(f/to the right) presents the C_p under Mode: III, in this case C_p had maintained the maximum value despite of wind speed variation. Figure.4.12-(g) displays the slip (S) behavior during the generator speed variation; figure.4.12-(g/to the left) illustrates the behavior of S under generator speed variation, in this case S varies between '+1' and '0' $\rightarrow 0 < S \leq +1$ means the generator speed did not reach the synchronous speed (always < 1500 rpm)), figure.4.12-(g/to the right) represents the S behavior under generator speed variation, in this case S varies between '+1' and '-1' $\rightarrow -1 < S \leq +1$ means the generator speed varies below and above the synchronous speed (superior and inferior 1500 rpm)), in the case when S reaches zero value means the mechanical speed $N_r=1500$ (rpm) this case called the synchronous mode (because S equals $(N_s-N_r)/N_s$), for exp: in the case of mechanical speed $N_r=1500$ (rpm) and $N_s =1500$ (rpm) $= (60*f)/P = (60*50)/2 = 1500$ (rpm) means $S = (1500-1500)/1500 = 0$) is the stable zone, please refer to Appendix: A, DFIG's parameters (Table.A.1). Figure.4.12-(h) displays the behavior of rotor currents under generator speed variation; figure.4.12-(h/to the left) illustrates the sinusoidal waveforms of rotor currents with few ripples (in this case the rotor currents did not change the sense because the S did not reach the zero value) and figure.4.12-(h/to the right) demonstrates the rotor currents behavior under generator speed variation, it can be seen the rotor currents had changed the sense in the case when S equals to zero value means when the generator speed varied near the synchronous speed.

Robustness tests⁹: In the left side of figure.4.13-(Mode: I/without MPPT strategy); the middle side of figure.4.13-(Mode: II/ using Step wind speed) and in right side of figure.4.13-(Mode: III/ using random wind speed). In Mode: I red color), figures.4.13-(a and b/to the left) illustrate the behavior of stator active and reactive powers under parameters variations. It can be noted big power in active and reactive power especially using the 2nd test (brown color/please refer to the bottom of the page) and 3rd test (green color) with remarkable undulations especially in transient and steady states (please refer to zoom) and the value of power error reaches

Table.4.3. Results recapitulation for conventional I/OLDC based on PI using two level converter¹⁰.

	THD I_{s_abc} (%) :	THD I_{r_abc} (%) :	Overshoot :	Response time (Sec):	Power Error (W_Var) :
Mode I:	0.76 %	177.25 %	Remarkable ($\approx 20\%$).	$2.3 * 10^{-4}$.	+/- 120.
Mode II:	0.40 %	60.45 %	Few ($\approx 10\%$).	$2.5 * 10^{-4}$.	+/- 160.
Mode III:	0.31 %	05.41 %	Few ($\approx 10\%$).	$2.5 * 10^{-4}$.	+/- 150.

⁹ Knowing that in this chapter the robustness tests are based on three tests as follows: [Test-1: without parameter changement \rightarrow Blue color, Test-2: +100% of R_r and -25% of (L_s, L_r and L_m) \rightarrow Brown color and Test-3: +100% of (J and R_r), -25% of (L_r, L_s and L_m) \rightarrow Green color] respectively.

³ Knowing that the recapitulations of tables.4-(3, 4 and 5) are taken without robustness test.

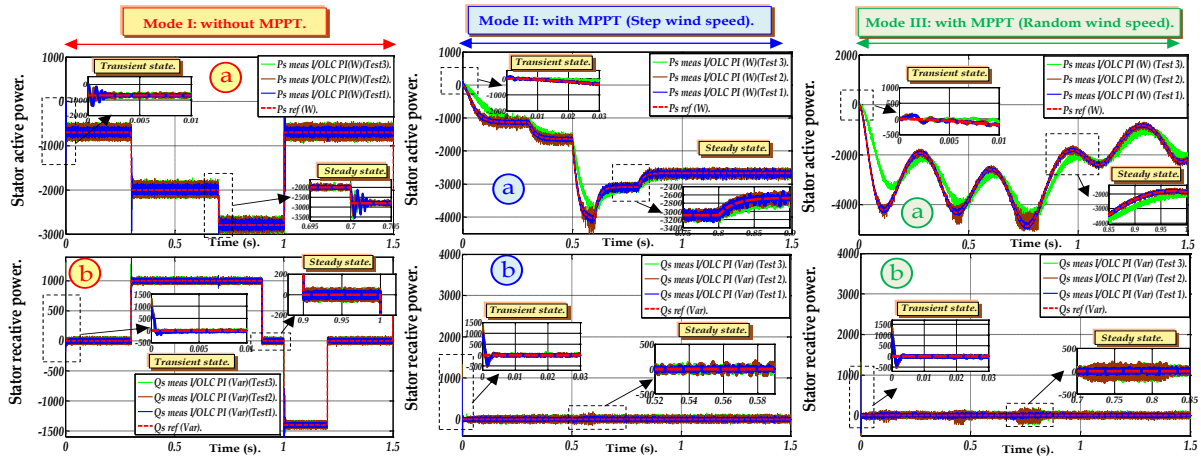


Figure.4.13 Robustness tests of proposed control (I/OLDC based on PI with PWM two levels) under three (03) modes; (a): sator active powers, (b): sator active powers.

nearly ± 120 (W_Var) in Test-1, and nearly ± 200 (W_Var) in Test-2 and Test-3. A remarkable overshoot is noted under all robustness tests especially at 0.3 (sec) and at 1.0 (sec). Figures.4.13-(a and b/to the middle) display the behavior of sator active and reactive powers under MPPT strategy by maintaining the reactive power equals to zero value. In this case the active power had taken the inverse step profile of wind speed. Using robustness tests a remarkable undulations are noted (using tests: 2 and 3) especially at 0.6 (sec) which presents the rated power of DFIG ($P=4$ (kW)), on other hand and in the same time a remarkable power error is noted in sator reactive power (which means that the PI controllers can not maintain the unity power factor under maximum wind power and parameters variation), also a few overshoot is noted in transient and steady states of active and reactive power. Figures.4.13-(a and b/to the right) display the behavior of sator active and reactive powers under MPPT strategy by maintaining the reactive power equals to zero value. In this case the active power had taken the inverse random profile of wind speed. Using robustness tests a remarkable undulations are noted (using tests: 2 and 3) especially at 0.75 (sec) and 0.8 (sec) which presents the over rated power of DFIG ($P=4$ (kW) and the measured active power maintain 4.6 (kW)), on other hand and in the same time a remarkable power error is noted in sator reactive power (which means that the PI controllers can not maintain the unity power factor under maximum wind power), also a few overshoot is noted in transient and steady states of active and reactive power.

4.4.2 Back-to-back two Level converter using MRAC controller

The simulation results of this topology (I/OLDC based on MRAC controller using 2LC) are described in details in figures.4-(14, 15 and 16). Figure.4.14 presents the behavior of the wind-system (using DFIG (4 kW) and wind turbine (4.5 kW)) under three modes in transient and steady states. Following are the detailed description of the simulation results under three (03) modes:

Mode 1 (red color/figure.4.14 to the left): The measured sator active and reactive powers (P_{s_meas} and Q_{s_meas}) and their references (P_{s_ref} and Q_{s_ref}) profiles are presented together in figure.4.14-(a) and are presented separately in figures.4.14-(b and c) respectively. The reference powers are indicated in Table.4.2. It is clear that the measured powers (active and reactive) have excellent tracking power (neglected power error with very short response time) compared to their reference powers in transient and steady states (refer to figures.4.14-(b and c)), a neglected overshoot is noted at all simulation time in measured sator reactive' and active power (P_{s_meas} and Q_{s_meas}) (in this case the MRAC controller is very robust in terms of overshoot especially if the step power' changement is big). The rotor direct and quadrature components of currents and flux (I_{rd} , I_{rq} and Φ_{rd} , Φ_{rq}) are presented respectively in figures.4.14-(e and g), which present the inverse diagrams compared to reactive and active powers. The inverse case for sator direct and quadrature currents (I_{sd} , I_{sq}) which have the same profiles of reactive and active powers, and they are presented in figure.4.14-(d). The power error is presented in figure.4.14-(f), we observe a lower power error of active and reactive powers: -50 (W_Var) $\leq \Delta P_s \Delta Q_s \leq +50$ (W_Var). The sator' and rotor currents; I_{s_abc} and I_{r_abc} are shown in figures.4.14-(h and i) respectively, we remark the perfect sinusoidal waveforms of the three rotor and sator phases currents. The power factor (PF) of the proposed control

is presented in figure.4.14-(j), had reached the top value when the reactive power equals to zero value; refer to these time interval in figures.4.14-(a, b, c and j): 0-0.3 (sec), 0.9-1.0 (sec) and 1.2-1.5(sec); and this is the main aim of MPPT strategy/keeping at any time the unity power factor regardless wind speed variation and parameters changement. In 1.0-1.2 (sec) neglected ripples are noted (the inverse case compared to conventional I/OLDC based on PI). Table.4.4 described in details the obtained results of the proposed I/OLDC based on MRAC using 2LC for Mode: I.

Mode 2 (blue color/figure.4.14 to the middle): The reference stator active power (P_{s_ref}) (figure.4.14-(a)) is extracted from MPPT strategy (in this case, the wind speed will take the step form); it takes the inverse profile of wind speed. The stator reactive power (Q_{s_ref}) equal to 0 (Var), represents power factor unity. It is clear that the measured powers (active and reactive) have good tracking with neglected undulations (neglected power error is noted with short response time) compared to their reference powers in transient and steady states, a neglected overshoot is noted at 0.6 (sec) in measured stator reactive' and active power (P_{s_meas} and Q_{s_meas}) (because the MRAC controller is so robust in terms of overshoot especially if the wind power' changement is big). The rotor direct and quadrature components of currents and flux (I_{rd} , I_{rq} and Φ_{rd} , Φ_{rq}) are presented respectively in figures.4.14-(e and g), which present the inverse diagrams compared to reactive and active powers. The inverse case for stator direct and quadrature currents (I_{sd} , I_{sq}) which have the same diagrams of reactive and active powers, and they are presented in figure.4.14-(d). The power error is presented in figure.4.14-(f), we observe a lower power error of active and reactive powers $-70 (W_Var) \leq \Delta P_s_Q_s \leq +70 (W_Var)$. The stator' and rotor currents; I_{s_abc} and I_{r_abc} are shown in figures.4.14-(h and i) respectively, we remark the sinusoidal form of the waveforms. The power factor (PF) of the proposed control is presented in figure.4.14-(j), knowing that PF is the ratio of P to S (apparent power), it reaches the top value when the reactive power equals to zero value (refer to these time interval in figures.4.14-(a, b, c and j): in this case the stator reactive power equals to zero value means the PF had taken always the unity; and this is the main aim of MPPT strategy/keeping at any time the unity power factor regardless wind speed variation and parameter variation. Table.4.4 described in details the obtained results of the proposed I/OLDC based on MRAC using 2LC for Mode: II.

Mode 3 (green color/figure.4.14 to the right): The reference stator active power (P_{s_ref}) (figure.4.15-(a)) is extracted from MPPT strategy (in this case, the wind speed will take the random form); it takes the inverse profile of wind speed. The stator reactive power (Q_{s_ref}) equal to 0 (Var), represents power factor unity. It is clear that the measured powers (active and reactive) have excellent tracking with neglected ripples (neglected power error is noted) compared to their reference powers in transient and steady states, a neglected overshoot is noted at 0.5 (sec) and 0.8 (sec) in measured stator reactive' and active power (P_{s_meas} and Q_{s_meas}) (because the MRAC controller is so robust in terms of overshoot especially if the wind power' changement is big). The rotor direct and quadrature components of currents and flux (I_{rd} , I_{rq} and Φ_{rd} , Φ_{rq}) are presented respectively in figures.4.14-(e and g), which present the inverse diagrams compared to reactive and active powers. The inverse case for stator direct and quadrature currents (I_{sd} , I_{sq}) which have the same profiles of reactive and active powers, and they are presented in figure.4.14-(d). The power error is presented in figure.4.14-(f), we observe a low power error of active and reactive powers $-85 (W_Var) \leq \Delta P_s_Q_s \leq +85 (W_Var)$. The stator' and rotor currents; I_{s_abc} and I_{r_abc} are shown in figures.4.14-(h and i) respectively, we remark the excellent sinusoidal waveforms of three phases currents. The power factor (PF) of the proposed control is presented in figure.4.14-(j), knowing that PF is the ratio of P to S (apparent power), it reached the top value when the reactive power equals to zero value (refer to these time interval in figures.4.14-(a, b and j)), and this is the main aim of MPPT strategy/keeping at any time the unity power factor regardless wind speed variation and parameter variation. Table.4.4 described in details the obtained results of the proposed I/OLDC based on MRAC using 2LC for Mode: III.

MPPT Strategy: Knowing that in the left side of figure.4.15 (Mode: II); the wind speed had taken the step form and the right side of figure.4.15 (Mode: III); the wind speed had taken the random form. Figure.4.15-(a) presents the stator active and reactive powers and its references profiles using of the proposed I/OLDC based on MRAC for pitch angle equals to 0° ($B^\circ=0^\circ$) which represents the maximum wind power. It can be seen that the measured powers (active and reactive) follow exactly theirs references despite the sudden variation of wind speed in transient and steady states with an excellent tracking power (neglected ripples are noted). Figures.4.15-(b) illustrate the stator active power under different pitch angle ($B^\circ=0^\circ, 1^\circ, 1.5^\circ, 2^\circ$ and 2.05°), it can be seen the

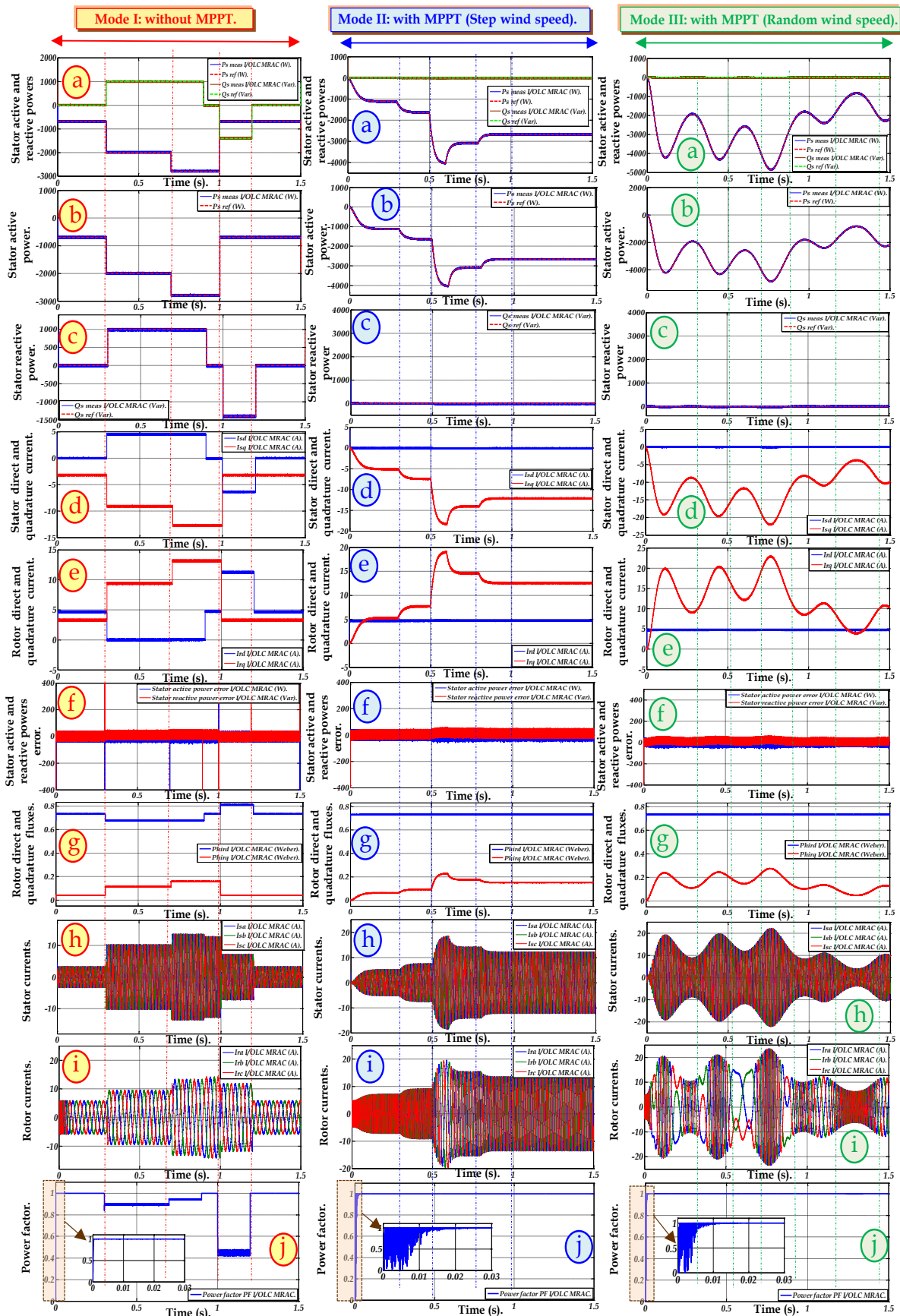


Figure.4.14 Simulations results for proposed control (I/O LDC based on MRAC with PWM two levels) under three (03) modes; (a) stator active and reactive powers, (b) stator active power, (c) stator reactive power, (d) stator direct and quadrature currents, (e) rotor direct and quadrature currents, (f) stator active and reactive power error, (g) rotor direct and quadrature fluxes, (h) stator currents, (i) rotor currents, (j) power factor.

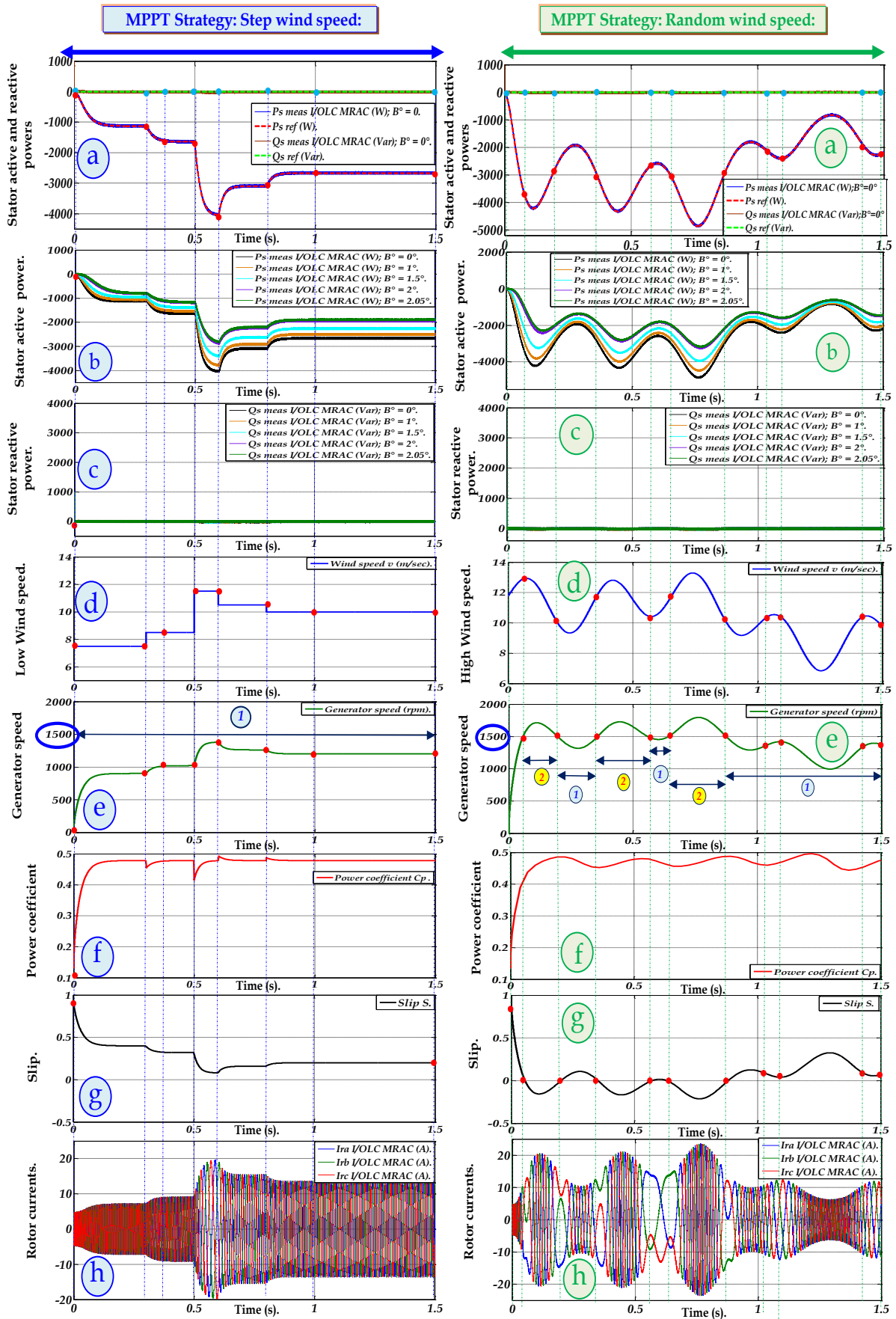


Figure.4.15 Simulations results of tow modes MPPT strategy for proposed control (I/OLDC based on MRAC with PWM two levels); (a): stator active and reactive powers, (b): stator active power using different B° pitch angles, (c): stator reactive power using different pitch angles B° , (d): wind speed, (e): generator speed, (f): power coefficient, (g): slip, (h): rotor currents.

inverse proportionality between the active powers and pitch angle. Figures.4.15-(c) illustrate the stator reactive power under different pitch angle ($B^\circ=0^\circ, 1^\circ, 1.5^\circ, 2^\circ$ and 2.05°), it is clear that the reactive power maintain the zero level despite the pitch angle variation (the maximum wind power is reached at $B^\circ=0^\circ$ (black color) as mentioned from MPPT strategy/refer to Chapter:2). Figure.4.15-(d) illustrate the wind speed forms; figure.4.15-(d/to the left) presents the step wind speed (maximum value equals to 11.5 m/sec) and figure.4.15-(d/to the right) displays the random wind speed (maximum value equals to 13.5 m/sec). Figure.4.15-(e) presents the generator speed (rpm); figure.4.15-(e/to the left) presents the generator speed (<1500 rpm) means the Sub-synchronous mode, noted by '1' and figure.4.15-(e/to the right) displays the generator speed (below and above the synchronous speed (1500 rpm) means the Sub-synchronous and Super-synchronous modes noted by '1' and '2' respectively). Figure.4.15-(f) displays the power coefficient (C_p); figure.4.15-(f/to the left) illustrates the power coefficient under Mode: II, it is clear that C_p had maintained the maximum value regardless (near than 0.48) the wind speed variation and figure.4.15-(f/to the right) presents the C_p under Mode: III, in this case C_p had maintained the maximum value despite of wind speed variation. Figure.4.15-(g) displays the slip (S) behavior during the generator speed variation, figure.4.15-(g/to the left) illustrates the behavior of S under generator speed variation, in this case S varies between '+1' and '0' $\rightarrow 0 < S \leq +1$ means the generator speed did not reach the synchronous speed (always < 1500 rpm)), figure.15-(g/to the right) represents the S behavior under generator speed variation, in this case S varies between '+1' and '-1' $\rightarrow -1 < S \leq +1$ means the generator speed varies below and above the synchronous speed (superior and inferior 1500 rpm)), in the case when S reaches zero value means the mechanical speed $N_r=1500$ rpm) this case called the synchronous mode, please refer to appendix: A, DFIG's parameters (Table.A.1). Figure.4.15-(h) displays the behavior of rotor currents under generator speed variation; figure.4.15-(h/to the left) illustrates the sinusoidal waveforms of rotor currents with few ripples (in this case the rotor currents did not change the sense because the S did not reach the zero value) and figure.4.15-(h/to the right) demonstrates the rotor currents behavior under generator speed variation, it can be seen the rotor currents had changed the sense in the case when S equals to zero value means when the generator speed varied near the synchronous speed.

Robustness tests¹¹: In the left side of figure.4.16-(Mode: I/without MPPT strategy); the middle side of figure.4.16-(Mode: II/ using Step wind speed) and in the right side of figure.4.16-(Mode: III/ using random wind speed). In Mode: I red color), figures.4.16-(a and b/to the left) illustrate the behavior of stator active and reactive powers under parameters variations. It can be noted lower power in active and reactive power especially using the 2nd test (brown color/please refer to the bottom of the page) and 3rd tests (green color) with neglected undulations especially in transient and steady states (please refer to zoom) and the value of power error reaches nearly ± 50 (W_Var) in Test-1, and nearly ± 60 (W_Var) in Test-2 and Test-3. A neglected overshoot is noted under all robustness tests especially at 0.3 (sec) and at 1.0 (sec). Figures.4.16-(a and b/to the middle) displays the behavior of the stator active and reactive powers under MPPT strategy by maintaining the reactive power equals to zero value. In this case the active power had taken the inverse step profile of wind speed. Using robustness tests a neglected undulations are noted (using tests: 2 and 3) in all simulation time (the inverse case of conventional I/OLDC based on PI), at 0.6 (sec) a neglected power error was noted which presents the rated power of DFIG ($P=4$ (kW)) in other hand in the same time a neglected power error is noted in stator reactive power (which means that the MRAC controllers can easily maintain the unity power factor under maximum wind power), also a neglected overshoot is noted in transient and steady states of active and reactive power.

Table.4.4. Results recapitulation for proposed I/OLDC based on MRAC using two level converter.

	THD I_s abc (%) :	THD I_r abc (%) :	Overshoot :	Response time (Sec) :	Power Error (W_Var) :
Mode I:	0.58 %	97.46 %	Neglected ($\approx 1\%$).	$1.35 * 10^{-3}$.	+/- 50.
Mode II:	0.45 %	60.34 %	Neglected ($\approx 1\%$).	$1.3 * 10^{-3}$.	+/- 70.
Mode III:	0.31 %	05.14 %	Neglected ($\approx 1\%$).	$8.0 * 10^{-4}$.	+/- 85.

¹¹ Knowing that in this chapter the robustness tests are based on three tests as follows: [Test-1: without parameter changement \rightarrow Blue color, Test-2: +100% of R_r and -25% of (L_s, L_r and L_m) \rightarrow Brown color and Test-3: +100% of (J and R_r), -25 % of (L_r, L_s and L_m) \rightarrow Green color] respectively.

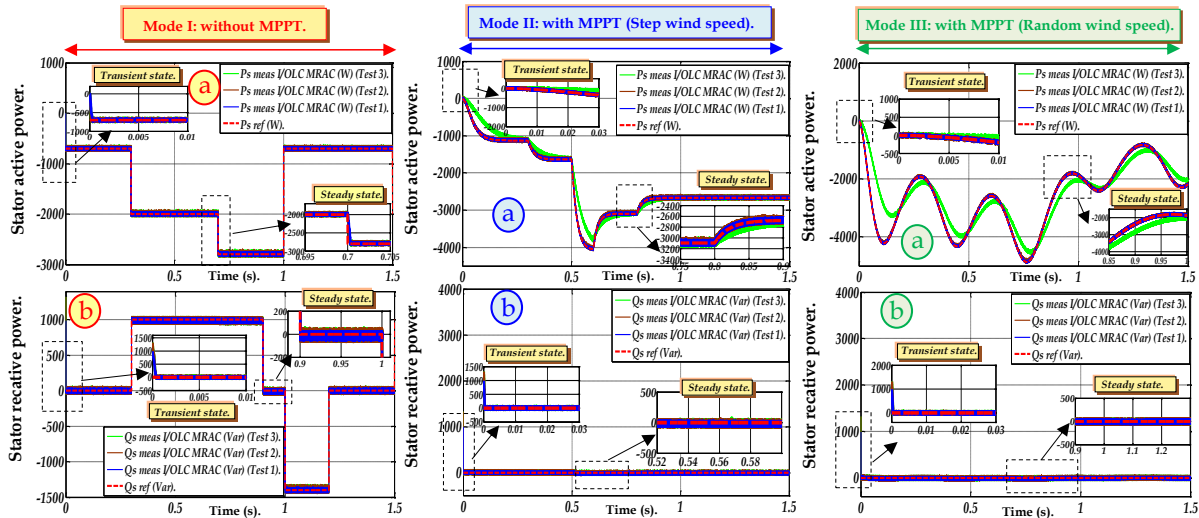


Figure.4.16 Robustness tests of proposed control (I/OLDC based on MRAC with PWM two levels) under three modes; (a): stator active powers, (b): stator active powers.

Figures.4.16-(a and b/to the right) displays the behavior of stator active and reactive powers under MPPT strategy by maintaining the reactive power equals to zero level. In this case the active power had taken the inverse random profile of wind speed. Using robustness tests a neglected ripples are noted (using tests: 2 and 3) especially at 0.75 (sec) and 0.8 (sec) which presents the over rated power of DFIG ($P=4$ (kW) and the measured active power maintain 4.6 (kW)) on the other hand and in the same time a neglected power error is noted in stator reactive power (which means that the MRAC controller can maintain the unity power factor under maximum wind power), also a neglected overshoot is not-ed in transient and steady states of active and reactive power.

4.4.3 Back-to-back three Level Inverter (NPC) based on MRAC controller

The simulation results of this topology (proposed I/OLDC based on MRAC controller using 3LC) are described in details in figures.4-(17, 18 and 19). Figure.4.17 presents the behavior of the wind-system (using DFIG (4 kW) and wind turbine (4.5 kW)) under three modes (that already presented above) in transient and steady states. Following are detailed description of the simulation results under three (03) modes:

Mode 1 (red color/figure.4.17 to the left): The measured stator active and reactive powers (P_{s_meas} and Q_{s_meas}) and their references (P_{s_ref} and Q_{s_ref}) profiles are presented together in figure.4.17-(a), are presented separately in figures.4.17.(b and c) respectively. The reference powers are indicated in table.4.2. It is clear that the measured powers (active and reactive) have excellent tracking power (a neglected power error with very short response time) compared to their reference powers in transient and steady states (refer to figures.4.17-(b and c)), a neglected overshoot is noted at all simulation time in measured stator reactive' and active power (P_{s_meas} and Q_{s_meas}) (because the MRAC controller is more robust in terms of overshoot). The rotor direct and quadrature components of currents and flux (I_{rd} , I_{rq} and Φ_{rd} , Φ_{rq}) are presented respectively in figures.4.17-(e and g), which present the inverse diagrams compared to reactive and active powers. The inverse case for stator direct and quadrature currents (I_{sd} , I_{sq}) which have the same diagrams of reactive and active powers, and they are presented in figure.4.17-(d). The power error is presented in figure.4.17-(f), we observe a low power error of active and reactive powers -90 (W_Var) $\leq \Delta P_s \Delta Q_s \leq +90$ (W_Var). The stator' and rotor currents; I_{s_abc} and I_{r_abc} are shown in figure.4.17-(h and i) respectively, we remark the perfect sinusoidal waveforms of the rotor and stator currents. The power factor (PF) of the proposed control is presented in figure.4.17-(j), knowing that PF is the ratio of P to S (apparent power), reached the top value when the reactive power equals to zero value; refer to these time interval in figures.4.17-(a, b, c and j): 0-0.3 (sec), 0.9-1.0 (sec) and 1.2-1.5(sec); and this is the main aim of MPPT strategy/keeping at any time the unity power factor regardless wind speed variation and parameters changement. In 1.0-1.2 (sec) neglected ripples are noted (the inverse case compared to I/OLDC based on PI). Table.4.5 described in details the obtained results of the proposed I/OLDC based on MRAC using 3LC Mode: I.

Mode 2 (blue color/figure.4.17 to the middle): The reference stator active power (P_{s_ref}) (figure.4.17-(a) to the middle) is extracted from MPPT strategy (in this case, the wind speed will take the step form); it takes the

inverse diagram of wind speed. The stator reactive power (Q_{s_ref}) equal to 0 (Var), represents power factor unity. It is clear that the measured powers (active and reactive) have good tracking with neglected undulations (neglected power error with short response time) compared to their reference powers in transient and steady states, a neglected overshoot is noted at 0.6 (sec) in measured stator reactive' and active power (P_{s_meas} and Q_{s_meas}) (because the MRAC controller is so robust in terms of overshoot especially if the wind power' changement is big). The rotor direct and quadrature components of currents and flux (I_{rd} , I_{rq} and Φ_{rd} , Φ_{rq}) are presented respectively in figures.4.17-(e and g), which present the inverse diagrams compared to reactive and active powers. The inverse case for stator direct and quadrature currents (I_{sd} , I_{sq}) which have the same diagrams of reactive and active powers, and they are presented in figure.4.17-(d). The power error is presented in figure.4.17-(f), we observe a low power error of active and reactive powers $-90 (W_Var) \leq \Delta P_s _ \Delta Q_s \leq +90 (W_Var)$. The stator' and rotor currents; I_{s_abc} and I_{r_abc} are shown in figures.4.17-(h and i) respectively, we remark the perfect sinusoidal waveforms of the currents. The power factor (PF) of the proposed control is presented in figure.4.17-(j), knowing that PF is the ratio of P to S (apparent power), it reaches the top value when the reactive power equals to zero value (refer to these time interval in figures.4.18-(a, b, c and j)): in this case the stator reactive power equals to zero value means the PF had taken always the unity; and this is the main aim of MPPT strategy/keeping at any time the unity power factor regardless wind speed variation and parameter variation. Table.4.5 described in details the obtained results of the proposed I/OLDC based on MRAC using 3LC of Mode: II.

Mode 3 (green color/figure.4.17 to the right): The reference stator active power (P_{s_ref}) (figure.4.18-(a)) is extracted from MPPT strategy (in this case, the wind speed is in the form of a random); it takes the inverse diagram of wind speed. The stator reactive power (Q_{s_ref}) equal to 0 (Var), represents power factor unity. It is clear that the measured powers (active and reactive) have excellent tracking (neglected power error with very short response time) compared to their reference powers in transient and steady states, a neglected overshoot is noted at 0.5 (sec) and 0.8 (sec) in measured stator reactive' and active power (P_{s_meas} and Q_{s_meas}) (because the MRAC controller is so robust in terms of overshoot especially if the wind power' changement is big). The rotor direct and quadrature components of currents and flux (I_{rd} , I_{rq} and Φ_{rd} , Φ_{rq}) are presented respectively in figures.4.17-(e and g), they present the inverse diagrams compared to reactive and active powers. The inverse case for stator direct and quadrature currents (I_{sd} , I_{sq}) which have the same diagrams of reactive and active powers, and they are presented in figure.4.17-(d). The power error is presented in figure.4.17-(f), we observe a low power error of active and reactive powers $-95 (W_Var) \leq \Delta P_s _ \Delta Q_s \leq +95 (W_Var)$. The stator' and rotor currents; I_{s_abc} and I_{r_abc} are shown in figures.4.17-(h and i) respectively, we remark the perfect sinusoidal form of the currents waveforms. The power factor (PF) of the proposed control is presented in figure.4.17-(j), knowing that PF is the ratio of P to S (apparent power), it reaches top the value when the reactive power equals to zero value (refer to these time interval in figures.4.17-(a, b and j)); and this is the main aim of MPPT strategy/keeping at any time the unity power factor regardless wind speed variation and parameter variation. Table.4.5 described in details the obtained results of the proposed I/OLDC based on MRAC using 3LC for Mode: III.

MPPT Strategy: Knowing that in the left side of figure.4.18 (Mode: II); the wind speed had taken the step form and the right side of figure.4.18 (Mode: III); the wind speed had taken the random form. Figure.4.18-(a) presents the stator active and reactive powers and its references profiles using of the proposed I/OLDC based on MRAC for pitch angle equals to 0° ($B^\circ=0^\circ$) which presents the maximum wind power. It can be seen that the measured powers (active and reactive) follow exactly theirs references despite the sudden variation of wind speed in transient and steady states with an acceptable tracking power (ripples and undulation are noted). Figures.4.198-(b) illustrate the stator active power under different pitch angle ($B^\circ=0^\circ, 1^\circ, 1.5^\circ, 2^\circ$ and 2.05°), it can be seen the inversely proportionality between the active powers and pitch angle. Figures.4.18-(c) illustrate the stator reactive power under different pitch angle ($B^\circ=0^\circ, 1^\circ, 1.5^\circ, 2^\circ$ and 2.05°), it is clear that the reactive power maintain the zero level despite the pitch angle variation (the maximum wind power is reached at $B^\circ=0^\circ$ (black color) as mentioned from MPPT strategy/refer to Chapter:2). Figure.4.18-(d) illustrate the wind speed forms; figure.4.18-(d/to the left) presents the step wind speed (maximum value equals to 11.5 m/sec) and figure.4.18-(d/to the right) displays the random wind speed (maximum value equals to 13.5 m/sec). Figure.4.18-(e) presents the generator speed (rpm); figure.4.18-(e/to the left) presents the generator speed (<1500 (rpm) means the Sub-synchronous mode, noted by '1') and figure.4.19-(e/to the right) displays the generator speed

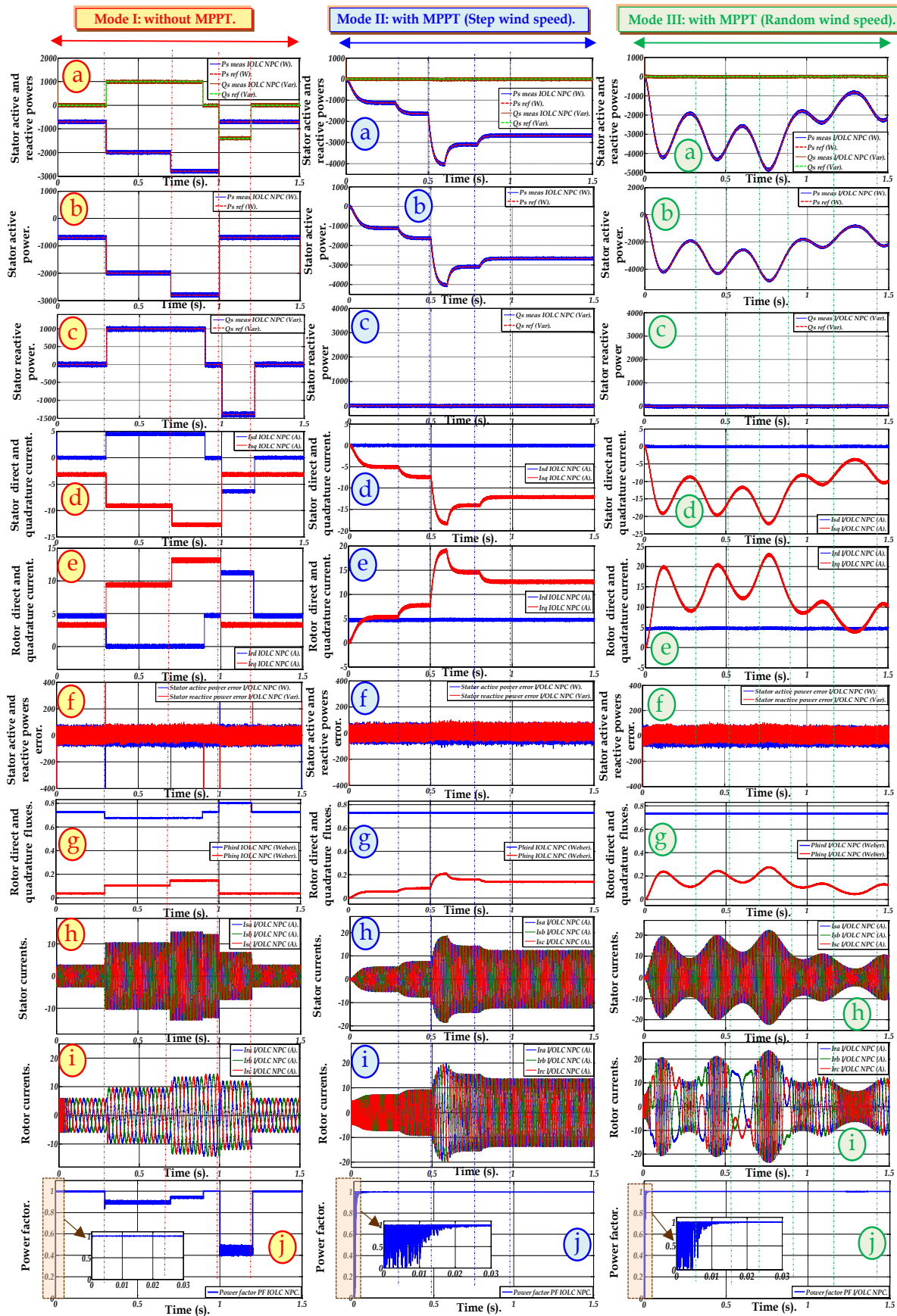


Figure.4.17 Simulations results for proposed control (I/O LDC based on MRAC with PWM three levels inverter/NPC) under three modes; (a): stator active and reactive powers, (b): stator active power, (c): stator reactive power, (d): stator direct and quadrature currents, (e): rotor direct and quadrature currents, (f): stator active and reactive power error, (g): rotor direct and quadrature fluxes, (h): stator currents, (i): rotor currents, (j): power factor.

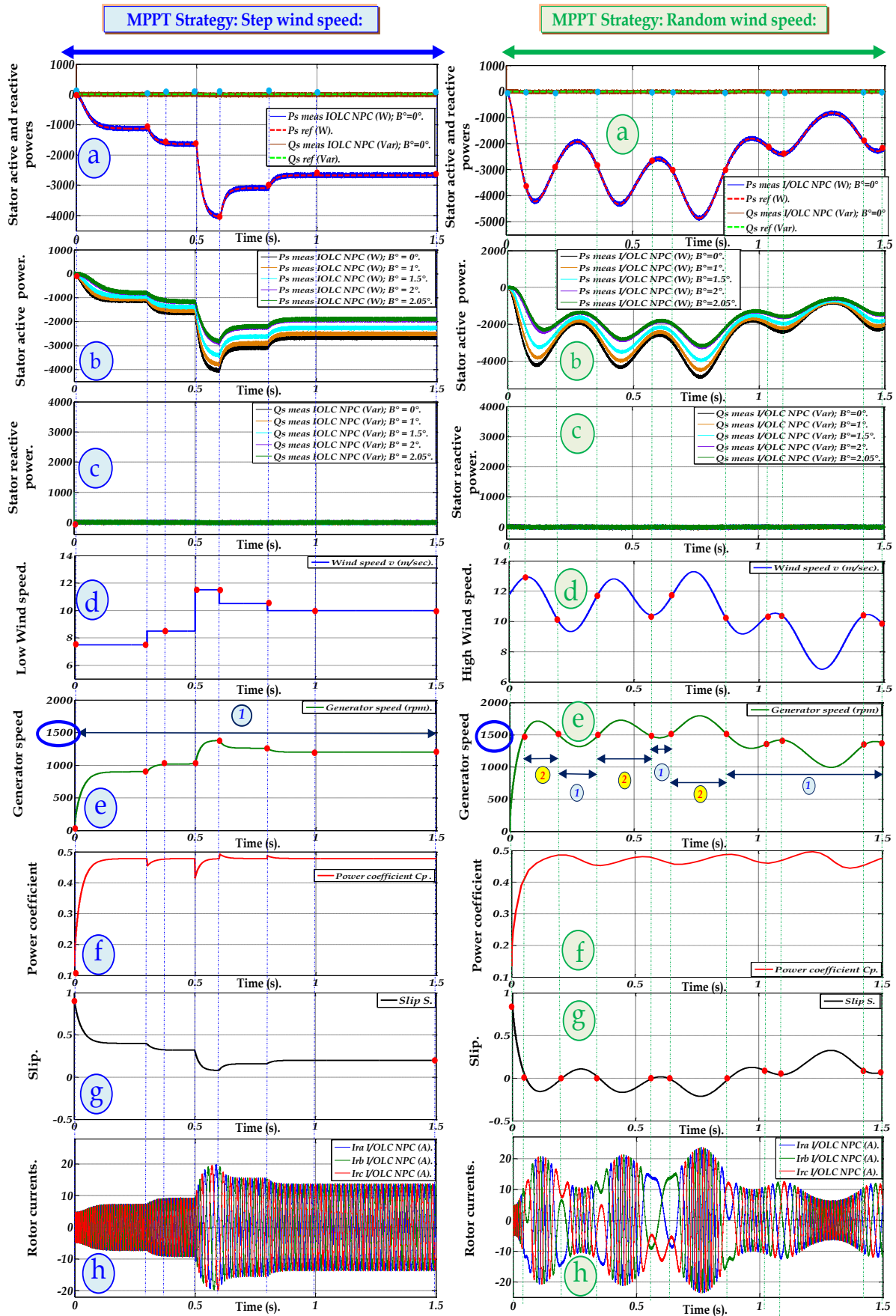


Figure.4.18 Simulations results of tow modes MPPT strategy for proposed control (I/OLDC based on MRAC with PWM three levels inverter/NPC); (a): stator active and reactive powers, (b): stator active power using different B° pitch angles, (c): stator reactive power using different pitch angles B° , (d): wind speed, (e): generator speed, (f): power coefficient, (g): slip, (h): rotor currents.

(below and above the synchronous speed (1500 rpm) means the Sub-synchronous and Super-synchronous modes noted by '1' and '2' respectively). Figure.4.18-(f) displays the power coefficient (C_p); figure.4.18-(f/to the left) illustrates the power coefficient under Mode: II, it is clear that C_p had maintained the maximum value regardless (near than 0.48) the wind speed variation and figure.4.18-(f/to the right) presents the C_p under Mode: III, in this case C_p had maintained the maximum value despite of wind speed variation. Figure.4.18-(g) displays the slip (S) behavior during the generator speed variation; figure.4.18-(g/to the left) illustrates the behavior of S under generator speed variation, in this case S varies between '+1' and '0' $\rightarrow 0 < S \leq +1$ means the generator speed did not reach the synchronous speed (always < 1500 (rpm)), figure.4.18-(g/to the right) represents the S behavior under generator speed variation, in this case S varies between '+1' and '-1' $\rightarrow -1 < S \leq +1$ means the generator speed varies below and above the synchronous speed (superior and inferior 1500 (rpm)), in the case when S reaches zero value means the mechanical speed $N_r=1500$ (rpm) this case called the synchronous mode, please refer to appendix: A, DFIG's parameters (Table. A.1). Figure.4.18-(h) displays the behavior of rotor currents under generator speed variation; figure.4.18-(h/to the left) illustrates the sinusoidal waveforms of rotor currents with few ripples (in this case the rotor currents did not change the sense because the S did not reach the zero value) and figure.4.18-(h/to the right) demonstrates the rotor currents behavior under generator speed variation, it can be seen the rotor currents had changed the sense in the case when S equals to zero value means when the generator speed varied near the synchronous speed.

Table.4.5. Results recapitulation for proposed I/OLDC based on MRAC using NPC three level converter.

	THD I_{s_abc} (%):	THD I_{r_abc} (%):	Overshoot :	Response time (sec) :	Power Error (W_Var) :
Mode I:	0.40 %	105.30%	Neglected ($\approx 1\%$).	$1.5 * 10^{-4}$.	+/- 90.
Mode II:	0.32 %	60.24 %	Neglected ($\approx 1\%$).	$2.1 * 10^{-4}$.	+/- 90.
Mode III:	0.23 %	05.21 %	Neglected ($\approx 1\%$).	$2.15 * 10^{-4}$.	+/- 95.

Robustness tests¹²: Knowing that in the left side of figure.4.19-(Mode: I/without MPPT strategy); the middle side of figure.4.19-(Mode: II/ using Step wind speed) and figure.4.19-(Mode: III/ using random wind speed). In Mode: I red color), figures.4.19-(a and b/to the left) illustrate the behavior of stator active and reactive powers under parameters variations. It can be noted a neglected power error in active and reactive power using the 2nd test (brown color/please refer to the bottom of the page) and 3rd tests (green color) with neglected undulations especially in transient and steady states (please refer to zoom) and the value of power error reaches nearly ± 90 (W_Var) in Test-1, and nearly ± 100 (W_Var) in Test-2 and Test-3. A neglected overshoot is noted under all robustness tests especially at 0.3 (sec) and at 1.0 (sec). Figures.4.19-(a and b/to the middle) display the behavior of stator active and reactive powers under MPPT strategy by maintaining the reactive power equals to zero value. In this case the active power had taken the inverse step profile of wind speed. Using robustness tests a neglected undulations are noted (using tests: 2 and 3) especially at 0.6 (sec) which presents the rated power of DFIG ($P=4$ (kW)) in other hand and in the same time a neglected power error is noted in stator reactive power (which means that the MRAC controllers can maintain the unity power factor under maximum wind power), also a neglected overshoot is noted in transient and steady states of active and reactive power. Figures.4.19-(a and b/to the right) display the behavior of stator active and reactive powers under MPPT strategy by maintaining the reactive power equals to zero value. In this case the active power had taken the inverse random profile of wind speed. Using robustness tests a neglected ripples are noted (using tests: 2 and 3) especially at 0.75 (sec) and 0.8 (sec) which presents the over rated power of DFIG ($P=4$ (kW)) and the measured active power maintain 4.6 (kW)) on other hand and in the same time a neglected power error (the inverse case compared to the conventional I/OLDC based on PI) is noted in stator reactive power (which means that the MRAC controllers can easily maintain the unity power factor under maximum wind power), also a neglected overshoot is noted in transient and steady states of active and reactive power.

¹² The robustness tests are based on three tests as follows: [Test-1: without parameter change \rightarrow Blue color, Test-2: +100% of R_r and -25% of (L_s , L_r and L_m) \rightarrow Brown color and Test-3: +100% of (J and R_r), -25 % of (L_r , L_s and L_m) \rightarrow Green color] respectively.

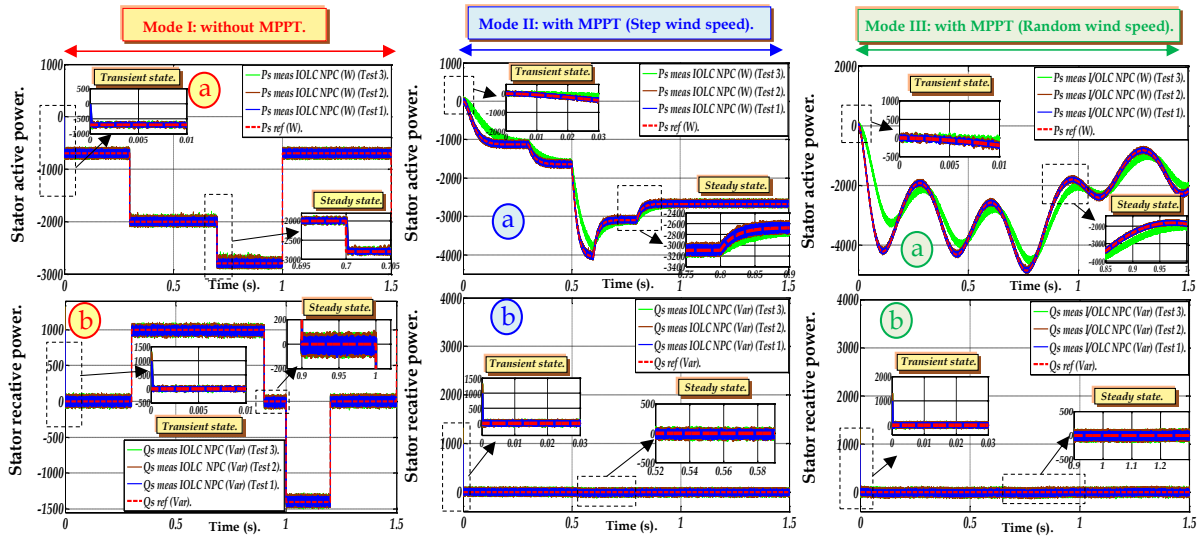


Figure.4.19 Robustness tests of proposed control (I/OLDC based on MRAC with PWM three levels inverter/NPC) under three modes; (a): stator active powers, (b): stator active powers.

4.5 The high power' evaluation tests (using improved I/OLDC with 2LC and 3LC):

This section presents the comparative study (refer to figures.4.20-(a, b, c and d) with their zoom) between power performance of 2LC and 3LC of proposed I/OLDC (based on MRAC) using new power profiles (Table.4.6). The main aim of this simulation study is to virify the behavior of each topology (2LC and 3LC) under high power profiles (max power values is: 6500 (W)). It is clear that the 3LC topology (figures.4.20-(c and d)) offres superior performance under high powers compared to 2LC topolgy (zoom of figures.4.20-(a and b)) illustrate that the 2LC topology follow high power reference and generated bad tracking power and power error, we confirm that the multilevel converter is the best solution in case of high wind-power.

Table.4.6 The proposed references profiles of high power.

Time (sec):	Stator active power (W):	Stator reactive power (Var):
[0 - 0.3]	-700.	0.
[0.3-0.7]	-2000.	+1000.
[0.7-1.0]	-6500.	0.
[1.0-1.2]	-700.	-1400.
[1.2-1.5]	-700.	0.

4.6 Decoupling parameter tests (using all the proposed control: chapter 2, chapter 3 and chapter 4):

In this section, a comparative study (refer to figures.4.21-(a, b, c, d, e, f, g and h) is presented to show the decoupling terms (under d and q axes) using all the proposed algorithmis in this thesis (chapters-(2, 3 and 4). The main aim of this simulation study is to show the high performance offred by the improved I/OLDC compared the those of imporoved power control in terms of perfect decoupling parameters, neglected power error and high tracking power by using another power propfiles, in order to show clearly the coupling terms between active and reactive power in each topology; knowing that in improved I/OLDC using the MRAC; it is clear that the relationship between the active and reactive power is perfectly decoupling (refer to figure.4.21-(h)).

It is clear that the proposed I/OLDC algorithm (based on MRAC) solved several problems such as; the coupling terms between d and q axis affected by the first proposed controls (chapters: 2 and 3), deleted the overshoot and offered an excellent wind-system performance especially using high power under multi-level converter and under robustness tests. Also, the THD of stator currents is more improved (Please refer to tables.4.4 and 4.5) in 3LC NPC compared to 2LC, means good power quality injected into the grid.

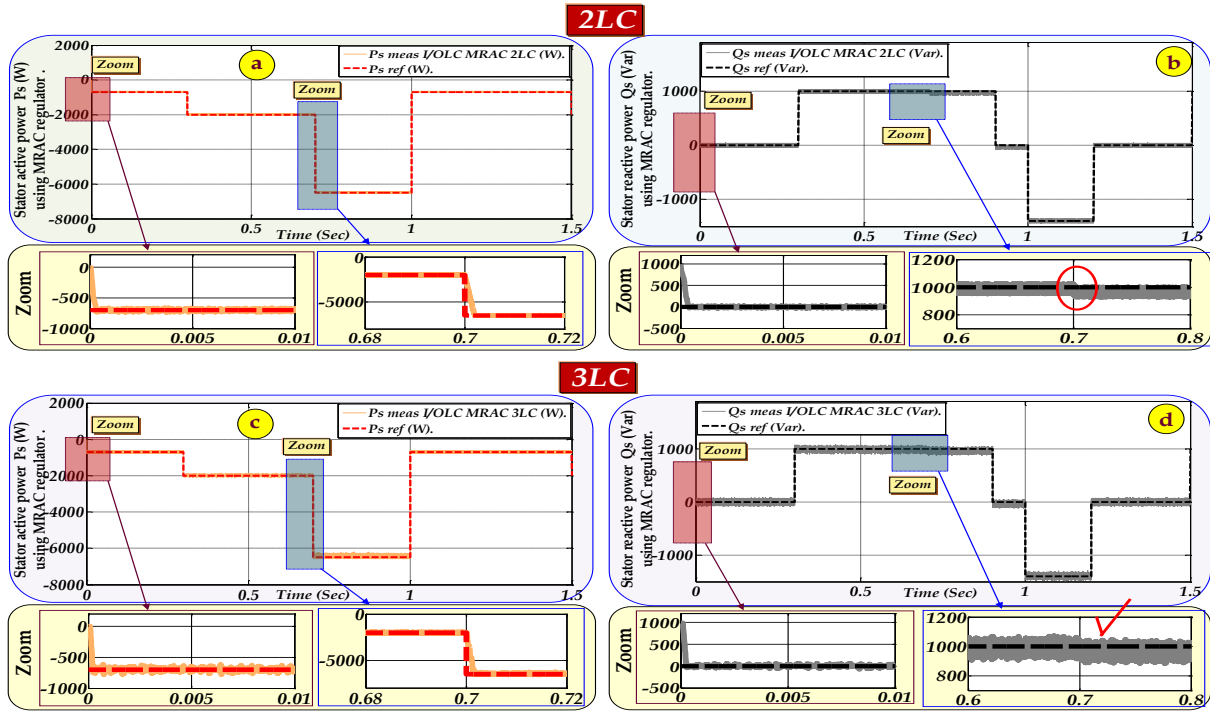
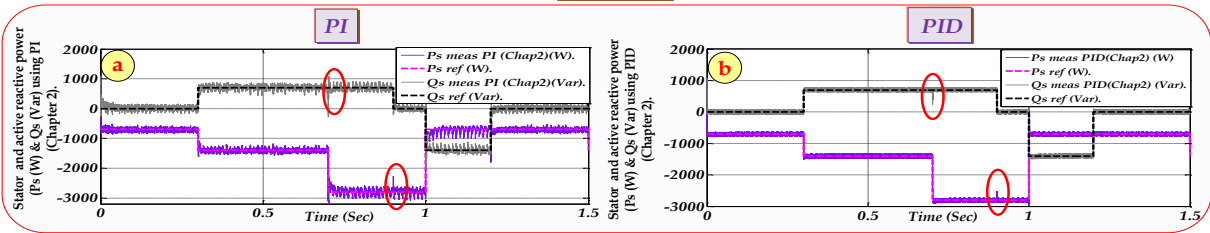
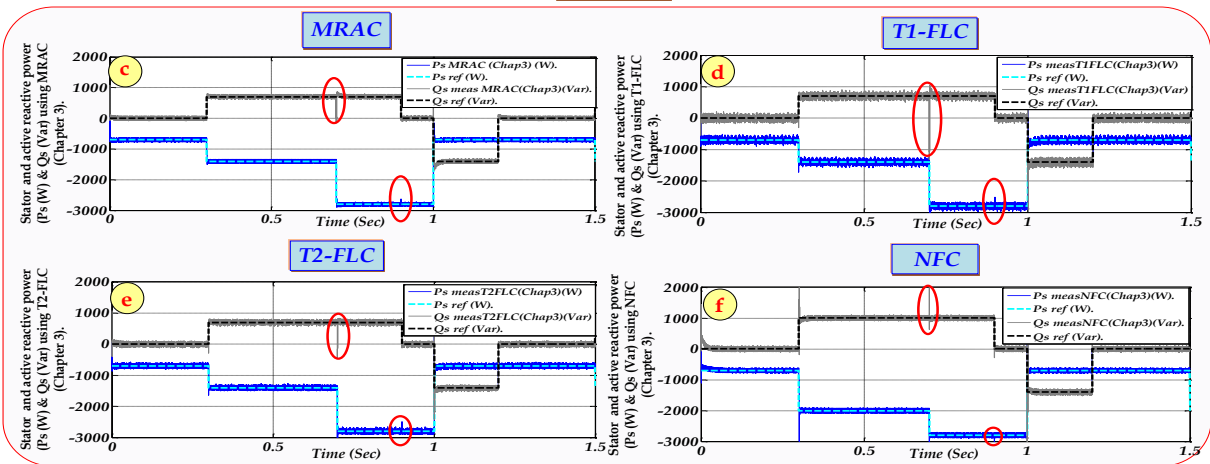


Figure.4.20 Simulations results of the high power' evaluation tests (using improved I/OLDC with 2LC and 3LC).

Chapter 2



Chapter 3



Chapter 4

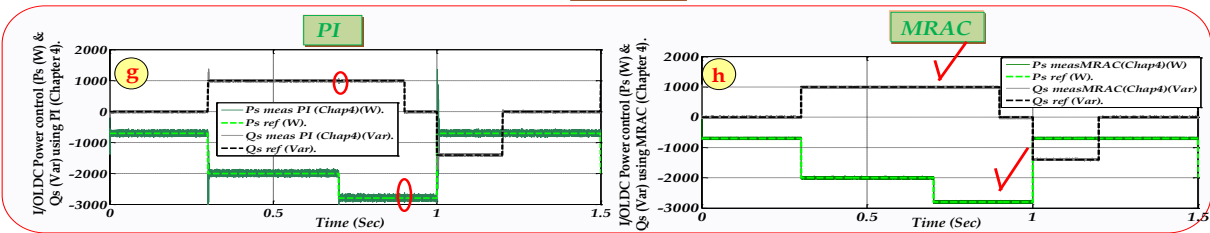


Figure.4.21 Simulations results of decoupling terms (between active and reactive power) in each topology.

4.7 Conclusion

In this chapter, the novel feedback decoupling and linearization control based on the model of wind-turbine DFIG has been proposed. MRAC is used to improve the performances of the classical nonlinear control. According the nonlinear control theory, the control algorithm can be more easily realized in comparison with the vector control, because the design of the controller depends only on the nonlinear theory. The results obtained by the validation platform using the MATLAB/Simulink®, prove that the decoupling terms problem is perfectly solved using robust improved controller and demonstrate the feasibility for multilevel converter with the high performances of the proposed algorithm.

4.8 References

- [1] Fayssal AMRANE, Azeddine CHAIBA and Khaled Eben el-Oualid. MEDANI: "Improved Input-Output Linearizing Control using MRAC in Variable Speed DFIG-based on WECS Fed by Three-Level Voltage Source Inverter" *International conference on electrical engineering and first workshop on robotics and controls, 9th CEE 2-4th October 2016 Batna-Algeria.*
- [2] Fayssal AMRANE, Azeddine CHAIBA and Ali CHEBABHI: "Robust and Simplified Input-Output Linearizing Control in Variable Speed DFIG using MRAC with Fixed Switching Frequency" *International Conference on Technological Advances in Electrical Engineering, ICTAEE 24-26th October 2016 Skikda-Algeria.*
- [3] M. JUJAWA, *Large wind rising, Renewable Energy World, no. 2, Vol: 6, Mars/April 2003, pp.39-51.*
- [4] Jun YAO, Hui LI, Yong LIAO, and Zhe CHEN, "An improved control strategy of limiting the DC-link voltage fluctuation for a doubly fed induction wind generator" *IEEE Transaction on Power Electronics, Vol: 23, no. 3, pp. 1205-1213, 2008.*
- [5] J. GUO, X. CAI, and Y. GONG, "Decoupled control of active and reactive power for a grid-connected doubly-fed induction generator," *Nanjing, China, pp. 2620-2625, 2008.*
- [6] Tarek GHENNAM, E.M. BERKOUK, Bruno FRANCOIS, "A Vector Hysteresis Current Control Applied on Three-Level Inverter. Application to the Active and Reactive Power Control of Doubly Fed Induction Generator Based Wind Turbine", *International Review of Electrical Engineering (I.R.E.E.), Vol: xx, no. x, 2007.*
- [7] Ahmed G. ABO-KHALIL, "Synchronization of DFIG output voltage to utility grid in wind power system", *Renewable Energy, Vol: 44, pp. 193-198, 2012.*
- [8] H. STEMMLER, P. GEGGENBACH, "Configurations of high power voltage source inverter drives", *proceeding of the 5th European conference on power electronics Brighton, UK, Vol: 5, pp 7-12, 1993*
- [9] Sheng HU, Yong KANG, DiHua LI and XinChun LIN, "Nonlinear control strategy for doubly-fed induction generator (DFIG) in wind power controller", *IEEE conference 2010.*
- [10] Stanislav E. ENEV, "Input-output linearization control of current-fed induction motors with rotor resistance and load torque identification," *in 1st IEEE ICEIE Hammamet, Tunisia, pp. 198-201, 2006.*
- [11] David M. BROD and Donald W. NOVOTNY, "Current control of VSI-PWM inverters", *IEEE Transactions on Industrial Application, Vol: 21 no. 4, pp. 562-570, 1985.*
- [12] Fayssal AMRANE, Azeddine. CHAIBA and Saad MEKHILEF, "High performances of Grid-connected DFIG based on Direct Power Control with Fixed Switching Frequency via MPPT Strategy using MRAC and Neuro-Fuzzy Control", *Journal of Power Technologies, Vol. 96, no.1, pp.27-39, 2016.*
- [13] Samuel Vasconcelos ARAÚJO, Alfred ENGLER, Benjamin SAHAN and Fernando Luiz Marcelo ANTUNES "LCL Filter design for grid-connected NPC inverters in offshore wind turbines", *IEEE conference, The 7th International Conference on Power Electronics, October 22-26, 2007 / EXCO, Daegu, Korea, 2007.*

Chapter 5 :

Experimental Design of IDPC of DFIG for Variable Speed Wind-Turbine in Isolated Mode with LCL-Filter.

5.1 Introduction	122
5.2 Proposed control (<i>Stand-alone topology</i>)	123
5.3 Indirect Power Control (IDPC) based on Integral-Proportional (IP) regulators	123
5.3.1 DFIG control (<i>Rotor Side Converter-RSC</i>)	123
5.3.2 Integral Proportional (IP) regulators	124
5.3.3 Emulator turbine control (<i>Induction motor torque and flux control</i>):.....	126
5.3.4 Hardware implementation.....	127
5.4 Experimental studies using a new inverter named SEMIKUBE (<i>100 kW, 2016 version</i>)	128
5.4.1 SEMIKUBE components description.....	128
5.4.2 Isolation card.....	129
5.4.3 SEMIKUBE with isolation card	130
5.4.4 dSPACE1103 and Control Desk software.....	130
5.4.5 SEMIKUBE with R-L load under open loop using dSPACE1103 card.....	131
5.5 Impact of Filters in RSC using the Fast Fourier Transform (FFT).....	133
5.5.1 Mode I: L Filter	134
5.5.2 Mode II: LC Filter	135
5.5.3 Mode III: LCL Filter.....	136
5.6 Robustness tests of proposed control (<i>under Trapezoid, Step form of rotor d-q axes rotor currents</i>)	139
5.6.1 Topology 1 : Stator not connected to R-L load	139
5.6.2 Topology 2 : Stator under load (connected to R-L load).....	141
5.7 Experimental results of proposed control under Sub- and Super-synchronous operations	143
5.7.1 Case 1 : $N_r = 0$ (rpm).....	144
5.7.2 Case 2 : $N_r = 500$ (rpm).....	146
5.7.3 Case 3 : $N_r = 1000$ (rpm).....	147
5.7.4 Case 4 : $N_r = 1500$ (rpm).....	148
5.7.5 Case 5 : $N_r = 1700$ (rpm).....	149
5.8 Conclusion	149
5.9 References	150

Abstract:

In this chapter, design and experimental study based on Indirect Power Control (IDPC) of DFIG is proposed for Stand-alone mode in Variable Speed Wind Energy Conversion System (VS-WECS). The proposed IDPC method based on robust IP (Integral-Proportional) controllers are used in order to control the Rotor Side Converter (RSC) by the means of the rotor current d-q axes components (I_{rd}^ and I_{rq}^*) of Doubly Fed Induction Generator (DFIG) through AC-DC-AC converter. The experimental test bench based on an emulator turbine represented by Asynchronous Motor (ASM) controlled by the Automatic Variable Regulator (AVR) which is coupled with DFIG. The implementation is realized using dSPACE dS1103 card under Sub and Super-synchronous operations (means inferior and superior of the synchronous speed 1500 rpm). To improve the waveforms of the stator and rotor voltages; L, LC and LCL-filters are proposed and implemented between the SEMIKUBE (Inverter) and the DFIG (Rotor) and described with experimental results. Different robustness tests are presented in details using speed and currents variation with/without RL-load to ensure the feasibility of the proposed algorithm. The experimental results show excellent performances in transient and steady states in terms of short response time, neglected overshoot, good power and current tracking with very small error despite for sudden variation of wind speed and rotor references currents.*

5.1 Introduction

Wind energy capacity is experiencing a massive growth in recent years, with a new installations amounted to 51 GW in 2015 [1]. Wind electric generation is one of the best alternative electric energy sources because it's economic benefits [2], and usefulness for power system in diverse areas. For a Variable Speed Wind Turbine (VSWT), there are many reasons to use a Doubly Fed Induction Generator (DFIG), such as noise reduction, efforts reduction on the aero-generator shaft, reduced inverters and the possibility of stator active and reactive powers control [3-4-5]. The main advantage is that the power converter is rated at only 25-30% of the generator rating, leading to lower converter cost and power losses [6-7-8]. It also allows controlling the active and reactive powers via stator powers regulators. The power electronics have become more advanced with the growing capacity coverage, and have brought significant performance improvements to wind turbines-not only reducing mechanical stress and increasing energy yield [9], but also enabling the WTS to act as a controllable generator much more suitable for integration with power grid.

The main DFIG's control topologies based on AC power generation for grid connected [10-11-12] and stand-alone systems [13-14-15-16] and [17] are widely available in literature. The popular control techniques, for control of DFIG, are stator flux based Field Oriented Control (FOC) and Direct Power Control (DPC). In [18-19] DPC is characterized by quick dynamic response, simple structure and low parameter dependency, so it has become an interest of both the academic and industry communities throughout the world. In [20] the authors have studied a new control for DC voltage regulation of stand-alone DFIG-DC system. The main idea of this research based on the DC link voltage regulation is achieved by control of stator voltage magnitude using flux loop by d -axis rotor current. The load current, reflected in stator current, will be directly supported by q -axis rotor current. In [21] the authors have proposed an interesting study known by Sensorless frequency and voltage control in stand-alone. The principle goal of this work was sensors number reduction, and the sensorless implementation was adopted to achieve field orientation and regulate stator frequency and dc voltage. In [22] the authors have propo-sed a novel analysis study of Stand-alone DFIG-system and DC voltage regulation with reduced sensors. The aim of this study was a modified control scheme for stand-alone DFIG which does not require sensing of stator voltages and stator currents. Due to the nonlinear nature of the wind-system, it is necessary to add the filters in order to reduce the ripples/undulations; especially between the generator and converters or the converters and the grid. Commonly a high-order filter has been used in place of the conventional L-filter for smoothing the output currents from a VSI [23-24]. Because of these advantages, this solution is now used widely in distributed generation (solar and wind) [25], [26] and power active filters.

The main contribution of this chapter is the experimental validation (via dSPACE1103 card and ControlDesk) of the proposed algorithm in stand-alone mode (under sudden wind speed variation tests) by the means the variation of the references rotor direct and quadrature currents (I_{rd} and I_{rq}) to overcome the drawbacks of conventional algorithm such as; power tracking, power quality and sensitivity to wind speed variation. In this chapter, a novel direct power control in stand-alone mode (figure.5.1) will be developed in real time. A new inverter version will be proposed (called SEMIKUBE 100 kW) to fed the rotor side converter (RSC) by the means of PWM strategy (using isolation card corresponding to this new inverter). IP controllers will be proposed to control I_{rd} and I_{rq} (images of Q_s and P_s respectively) and this choice will be justified compared to others regulators (experimental conditions). Several experimental validation tests will be established under deffirent condicions (stator is/ is not connected to RL-load)to ensure the wind-system high performances.

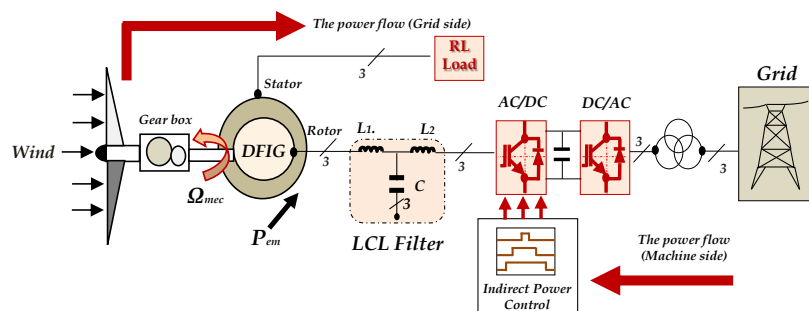


Figure.5.1 Schematic diagram of DFIG using indirect power control in stand-alone mode.

5.2 Proposed Control (stand-alone topology)

Figure.5.2 presents the proposed control scheme of wind-system based on DFIG¹. Rotor side converter is controlled via the Indirect power control (by the means of IP regulator via rotor currents “ I_{rd} and I_{rq} ”) to generate the PWM switching signals to control the SEMIKUBE (inverter). The stator of DFIG is connected into the RL-load, this case called: isolated-mode (or stand-alone mode), the objective is to ensure the high performances of the proposed control under robustness currents/speed tests in terms of good tracking, no overshoot, short response time, low current’ and power error (The LCL filter is connected between DFIG’s rotor and the SEMIKUBE to improve the stator’ and rotor voltages waveforms). To ensure these performances regarding the references currents’ and speed variation, it is necessary to use very robust regulators to control d - q axes rotor currents components (I_{rd} and I_{rq}) named by IP (Integral-Proportional) controllers. The second section describes the transfert function of IP in closed loop.

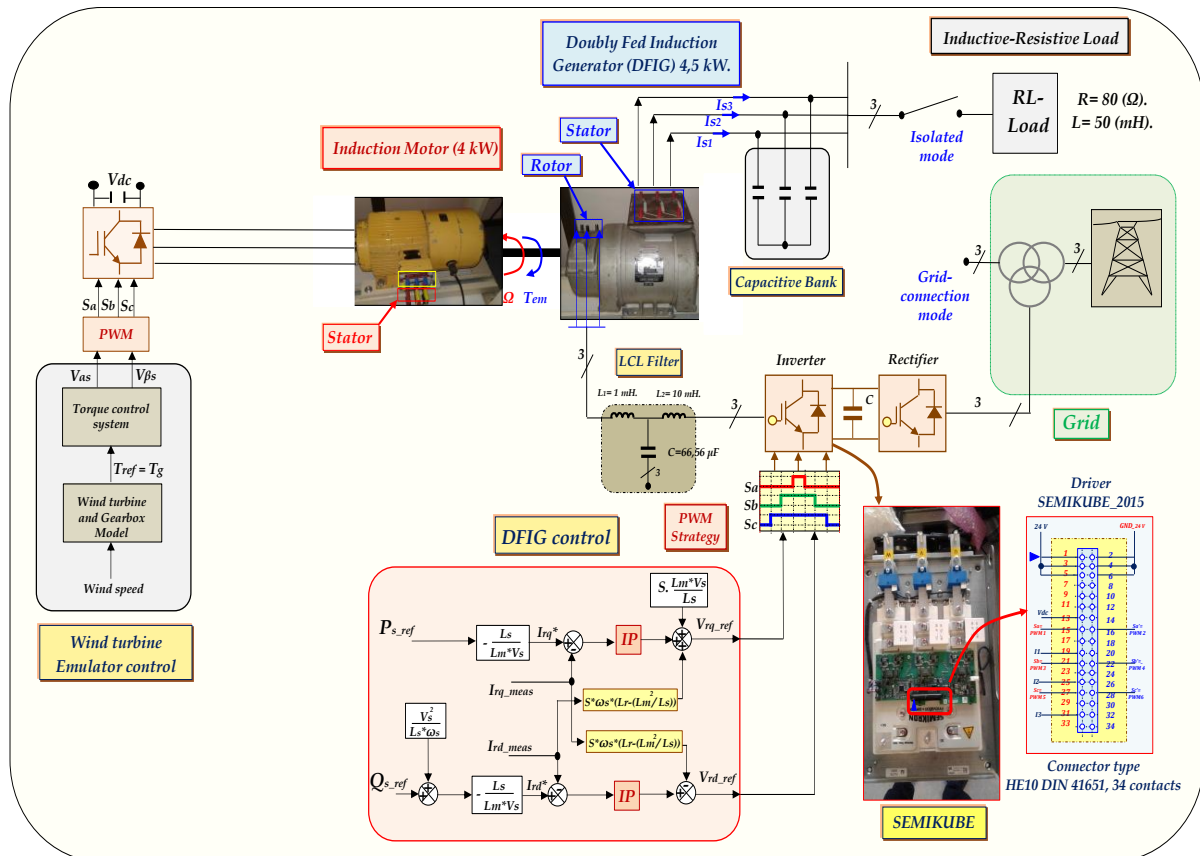


Figure.5.2 Proposed control scheme based on DFIG power control in stand-alone mode.

5.3 Indirect Power Control (IDPC) based on Integral-Proportional (IP) regulators

5.3.1 DFIG control (Rotor side converter)

The control of the DFIG through the DC-AC converter connected to its rotor must ensure the necessary torque to vary the mechanical generator speed (Ω_{mec}) in order to extract the maximum power, by imposing adequate rotor voltages to the DFIG [27]. The reference reactive power is generally equals to zero value for the MPPT control strategy (already explain in §.2.4.1). From equation: (2.36)-(chapter-2), it is clear that the torque can be controlled by acting on the rotor quadrature current component (I_{rq}) of the DFIG.

In a similar manner, the rotor direct current component (I_{rd}) is used to control the generated reactive power (equation: (2.50)-(Chapter-2)). We can therefore write the following [27]:

$$I_{rq}^* = -\frac{L_s}{P \cdot L_m \cdot \Phi_s} * T_{em}^* \quad (5.1)$$

¹ Please refer to Appendix-“C-Section.C-1”: (There are real photos of DFIG and the wind turbine emulator and their nameplates (Figures.C-(1&2)).

$$I_{rd}^* = \frac{\Phi_s}{L_m} - \frac{L_s}{V_s \cdot L_m} * Q_s^* \quad (5.2)$$

$$I_{rq}^* = \frac{L_s}{V_s \cdot L_m} * P_s^* \quad (5.3)$$

In contrast to the MPPT control strategy where the reference quadrature (or transversal) component I_{rq}^* represents the image of the torque to be produced, the power controller for this algorithm calculates and sends at its output the rotor reference quadrature & direct components (I_{rq}^* and I_{rd}^*) of the DFIG, are images of the stator active and reactive power respectively. These are derived respectively from equation: (2.49) & (2.50)-(Chapter:2)

5.3.2 Integral Proportional (IP) regulators²

In this part IP regulators are proposed to control I_{rq} and I_{rd} respectively of DFIG (figure.5.4). IP regulators are similar to PI regulators (is described in details in chapter 2) except that the proportional and integral actions are serialized unlike PI regulators, where these actions are paralleled (figures.5.3-(a and b) respectively). As described above, the system is first regulated by simplifying the system into a monovariabile model. Thus the simplified model used for IP dimensioning is as flows (figure.5.4-(a & b)), and the global proposed control scheme is described in figure.5.4-(c). The closed loop transfer function (CLTF) with the IP controller is then written:

$$CLTF = \frac{Output}{Input_{ref}} = \frac{k_i * k_p * A}{p^2 + (k_p * A + B)p + k_i * k_p * A} \quad (5.4)$$

Such as:
$$\begin{cases} A = \frac{L_m * V_s}{L_s * L_r - L_m^2} \\ B = \frac{L_s * R_r}{L_s * L_r - L_m^2} \end{cases}$$

By identification with a second order system of transfer function:

$$CLTF = \frac{Input_{ref}}{Output} = \frac{k * \omega_n^2}{p^2 + 2 * \xi * \omega_n * p + \omega_n^2} \quad (5.5)$$

The gains³ of the correctors will be expressed as a function of the parameters of the machine as follows:

$$\begin{cases} k_i = \frac{\omega_n^2}{k_p * A} \\ k_p = \frac{2 * \xi * \omega_n - B}{A} \end{cases} \quad (5.6)$$

Hence replacing A and B by their respective expressions we obtain:

$$\begin{cases} k_i = \frac{\omega_n^2 * (L_s * L_r - L_m^2)}{k_p * L_m * V_s} \\ k_p = \frac{2 * \xi * \omega_n * (L_s * L_r - L_m^2) - L_s * R_r}{L_m * V_s} \end{cases} \quad (5.7)$$

The choice of ξ is made so that the damping coefficient of the closed loop system is optimal (about 0.7). As for the dynamics of the system (ω_n), it will be chosen during the simulation in order to have the best performances.

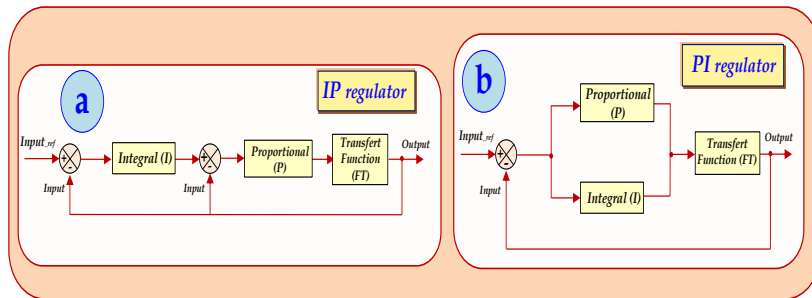


Figure.5.3 Schematic diagram of IP and PI regulators.

² The choice of IP controllers is based on the high performances despite the references variation instead PI controllers, in construct of chapters-2 and 3 (PID controllers are used to control I_{rd} and I_{rq}) PID controllers are not used in chapter: 5, due to the real time implementation calculation (Experimental study limitations) which takes more time using three parameters (PID) instead only two (for IP) for each loop/period.

³ Please refer to Appendix.C-"Section.C-3": (the values of gains: K_i and K_p of proposed IP controller in Table.C.2).

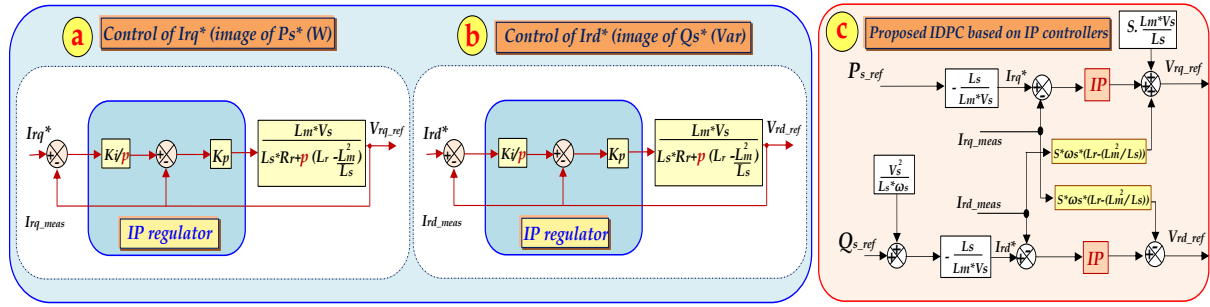


Figure.5.4 Controlled system by IP regulator (according to d and q axis).

Table.5.1 The advantages and disadvantages (difficulties) of the proposed controls in Chapters 3, 4 and 5.

		Proposed controls:		
		Novel Indirect Power Control (in CLTF):	Novel Input/output Linearizing control:	Enhanced Indirect Power Control (in OLTF):
Chapter 3:	Control's mathematical model:	Easy.	-	-
	Schematic structure (Loops):	04.	-	-
	Experimental implementation:	Medium (take more time)	-	-
Chapter 4:	Control's mathematical model:	-	Medium.	-
	Schematic structure (Loops):	-	02.	-
	Experimental implementation:	-	Medium.	-
Chapter 5:	Control's mathematical model:	-	-	Easy.
	Schematic structure (Loops):	-	-	02.
	Experimental implementation:	-	-	Easy

Figure.5.5-(a and b) presents simulation results of the Stator active' and reactive' powers under IDPC using PI and IP controllers (to control I_{rq} & I_{rd}) respectively. Figure.5.5-(a) illustrates the the behavior of stator active measured power (using PI and IP respectively) in steady and transient states in the period of 1.5 (sec). The performances of the stator active power (zoom) using IP controllers is more powerfull in terms of good tracking, very short response time and neglected overshoot despite the sudden variation of the stator active reference power, in the inverse case. in stator active power using the PI controler; rematkables overshoot and power error are noted. Figure.5.5-(b) illustrates the the behavior of stator reactive measured power (using PI and IP respectively) in steady and transient states in the period of 1.5 (sec). The stator reactive measured power (using IP controllers) follows exactly its refernce (zoom) despite of the sudden variation the stator power reference, it can be seen improved perfromnces using IP controller especially in tracking power, power error and response time. Table.5.1 describes in details the advantages and disadvantages of each proposed controls, so it is clear that the best control for experimental study is the third one (Enhanced IDPC in open loop transfert function 'OLTF')⁴.

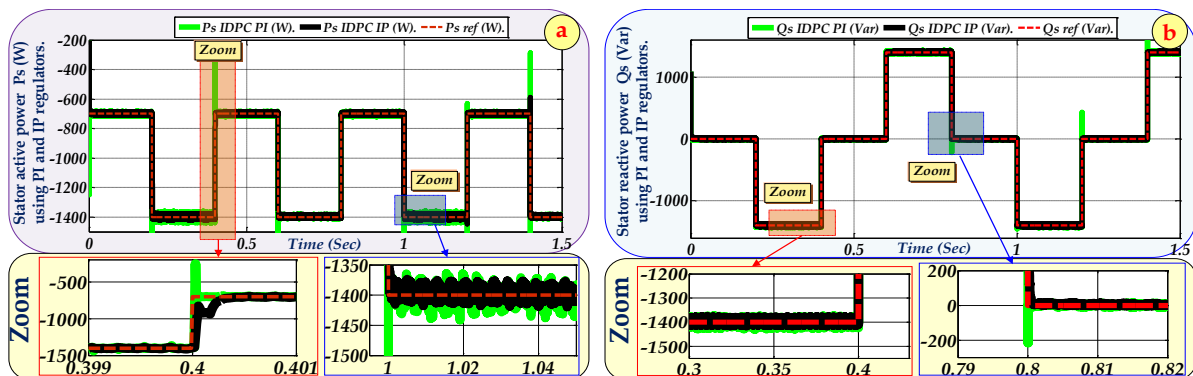


Figure.5.5-(a and b): The stator active and reactive power controlled by 'PI and IP' controllers respectively.

⁴ In this chapter, the proposed Indirect Power Control (in OLTF) is based on IP controllers for two raisons; 1st: take little calculation time (only two loops) and 2nd: IP controllers overcome the overshoot drawback (PID is also an excellent solution but takes more calculation time).

5.3.3 Emulator turbine control (Induction motor torque and flux control):

In proposed system drive, the induction motor imposes torque in electrical generator shaft according to a reference torque signal generated by wind turbine model from a reference wind speed. The whole motor induction torque and rotor flux control system is shown in figure.5.6. The system includes closed loop stator current control with PI regulators with outer loop torque and rotor flux control. The torque control is realized by acting over the amplitude of the stator current and its frequency command is generated by the rotor flux control loop. Instead of constant rated flux, the reference rotor flux control loop can be programmed with the speed motor operation for efficient improvement. For torque and rotor flux calculation, stator current in 3-phase system (a, b and c) is decomposed in two dimension orthogonal system (α, β) [28]. This change of variables is well known as Clarke transformation and can be used to reduce the complexity of the system control implementation. After the acquisition, the stator 'abc' voltage and current are transformed into a stationary αβ coordinate system. The voltage $V_{\alpha s}$ is aligned with the voltage $V_{\alpha s}$ (as shown in figure.5.6). Then, the αβ stator voltages are calculated as:

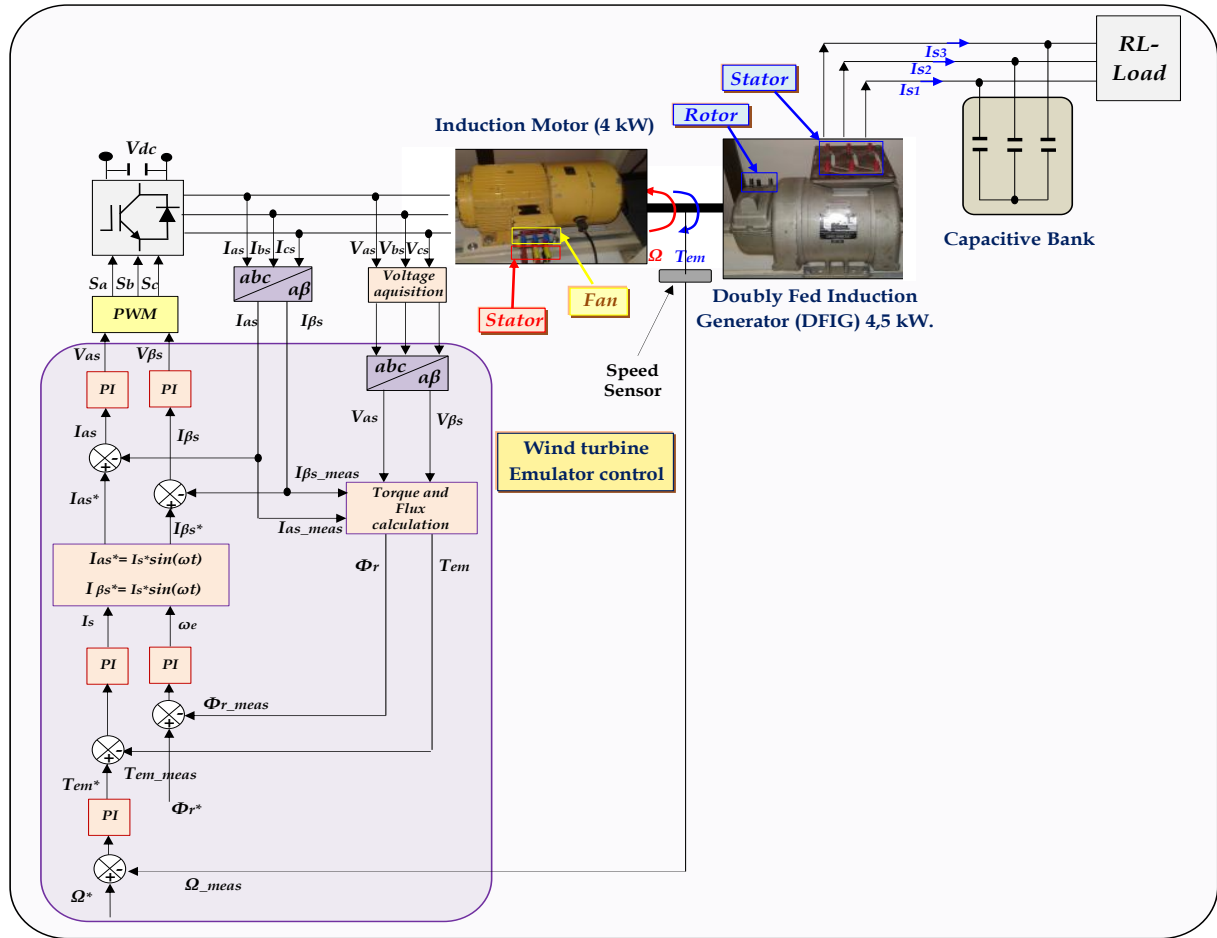


Figure.5.6 Induction motor torque and rotor flux control system.

$$V_{\alpha s} = \frac{1}{3}(V_{ab} - V_{ca}) \quad \text{and} \quad V_{\beta s} = \frac{\sqrt{3}}{3}V_{cb} \tag{5.8}$$

The currents in αβ axes are calculated as:

$$I_{\alpha s} = I_{as} \quad \text{and} \quad I_{\beta s} = \frac{\sqrt{3}}{3} \cdot (I_{as} + 2 \cdot I_{bs}) \tag{5.9}$$

With the stator voltages and currents, the stator flux is calculated in the stationary αβ axes:

$$\Phi_{\alpha s} = \int (V_{\alpha s} - r_s \cdot I_{\alpha s}) dt \quad \text{and} \quad \Phi_{\beta s} = \int (V_{\beta s} - r_s \cdot I_{\beta s}) dt \tag{5.10}$$

The rotor flux in the stationary αβ axes can be calculated according to following equations:

$$\Phi_{\alpha r} = \frac{L_r}{L_m} \cdot (\Phi_{\alpha s} - \sigma \cdot L_s \cdot I_{\alpha s}) \quad \text{and} \quad \Phi_{\beta r} = \frac{L_r}{L_m} \cdot (\Phi_{\beta s} - \sigma \cdot L_s \cdot I_{\beta s}) \tag{5.11}$$

5.3.4 Hardware implementation

In this section, the experimental wind-turbine emulator control has been presented in order to explain the hardware relationship between the emulator turbine control (*Digital Control Interface*) and *dSPACE1103* panel via the wires connexion as shown in *figure.5.7*. Knowing that the incremental sensor pins (*pins*→*signal*) are described in details in *table.5.2*; such as *V_{cc}*, *GND* and the position/angle at 0°, 90° or *Index*. *Figure.5.8* illustrates the electric /mechanic WECS hardware connection of the proposed control (*DFIG and Wind turbine emulator: 'Induction motor'*)⁵. It can be seen also, the *L-filter* (*L=10 mH*) to the left, is implemented between the *SEMIKUBE* (*Inverter*) and the *DFIG's* rotor. *Figure.5.9* illustrates the experimental tests bench developed in *L2EP Laboratory*. The different devices and materials used are as follows; **1**: *PC*(with control desk interface to the right), **2**: *Oscilloscope*, **3**: *dSPACE1103* panel, **4**: *PLL synchronization hardware*, **5**: *Resistive load*, **6**: *SEMIKUBE Driver Power supply (+24)*, **7**: *DC bus voltage SEMIKUBE (0 V-600 V)* **8**: *Emulator turbine control (Rotor flux control)*, **9**: *DFIG (4.5 kW)*, **10**: *Emulator turbine /Induction motor (4 kW)*, **11**: *SEMIKUBE (Inverter)*, **12**: *Isolation card DC*, **13**: *Current sensors*, **14**: *Grid AC (0-400 V)*.

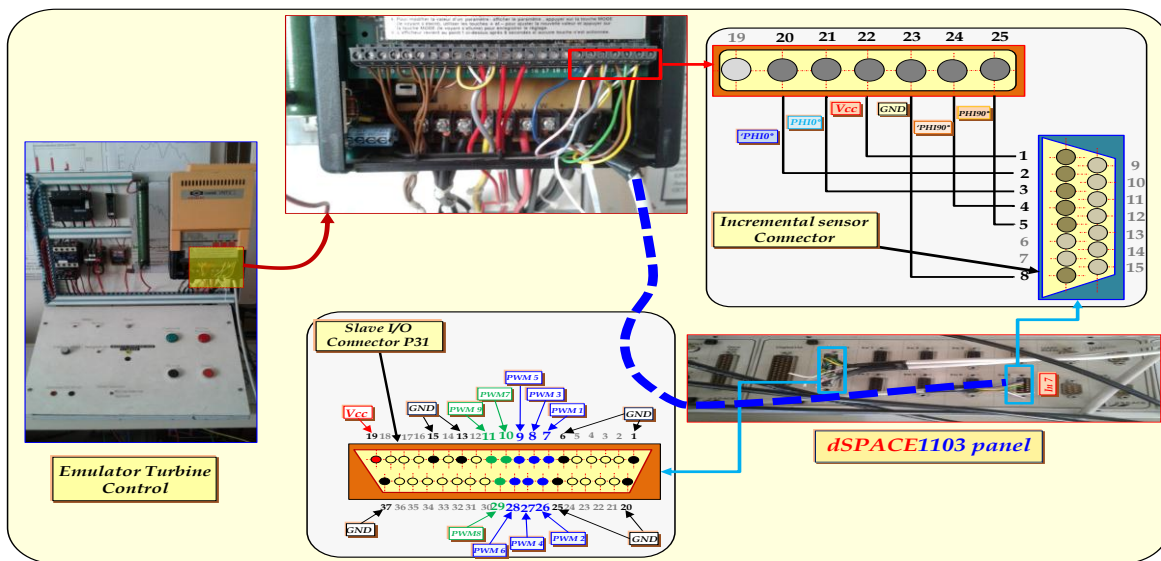


Figure.5.7 Hardware connexion of emulator wind turbine and dSPACE1103 panel via incremental sensor connector.

Table.5.2 Incremental sensor' connectors.

Pin:	Signal:	Pin:	Signal:
1	V _{cc} .	9	V _{cc} .
2	PHI 0(x).	10	GND.
3	/PHI 0(x).	11	GND.
4	PHI 90(x).	12	GND.
5	/PHI 90(x).	13	GND.
6	INDEX (x).	14	GND.
7	/INDEX (x).	15	GND.
8	GND.		

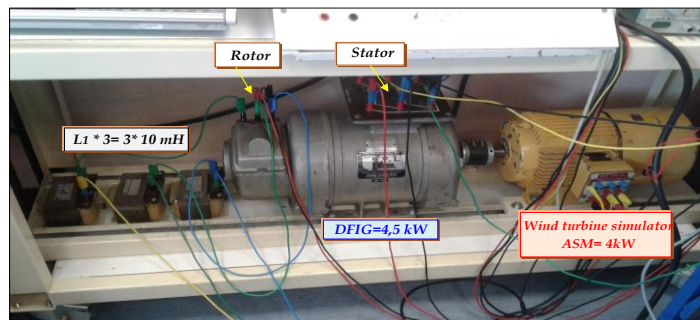


Figure.5.8 WECS hardware implementation: (emulator turbine + DFIG + inductances (L-Filter)).

⁵ Please refer to Appendix.A-“Section.A-2”; Parameters of the DFIG and wind turbine emulator (Table.A.3 + Table.A.4).

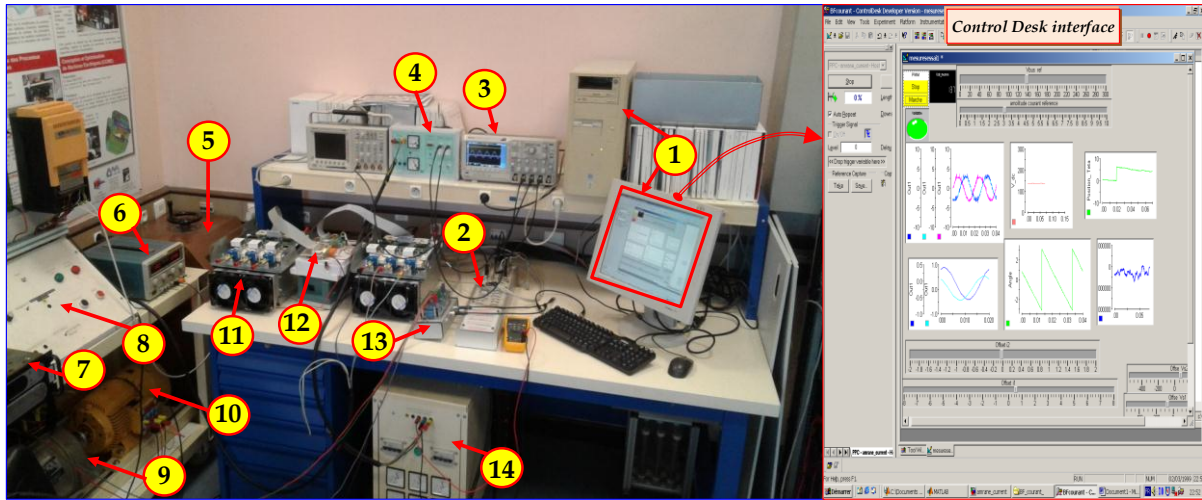
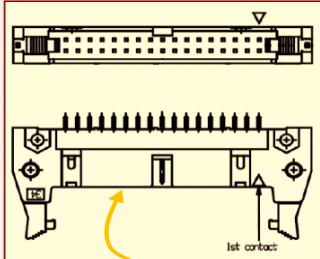



Figure.5.9 Experimental test bench developed in L2EP Laboratory (Ecole Centrale de Lille/France).

5.4 Experimental studies using a new inverter named SEMIKUBE (100 kW, 2016 version)

5.4.1 SEMIKUBE components description

Table.5.3 SEMIKUBE connector pin assignment.

Pin	Signal:	Function:	SEMIKUBE® Photo:
1	F_PWR_VP	Power supply	<p>Connector type HE10 DIN 41651, 34 contacts</p>  
2	IF_PWR_GND	GND for IF_PWR_VP	
3	IF_PWR_VP	Power supply	
4	IF_PWR_GND	GND for IF_PWR_VP	
5	IF_PWR_VP	Power supply	
6	IF_PWR_GND	GND for IF_PWR_VP	
7	IF_CMN_GPIO1	Reserved	
8	IF_CMN_GND	GND for IF_CMN_nHALT, Status signal	
9	IF_CMN_nHALT	Status signal	
10	IF_CMN_GPIO0	Status signal inverted HALT	
11	IF_ANLG_Temp	Temperature analog out	
12	IF_ANLG_Temp_GND	GND for IF_ANLG_Temp	
13	IF_ANLG_UDC	UDC analog out	
14	F_ANLG_UDC_GND	GND for IF_ANLG_UDC	
15	IF_HB1_TOP	Switching signal input	
16	IF_HB1_BOT	Switching signal input	
17	IF_HB1_rsvrd	Reserved	
18	IF_HB1_GND	GND for IF_HB1_TOP, I analog out HB1	
19	F_HB1_ANLG	I analog out HB1	
20	IF_HB1_AGND	GND for IF_HB1_ANLG	
21	IF_HB2_TOP	Switching signal input (HB2 TOP switch)	
22	IF_HB2_BOT	Switching signal input (HB2 BOT switch).	
23	IF_HB2_rsvrd	Reserved	
24	IF_HB2_GND	GND for IF_HB2_TOP, I analog out HB2	
25	IF_HB2_ANLG	I analog out HB2	
26	IF_HB2_AGND	GND for IF_HB2_ANLG	
27	IF_HB3_TOP	Switching signal input (HB3 TOP switch)	
28	F_HB3_BOT	Switching signal input (HB3 BOT switch)	
29	IF_HB3_rsvrd	Reserved	
30	IF_HB3_GND	GND for IF_HB3_TOP, analog out HB3	
31	F_HB3_ANLG	analog out HB3	
32	IF_HB3_AGND	GND for IF_HB3_ANLG	
33	IF_CAN_H	Configuration/diagnostic CAN interface I/O	
34	IF_CAN_L	Configuration/diagnostic CAN interface I/O	

A. PWM input signals

The SEMIKUBE SL drivers are available as GD (Six packs – SL20, SL40) and GB (half bridge –SL80, SL150) type. Overlapping of Top and Bot signals is avoided by an internal dead time generation. The input signals are filtered by digital short pulse suppression.

B. Dead time generation

The interlock dead time is defined as t_{TD} in the data sheet. The dead time circuit prevents those high and

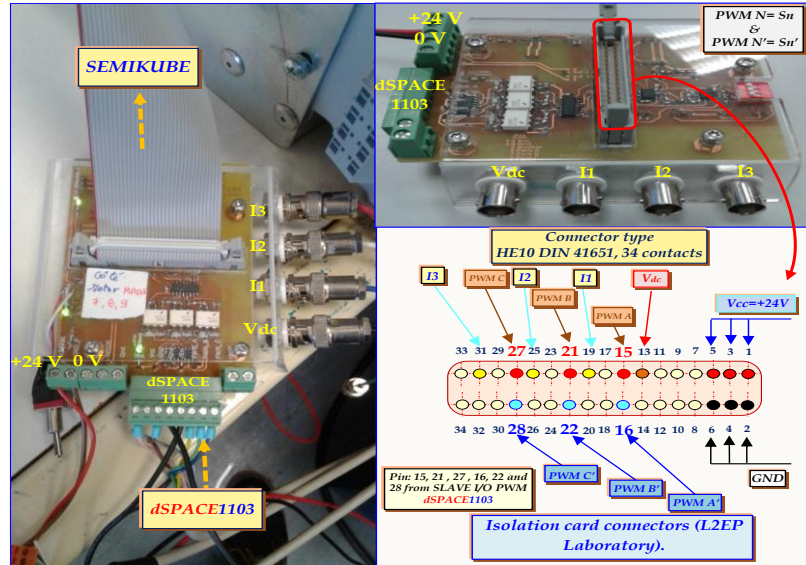


Figure.5.10 Isolation card for the dSPACE1104 realizing in L2EP Laboratory (Ecole Centrale de Lille).

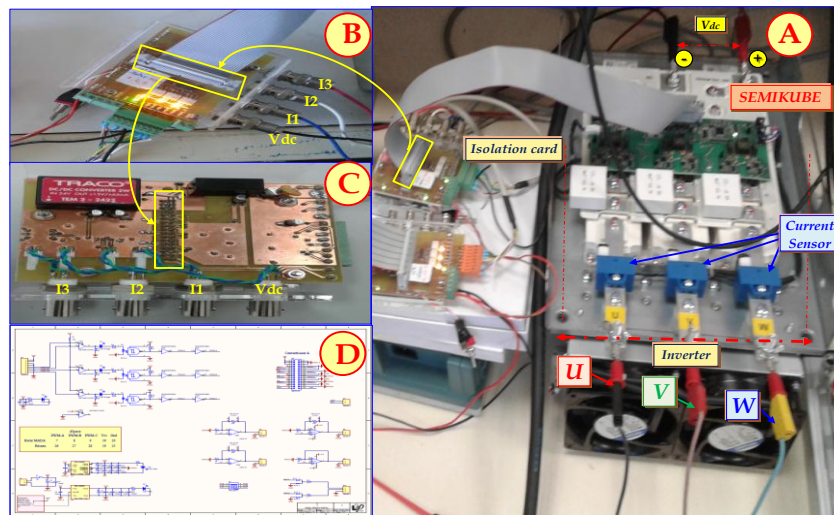


Figure.5.11 Inverter type SEMIKUBE® with isolation card developed in L2EP Laboratory (Ecole Centrale de Lille), A: Inverter + Isolation card, B: Isolation card is connected, C: The isolation card components and D: Printed circuit board (copper side)

low sides IGBT of one half bridges are switched on at the same time. It is allowed to control the SEMIKUBE by inverted pulses that means without controller dead time. t_{TD} is not added to a dead time given by the controller.

C. LED Diagnostic

The system status during system power on, normal operation or failure event is illuminated by one LED. The LED indicates the following conditions. During the sequence, a red LED indicates a current error. An orange LED an error in the past. The sequence is only to support finding the error cause. A proper measurement (esp. HALT-Signal) has to be done to determine the cause.

5.4.2 Isolation card⁶

To generate the switching signals from the dSPACE1103 into the SEMIKUBE, we need the isolation card to separate the power stage from the control stage by using two different grounding panel sockets via the Optocoupler. Figure.5.10 illustrates the isolation card and different dSPACE1103's connectors.

⁶ Please refer to Appendix.B-“Section.B.1”: (Figure.B.1 + Table.B1/for more information about components/copper circuit of the dSPACE1103's isolation card).

5.4.3 SEMIKUBE with isolation card

Figure.5.11 demonstrates the electric connection between the isolation card and the SEMIKUBE using 34 panel connectors. The SEMIKUBE used in this test is from ‘SlimeLine from Semikron, 2016 Version’.

5.4.4 dSPACE1103 and ControlDesk software [29]

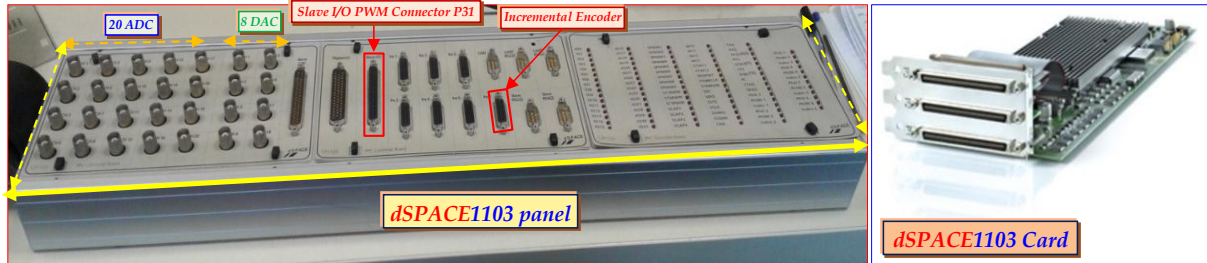


Figure.5.12 dSPACE1103 panel (to the left) and dSPACE1103 Card (to the right).

A. PWM Outputs

The 3-phase and 1-phase PWM outputs are provided at the front panel, after signal conditioning from +5 V generated by the dSPACE card (figure.5.12 and table.5.4) to +15 V required by the IGBT drivers.

B. ADC Inputs

The ADC inputs are present to interface with the transducers. They consist of 8 channels. ADCH1 to ADCH4 are multiplexed, 16-bit resolution, to a single ADC while ADCH5 to ADCH8 are four independent ADCs, each with 12-bit resolution. The input voltage limit is ±10 V. The conversion time for the multiplexed channels is 2 (μs) while for the parallel channels it is 800 ns.

C. DAC Outputs

The DAC outputs are present to interface with actuators. There are 8 independent DAC channels. DACH1 through DACH8 have a 16-bit resolution and voltage output limits of ±10 V. The output current limit is ±5 mA.

D. Master PPC Digital I/Os

Inputs and outputs controlled by the master processor PPC are indicated as ‘Digital I/O’.

Table.5.4 Slave I/O PWM connector (dSPACE1103).

CP18 (37 pins):	Pin:	Signal:	Pin:	Signal:
	1	GND.	20	GND.
	2	SCAP1.	21	SCAP2.
	3	SCAP3.	22	SCAP4.
	4	GND.	23	ST1PWM.
	5	ST2PWM.	24	ST3PWM.
	6	GND.	25	GND.
	7	SPWM1.	26	SPWM2.
	8	SPWM3.	27	SPWM4.
	9	SPWM5.	28	SPWM6.
	10	SPWM7.	29	SPWM8.
	11	SPWM9.	30	GND.
	12	STMRCLK.	31	STMRDIR.
	13	GND.	32	SPDPINT.
	14	STINT1.	33	STINT2.
	15	--	34	--
	16	--	35	--
	17	--	36	GND.
	18	Vcc (+5 V).	37	GND.
	19	GND.		

Figure.5.13 illustrates the ControlDesk interface using in this experimental study (for proposed DPC based on IP regulators in stand-alone mode). By using ControlDesk software, it can be easy to manipulate all the outsider parameters (voltages, currents and speed). It can be very helpful using the ON/OFF (top-left side of figure.5.13) option to stop the hardware system in only one second in the case of accident (an overvoltage, overcurrent or short-circuit).

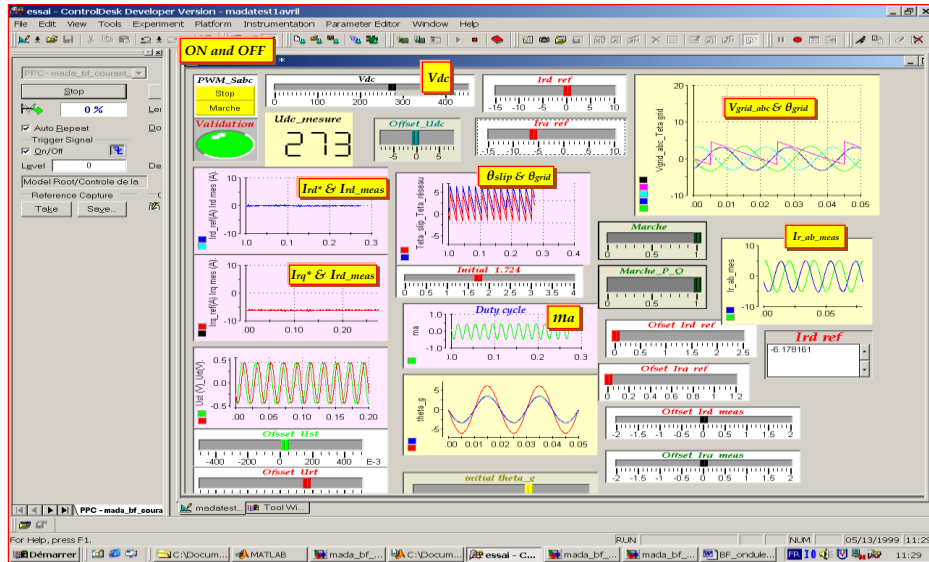


Figure.5.13 ControlDesk interface (for the proposed control).

5.4.5 SEMIKUBE with R-L load under open loop using dSPACE1103 card

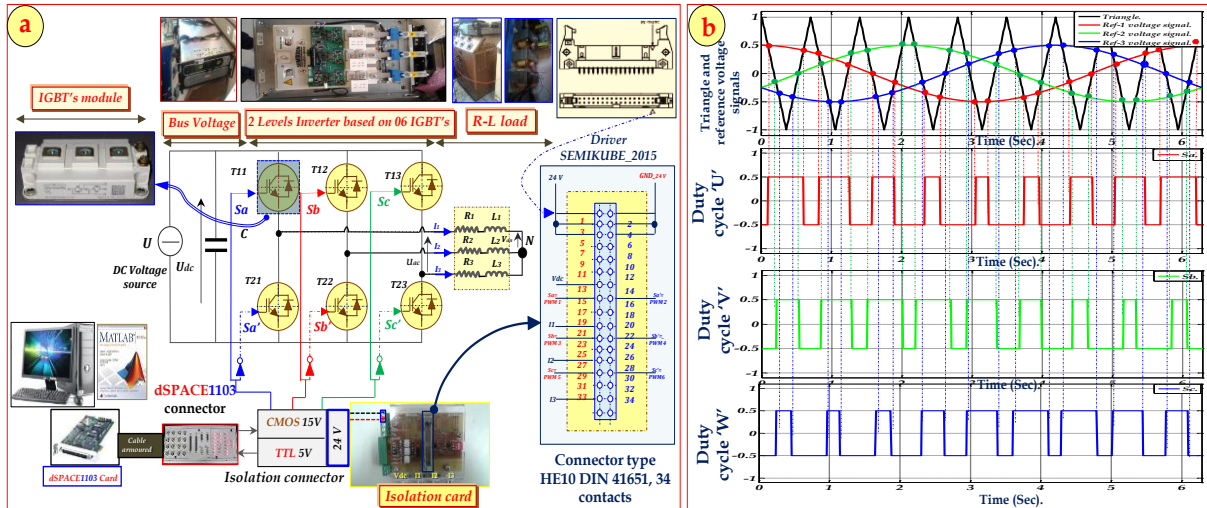


Figure.5.14 a: Open loop hardware scheme using SEMIKUBE with R-L Load (Stand-alone) and b: PWM signals for three SEMIKUBE Legs.

Before using the switching gates generated by the PWM algorithm to control rotor side converter (RSC) of the DFIG, it is necessary to test the SEMIKUBE (novel inverter version) in open loop with only R-L load (figure.5.18) under real time dSPACE1103 card. Figure.5.14-(a) presents the hardware implementation of the proposed algorithm tests, to ensure the good performances of the SEMIKUBE using PWM strategy before feeding the rotor side converter (RSC) of DFIG. As shown in figure.5.14-(b), the signals switching 'S_n' are generated via isolation card (24 V/connector type HE10 DIN 41651, 34 contacts). The different parameters used in this test are: $V_{dc_Test}=80$ (V), $R_{0_Test}= 80$ (Ω), $L_{0_Test}= 50$ (m H), $I_{0_Test}= 4$ (A), switching frequency $f_{s_Test}= 5$ (KHz) and the rated load power $P_{0_Test}= 1,28$ (KW). The power circuit of the three-phase voltage source inverter is obtained by adding a third leg to the single-phase inverter. Assuming that of the two power switches in each leg (phase) of the SEMIKUBE, one and only one is always on, that is, neglecting the time intervals when both switches are off (blanking time), three switching variables, *a*, *b* and *c* can be assigned to the inverter. A state of the inverter is assigned as 'abc', making for a total of eight states, from state 0, when all output terminals are clamped to the negative DC bus, through state 7 when they are clamped to the positive bus V_{dc_Test} (V). In this case, it is assumed that the R-L (resistive-inductive) load is three phases balanced load, the line to line voltage in each phase equals to:

$$\begin{pmatrix} V_{AB} \\ V_{BC} \\ V_{CA} \end{pmatrix} = R_{Load} * \begin{pmatrix} I_A \\ I_B \\ I_C \end{pmatrix} + L_{Load} * \frac{d}{dt} \cdot \begin{pmatrix} I_A \\ I_B \\ I_C \end{pmatrix} \tag{5.12}$$

$$I_A + I_B + I_C = 0 \tag{5.13}$$

The instantaneous line to line output voltages; V_{AB} , V_{BA} and V_{CA} are given by:

$$\begin{pmatrix} V_{AB} \\ V_{BC} \\ V_{CA} \end{pmatrix} = \frac{1}{3} V_{dc} * \begin{pmatrix} +2 & -1 & -1 \\ -1 & +2 & -1 \\ -1 & -1 & +2 \end{pmatrix} * \begin{pmatrix} V_{AN} \\ V_{BN} \\ V_{CN} \end{pmatrix} \tag{5.14}$$

Figure.5.14-(b) presents the PWM strategy for the three leg inverter under Matlab/Simulink® R2009b software. Figure.5.15 illustrates the real photos of resistances and inductors for the proposed SEMIKUBE control tests are coupled together in star shape. Figure.5.16 illustrates the switching signals of the three (03) legs of the inverter; in high side (S_a , S_b and S_c) and low side (S_a' , S_b' and S_c') with their zoom. Figure.5.17 displays the dead time between the switching signals (2 (μ sec)) for each leg, for example the dead time between S_a and S_a' (leg 'a') equals to 2 (μ sec) and the same thing in the rest of legs.

Figure.5.18 presents the load waveforms and their zoom under open loop topology. The top graph displays the current, simple and compound voltage and switching signal respectively in steady state and transient states. The fourth (04) bottom graphs represent only one cycle for each of them (2 (msec) *10= 1 cycle). It can be seen an excellent sinusoidal form of the load current (peak to peak load current equals to 4 (A)) with very neglected ripples.

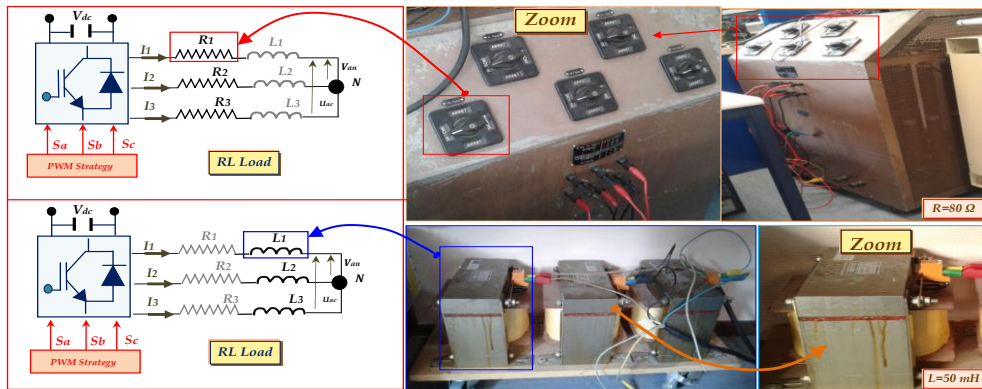


Figure.5.15 The R-L load used in SEMIKUBE performance tests.

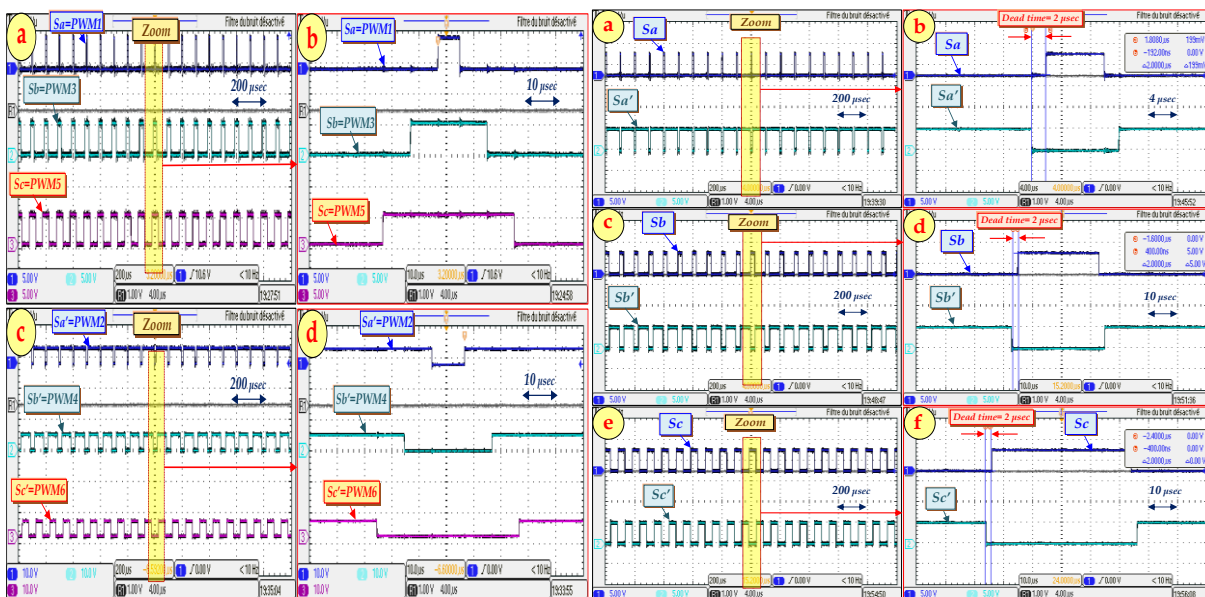


Figure.5.16 Switching signals: high (S_a , S_b and S_c) and low (S_a' , S_b' and S_c').

Figure.5.17 Dead time between the switching signals for each leg.

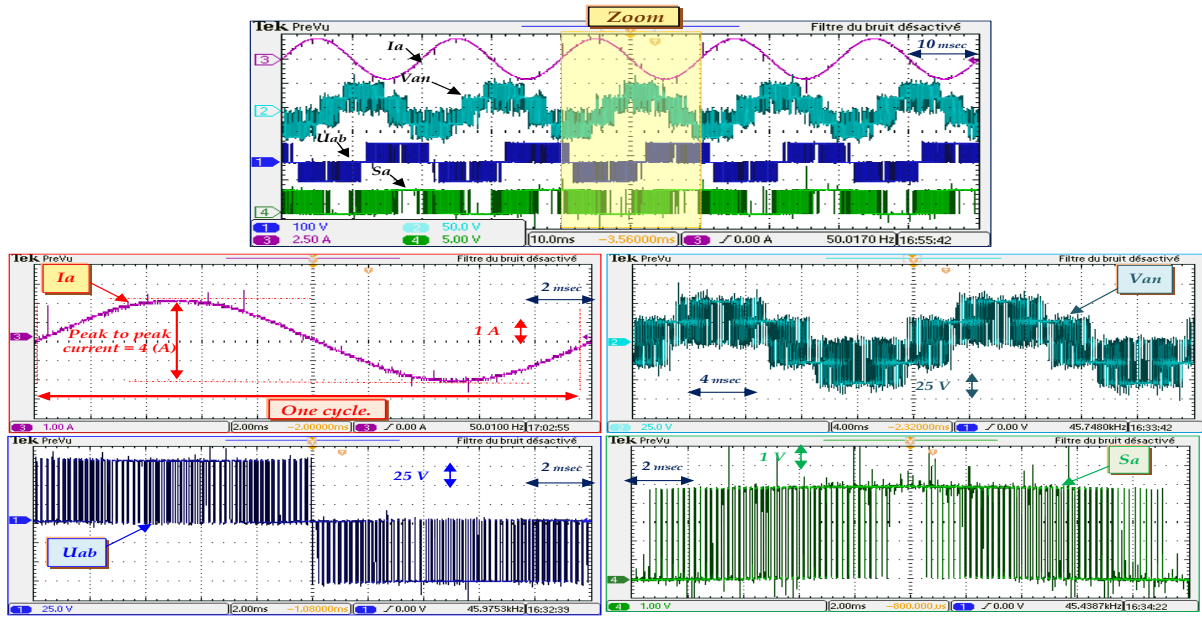


Figure.5.18 Current and voltage waveforms of RL-load under $V_{dc}= 80$ (V).

5.5 Impact of Filters in RSC using the Fast Fourier Transform (FFT)

In order to choose an optimal filter topology for variable speed wind-turbines (VS-WT) to feed the DFIG's rotor via SEMIKUBE (inverter), parameters like efficiency, weight and volume have to be considered. Regarding efficiency, filter topologies with reduced losses are required, though those are relatively small when compared to losses in the inverter [30]. Weight and volume are considered as critical characteristics at offshore applications due to difficulties with transportation, installation and maintenance. The filter cost depends basically on the amount of components and materials used, for example the magnetic material for the core of inductors. Filters connected to the output of an inverter have basically the following four-pole circuit configuration as seen in figure.5.19-(a).

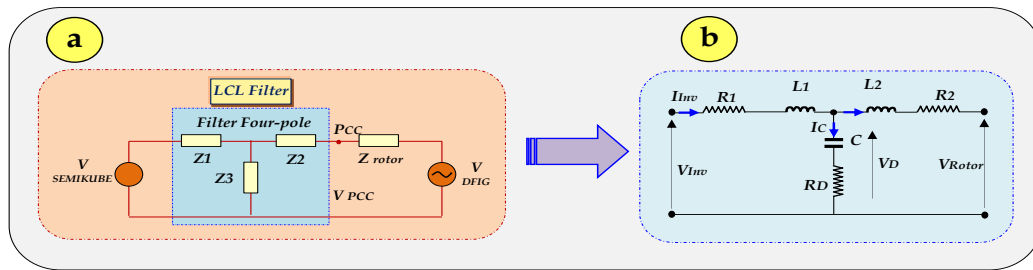


Figure.5.19 Single phase LCL-Filter schematic.

Figure.5.20 illustrates the different filters (L, LC and LCL) used in experimental test bench between the SEMIKUBE (inverter) and the DFIG's rotor.

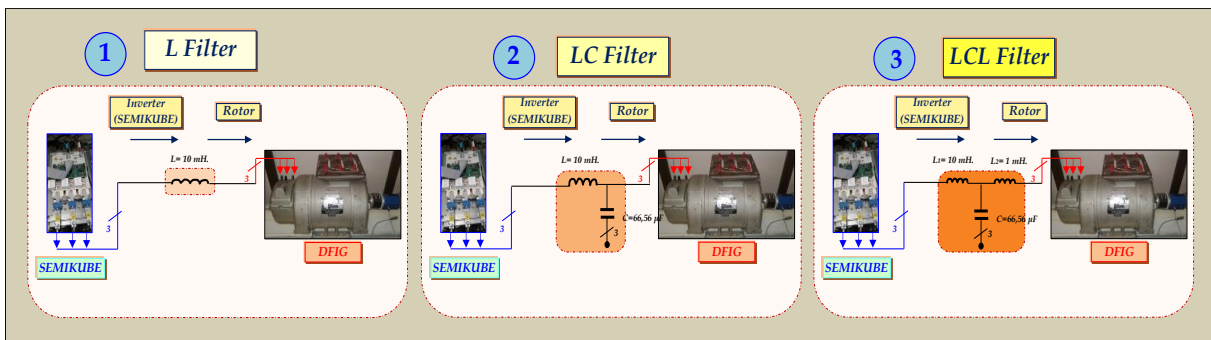


Figure.5.20 Proposed filters (L, LC and LCL) topologies.

5.5.1 Mode I: L Filter

The L-Filter (figure.5.20-(1)) is the first order filter with attenuation 20 dB/decade over the whole frequency range. Therefore the application of this filter type is suitable for converters with high switching frequency, where the attenuation is sufficient. On the other side inductance greatly decreases dynamics of the whole system converter-filter. In this case $L = 10$ (mH).

Figure.5.21 illustrates the experimental results of rotor' and stator voltages (V_r and V_s) waveforms respectively of whole system: Converter (SEMIKUBE) + Filter (L) + DFIG (Rotor); in transient and steady states under four (04) cases in term of current variation (I_{rd}^* and I_{rq}^*) as described in table.5.5:

Table.5.5 References rotor current variation using L-filter.

Cases:	Reference rotor current variation (I_{rd}^* and I_{rq}^*):
Case 1:	$I_{rd}^* = 0(A)$ and $I_{rq}^* = 0(A)$; (refer to figure.5.21-(a and b)).
Case 2:	$I_{rd}^* = -5 (A)$ and $I_{rq}^* = -5 (A)$; (refer to figure.5.21-(c and d)),
Case 3:	$I_{rd}^* = -10 (A)$ and $I_{rq}^* = 0 (A)$; (refer to figure.5.21-(e and f)),
Case 4:	$I_{rd}^* = 0 (A)$ and $I_{rq}^* = -10 (A)$; (refer to figure.5.21-(g and h)),

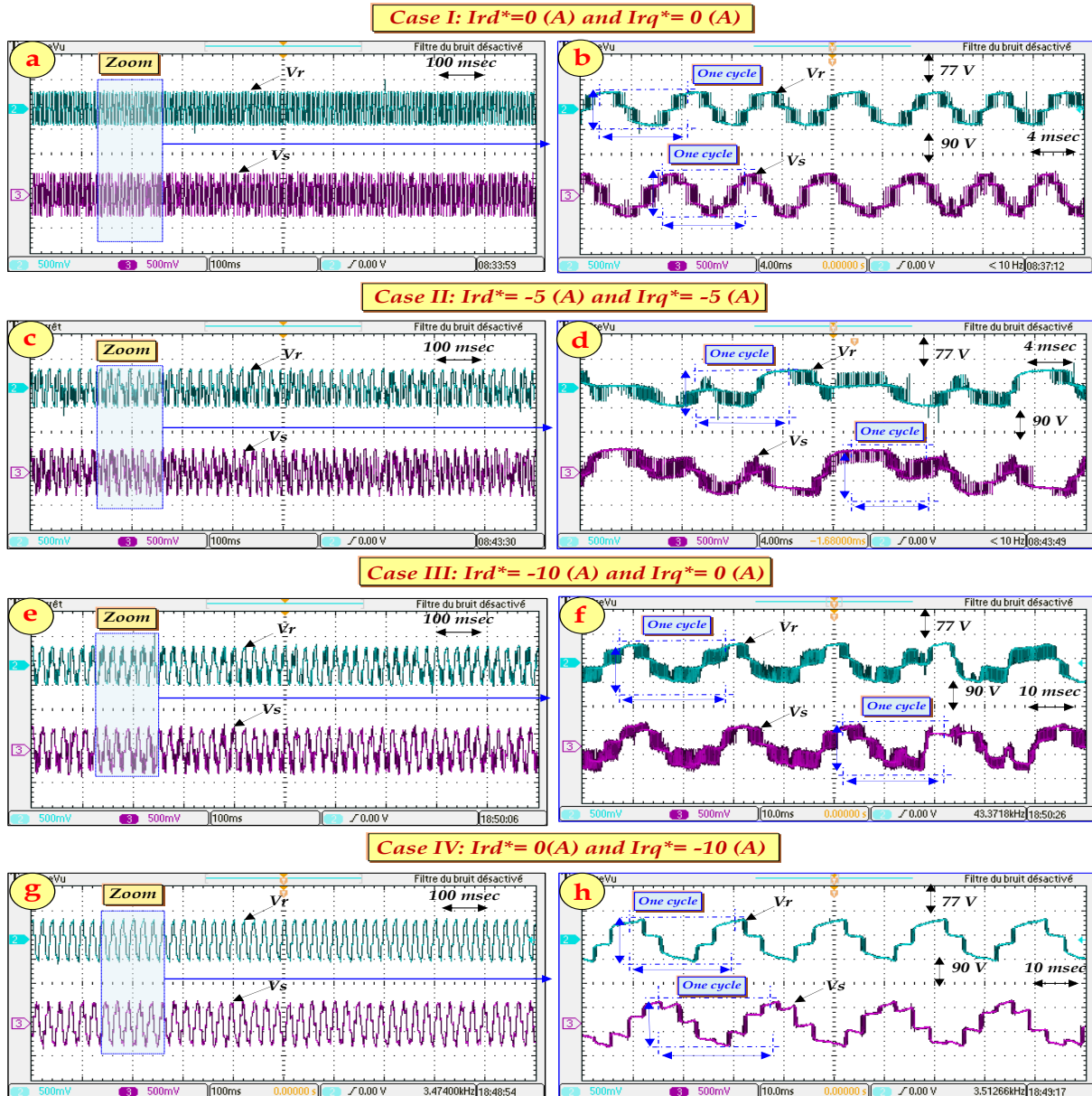


Figure.5.21 Experimental results of the rotor' and stator voltages in transient and steady states (under d-q axes rotor currents variation using L-Filter).

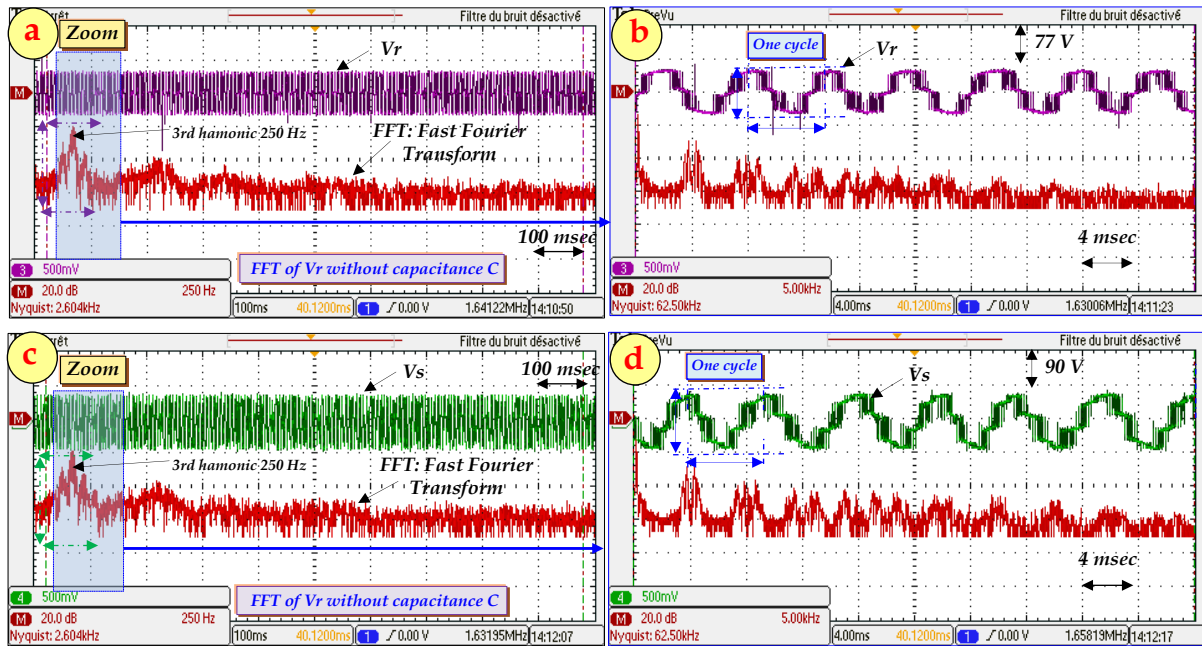


Figure.5.22 Experimental results of the rotor' and stator voltages FFT in transient and steady states (under d - q axes rotor currents variation using L-Filter).

It is clear that the waveforms of rotor' and stator voltages (V_r and V_s) have taken the same inverter's waveforms in the case of only RL-load⁷ (in zoom of each figure-case/to the right) with amplitude equals to 77 (V) for V_r and 90 (V) for V_s , means that the L-filter can't provide the sinusoidal waveforms of the rotor' and stator' voltages under currents variation (d - q axis components).

Figure.5.22 demonstrates the experimental results of rotor' and stator' voltages (V_r and V_s) waveforms respectively of whole system and theirs Fast Fourier Transform (FFT) via L-Filter in transient and steady states using the first case (same as the figure.5.21-(a and b)) in term of current variation (I_{rd}^* and I_{rq}^*) as follows:

FFT Study case⁸: $I_{rd}^* = 0(A)$ and $I_{rq}^* = 0(A)$; (refer to figure.5.22-(a and b)) illustrates the rotor waveform and it's FFT and figure.5.22-(c and d) illustrates the stator waveform and its FFT with amplitude equals to 77 (V) for V_r and 90 (V) for V_s .

It can be seen that the FFT demonstrates different impairs harmonics, in figure.5.22-(a and b) the FFT of rotor voltage (V_r) show that the 3rd harmonic equals to 250 (Hz), means the fundamental voltage signal is affected by the ripples, and it is necessary to remove/overcome this power quality drawback.

In figure.5.22-(c and d) the FFT of stator voltage (V_s) show that the 3rd harmonic equals also to 250 (Hz), means the fundamental voltage signal is affected by the undulations/ripples, and it is necessary to remove/overcome this power quality disadvantage. To overcome the 3rd harmonic, LC-Filter is proposed (refer to figure.5.20-(2)) with same system-structure.

5.5.2 Mode II: LC Filter

The LC-Filter (figure.5.20-(2)) is second order filter and it has better damping behaviors than L-Filter. This simple configuration is easy to design and it works mostly without problems. The second order filter provides 12 (dB), knowing that in this case the values of inductance and capacitance are: $L = 10$ (mH) and $C = 16.56$ (μF).

The own design of the LC-Filter is a compromise between the value of the capacity and inductance. The high capacity has positive effects on the voltage quality. On the other hand higher inductance value is required to achieve demanded cut-off frequency of the filter. Connecting system with this kind

⁷ Please refer to figure.5.18; it is clear that the stator' and rotor voltages waveforms (figure.5.21) in four cases using L-filter took the same waveforms of RL-load voltages (in the case of inverter under stand-alone mode).

⁸ In experimental study, FFT (Fast Fourier Transform) is developed using the Digital Oscilloscope. It is commonly used in digital signal processing to transform discrete time domain data to the frequency domain.

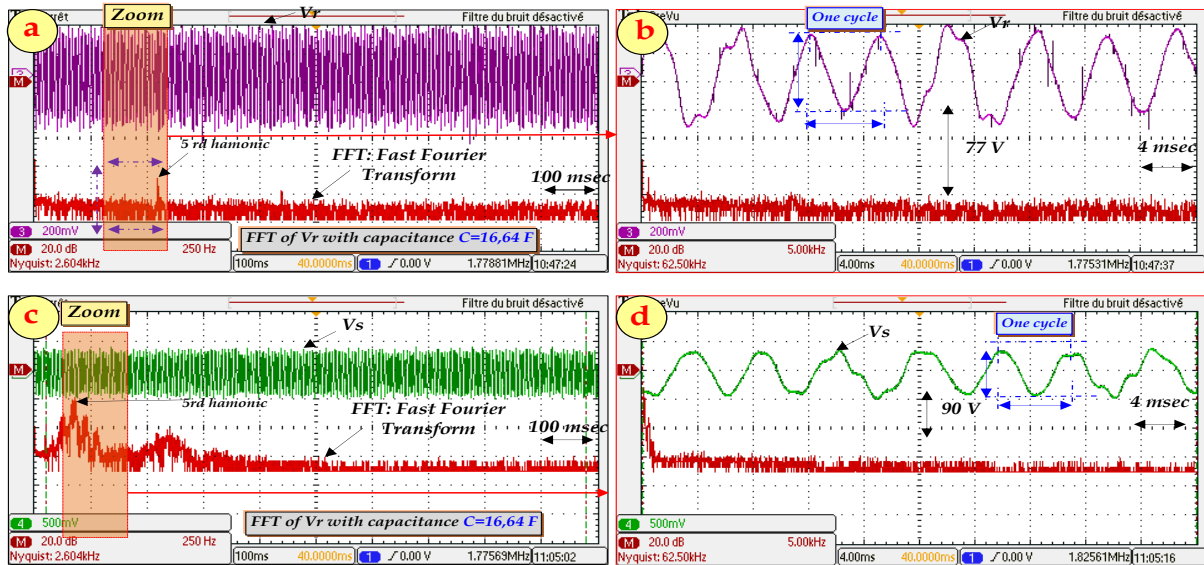


Figure.5.23 Experimental results of the rotor and stator voltages FFT in transient and steady states under d - q axes rotor currents variation using LC-Filter.

of filter to the supply grid, the resonant frequency of the filter becomes dependent on the grid impedance and therefore this filter is not suitable, too.

Figure.5.23 demonstrates the experimental results of rotor' and stator' voltages (V_r and V_s) waveforms respectively of whole system and theirs Fast Fourier Transform (FFT) via LC-Filter in transient and steady states keeping d - q axis components rotor current constant (I_{rd}^* and I_{rq}^*) as follows:

FFT Study case: $I_{rd}^* = 0(A)$ and $I_{rq}^* = 0(A)$; figure.5.23-(a and b) illustrates the rotor voltage waveform and it's FFT and figure.5.23-(c and d) illustrates the stator voltage waveform and it's FFT with amplitude equals to 77 (V) for V_r and 90 (V) for V_s .

It can be seen that the FFT demonstrates the different impairs harmonics, in figure.5.23-(a and b) the FFT of rotor voltage (V_r) show that the 5th harmonic equals to 250 (Hz), means the fundamental voltage signal is less affected by the ripples, contrary to FFT of rotor and stator voltage using L-Filter (figure.5.22).

In figure.5.23-(c and d) the FFT of stator voltage (V_s) show that the 5th harmonic equals also to 250 (Hz), means the fundamental voltage signal is less affected by the undulations/ ripples, and it is necessary to remove/or overcome this power quality drawback, contrary to FFT of rotor' and stator' voltage using L-Filter (figure.5.22).

To solve this problem, 3rd order filter is proposed; named by LCL-Filter; to make the sinusoidal waveforms of the stator' and rotor voltages with neglected harmonics (the main objective).

5.5.3 Mode III: LCL Filter

When compared with the previous topology, the LCL-filter (figure.5.20-(3)) has the advantage of providing a better decoupling between filter and DFIG impedance (reducing the dependence on DFIG parameters) and a lower ripple current stress across the grid inductor (since the current ripple is reduced by the capacitor, the impedance at the rotor side suffers less stress when compared with the LC topology). Like the LC-filter, increasing the capacitor value reduces filter cost and weight but with similar drawbacks. The split factor between the inductances at the inverter and grid side offers a further design flexibility. The attenuation of the LCL-Filter is 60 dB/decade for frequencies above resonant frequency, therefore lower switching frequency for the converter can be used. Knowing that in this case the values of inductance and capacitance are: $L_1 = 10$ (mH), $C = 66.68$ (μ F) and $L_2 = 1$ (mH). Figure.5.24 demonstrates in details the different element/parameter and values of the LCL filter (connected between the SEMIKUBE and the Rotor of DFIG). [30]

Following are a few important criteria for designing the LCL filter:

- Fulfillment of reactive volt-ampere reactive (VAR) limits (power factor nearly equals to 1).
- Optimal volume and weight with resulting minimum cost of passive (inductive and capacitive) components

- Attenuation of higher order harmonics from the output current ($THD \leq 3\%$).
- Proper choice of resonance frequency such that the switching harmonics are sufficiently attenuated and the size of the filter components is not too large.

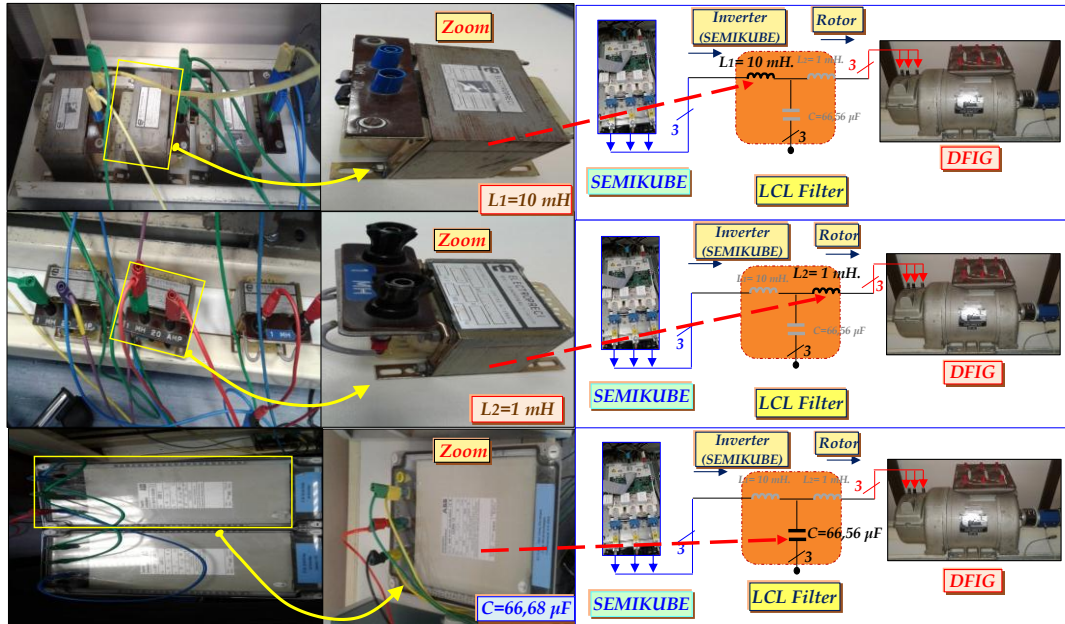


Figure.5.24 LCL's elements filter with their values.

Transfer functions are the ratios between various input to output Laplace-transformed complex currents and voltages. The most pertinent transfer function for this LCL filter (knowing that the LCL components/parameters and values are described in table.5.6) is from the inverter voltage to the rotor current that is injected and is given by:

Tbale.5.6 LCL Filter's elements with their values.

LCL components:	Description and values:
V_{Inv}	Voltage inverter (SEMIKUBE).
V_{Rotor}	Rotor voltage (80 (V))
I_{Inv}	Inverter current (A).
I_c	Capacitance current (A).
I_{Rotor}	Rotor currant (10 (A)).
L_1	Inverter side inductor (10 (mH)).
L_2	Rotor side inductance (1 (mH)).
R_1	Inverter side resistance (0.5 (Ω)).
R_2	Rotor side resistance (0.2 (Ω)).
R_D	Damping resistance (0.3 (Ω)).
C	Capacitance (66.68 (μF)).

$$H_{LCL}(p) = \frac{I_{rotor}(p)}{V_{inv}(p)} = \frac{C \cdot R_D \cdot p + 1}{D_{LCL}} \quad (5.15)$$

Where:

$$D_{LCL} = C \cdot L_1 \cdot L_2 \cdot p^3 + (C \cdot L_1 \cdot R_2 + C \cdot L_2 \cdot R_1 + C \cdot L_1 \cdot R_D + C \cdot L_2 \cdot R_D) \cdot p^2 + (L_1 \cdot L_2 + C \cdot R_1 \cdot R_2 + C \cdot R_1 \cdot R_D + C \cdot R_2 \cdot R_D) \cdot p + (R_1 \cdot R_2) \quad (5.16)$$

Obtained using the equation:

$$H_{LCL}(p) = C \cdot (p \cdot I - A)^{-1} \cdot B + D \quad (5.17)$$

Where A, B, C and D are matrices.

Figure.5.19-(b) describes the topology of an LCL filter. $V_{inv}(V)$ and $V_{Rotor}(V)$ are the inverter voltage (input) and grid voltage, respectively. Similarly, $I_{inv}(A)$, $I_c(A)$ and $I_{Rotor}(A)$ are the inverter, capacitor and the grid currents, respectively. Applying Kirchoff's voltage and current laws to figure.5.19-(b), we obtain the following:

$$I_{Inv} - I_{Rotor} = I_C \quad (5.18)$$

$$I_C = C * \frac{dV_C}{dt} \quad (5.19)$$

$$V_{L1} = L_1 * \frac{dI_{Inv}}{dt} = V_{Inv} - R_1 \cdot I_{Inv} - V_C - R_D \cdot I_C \quad (5.20)$$

$$V_{L2} = L_2 * \frac{dI_{Rotor}}{dt} = V_C - V_{Rotor} + R_D \cdot I_C - R_2 \cdot I_{Rotor} \quad (5.21)$$

Rearranging these, we get:

$$\frac{dI_{Inv}}{dt} = \frac{1}{L_1} \cdot [-(R_1 + R_D)I_{Inv} + R_D \cdot I_{Rotor} - V_C + V_{Inv}] \quad (5.22)$$

$$\frac{dI_{Rotor}}{dt} = \frac{1}{L_2} \cdot [R_D \cdot I_{Inv} - (R_2 + R_D) \cdot I_{Rotor} + V_C - V_{Rotor}] \quad (5.23)$$

$$\frac{dV_C}{dt} = \frac{1}{C} \cdot [I_{Inv} - I_{Rotor}] \quad (5.24)$$

The representation of equations: ((5.22), (5.23) and (5.24)) in state space form is:

$$\begin{pmatrix} \frac{dI_{Inv}}{dt} \\ \frac{dI_{Rotor}}{dt} \\ \frac{dV_C}{dt} \end{pmatrix} = \begin{pmatrix} -\frac{(R_1 + R_D)}{L_1} & \frac{R_D}{L_1} & -\frac{1}{L_1} \\ \frac{R_D}{L_2} & -\frac{(R_2 + R_D)}{L_2} & \frac{1}{L_2} \\ \frac{1}{C} & -\frac{1}{C} & 0 \end{pmatrix} \cdot \begin{pmatrix} I_{Inv} \\ I_{Rotor} \\ V_C \end{pmatrix} + \begin{pmatrix} \frac{1}{L_1} & 0 \\ 0 & -\frac{1}{L_2} \\ 0 & 0 \end{pmatrix} \cdot \begin{pmatrix} V_{Inv} \\ V_{Rotor} \end{pmatrix} \quad (5.25)$$

We define the state vector as:

$$x = \begin{pmatrix} I_{Inv} \\ I_{Rotor} \\ V_C \end{pmatrix} \quad (5.26)$$

And the input vector as:

$$u = \begin{pmatrix} V_{Inv} \\ V_{Rotor} \end{pmatrix} \quad (5.27)$$

The output (Y) equation:

$$Y = I_{Rotor} = (0) \cdot I_{Inv} + (1) \cdot I_{Rotor} + (0) \cdot V_C + (0) \cdot V_{Inv} + (0) \cdot V_{Rotor} \quad (5.28)$$

The state space representation of this equation is:

$$Y = (0 \quad 1 \quad 0) \cdot \begin{pmatrix} I_{Inv} \\ I_{Rotor} \\ V_C \end{pmatrix} + (0 \quad 0) \cdot \begin{pmatrix} V_{Inv} \\ V_{Rotor} \end{pmatrix} \quad (5.29)$$

Now, we write the complete state space form of the LCL filter model (equations (5.25) and (5.29) as:

$$\begin{cases} \dot{x} = A \cdot x + B \cdot u \\ y = C \cdot x + D \cdot u \end{cases} \quad (5.30)$$

Where the matrices A, B, C and D are defined as:

$$A = \begin{pmatrix} -\frac{(R_1 + R_D)}{L_1} & \frac{R_D}{L_1} & -\frac{1}{L_1} \\ \frac{R_D}{L_2} & -\frac{(R_2 + R_D)}{L_2} & \frac{1}{L_2} \\ \frac{1}{C} & -\frac{1}{C} & 0 \end{pmatrix} \quad (5.31)$$

$$B = \begin{pmatrix} \frac{1}{L_1} & 0 \\ 0 & -\frac{1}{L_2} \\ 0 & 0 \end{pmatrix} \quad (5.32)$$

$$C = (1 \quad 0 \quad 1) \quad (5.33)$$

$$D = (0 \quad 0) \quad (5.34)$$

Neglecting all the three resistances, equation (5.15) reduces to:

$$H_{LCL}(p) = \frac{1}{C \cdot L_1 \cdot L_2 \cdot p^3 + (L_1 + L_2) \cdot p} \quad (5.35)$$

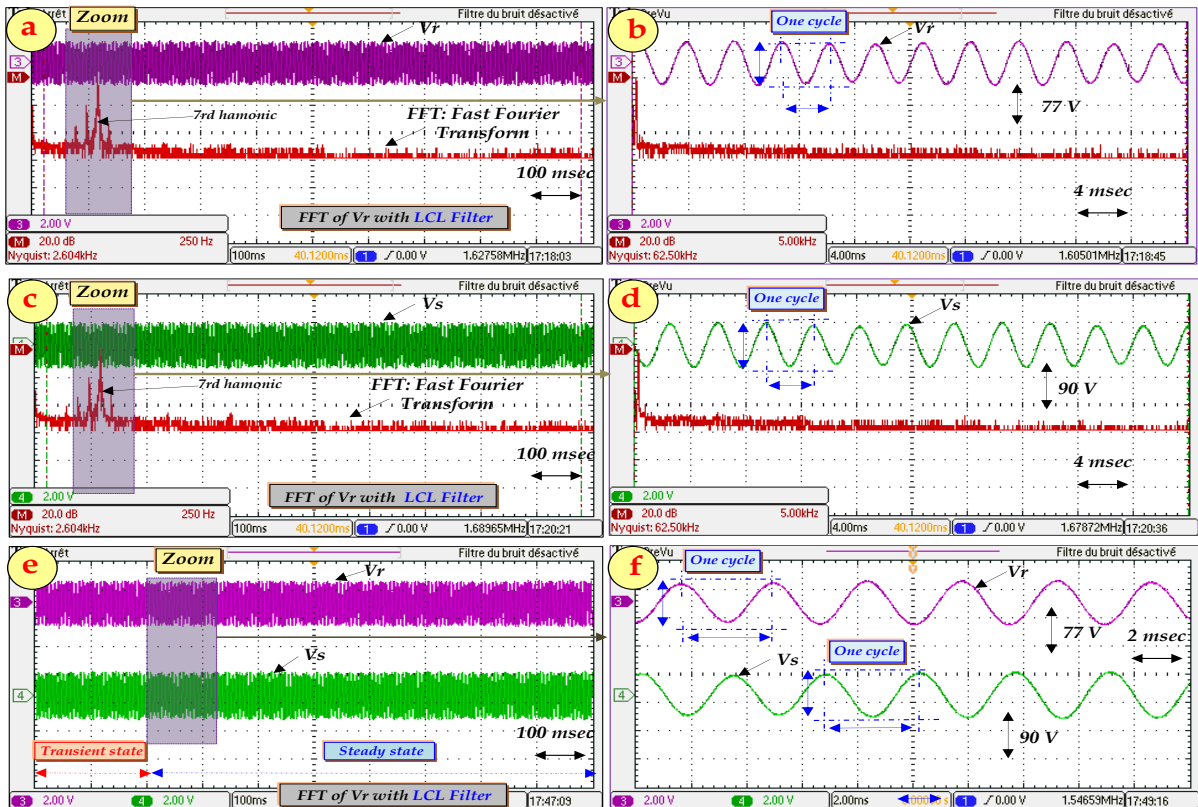


Figure.5.25 Experimental results of the rotor and stator voltages FFT in transient and steady states under d - q axis rotor currents variation using LCL-Filter.

Figure.5.25 demonstrates the experimental results of rotor’ and stator voltages (V_r and V_s) waveforms respectively of whole system and theirs Fast Fourier Transform (FFT) via LCL-Filter in transient and steady states by keeping d - q axis components rotor current constant (I_{rd}^* and I_{rq}^*) as follows:

FFT Study case: $I_{rd}^* = 0(A)$ and $I_{rq}^* = 0(A)$; (refer to figure.5.25-(a and b) illustrates the rotor voltage waveform and it’s FFT and figure.5.25-(c and d) illustrates the stator voltage waveform and its FFT with amplitude equals to 77 (V) for V_r and 90 (V) for V_s .

It can be seen that the FFT demonstrates the different impairs harmonics, in figure.5.25-(a and b) the FFT of rotor voltage (V_r) show that the 7th harmonic equals to 250 (Hz), means the fundamental voltage signal is not affected by the ripples, contrarily the FFT of rotor and stator voltage using LC-Filter (figure.5.23).

In figure.5.25-(c and d) the FFT of stator voltage (V_s) show that the 7th harmonic equals also to 250 (Hz), means the fundamental voltage signal is not affected by the undulations/ ripples. In figure.5.25-(e and f) it can be seen an excellent sinusoidal waveforms (in zoom/figure.5.25-(f)) in steady and transient states.

So, it is necessary to keep the LCL-filter in the future robustness tests especially in current and speed variation tests (Sub- and Super-synchronous operation modes).The main information which can be inspired from these experimental tests is that the DFIG’s behavior is the same as the transformer; in terms of voltage waveforms (Good/ or poor rotor voltage waveforms “presents the primary” automatically we will have as results good/ or poor stator voltage waveforms “presents the secondary”).

5.6 Robustness tests of proposed control (under Trapezoid, Step form of rotor d - q axes rotor currents)

5.6.1 Topology 1 : Stator not connected to R-L load

The objective of this case is to apply the proposed control without load (means that stator will not be connected to the R-L load (figure.5.26)), to ensure that the proposed control can work in all conditions with high performances. Knowing that the image of “torque and stator active power ($P_s^*(W)$)” is $I_{rq}^*(A)$ and the image of “flux and stator reactive power ($Q_s^*(Var)$)” is $I_{rd}^*(A)$. In this work, $I_{rq}^*(A)$ and $I_{rd}^*(A)$ take negative values (means generator mode).

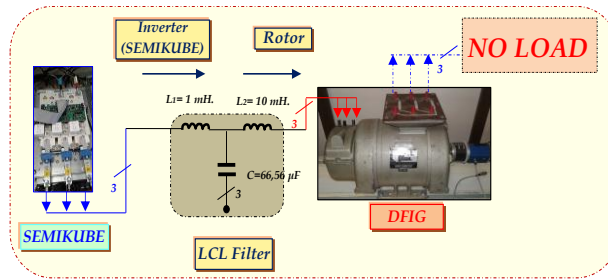


Figure.5.26 SEMIKUBE-LCL-DFIG topology without load.

Figure.5.27-(a, b and c) illustrates the experimental results of rotor current ($I_{rq}^*(A)$) variation (0 (A), -5 (A), -8 (A), -10 (A), -5 (A), 0 (A), -5 (A), -10 (A), -5 (A) and 0 (A)) in transient and steady states in the period of 100 (sec) = (10 (sec) *10). It can be seen that the rotor sinusoidal currents ($I_{r_meas}(A)$) takes the same step taking in consideration that the d-axis rotor currents component is keeping at zero level ($I_{rq}^* = 0$ (A)) (else it can be seen the amplitude variation in sinusoidal rotor current waveform $I_{r_meas}(A)$). In figure.5.27-(c) it is clear to see the good sinusoidal waveforms with excellent THD $_{I_r} \% < 5$ (%) despite the rotor current variation.

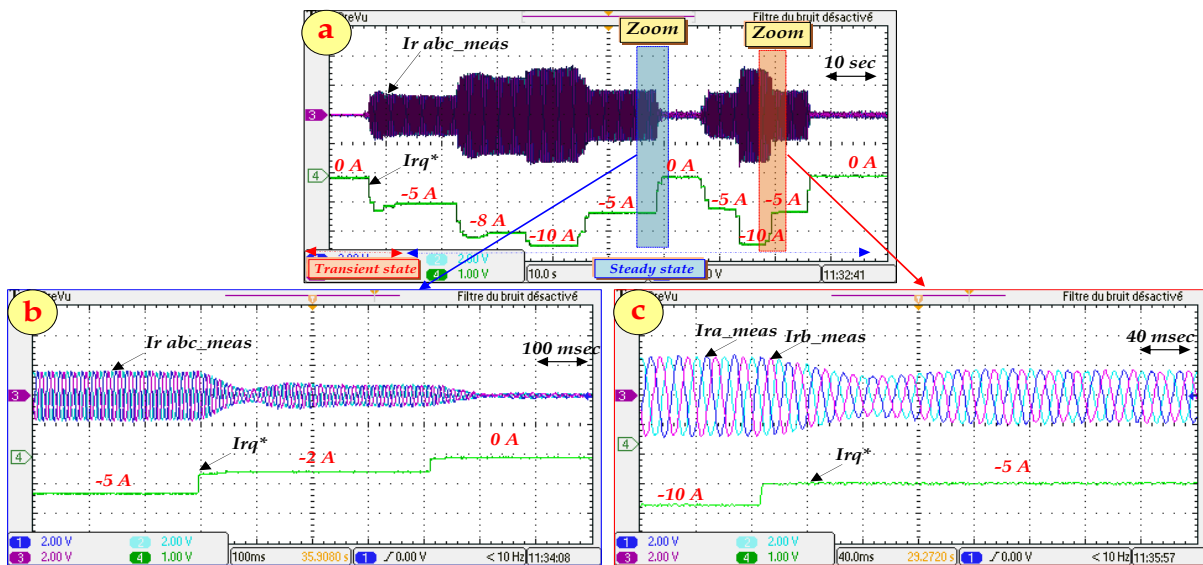


Figure.5.27 Robustness tests (rotor currents variation: $I_{r_meas}(A)$ and $I_{rq}^*(A)$) in steady and transient states without RL-load.

A- Trapezoid form:

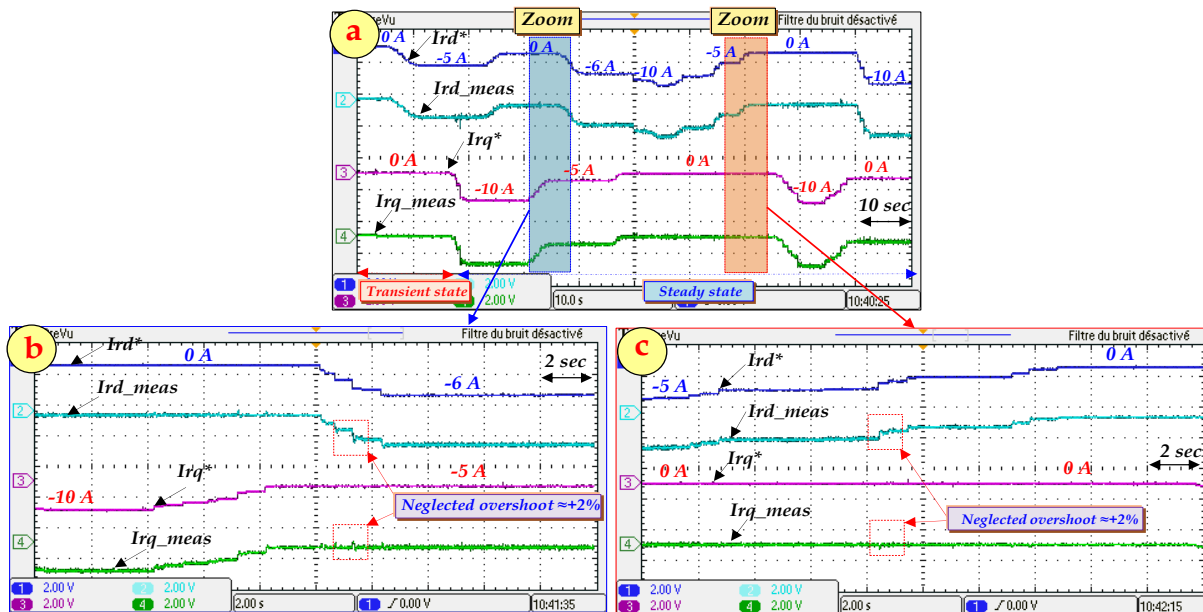


Figure.5.28 Robustness tests under Trapezoid form (rotor currents variation: $I_{rd}^*(A)$, $I_{rd_meas}(A)$ and $I_{rq}^*(A)$, $I_{rq_meas}(A)$) without RL-load.

Figure.5.28-(a) shows the experimental results of rotor direct and transversal currents ($I_{rd}^*(A)$ and $I_{rq}^*(A)$) variation ($I_{rd}^*(A)$ variation are: 0 (A), -5 (A), 0 (A), -6 (A), -10 (A), -5 (A), 0 (A), -10 (A) and $I_{rq}^*(A)$ variation are: 0 (A), -10 (A), -5 (A), 0 (A), -10 (A), 0 (A)) using trapezoid form in transient and steady states in the period of 100 (sec)=(10 (sec)*10). It can be seen that the rotor direct and transversal measured currents (I_{rd_meas} (A) and I_{rq_meas} (A)) follow exactly their reference ($I_{rd}^*(A)$ and $I_{rq}^*(A)$) respectively despite the quick variation of the $I_{rd}^*(A)$ and $I_{rq}^*(A)$ and the zoom in figure.5.28-(b) shows that the overshoot is neglected ($\approx +2\%$). In figure.5.28-(c) illustrates a perfect decoupled control between d-q axis currents components ($I_{rd}^*(A)$ and $I_{rq}^*(A)$) despite currents references variation.

B- Step form:

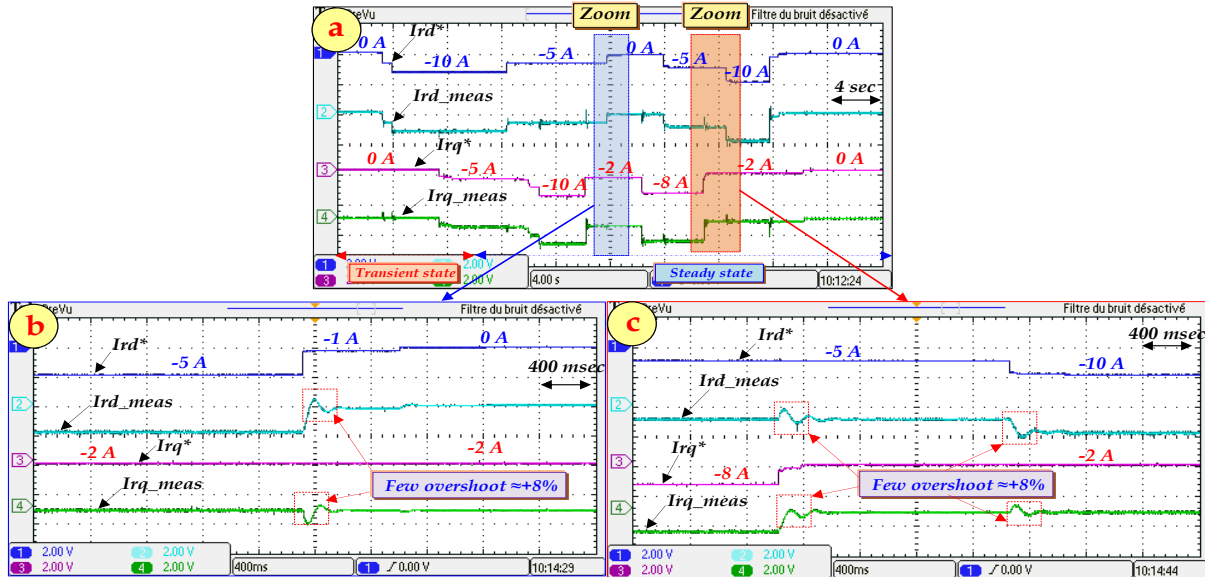


Figure.5.29 Robustness tests under Step form (rotor currents variation: $I_{rd}^*(A)$, I_{rd_meas} (A) and $I_{rq}^*(A)$, I_{rq_meas} (A)) without RL-load.

Figure.5.29-(a) shows the experimental results of rotor direct and transversal currents ($I_{rd}^*(A)$ and $I_{rq}^*(A)$) variation ($I_{rd}^*(A)$ variation are: 0 (A), -5 (A), -10 (A), -5 (A), 0 (A), -5 (A), -10 (A), 0 (A) and $I_{rq}^*(A)$ variation are: 0 (A), -5 (A), -10 (A), -2 (A), -8 (A), -2 (A), 0 (A)) using step form in transient and steady states in the period of 40 (sec)=(4 (sec)*10). It can be seen that the rotor direct and transversal measured currents (I_{rd_meas} (A) and I_{rq_meas} (A)) follow exactly their reference ($I_{rd}^*(A)$ and $I_{rq}^*(A)$) respectively despite the sudden variation of the $I_{rd}^*(A)$ and $I_{rq}^*(A)$ and the zoom in figure.5.29-(b) shows that the overshoot is few ($\approx +8\%$). In figure.5.29-(c) demonstrates a good decoupled control between d-q axis currents components ($I_{rd}^*(A)$ and $I_{rq}^*(A)$) in spite of currents reference variation. The response time is very short < 70 (msec), good tracking currents and neglected current error.

5.6.2 Topology 2 : Stator under load (connected to R-L load)

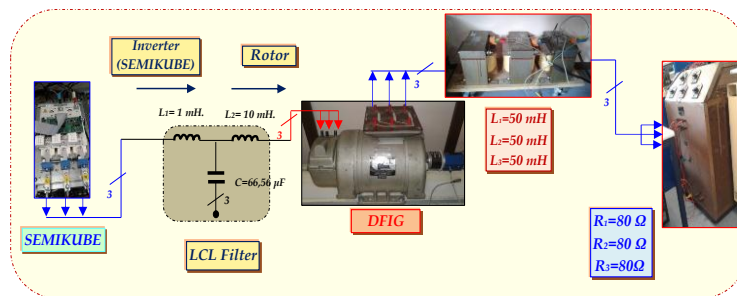


Figure.5.30 SEMIKUBE-LCL-DFIG topology with R-L load.

The main objective of this case is to apply the proposed control with R-L load, means that stator will be connected to the R-L load and this proposed control named by "Indirect power control of DFIG in Stand-alone mode (figure.5.30)"; to ensure that the proposed control can work with high performances.

A- Trapezoid form:

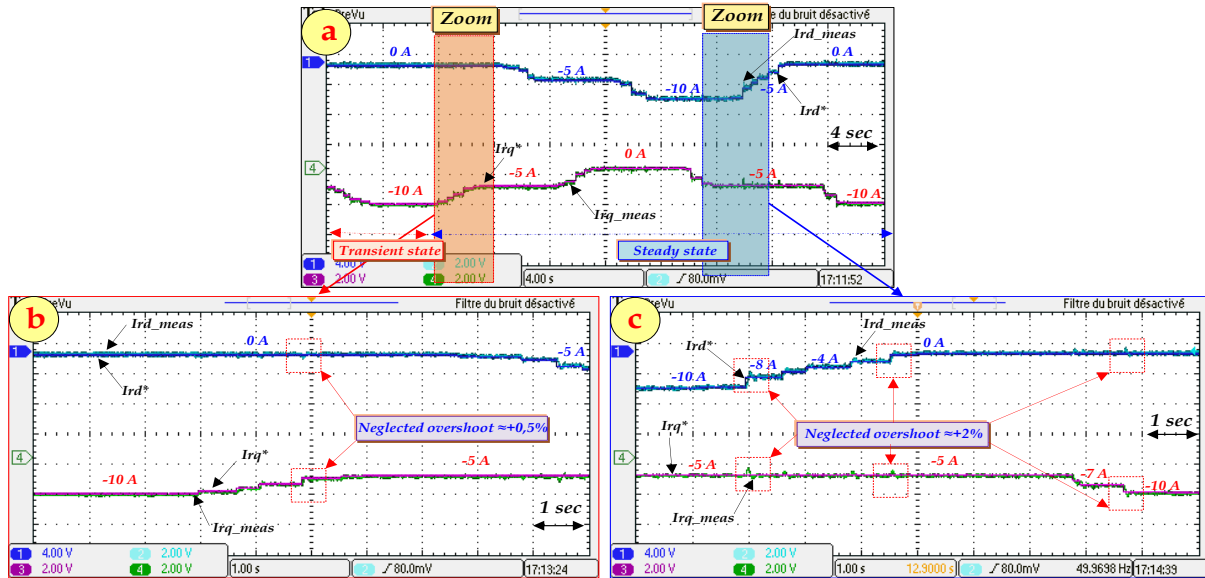


Figure.5.31 Robustness tests under trapezoid form (rotor currents variation: $I_{rd}^*(A)$, $I_{rd_meas}(A)$ and $I_{rq}^*(A)$, $I_{rq_meas}(A)$) with RL-load.

Figure.5.31-(a) shows experimental results of rotor direct and quadrature currents ($I_{rd}^*(A)$ and $I_{rq}^*(A)$) variation ($I_{rd}^*(A)$ variation are: 0 (A), -5 (A), -10 (A), -5 (A), 0 (A) and $I_{rq}^*(A)$ variation are: 0 (A), -10 (A), -5 (A), 0 (A), -5 (A), -10 (A)) using trapezoid form in transient and steady states in the period of 40 (sec)=(4 (sec)*10). It can be seen that the rotor direct and quadrature measured currents ($I_{rd_meas}(A)$ and $I_{rq_meas}(A)$) follow exactly their reference ($I_{rd}^*(A)$ and $I_{rq}^*(A)$) respectively despite the sudden variation of the $I_{rd}^*(A)$ and $I_{rq}^*(A)$ and the zoom in figure-5.31-(b) shows that the overshoot is neglected (between +0.5% and +2 %). In figure.5.31-(c) demonstrates a perfect decoupled control between d-q axis currents components ($I_{rd}^*(A)$ and $I_{rq}^*(A)$) despite currents reference variation. Knowing that the response time is short < 0.025 (sec), good current tracking and low power/current error.

B- Step form:

Figure.5.32 shows the experimental results of rotor direct and quadrature currents ($I_{rd}^*(A)$ and $I_{rq}^*(A)$) variation ($I_{rd}^*(A)$ variation are: 0 (A), -5 (A), -10 (A), 0 (A) and $I_{rq}^*(A)$ variation are: 0 (A), -10 (A), 0 (A), -5 (A), -10 (A), -5 (A), 0 (A)) under step form in transient and steady states in the period of 40 (sec) = (4 (sec)*10). It can be seen that the rotor direct and quadrature measured currents ($I_{rd_meas}(A)$ and $I_{rq_meas}(A)$) follow exactly their reference ($I_{rd}^*(A)$ & $I_{rq}^*(A)$) respectively inspite of the sudden variation of the $I_{rd}^*(A)$ & $I_{rq}^*(A)$ and the zoom in figure.5.32-

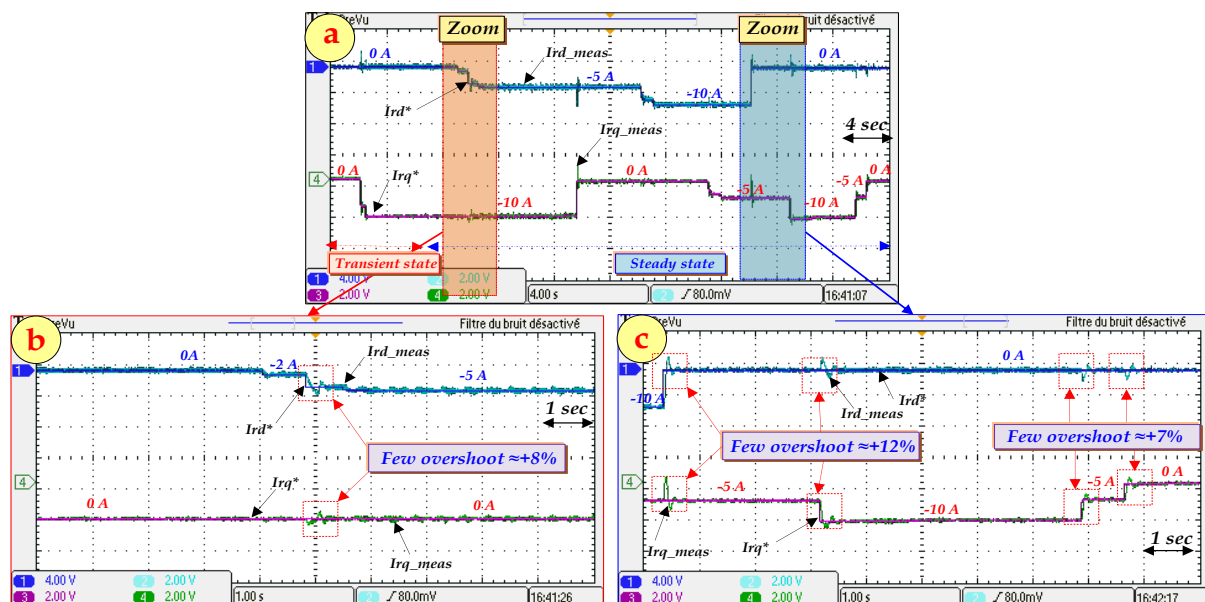


Figure.5.32 Robustness tests under Step form (rotor currents variation: $I_{rd}^*(A)$ and $I_{rd_meas}(A)$ and $I_{rq}^*(A)$, $I_{rq_meas}(A)$) with RL-load.

(b) shows that the overshoot is acceptable (not remarkable/between +7%, 8% and 12 %). In figure.5.32-(c) demonstrates a good decoupled control between d - q axes currents components ($I_{rd}^*(A)$ and $I_{rq}^*(A)$) in spite of currents reference variation. The response time is very short < 35 (msec), good tracking currents and neglected current error are noted.

5.7 Experimental results of proposed control under Sub- & Super-synchronous operations

In this section, a demonstration of Sub- and Super-synchronous operations is presented in figures.5-(33 and 35). Figure.5.34⁹ explains the relationship between: electromagnetic torque, synchronous speed and mechanical speed values in four modes (especially in generator modes/ under negative). Figures.5.33-(a and b) illustrate the experimental results of the rotor sinusoidal current variation in transient and steady states (I_{ra_meas} (A)) phase 'A' (The variation of I_{ra_meas} (A) are: with absolute values $|\pm|$: 0 (A), 5 (A), 10 (A), 6 (A), 2 (A), 0.5 (A), 10 (A), 6 (A), 0 (A), 5(A), 0 (A)”) and the slip angle variation (θ_{slip} (rad)) in transient and steady states under in the period of 40 (sec)=(4 (sec)*10). It can be seen that the variation of I_{ra_meas} (A) has no effect because

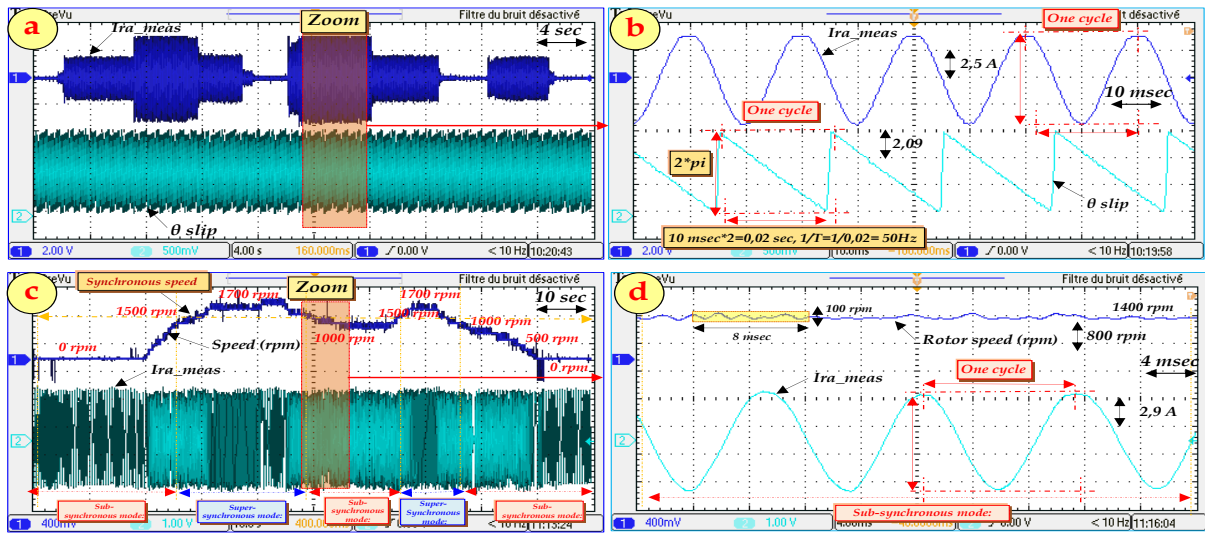


Figure.5.33 a and b: Measured rotor current variation and slip angle, c and d: Rotor speed variation and measured rotor current.

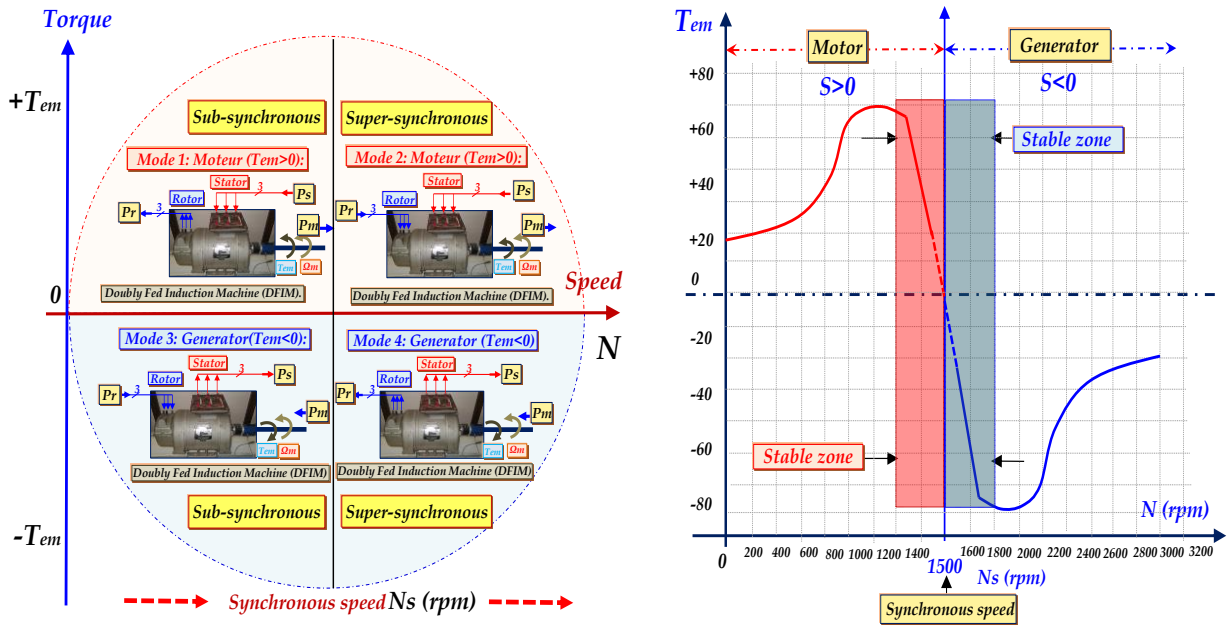


Figure.5.34 DFIG's operating modes (Motor/Generator) using Doubly Fed Induction Machine (DFIM) and Torque/speed characteristic.

⁹ Knowing that the stable zone for generator' and motor' modes (please refer to figure.5.34) is within this range (band) 1400 (rpm); 1600 (rpm). From the stable zone it can be deduced that the slip $S = (N_s - N) / N_s$ is equals to $\pm \approx (0.05 \text{ to } 0.07)$ means $\pm (5\% \text{ to } 7\%)$.

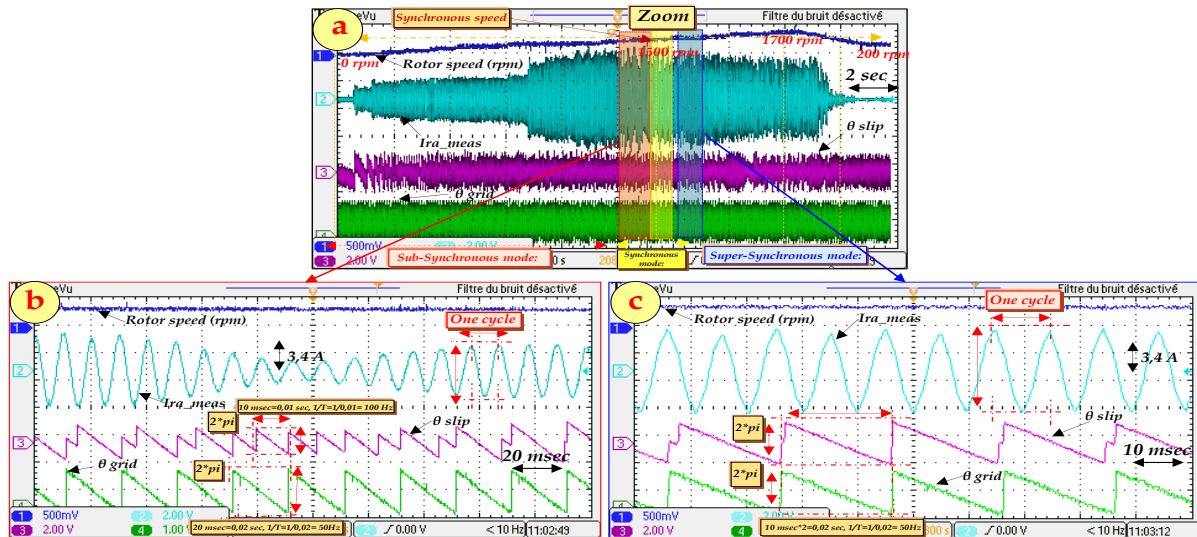


Figure.5.35 Rotor speed tests: 0 rpm, 1500 rpm, 1700 rpm and 200 rpm (Sub and Super synchronous modes) with slip' and grid angle.

because the value of slip angle theoretically based on rotor angle and grid angle (knowing that in this case the rotor angle equals to zero; means that the slip angle equal directly to grid angle because the rotor speed $\Omega_r(\text{rad/sec}) = N_r^{10}(\text{rpm}) = 0 (\text{rpm})$; please refer to equation.6.25/Chapter.6). Figures.5.33-(c and d) present the behavior of the rotor measured current waveform in transient and steady states in the period of 100 (sec) = (10 (sec)*10) (I_{ra_meas} (A); knowing that the peak to peak current magnitude equals to 10 (A) under rotor speed variation (The variation of N_r (rpm): 0, 1500, 1700, 1000, 1500, 1700, 1000, 500 and 0 respectively); knowing that 1500 (rpm) presents the synchronous speed, it can be seen the Sub-synchronous operation (less than 1500 (rpm)) and Super-synchronous operation (more than 1500 (rpm)) . From figure.5.33-(d) it can be zoom of steady state of the figure.5.33-(c) in synchronous speed ($N_r = 1500$ (rpm)). It can be seen also that the rotor current frequency varied as-for-as the variation of speed between the Sub- and Super-synchronous operations.

Figure.5.35 shows the experimental results of the behavior of the rotor currents waveform, slip angle and grid angle under rotor speed variation in transient and steady states in the period of 20 (sec) = (2 (sec) *10). It is easy to determinate the rotor frequency from the rotor current waveforms and from the grid and slip angles. Figure.5.35-(a) is divided into 3 modes as-for-as the rotor speed Ω_r (rpm) as follows; the Sub-synchronous mode $N_r < 1500$ (rpm), Synchronous mode $N_r = 1500$ (rpm) and the Super-synchronous mode >1500 (rpm). Figure.5.35-(b) illustrates the Sub-synchronous mode it can be seen the rotor current magnitude nearly 6 (A) with an speed rotor increasing in 160 (msec) = (20 (msec)*8) on to 1700 (rpm), in this case the slip angle frequency ($f_{slip} = 1/T_{slip} = 1/0.01(\text{msec}) = 100$ (Hz)) is more than the grid angle frequency ($f_{grid} = 1/T_{grid} = 1/0.02(\text{msec}) = 50$ (Hz)). Figure.5.35-(c) presents the Synchronous mode based on synchronous speed $N_r = 1500$ (rpm) in the period of 100 (msec) = (10 (sec)*10), it can be seen that the rotor current magnitude equals to 10 (A) and the slip angle frequency equals to the grid angle frequency ($f_{slip} = f_{grid} = 50$ (Hz)).

5.7.1 Case 1 : $N_r = 0$ (rpm)

Figure.5.36-(a, b and c) shows the experimental results of the behavior (at zero rotor speed $N_r = 0$ (rpm) $\ll N_{Synchronous} = 1500$ (rpm)) of measured rotor and stator currents waveforms (I_{ra_meas} (A) and I_{sa_meas} (A)) under direct and quadrature currents ($I_{rd}^*(A)$ and $I_{rq}^*(A)$) variation ($I_{rd}^*(A)$ variation are: -5 (A), -10 (A), 0 (A), -5(A), -10 (A) and $I_{rq}^*(A)$ variation are: 0 (A), -5 (A), -10 (A), 0 (A)) using Step form in transient and steady states in the period of 40 (sec) = (4 (sec)*10); "Knowing that in this case the stator is connected into the RL-load". Figure.5.36-(b) presents the zoom of figure.36.(a) in steady state in the period of 400 msec (40 (msec)*10), it can be seen an excellent sinusoidal waveform of rotor and stator currents and the angle between them is nearly equals to $+180^\circ$; "knowing that in this case: $I_{rd}^*(A) = 0$ (A) and $I_{rd}^*(A) = -10$ (A), and at on cycle it can be concluded the rotor and stator frequencies; f_{rotor} (Hz) = $1/T_{rotor}(\text{msec}) = 1/0.5*40(\text{msec}) = 1/20$ (msec) = 50 (Hz), and f_{stator} (Hz)=

¹⁰ Knowing that N_r is measured in 'rpm' and Ω_r in 'rad/sec', Exp: in synchronous speed, we have $N_s = 1500 * (2.\pi) (\text{rad}) / 60 (\text{sec}) = 157 (\text{rad/sec}) = \Omega_s$.

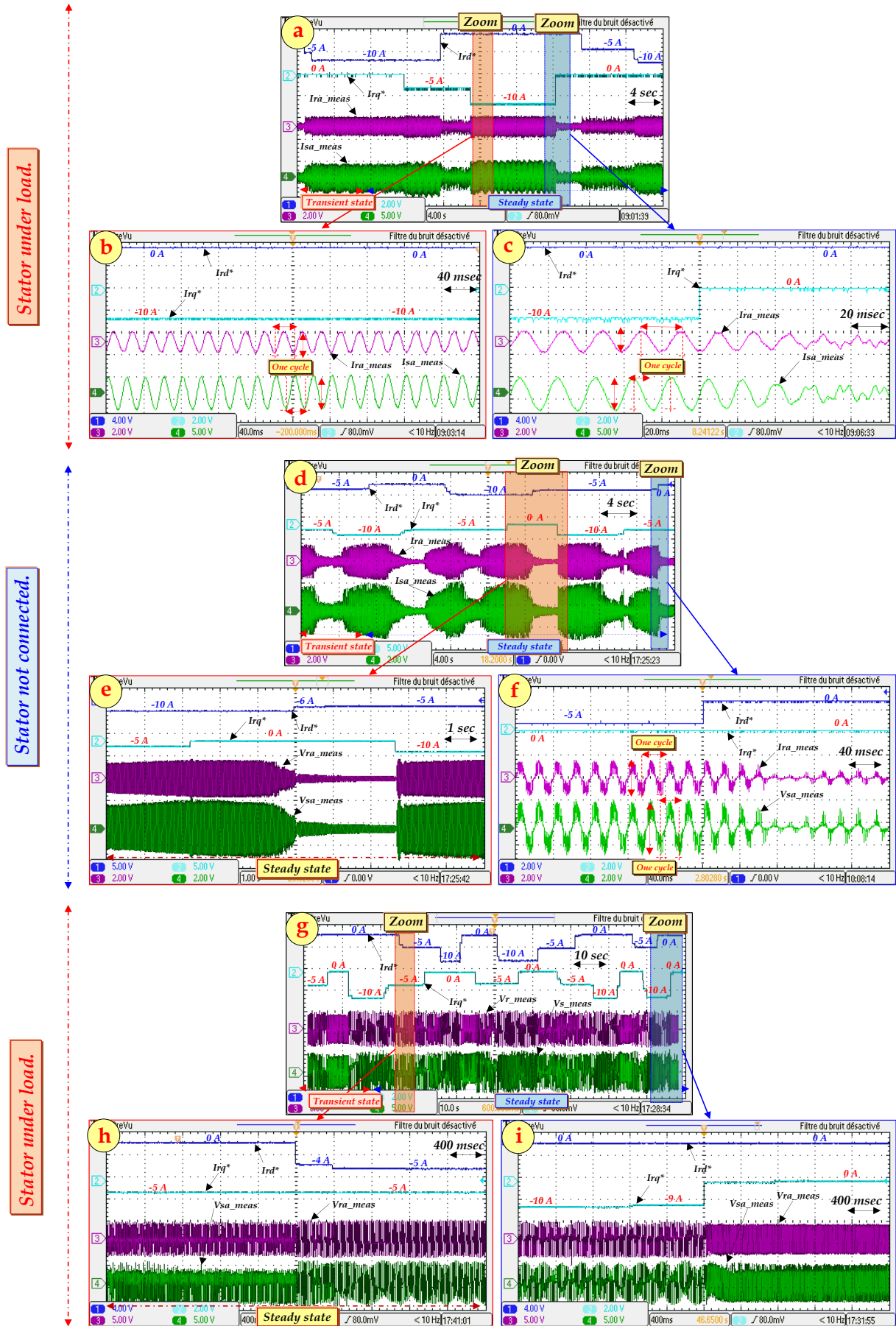


Figure.5.36 Rotor and stator voltages behavior under currents variation ($I_{rd}^*(A)$ and $I_{rq}^*(A)$) at 0 rpm with/without load.

$f_{grid}(Hz)=1/0.5*40$ (msec) = 50 (Hz), means f_{rotor} (Hz) = f_{stator} (Hz)". Figure.5.36-(c) presents the zoom of figure.36-(a) in steady state in the period of 200 (msec) = (20 (msec)*10) but using another conditions. It can be seen an excellent sinusoidal waveforms of rotor and stator currents and the angle between them is nearly +120°; due the rotor quadrature $I_{rq}^*(A)$ current variation from -10 (A) to 0 (A) and be keeping rotor direct current equals to zero level ($I_{rd}^*(A) = 0(A)$) in the period of 200 (msec) = (20 (msec)*10).

Figure.5.36-(d, e and f) illustrate the behavior (at zero rotor speed $N_r = 0$ (rpm)) of measured rotor and stator voltages ($I_{ra_meas}(A)$ and $I_{sa_meas}(A)$) waveforms under direct and quadrature currents ($I_{rd}^*(A)$ and $I_{rq}^*(A)$) variation ($I_{rd}^*(A)$ variation are: -5 (A), 0 (A), -10 (A), -5(A), 0 (A) and $I_{rq}^*(A)$ variation are: -5 (A), -10 (A), -5 (A), 0 (A) -10 (A), -5 (A)) using Step form in transient and steady states in the period of 40 (sec) = (4 (sec)*10); "Knowing that in this case the stator is not connected into the RL-load and L-filter is connected between the DFIG's rotor and the SEMIKUBE". Figure.5.36-(e) presents the zoom of figure.36.(d) in steady state in the period of 400 (msec) = (40 (msec)*10), it can be seen a bad sinusoidal waveform of rotor and stator voltages and to overcome these ripples/harmonics; refer to § 5.5.3¹¹ (using LCL-filter to improve the rotor and stator voltages); knowing that in this case: $I_{rd}^*(A)$ is varying in these values: -10 (A), -6 (A), -5 (A) and $I_{rq}^*(A)$ is varying in these values: -5 (A), 0 (A), -10 (A), it can be seen also that in each d-q axes current components variation the rotor and stator voltages follow exactly these variation. Figure.5.36-(f) presents the zoom of figure.36-(d) in steady state in the period of 400 (msec) = (40 (msec)*10) but in another conditions; knowing that in is this case: $I_{rd}^*(A)$ is varying in these values: -5 (A), 0 (A) and $I_{rq}^*(A)$ is keeping at zero level: 0 (A), it clear that rotor and stator voltage follow exactly the d-q axes currents variation in terms of magnitude and frequency.

Figure.5.36-(g, h and i) shows the experimental results of the behavior (at zero rotor speed $N_r = 0$ (rpm)) of measured rotor and stator voltages ($I_{ra_meas}(A)$ and $I_{sa_meas}(A)$) waveforms under direct and quadrature currents ($I_{rd}^*(A)$ and $I_{rq}^*(A)$) variation ($I_{rd}^*(A)$ variation are: 0 (A), -5 (A), -10 (A), 0 (A), -10 (A), -5 (A), 0 (A), -5 (A), 0 (A) and $I_{rq}^*(A)$ variation are: -5 (A), 0 (A), -10 (A), 0 (A), -5 (A), 0 (A), -5 (A), -10 (A), 0 (A), -10 (A), 0 (A)) using Step form in transient and steady states in the period of 100 (sec) = (10 sec*10); "Knowing that in this case the stator is connected into the RL-load and L-filter is connected between the DFIG's rotor and the SEMIKUBE". Figure.5.36-(h) presents the zoom of figure.36.(g) in steady state in the period of 400 (msec) = (40 (msec)*10); knowing that in is this case: $I_{rd}^*(A)$ is varying in these values: 0 (A), -4 (A), -5 (A) and $I_{rq}^*(A)$ is keeping at: -5 (A), it can be seen also that in each d-q axes current components variation the rotor and stator voltages follow exactly these variation. Figure.5.36-(i) presents the zoom of figure.36-(g) in steady state in the period of 400 (msec) = (40 (msec)*10) but in another conditions; knowing that in this case: $I_{rd}^*(A)$ is keeping at zero level: 0 (A) and $I_{rq}^*(A)$ is varying in these values: -10 (A), -9 (A), 0 (A), it clear that rotor and stator voltage follow exactly the d-q axes currents variation in terms of magnitude and frequency.

5.7.2 Case 2 : $N_r = 500$ (rpm)

Figure.5.37 shows the experimental results of the behavior (at rotor speed $N_r = 500$ (rpm) < $N_{Synchronous} = 1500$ (rpm)) of measured rotor and stator currents ($I_{ra_meas}(A)$ and $I_{sa_meas}(A)$) waveforms under direct and quadrature currents ($I_{rd}^*(A)$ and $I_{rq}^*(A)$) variation ($I_{rd}^*(A)$ variation are: 0 (A), -4 (A), -5 (A), 0 (A) and $I_{rq}^*(A)$ variation are: 0 (A), -6 (A), -10 (A), 0 (A)) using Step form in transient and steady states in the period of 40 (sec) = (40 sec*10); "Knowing that in this case the stator is connected into the RL-load". Figure.5.37-(b) presents the zoom of figure.37.(a) in steady state in the period of 200 (msec) = (20 (msec)*10), it can be seen an excellent sinusoidal waveforms of rotor and stator currents despite the d-q axes current's components variation; knowing that in this case: $I_{rd}^*(A)$ is keeping at value: -5 (A) and $I_{rq}^*(A)$ is keeping at: -10 (A), and at one cycle it can be concluded the rotor and stator frequencies; " f_{rotor} (Hz) = $1/T_{rotor}(msec) = 1/1.5 * 20(msec) = 1/30$ (msec) = 33.33 (Hz), and f_{stator} (Hz)= f_{grid} (Hz)= $1/1*20$ (msec) = 50 (Hz) means f_{rotor} (Hz) < f_{stator} (Hz)". Figure.5.37-(c) presents the zoom of figure.37-(a) in steady state in the period of 400 (msec) = (40 (msec)*10) but in another conditions; knowing that in this case: $I_{rd}^*(A)$ is keeping at zero level: 0 (A) and $I_{rq}^*(A)$ is varying in these values: -10 (A), 0 (A), it can be seen an excellent sinusoidal waveforms of rotor and stator currents in steady state despite the d-q axes current's components variation, and at one cycle it can be concluded the rotor and stator frequencies; " f_{rotor} (Hz)

¹¹ Please refer to paragraph § 5.5.3 (Mode III: LCL Filter).

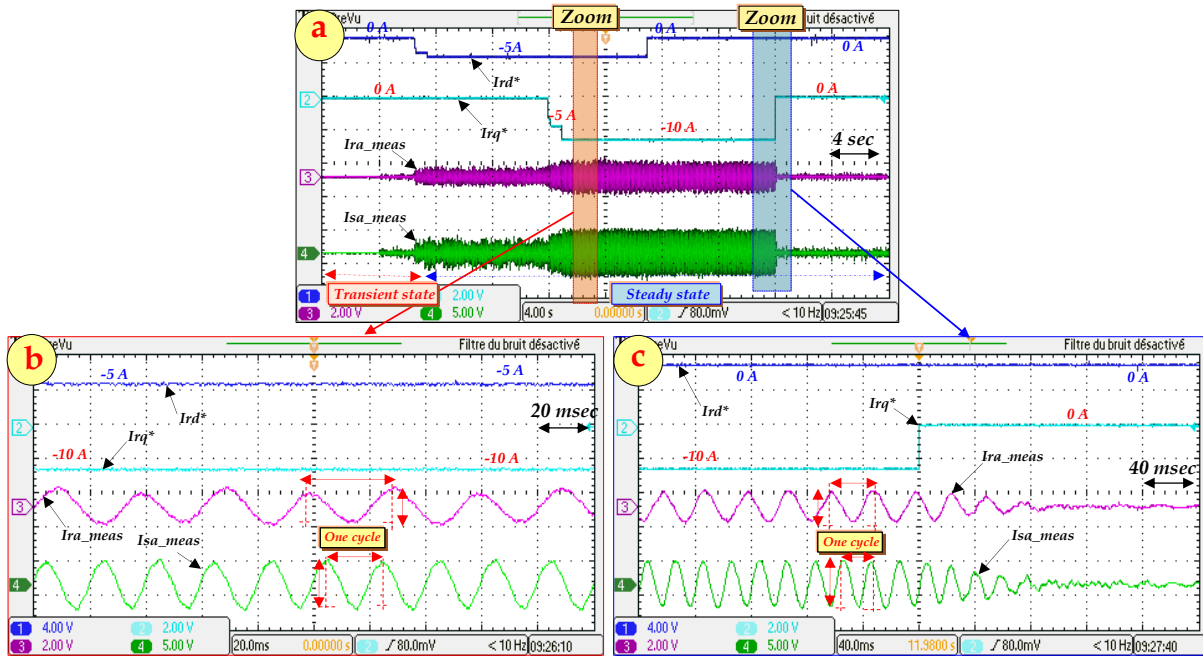


Figure.5.37 Rotor currents variation ($I_{rd}^*(A)$ and $I_{rq}^*(A)$) under 500 (rpm) with RL-load.

= 33.33 (Hz) means f_{rotor} (Hz) < f_{stator} (Hz)''.

5.7.3 Case 3 : $N_r = 1000$ (rpm)

Figure.5.38 shows the experimental results of the behavior (at rotor speed $N_r = 1000$ (rpm) < $N_{Synchronous} = 1500$ (rpm)) of measured rotor and stator currents ($I_{ra_meas}(A)$ and $I_{sa_meas}(A)$) waveforms under direct and quadrature currents ($I_{rd}^*(A)$ and $I_{rq}^*(A)$) variation ($I_{rd}^*(A)$ variation are: 0 (A), -4 (A), -5 (A), 0 (A) and $I_{rq}^*(A)$ variation are: 0 (A), -5 (A), -10 (A), 0 (A)) using Step form in transient and steady states in the period of 40 (sec) = (40 (sec) * 10); "Knowing that in this case the stator is connected into the RL-load". Figure.5.38-(b) presents the zoom of figure.38-(a) in steady state in the period of 400 (msec) = (40 (msec) * 10), it can be seen an excellent sinusoidal wa-

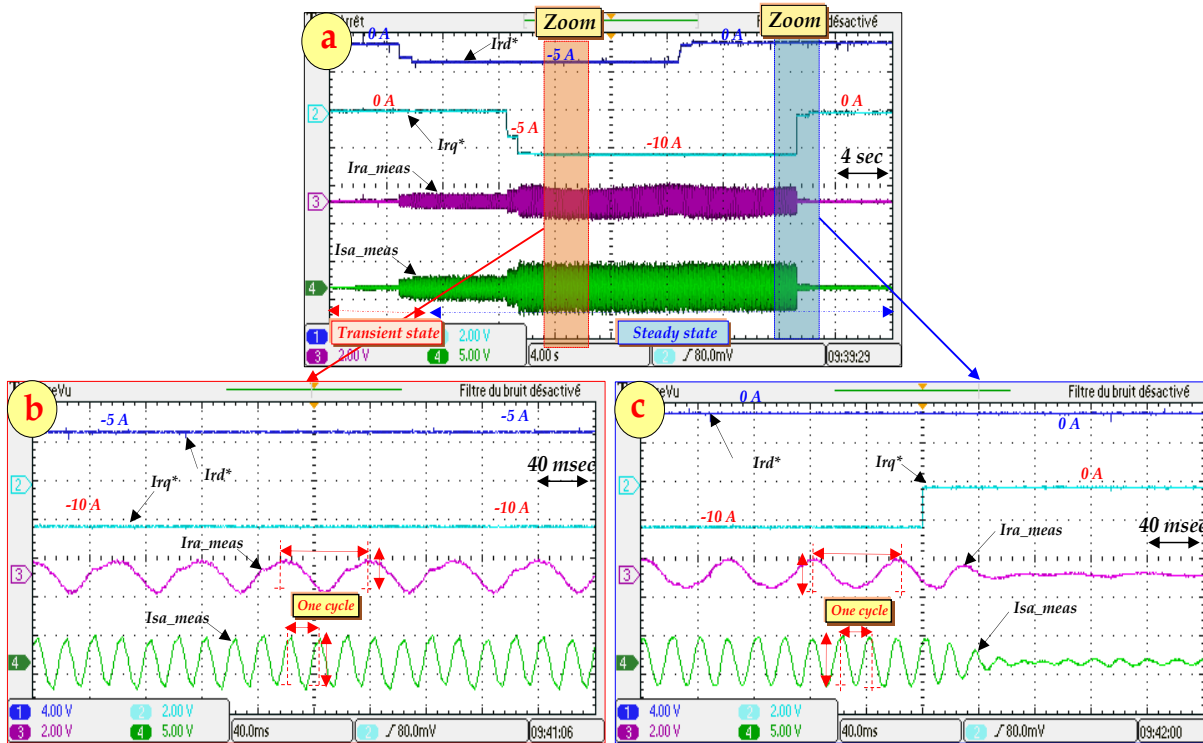


Figure.5.38 Rotor currents variation ($I_{rd}^*(A)$ and $I_{rq}^*(A)$) under 1000 (rpm) with RL-load.

-veforms of rotor and stator currents despite the d-q axes current's components variation with neglected ripples; knowing that in this case: $I_{rd}^*(A)$ is keeping at value: -5 (A) and $I_{rq}^*(A)$ is keeping at: -10 (A), and at one cycle it can be concluded the rotor and stator frequencies; " $f_{rotor} (Hz) = 1/ T_{rotor}(msec) = 1/1.5 * 40(msec) = 1/60 (msec) \approx 16.67 (Hz)$, and $f_{stator} (Hz)= f_{grid} (Hz)=1/0.5*40 (msec) = 50 (Hz)$ means $f_{rotor} (Hz) < f_{stator} (Hz)$ ". Figure.5.38-(c) presents the zoom of figure.38-(a) in steady state in the period of 400 (msec) = (40 (msec)*10) but in another conditions; knowing that in this case: $I_{rd}^*(A)$ is keeping at zero level: 0 (A) and $I_{rq}^*(A)$ is varying in these values: -10 (A), 0 (A), it can be seen an excellent sinusoidal waveforms of rotor and stator currents in steady state despite the d-q axes current's components variation, and at one cycle it can be concluded the rotor and stator frequencies; " $f_{rotor} (Hz) = 1/ T_{rotor}(msec) = 1/1.5 * 40(msec) = 1/60 (msec) \approx 16.67 (Hz)$, and $f_{stator} (Hz)= f_{grid} (Hz)=1/0.5*40 (msec) = 50 (Hz)$ means $f_{rotor} (Hz) \ll f_{stator} (Hz)$ ".

5.7.4 Case 4 : $N_r = 1500 (rpm)$

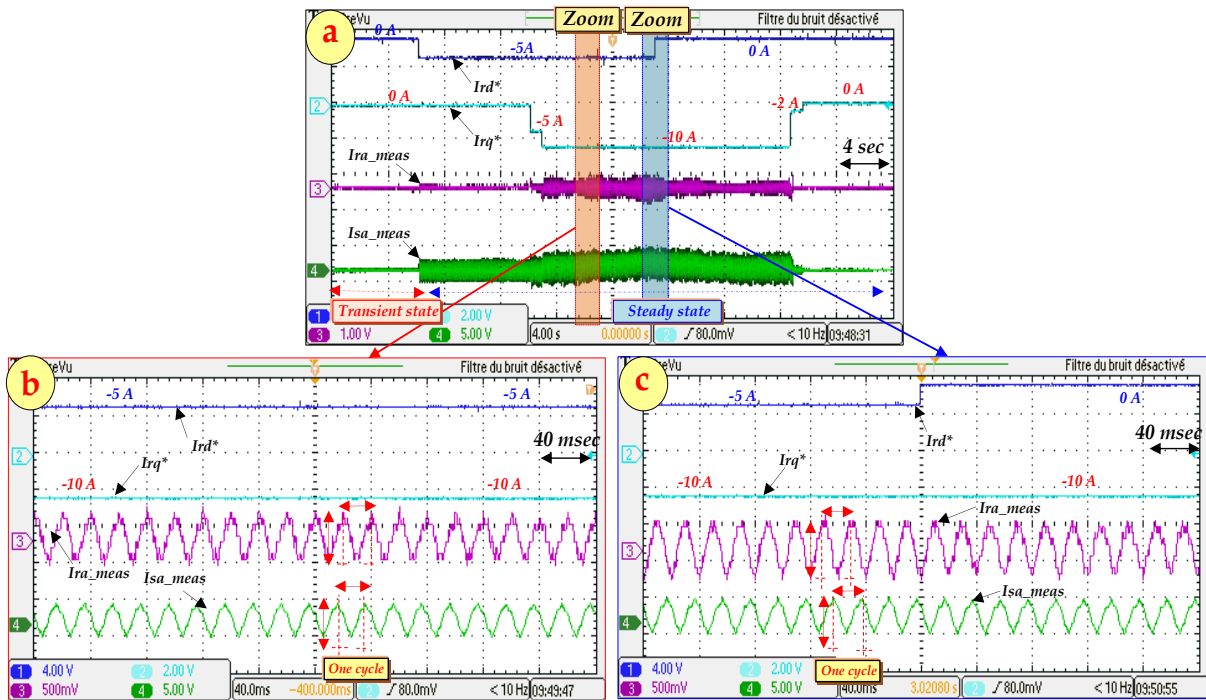


Figure.5.39 Rotor currents variation ($I_{rd}^*(A)$ and $I_{rq}^*(A)$) under 1500 (rpm) with RL-load.

Figure.5.39 shows the experimental results of the behavior (at rotor speed $N_r = 1500 (rpm)$ = Synchronous speed $N_{Synchronous} (rpm)$) of measured rotor and stator currents ($I_{ra_meas}(A)$ and $I_{sa_meas}(A)$) waveforms under direct and quadrature currents ($I_{rd}^*(A)$ and $I_{rq}^*(A)$) variation ($I_{rd}^*(A)$ variation are: 0 (A), -5 (A), 0 (A) and $I_{rq}^*(A)$ variation are: 0 (A), -5 (A), -10 (A), -2 (A), 0 (A)) using Step form in transient and steady states in the period of 40 (sec) = (40 (sec)*10); "Knowing that in this case the stator is connected into the RL-load". Figure.5.39-(b) presents the zoom of figure.39.(a) in steady state in the period of 400 (msec) = (40 (msec) *10), it can be seen good sinusoidal waveforms of rotor and stator currents despite the d-q axis current's components variation with neglected ripples; knowing that in this case: $I_{rd}^*(A)$ is keeping at value: -5 (A) and $I_{rq}^*(A)$ is keeping at: -10 (A), and at one cycle it can be concluded the rotor and stator frequencies; " $f_{rotor} (Hz) = 1/ T_{rotor}(msec) = 1/0.5 * 40(msec) = 1/20 (msec) \approx 50 (Hz)$, and $f_{stator} (Hz)= f_{grid} (Hz)=1/0.5*40 (msec) = 50 (Hz)$ means $f_{rotor} (Hz) = f_{stator} (Hz)$ ", knowing that the angle between the rotor and stator currents is nearly to 0° , this is the inverse case comparing to Case I " $\Omega_r = 0 (rpm)$ ". Figure.5.39-(c) presents the zoom of figure.39-(a) in steady state in the period of 400 (msec) = (40 (msec)*10) but in another conditions; knowing that in this case: $I_{rd}^*(A)$ is varying in these values: -5 (A), 0 (A) and $I_{rq}^*(A)$ is keeping at this value: -10 (A), it can be seen good sinusoidal waveforms of rotor and stator currents in steady state despite the d-q axis current's components variation, and at one cycle it can be concluded the rotor and stator frequencies; " $f_{rotor} (Hz) = 1/ T_{rotor}(msec) = 1/0.5 * 40(msec) = 1/20 (msec) = 50 (Hz)$, and $f_{stator} (Hz)= f_{grid} (Hz)=1/0.5*40 (msec) = 50 (Hz)$ means $f_{rotor} (Hz) = f_{stator} (Hz)$ ".

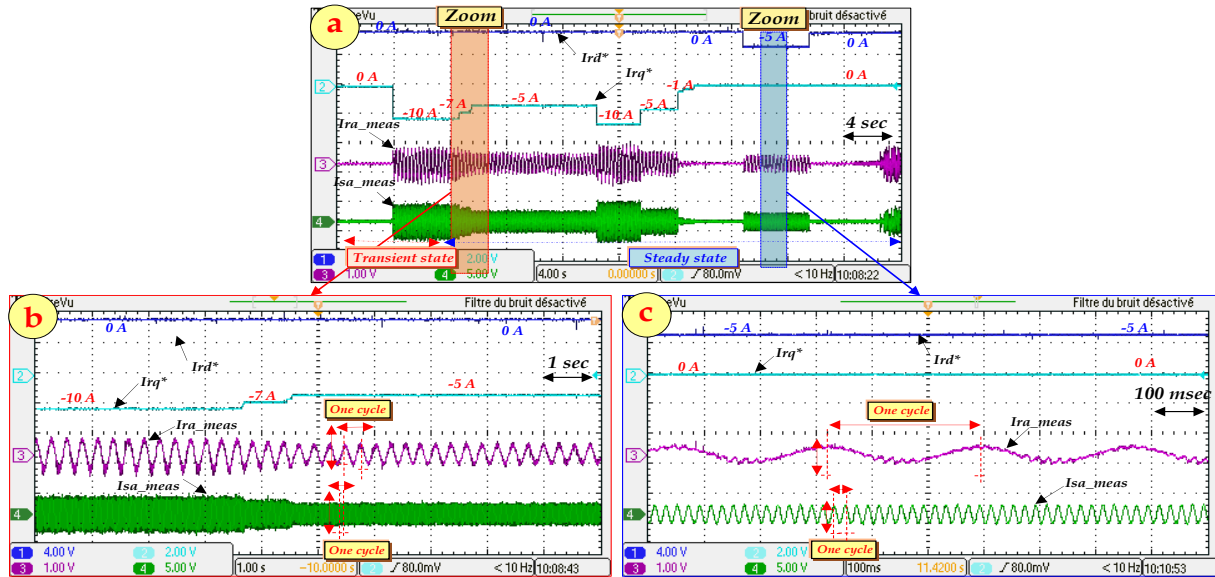
5.7.5 Case 5 : $N_r = 1700$ (rpm)

Figure.5.40 Rotor currents variation ($I_{rd}^*(A)$ and $I_{rq}^*(A)$) under 1700 (rpm) with RL-load.

Figure.5.40 shows the experimental results of the behavior (at rotor speed $N_r = 1700$ (rpm) $> N_{Synchronous}$ (rpm)) of measured rotor and stator currents ($I_{ra_meas}(A)$ and $I_{sa_meas}(A)$) waveforms under direct and quadrature currents ($I_{rd}^*(A)$ and $I_{rq}^*(A)$) variation ($I_{rd}^*(A)$ variation are: 0 (A), -5 (A), 0 (A) and $I_{rq}^*(A)$ variation are: 0 (A), -10 (A), -7 (A), -5 (A), -10 (A), -5 (A), -1 (A), 0 (A)) using Step form in transient and steady states in the period of 40 (sec) = (40 (sec)*10); "Knowing that in this case the stator is connected into the RL-load". Figure.5.40-(b) presents the zoom of figure.40.(a) in steady state in the period of 10 (msec) = (1 (msec) *10), it can be seen good sinusoidal waveforms of rotor and stator currents despite the d-q axes current's components variation with neglected ripples; knowing that in is this case: $I_{rd}^*(A)$ is keeping at zero level: 0 (A) and $I_{rq}^*(A)$ is varying in these values: -10 (A), -7 (A), -5 (A) and at one cycle it can be concluded the rotor and stator frequencies; " f_{rotor} (Hz) = $1/T_{rotor}(msec) = 1/0.3 * 1(sec) = 1/0.3$ (sec) ≈ 3.33 (Hz), and f_{stator} (Hz) = f_{grid} (Hz) = $1/((1/50)*1 (sec)) = 1/20$ (msec) = 50 (Hz) means f_{rotor} (Hz) $\ll f_{stator}$ (Hz)". Figure.5.40-(c) presents the zoom of figure.40-(a) in steady state in the period of 1 (sec) = (100 (msec)*10) but in another conditions; knowing that in is this case: $I_{rd}^*(A)$ is keeping at this value : -5 (A) and $I_{rq}^*(A)$ is keeping at zero level: 0 (A), it can be seen excellent sinusoidal waveforms of rotor and stator currents in steady state despite the d-q axes current's components variation, and at one cycle it can be concluded the rotor and stator frequencies; " f_{rotor} (Hz) = $1/T_{rotor}(msec) = 1/(3 * 100(msec)) = 1/300$ (msec) ≈ 3.33 (Hz), and f_{stator} (Hz) = f_{grid} (Hz) = $1/((1/5)*100 (msec)) = 1/20$ (msec) = 50 (Hz) means f_{rotor} (Hz) $\ll f_{stator}$ (Hz)".

The proposed experimental algorithm (IDPC based on stand-alone mode) offered superior wind-system performance and high power quality injected in-RL-load. Several experimental tests (stator is/is not connected to RL-load) are established to ensure the robustness of proposed control (based on IP regulators) using different currents profiles (step and trapezoid forms) in transient tests. Also, different wind speed variation was established to illustrate the Sub- and Super-synchronous operations also to prove the high efficiency of the proposed algorithm. In order to improve the power quality of stator and rotor voltages; the LCL-filter is connected between the DFIG's rotor and SEMIKUBE. All experimental results are established using DSP (dSPACE 1103 card in real time) confirm that the wind-system has the high dynamics responses in transient and steady states.

5.8 Conclusion

In this chapter, the experimental validation of high performances IDPC in stand-alone mode has been presented for variable speed wind turbine using DFIG. A robust approach based on IP regulators is proposed to control the rotor side converter (SEMEKUBE) using PWM strategy by the means of the rotor direct and quadrature currents (I_{rd}^* and I_{rq}^*) variation for two topologies: stator connected to the RL-load and stator not connected to the RL-load in order to ensure the good current tracking and low current error. LCL is selected as the best filter after have being compared to L and LC filters under different experimental tests using the FFT of rotor' and stator voltages, knowing that the main aim of adding LCL filter between the SEMIKUBE (inverter)

and the DFIG's rotor was that the LCL provided a good sinusoidal stator and rotor voltages waveforms and to smooth the stator' and rotor currents. Different experimental tests has been established by rotor speed and currents variation in order to display the Sub-synchronous and Super-synchronous operations, in other hand to be sure that the proposed control is able to work in different wind-speed conditions. Experimental results proved high performances of the proposed control in terms of power quality, response time, overshoot, current error and power error.

5.9 References

- [1] "Global wind report: Annual market update 2014," Global Wind Energy Council, Brussels, Belgium, Tech. Rep., 2014.
- [2] A. P. FARROKH, N. HASHEMNIA, and A. KASHIHA, "Robust Speed Sensorless Control of Doubly-fed Induction Machine Based on Input-output Feedback Linearization Control Using a Sliding-mode Observer", World Applied Sciences Journal, vol: 10, no:11, pp.:1392-400, 2010.
- [3] Yipeng SONG; Frede BLAABJERG, "Overview of DFIG-Based Wind Power System Resonances Under Weak Networks", IEEE Transactions on Power Electronics, vol: 32, no: 6, pp: 4370 – 4394, 2017.
- [4] Dao ZHOU; Frede BLAABJERG; Toke FRANKE; Michael TONNES and Mogens LAU, "Reduced Cost of Reactive Power in Doubly Fed Induction Generator Wind Turbine System with Optimized Grid Filter", IEEE Transactions on Power Electronics, vol: 30, no: 10, pp.: 5581 – 5590, 2015.
- [5] Abdelhak DJOUDI, Seddik BACHA, Hachemi CHEKIREB, Hossein IMAN-EINI and Cédric BOUDINET, "Adaptive Sensorless SM-DPC of DFIG-Based WECS under Disturbed Grid: Study and Experimental Results", IEEE Transactions on Sustainable Energy, vol: XX, no: XX, DOI: 10.1109/TSTE.2017.2748966, 2017.
- [6] Gonzalo ABAD and Grzegorz IWANSKI, "Properties and Control of a Doubly Fed Induction Machine", Power Electronics for Renewable Energy Systems, Transportation and Industrial Applications, First Edition, John Wiley & Sons, 2014.
- [7] C. EVANGELISTA, F. VALENCIAGA and P. PULESTON. "Active and reactive power control for wind turbine based on a MIMO 2-sliding mode algorithm with variable gains" IEEE Transactions Energy Conversion, vol: 28, no: 3, pp.: 882-889, 2013.
- [8] H. NIAN, Y. SONG, P. ZHOU and Y. HE. "Improved direct power control of a wind turbine driven doubly fed induction generator during transient grid voltage unbalance" IEEE Transactions Energy Conversion, vol: 26, no: 3, pp.: 976-986, 2011.
- [9] Frede BLAABJERG and Ke MA, "Wind Energy Systems", proceeding of the IEEE, vol: 105, no: 11, 2017.
- [10] Dan SUN and Xiaohe WANG, "Sliding-mode DPC using SOGI for DFIG under unbalanced grid condition", IEEE Electronics Letters, vol: 53, no: 10, pp: 674–676, 2017.
- [11] W. LEONHARD, "Control of Electrical Drives", 3rd ed. Berlin, Germany: Springer Verlag, 2003.
- [12] R. DATTA and V. T. RANGANATHAN, "Direct power control of grid-connected wound rotor induction machine without rotor position sensors" IEEE Transactions on Power Electronics, vol: 16, no: 8, pp.: 390–399, May. 2001.
- [13] Van-Tung PHAN, Dinh-Tuyen NGUYEN, Quoc-Nam TRINH, Cong-Long NGUYEN and Thillainathan LOGENTHIRAN, "Harmonics Rejection in Stand-Alone Doubly-Fed Induction Generators With Nonlinear Loads", IEEE Transactions on Energy Conversion, vol: 31, no:2, pp. 815-817, 2016.
- [14] V. -T. PHAN and H. -H. LEE "Stationary frame control scheme for a stand-alone doubly fed induction generator system with effective harmonic voltages rejection", IET Electric Power Applications, vol: 5, no: 9, pp. 697-707, 2011.

- [15] Fayssal AMRANE, Azeddine CHAIBA, Bruno FRANCOIS and Badreddine BABES, "Experimental Design of Stand-alone Field Oriented Control for WECS in Variable Speed DFIG-based on Hysteresis Current Controller", IEEE 2017 15th International Conference on Electrical Machines, Drives and Power, Bulgaria, 2017.
- [16] R. PENA, J. C. CLARE, and G. M. ASHER, "A doubly fed induction generator using back-to-back PWM converters supplying an isolated load from a variable speed wind turbine" IEE Proceeding. - Electronics Power Applications, vol. 143, no. 1, pp. 380-387, 1996.
- [17] Roberto CARDENAS; Rubén PENA; Salvador ALEPUZ and Greg ASHER, "Overview of Control Systems for the Operation of DFIGs in Wind Energy Applications", IEEE Transactions on Industrial Electronics, vol: 60, no: 7, pp.: 2776-2798, 2013.
- [18] Lie XU and Phillip CARTWRIGHT, "Direct Active and Reactive Power Control of DFIG for Wind Energy Generation", IEEE Transactions on Energy Conversion, vol. 21, no: 3, 2006.
- [19] Yongchang ZHANG, Jiefeng HU and Jianguo ZHU, "Three-Vectors-Based Predictive Direct Power Control of the Doubly Fed Induction Generator for Wind Energy Applications", IEEE Transactions on Power Electronics, vol: 29, no: 7, pp.: 3485-3500, 2014.
- [20] Himanshu MISRA, Akhila GUNDAVARAPU and Amit Kumar JAIN, "Control Scheme for DC Voltage Regulation of Stand-Alone DFIG-DC System", IEEE Transactions on Industrial Electronics, vol: 64, no: 4, pp.: 2700-2708, DOI: 10.1109/TIE.2016.2632066, 2017.
- [21] Gil D. MARQUES, and Matteo F. IACCHETTI, "Sensorless Frequency and Voltage Control in Stand-Alone DFIG-DC System", IEEE Transactions on Industrial Electronics, vol: 64, no: 3, pp.: 1949-1957, DOI: 10.1109/TIE.2016.2624262, 2017.
- [22] Himanshu MISRA and Amit Kumar JAIN, "Analysis of Stand-Alone DFIG-DC System and DC Voltage Regulation With Reduced Sensors", IEEE Transactions on Industrial Electronics, vol: 64, no: 6, pp.: 4402-4412, DOI: 10.1109/TIE.2017.2669889, 2017.
- [23] F. BOUCHAFAA, D. BERIBER, and M. S. BOUCHERIT, "Modeling and control of a grid connected PV generation system," in Control & Automation (MED), 18th Mediterranean Conference, pp.315 - 320, 2010.
- [24] M. LISERRE, F. BLAABJERG, and S. HANSEN, "Design and Control of an LCL-Filter-Based Three-Phase Active Rectifier," IEEE Transactions on Industry Applications, vol. 41, no. 5, pp. 1281-1291, Sep. 2005.
- [25] J. GUERRERO, F. BLAABJERG, T. ZHELEV, K. HEMMES, E. MONMASSON, S. JEMEI, M. COMECH, R. GRANADINO, and J. FRAU, "Distributed generation: Toward a new energy paradigm," IEEE Industrial on Electronics Mag., vol. 4, no. 1, pp. 52 -64, march 2010.
- [26] J. HE and Y. W. LI, "Hybrid voltage and current control approach for DG grid interfacing converters with LCL filters," IEEE Transactions on Industrials Electronics, vol. 60, no. 5, pp. 1797-1809, 2013.
- [27] Tarak GHENNAM, "Supervision d'une ferme éolienne pour son intégration dans la gestion d'un réseau électrique, Apports des convertisseurs multi niveaux au réglage des éoliennes à base de machine asynchrone à double alimentation," PhD Thesis (in French language), 2011.
- [28] Hélio VOLTOLINI, Marcelo H. GRANZA, Josmar IVANQUI and Renato CARLSON, "Modeling and Simulation of the Wind-Turbine Emulator using Induction Motor Driven by Torque Control Inverter", 10th IEEE Conference/IAS International Conference on Industry Applications, 2012.
- [29] <https://www.dspace.com/en/pub/home/products>
- [30] Y. TANG, P. C. LOH, P. WANG, F. H. CHOO, F. GAO, and F. BLAABJERG, "Generalized design of high performance shunt active power filter with output LCL filter," IEEE Transactions on Industrial Electronics, vol. 59, no. 3, pp. 1443- 1452, 2012.

Chapter 6 :

Design and Real Time Implementation of FOC based on HCC in WECS Variable Speed DFIG for Grid-connection and Stand-alone Modes.

6.1 Introduction	153
6.2 Field Oriented Control (FOC).....	155
6.3 Hysteresis Current Controllers (HCC) Topology.....	155
6.4 Experimental Studies using a SEMIKRON Inverter (60 kW, 2008 version)	156
6.4.1 SEMIKRON Components Description	157
6.4.2 Isolation card (realized in LAS Laboratory).....	159
6.4.3 dSPACE1104.....	159
6.4.4 SEMIKRON with Isolation Card	159
6.5 Proposed control strategies.....	160
6.5.1 Mode I: Stand-alone topology	160
6.5.2 Mode II: Grid-connection topology	161
6.6 Hardware implementation (Stand-alone and Grid-connection Topologies).....	163
6.7 Experimental results	164
6.7.1 Stand-alone mode.....	164
6.7.2 Grid-connection mode.....	166
6.8 Conclusion	170
6.9 References	170

Abstract:

In this chapter, an experimental study based on Field Oriented Control (FOC) of Doubly Fed Induction Generator (DFIG) for both modes Stand-alone and Grid-connection are proposed in Variable Speed Wind Energy Conversion System (VS-WECS). The proposed FOC method based on Hysteresis Current Controller (HCC) is used in order to control Rotor Side Converter (RSC) by the means of the rotor current components (I_{rd}^ and I_{rq}^*) of DFIG through AC-DC-AC converter. Two topologies are proposed in this chapter; Stand-alone and grid-connection. The first topology is based on rotor current components using an independently rotor angle (no relationship with the grid angle) and the stator is connected to the nonlinear load (R-L) via rectifier to create a micro-grid. And the second one is based on robust Phase Locked Loop (PLL) to make synchronization between the stator and the grid in terms of phase, sequence and frequency and to inject stator current with high power quality. The experimental test bench based on emulator turbine represented by Direct Current Motor (DCM) which is coupled with DFIG. The implementation is realized using dSPACE1104 card below and above the synchronous speed (< 1500 rpm and >1500 rpm) named the Sub-synchronous and Super-synchronous operations respectively for both proposed modes. The experimental results show high performances in transient and steady states in both topologies under fluctuating wind speed with minor stator current THD injected to the grid (3.7 %) and the Grid Side Converter (GSC) exchanges only active power with grid to ensure unity power factor. The implementation simplicity and lower switching frequency converter are the main advantages of the proposed control.*

6.1 Introduction

Several installed wind turbines today are equipped with doubly fed induction machine (DFIM). However, most of these machines are connected directly to the network to avoid the presence of converter. The major advantage of this configuration lies in the fact that the power rating of the inverters is around 25-30% of the nominal generator power [1-2-3]. A Doubly Fed Induction Generator (DFIG) is the most important generator used for variable-speed wind energy generation. It consists of a wound rotor induction generator (WRIG) with the stator windings directly connected to a three-phase power grid and with the rotor windings mounted to a bidirectional back-to-back IGBT frequency converter [4-5].

The vector control is the most common method used in the DFIG-based wind turbines [6]. Precise steady-state performance and lower converter switching frequency are the advantages of this method. However, it has some disadvantages, such as its dependence on the machine parameters variation due to the decoupling terms [6]. A new modeling approach based on the flux measurement has been proposed in [7] in order to conclude input-to-state stability and convergence to the desired equilibrium. Control strategies of DFIG have been discussed in details in literatures; Direct Power Control (DPC) [7-8], Model Predictive Direct Power Control (MPDPC) [9-10], Sliding mode Direct Power Control [11], Sliding mode control [12] and Backstepping Control [13]. A schematic diagram of variable speed wind turbine system with a DFIG is shown in figure.6.1.

Many researchers focus their studies based on field oriented control (FOC) using linear regulator Proportional Integrator (PI) in order to control Rotor Side Converter (RSC) as mention in [7,14,15-16], by calculating K_p and K_i . Linear regulator as Proportional Integrator (PI) needs the full system parameters knowledge and also involve with more computation. While the Nonlinear regulator as hysteresis regulator does not need the information about the system parameters and also gives better dynamic response [17]. Most of the researchers in this area are concentrated on analyzing network dynamics, system transients, fault conditions, or grid disturbances [18-19]. Vector control utilizes the dynamic state relationships of DFIG to define angular speed, amplitude and instantaneous position of current, voltage and flux linkage vectors [20]. In contrast scalar control method, proposition employs steady-state relationships to determine angular speed and amplitude of current, voltage and flux vectors [21]. In [22], the authors propose enhanced hysteresis-based current regulators for vector control DFIG-based Wind Energy Conversion System (WECS), used to control the output currents of the rotor-side and grid-side converters. This proposed Hysteresis-based technique has excellent steady-state performances.

There are two common methods for DFIGs employment in wind power systems such as: Stand-alone installation [23] and Grid-connected usage [24-25]. A lot of researches have been performed on doubly fed induction generators' operation as grid-connected systems [26]. A new synchronization algorithm for grid connection of a DFIG based on Stator flux-oriented vector control for back to-back PWM converters in the DFIG has been proposed by [27]. This method gives fast starting and takes just 2 cycles to be performed and better robustness and has satisfactory performance than existing methods. One of the most advantages of Grid-connection usage is an appropriate method for large power networks and consequently many researches are in hand in this area.

In this chapter, we propose two novel and robust topologies; stand-alone mode and Grid-connected usage for

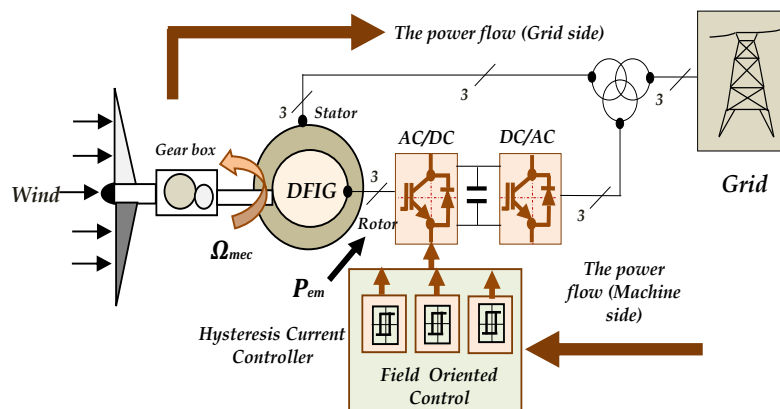


Figure.6.1 Schematic diagram of wind energy conversion system based on DFIG using field oriented control.

Wind Energy Conversion Systems (WECS's). We used the Hysteresis current controllers to obtain the switching signals to command the Rotor Side Converter (RSC). The main contribution in this chapter is the real time implementation for WECS based on DFIG using hybrid Hysteresis Current (HC) with Field Oriented Control (FOC). The decoupling terms in control approach is not needed; because the hysteresis controllers have nonlinear nature also we don't use the stator side converter (to minimize the stator power losses). The purpose is to build in real time a hybrid Field oriented control (FOC) with Hysteresis current controller using doubly fed induction generator (DFIG), to provide good tracking of the predefined references regardless the wind speed changing, and to guarantee converter with unity power factor (zero reactive power), means that the Grid Side Converter (GSC) exchanges only active power with grid.

The main contribution of this chapter is the experimental implementation (via dSPACE1104 card) of the proposed algorithm using both modes (Stand-alone mode and Grid-connection mode) under robustness tests by the means of the references direct and quadrature currents variation (I_{rd}^* and I_{rq}^*) to ensure high WECS performances in terms of; excellent current tracking by the mean of the hysteresis band (0.01 A), no overshoot, excellent Stator current THD (<5%) will be injected into the grid and very short response time (<0.001 sec).

In this chapter, a comparative study between Stand-alone and Grid-connection topology is proposed. The proposed control is based on Hysteresis controller to generate the switching signals in order to control the rotor side converter (RSC). The proposed schematic diagram based on FOC-HCC of DFIG-Wind turbine with 2 cases is shown in figure.6.2, is composed on four (04) parts:

- 1- Grid.
- 2- Wind turbine.
- 3- Combination between FOC and HCC.
- 4- Proposed control strategies:
 - 4.1- Mode I: Stand-alone (or Load connection topology).
 - 4.2- Mode II: Grid connection topology.

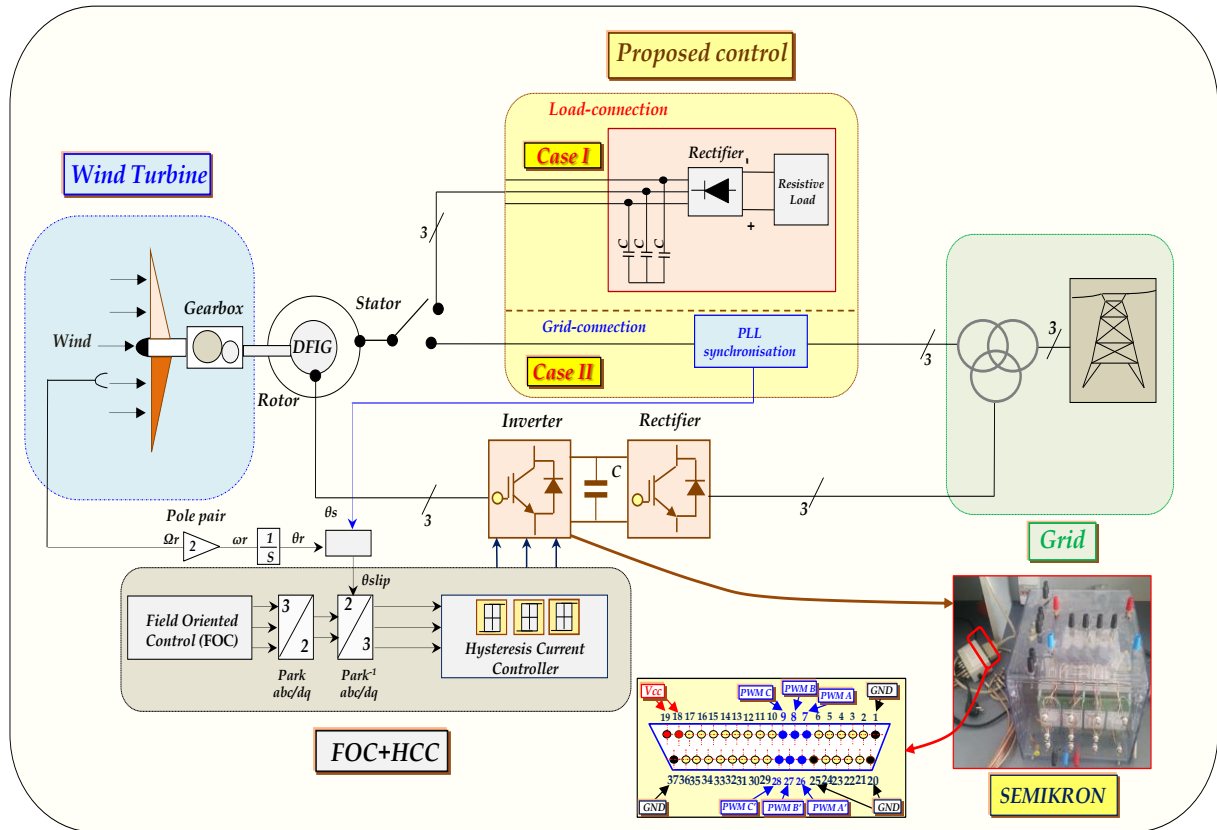


Figure.6.2 Proposed FOC-HCC for wind turbine-DFIG for both modes: stand-alone and grid-connection.

6.2 Field Oriented Control (FOC)

The DFIG model can be described by the following state equations in synchronous reference frame (*figure.6.3*) whose axis d is aligned with the rotor flux vector ($\Phi_{rq} = 0$) and ($\Phi_{rd} = \Phi_r$) [23-24-25].

$$I_{rq} = -\frac{L_m}{L_r} \cdot I_{sq} \text{ and } I_{sq} = -\frac{L_r}{L_m} \cdot I_{rq} \quad (6.1)$$

The arrangement of the equations gives the expressions of the rotor flux and the electromagnetic torque:

$$\Phi_{sd} = -\sigma \frac{L_s \cdot L_r}{L_m} \cdot I_{rq} \text{ and } T_{em} = P \cdot L_m \cdot (I_{sq} \cdot I_{rd} - I_{sd} \cdot I_{rq}) = P \cdot \Phi_{rd} \cdot I_{rq} \quad (6.2)$$

$$\text{With: } \sigma = 1 - \frac{L_m^2}{L_s \cdot L_r}$$

$$\text{If: } \Phi_{sd} = 0 \text{ (via stator)} \equiv \Phi_{sd} = L_m \cdot I_{sd} \quad (6.3)$$

$$\text{If: } I_{sd} = 0 \text{ (via rotor)} \equiv \Phi_{rd} = L_r \cdot I_{rd} \quad (6.4)$$

$$\text{(via stator and rotor)} \equiv \Phi_{rd} = L_r \cdot I_{rd} + L_m \cdot I_{sd} \quad (6.5)$$

From equation (2.2) the rotor reference transversal current

$$I_{rq}^* = \frac{T_{em}^*}{P \cdot \Phi_{rd}} \quad (6.6)$$

6.3 Hysteresis Current Controllers (HCC) Topology

T_i and T'_i are switches connected, one to the output of a hysteresis comparator, the other to this same output via an inverter [23-27-28] and [29]. The sign of the difference of change between the reference and the measured current does not instantaneously results in the tilting of the comparison due to the effect of the hysteresis, which means the measured current is changing by increasing until ΔI is equal to h . The comparator switches over either switch comes into conduction in turn as $\Delta I < h$ illustrated in (*figure.6.4-(b)*). The switching conditions are defined in terms of logical states corresponding [24]. The two-level hysteresis current control is the simplest non-linear controller which operates by comparing tracking error $e(t)$ with the fixed hysteresis bands ($\pm h$) illustrated in *figure.6.4.(a)*; where, $e(t)$ is the difference between the reference current $I_{ref}(t)$ and the actual current $I_{act}(t)$. The graphical representation of the two-level hysteresis modulation is shown in *figure.6.4-(b)*.

$$u(t) = +1 \text{ For } I_{act}(t) < I_{ref}(t) - h \text{ or } e(t) > +h \quad (6.7)$$

$$u(t) = -1 \text{ For } I_{act}(t) > I_{ref}(t) + h \text{ or } e(t) > -h \quad (6.8)$$

Figure.6.5 presents transient and steady states of rotor currents under hysteresis current topology. Four (04) hysteresis band (HB) are used to show the influence of the HB performances. *Table.6.1* describes in details the performances of each case. From this table, it can be seen that the fourth case ($\Delta I_r = 0.01$ (A)) presents high performances (*low THD rotor current = 02.89 %*, *neglected overshoot and fast response time*). The case n°04 is validated experimentally using a hybrid FOC-HCC control in both cases (*stand-alone and grid-connection topologies*).

Table.6.1. Recapitulation results for proposed hysteresis band (HB) performances using 04 cases.

Performances: Cases:	Hysteresis Band (HB):	Response time (sec):	Overshoot :	THD I_r abc (%):
Case 1:	$\Delta I_r = \pm 2$ (A).	$1.786 \cdot 10^{-1}$.	Remarkable.	03.49%
Case 2:	$\Delta I_r = \pm 1$ (A).	$1.785 \cdot 10^{-1}$.	Few.	03.09 %
Case 3:	$\Delta I_r = \pm 0.1$ (A).	$1.784 \cdot 10^{-1}$.	Neglected.	02.91 %
Case 4:	$\Delta I_r = \pm 0.01$ (A).	$1.784 \cdot 10^{-1}$.	Neglected.	02.89%

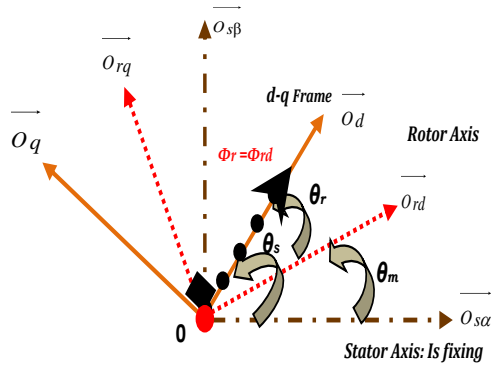


Figure.6.3 Rotor flux vector in the synchronous d-q frame.

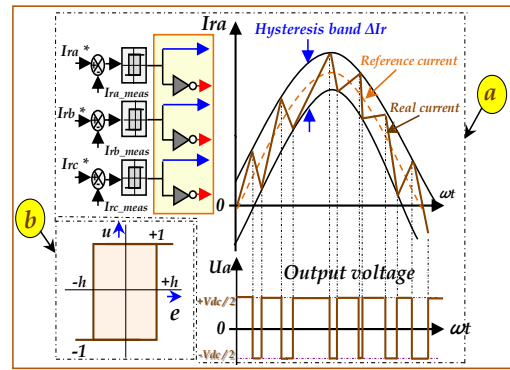


Figure.6.4 Hysteresis current control structure for two-level inverter.

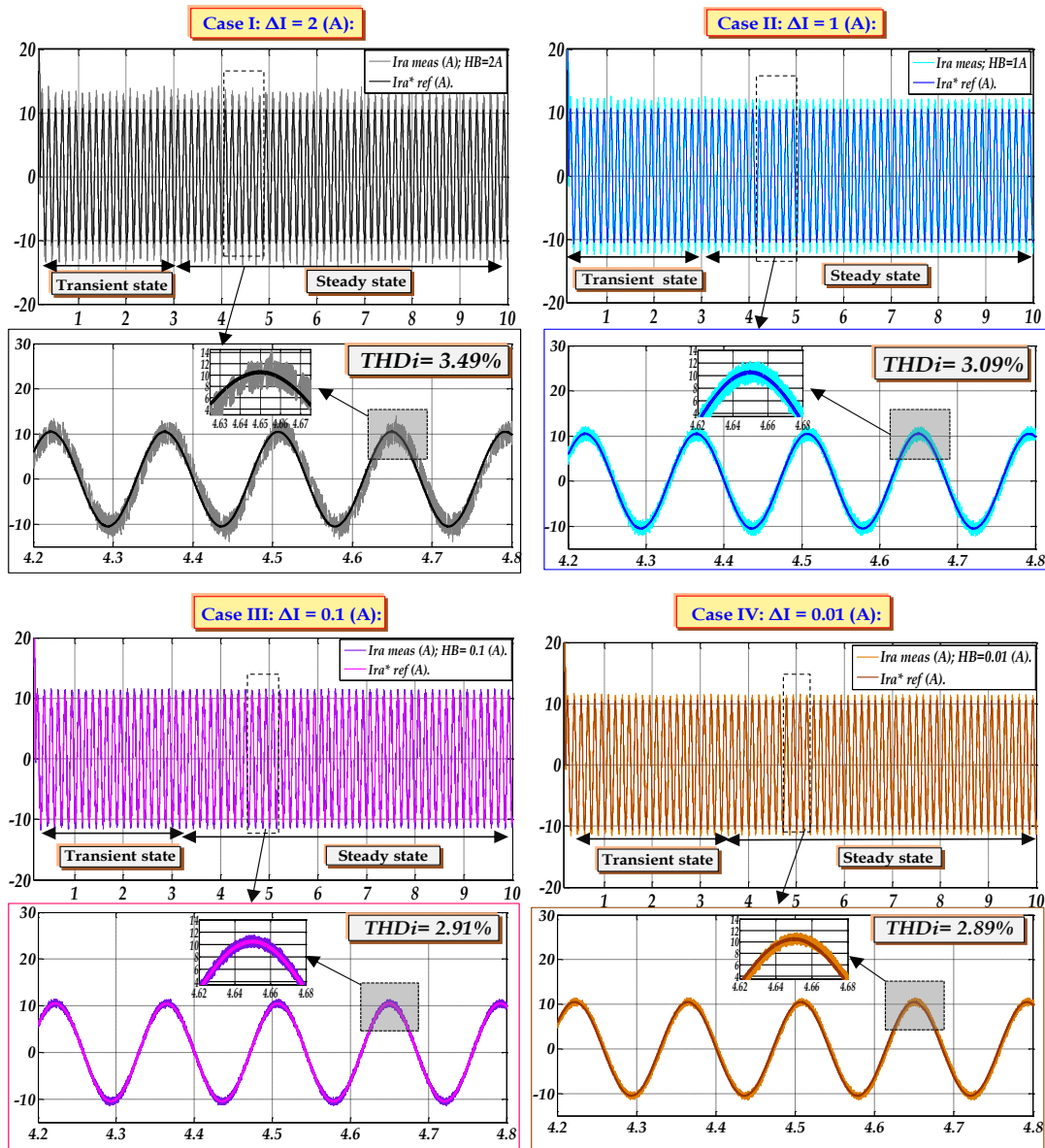


Figure.6.5 Hysteresis band validation using four (04) cases.

6.4 Experimental Study using a SEMIKRON Inverter (60 kW, 2008 version)

In this part, we use the inverter (type SEMIKRON) to feed the rotor of the DFIG, but before realizing this step we should realize the isolation card to generate the switching signals corresponding to this inverter.

6.4.1 SEMIKRON Components Description

Table.6.2 describes the interfaces and the connectors in details; the SEMIKRON is composed by three (03) Modules type: SKM50GB123-D, which parameters are; $V_{CE}=1200$ (V), $I_C= 50$ (A), $V_{GE}= 15$ (V), $V_{in(max)} = 3*380$ (V) and $T^{\circ}_{dissipation}=80^{\circ}$.

A. Diode Bridge

By default, the SKD 51/14, 380 (V), 50 (A), diode bridge rectifier is not connected to the IGBT converter. To operate the rectifier with the converter, its output has to be connected to the DC-link terminals. The rectifier can also be operated as a single phase bridge.

B. DC-link Capacitors

The electrolytic DC-link capacitors are each rated at 2200 (μ F), 400 (V) and connected in series to provide an equivalent 1100 (μ F), 800 (V) rating. The capacitor voltage balancing resistors are 22 (k Ω) each. The DC-link capacitor will discharge through the voltage balancing resistor across it, in about 46 (sec).

C. IGBT Modules

The IGBT modules, SKM 50 GB 123 D, are rated at 1200 V, 50 A, but the maximum current recommended by the manufacturer is 30 A. The input voltage signal level required to turn the IGBT on and off is +15 V and -15 V respectively. The typical turn-on threshold voltage is 5.5 V. The maximum saturation collector to emitter voltage is 3V (3.7V), for junction temperature of 25°C (125°C), at the rated current of 50 A. The turn-on and turnoff time delay is 70 ns and 400 ns respectively while the rise and fall times are 60 ns and 45 ns respectively, with a gate resistance of 27 Ω and a current of 40 A. The peak collector current can be 80 A, but with a maximum pulse duration of 1 msec. The IGBTs have a high short circuit current capability of 500 A, at full DC voltage of 1200 V, but this short-circuit must be detected within 10 μ s otherwise there is a risk of thermal breakdown.

D. IGBT Drivers

The SKHI 22A drivers can provide an output peak current of 8A and provide the +15V and -15 V required to switch the IGBT. The gate resistor value is 30 Ω . The drivers require a supply voltage of 15 V and consume 160 mA per driver. The maximum switching frequency, for the driver, is 50 kHz. There is interlocking to prevent the simultaneous switch-on for IGBTs in the same inverter leg. The driver inserts an interlock dead time of 3.3 – 4.3 μ s by default. The drivers also provide the error outputs for protection at faults like short-circuits of the IGBT, by monitoring the collector to emitter voltage VCE, and driver supply under-voltage 13 V. The short-circuit is detected within 5 μ s. The error input to output propagation time is 0.6 μ s.

E. Snubber Capacitors

The MKP type snubber capacitors, rated at 22 μ F, 1600 V, are mounted directly between the collector and

Table.6.2. The interfaces / connectors of the SEMIKRON®.

N°	Type:	Function:	Voltage Level:	Max Current level:	SEMIKRON® Inverter Photo:
0	Grounding panel socket.	Earth connection	0 V.	30 A	
1	Connector 4 mm.	Fan power supply.	230 V/50 Hz	1 A	
2	Connector 4 mm.	Thermal trip.	15 V	5 A	
3	Connector 4 mm.	Rectifier input.	230/400 V	30 A	
4	Connector 4 mm.	DC rectifier outputs.	600 VDC	30 A	
5	Connector 4 mm.	DC IGBT inverter inputs.	600 VDC	30 A	
6	Connector 4 mm.	AC IGBT inverter+ chopper outputs.	400 VAC/600 VDC	30 A	
7	BNC coaxial insulated.	PWM input of inverter.	C-MOS logic 0/15 V	1 A	
8	BNC coaxial insulated.	PWM input of brake chopper	C-MOS logic 0/15 V	1 A	
9	BNC coaxial insulated.	Error output.	C-MOS logic 0/15 V	1 A	
10	Connector 4 mm.	15 V driver power supply.	15 V	5 A	
11	Connector 4 mm.	0 V driver power supply	15 V	5 A	
12	Connector 4 mm.	Temperature sensor	0-5 V	1 A	

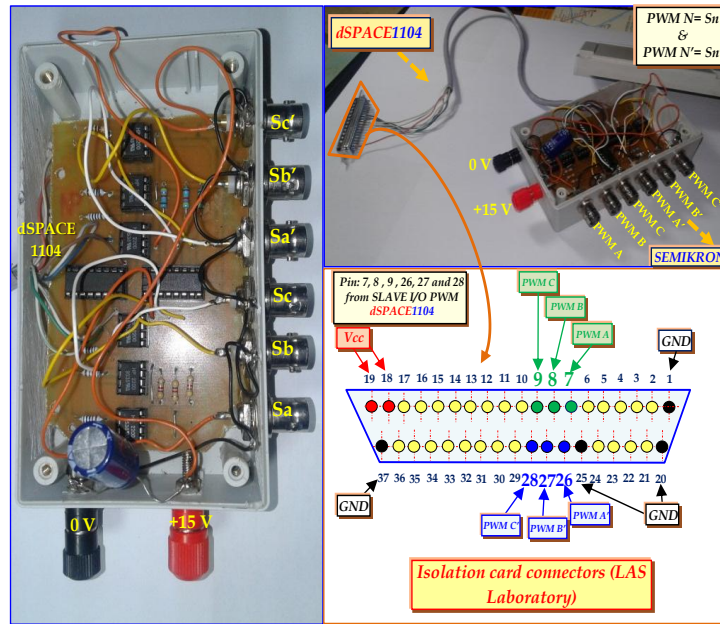


Figure.6.6 Isolation card for the dSPACE1104 realizing in LAS laboratory (UFASetif-1).

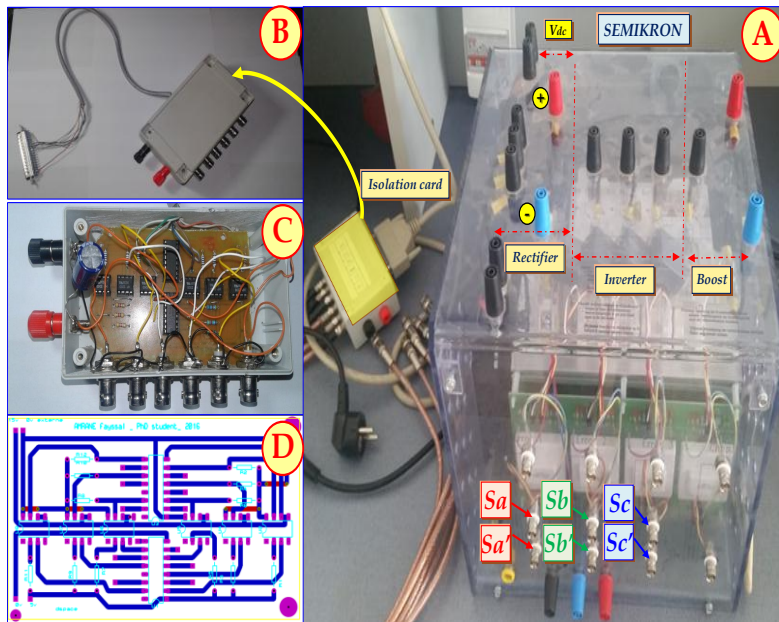


Figure.6.7 Inverter type SEMIKRON® with isolation card developed in LAS laboratory (UFASetif-1), A: Inverter + Isolation card, B: Isolation card not connected, C: The isolation card components and D: Printed circuit board (copper side).

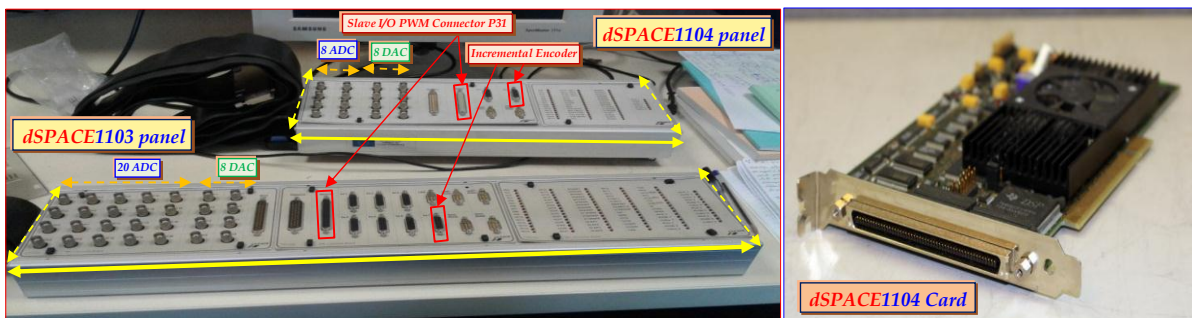


Figure.6.8 Deference between dSPACE1103 panel and dSPACE1104 panel.

emitter terminals of the IGBT modules. They absorb the high frequency harmonics and limit the overvoltages, due to the parasitic inductances. A snubber also reduces the switching losses but this

function is less important, for an IGBT, since it can be switched at full current with full rated voltage e.g. 1200 V.

6.4.2 Isolation card (realized in LAS Laboratory)¹

To generate the switching signals from the dSPACE1104 into the SEMIKRON, we need the isolation card to separate the power stage from the control stage by using two different Grounding panel socket via the Optocoupler. Figure.6.6 illustrates the isolation card and its different dSPACE1104’s connectors.

6.4.3 SEMIKRON with Isolation Card

Figure.6.7 demonstrates the electric connection between the isolation card and the SEMIKRON using the BNC connectors (The input BNC connector shields and the temperature sensor reference are connected to the driver 0 V. The temperature probe is LM3352 with a gradient of 10 (mV/°C). It measures the temperature of the heat sink, at its hottest point).

6.4.4 dSPACE1104 [37-38-39] and [40]

The main difference² between the dSPACE1103 (used in chapter n°5) and dSPACE1104 (used in chapter n°6) is that the 1103 contain more Analog Digital Converter (ADC); **20 ADC** for dSPACE1103 and only **08** for dSPACE1104 (as illustrate in figure.6.8). Table.6.3 illustrates the slave I/O PWM connectors.

A. PWM Outputs

The 3-phase and 1-phase PWM outputs are provided at the front panel, after signal conditioning from +5 V generated by the dSPACE card to +15 V required by the IGBT drivers.

B. ADC Inputs

The ADC inputs are present to interface with the transducers. They consist of 8 channels. ADCH1 to ADCH4 are multiplexed, 16-bit resolution, to a single ADC while ADCH5 to ADCH8 are four independent ADCs, each with 12-bit resolution. The input voltage limit is ±10 V. The conversion time for the multiplexed channels is 2µs while for the parallel channels it is 800 ns.

C. DAC Outputs

The DAC outputs are present to interface with actuators. There are 8 independent DAC channels. DACH1 through DACH8 have a 16-bit resolution and voltage output limits of ±10 V. The output current limit is ±5 mA.

D. Master PPC Digital I/Os

Inputs and outputs controlled by the master processor PPC are indicated as ‘Digital I/O’.

Table.6.3 Slave I/O PWM connector (dSPACE1104).

CP18 (37 pins):	Pin:	Signal:	Pin:	Signal:
	1	GND.	20	GND.
	2	SCAP1.	21	SCAP2.
	3	SCAP3.	22	SCAP4.
	4	GND.	23	ST1PWM.
	5	ST2PWM.	24	ST3PWM.
	6	GND.	25	GND.
	7	SPWM1.	26	SPWM2.
	8	SPWM3.	27	SPWM4.
	9	SPWM5.	28	SPWM6.
	10	SPWM7.	29	SPWM8.
	11	SPWM9.	30	GND.
	12	GND.	31	GND.
	13	GND.	32	GND.
	14	GND.	33	GND.
	15	GND.	34	SSOMI.
	16	SSIMO.	35	SSTE.
	17	SCLK.	36	GND.
	18	Vcc (+5 V).	37	GND.
	19	Vcc (+5 V).		

¹ Please refer to Appendix B (Figure.B.2 + Table.B2/there are more information about components/copper circuit of the dSPACE1104’s isolation card).
² There is another difference; the sampling time is more small (until 1e-6 (sec) in each loop calculation) in dSPACE1103 than dSPACE1104.

6.5 Proposed control strategies

In this section, two FOC-HCC topologies are proposed to control Rotor Side Converter (RSC). Figure.6.9 presents the mechanic WECS hardware connection of the proposed control (DFIG and Wind turbine emulator used in this work)³. Figures.6.10 and figures.6.11 illustrate detailed control scheme of proposed FOC-HCC under dSPACE1104 card for both cases: I: Stand-alone and II: Grid-connection:

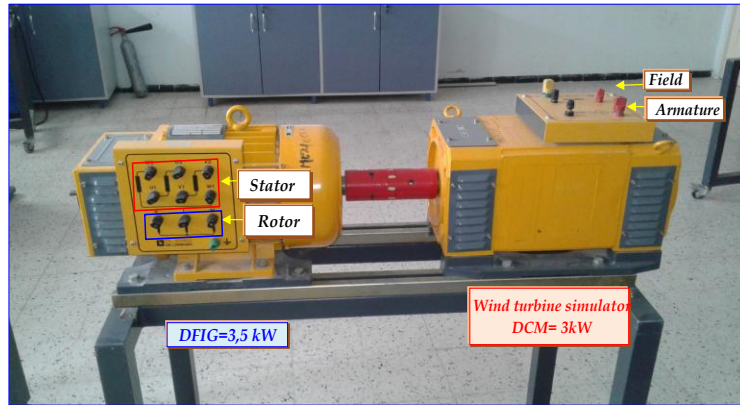


Figure.6.9 WECS Hardware implementation (Emulator turbine + DFIG)⁴.

6.5.1 Mode I: Stand-alone topology

In this case, the RSC is controlled via switching signals generated by hysteresis rotor current controller and the stator side is connected into the nonlinear load as shown in figure.6.10. In the case of stand-alone DFIG system, stator voltage is not given by the power grid, but abstained as a consequence of the excited machine loaded on the stator side. The stator voltage during a resistive load supply is calculated as [23]:

$$V_s = -R_0 * I_s \tag{6.9}$$

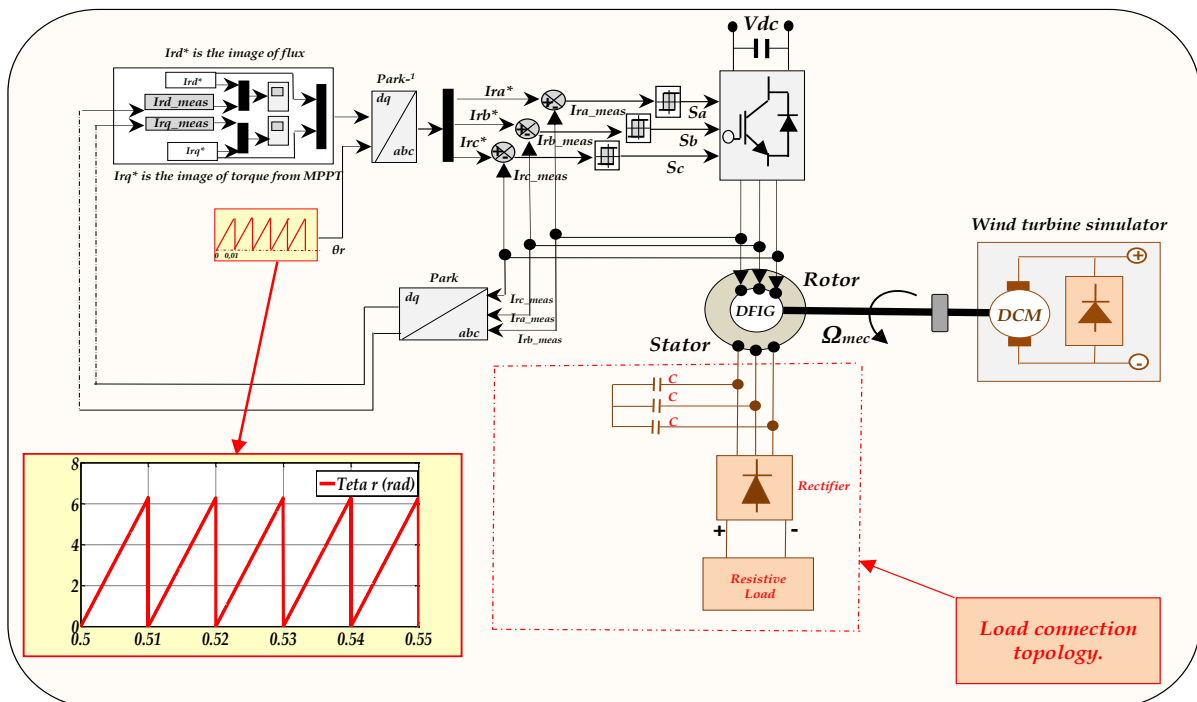


Figure.6.10 Detailed scheme of proposed stand-alone of FOC-HCC based on DFIG.

³ Please refer to Appendix A-“Section-A.2”; Parameters of the DFIG and wind turbine emulator (Table.A.5 + Table.A.6).

⁴ There are real photos of DFIG and the wind turbine emulator with their nameplates, please refer to figures.C-(3 and 4).

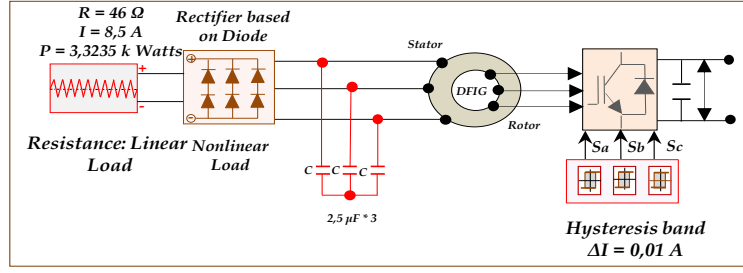


Figure.6.11 Stator side converter of stand-alone topology.

Where R_{Load} is the load resistance and the stator current also represents the load current. From equation (2.1, 2.2, 2.5 and 2.6) and with a resistive load and neglected stator resistance the dependence of the rotor current on the stator voltage represented in dq frame can be described by:

$$V_s = \frac{R_{Load} \cdot L_m}{Z_s} \cdot \frac{dI_r}{dt} + j \left(\frac{\omega_s \cdot R_{Load} \cdot L_s}{Z_s} \right) \cdot I_r - \frac{L_s}{Z_s} \cdot \frac{dV_s}{dt} \quad (6.10)$$

Where R_{Load} is the load resistance, stator resistance is neglected and Z_s is the stator side impedance $Z_s = R_{Load} + j\omega_s \cdot L_m \cdot I_r$. For an unloaded system, we have

$$V_s = L_m \cdot \frac{dI_r}{dt} + j\omega_s \cdot L_m \cdot I_r \quad (6.11)$$

The stand-alone topology is described in details with parameter values in figures.6.11. The stator is connected to the nonlinear load which compound by the unidirectional rectifier (based on six diodes) and resistive load ($R_{Load}=46$ (Ω), $I_{Load}=8.5$ (A), $P_{Load}=3.325$ (KW)) and the bank capacitances $C=3 \cdot 2.5$ (μF) (under star coupling) used between the stator and the nonlinear load for voltage filtering.

6.5.2 Mode II: Grid-connection topology

The grid synchronization method has been proposed as this system needs some care during the machine start-up and integration with the grid. The main goal of the synchronization control process is to avoid heavy start-up currents and mechanical stresses on the turbine shaft and other integrated components. This is achieved by properly matching the phase angle, frequency, and magnitude of the grid voltage and the stator induced voltage irrespective of whether it is a stator-voltage or stator-flux oriented frame used for modeling the generator [24-25].

Instead of a traditional control scheme using a PLL (phase-locked loop), the rotor $d-q$ reference current is generated with grid voltage as the reference so as to induce identical voltage in the stator as that of the grid. The machine is started by a driving torque and the switch between stator and the grid can be closed for synchronization. However, appropriate timing of switch closure plays a critical role in satisfying the magnitude condition of synchronization [33-34]. The stator connection is the most critical stage of the synchronization process. The time at which the three-phase circuit breaker (K) needs (as shown in figures.6.12) to be closed for connecting the stator is very important. Care has to be taken that the breaker is closed at a point of time when the stator induced voltage is exactly equal in magnitude to the grid voltage. The stator induced voltage would be in phase with grid voltage and so would be the frequency, but the magnitude needs to be monitored. If the circuit breaker is closed with a stator induced voltage less than the grid voltage, heavy transient stator and rotor currents would be observed which indicates unsuccessful synchronization. These conditions can be summarized in form of equations given below. [35]

$$V_{grid} \cdot \sin(\omega t + \varphi) = V_{stator} \cdot \sin(\omega t + \varphi) \quad (6.12)$$

$$f_{grid} = f_{stator} \text{ and } |V_{grid}| = |V_{stator}| \quad (6.13)$$

Where: φ , V_{grid} , V_{stator} , f_{grid} , f_{stator} , $|V_{grid}|$ and $|V_{stator}|$ are the phase angle, peak value, frequency and magnitude of the grid and stator voltage respectively. [34]

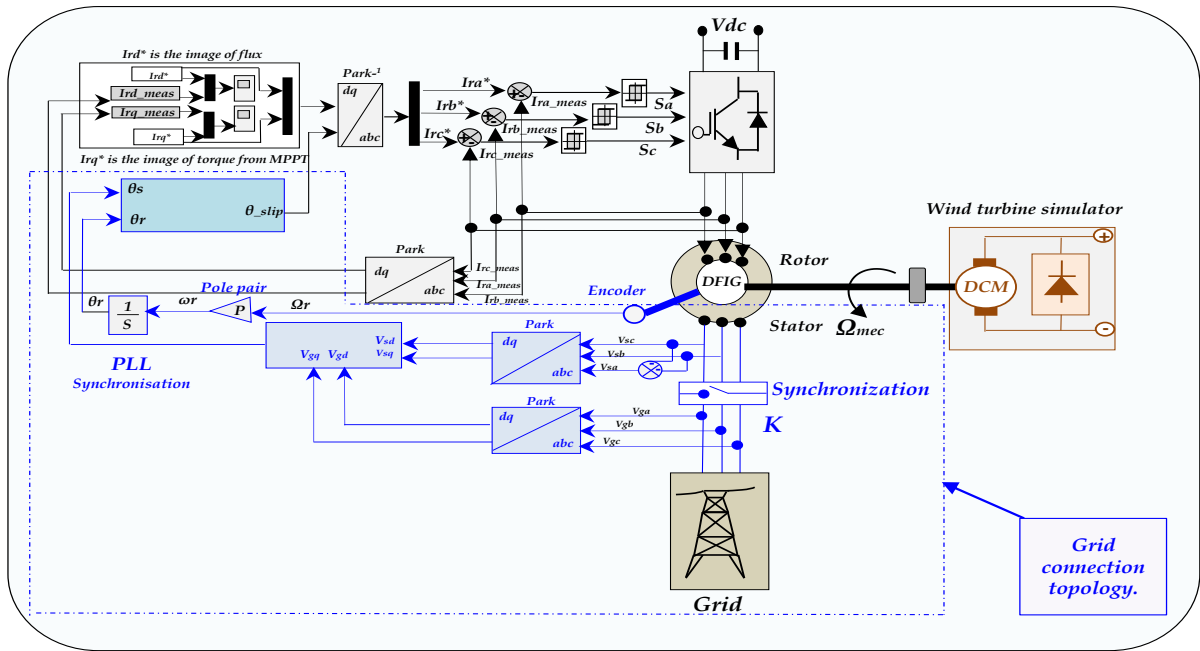


Figure.6.12 Detailed scheme of proposed grid-connection of FOC-HCC based on DFIG.

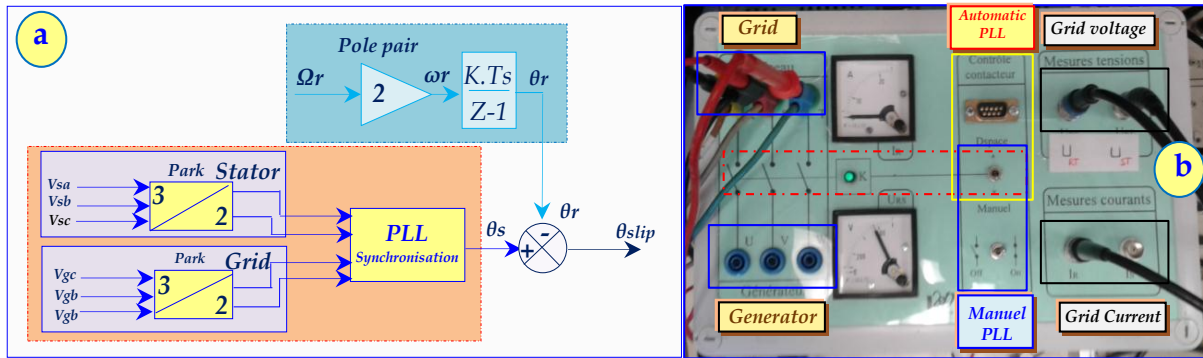


Figure.6.13 PLL structure scheme; a: Scheme of slip angle calculation and b: Hardware PLL implementation.

The slip angle [68] is calculated as shown in figure.6.13-(a):

$$\theta_{slip} = \theta_s - \theta_r = \theta_s - \int \omega_r . dt \tag{6.14}$$

With: $\omega_r = \Omega_{mec} * P$ (P: number of pair pole).

Figure.6.13-(b) presents a hardware PLL implementation, which based on voltage inputs (Grid voltage and Generator voltage respectively) and the measured outputs (grid currents).

a. Synchronous Reference Frame Phase Locked Loop (SRF-PLL):

The Synchronous Reference Frame Phase Locked Loop (SRF PLL) is modeled in MATLAB/Simulink® R2009b as shown in figure.6.14. The block takes phase voltage of the grid as input. The block outputs are instantaneous frequency, grid phase angle θ , $\sin(\theta)$ and $\cos(\theta)$. Second order filter used to remove ripples in frequency estimate. [33]

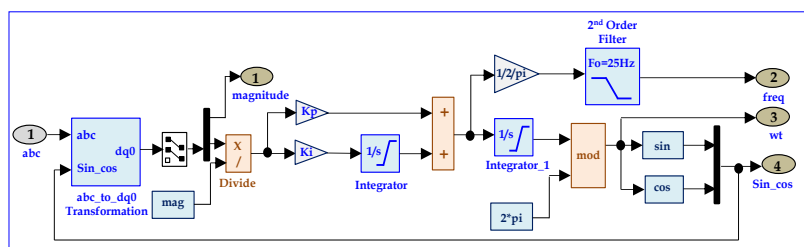


Figure.6.14 PLL block implementation in Matlab/Simulink®.

b. Selection of switching frequency:

Switching frequency is selected as 5 (kHz) that in most applications the switching frequency is selected either less than 6 (kHz) or greater than 20 (kHz) to be above the audible range. A relatively low value of switching frequency is selected for the current research work so as to reduce the switching losses as well as the 77 sampling frequency of the ADC of the microcontroller while hardware implementing. [36]

6.6 Hardware implementation (Stand-alone and Grid-connection Topologies)

Figures.6.17 presents the experimental test bench (to the left present stand-alone mode and to the right presents the Grid-connection mode, developed in LAS laboratory/UFASétif-1) for Wind Energy Conversion System (WECS) under two modes (left: stand-alone, and right: grid-connection). The DFIG used in this real time implementation is a 3.5 (kW) (whose parameters are described in Appendix A) not designed especially for generation. And DCM (Direct Current Motor) as shown in figure.6.17-(N°:10), is a 3 (kW) who's represented wind turbine simulator, to reproduce the aerodynamic torque of a wind turbine. The right part of figures-(6.15 and 9.16) respectively is composed of a data acquisition system connected to the control board. The FOC algorithm is implemented on real time board (dSPACE-RT1104) from Texas Instrument with a TMS320F240 DSP (20 MHz) and a microprocessor Power PC 603e (250 MHz); with a sampling time (fixed step); the controller is executed at 10 kHz. The connections between the dSPACE1104 card and the power converter are carried out by an interface card, which adapts the control signal levels. The current and voltage are ensured by the (Fluke i30S) and (ST1000-II) sensors, whereas, both the rotor position and speed are given by a 1024-pulse incremental encoder implemented on the DC motor shaft.

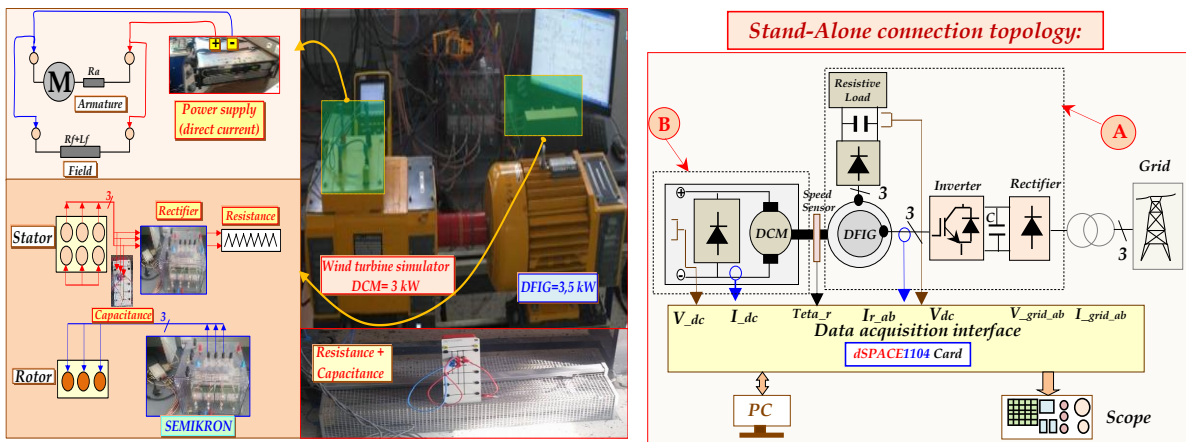


Figure.6.15 Hardware connection of proposed FOC-HCC for stand-alone topology.

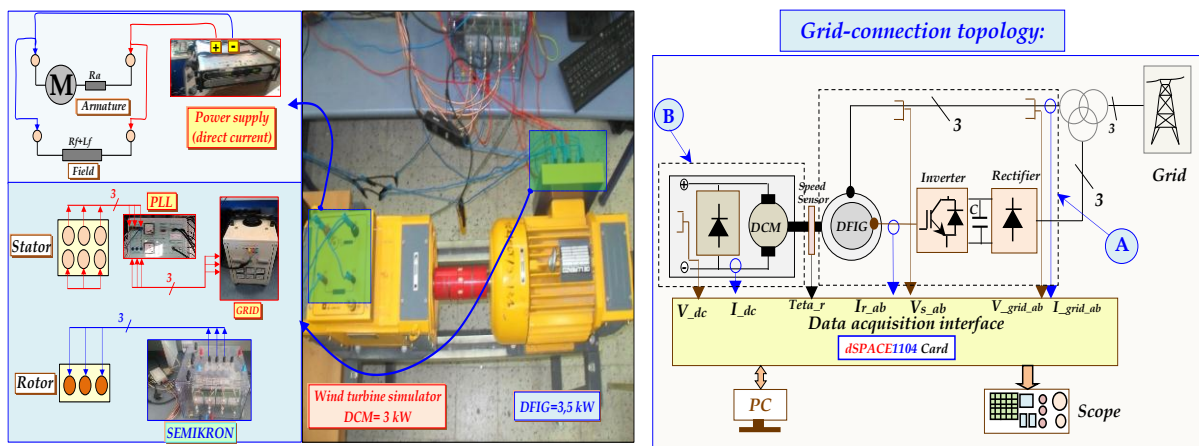


Figure.6.16 Hardware connection of proposed FOC-HCC for grid-connection topology.

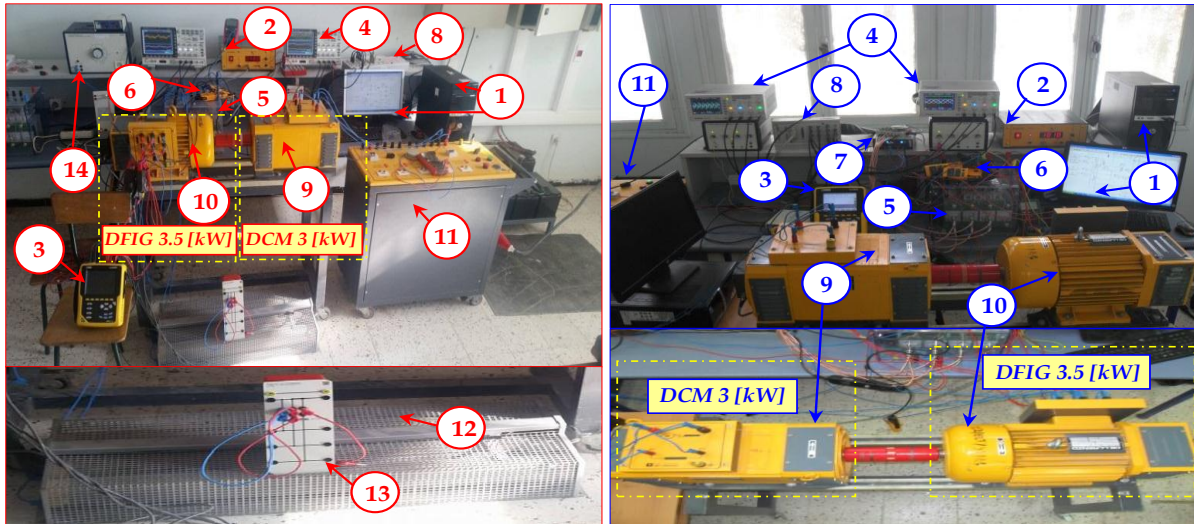


Figure.6.17 Experimental test bench developed in LAS Laboratory (UFASétif/Algeria) 1: PC, 2: Speed sensor, 3: Power analyzer, 4: Oscilloscopes, 5: inverter (SEMIKRON), 6: Current sensors, 7: Voltage sensors, 8: dSPACE1104, 9: DCM, 10: DFIG, 11: Grid, 12: Resistive load (Resistance), 13: Capacitor, 14: DC variable supply power).

6.7 Experimental results

The following experimental results are giving under *Sub-synchronous and Super-synchronous* operations for *Stand-alone* and *Grid-connection* modes respectively, using *dSPACE1104* card and *Matlab/Simulink®*. It is noted that; I_{rd}^* (Rotor direct reference current) is the image of flux, and I_{rq}^* (Rotor quadrature reference current) is the image of torque from the MPPT (Maximum Power Point Tracking).

6.7.1 Stand-alone mode

A. Rotor side converter (Stand-alone topology)

In the rotor side converter, we used several tests, as shown in figures.6.18-(a, b, c, d, e and f). Figure.6.18-(a) displays the behavior of rotor speed (N_r (rpm)⁵) and rotor current (I_{ra} (A)) under variation condition. It can be seen the variation (increasing) of speed from 400 (rpm) to 980 (rpm) (transient and steady state) during 5 (sec) less than synchronous speed (1420 (rpm) < 1500 (rpm)) means the sub-synchronous operation, and after that the decreasing of rotor speed from 980 (rpm) to 400 (rpm) during also 5 (sec), also it noted also the decreasing and increasing frequency respectively of rotor currents ($f_{rotor} < 50$ (Hz)). Figure.6.18-(b) and figure.6.18-(c) present the zoom of figure.6.18-(a) during the period of 1 (sec) = (10*100 (msec)) and 0.2 (sec) = (10*20 (msec)) respectively. In figure.6.18-(c) it is absolutely clear that the rotor currents I_{ra} (A) took sinusoidal form with few harmonics under speed variation. Figure.6.18-(d) illustrates the behavior of the rotor speed and the sinusoidal rotor current I_{ra} (A) under variation (increasing) of the reference quadrature rotor current I_{rq}^* (A) from 2 (A) to 3 (A); means the rotor torque with negative value to ensure the generator mode, on the other hand we keep the reference direct rotor current I_{rd}^* (A) at zero value (0 (A)) means the image of the rotor flux to ensure the exchange of the active power to the nonlinear load, in the same test the rotor speed is constant equals to 600 (rpm) during the variation of the currents references (I_{rd}^* (A) and I_{rq}^* (A)). Rotor current I_{ra} (A) takes the sinusoidal form using the hysteresis current controller (hysteresis band $\Delta I_r = \pm 0.01$ (A) mentioned in table.6.1 in case.IV). Figure.6.18-(e) displays the zoom of figure.6.18-(d) during 0.2 (sec) = (10*20(msec), it can be seen the sinusoidal for of the rotor current, that validated the good choice of the hysteresis band ΔI_r (A). The behavior of the bus voltage ($V_{dc} = 150$ (V)) with fluctuation of ± 10 (V) and the rotor speed ($\Omega_r = 600$ (rpm)) are shown in figure.6.18-(f) during the stand-alone conditions.

B. Stator side converter (Stand-alone topology):

In the Stator side converter, we used several tests, as shown in figures.6.19-(a, b, c, d, e, f, g, h, i and j).

⁵ Knowing that N_r is measured in 'rpm' and Ω_r in 'rad/sec', Exp: in synchronous mode, we have $N_s = 1500 * (2\pi) / 60$ (rad) / 60 (sec) = 157 (rad/sec) = Ω_s .

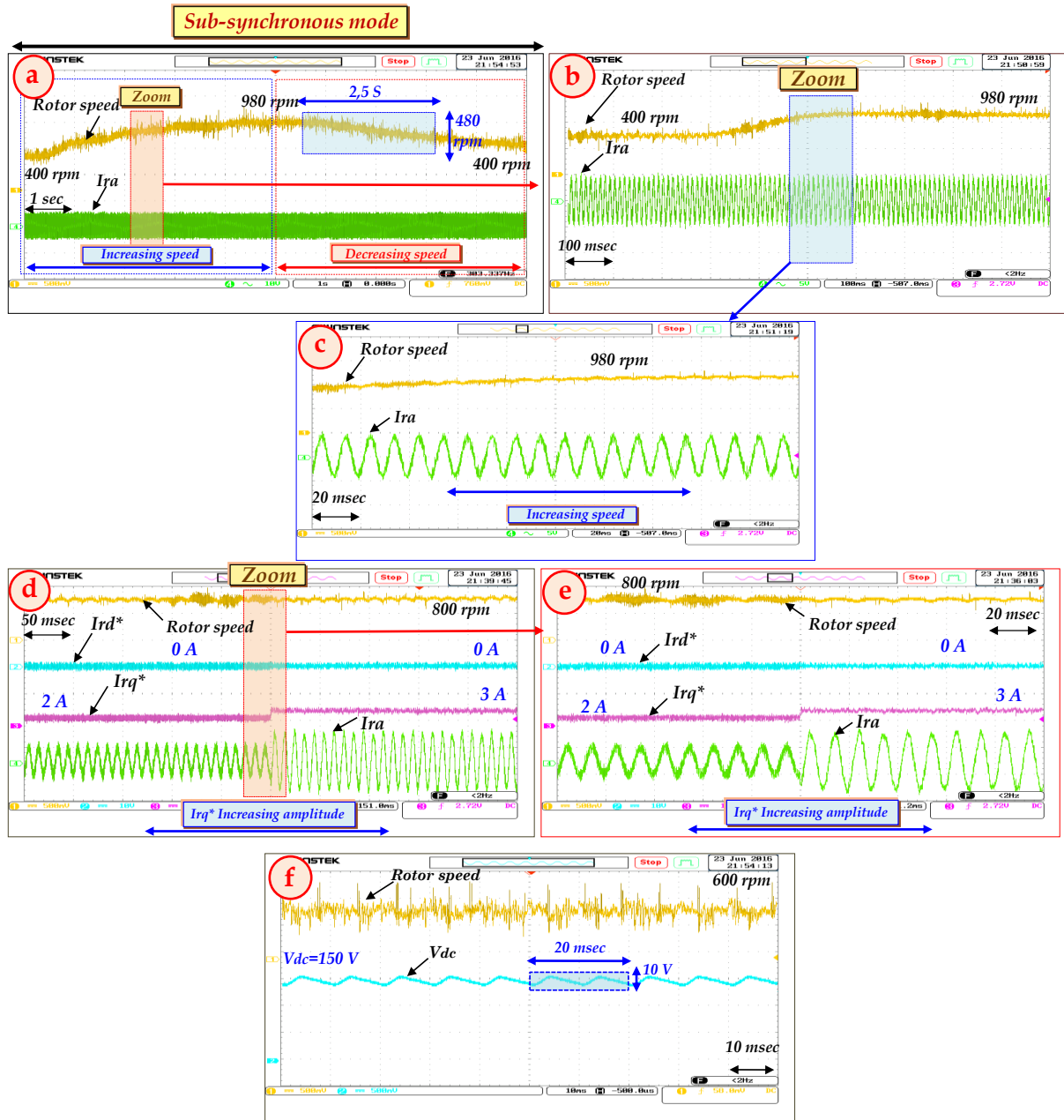


Figure.6.18 Steady and transient states of the RSC parameters under the variation of the speed and rotor direct and quadrature respectively (stand-alone mode).

Figure.6.19-(a) illustrates the behavior of the three stator currents phases (I_{s_abc} (A) under magnitude variation (decreasing amplitude) during the stand-alone topology, due to the decreasing of the rotor reference quadrature current I_{rq}^* (A) magnitude during the period of 0.5 (sec) = (10*50 (msec)). Figure.6.18-(b) displays the zoom of the figure.6.19-(a), it can be seen the excellent sinusoidal form of the three stator current I_{s_abc} (A) with few ripples (THD I_{s_abc} (%) < 5(%)) in the period of 0.1 (sec) = (10*10 (msec)). Figure.6.19-(c) shows the variation of the stator currents I_{s_abc} (A) under magnitude variation (increasing amplitude) during the stand-alone topology, due to the increasing of the rotor reference quadrature current I_{rq}^* (A) magnitude during the period of 1(sec) = (10*100 (msec)). It is absolutely clear (as shown in figure.6.18-(d)) that despite the rotor reference quadrature currents I_{rq}^* (A) variation the three stator currents I_{s_abc} (A) have the sinusoidal waveform with neglected undulations during the period of 0.2 (sec) = (10*20 (msec)). Figures.6.19-(e, f, g, h, i and j) are experimental results obtained from the power quality analyzer, which shows the waves form of the stator currents and voltages respectively under Stand-alone conditions. Figures.6.19-(e, f and g) present the behavior of stator current (I_s (A)) and the stator voltage (V_s (V)) for three phases (a, b, and c) respectively during stand-alone connection. Figures.6.19-(h) shows the three sinusoidal stator currents I_{s_abc} (A) under speed variation. Figures.6.19-(i and j)

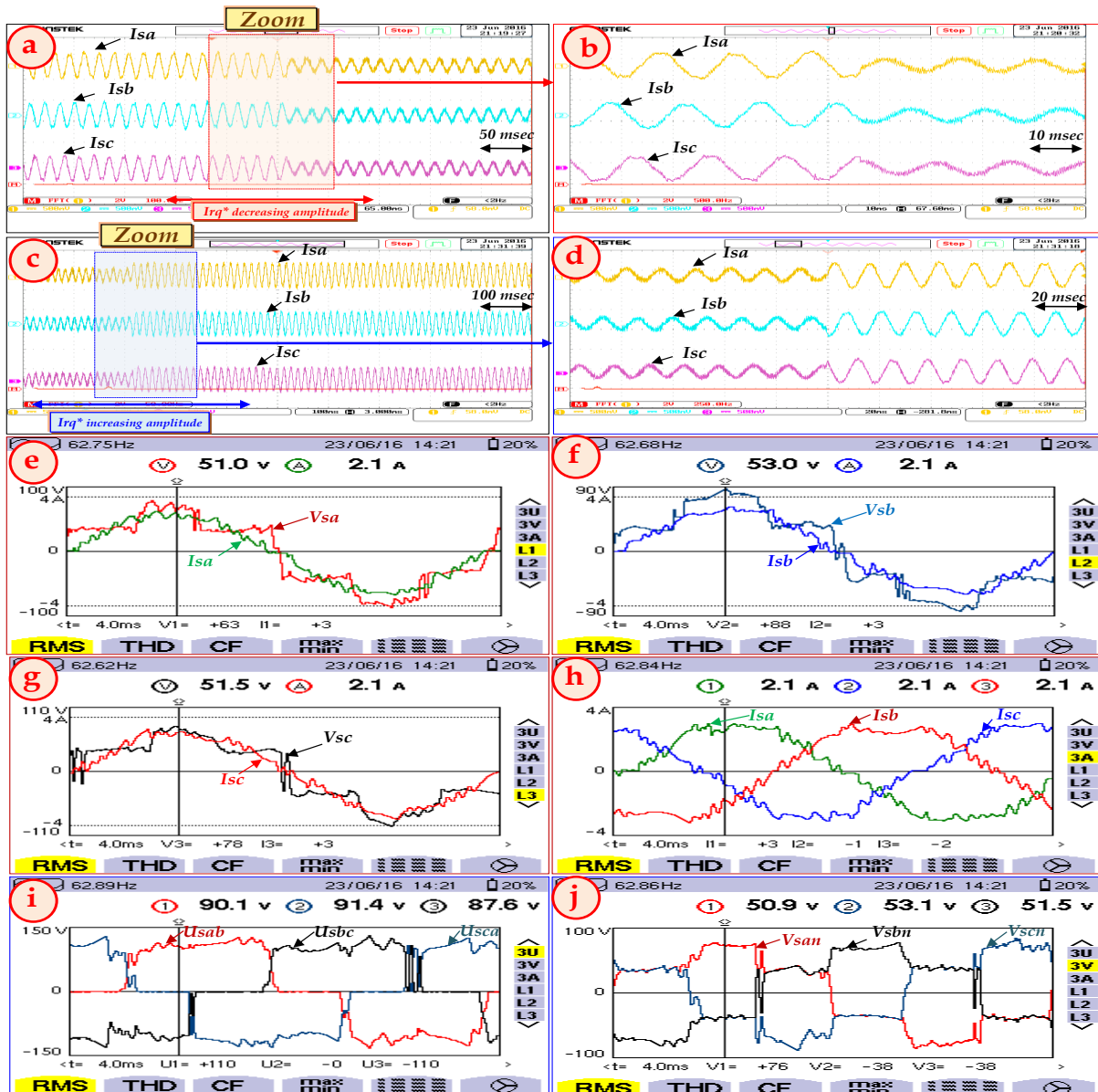


Figure.6.19 The performances of SSC under rotor direct and quadrature currents variation in both steady and transient states (stand-alone mode).

illustrate the stator line-to-line voltage U_{s_abc} (V) and the line-to-neutral voltage V_{sn_abc} (V) under stand-alone strategy.

6.7.2 Grid-connection mode

After having synchronized and connected the DFIG to the grid using PLL (Phase locked loop). Several tests have been carried out to study the performance of the supply-side converter in both transient and steady-state conditions, including bidirectional power flow with lagging, leading and a unity displacement factor.

A. Grid side converter (Grid-connection topology)

In the grid side converter, we used several tests, as shown in figures.6.20-(a, b, c, d, e and f). Figure.6.20-(a) displays the transient and steady states respectively of stator currents I_{s_abc} (A) in the period of 0.1 (sec) = (10*10 (msec)). Figure.6.20-(b) illustrates the behavior of the three phase's stator currents I_{s_abc} (A) under rotor reference quadrature I_{rq}^* (A) variation. Figure.6.20-(c) represents the zoom of the figure.6.20-(a) in steady state during the period of 0.05 (sec) = (10*5(msec)), it is clear that waveforms took sinusoidal form with neglected harmonics and ripples and represent an excellent stator current that will be injected in the grid with good power quality. Figure.6.20-(d) shows the stator currents I_{s_abc} (A) and the stator voltage V_{sb} (V), it is clear

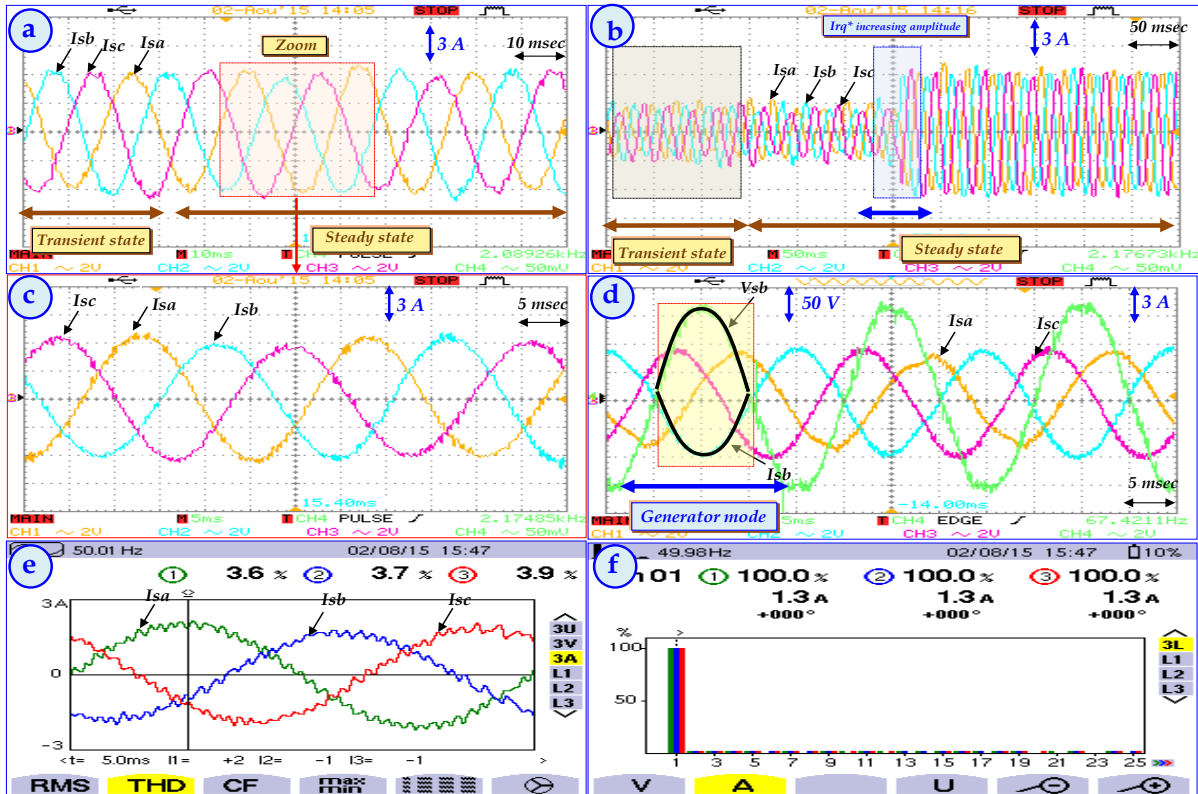


Figure.6.20 The performances of GSC under rotor direct and quadrature currents variation in both steady and transient states (grid-connection mode).

that the stator current I_{sb} (A) and stator voltage V_{sb} (V) are 180° out-of-phase, which proves that only the active power flows to the grid (that means: the generator mode; which stator reactive power Q_s (Var) equal to 0 (Var)). Figure.6.20-(e and f) are experimental results obtained from the power quality analyzer that shows the THD of the stator current (THD_ I_{s_abc} (%)) equal to 3.7 (%); less than 5 (%) satisfies the IEEE harmonic Standard 519.

B. Rotor side converter (Grid-connection topology):

In the Rotor side converter, we used several tests, divided into two steps:

- **Step 1:** The RSC experimental results are described as shown in figures.6.21-(a, b and c):

Figure.6.21-(a) shows the behavior of the Sub-synchronous mode (means below the synchronous speed N_n (rpm) < 1500 (rpm)) and Super-synchronous operation (means above the synchronous speed N_n (rpm) > 1500 (rpm)) under steady and transient states during the period of 10 (sec) = (10* 1 (sec)). It can be seen a proportionality between rotor speed N_n (rpm) and rotor currents I_{r_abc} (A) in terms of rotor frequency f_{rotor} (Hz). It can be seen the behavior of the rotor currents I_{r_abc} (A) under the speed increasing from 1300 (rpm) to 1700 (rpm) and then the speed decreasing with the same speed value (1700 (rpm) to 1300 (rpm)), it is obvious that

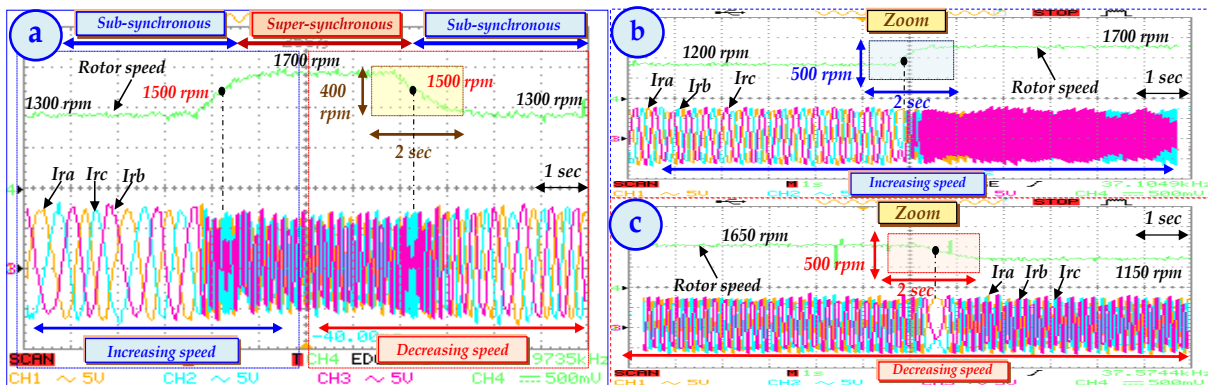


Figure.6.21 Sub-synchronous and Super-synchronous operations under rotor speed variation (grid-connection mode).

inverse rotor currents had the opposite direction when the rotor speed had passed through the synchronous speed (1500 (rpm)) because the slip is equal to the ratio $((N_s - N_r) / N_s)$ (Please refer to § 5.7 (Chapter.5)). In the extremity it can be observed the sinusoidal waveforms of the rotor currents I_{r_abc} (A) despite the rotor speed variation N_r (rpm) with neglected ripples. Figure.6.21-(b) presents only the speed increasing (from 1200 (rpm) to 1700 (rpm)) and the increasing period equal to 2 (sec). It clear that the rotor frequency f_{rotor} (Hz) is increasing. Figure.6.21-(c) shows only the speed decreasing (from 1650 (rpm) to 1150 (rpm)) and also the decreasing period equal to 2 (sec). It clear that the rotor frequency is decreasing f_{rotor} (Hz).

• **Step 2:** The RSC experimental results are described as shown in figures.6.22-(a, b, c, d, e, f, g, h, i and j):

Figure.6.22-(a) presents a behavior of the rotor reference and measured current (I_{ra}^* (A) and I_{ra_meas} (A)) in the transient and steady states under increasing and decreasing of the rotor reference quadrature current I_{rq}^* (A); from -5 (A) to -7 (A) and by keeping the rotor direct current to the zero value I_{rd}^* (A) = 0 (A) during the period of 0.25 (sec) = (10*25 (msec)). Figure.6.22-(b) illustrates the steady state of the behavior of the reference and measured rotor current under increasing and decreasing of the rotor quadrature current I_{rq}^* (A) from -7 (A) to -5 (A) and also by keeping at zero value the rotor reference direct current I_{rd}^* (A) = 0 (A) during 0.25 (sec) (=10*25 (msec)). For both figures (figures.6.22-(a and b)) it is absolutely clear that the measured rotor current follows exactly its reference with neglected current error using smooth hysteresis band equals to $\Delta I_r = 0.01$ (A) (as shown in table.6.1; case.IV). And the reason of keeping the rotor reference direct current equals to zero value is to ensure the exchange only of the active power; that means to guarantee the unity power factor (PF \approx 1). Figures.6.22 (c and d) illustrates the behavior of the stator and rotor measured sinusoidal currents (I_{sa_meas} (A) and I_{ra_meas} (A)) under rotor reference quadrature current I_{rq}^* (A) variation from -5 (A) to -7 (A) to -5 (A) again in the case of figure.6.22-(c) and from 0 (A) to +4 (A) to 0 (A) again in the case of figure.6.22-(d). It can be seen that for both figures the rotor frequency is less than the stator frequency (f_{rotor} (Hz) < f_{stator} (Hz)) during the period of 0.25 (sec) (=10* 25 (msec)). Figures.6.22-(e-f and g) display the same steady and transient states of the performance of reference direct current I_{rd}^* (A). It is clear that the rotor sinusoidal measured current I_{ra_meas} (A) follows exactly its reference I_{ra}^* (A) with neglected ripples. By using hysteresis band that equals ΔI_r (A) = 0.01 (A), this later is sufficient to maintain a good reference rotor current tracking despite rotor current and speed variation. Figure.6.22-(g) displays the zoom of the figure.6.22-(e) which show the behavior of the steady state of tracking reference current I_{ra}^* (A) under rotor direct I_{rd}^* (A) variation from 0 (A) to +7 (A) to 0 (A) again and by keeping negative value of the rotor quadrature current I_{rq}^* (A) equals to -5 (A) (to ensure the generator mode). Figure.6.21-(f) illustrates one period ($\omega t = \pi$) from Figure.6.22-(e) the tracking reference current is very clear and it can be seen the high performance of the validated hysteresis band during 0.05 (sec) (= 10*5 (msec)). Figure.6.22-(h) shows a simultaneity waveforms of stator and rotor measured currents (I_{sa_meas} (A) and I_{ra_meas} (A)) under variation of reference direct and quadrature reference currents (I_{rq}^* (A) and I_{rd}^* (A)) respectively. In the case of I_{rq}^* (A) from -7(A) to -3(A) at $t = (50 \text{ (msec)} * 2) = 0.1$ (sec), the rotor quadrature current equals to negative Torque means produced by the turbine emulator (DCM) to maintain the generator mode. And in the case of I_{rd}^* (A) from 0 (A) to -5(A) at $t = (50 \text{ (msec)} * 5.75) = 0.2875$ (sec) and from -5 (A) to 0 (A) again at $t = (50 \text{ (msec)} * 9.2) = 0.46$ (sec). Figure.6.22-(i) represents tracking reference direct and quadrature rotor current under variation (decreasing magnitude) of I_{rq}^* (A) from -7 (A) to -3(A) at $t = 50 \text{ (msec)} * 6 = 0.3$ (sec) and by keeping at zero value of the I_{rd}^* (A) = 0 (A) to ensure exchange only the active power to the grid in the case of generator mode. Figure.6.22-(j) displays the zoom of the figure.6.22-(i) that show an excellent tracking rotor current of direct and quadrature measured component as for as theirs references. It can be seen a good tracking of measured current with a neglected overshoot. It can be seen also an exchange of stator active power by keeping zero value of reference direct current.

The proposed FOC using hysteresis controllers offered excellent wind-system performances for grid-connection and stand-alone modes in transient and steady states. All experimental results (using dSPACE 1104 card in real time) especially the rotor' speed and currents variation confirm the robustness of proposed algorithm in terms of: power quality (excellent THD: < 5% respect the IEEE 519 Standard), overshoot, short response time, good tracking current and excellent power factor (PF \approx 0.96) in transient and steady states.

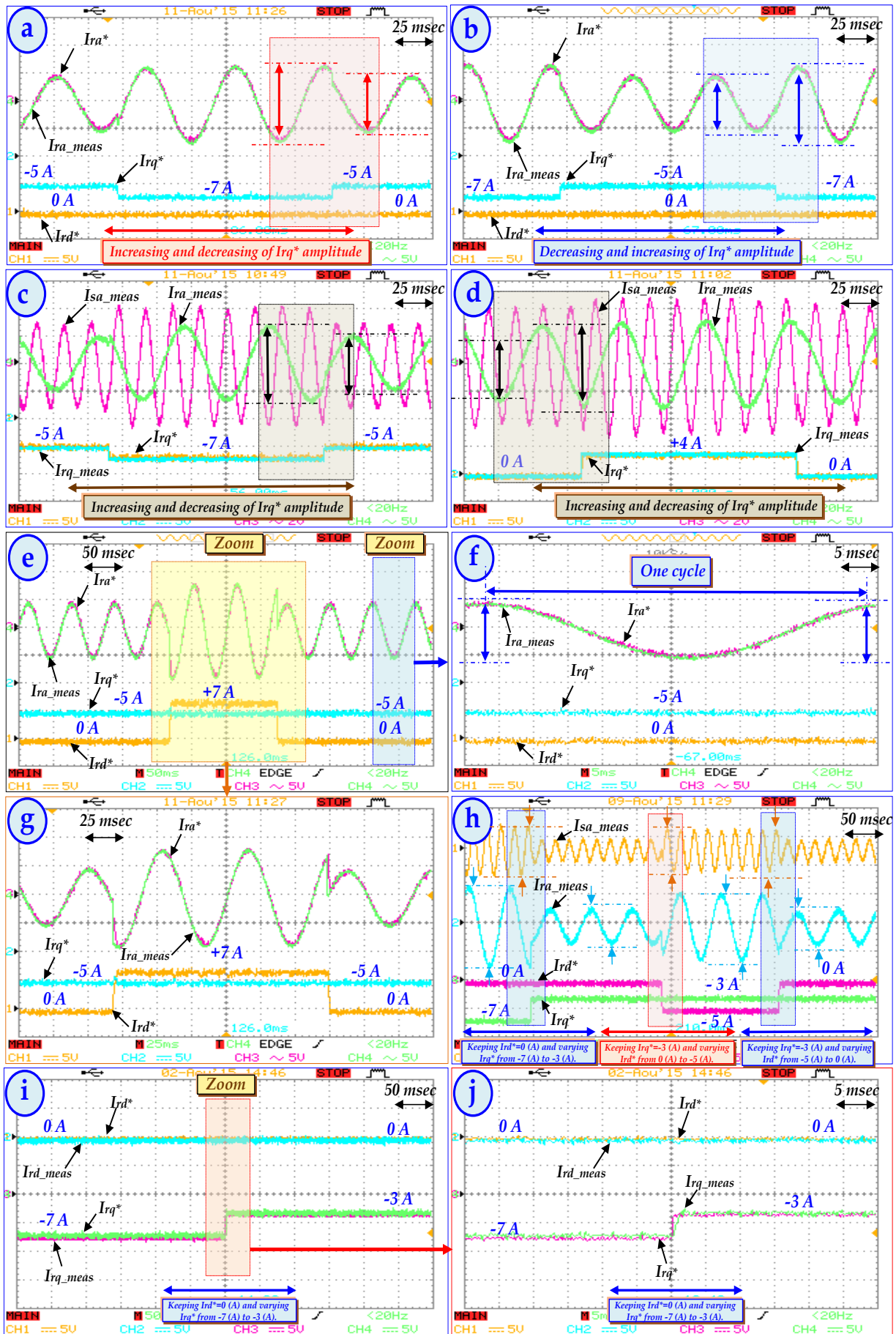


Figure.6.22 Robustness tests by variation of reference quadrature current to ensure the unity power factor (grid-connection mode).

6.8 Conclusion

In this chapter, the experimental real time implementation of high performances FOC based HCC for variable speed wind turbine-DFIG has been presented. Two approach are proposed to control the rotor side converter by the means direct and quadrature components (I_{rd} and I_{rq}). The first topology based on stand-alone, means the DFIG's stator is connected to resistive load by the mean of nonlinear load (rectifier converter) using bank capacitance between the resistance linear and nonlinear load for feltring the stator voltage regardless the load variation. In contrary to stand-alone, the grid-connection topology allows the connection of the stator directly to the grid by respecting the synchronization law (sequence, magnitude and frequency) with grid in order to ensure stator current injection in to the grid despite the wind speed fluctuating. Moreover, in steady state, it is shown that the proposed controller achieves sinusoidal grid current, THD (3.7 %) irrespective to the load variations and grid conditions compared to some of published literatures. The proposed control could be an excellent alternative in regulation system for variable speed wind energy conversion system.

6.9 References

- [1] Heng NIAN, and Yipeng SONG, "Direct Power Control of Doubly Fed Induction Generator under Distorted Grid Voltage", *IEEE Transactions on Power Electronics*, vol. 29, no. 2, 2014.
- [2] Heng NIAN, Peng CHENG, Z.Q. ZHU, "Coordinated Direct Power Control of DFIG System without Locked Loop under Unbalanced Grid Voltage Conditions", *IEEE Transactions on Power Electronics*, 2015.
- [3] Fayssal AMRANE, Azeddine CHAIBA and Saad MEKHILEF: "High performances of grid-connected DFIG based on direct power control with fixed switching frequency via MPPT strategy using MRAC and Neuro-Fuzzy control" *JPT Journal of power technologies*, vol, 96, n°: 1, 2016.
- [4] Roberto CÁRDENAS, Rubén PEÑA, Salvador ALEPUZ, and Greg ASHER, "Overview of Control Systems for the Operation of DFIGs in Wind Energy Applications", *IEEE Transactions on Industrial Electronics*, vol. 60, no. 7, 2013
- [5] Fayssal AMRANE, Azeddine CHAIBA and Ali CHEBABHI: "Improvement Performances of Doubly Fed Induction Generator via MPPT Strategy using Model Reference Adaptive Control based on Direct Power Control with Space Vector Modulation", *JEE Journal of Electrical Engineering*, vol: 16, n°: 3, pp. 218-225, 2016.
- [6] Jafar MOHAMMADI, Sadegh VAEZ-ZADEH, Saeed AFSHARNIA, and Ehsan DARYABEIGI, "A Combined Vector and Direct Power Control for DFIG-Based Wind Turbines", *IEEE Transactions On Sustainable Energy*, vol. 5, no. 3, 2014.
- [7] Michael K. BOURDOULIS, and Antonio T. ALEXANDRIDIS, "Direct Power Control of DFIG Wind Systems Based on Nonlinear Modeling and Analysis", *IEEE Journal of Emerging and Selected Topics in Power Electronics*, vol. 2, No. 4, 2014.
- [8] Bhim SINGH, and N. K. SWAMI NAIDU, "Direct Power Control of Single VSC-Based DFIG without Rotor Position Sensor", *IEEE Transactions On Industry Applications*, vol. 50, no. 6, 2014
- [9] Jiefeng HU, Jianguo ZHU, and David G. DORRELL, "Predictive Direct Power Control of Doubly Fed Induction Generators Under Unbalanced Grid Voltage Conditions for Power Quality Improvement", *IEEE Transactions on Sustainable Energy*, vol. 6, no. 3, 2015
- [10] Jiefeng Hu, Jianguo ZHU and David G. DORRELL, "Model-predictive direct power control of doubly-fed induction generators under unbalanced grid voltage conditions in wind energy applications". *IET Renewable Power Generation*, vol. 8, pp. 687-695, 2014
- [11] E.G. SHEHATA, "Sliding mode direct power control of RSC for DFIGs driven by variable speed wind turbines". *Alexandria Engineering Journal*, 2015.

- [12] S. TARAFT , Djemela. REKIOUA, D. AOUZELLAG and Seddik. BACHA, "A proposed strategy for power optimization of a wind energy conversion system connected to the grid", *Energy Conversion and Management*, 2015.
- [13] Badre BOSSOUFI, Mohammed KARIM, Ahmed LAGRIOUI, Mohammed TAOUSSI, and Aziz DEROUICH, "Observer Backstepping control of DFIG-Generators for wind turbines variable-speed: FPGA-based implementation", *Renewable Energy*, 2015.
- [14] G. D. MARQUES and Matteo F. IACCHETTI, "Stator Frequency Regulation in a Field-Oriented Controlled DFIG Connected to a DC Link", *IEEE Transactions on Industrial Electronics*, vol. 61, no. 11, pp.5930-5939, 2014.
- [15] Matteo F. IACCHETTI, Gil D. MARQUES and Roberto PERINI, "A Scheme for the Power Control in a DFIG Connected to a DC Bus via a Diode Rectifier", *IEEE Transactions on Power Electronics*, vol. 30, no. 3, pp. 1286-1296, 2015.
- [16] P.K. GAYEN, D. CHATTERJEE and S.K. GOSWAMI, "Stator side active and reactive power control with improved rotor position and speed estimator of a grid connected DFIG (doubly-fed induction generator)", *Energy*, 2015.
- [17] Rishabh Dev SHUKLA and Ramesh Kumar TRIPATHI, "Isolated Wind Power Supply System using Double-fed Induction Generator for remote areas", *Energy Conversion and Management*, vol. 96, pp. 473-489, 2015
- [18] Minh Quan DUONG, Francesco GRIMACCIA, Sonia LEVA, Marco MUSSETTA and Kim Hung LE, "Improving Transient Stability in a Grid-Connected Squirrel-Cage Induction Generator Wind Turbine System Using a Fuzzy Logic Controller", *Energies*, 8, pp. 6328-6349, 2015.
- [19] Fan XIAO, Zhe ZHANG and Xianggen YIN. "Fault Current Characteristics of the DFIG under Asymmetrical Fault Conditions", *Energies*, 8, pp. 10971-10992, 2015.
- [20] Buja GS, Kazmierkowski MP. "Direct torque control of PWM inverter-fed AC motors-survey", *IEEE Transactions on Industrial Electronics*, Vol. 51:744-57, 2004.
- [21] Trzynadlowski AM. "Scalar control methods, Control of induction motors", San Diego: Academic Press, pp. 93-105 [chapter5], 2001.
- [22] Mansour MOHSENI, Syed M. ISLAM, Mohammad A. S. MASOUM, "Enhanced Hysteresis-Based Current Regulators in Vector Control of DFIG Wind Turbines", *IEEE Transactions on Power Electronics*, vol. 26, pp. 223-234, 2011.
- [23] Fayssal AMRANE, Azeddine CHAIBA, Bruno FRANCOIS and Badr Eddine BABES, "Experimental Design of Stand-alone Field Oriented Control for WECS in Variable Speed DFIG-based on Hysteresis Current Controller", *IEEE conference, 15th International Conference on Electrical Machines, Drives and Power Systems ELMA, 1-3th June 2017 Sofia-Bulgaria*.
- [24] Fayssal AMRANE, Azeddine CHAIBA, Badr Eddine BABES and Saad MEKHILEF, "Design and Implementation of High Performance Field Oriented Control for Grid-Connected Doubly Fed Induction Generator via Hysteresis Rotor Current Controller", *Rev. Roum. Sci. Techn.- Électrotechn. et Énerg* vol: 61, n°: 4, pp. 319-324, 2016.
- [25] Fayssal AMRANE, Azeddine CHAIBA, Bruno FRANCOIS and Badreddine BABES, "Real Time Implementation of Grid-connection control using Robust PLL for WECS in Variable Speed DFIG-based on HCC", *5th International Conference on Electrical Engineering, IEEE Conference, ICEE 29-31th Oct 2017 Boumerdes-Algeria*.
- [26] Abdullah Asuhaimi B. MOHD ZIN , Mahmoud PESARAN H.A, Azhar B. KHAIRUDDIN ,Leila JAHANSHALOO, Omid SHARIATI, "An overview on doubly fed induction generators' controls and contributions to wind based electricity generation", *Renewable and Sustainable Energy Reviews*, vol 27, pp.692-708, 2013.
- [27] Ahmed G. ABO-KHALIL, "Synchronization of DFIG output voltage to utility grid in wind power system", *Renewable Energy*, Vol 44, pp. 193-198, 2012.

- [28] Gonzalo Abad Jesus LOPEZ, Miguel A. RODRIGUEZ, Luis MARROYO, Grzegorz IWANSKI, "Doubly fed induction machine: Modeling and control for wind energy generation", IEEE pressSeries on Power Engineering, 2011.
- [29] Jiefeng HU, Jianguo ZHU, and DAVID G. DORRELL. "Predictive Direct Power Control of Doubly Fed Induction Generators Under Unbalanced Grid Voltage Conditions for Power Quality Improvement", IEEE Transactions on Sustainable Energy, Vol. 6, no. 3, 943- 950, 2015.
- [30] Mahesh K. MISHRA and K. KARTHIKEYAN. "An Investigation on Design and Switching Dynamics of a Voltage Source Inverter to Compensate Unbalanced and Nonlinear Loads", IEEE Transaction. On Industrial Electronics, vol.56, no.8, pp. 2802-2810, 2009.
- [31] Ali CHEBABHI, Mohammed-Karim FELLAH, Mohamed-Fouad BENKHORIS, "3d Space Vector Modulation Control Of Four-Leg Shunt Active Power Filter Using Pq0 Theory", Rev. Roum. Sci. Techn. – Électrotechn. et Énerg., 60, 2, p. 185–194, Bucarest, 2015.
- [32] Tarak BENSLIMANE, "Open Switch Faults Detection and Localization In Three Phases Shunt Active Power Filter", Rev. Roum. Sci. Techn.– Électrotechn. et Énerg., vol: 52, 3, p. 359–370, Bucarest, 2007.
- [33] Yipeng SONG; Frede BLAABJERG, 'Analysis of Middle Frequency Resonance in DFIG System Considering Phase Locked Loop', IEEE Transactions on Power Electronics, col: xx, no: xx, pp.: xx-xx, DOI: 10.1109/TPEL.2017.2672867, 2017.
- [34] Jing MA; Yang QIU; Yinan LI; Weibo ZHANG; Zhanxiang SONG; James S. THORP, 'Research on the Impact of DFIG Virtual Inertia Control on Power System Small-Signal Stability Considering the Phase-Locked Loop', IEEE Transactions on Power Systems, vol: 32, no: 3, pp.: 2094 - 2105, 2017.
- [35] Xiangyu ZHANG; Yuan FU; Shuang WANG; Yi WANG, 'Effects of two-area variable inertia on transient stabilisation in interconnected power system with DFIG-based wind turbines', IET Renewable Power Generation, vol: 11, no: 5, pp.: 696 - 706, 2017.
- [36] Dawei XIANG; Chuandong WANG; Yeke LIU, 'Switching Frequency Dynamic Control for DFIG Wind Turbine Performance Improvement around Synchronous Speed', IEEE Transactions on Power Electronics, vol: 32, no: 9, pp: 7271 - 7283, 2017.
- [37] <https://www.dspace.com/en/pub/home/products>
- [38] Rakhee PANIGRAHI; Bidyadhar SUBUDHI, 'Performance Enhancement of Shunt Active Power Filter Using a Kalman Filter-Based Adaptive Control Strategy', IEEE Transactions on Power Electronics, Vol: 32, no: 4, pp: 2622 – 2630, 2017.
- [39] Subashini NALLUSAMY; Dharmalingam VELAYUTHAM; Uma GOVINDARAJAN; Deivasundari PARVATHYSHANKAR, 'Power quality improvement in a low-voltage DC ceiling grid powered system', IET Power Electronics, vol: 8, no: 10, pp: 1902 – 1911, 2015.
- [40] Rakhee PANIGRAHI; Bidyadhar SUBUDHI; Prafulla Chandra PANDA, 'A Robust LQG Servo Control Strategy of Shunt-Active Power Filter for Power Quality Enhancement', IEEE Transactions on Power Electronics, vol: 31, no: 4, pp: 2622 – 2860, 2866, 2016.

Chapter 7 :

General Conclusion and Future Works.

7.1 General Conclusion

This dissertation deals with the enhancement of the power control of WECS based on DFIG. The conventional IDPC is a control method which offers a decoupled active and reactive power control for wind system drives. IDPC is featured by simple structure, fast power dynamic. However, it suffers from the high sensitivity to the machine parameters variation and wind speed variation.

Due to the non-linearity of wind system, the power control of DFIG presents a big challenge under wind-speed variation and sensibility parameter. To overcome these problems an improved IDPC (based on classical PID controller) was proposed, in order to enhance the wind-system performances in terms; power error, tracking power and overshoot. Unfortunately using robustness tests (via severe tests); the wind-system offers non-satisfactory simulation results which were illustrated by the very bad power tracking and very big overshoot (>50%). In this context; adaptive, robust and intelligent controllers were proposed to control direct and quadrature currents (I_{rd} and I_{rq}) under MPPT strategy. In this case, the new IDPC based on intelligent controllers offered an excellent wind-system performance especially using robustness tests, which offered a big improvement especially using T2-FLC and NFC. Unfortunately the decoupling d-q axes component was not definitively resolved for this reason a new power control was necessary to overcome it. In this context, a new I/OLDC was proposed also to control DFIG's stator powers (P_s and Q_s) using MRAC controller. The algorithm offered a perfect performances with/without robustness tests in terms; power quality an excellent THD for the stator currents injected to the grid, a neglected overshoot (<1%), a neglected power error (<100 W_Var) and very short response time. To generate a big electric power with high quality; 3L-NPC was the best technical-economic solution, which satisfied the high wind-system performances using robustness tests.

To validate these algorithms, two experimental tests bench have been developed in laboratories using two wind turbine emulators in order to ensure the high performance of the proposed controls under robustness tests of rotor current reference tracking and speed under Sub- and Super-synchronous operation modes. Experimental tests (under IDPC using IP and FOC-HCC) prove the robustness and high efficiency of the proposed controls in which several wind system problems have been remedied in terms of; decoupling the variables state of the two axes (d and q), sensitivity to the parametric variation, references tracking, power error, response time and overshoot.

The main objective of this thesis is the improvement of the WECS' performances based on DFIG' drive, under power control using various control approaches. In this context, the research work has been addressed these principal points concerning the conventional control algorithm' drawbacks to will be treated:

- *The parameters changement sensibility (noted in conventional IDPC) is solved using intelligent and robust controllers (Improved IDPC and Novel I/OLDC).*
- *The important overshoot noted especially in conventional IDPC, is overcome using adaptive and artificial controllers (especially using T2-FLC and NFC).*
- *The coupling terms under both axes (d and q) is applied especially in high wind-power generation (HWPG) is treated through novel I/OLDC using an adaptive regulators (MRAC).*
- *The response time is improved (from the order of $10e^{-2}$ (sec) to $10e^{-3}$ (sec)).*
- *The power tracking also is more improved especially using the improved IDPC and the Novel I/OLDC,*
- *Good power/voltage quality which will be transmitted to the grid (excellent THD that respect IEEE standards (< + 5%)) and Power factor is maintain to the unitary ($PF \approx 1$) despite the wind-system variation.*
- *A neglected power error less than 100 (W_Var) which presents < 2.5 % of the rated power.*

7.2 Future Works

- *Improve the hardware implementation ground by the use of the Field Programmable Gate Array (FPGA) instead of dSPACE 1104 signal card. The new FPGA technology is featured by very high sampling frequency (less than $1e^{-6}$) and it can be offered with lower cost.*
- *The load variation is interesting study in the case of both proposed algorithms (FOC-HCC and IDPC) in order to ensure the power transmitted limit. Secondly, stator voltage control is necessary (at the load level) to improve the energy management at all times.*
- *Artificial intelligence (Fuzzy Control and Neuro-Fuzzy Control) is an adequate solution in an experimental implementation (using the same experimental test bench) to improve the stator powers and the rotor currents control, despite of the sudden wind variation, parameters variation and load variation respectively.*
- *Experimental implementation of the MPPT strategy (via Emulator turbine), in order to extract the maximum wind power despite the wind-speed variation by the means of artificial intelligent controllers.*
- *In order to rise the output power of WECS, the 3L-NPC converters are the best solutions in experimental validation especially if the aerodynamic power is high.*
- *In order to ensure the accuracy of PI', IP', PID' and MRAC' gains; Genetic algorithms (GA) and Particle Swarm Optimization (PSO) will be proposed to minimize the calculation error and to offer optimal values for the proposed algorithm.*
- *The predictive control is an excellent alternative for the Wind-system based on the independently control the active and reactive powers. The basic principle of this command does not require the PWM modulation (contrary case of IDPC and I/OLDC) which minimizes the calculation time also it is easy to implement.*
- *In order to minimize the cost, the observers (speed ...ect) will be interesting idea in experimental implementation instead the sensors.*

Appendix :

A, B and C

Appendix.A. WECS Parameters (<i>Chapters n°: 2, 3, 4, 5 and 6</i>) + Real time implementation (<i>PWM and SVM Strategies</i>) + Parameters' identification topology + List of Wind Turbine Manufacturers	176
A.1 Simulation part.....	176
A.2 Experimental part.....	176
A.3 Real time implementation.....	176
A.4 Parameters' identification topology of the Experimental part (<i>chapter n°5 and Chapter n°6</i>)	178
Appendix.B. Isolation cards of dSPACE1103 and dSPACE1104.....	180
B.1 dSPACE1103 Isolation Card (<i>L2EP Laboratory/ France</i>)	180
B.2 dSPACE1104 Isolation Card (<i>LAS Laboratory, UFASétif-1/Algeria</i>)	181
Appendix.C. DFIG and Emulator turbine using in chapter n°5 and Chapter n°6	182
C.1 Wind Energy conversion system used in Chapter n°5 (<i>L2EP Laboratory</i>).....	182
C.2 Wind Energy conversion system used in Chapter n°6 (<i>LAS Laboratory</i>).	182
C.3 The gains's values of the proposed controllers (<i>chapters n°; 2, 3, 4, 5 and 6</i>).....	182
C.4 Neutral Point Clamped (NPC) realized in L2EP Laboratory.	183

A.1 Simulation part:**Table.A.1** Parameters of the DFIG (Chapter: 2, 3 and 4).

Rated Power:	4.0 kW
Stator Resistance:	$R_s = 1.2 \Omega$
Rotor Resistance:	$R_r = 1.8 \Omega$
Stator Inductance:	$L_s = 0.1554 H.$
Rotor Inductance:	$L_r = 0.1558 H.$
Mutual Inductance:	$L_m = 0.15 H.$
Rated Voltage:	$V_s = 220/380 V$
Number of Pole pairs:	$P = 2$
Rated Speed:	$N = 1440 \text{ rpm}$
Friction Coefficient:	$f_{DFIG} = 0.00 \text{ N.m/sec}$
The moment of inertia	$J = 0.2 \text{ kg.m}^2$

Table.A.2 Parameters of the wind turbine (Chapter: 2, 3 and 4).

Rated Power:	4.5 kW
Number of blades:	$P = 3$
Blade diameter	$R = 3 \text{ m}$
Gain:	$G = 4.15$
The moment of inertia	$J_f = 0.00065 \text{ kg.m}^2$
Friction coefficient	$f_f = 0.017 \text{ N.m/sec}$
Air density:	$\rho = 1.22 \text{ Kg/m}^3$

A.2 Experimental part:**Table.A.3** Parameters of the DFIG (L2EP Laboratory/France) (Chapter: 5).

Rated Power:	4.5 kW
Stator Resistance:	$R_s = 0.4 \Omega$
Rotor Resistance:	$R_r = 0.8 \Omega$
Stator Inductance:	$L_s = 0.082 H.$
Rotor Inductance:	$L_r = 0.082 H.$
Mutual Inductance:	$L_m = 0.081 H.$
Rated Voltage:	$V_s = 220/380 V$
Number of Pole pairs:	$P = 2$
Rated Speed:	$N = 1395 \text{ rpm}$
Friction Coefficient:	$f_{DFIG} = 0.00 \text{ N.m/sec}$
The moment of inertia	$J = 0.2 \text{ kg.m}^2$

Table.A.4 Parameters of the emulator wind turbine "Asynchronous MOTOR: ASM" (Chapter: 5).

Rated Power:	4.0 kW
Y/Δ:	380/220 V
Cos θ:	0.82
Rated speed:	$N = 1440\text{-}2000 \text{ rpm}$

Table.A.5 Parameters of the DFIG (LAS Laboratory/Algeria) (Chapter: 6).

Rated Power:	3.5 kW
Stator Resistance:	$R_s = 2.3 \Omega$
Rotor Resistance:	$R_r = 4.95 \Omega$
Stator Inductance:	$L_s = 0.04 H.$
Rotor Inductance:	$L_r = 0.039 H.$
Mutual Inductance:	$L_m = 0.041 H.$
Rated Voltage:	$V_s = 220/380 V$
Number of Pole pairs:	$P = 2$
Rated Speed:	$N = 1420 \text{ rpm}$
Friction Coefficient:	$f_{DFIG} = 0.00 \text{ N.m/sec}$
The moment of inertia	$J = 0.2 \text{ kg.m}^2$

Table.A.6 Parameters of the emulator wind turbine 'Direct Current Motor: DCM' (Chapter: 6).

Rated Power:	3.0 kW
Rated speed:	$N = 1500 \text{ rpm}$
Armature:	220 V/15.4 A
Field:	170 V/0.71
Coupling	Shunt.

A.3 Real Time Implementation

Figure.A.1 presents the experimental results of triangular carrier using dSPACE1103 for a frequency equals to 10 (kHz). Figures.A-(2 and 3) present an experimental results of switching signals generated by PWM and SVM strategies respectively to control the six IGBTs of inverter (SEMIKRON or SEMIKUBE).

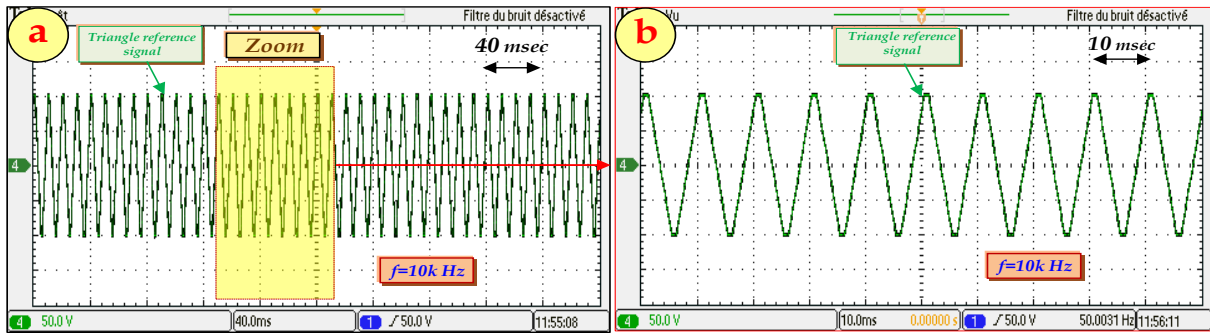


Figure.A.1 Experimental result of triangular carrier ($f=10\text{ KHz}$).

- PWM (Pulse Width Modulation) and SVM (space vector modulation) strategies using Matlab/Simulink® R2009a for experimental tests:

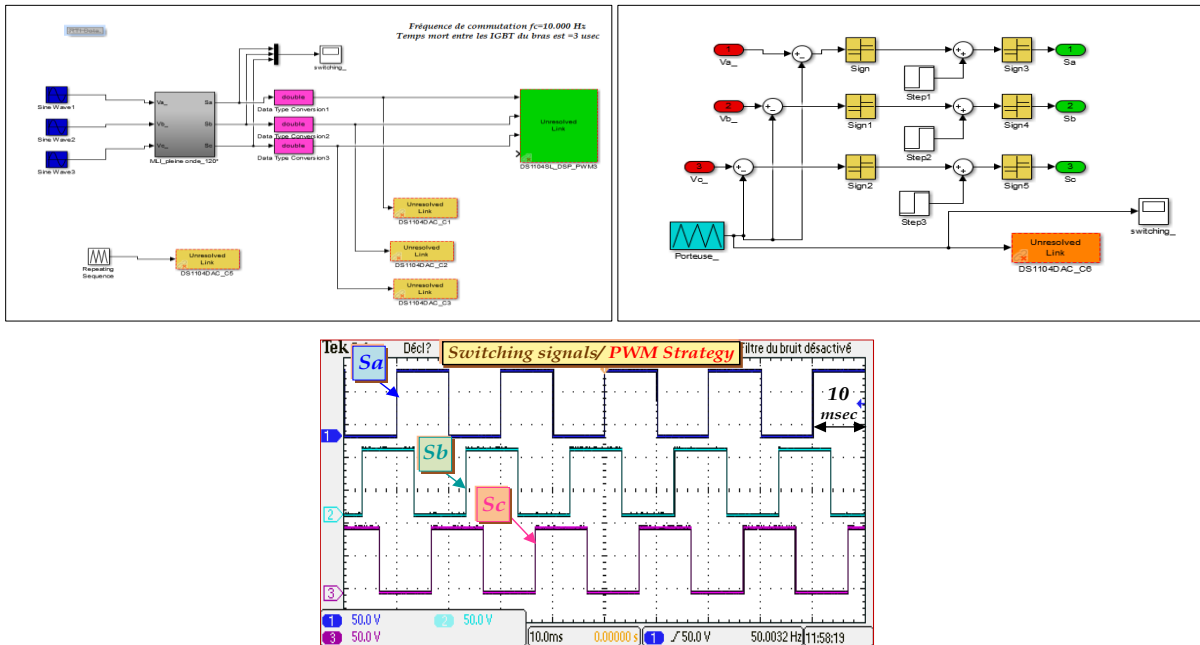


Figure.A.2 Block diagram of the PWM strategy under Matlab/Simulink® and experimental result of switching signals Sa, Sb and Sc.

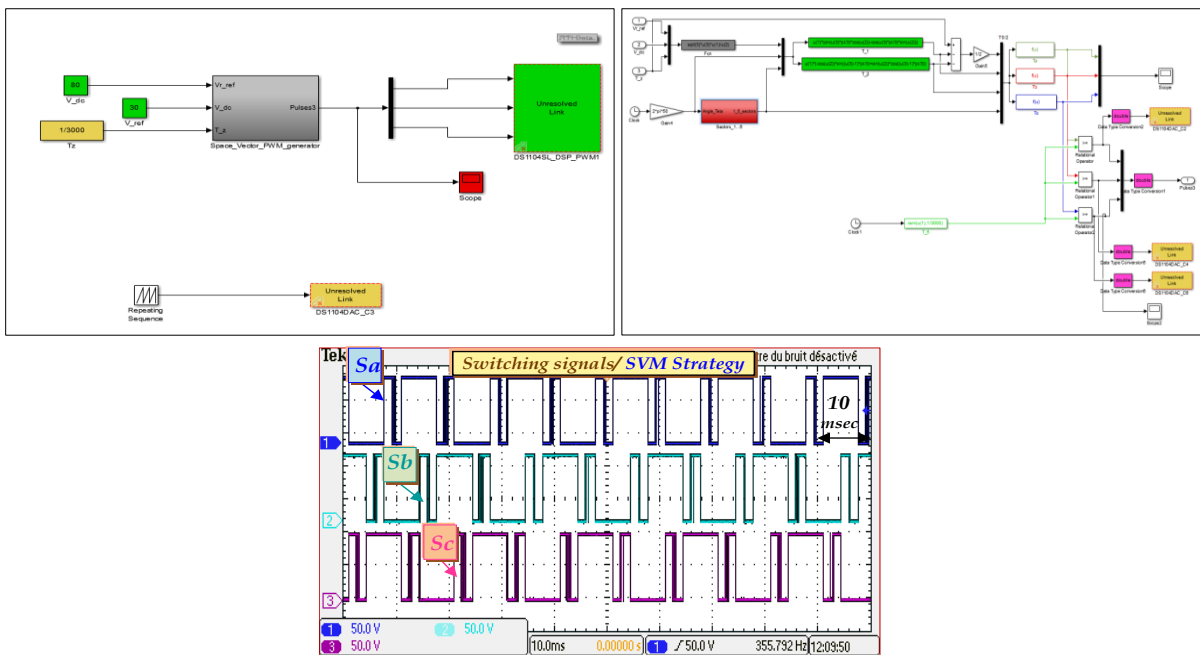


Figure.A.3 Block diagram of the SVM strategy under Matlab/Simulink® and experimental result of the switching signals Sa, Sb and Sc.

A.4 Parameters' identification topology of the Experimental part (chapter n°5 and Chapter n°6):¹

The electrical model of the doubly fed induction machine is equivalent to that of the asynchronous cage machine. However, the methods for identifying the parameters of the two machines are different since, in the case of the cage machine, the cage is a three-phase winding but without it being possible to determine by direct measurement the values of the current flowing in the bars. For the doubly fed induction machine the rotor is wound and accessible for the measurement of currents and voltages. In this case, the identification of the electrical parameters differs from that of the cage machine. The identification of the mechanical parameters J and f (respectively moment of inertia and coefficient of viscous friction) and the resistances of stator and rotor phases are, however, identical and will not be described in this appendix.

- **Measurement of the inductance of a stator phase l_s , of the mutual stator-stator L_{ms} , of the mutual stator-rotor L_{msr} and the magnetizing inductance L_m :**

The basic diagram of this test is given in figure.A.4. Since the rotor of the machine is open, a single phase of the stator is fed in order to deduce the proper inductance L_s . The measurement of the voltage at the terminals of one of the other two rotor windings makes it possible to deduce the mutual stator L_{ms} and the measurement of a composite rotor voltage gives the mutual stator-rotor L_{msr} .

The self-inductance can't be measured for the rotor phases because the neutral point is not accessible. The supply of a single rotor phase is therefore not conceivable.

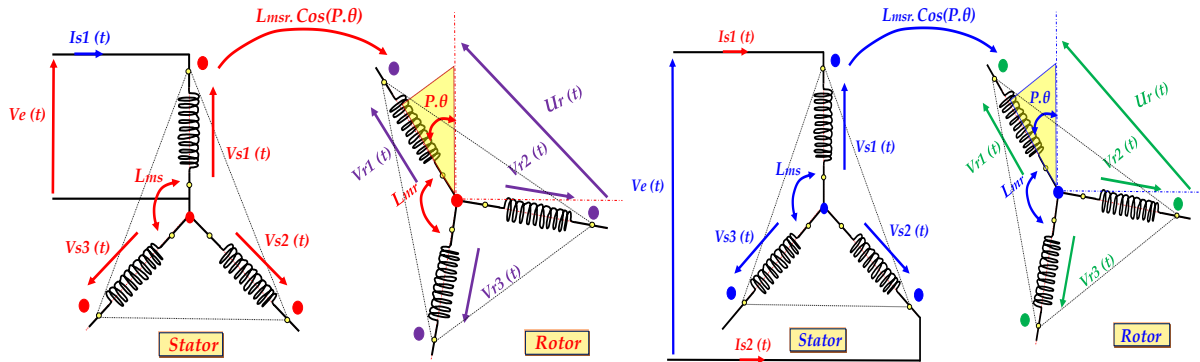


Figure.A.4 Measurement of l_s , L_{ms} , L_{msr} and L_m .

Figure.A.5 Measurement of L_s and L_r .

Note that the determination of mutual inductance L_{msr} requires a rotation the rotor in order to obtain the maximum voltage between two phases of the rotor. Moreover, the influence of the stator resistance R_s and that of the resistance R_f modeling the iron losses must be negligible, it is then necessary to check with a wattmeter that $P < 0.14 \cdot S$ ($P \ll Q$).

The relations giving l_s , L_{ms} and L_{msr} are:

$$l_s = \frac{V_{s1}}{I_{s1} \cdot \omega_s}; L_{ms} = \frac{V_{s2}}{I_{s1} \cdot \omega_s}; L_{msr} = \frac{U_r}{I_{s1} \cdot \omega_s \cdot \sqrt{3}} \quad (\text{A.1})$$

We can deduce:

$$L_m = \frac{3}{2} * L_{msr}; L_s = l_s - L_m \quad (\text{A.2})$$

- **Measurement of stator or rotor cyclic inductance:**

The basic diagram of this test is given in figure.A.5. Two phases of the stator are supplied in series and the rotor is open. Equation (A.3) shows how the stator cyclic inductance can be obtained on the one hand and the rotor cyclic inductance on the other hand if the test is transposed to the rotor (two phases of the rotor supplied in series).

$$L_s = \frac{V_{s1}}{I_{s1} \cdot \omega_s}; L_r = \frac{U_r}{I_{r1} \cdot \omega_s} \quad (\text{A.3})$$

¹ The main idea of parameters' identification topology was inspired from PhD Thesis of Mr. Frédéric POITIER "Etude ET Commande De Generatrices Asynchrones Pour L'Utilisation de L'Energie Eolienne, -Machine asynchrone à cage autonome, -Machine asynchrone à double alimentation reliée au réseau" pp. 166, year: 2003, in French language.

Table.A.7 List of wind turbine manufacturers.

Manufacturer	Web page
AAER (Canada)	http://www.pioneerwindenergy.com/
Acciona (Spain)	http://www.acciona-energia.es
ACSA (Spain)	http://www.acsaeolica.com
Alstom-Ecotecnia (France, Spain)	http://www.alstom.com/power
Areva Wind (France, Germany)	http://www.areva-wind.com/
AMSC (USA)	http://www.amsc.com/products/applications/eneable/
Aeronautica Windpower (USA)	http://aeronauticawind.com
Alizeo (France)	http://www.groupe-alizeo.com
Avantis (China, Germany, Austria)	http://www.avantis-energy.com
AWE (Canada)	http://www.awe-wind.com/
Bard (Germany)	http://www.bard-offshore.de/
Blaster (Norway)	http://www.blaaster.no
China Creative Wind Energy (China)	http://ccwewind.com
Clipper (UK)	http://www.clipperwind.com
Cwel (India)	http://www.cwel.in
Darwind (Netherland, China)	http://www.xemc-darwind.com/
Ddis (France)	http://www.ddiswt.com
Doosan (South Korea)	http://www.doosanheavy.com/
Dong Fang (China)	http://www.dongfang.com.cn
Elecon Engineering (India)	http://www.elecon.com
Elsewedy (Egypt)	http://www.elsewedyelectric.com/
Enercon (Germany)	http://www.enercon.de
Envision (China)	http://www.envisioncn.com
Eviag (Germany)	http://www.eviag.com/
EWT (Netherland)	http://www.ewtinternational.com/
Fuhrlander (Germany)	http://www.fuhrlander.de/
Gamesa (Spain)	http://www.gamesacorp.com
GC China Turbine Corporation (China)	http://www.gcchinaturbine.com
Ghodwat (India)	http://www.ghodawatenergy.com
Hewind (China)	http://www.hewind.com
IMPESA (Argentina)	http://www.impesa.com.ar/
Mitsubishi (Japan)	http://www.mhi.co.jp/
Mingyang (China)	http://www.mywind.com.cn
GE Energy (USA)	http://www.ge-energy.com/
Hyundai (South Korea)	http://www.hyundai-elec.com
Hyosung (South Korea)	http://www.hyosung.com
Jeumont (France)	http://www.jeumontelectric.com
Leitwind (Italia)	http://www.leitwind.com
Mervoento (Finland)	http://www.mervoento.fi
Moncada Energy Group (Italy)	http://www.moncadaenergy.com/
Mtorres	http://www.mtorres.es/
Multibrid	http://www.multibrid.com
Nordex (Germany)	http://www.nordex-online.com/
Northern Power (USA)	http://www.northernpower.com/
Norwin (Denmark)	http://www.norwin.dk/
RePower (Germany)	http://www.repower.de/
Samsung (South Korea)	http://www.shi.samsung.co.kr/
Sany (China)	http://www.sanyse.com.cn
Shanghai Electric Company (China)	http://www.shanghai-electric.com
Schuler (Germany)	http://www.schulergroup.com
Siemens (Germany)	http://www.energy.siemens.com/
Sinovel (China)	http://www.sinovel.com
Statoil (Norway)	http://www.statoil.com
Subaru (Japan)	http://www.fhi.co.jp
Suzlon (India)	http://www.suzlon.com
Vensys (Germany)	http://www.vensys.de/
Vestas (Denmark)	http://www.vestas.com
Unison (South Korea)	http://www.unison.co.kr/
W2E (Germany)	http://www.w2e-rostock.de/
Wikow (Czech republic)	http://www.wikov.com
Windflow (New Zeland)	http://www.windflow.co.nz/
WinWinD (Finland)	http://www.winwind.fi/
Wind Direct (Austria)	http://www.windtec.at
Zephyros (Netherlands)	http://www.peeraer.com/zephyros/

B.1 dSPACE1103 Isolation Card (L2EP Laboratory/ France):

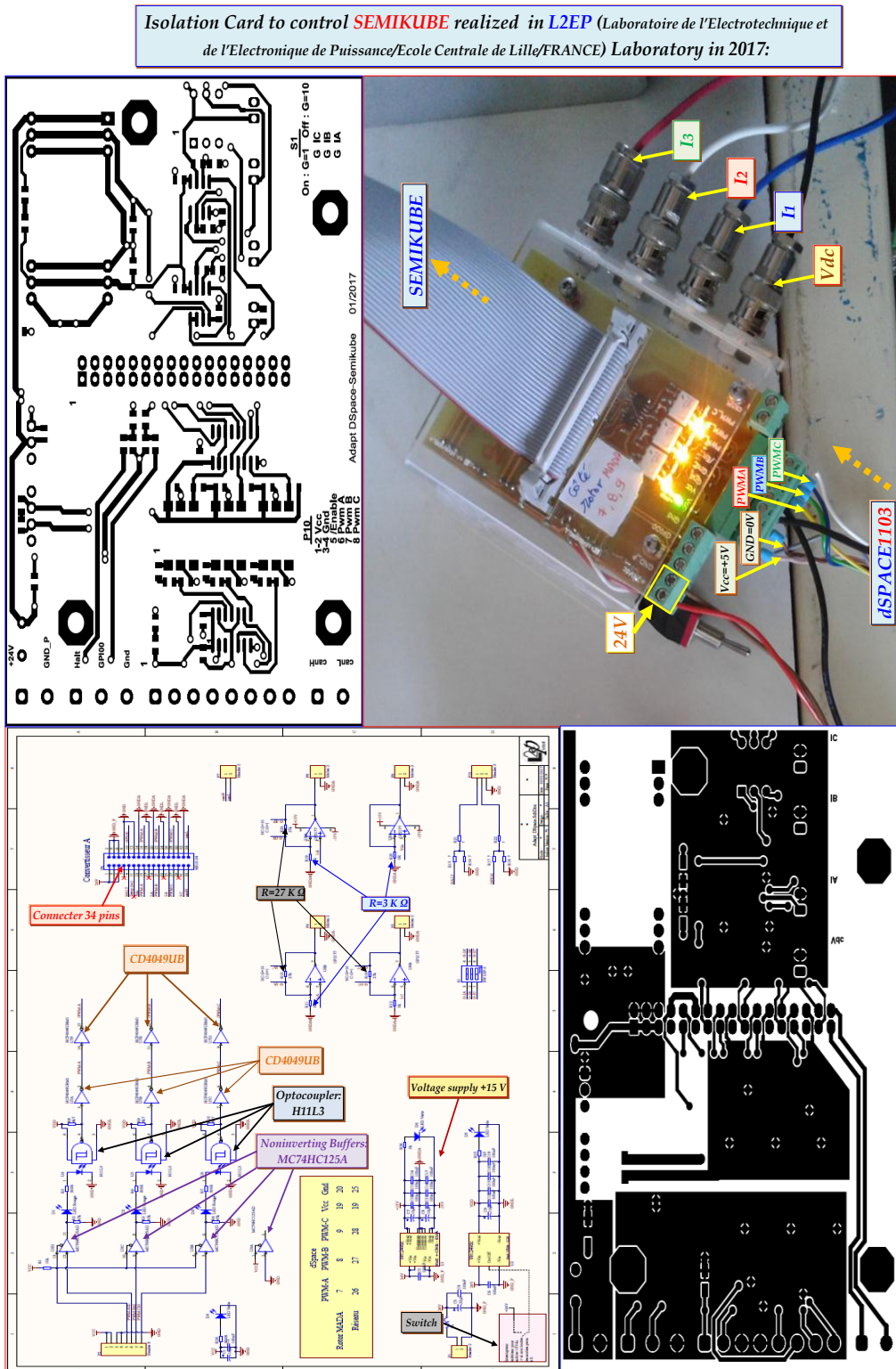


Figure.B.1 dSPACE1103's isolation card.

Table.B.1 Components of the dSPACE1103's isolation card.

Components of the SEMIKUBE® Isolation Card:
-Connector: 34 pins, Resistances: (3* R1=27 K Ω), (3* R2=3 K Ω), - Buffer/amplifier: 3* CD4049UB, Switch (*1), - Optocoupler: (3* H11L3), voltage supply +15 V, Non-inverting Buffers MC74HC125A (*4).

B.2 dSPACE1104 Isolation Card (LAS Laboratory, UFASétif-1/Algeria):

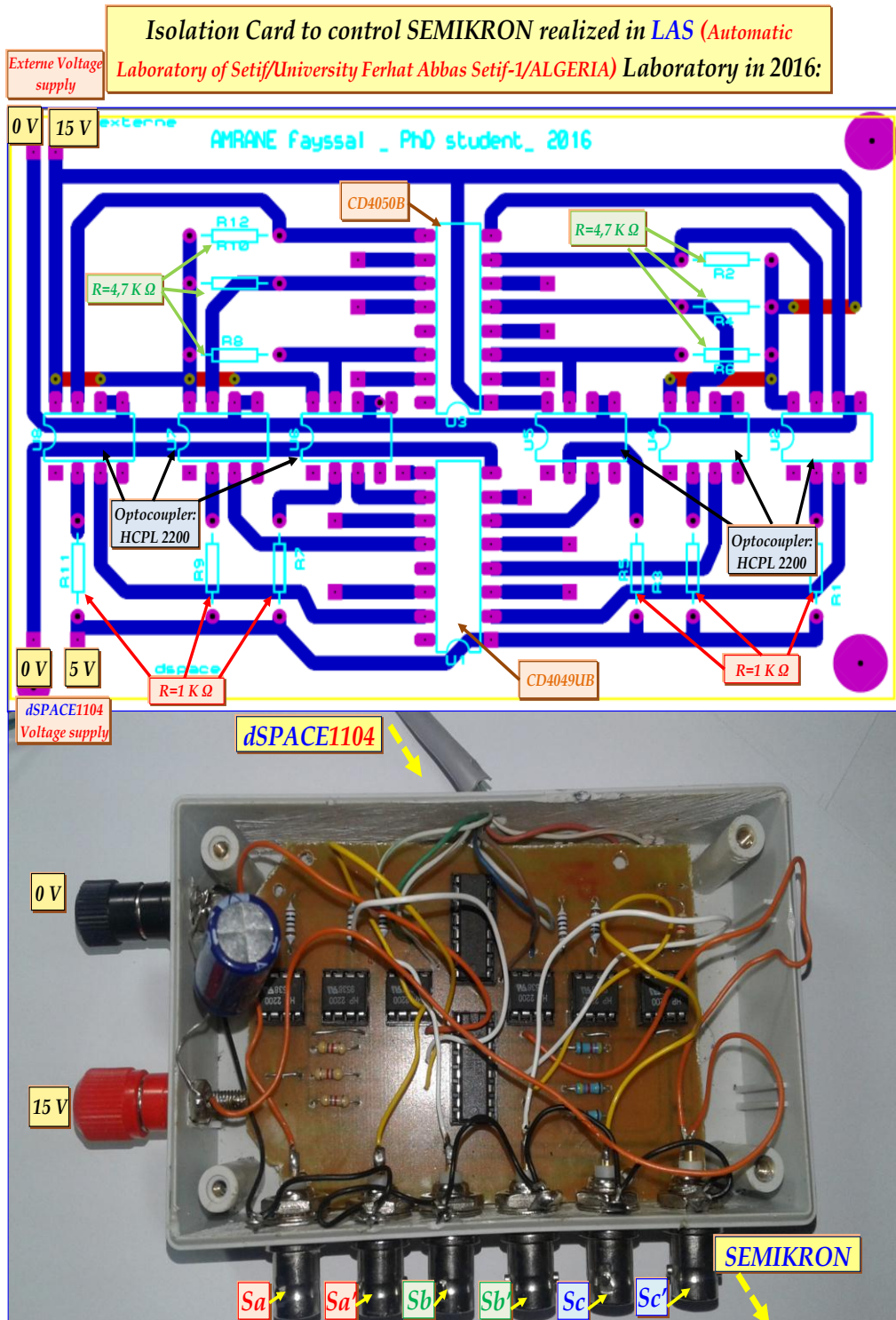


Figure.B.2 dSPACE1104's isolation card.

Table.B.2 Components of the dSPACE1104's isolation card.

Components of the SEMIKRON® isolation card:
-Resistances: (6* R1=4.7 K Ω), (6* R2=1 K Ω) and 6* BNC (connector).
-Optocoupler: (6* HCPL2200).
-Buffer/amplifier and inverse: 1* CD4050B and 1*CD4049UB.

C.1 Wind Energy conversion system used in Chapter N°5 (L2EP Laboratory)

1- DFIG (4.5 kW):

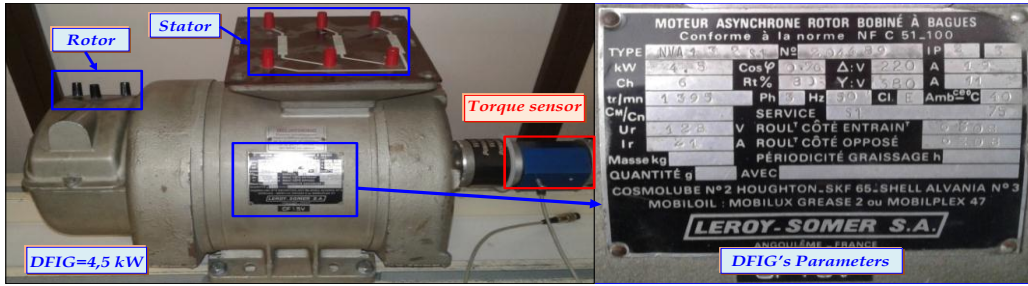


Figure.C.1 The DFIG' nameplate used in chapter 5.

2- Wind Turbine Emulator/Asynchronous Motor (4 kW):

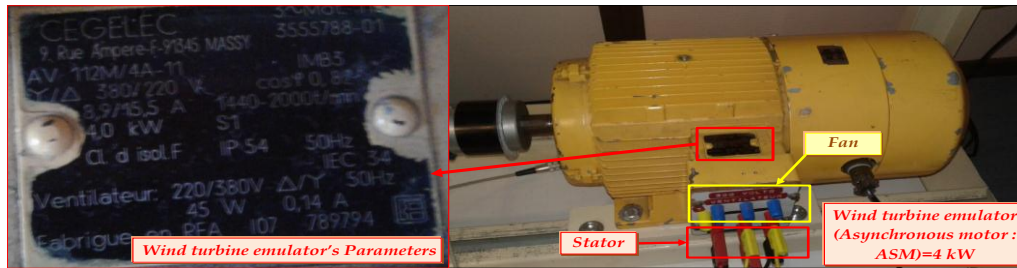


Figure.C.2 The Wind turbine emulator' nameplate used in chapter 5.

C.2 Wind Energy conversion system used in Chapter N°6 (LAS Laboratory)

1- DFIG (3.5 kW):

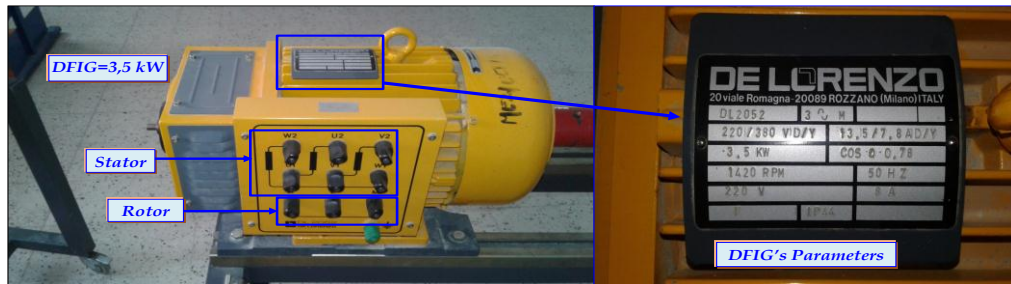


Figure.C.3 The DFIG' nameplate used in chapter 6.

2- Wind Turbine Emulator/Direct current motor (3 kW):

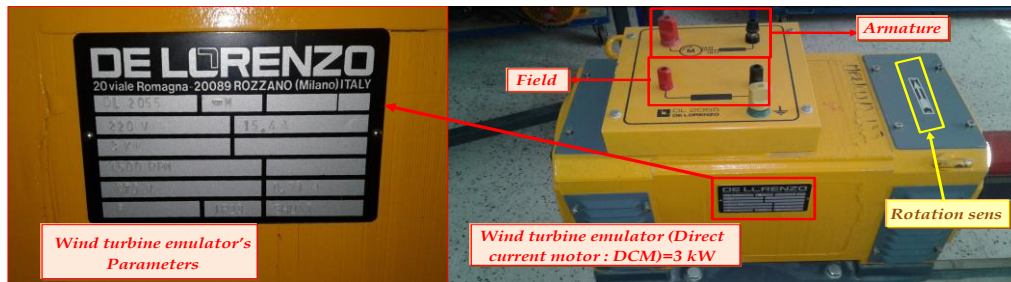


Figure.C.4 The Wind turbine emulator' nameplate used in chapter 6.

C.3 The gains's values of the proposed controllers (chapters; 2, 3, 4, 5 and 6):

"Knowing that: the simulation conditions are detailed below (using Matlab/Simulink® R2009a)"

Table.C.1 The simulation conditions using Matlab/Simulink® R2009a

Type:	Fixed-step.
Ode-4:	Range Kutta Order4
Fixed-step Size (Fundamental sample time):	Simulation studies: 1e-5.
Fixed-step Size (Fundamental sample time):	Experimental studies: 1e-4.
Tasking mode for periodic sample time:	Auto.

Table.C.2 The gains's values of the proposed controllers (chapters; 2, 3, 4, 5 and 6).

Gain's controllers								
	PI	IP	PID	MRAC	T1-FLC	T2-FLC	NFC	HCC
Chapter 2:	P_s and Q_s $K_p=30$ $K_i=1200$ I_{rq} and I_{rd} $K_p=2500$ $K_i=1250$	-	P_s and Q_s $K_p = 30$ $K_i = 1200$ $K_d = 0.0077$ I_{rq} and I_{rd} $K_p = 2500$ $K_i = 1250$ $K_d = 0.000055$	-	-	-	-	-
Chapter 3:	-	-	P_s and Q_s $K_p = 41$ $K_i = 2000$ $K_d = 0.007099$	I_{rq} and I_{rd} $K=5e^{+5}$, $K_a=0.55$, $K_{G1}=0.0002$, $K_{G2}=0.0001$.	I_{rq} and I_{rd} $G_1 = 1/2000$ $G_2 = 1/2000$ $G_3 = 2000$	I_{rq} and I_{rd} $G_1 = 1/2000$ $G_2 = 1/2000$ $G_3 = 2000$	I_{rq} and I_{rd} $G_1 = 1/2500$ $G_2 = 1/2500$ $G_3 = 1500$	-
Chapter 4:	P_s and Q_s $K_p=2100$ $K_i=10e^{+7}$.	-	-	P_s and Q_s $K=5e^{+5}$, $K_a=0.9$, $K_\beta=5$, $K_{G1}=0.9$, $K_{G2}=5$.	-	-	-	-
Chapter 5:	I_{rq} and I_{rd} $K_p = 700e^{-2}$ $K_i = 5350e^{-3}$ <i>Experimental study</i>	I_{rq} and I_{rd} $K_i = 10$ $K_p = 30$ <i>Experimental study</i>	I_{rq} and I_{rd} $K_p = 720e^{-3}$ $K_i = 5350e^{-2}$ $K_d = 5e^{-6}$ <i>Experimental study</i>	-	-	-	-	-
Chapter 6:	-	-	-	-	-	-	-	ΔIr ± 0.01 <i>Experimental study</i>

C.4 Neutral Point Clamped (NPC) realized in L2EP Laboratory:

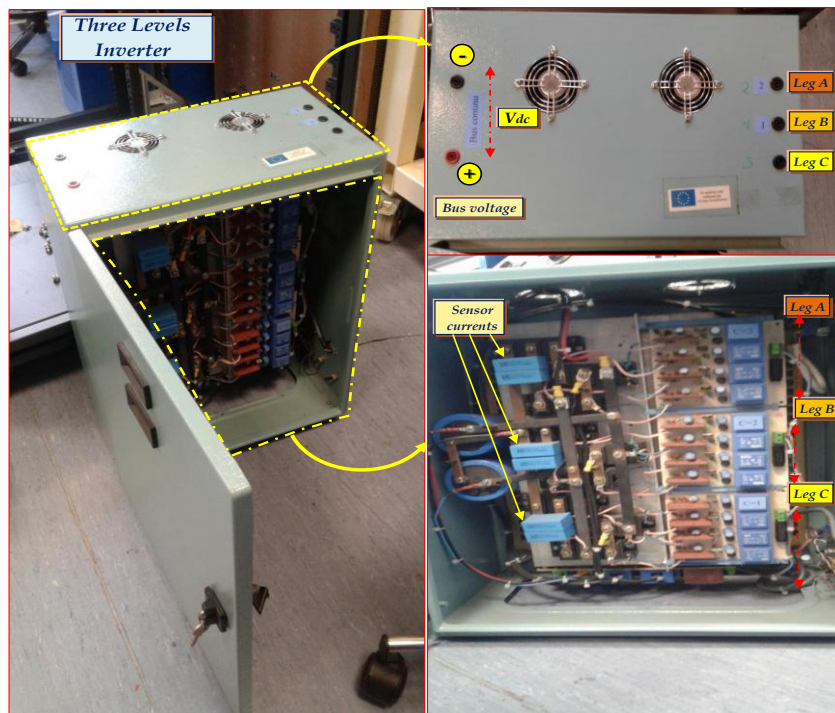


Figure.C.5 Neutral Point Clamped (NPC).